

Reduction of Radon-daughter Backgrounds for the Super Cryogenic Dark Matter Search Experiment

by
Joseph A. Street

A thesis submitted to the Graduate Division
in partial fulfillment of the requirements for the degree of

Doctor of Philosophy in Physics

South Dakota School of Mines and Technology
Rapid City, South Dakota

Date Defended: March 27, 2023

Approved by:

Major Professor — Richard Schnee, Ph.D., Department
of Physics

Date

Graduate Division Representative — William Cross,
Ph.D., Department of Materials and Metallurgical
Engineering

Date

Committee Member — Juergen Reichenbacher, Ph.D.,
Department of Physics

Date

Committee Member — Frank Strieder, Ph.D.,
Department of Physics

Date

Committee Member — Wolfgang Rau, Ph.D.,
TRIUMF, Vancouver, Canada

Date

Head of the Department of Physics — Richard Schnee,
Ph.D.

Date

Dean of Graduate Education — Maribeth Price, Ph.D.

Date

Copyright © 2023, Joseph A. Street
All Rights Reserved

Abstract

The Super Cryogenic Dark Matter Search (SuperCDMS) SNOLAB experiment will search for interactions of dark matter particles in solid-state detectors. The dominant expected background at low energy for SuperCDMS SNOLAB comes from radon daughters. This dissertation provides improved understanding to help SuperCDMS achieve its goal of $\leq 50 \text{ nBq/cm}^2$ of ^{210}Pb contamination.

My analysis of SuperCDMS Soudan (the predecessor to SuperCDMS SNOLAB) indicates that the ^{210}Pb contamination of the detector faces and side regions were $62 \pm 5 \text{ nBq/cm}^2$ and $231 \pm 8 \text{ nBq/cm}^2$ respectively. Bulk ^{210}Pb contamination in surrounding materials was $347 \pm 7 \text{ mBq/kg}$ and likely produced an even larger background than the surface contamination. The angular position of these background events indicated that the detector interface boards (DIBs) mounted on opposing sides of each detector produced $\sim 5\times$ the bulk event rate as compared with other locations. For SuperCDMS SNOLAB, bulk contamination is being reduced by choosing sufficiently radio-pure materials; surface contamination is being reduced by minimizing exposure to high-radon environments and reducing the radon concentration of the underground cleanroom where detectors are installed.

In order to reduce the radon concentration of such environments, I led the construction and optimization of the SD Mines radon-reduction system (RRS), which achieved a $4000\times$ reduction in the radon concentration to an activity of $\sim 25 \text{ mBq/m}^3$ (four times lower than the SuperCDMS SNOLAB goal of 100 mBq/m^3). I have also helped develop and install the SuperCDMS SNOLAB RRS.

In order to optimize existing systems and inform development of future systems, I have written a highly configurable simulation of the RRS based on the principles of adsorption and diffusion physics. The RRS simulation has been used to guide operation of the SD Mines RRS and predict the performance of future systems for several compelling hardware changes; these predictions indicate that a radon reduction similar to that of the SD Mines RRS could be achieved at more than double the through-system flow after installing longer columns or an active heating system, or by increasing the pumping speed.

Finally, I have demonstrated that a post-fabrication, acid-etch cleaning of detector sidewalls can reduce ^{210}Pb surface contamination by $> 99\times$ at 90% C.L., potentially reducing the ^{210}Pb contamination from $\sim 50 \text{ nBq/cm}^2$ to $\sim 20 \text{ nBq/cm}^2$.

Acknowledgments

I want to express my most sincere gratitude to my advisor, Professor Richard Schnee, for allowing me to make small mistakes that I can learn from, while protecting me from the larger ones. He is the most patient teacher I have known (or seen, for that matter), and I feel incredibly fortunate to have had the opportunity to learn from him during my graduate studies. Professor Schnee has a truly brilliant mind, and while sometimes quite daunting, it has been a joy to witness such a high level of ability in scientific research. He has been a central role model to me, and I hope that I might reflect some of his many qualities. The successes that I have enjoyed in the sciences and hope to enjoy in the future I owe to him.

I am also incredibly grateful to Professor Juergen Reichenbacher, who has acted as a second advisor to me and also a close friend. He is without question a brilliant physicist and, naturally, has many demands on his time. Nonetheless, Professor Reichenbacher has generously made time to work with me on research goals and provide guidance on key life decisions. It has been an honor and a great pleasure to have had the opportunity to learn from him, and his thoughtful counsel has shaped my life.

I am truly grateful to my dissertation committee members: Professor Richard Schnee, Professor Juergen Reichenbacher, Professor Frank Strieder, Professor William Cross, and Dr. Wolfgang Rau. They demonstrated incredible patience and flexibility while scheduling my defense and were always prompt in responding (usually within just an hour!) to urgent emails, which provided me with much relief. Their excellent suggestions have significantly enhanced both the content and readability of my dissertation.

Much of my work, particularly in the early years, has been made possible by the incredibly talented post-doctoral researchers that have worked in our group. Dr. Raymond Bunker was a driving force during my early years. An expert in both hardware and

analysis, he provided excellent examples of lab etiquette and worked patiently with me in the lab and on analysis alike. Dr. Eric Miller provided me with important guidance early on in my simulation work that was critical to its development. He always impressed me with his knowledge of fundamental physics and was a generous and patient teacher. With his door always open, Dr. Miller would smile and say, “Please, come into my office,” whenever I had a question, even when his desk was full. Dr. Nicholas Chott has been a pleasure to work with and is always willing to work with me on physics problems or help me in the lab. Over the last few years, he has been closely involved with my work and has provided me with important checks and discussion that has been key in overcoming many challenges. I am truly grateful to Dr. Bunker, Dr. Miller, and Dr. Chott and fortunate to have worked so closely with each of them.

I want to especially thank our group’s lab technician, Mr. David Molash, who lead the assembly of the SuperCDMS SNOLAB Radon-Reduction System (RRS) at SD Mines and, along with Dr. Bunker, Dr. Chott, and me, worked to install the system underground at SNOLAB. The work done by Mr. Molash enabled me to put more of my effort into the RRS simulation, and I am very grateful for his hard work and expertise.

I want thank Mr. Eric Morrison for diligently processing Radon Monitor data that was critical in understanding the SD Mines RRS and developing the RRS simulation. Mr. Morrison’s incredible competence is matched by his patience and friendly demeanor, and it has been a great pleasure to have him as a colleague and close friend.

I want to thank Dr. Michael Bowles for providing me with important insights and suggestions that led to improvements in my understanding of physics and programming. Dr. Bowles has been a cornerstone of my graduate years and a close friend, and I owe him a great deal of gratitude.

While I have been fortunate to have worked with many undergraduates, I want to especially thank Mr. Noah Everett for his work on the Cleanroom Monitoring System (CMS). Mr. Everett immediately took ownership of the project, working through chal-

lenges offline and then reporting on results. I was incredibly impressed by how quickly he made progress and the quality of his work; the result of his efforts have provided important cleanroom environmental data that can be key in problem-solving. It was a pleasure working with Mr. Everett and am very grateful for his diligence and hard work.

I want to extent my appreciation to Dr. Ian Walters for his time and expertise in helping me perform an assay of the specific-surface area of the activated carbon used for the SD Mines Radon-Reduction System. Dr. Walters even provided me with literature on the relevant theory and spent additional time in the lab answering my questions.

About fifteen years ago, I knew very little of the field of physics. It was then that I met my soon-to-be brother-in-law, Adam Stoll—a physicist turned jet pilot. Adam is a profoundly thoughtful and generous person and took the time to give me much-needed career advice. Even now, I recall the conversation with excitement; he described the field of physics, detailing the tough coursework encountered while pursuing a degree, the challenging lab work exploring various questions, and some of his contributions (including work on the Large Hadron Collider). I was filled with enthusiasm for the field and, from that point forward, directed my efforts in obtaining an excellent physics education and engaging with the subject at every opportunity. Just a couple years ago, I learned that Adam’s detailed explanation of the physics field was meant to persuade me to pursue a more practical degree in, for example, engineering. In any event, I am truly grateful to Adam for giving me a clear and focused career goal that I have pursued successfully for almost 15 years without the slightest loss of enthusiasm—even if it was not the career he had originally intended.

Finally, I want to thank my family and close friends. It seems unlikely that I would have been able to get through such a tough physics program (especially while keeping most of my sanity) without their loving support. I owe many thanks to my Mom, who taught me, in spite of my greatest efforts to play outside, how to read, write, and perform arithmetic. Similarly, I want to thank my Dad for his gentle encouragement, telling me

at a young age that I appeared to have a passion for complex topics and that I should pursue them, making said topics seem much less daunting. I am especially grateful to my brother Jared, who has on countless occasions given me guidance and support that has been critical to my success; without his generosity and wisdom, I would have surely faltered and been overwhelmed. I am also grateful to my dear friend Dr. Jon Fisher for providing me with much encouragement and the often-needed reality check. Jon has been the wise sage in my life; his profound wisdom has sometimes required several days for me to fully appreciate and understand, but has always, in the end, been exactly what I needed to hear. Jon has been the cornerstone of my adult years, and I am truly in his debt. Thank you everyone!

This material is based upon work supported in part by the U.S. Department of Energy, Office of Science, Office of High Energy Physics, under Award Numbers DE-SC0014223 and DE-AC02-76SF00515, and by the U.S. National Science Foundation NSF grants PHY-1506033 and NSF-1546843.

Table of Contents

Abstract	i
Acknowledgments	ii
Table of Contents	vi
List of Tables	x
List of Figures	xii
Dedication	xxiii
1 Dark Matter	1
1.1 Astrophysical Evidence	1
1.2 Cosmological Evidence	2
1.3 Summary of Dark Matter Properties and the WIMP	4
2 The SuperCDMS Experiment	7
2.1 SuperCDMS Soudan	7
2.1.1 Detector Shielding	9
2.1.2 The SuperCDMS Soudan Detectors	10
2.1.3 Detector Physics	11
2.1.3.1 Charge	11
2.1.3.2 Phonons	12
2.1.4 Surface Rejection Power of the Soudan iZIP	14
2.1.5 Soudan iZIP Detector Geometry	15
2.1.6 Soudan iZIP Detector Housings	18
2.2 SuperCDMS SNOLAB	19
2.2.1 Expected Backgrounds for SuperCDMS SNOLAB	20
3 Surface Contamination of SuperCDMS Soudan Detectors	25
3.1 SuperCDMS Soudan Science Runs and Data Processing	26
3.1.1 Data Quality Cuts	26
3.1.2 Detector Selection	27
3.2 ^{210}Po Event Selection	27
3.3 Event Energy Reconstruction and Estimates of ^{210}Po Contamination	32
3.4 Toy Monte Carlo Simulation for Buried ^{210}Po Alphas	37
3.5 Improved Estimates of Buried and Surface ^{210}Pb Contamination	48
3.6 Event Position Reconstruction from Phonons	52
3.7 ^{210}Po Event Rate Versus Time	59

3.8 Assay of ^{210}Po on Detector Sidewalls by the AlphaBACH	64
3.9 Inferred Contamination and Conclusions	66
4 Radon Removal From Breathable Air	73
4.1 Adsorption Physics	76
4.1.1 Langmuir Adsorption from the Kinetic Theory of Gases	78
4.2 Diffusion Physics	87
4.2.1 The error-function form of $C(x, t)$	91
4.2.2 The Diffusion Coefficient, D	93
4.3 The Velocity Within Empty and Packed Columns	94
4.3.1 For an Incompressible Fluid	95
4.3.2 For a Compressible Fluid	98
4.4 Types of Radon Mitigation Systems	102
5 The SD Mines Demonstration Radon-Reduction System	104
5.1 The SD Mines Radon Monitor	109
5.2 Performance of the SD Mines RRS	115
5.3 Vacuum Pumps and Measured Pressure in Columns	118
5.4 Temperature Measurements Within the Carbon Bed: Dependencies and Discussion	120
5.4.1 Cooling During Regeneration	125
5.4.2 Temperature Change due to Water Vapor in the Input Air	139
5.5 Long or Short Columns?	143
6 The SD Mines Low-Radon Cleanroom	147
6.1 Sources of Radon Within the SD Mines Cleanroom	153
6.2 Radon Concentration During Entry/Exit and Back Diffusion	155
6.2.1 Radon Concentration During Entry and Exit	155
6.2.2 Back Diffusion	158
6.3 Low-radon Water Source for Cleanroom Humidification	159
6.3.1 Water Consumption	160
6.3.2 The Radon Bubbler	163
6.4 SD Mines Cleanroom Environmental Monitoring	167
7 The RRS Simulation	170
7.1 Brief Overview of RRS Simulation Modules	172
7.2 The Generator: A Distribution Function Governing the Translation and Diffusion of Radon Atoms	173
7.3 Operators	177
7.3.1 More on the Matrix Operator	183
7.4 RRS Simulation: Modes of Operation	186
7.4.1 The Break-through Curve	187
7.4.2 The “Swing” Mode	193
7.5 Padded Columns	198
7.6 The Radon Velocity Within a Column	201

7.6.1	An Optional Correction: The Time-averaged Velocity	205
7.7	The Diffusion Coefficient Within a Column	207
7.8	The Temperature Within a Column	209
7.8.1	The SD Mines RRS Column Temperature During BTCs	213
7.8.2	The SD Mines RRS Column Temperature During Swing Mode . .	215
7.9	The Pressure Within a Column	216
7.10	Radon Emanation from Carbon Beds	227
7.11	Radon Distribution Within a Column After Break-through Curve Completion	234
7.12	Checking Simulation Consistency by Counting Atoms	238
7.13	Determination of Simulation Parameters	248
7.13.1	Break-through Curves: Simulation versus Measurement	249
7.13.2	Possible Simulation Shortcomings	257
7.13.3	Using Break-through Curve Data to Constrain Simulation Parameters	260
7.13.4	Regeneration Curves: Simulation versus Measurement	270
7.14	Future Work on the Simulation	292
7.15	RRS Simulation Predictions	294
7.15.1	Improving RRS Performance by Optimizing Operational Parameters	297
7.15.2	Improving RRS Performance Through Hardware Changes	301
7.15.3	Using the Simulation to Inform Leak-tightness Criteria	321
8	The SD Mines Table-top System	325
8.1	An Overview of the Physical TTS	325
8.2	Details Important to TTS Operation	327
8.3	Sensors and Their Readout	330
8.3.1	Early Results: Water Vapor Passing Through A Carbon Column .	331
8.4	Future Studies and Discussion	333
9	Assay of Interposer Boards	336
10	Removal of ^{210}Pb by Etch of Crystalline Detector Sidewalls	344
10.1	^{210}Pb Deposition from High-Radon Air Exposure	344
10.2	Alpha Duo α Spectrometer	347
10.2.1	Detection Efficiency for a Si Core	350
10.3	Pre-etch Assay	353
10.4	Fitting the Pre-etch Data	354
10.4.1	The Number of Free Parameters and Relative Abundance	356
10.4.2	Toy Monte Carlo Simulation of the Time-dependent ^{210}Po Rate .	360
10.5	Etching Technique	363
10.6	Post-etch Assay and Observed ^{210}Pb Reduction	365
10.7	Conclusions	367
Bibliography		368

Appendices	380
Appendix A	380
Appendix B	384
Appendix C	409
Vita	412

List of Tables

2.1	SuperCDMS Soudan detector surface areas.	18
3.1	Quality cuts used for the Soudan Science runs used in this analysis.	27
3.2	Operational status of SuperCDMS Soudon detectors.	28
3.3	Inferred ^{210}Po contamination for detector 1101 (using an event selection cut on recoil energy).	51
3.4	Inferred ^{210}Po contamination on the sidewall of detector 1101 as a function of sidewall location.	56
3.5	Inferred initial ^{210}Pb and ^{210}Po surface (S) contamination for all functional detectors as a function of location.	67
3.6	Inferred initial ^{210}Pb and ^{210}Po buried (B) contamination for all functional detectors as a function of location.	68
4.1	Viscosity for different gases.	96
5.1	The mixing fraction for varying flow rate and time sampled.	114
5.2	Numerical values of relevant system parameters for estimating the temperature measured by an RTD within the carbon bed during the regeneration stage.	135
6.1	Best-fit parameters for the linear and exponential functions fit to the increase and decrease in radon concentration due to opening and closing the outer cleanroom door respectively.	158
6.2	Sensors used for the Cleanroom Monitoring System (CMS).	168
7.1	Simulation modules with high-level descriptions.	174
7.2	Best-fit values of parameters m and b from Eq. 7.51 and c from Eq. 7.53.	222
7.3	The goodness-of-fit statistics for each BTC run used to infer models for f_A , f_D , and T_0	269
7.4	The default simulation parameter values.	295
7.5	Cost-benefit analysis for potential hardware changes.	319
8.1	Table-top system column geometry.	326
9.1	Dimensions of interposer boards.	337
9.2	Detection efficiencies for alpha decays on interposer surfaces.	338
9.3	Integrated rate (in counts per day) within the 200 keV ^{210}Po ROI for each run. Uncertainties are found as \sqrt{N}/t_{live} , where N is the total number of counts within the ROI during the live-time t_{live} . The “Run Number” column is included for posterity (and will agree with the logs taken during these assays).	340
9.4	95% upper-confidence limits of interposer ^{210}Po assays.	343

10.1 Angle dependence and reproducibility.	357
10.2 Domains and best-fit value for each thrown parameter.	361

List of Figures

2.1	Muon flux Φ_{μ} as a function of depth for many underground facilities.	8
2.2	Side and top cross-sectional diagrams of SuperCDMS Soudan shielding.	8
2.3	SuperCDMS Soudan detector array consisted of five detector towers with three detectors per tower.	9
2.4	Newly-fabricated SuperCDMS Soudan iZIP detectors, with one installed inside of its copper housing.	10
2.5	Side 1 ($+z$) and side 2 ($-z$) of the Soudan iZIP detectors are outfitted with both charge and phonon sensors.	10
2.6	Phonon and charge sensor layout.	14
2.7	The electric field within a Soudan iZIP and side-symmetric event selection.	15
2.8	Top and side dimensions for the SuperCDMS Soudan iZIP detectors.	16
2.9	Diagram of a Soudan iZIP within its copper housing.	18
2.10	Diagram of a Soudan detector copper housing.	19
2.11	Image and diagram of a Soudan detector tower holding three iZIP detectors.	20
2.12	Projected sensitivity to the spin-independent dark matter-nucleon scattering cross-section as a function of dark matter mass for Si and Ge iZIP and Si and Ge HV detectors of the SuperCDMS SNOLAB experiment.	21
2.13	The SuperCDMS SNOLAB HV and iZIP detectors.	21
2.14	Projected sensitivity to the spin-independent dark matter-nucleon scattering cross-section as a function of dark matter mass for Si and Ge iZIP and Si and Ge HV detectors of the SuperCDMS SNOLAB experiment showing the effect of ^{210}Pb surface contamination.	22
2.15	Background spectra before and after analysis cuts for Ge HV detectors shown as a function of nuclear recoil energy.	23
3.1	Ionization yield Y as a function of recoil energy E_r	30
3.2	Total charge (from sides 1 and 2) from the outer channels versus the inner channels.	30
3.3	The charge versus (phonon) recoil-energy phase space for all events.	31
3.4	The recoil energy spectrum for selected alphas is compared with the energy spectrum of all events.	32
3.5	The z location of each event versus recoil energy.	35
3.6	The z location of each event versus recoil energy with quadratic fit $f_{\text{peak}}(z)$	36
3.7	the z -corrected alpha spectrum compared with the uncorrected alpha spectrum.	37
3.8	Exploded-view rendering of a SuperCDMS SNOLAB detector within its copper housing as reference for the toy Monte Carlo simulation geometry used in estimating deposited energy of buried ^{210}Po alphas.	38
3.9	AFM image of milled copper and corresponding simulation of the energy spectrum for ^{210}Po alphas originating on the surface.	40

3.10 A 3D scatter plot viewed from the top and side representing the toy MC for buried ^{210}Po alphas.	43
3.11 The number of incident trajectories is shown as a function of the initial depth $r_{\text{cs}} - r_c$ the alpha was located within the copper housing.	43
3.12 The projected range R of an alpha particle in copper versus kinetic energy E and the remaining kinetic energy of an alpha E_{rem} after traveling a distance R_i through the copper.	45
3.13 The remaining kinetic energy of an alpha as a function of its distance traveled through copper and its stopping power.	46
3.14 The z -corrected energy spectrum for selected alphas is fit by the predicted spectrum model $F(E_r)$	49
3.15 Examples of phonon pulses with illustration of their 20% rise-time.	51
3.16 Position reconstruction for inner and outer selected alphas for both side 1 and side 2.	53
3.17 Soudan detector phonon channel diagram and $x - y$ event position reconstruction shown as a heatmap.	54
3.18 Event rate for all alphas as a function of angle θ	55
3.19 Event rate for buried and surface alphas as a function of angle θ	55
3.20 Image of a detector interface board (DIB) used for SuperCDMS Soudan. .	57
3.21 Soudan alpha spectrum shown with selection cuts for buried and surface events used for the time-series analysis.	58
3.22 The inferred ^{210}Po rate (after correcting for data-selection cut inefficiencies) shown for all selected alphas, surface and buried alphas in the side region, and surface and buried alphas in the major flat regions.	62
3.23 The inferred ^{210}Po rate (after correcting for data-selection cut inefficiencies) shown for the sidewall regions, excluding both major flats, for both the surface and buried events.	63
3.24 The inferred ^{210}Po rate (after correcting for data-selection cut inefficiencies) shown for inner (face) events.	63
3.25 Soudan detector 1110, 1111, and 1112 are seen placed on their sides, face-to-face, with major flats facing up, toward the AlphaBACH's 52 mm Si detector.	65
3.26 A 3-D rendering of origins and hits resulting from the Monte Carlo simulation used to estimate the detection efficiency for ^{210}Po decays on the surface of three Soudan detectors within the AlphaBACH.	65
 4.1 The ^{222}Rn decay chain.	73
4.2 Diagram of a surface showing adsorption and desorption with nomenclature. .	76
4.3 The Lennard-Jones potential.	77
4.4 Probability and cumulative distribution functions for the Maxwellian speed distribution.	81
4.5 The impingement rate J_{imp} is shown as a function of pressure P	83
4.6 Illustration of adsorption and desorption to a perfect surface.	84
4.7 Cartoon of nitrogen and radon passing through a carbon bed, with radon spending more time than nitrogen on the carbon surface.	86

4.8	The solution to Fick's second law with initial radon spike at $x = 0$ of $C_0 = 100 \text{ Bq/m}^3$	90
4.9	The solution to Fick's second law with initial step radon concentration.	91
4.10	The solution to Fick's second law with initial radon concentration $C_0 = 100 \text{ Bq/m}^3$ with $h = 5$ and centered at $x = 0$	92
4.11	Velocity profiles for empty and packed columns.	94
4.12	Gas incompressibility test versus input pressure.	101
5.1	The SD Mines Radon-Reduction System	105
5.2	Schematic of Radon-Reduction System.	106
5.3	A full cycle of RRS operation is represented by four steps.	108
5.4	Diagram of the SD Mines Radon Monitor.	109
5.5	Measured radon concentration by the SD Mines Radon Monitor of the Radon-Reduction System output during swing mode operation and, later, boil-off nitrogen.	110
5.6	The measured response by the Radon Monitor to an approximate step-change in the sampled radon concentration.	114
5.7	The mixing fraction of the Radon Monitor detection volume as a function of time.	115
5.8	Radon concentration measurement diagram for the SD Mines RRS.	115
5.9	Selected Regeneration Curves from the SD Mines Radon-Reduction System	117
5.10	SD Mines Radon-Reduction System Performance	118
5.11	Pressure and pumping speed versus time during column pump down.	119
5.12	The measured pressure at the Top and the Bottom of a column during swing mode.	120
5.13	Diagram showing the locations of resistive-temperature devices (RTDs) within a column.	122
5.14	Cartoon of resistive-temperature devices (RTDs) installed inside the activated carbon within a column.	122
5.15	Temperature measured by RTDs at four locations within one carbon column.	123
5.16	RTD temperature measurements at $F = 28.8 \text{ cfm}$	124
5.17	RTD temperature measurements at $F = 90.1 \text{ cfm}$	125
5.18	Diagram of column showing regions as a function of their temperature, pressure, and air density.	126
5.19	Measured RTD temperature during RRS operation compared with measured column pressure.	126
5.20	Diagram showing two insulated volumes (regions 1 and 2) initially isolated by the valve connecting them.	129
5.21	Diagram of two pipes connected by a valve with imaginary pistons moving a volume between them.	131
5.22	Measured RTD temperature during RRS operation compared with inferred carbon temperature.	138
5.23	Saturation vapor density versus temperature.	140
5.24	Temperature measured within a single column during a break-through curve run.	141

5.25 Cartoons of columns with differing geometry.	143
6.1 Images of the low-radon cleanroom at SD Mines seen from outside and inside.	147
6.2 Schematic of the SD Mines cleanroom illustrating the location and approximate size (± 1 inch) of important components.	148
6.3 The time to reach 95% replacement of the SD Mines cleanroom due only to internal circulation by the HVAC.	149
6.4 The cleanroom overpressure is measured for both the main room (black circles) and anteroom (blue squares) as a function of make-up air flow F . .	151
6.5 Cleanroom volume replacement fraction and time to reach 95% replacement.	153
6.6 Radon concentration within the SD Mines cleanroom during an entry-exit test with internal recirculation set to 75%.	156
6.7 Radon concentration within the SD Mines cleanroom during an entry-exit test with internal recirculation set to zero.	157
6.8 Radon concentration as a function of distance in SD Mines cleanroom pressure relief pipe.	159
6.9 The amount of water that must be added to achieve the relative humidity ϕ_{out} given the make-up air flow F	162
6.10 A water volume sharing an interface with an air volume.	163
6.11 Diagram of the SD Mines Radon Bubbler.	165
6.12 Diagram of the Durridge RAD Aqua measurement setup.	166
6.13 Inferred radon concentration of water passing through the Radon Bubbler with and without air flowing through it.	167
6.14 Diagram of the Cleanroom Monitoring System (CMS).	168
7.1 RRS simulation module flow chart.	173
7.2 Example rows of the Generator matrix.	176
7.3 Cartoon showing how simulation operators propagate and diffuse radon atoms.	178
7.4 First example of radon propagation and diffusion.	181
7.5 Second example of radon propagation and diffusion.	182
7.6 Operator dependency flow chart.	183
7.7 Heatmap illustration of matrix operator.	184
7.8 Example of radon propagation and diffusion using operators with a spatially dependent diffusion coefficient.	185
7.9 Cartoon illustrating the stages of swing mode operation.	186
7.10 Diagram and cartoon illustration of break-through curves as a function of space and time.	188
7.11 An idealized break-through curve.	190
7.12 A simulated break-through curve produced with a time-varying input radon concentration.	191
7.13 A simulated BTC is compared to an ideal BTC.	193
7.14 One full period of swing mode represented by four states.	194

7.15 Three regeneration curves created with input air flow set to 30, 60, and 90 cfm.	196
7.16 Diagram showing the padded regions of a simulated column.	198
7.17 Radon atoms within a column with padded regions.	199
7.18 Radon atoms within a column with and without padded regions.	201
7.19 Cartoon of radon atoms moving across an interface separating regions within a column that where radon moves with different velocities.	205
7.20 Instantaneous and time-averaged velocity as a function of distance in a column.	206
7.21 Radon velocity within a column during each stage of swing mode.	207
7.22 Radon diffusion coefficient within a column during each stage of swing mode.	208
7.23 Diagram showing RTD locations within a physical column and their mapping to locations within a simulated column.	210
7.24 The expected change in the radon velocity and diffusion coefficient for a change in temperature T	212
7.25 Temperature within a column used to build the first six filtering operators.	212
7.26 Temperature within a column used to build the first six regeneration operators.	213
7.27 Measured and processed temperature as a function of time during a BTC.	214
7.28 Measured temperature during swing mode operation at $F = 28.8 \text{ scfm}$	215
7.29 Measured and processed temperature as a function of time during a RC.	216
7.30 The measured temperature at the Top and Bottom of a column during swing mode operation as a function of time.	217
7.31 The pressure during regeneration at the pump side and purge side of a column.	219
7.32 Pressure measured on the purge-flow and pump sides of the column versus time during during the slow-fill mode with varying values of the purge flow.	220
7.33 The slope a found from the fits in Fig. 7.32 versus purge flow.	220
7.34 The time needed to raise a column to atmospheric pressure as a function of purge flow and the ratio of pressures at the pump and purge sides versus time.	223
7.35 Cartoon of the pressure within a column versus time.	223
7.36 The simulation-modeled pressure during the swing mode for each stage.	226
7.37 Comparison between simulated and the measured pressure.	226
7.38 Cartoon of radon emanation from carbon within a column.	229
7.39 Equilibrium radon concentration from radon emanating from the carbon as a function of through-column flow F	229
7.40 Break-through curves are simulated for flow rates of 30 and 60 scfm, but with the input radon concentration set to zero.	231
7.41 The equilibrium radon concentration is simulated versus air flow rate for several choices of filtering time.	232
7.42 Equilibrium output radon concentration generated as a function of flow F , with the simulation set to perfect regeneration.	233
7.43 Radon concentration and atoms entering, within, and exiting a column as a function of time during a BTC.	235

7.44 The distribution of radon in a column after a BTC has completed normalized by its maximum value.	236
7.45 The inferred slope from the simulated radon distribution within a column after BTC completion.	237
7.46 Simplified Radon-Reduction System diagram emphasizing the number of atoms throughout the system.	240
7.47 The number of atoms introduced at time t to the RRS simulation per Δt is $N_{\text{in}}(t)$ for the first 4 hours.	242
7.48 The number of atoms introduced at time t to the RRS simulation per Δt is $N_{\text{in}}(t)$ for the first 48 hours.	243
7.49 The number of atoms introduced at time t to the RRS simulation per Δt is $N_{\text{in}}(t)$ at late time (between 50 and 54 hours).	244
7.50 Radon atoms exiting the system to the cleanroom and purge flow as a function of time.	245
7.51 Radon atoms exiting the system to the cleanroom and purge flow as a function of time at late time (between 50 and 54 hours).	245
7.52 The number of radon atoms lost and their fractional loss as a function of time.	246
7.53 Measured input and output of a BTC.	250
7.54 Measured input and output of a BTC compared with an ideal BTC.	252
7.55 Measured input and output of a BTC compared with a simulated BTC built with the input concentration.	252
7.56 Measured input and output of a BTC compared with a simulated BTC built with the input concentration and temperature.	253
7.57 Measured input and output of a BTC compared with a simulated BTC with varying incomplete regeneration.	254
7.58 Measured input and output of a BTC compared with a simulated BTC with varying adsorption.	255
7.59 Measured input and output of a BTC compared with a simulated BTC with varying diffusion.	255
7.60 Measured input and output of a BTC compared with a simulated BTC with varying T_0	257
7.61 χ^2 as a function of f_A and f_D	261
7.62 Best-fit values of the adsorption factor f_A for several BTC runs that were performed at differing air flow rates F through the column.	262
7.63 Best-fit values of the adsorption factor f_A for several BTC runs that were performed at differing air flow rates F through the column (with projection to higher flow).	263
7.64 Best-fit values of the diffusion factor f_D for several BTC runs that were performed at differing air flow rates F through the column.	264
7.65 Best-fit values of the diffusion factor f_D for several BTC runs that were performed at differing air flow rates F through the column (with projection to higher flow).	264

7.66 Comparison of a simulated and measured BTC using best-fit parameters for the particular run and from the average best-fit parameters from all runs.	265
7.67 Best-fit values of the adsorption factor f_A found from the 3-parameter minimization routine are plotted for several BTC runs that were performed at differing air flow rates F through the column.	267
7.68 Best-fit values of the diffusion factor f_D found from the 3-parameter minimization routine are plotted for several BTC runs that were performed at differing air flow rates F through the column.	267
7.69 Best-fit values of the critical temperature of adsorption T_c found from the 3-parameter minimization routine are plotted for several BTC runs that were performed at differing air flow rates F through the column.	268
7.70 Measured input and outer radon concentration for a RC.	270
7.71 Measured input and outer radon concentration for a RC at early time compared with a simulated RC.	274
7.72 Measured input and outer radon concentration for a RC at early time compared with a simulated RC (but with the Radon Monitor mixing time varied).	276
7.73 The number of radon atoms throughout a column after a BTC compared with a flat distribution.	277
7.74 Measured input and outer radon concentration for a RC at early time compared with a simulated RC with varying diffusion coefficient.	278
7.75 Measured input and outer radon concentration for a RC at early time compared with a simulated RC with varying diffusion coefficient (for a larger time domain).	279
7.76 Measured input and outer radon concentration for a RC at early time compared with a simulated RC with varying adsorption.	280
7.77 [Measured input and outer radon concentration for a RC at early time compared with a simulated RC with varying adsorption (for a larger time domain).	280
7.78 Measured input and outer radon concentration and column temperature for a second RC (at high flow) compared with simulation.	281
7.79 Measured input and outer radon concentration and column temperature for a third RC (at medium flow) compared with simulation.	282
7.80 Measured input and outer radon concentration and column temperature for a second RC (at low flow) compared with simulation.	283
7.81 Measured input and outer radon concentration and column temperature for a RC compared with simulation with a relative humidity correction. .	287
7.82 Relative humidity correction as a function of time.	287
7.83 Comparison of measured and simulated equilibrium radon concentrations. .	290
7.84 The equilibrium radon concentration and its fractional change as a function of flow for varying input concentration.	297
7.85 The equilibrium radon concentration as a function of flow for varying regeneration time.	298

7.86 The equilibrium radon concentration as a function of regeneration time and purge flow.	299
7.87 The equilibrium radon concentration as a function of flow for varying slow-fill time.	299
7.88 The equilibrium radon concentration as a function of flow for varying purge flow.	300
7.89 The equilibrium radon concentration as a function of flow for varying filtering temperature.	301
7.90 The equilibrium radon concentration as a function of flow for varying regeneration temperature.	303
7.91 The equilibrium radon concentration as a function of flow for varying slow-fill temperature.	304
7.92 The equilibrium radon concentration as a function of flow for varying column length.	305
7.93 The equilibrium radon concentration as a function of flow for varying column length (fixed volume).	306
7.94 The equilibrium radon concentration as a function of column length and column length with fixed volume.	308
7.95 Required cycles to reach equilibrium as a function of flow for varying column length, column length (fixed volume), input concentration, and purge flow.	310
7.96 The equilibrium radon concentration as a function of flow for varying column diameter.	311
7.97 The equilibrium radon concentration as a function of flow for varying pumping speed.	314
7.98 Diagram of a compound column.	316
7.99 The equilibrium radon concentration as a function of flow for varying radon emanation from the carbon.	318
7.100 The equilibrium radon concentration as a function of flow for varying fractions of the carbon replaced with low-emanation carbon.	318
7.101 The equilibrium radon concentration as a function of flow for varying leak rates during filtering.	322
7.102 The equilibrium radon concentration as a function of flow for varying leak rates during regeneration.	323
7.103 The equilibrium radon concentration as a function of flow for varying leak rates during slowfill.	324
8.1 Table-top System diagram.	326
8.2 The radon concentration due to the Pylon radon source passing into a column or columns as a function of the flow passing through and, when using the dilution line, around the source.	328
8.3 Radon break-through time as a function of flow.	330
8.4 Measured relative humidity at the input and output of the TTS large column as a function of time.	333
9.1 Images of small, long, and large interposer boards.	336

9.2	Interposer faces, with clear plastic removed, exposed to the detector with a separation of 4 mm.	337
9.3	Interposer sidewalls exposed to the detector with a separation of 4 mm.	337
9.4	Renderings for the interposer detection efficiency toy Monte Carlo simulation.	338
9.5	Diagrams illustrating the solid angle for a point and disc source.	339
9.6	Event rate as a function of time for interposer assay runs.	340
9.7	Energy histogram for large interposer sidewall assay.	341
9.8	Energy histogram for small and long interposers sidewall assay.	342
9.9	Energy histogram for large interposer face assay.	342
9.10	Energy histogram for small and long interposer face assay.	342
10.1	Diagram of high-radon exposure setup.	346
10.2	Radon decay chain.	346
10.3	Si core preparation and exposure geometry.	347
10.4	The Ortec Alpha Duo alpha spectrometer is shown with one detector bay closed and the other open.	348
10.5	Background energy spectrum of the SD Mines Alpha Duo detector 1. . .	349
10.6	The toy MC with $N = 5000$ (for clarity) represented as a 3D scatter plot. .	351
10.7	The number of alpha particles that are incident on the Alpha Duo Si detector (or not) depending on the angle θ where the parent decayed on the Si core surface.	351
10.8	The number of alpha particles incident on the Alpha Duo Si detector (or not) depending on decay location x and y	352
10.9	Si core sitting inside the Alpha Duo counter detector bay.	354
10.10	Energy spectrum of post-exposure assay.	355
10.11	Detected ^{210}Po rate of pre-etch data at varying core rotations.	355
10.12	Atoms as a function of time for each radon daughter (down to ^{210}Po) due to the inferred, time-dependent high-radon exposure.	358
10.13	Comparison of best-fit curves for a 13 and 15 day exposure (as a ratio) as a function of time.	359
10.14	Overview of the first and second exposure and pre-etch assay presented as a time-series.	360
10.15	The p-values and χ^2 values for the generated curves built on Eq. 10.4 that have passed the 1σ cut.	361
10.16	Histograms of the passed parameter combinations of $N_{\text{Pb}}^{(1)}$, $N_{\text{Bi}}^{(1)}$, $N_{\text{Po}}^{(1)}$, and $N_{\text{Pb}}^{(2)}$	362
10.17	Distributions of total inferred N_{Pb} , N_{Bi} , and N_{Po} at the start of the pre-etch assay for 1σ solutions.	362
10.18	The correlation between the free parameters of the toy MC used to obtain contamination uncertainties shows expected trends.	364
10.19	Observed reduction in the ^{210}Po rate between the pre-etch and post-etch assays.	365
10.20	After etching the Si core sidewall, the measured ^{210}Po rate at the rotation of zero degrees is consistent with the background rate.	366

A.1	CalgonCarbon OVC 4x8 activated carbon.	380
A.2	Selected parts of the CalgonCarbon OVC 4x8 activated carbon datasheet.	381
A.3	Specific-surface-area assay of the SD Mines RRS activated carbon (sample A).	382
A.4	Specific-surface-area assay of the SD Mines RRS activated carbon (sample B).	383
B.1	Ionization yield versus recoil energy for SuperCDMS Soudan detector 1101 showing ^{210}Po alpha selection.	384
B.2	Ionization yield versus recoil energy for SuperCDMS Soudan detector 1104 showing ^{210}Po alpha selection.	385
B.3	Ionization yield versus recoil energy for SuperCDMS Soudan detector 1105 showing ^{210}Po alpha selection.	385
B.4	Ionization yield versus recoil energy for SuperCDMS Soudan detector 1106 showing ^{210}Po alpha selection.	386
B.5	Ionization yield versus recoil energy for SuperCDMS Soudan detector 1108 showing ^{210}Po alpha selection.	386
B.6	Ionization yield versus recoil energy for SuperCDMS Soudan detector 1111 showing ^{210}Po alpha selection.	387
B.7	Ionization yield versus recoil energy for SuperCDMS Soudan detector 1112 showing ^{210}Po alpha selection.	387
B.8	Ionization yield versus recoil energy for SuperCDMS Soudan detector 1114 showing ^{210}Po alpha selection.	388
B.9	Recoil energy spectrum for ^{210}Po alphas for SuperCDMS Soudan detector 1101 with spectrum fit.	388
B.10	Recoil energy spectrum for ^{210}Po alphas for SuperCDMS Soudan detector 1104 with spectrum fit.	389
B.11	Recoil energy spectrum for ^{210}Po alphas for SuperCDMS Soudan detector 1105 with spectrum fit.	389
B.12	Recoil energy spectrum for ^{210}Po alphas for SuperCDMS Soudan detector 1106 with spectrum fit.	390
B.13	Recoil energy spectrum for ^{210}Po alphas for SuperCDMS Soudan detector 1108 with spectrum fit.	390
B.14	Recoil energy spectrum for ^{210}Po alphas for SuperCDMS Soudan detector 1111 with spectrum fit.	391
B.15	Recoil energy spectrum for ^{210}Po alphas for SuperCDMS Soudan detector 1112 with spectrum fit.	391
B.16	Recoil energy spectrum for ^{210}Po alphas for SuperCDMS Soudan detector 1114 with spectrum fit.	391
B.17	The ^{210}Po event rate versus angle θ for SuperCDMS Soudan detector 1101.	392
B.18	The ^{210}Po event rate versus angle θ for SuperCDMS Soudan detector 1104.	392
B.19	The ^{210}Po event rate versus angle θ for SuperCDMS Soudan detector 1105.	392
B.20	The ^{210}Po event rate versus angle θ for SuperCDMS Soudan detector 1106.	393
B.21	The ^{210}Po event rate versus angle θ for SuperCDMS Soudan detector 1108.	393

B.22 The ^{210}Po event rate versus angle θ for SuperCDMS Soudan detector 1111.	393
B.23 The ^{210}Po event rate versus angle θ for SuperCDMS Soudan detector 1112.	394
B.24 The ^{210}Po event rate versus angle θ for SuperCDMS Soudan detector 1114.	394
B.25 Efficiency-corrected ^{210}Po rate versus time for SuperCDMS Soudan detector 1101.	395
B.26 Efficiency-corrected ^{210}Po rate versus time for SuperCDMS Soudan detector 1104.	396
B.27 Efficiency-corrected ^{210}Po rate versus time for SuperCDMS Soudan detector 1105.	397
B.28 Efficiency-corrected ^{210}Po rate versus time for SuperCDMS Soudan detector 1106.	398
B.29 Efficiency-corrected ^{210}Po rate versus time for SuperCDMS Soudan detector 1108.	399
B.30 Efficiency-corrected ^{210}Po rate versus time for SuperCDMS Soudan detector 1111.	400
B.31 Efficiency-corrected ^{210}Po rate versus time for SuperCDMS Soudan detector 1112.	401
B.32 Efficiency-corrected ^{210}Po rate versus time for SuperCDMS Soudan detector 1114.	402
B.33 Efficiency-corrected ^{210}Po inner (face) event rate versus time for SuperCDMS Soudan detectors 1101-1106.	403
B.34 Efficiency-corrected ^{210}Po inner (face) event rate versus time for SuperCDMS Soudan detectors 1108-1114.	404
B.35 Efficiency-corrected ^{210}Po (neither-major-flat) event rate versus time for SuperCDMS Soudan detectors 1101 and 1104.	405
B.36 Efficiency-corrected ^{210}Po (neither-major-flat) event rate versus time for SuperCDMS Soudan detectors 1105-1106.	406
B.37 Efficiency-corrected ^{210}Po (neither-major-flat) event rate versus time for SuperCDMS Soudan detectors 1108 and 1111.	407
B.38 Efficiency-corrected ^{210}Po (neither-major-flat) event rate versus time for SuperCDMS Soudan detectors 1112 and 1114.	408
C.1 Temperature measured within a single column during BTC operation.	409
C.2 Temperature measured within a single column during swing mode.	411

Dedication

To my Dad and Mom, Randall and Belinda.

Chapter 1

Dark Matter

Abundant observational and theoretical evidence supports the existence of a particle-like dark matter. Indeed, dark matter has been included in the standard cosmology model Λ CDM, where “CDM” refers to “Cold Dark Matter” [1]. The existence of dark matter is often inferred through observations of galaxies, galaxy clusters, collisions of galaxy clusters, and other astrophysical phenomena (see section Section 1.1). Studies that probe the early universe also provide compelling evidence for dark matter (see section Section 1.2). This section will provide an overview of a few of the astrophysical and cosmological motivations for the existence of dark matter.

1.1 Astrophysical Evidence

Dwarf galaxies are small objects found in abundance surrounding larger structures, such as our own galaxy. Interestingly, dwarf galaxies are the most dark-matter-dominated objects currently known [2]. Because dwarf galaxies have such little mass, baryon cooling and star formation are suppressed, leaving a diffuse baryonic gas amongst a halo of dark matter [2]. Over time, interactions with the larger central galaxy (and perhaps other objects) strip away the baryonic gas leaving an object made nearly entirely of dark matter. These resulting objects, called ‘ultra-faint’ dwarf galaxies, have been seen [2] using data from the Sloan Digital Sky Survey [3]. By measuring the velocities of stars within these ultra-faint dwarf galaxies, the gravitational potential (and therefore the mass) of these galaxies may be inferred from the virial theorem. From this, the mass-to-light ratio of ultra-faint dwarf galaxies is \sim 100 times that of typical spiral or elliptical galaxies [2].

Galaxies such as our own tend to have much more mass than is implied by their luminosity. Newtonian dynamics provides a relationship between the circular velocity at a distance r from the galactic center, $v_c(r)$. Beyond the luminous end of the galaxy (15 kpc for the Milky Way), the circular velocity of objects was expected to be $v_c(r) \propto r^{-1/2}$. However, the velocity profile, found by measuring the Doppler shifting of spectral lines, is that $v_c \propto \text{constant}$ [4]. This disagreement implies that there is additional, unseen mass modifying the mass distribution [5]. These studies provide evidence that dark matter is electrically neutral and stable on galactic timescales [6].

Evidence for the pervasive presence of dark matter is observed in gravitational lensing. A most compelling case is that of the Bullet Cluster (which is actually two colliding galaxy clusters). During this collision, the gravitational center of mass is displaced from the luminous centers of mass [7]. The disagreement in the locations of baryonic matter and gravitational potentials may be explained by the far greater likelihood for baryonic matter to interact as compared to dark matter. The dark matter and stars in each cluster essentially pass through the other unimpeded, while the baryonic gas is slowed greatly due to electromagnetic interactions. This provides evidence that dark matter is electrically neutral and appears to be no more than weakly interacting.

1.2 Cosmological Evidence

Big-bang nucleosynthesis (BBN) describes an epoch of primordial nuclear transformation during the early universe. BBN precisely predicts the abundance of light nuclei D, ^3He , ^4He , ^7Be , and ^7Li , that are synthesized during the first three minutes of our universe [8]. Constraints on the primordial abundance of D is obtained by measuring the absorption lines (called the Lyman- α forest) in the spectrum of light produced by excited hydrogen in galaxies and quasars that then passes through molecular gas clouds [9, 10, 11, 12]. Comparisons with the light nuclei abundance predictions provide constraints on the baryonic matter density [13, 14, 15] and find $0.021 \leq \Omega_b h^2 \leq 0.024$, at 95% C.L., for the Hubble parameter $h \equiv H(t_0)/100 \text{ km s}^{-1} \text{Mpc}^{-1}$ at the present time

t_0 [8]. In comparison to the total matter density of the universe of $\Omega_m \sim 0.3$, it may be inferred that the vast majority ($\sim 85\%$ [16]) of matter is non-baryonic.

Long after the nucleon freeze-out of BBN, the universe was still very hot, and collisions between photons and electrons kept radiation and matter in thermal equilibrium. At ~ 3000 K, the so-called *time of last scattering*, photons no longer had enough energy to ionize hydrogen, so the number of free electrons decreased, allowing photons to “free-stream.” Since then, the universe has further cooled to the current temperature of $T = 2.7255$ K to form the Cosmic Microwave Background (CMB) [1].

The CMB is a window to the early universe, revealing its composition and structure [17, 18, 19, 20, 21, 22, 23]. Even early measurements of the CMB (a nice historical overview of CMB experiments is presented in Ref. [24]), that were crude compared to those taken by Planck or WMAP, presented an early universe that was very nearly without structure. When we compare that early universe with the universe today, a universe filled with large and small structures, stars and galaxies, and clusters of galaxies, we come to a profound realization. The age of the universe is not long enough for the present structures to have formed from such a structureless early universe—not unless there was a large fraction of optically-unseen dark matter [24]. These studies of the CMB show that dark matter cannot be relativistic, thus supporting the assertion that dark matter be mostly cold made through numerical simulations of the formation of the observed large-scale structures.

Theoretical cosmological models fit to the recent Planck measurement of the CMB provide precise estimates of cosmological parameters. Of particular interest, they find the total matter density $\Omega_m h^2 = 0.1415 \pm 0.0019$ and the baryon density $\Omega_b h^2 = 0.02226 \pm 0.00023$, for $h = 0.6781 \pm 0.0092$ (at 68% C.L.) [1]. This result supports, with tighter constraints, the conclusions of BBN studies.

1.3 Summary of Dark Matter Properties and the WIMP

Studies of dark matter provide evidence of its existence and even some knowledge of its properties:

- The majority of the matter in the universe is dark, most of which is non-baryonic. Non-baryonic dark matter accounts for $\sim 85\%$ of the total matter density of the universe and is found in particularly high densities at the location of, and forming a gravitational well for, large-scale structures such as galaxies. Stellar kinematics constrain the local dark matter density to be $\rho_0 \sim 0.3 \text{ GeV/cm}^3$ [25, 16, 26].
- Dark matter is likely to be *cold* (*i.e.*, non-relativistic), or perhaps slightly warm. Relativistic *hot* dark matter is largely ruled out by the observed gravitationally-bound structures in our universe [23].
- Dark matter appears stable over cosmological timescales [6, 27].
- The ratio of dark matter to baryonic matter appears to be non-varying in that modern estimates of the dark matter ratio agree with estimates from the early universe [21].
- Dark matter appears to be electrically neutral. The absence of dark matter galaxies or stars implies dark matter does not radiate energy as baryonic matter does. The size and form of dark matter halos also provide insight into its inability to lose energy efficiently [5].
- Dark matter appears to be non-collisional, as seen in the Bullet Cluster [7].

Weakly Interacting Massive Particles (WIMPs) represent a generic class of new-particle candidates. The WIMP hypothesis naturally provides the inferred amount of non-baryonic dark matter [28], colloquially dubbed the “WIMP miracle” [29]. Because

WIMPs interact only through weak mediators, their annihilation rate becomes insignificantly small as the Universe expands, thus “freezing-out” a relic abundance of the particles [30, 31, 29]. Demanding that the WIMP density is the same as the non-baryonic dark matter density implies a WIMP velocity-averaged annihilation cross section of $\sim 1 \text{ pb}$ and therefore a WIMP mass of $\sim 100 \text{ GeV}/c^2$ [32].

The Super Cryogenic Dark Matter Search (SuperCDMS) experiment is designed to detect Dark Matter as it scatters off detector nuclei, resulting in measured energy produced by the recoiling nucleus. SuperCDMS is the focus of this thesis and is introduced in Chapter 2. Because Dark Matter is expected to interact infrequently, it is critical to understand and minimize detector backgrounds that might be mistaken as Dark Matter interactions. The expected backgrounds for SuperCDMS SNOLAB (the current generation of SuperCDMS) are presented in Section 2.2.1. Radon-induced backgrounds are expected to dominate at low energy (corresponding to a $\sim 1 \text{ GeV}$ WIMP) due to the long-lived radon daughter ^{210}Pb embedded on and within detector materials. In order to meet the SuperCDMS SNOLAB goal of at most $50 \text{ nBq}/\text{cm}^2$ of ^{210}Pb contamination, the ^{210}Pb contamination on and around detectors from the previous generation experiment, SuperCDMS Soudan, is determined as a function of location and is described in Chapter 3. Radon-induced surface backgrounds may be reduced by limiting the exposure time to or the radon concentration of environments where detectors are assembled and installed. Chapter 4 introduced the relevant physics of adsorption and diffusion. Chapter 5 describes the SD Mines Radon-Reduction System (RRS), with the the SD Mines low-radon cleanroom described in Chapter 6. The RRS has demonstrated a $4000 \times$ reduction in the radon concentration of breathable air to the steady-state radon concentration of $\sim 25 \text{ mBq}/\text{m}^3$. A close copy of the SD Mines RRS has been built and installed at the SNOLAB facility where SuperCDMS SNOLAB is being commissioned and is expected to surpass the SuperCDMS SNOLAB goal of a radon concentration of $\leq 100 \text{ mBq}/\text{m}^3$ during detector installation. In order to guide the optimization of an existing RRS and

inform the development of future systems, a simulation of the RRS has been written and is presented in Chapter 7. Section 5.1 introduces the SD Mines Radon Monitor, a high-sensitivity radon detector that has been employed extensively in this work. Chapter 8 introduces the SD Mines Table-top System, which was commissioned to further explore radon adsorption and diffusion as radon passes through a column filled with activated carbon. As part of reducing radon-induced backgrounds for SuperCDMS SNOLAB, so-called interposer boards were assayed for ^{210}Pb contamination; this work is described in Chapter 9. Finally, Chapter 10 presents published work that demonstrates that ^{210}Pb on detector sidewalls can be reduced by $> 99\times$ at 90% C.L. after detector fabrication (without damaging detector sensors); this sidewall etch could be employed to reduce radon-induced backgrounds as part of a future upgrade to SuperCDMS.

Chapter 2

The SuperCDMS Experiment

The Cryogenic Dark Matter Search (CDMS) experiment was first conceived in 1990 [33, 34] and was operated in the Stanford Underground Facility (SUF) [35]. Using Ge solid-state detectors sensitive to ionization and thermal phonons, a WIMP exclusion limit was measured between 1998-1999 and reported in early 2000 [35]. This exclusion limit was of particular interest as it disagreed with a measurement made by DAMA [36, 37, 38]. Without delay, the CDMS collaboration began working on the CDMS II experiment (for example, see [39]), which was located at the considerably deeper Soudan Underground Laboratory. The Soudan Mine provided an overburden of 2090 meter-water-equivalent that greatly reduced the muon-induced cosmogenic neutron background for the experiment (see Fig. 2.1). The CDMS II experiment used 19 Ge and 11 Si detectors, about 230 and 100 g respectively, operated at $< 50 \text{ mK}$, and housed inside an active muon-veto shield and substantial polyethylene [40]. The CDMS II detectors provided better rejection of surface events through phonon-pulse timing and the ratio of ionization to recoil energy [41]. The result of the final exposure of CDMS II was published in late 2009 [41].

2.1 SuperCDMS Soudan

Using the same detector shielding and site as CDMS II [40], the SuperCDMS Soudan experiment (at the time, referred to as just SuperCDMS) was commissioned to reduce the surface backgrounds that were dominant for its predecessor [41]. New detectors were designed that could better discriminate between surface and bulk events (see Section 2.1.2). The experiment consisted of fifteen detectors grouped into five towers, each tower containing three crystalline Ge detectors (see Fig. 2.3). Each detector had a mass of 600 g (resulting in a total target mass of 9 kg) and was sensitive to ionization (charge)

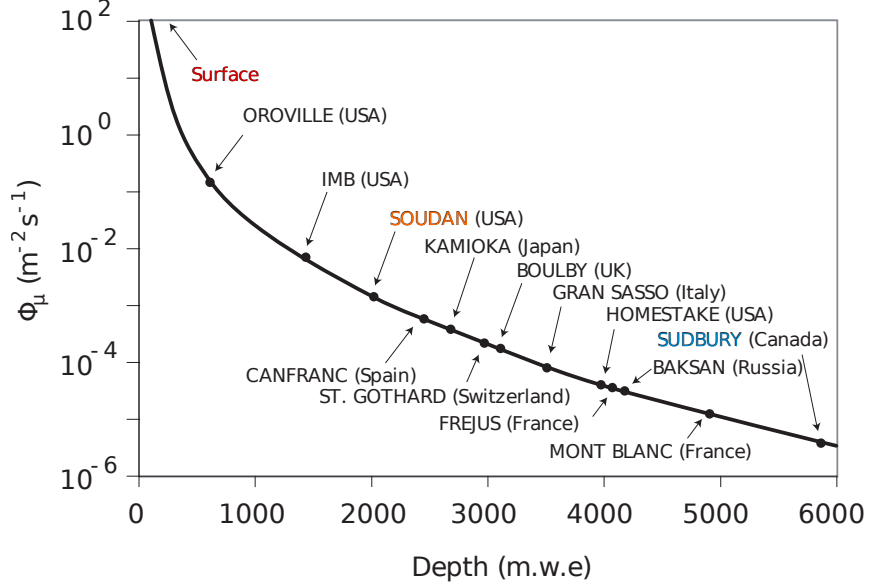


Figure 2.1: Muon flux Φ_μ as a function of depth for many underground facilities [42]. The muon flux at the surface (red) is about $200 \text{ m}^{-2}\text{s}^{-1}$. As compared to the surface, the Soudan Underground Laboratory (orange) and SNOLAB facility in Sudbury (blue) see a reduction in the muon flux of 10^5 and 10^7 respectively. This figure is reprinted from [42], with permission from Elsevier.

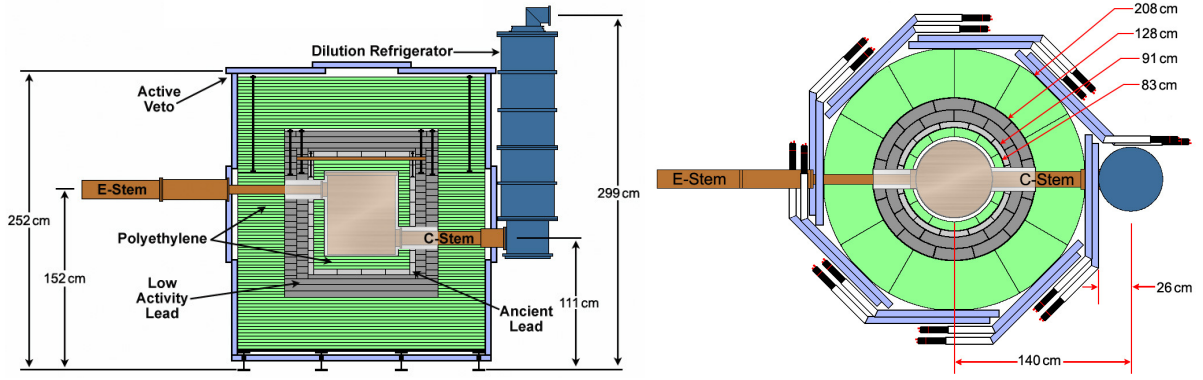


Figure 2.2: **Left:** Side cross-sectional view of the SuperCDMS Soudan shielding (reprinted from [49]). Moving toward the copper box that contains the detector towers, there was an active muon veto and then a layer of polyethylene, low-activity lead, ancient lead, and finally more polyethylene. There were two penetrations through the shielding: the E-Stem, containing the read-out cables, and the C-Stem, containing the dilution refrigerator's cold finger. **Right:** top-down cross-sectional view, with the diameters of shielding layers shown in the top right. The inner poly, ancient lead, low-activity lead, and finally outer-most poly have outer diameters 83, 91, 128, and 208 cm respectively.

and athermal phonons. The SuperCDMS Soudan experiment set the strongest limits for WIMP-germanium-nucleus interactions for masses $> 12 \text{ GeV}/c^2$ [43, 44, 45, 46, 47, 48].

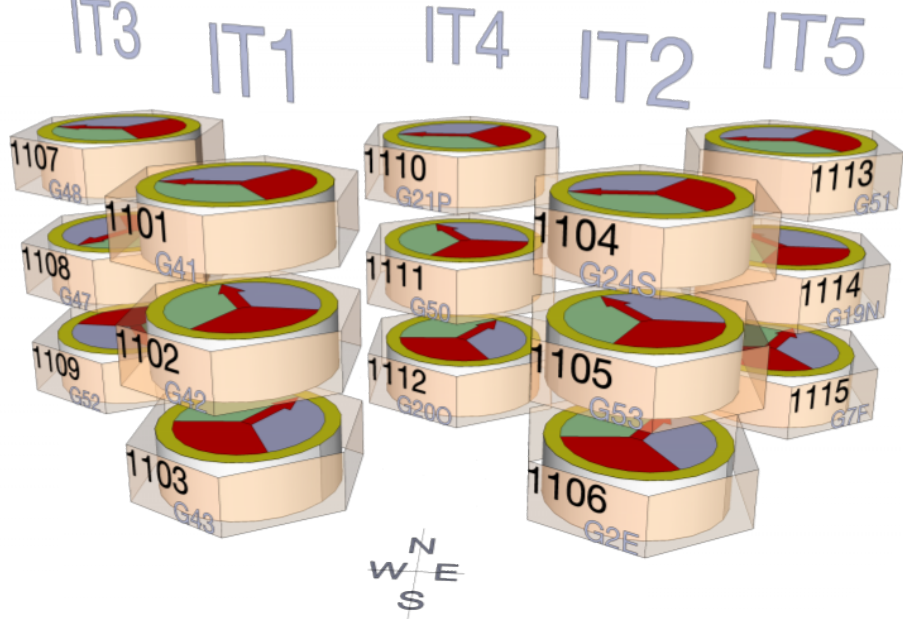


Figure 2.3: SuperCDMS Soudan detector array consisted of five detector towers with three detectors per tower. Detectors within each tower were rotated with respect to the detector above or below, as indicated by the red arrow. Each detector was given a numeric label and ID. For example, detector 1101 was also referred to as G41. For this work, only the numeric naming method will be used. The fifteen detector are numbered 1101, 1102, ..., 1115. Figure reprinted from [51], with permission from Dr. Scott Hertel.

2.1.1 Detector Shielding

SuperCDMS Soudan used the CDMS II shielding (see Fig. 2.2). An active muon veto enclosed inner layers of polyethylene and lead [50]. The outer-most layer (40 cm) of polyethylene was used to moderate cavern neutrons. Closer to the detectors, a layer of low-activity (17.8 cm) and then ancient (4.4 cm) lead shielded against gammas. The ancient lead, frequently obtained from the salvaged keels of long-sunken ships, has even less radioactive ^{210}Pb than the low-activity lead, and was thus nearer the detector. The inner-most layer of polyethylene (10 cm) moderated neutrons produced by (γ, n) reactions and (α, n) from the lead, but primarily cosmogenic neutrons produced through spallation of high-energy muons penetrating the outer polyethylene.

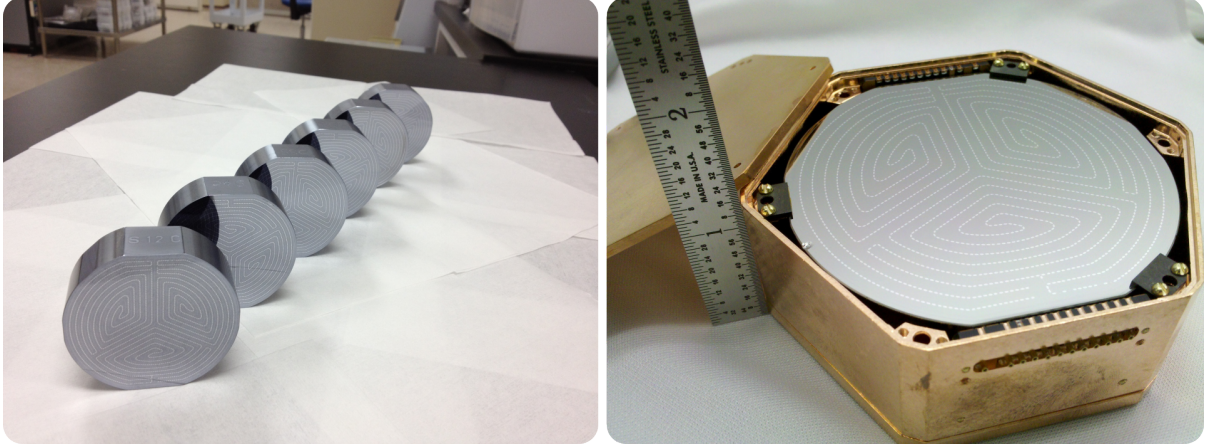


Figure 2.4: Newly-fabricated SuperCDMS Soudan iZIP detectors (left), with one installed inside of its copper housing (right). Figures courtesy of the SuperCDMS collaboration.

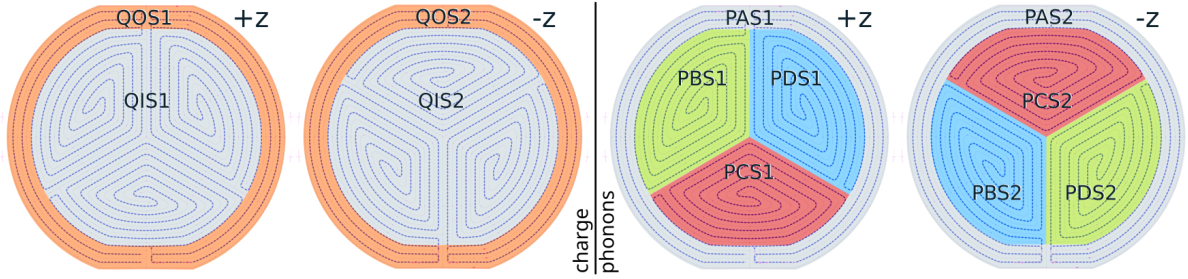


Figure 2.5: Side 1 ($+z$) and side 2 ($-z$) of the Soudan iZIP detectors are outfitted with both charge and phonon sensors. **Left:** Each face has a large inner charge channel (labeled QIS1 and QIS2, for side 1 and 2 respectively) and smaller outer charge channels (labeled QOS1 and QOS2). **Right:** Each face has four phonon sensors: one along the outer region (labeled PAS1 for side 1) and the other three occupying equal space in the inner region (labeled PBS1, PCS1, and PDS1 for side 1). Figure built upon the sensor image from [51], with permission from Dr. Scott Hertel.

2.1.2 The SuperCDMS Soudan Detectors

The SuperCDMS Soudan detector array consisted of five towers, with each containing three detectors. Each detector was encased in a copper housing (see Fig. 2.4), and then stacked to form a tower. The detectors were roughly cylindrical, with a diameter of 76 mm and thickness of 25.4 mm, and made from high-purity crystalline germanium, with band-gap energy $E_{\text{gap}} = 0.74 \text{ eV}$ at 0 K and 0.66 eV at 300 K (see page 190 of [52]).

Each detector was sensitive to both ionization (charge) and phonons. Sensors were located on the detector faces as illustrated by Fig. 2.5. Each face had an inner and outer

charge channel and four phonon channels. The Soudan detectors employed a powerful surface-event-rejection technology that is discussed in Section 2.1.4.

2.1.3 Detector Physics

For a detailed review of SuperCDMS detector physics, I refer the reader to the many excellent theses by my fellow SuperCDMS collaborators (for example, [51, 49, 53], with a complete listing of CDMS theses archived at <https://supercdms.slac.stanford.edu/dissertations>). For this work, only a brief introduction to detector physics is presented (mostly following Chapter 2 of D'Ann Barker's thesis [53]), as is necessary for the ^{210}Pb contamination analysis discussed in Chapter 3.

2.1.3.1 Charge

The recoil energy E_r is the total kinetic energy of a particle moving into the detector. If this particle interacts electronically (referred to as an electron recoil, ER), its kinetic energy is given up to the creation of electron-hole pairs (ionization) and producing phonons [54]. The electrons and holes drift through the electric potential and are eventually collected by ionization electrodes, producing a measured voltage for the event. The ionization energy E_Q is defined to be equal to the average recoil energy for an ER interaction that creates N_{eh} electron-hole pairs, so that

$$E_Q = N_{\text{eh}} \epsilon_{\text{eh}}, \quad (2.1)$$

where the average energy required to free an electron-hole pair $\epsilon_{\text{eh}} = 3 \text{ eV}$ [55].

The ionization yield is defined as the ionization energy divided by the recoil energy:

$$Y(E_r) \equiv \frac{E_Q}{E_r}, \quad (2.2)$$

with $Y(E_r) \approx 1$ for an ER and $Y(E_r) < 1$ for a nuclear recoil (NR); the value of the ionization yield for NRs is estimated by the Lindhard theory [56], given by

$$f = \frac{kg(\epsilon)}{1 + kg(\epsilon)}, \quad (2.3)$$

where $\epsilon = 11.5E_r Z^{-7/3}$ with E_r in units of keV, $k = 0.133Z^{2/3}A^{-1/2}$, and $g(\epsilon) = 3\epsilon^{0.15} + 0.7\epsilon^{0.6} + \epsilon$ [54], where Z is the atomic number and A is the atomic mass.

2.1.3.2 Phonons

There are three important instances where phonons are created: the primary recoil at the time of scattering, during carrier relaxation, and via the Neganov-Trofimov-Luke (NTL) effect [53]. When a particle scatters off an electron or a nucleus, primary (or prompt) phonons are created by the direct recoiling of that electron or nucleus. The primary phonon energy

$$E_P = E_r - N_{eh}E_{gap}, \quad (2.4)$$

with $N_{eh}E_{gap}$ representing the energy used in exciting N_{eh} electrons into the conduction band at the time of scattering.

By energy conservation, energy used in exciting electrons from the valance to the conduction band must be given back to the crystal [53, 57]. When charges reach the surface they relax back to the Fermi level, and any remaining energy E_{kin} is transferred to the lattice [53]. This *carrier relaxation* results in high-energy phonons being produced and quickly interacting with the nearby phonon sensors [53], depositing energy

$$E_{rel} = N_{eh}E_{gap} + E_{kin}. \quad (2.5)$$

Finally, electrons and holes created within the crystal are accelerated according to the detector bias voltage $\Delta V_b = 4V$. The work done by the static electric field \vec{E} to move a single electron the distance d_e across the crystal is

$$e|\vec{E}|d_e, \quad (2.6)$$

where e is an elementary charge. If the final kinetic energy of the electron is $E_{kin,e}$, the energy used in shedding phonons is

$$E_e = e|\vec{E}|d_e - E_{kin,e}. \quad (2.7)$$

Similarly, for a hole

$$E_h = e|\vec{E}|d_h - E_{\text{kin},h}. \quad (2.8)$$

The total NTL energy is the sum over all electrons and holes (presuming, for now, that all pairs are created at the same location, as it will drop out):

$$E_{\text{NTL}} = \sum_e E_e + \sum_h E_h = e|\vec{E}|d_e N_{\text{eh}} + e|\vec{E}|d_h N_{\text{eh}} - E_{\text{kin}} \quad (2.9)$$

$$= e|\vec{E}|N_{\text{eh}}(d_e + d_h) - E_{\text{kin}}, \quad (2.10)$$

where E_{kin} is the total kinetic energy transferred to the lattice during relaxation [53].

The energy collected per electron-hole pair is independent of where the electron-hole pair is created, because

$$e|\vec{E}|d_e + e|\vec{E}|d_h = e|\vec{E}|d, \quad (2.11)$$

where d_e and d_h are the distances the electron and hole must travel to reach their respective sides of the detector, adding up to the total distance across the detector d [51]. Therefore, with $|\vec{E}| = \Delta V_b/d$ and $d = d_e + d_h$,

$$E_{\text{NTL}} = e\Delta V_b N_{\text{eh}} - E_{\text{kin}}. \quad (2.12)$$

The total phonon energy E_t is the sum of phonon energy from each source of phonons:

$$E_t = E_p + E_{\text{rel}} + E_{\text{NTL}} \quad (2.13)$$

$$= (E_r - N_{\text{eh}}E_{\text{gap}}) + (N_{\text{eh}}E_{\text{gap}} + E_{\text{kin}}) + (e\Delta V_b N_{\text{eh}} - E_{\text{kin}}) \quad (2.14)$$

$$= E_r + e\Delta V_b N_{\text{eh}}. \quad (2.15)$$

Substituting Eq. 2.1 into Eq. 2.15 yields the total phonon energy as the recoil energy plus the NTL amplification energy:

$$E_t = E_r + \frac{e\Delta V_b}{\epsilon_{\text{eh}}} E_Q. \quad (2.16)$$

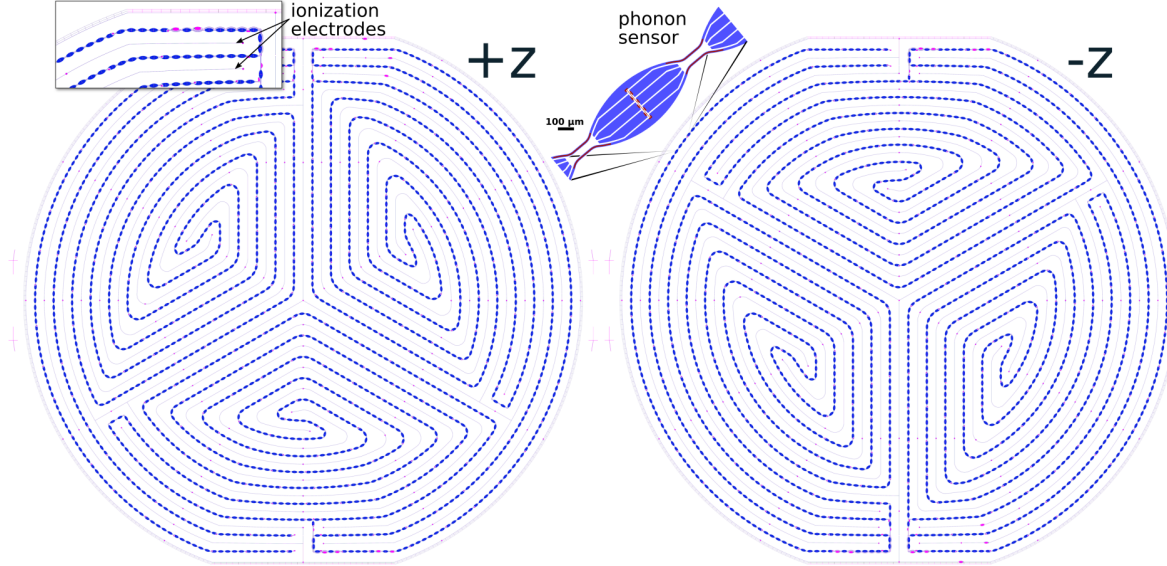


Figure 2.6: Phonon and charge sensor layout. Sensors on the top (left) and bottom (right) faces are identical, except rotated by 120° . Both faces are instrumented with ionization lines (one face with $+2\text{ V}$ and the other with -2 V) that are interleaved with phonon sensors (0 V) on a $\sim 1\text{ mm}$ pitch. The phonon sensors (zoomed-in inset) are arranged to give 4 phonon readout channels for each face, an outer sensor surrounding three inner ones. Figure built upon the sensor image from [51], with permission from Dr. Scott Hertel.

2.1.4 Surface Rejection Power of the Soudan iZIP

SuperCDMS Soudan used so-called Inter-digitated, Z-sensitive, Ionization and Phonon (iZIP) detectors. By employing these iZIP detectors, identification of surface backgrounds was substantially improved [58]. As shown in Fig. 2.6, each face of the detector (with top and bottom faces denoted as $+z$ and $-z$) has ionization and phonon sensors. The phonon sensors on both sides are held at 0 V , while the ionization sensors (or electrodes) are held at $+2\text{ V}$ on the $+z$ face and -2 V on the $-z$ face. This creates the electrical field profile shown in Fig. 2.7.

If an event takes place in the detector bulk, the electron-hole pairs are read out by both the $+2\text{ V}$ and -2 V electrodes and the event is called *side-symmetric*. If an event takes place near the detector face, the electron-hole pairs collect on the 0 V and $+2\text{ V}$ (-2 V) electrodes on the $+z$ ($-z$) face and the event is called *side-asymmetric* [58]. Side-asymmetric events are most likely due to radon-daughter backgrounds on or near the detector surface and can be discarded.

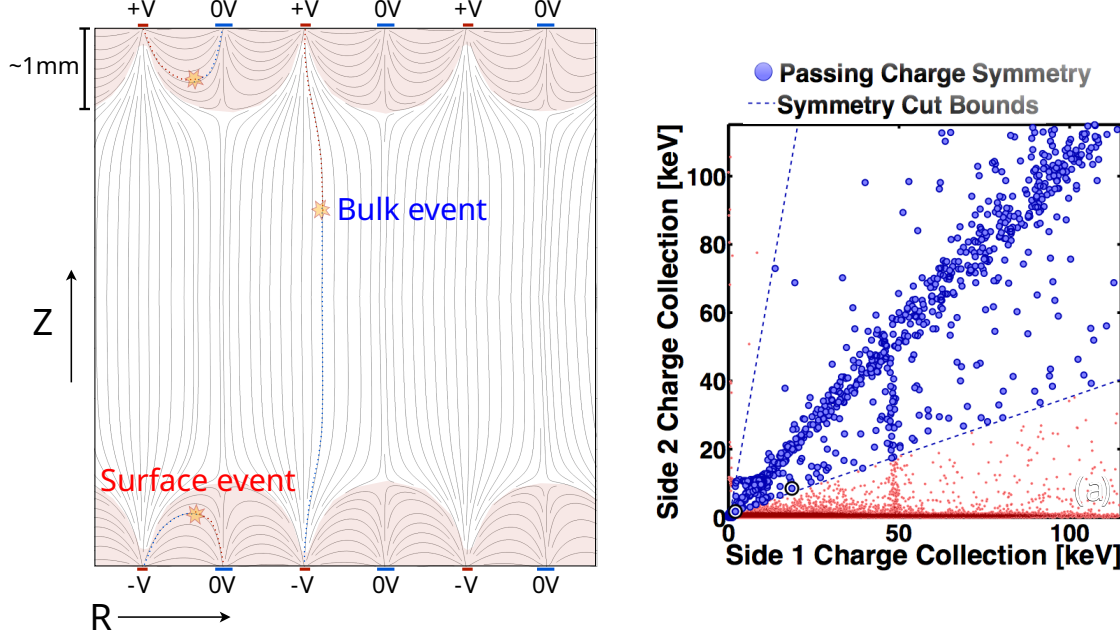


Figure 2.7: **Left:** The electric field within a Soudan iZIP is uniform up to about 1 mm from each face. Alternating ionization electrodes (small red regions, held at $\pm 2\text{V}$) and phonon sensors (small blue regions, held at 0 V) create a non-uniform field near the detector faces. Electrons (tiny red dots) and holes (tiny blue dots) follow the electric field lines to their respective electrodes. Electrons and holes from surface events (near one of the faces) are collected at electrodes on the nearby face. Electrons and holes from bulk events are collected at electrodes on apposing faces. This side-symmetric and side-asymmetric charge collection provides a powerful means to reject surface events. Figure reprinted from [51], with permission from Dr. Scott Hertel. **Right:** The data shown are from ~ 800 live hours of running an iZIP with a ^{210}Pb plate source under side 1 of the detector. Side-symmetric charge events (blue dots) in the interior of the crystal are clearly distinguished from those that fail the cut (red dots), which include surface events from betas, gammas and lead nuclei incident on side 1 from the source. The symmetry cuts (dotted blue lines) flare out near the origin so that events are accepted down to the noise wall [58]. The band of events just below 50 keV is from the 46.5 keV gammas from the source [58]. Figure reprinted from [58], with permission from Copyright Clearance Center, Inc.

2.1.5 Soudan iZIP Detector Geometry

Figure 2.8 shows a diagram of the Soudan iZIP detector. For the purpose of discussing surface contamination, the Soudan detector surface can be comprised of the following four regions:

1. **The inner detector face** is the surface of the inner charge channel (and inner three phonon channels); this surface is on both the top ($+z$) and bottom ($-z$) of

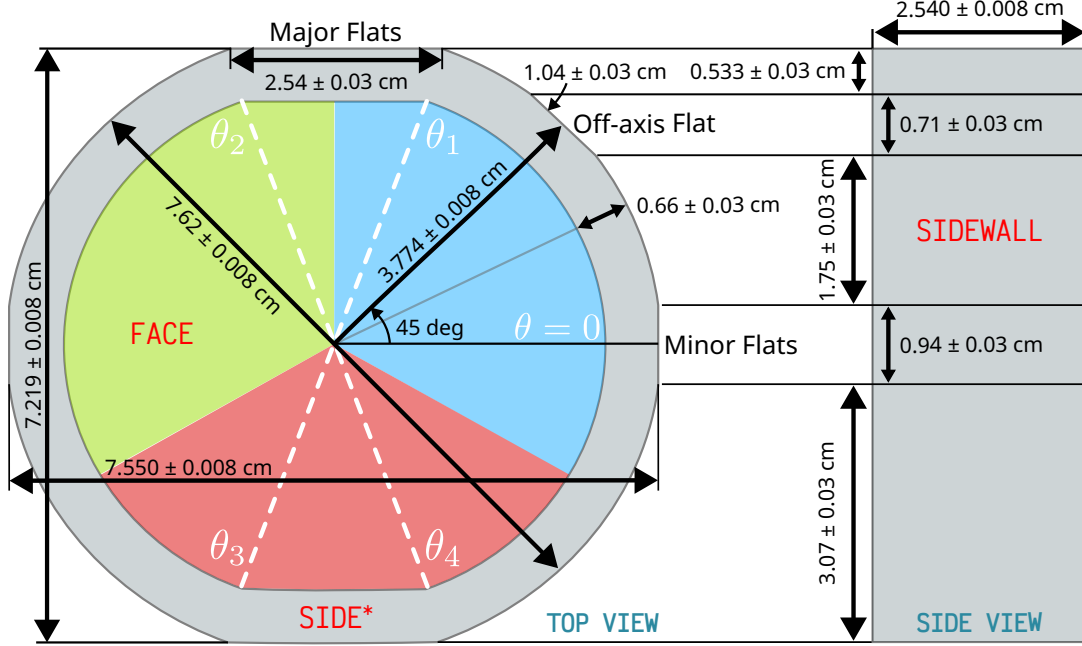


Figure 2.8: Top and side dimensions for the SuperCDMS Soudan iZIP detectors. The label SIDE has an asterisk to emphasize that sides region includes the sidewall and the outer charge-channel regions on both faces. One major flat is bound between $\theta_1 = 70^\circ$ and $\theta_2 = 110^\circ$ and the other is bound between $\theta_3 = 250^\circ$ and $\theta_4 = 290^\circ$.

the detector and is calculated as

$$a_{\text{inner}} = \pi r_{\text{inner}}^2, \quad (2.17)$$

where the radius of the inner channels $r_{\text{inner}} = 3.15 \pm 0.03 \text{ cm}$.

2. **The outer detector face** is the surface of the outer charge channel (and outer phonon channel), calculated as

$$a_{\text{outer}} = \pi r_{\text{det}}^2 - a_{\text{inner}}, \quad (2.18)$$

where the detector diameter $2r_{\text{det}} = 7.620 \pm 0.008 \text{ cm}$.

3. **The major flat region of the sidewall** refers to either of the two identical flat regions on apposing parts of the detector sidewall, with its area calculated as

$$a_{\text{singleFlat}} = h_{\text{det}} \ell_{\text{flat}}, \quad (2.19)$$

where the detector thickness $h_{\text{det}} = 2.540 \pm 0.008 \text{ cm}$ and the length of a flat region $\ell_{\text{flat}} = 2.54 \pm 0.03 \text{ cm}$.

4. **The side** refer to the detector surface of the detector sidewall *excluding* the major flat regions (but including the minor flat regions and off-axis region) and is calculated as

$$a_{\text{sidewall}} = 2\pi r_{\text{det}} h_{\text{det}} - 2a_{\text{singleFlat}}. \quad (2.20)$$

While the total face area $A_{\text{faces}} = 2a_{\text{inner}}$, the total sidewall area includes the outer face region a_{outer} on both faces, as the outer charge and phonon channels cannot discriminate between events that are truly located on the sidewall or on the outer face region. Therefore,

$$A_{\text{sides}} = 2a_{\text{singleFlat}} + a_{\text{sidewall}} + 2a_{\text{outer}}, \quad (2.21)$$

where the outer channel surfaces from both faces are added to the sides and two flat regions. The total surface area used for estimated contamination on the flat regions similarly includes a fraction $\phi_{\text{singleFlat}}$ of the outer channel regions from both faces. Therefore, the total area of both flat regions is

$$A_{\text{flats}} = 2 \times [a_{\text{singleFlat}} + \phi_{\text{singleFlat}}(2a_{\text{outer}})], \quad (2.22)$$

where

$$\phi_{\text{singleFlat}} \equiv \frac{\theta_2 - \theta_1}{2\pi} = 0.108 \quad (2.23)$$

with θ_1 and θ_2 given by Fig. 2.8. The total area of the sides (excluding the flat regions) is similarly

$$A_{\text{sidesNoFlats}} = a_{\text{sides}} + \phi_{\text{sidesNoFlats}}(2a_{\text{outer}}), \quad (2.24)$$

where the fraction of the outer face region that is included in the estimate of the total side area

$$\phi_{\text{sidesNoFlats}} \equiv 1 - 2\phi_{\text{singleFlat}}. \quad (2.25)$$

Table 2.1 presents the numerical values for each surface region of a SuperCDMS Soudan detector.

Face or Side	Surface	Symbol	Area [cm ²]
Face	Inner Channels (single)	a_{inner}	31 ± 1
	Outer Channels (single)	a_{outer}	14.4 ± 0.4
	Total inner face area	A_{faces}	62 ± 1
Side	Major flat region (single)	$a_{\text{singleFlat}}$	6.4 ± 0.2
	Sidewall (excluding flats)	a_{sidewall}	70 ± 1
	Both major flats + outer face regions	A_{flats}	19.1 ± 0.6
	Sidewall [†] + outer face regions	$A_{\text{sidesNoFlats}}$	70 ± 2
	Total side area	A_{sides}	89 ± 3

Table 2.1: SuperCDMS Soudan detector surface areas. [†]Minor flats are ignored for estimations of sidewall area.

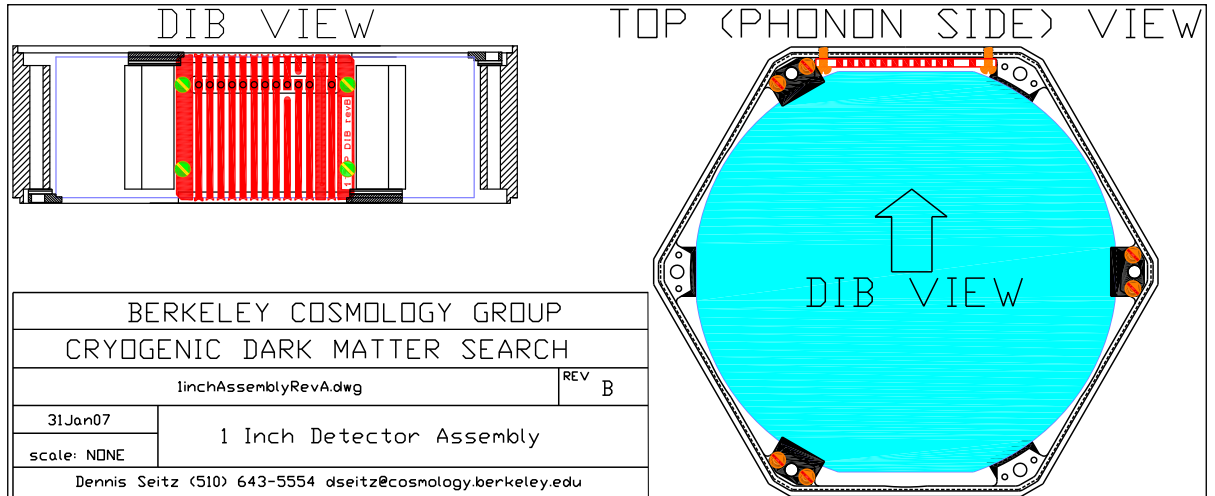


Figure 2.9: Diagram of a Soudan ZIP (teal), a predecessor to the Soudan iZIP, within its copper housing (black and white outlines). This housing is the same as what was used for the Soudan experiment, but with one important change: a readout-cabling DIB is placed between the detector and inner surface of the copper housing at the location of *each* major flat (as shown in Fig. 2.8), while this diagram shows only one DIB at one of major flat. Figure courtesy of Dennis Seitz.

2.1.6 Soudan iZIP Detector Housings

The Soudan iZIP detectors are contained within copper housing (see Fig. 2.9 with measurements shown by Fig. 2.10). Each detector is held in place by small, plastic pieces that gently press against the detector faces, such that no part of the detector touches the copper. Each detector and its housing is stacked to form a detector tower, as shown by Fig. 2.11. In Chapter 3, the copper housing geometry is simplified to a cylindrical shell (with an inner radius of 4.31 cm and height of 2.54 cm) for the purpose of estimating

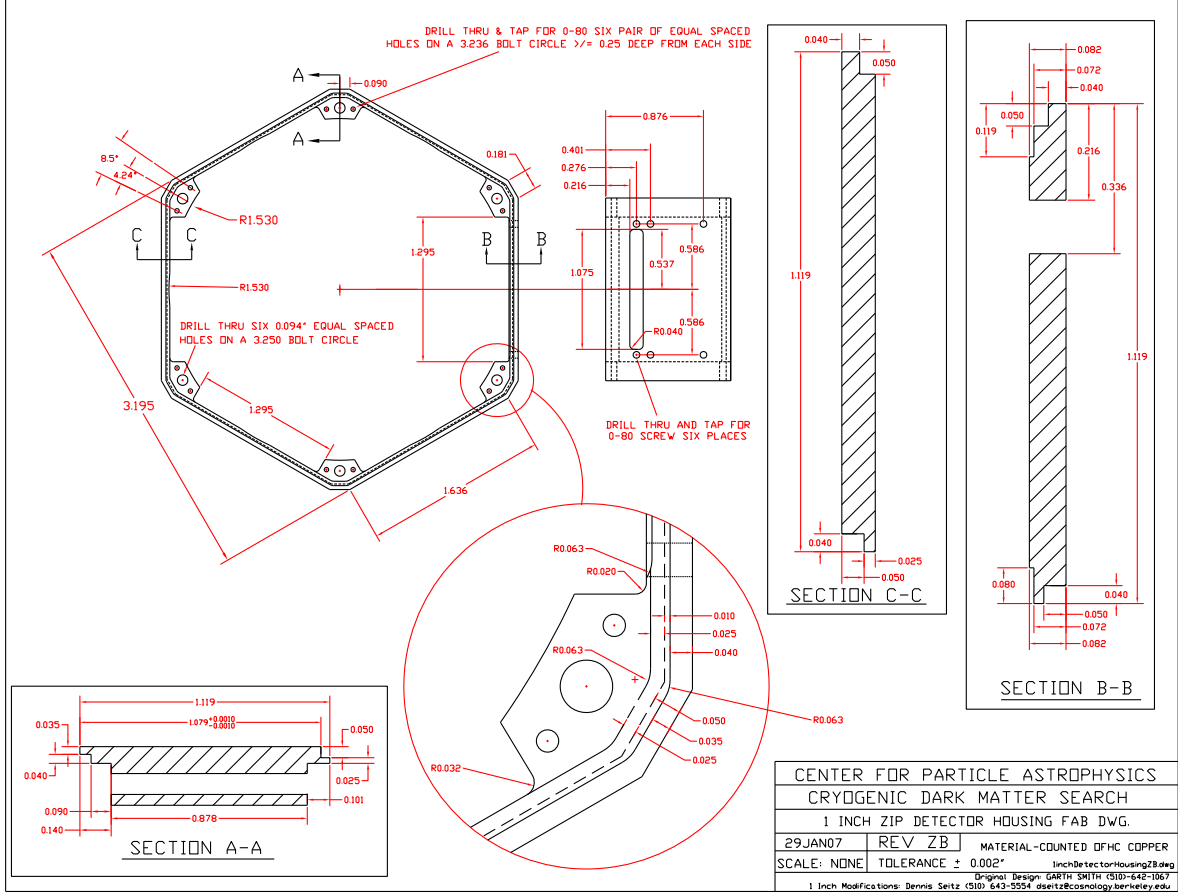


Figure 2.10: Diagram of a Soudan detector copper housing, with lengths given in inches and angles in degrees. Figure courtesy of Dennis Seitz.

^{210}Pb contamination on the inner surface of the copper housing and within the copper bulk.

2.2 SuperCDMS SNOLAB

The next generation of SuperCDMS is being installed at the SNOLAB underground facility in Sudbury, Canada. Projected sensitivities for SuperCDMS SNOLAB are unmatched at low WIMP masses (see Fig. 2.12) [59, 47]. The Ge and Si detectors (shown in Fig. 2.13) used in SuperCDMS SNOLAB detectors have many upgrades compared with SuperCDMS Soudan detectors, including a lower operating temperature, more channels, a larger mass, and an optimized phonon sensor layout for the HV mode [59]. Similar to SuperCDMS Soudan, the SNOLAB detectors will operate in either of two modes: the

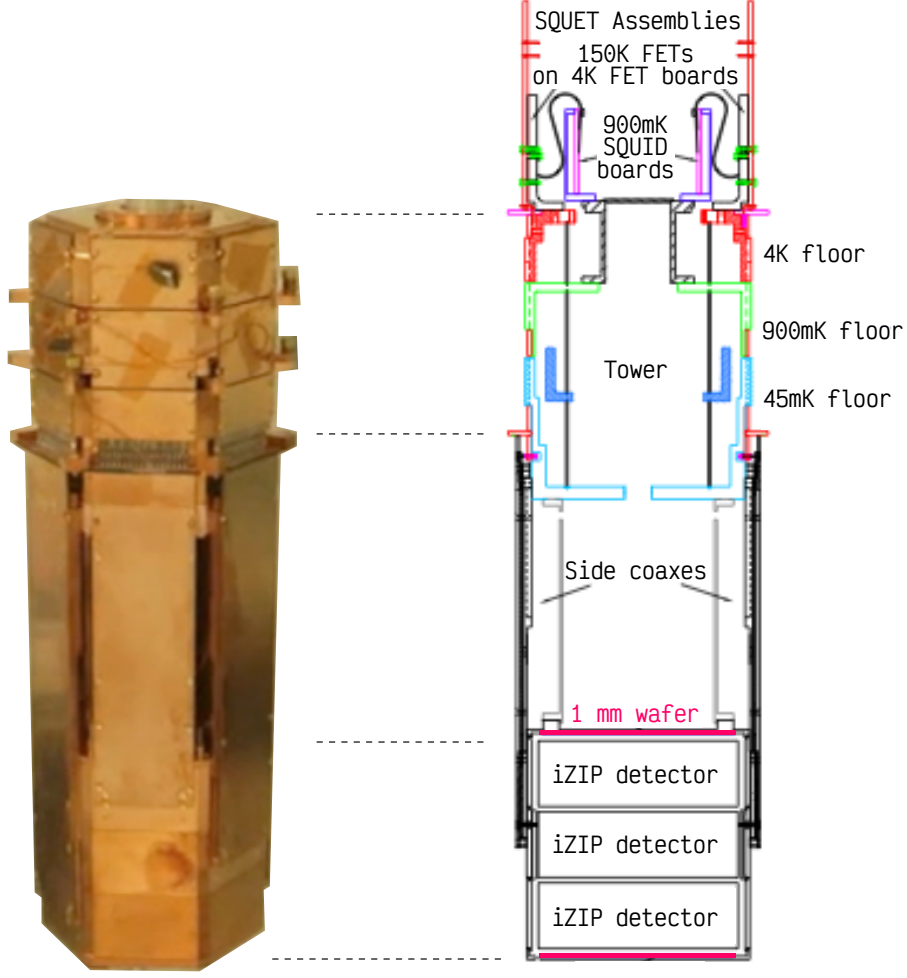


Figure 2.11: Image (left) and diagram (right) of a Soudan detector tower holding three iZIP detectors (in the base). The tower is suspended from the upper portion during operation [51]. Silicon wafers are shown above and below the iZIP detectors (in pink), but were not installed when commissioned. Figure adapted from [51], with permission from Dr. Scott Hertel.

low-voltage (iZIP) mode, providing better sensitivity above $\sim 5 \text{ GeV}/c^2$ due to its ability to discriminate between electron and nuclear recoils [46], and the high-voltage (HV) mode that provides better sensitivity for mass $\lesssim 5 \text{ GeV}/c^2$ [60, 66, 59, 47].

2.2.1 Expected Backgrounds for SuperCDMS SNOLAB

A potential source of dominant backgrounds for many rare-event searches is from radon daughter plate-out [67, 68]. Backgrounds from ^{210}Pb and the recoiling ^{206}Pb nucleus from the α decay of ^{210}Po were the dominant low-energy backgrounds for SuperCDMS Soudan [46]. Chapter 3 investigates the ^{210}Pb contamination of the SuperCDMS

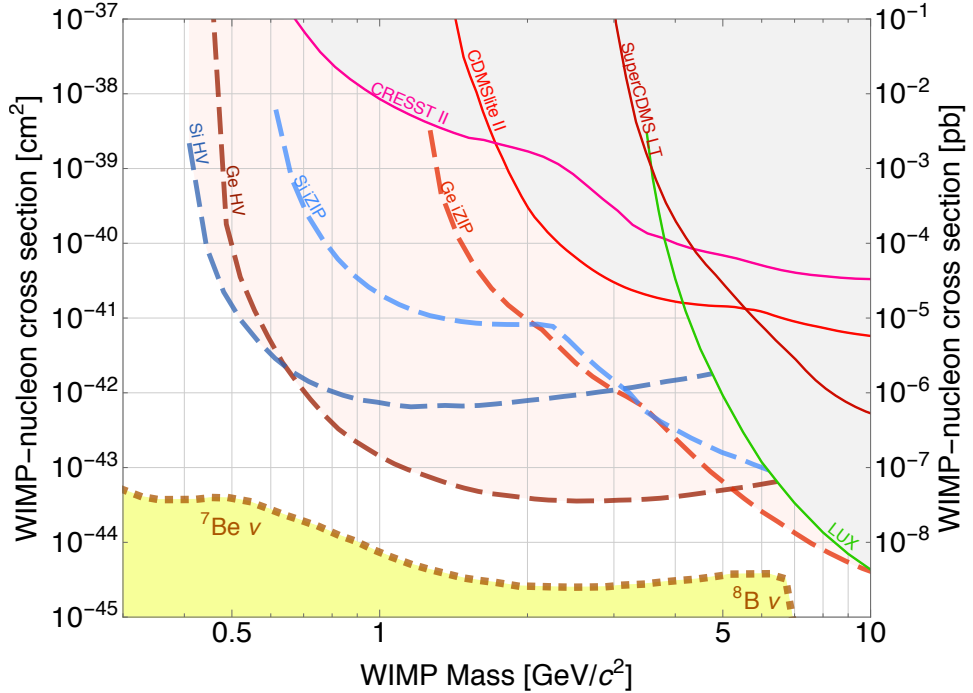


Figure 2.12: Projected sensitivity to the spin-independent dark matter-nucleon scattering cross-section as a function of dark matter mass for Si and Ge iZIP and Si and Ge HV detectors of the SuperCDMS SNOLAB experiment [59, 60]. The solid lines are the current exclusion limits set by the CRESST II [61], SuperCDMS [62, 63], and LUX [64] experiments. Reprinted figure with permission from [59]. Copyright 2016 by the American Physical Society.



Figure 2.13: The SuperCDMS SNOLAB HV (left) and iZIP (right) detectors [65].

Soudan detectors and their housings to further inform background reduction for Super-CDMS SNOLAB.

Radon-induced backgrounds are important to the expected low-mass sensitivity of the SuperCDMS SNOLAB experiment [59]. Although the SuperCDMS iZIP detectors pro-

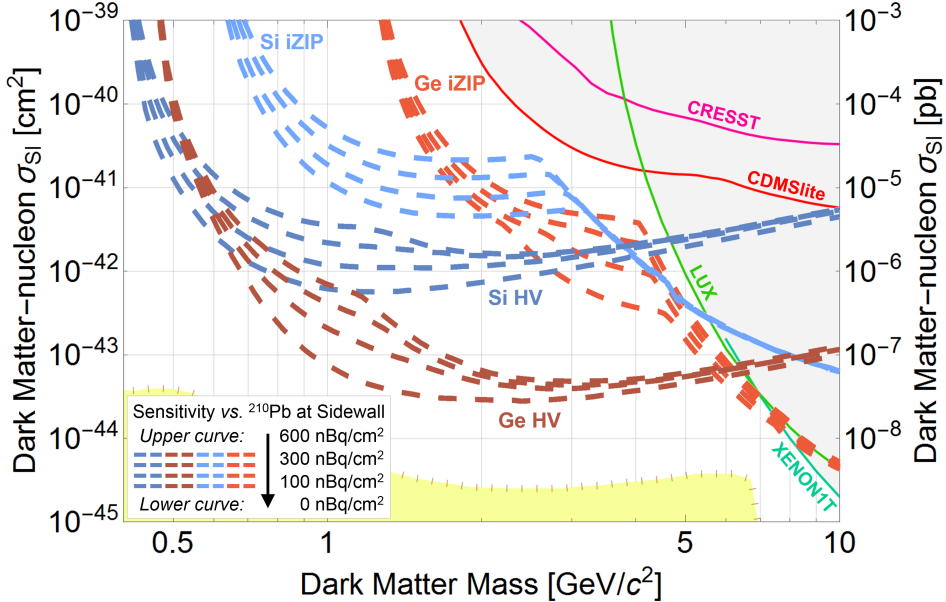


Figure 2.14: Projected sensitivity to the spin-independent dark matter-nucleon scattering cross-section as a function of dark matter mass for Si and Ge iZIP and Si and Ge HV detectors of the SuperCDMS SNOLAB experiment [59, 60]. Each set of four dashed lines represents projected sensitivities for (from bottom to top) 0, 100, 300, and 600 nBq cm^{-2} ${}^{210}\text{Pb}$ surface contamination on the detector sidewalls (*i.e.*, a sum across the detector and copper surfaces). At low masses, the sensitivity degrades significantly with increasing ${}^{210}\text{Pb}$ contamination above 50nBq cm^{-2} .

vide excellent rejection of surface events above 8 keV [58], at lower energies the rejection is expected to worsen to the point that radon-daughter backgrounds may dominate [59]. The situation is similar for the SuperCDMS high-voltage (HV) detectors, which provide the experiment’s lowest energy threshold by amplifying the ionization signal [46, 44]. Figure 2.14 shows how the expected sensitivity of SuperCDMS SNOLAB varies for different surface concentrations of ${}^{210}\text{Pb}$. Figure 2.15 shows the expected backgrounds (before and after analysis cuts) for the germanium detectors in HV mode. Below energies of $\sim 0.5 \text{ keV}$, rejection of events on the detector sidewall surface, based on the relative sizes of signals in the detectors’ phonon sensors, becomes ineffective, so radon-daughter surface backgrounds are expected to dominate over bulk backgrounds for ${}^{210}\text{Pb}$ concentrations $\gtrsim 50 \text{nBq cm}^{-2}$ [59].

Without mitigation, radon-daughter plate-out during assembly underground at SNO-LAB could dominate the expected background. The duration of the SNOLAB assembly

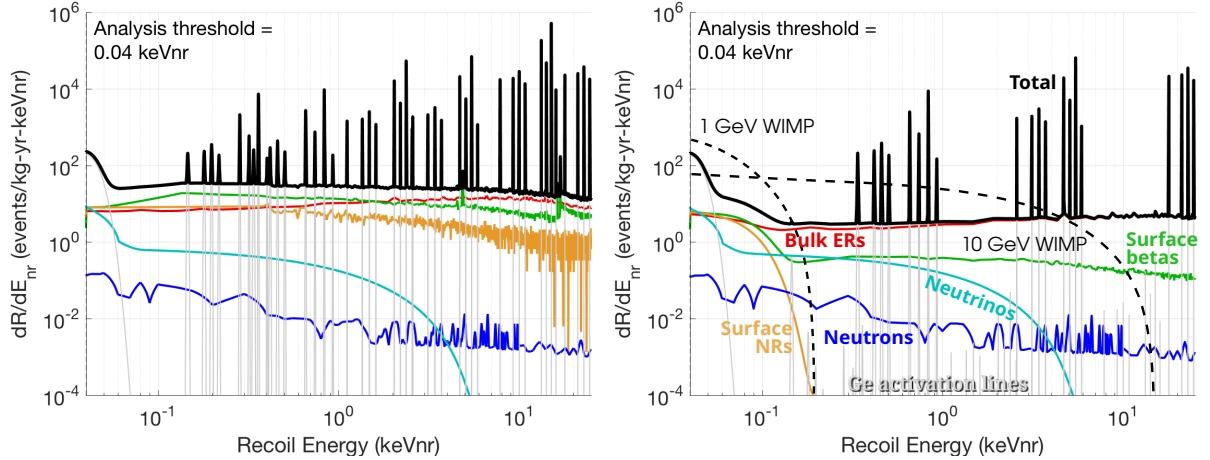


Figure 2.15: Background spectra, before (left) and after (right) analysis cuts for Ge HV detectors, shown as a function of nuclear recoil energy (keVnr). The thick black line represents the total background rate. Electron recoils from Compton gamma-rays and ${}^3\text{H}$ are grouped together (red). The Ge activation lines (grey) are shown convolved with a 10-eV r.m.s. resolution. The remaining components are surface betas (green), surface ${}^{206}\text{Pb}$ recoils (orange), neutrons (blue), and coherent neutrinos (cyan). Possible rates from 1- and 10-GeV WIMPs are represented by dashed lines. Reprinted figure with permission from [59]. Copyright 2016 by the American Physical Society.

is estimated at about 150 hours [69]. At the average SNOLAB radon concentration of 130 Bq/m³, the expected plate-out would be about 70 nBq/cm² of ${}^{210}\text{Pb}$ [69]. To make this plate-out rate negligible, SuperCDMS SNOLAB has a goal of achieving a radon concentration underground of <0.1 Bq/m³ in its assembly cleanroom underground [69]. Without radon mitigation, the expected ${}^{210}\text{Pb}$ contamination on detector surfaces from all steps in detector fabrication and during installation is about 117 nBq/cm². With radon mitigation during the installation stage (using the radon-reduction system discussed in Chapter 5), the estimated contamination is about 47 nBq/cm². Though not planned for SuperCDMS SNOLAB, using the post-fabrication sidewall etching technique (described in Chapter 10), the ${}^{210}\text{Pb}$ contamination could be further reduced to about 24 nBq/cm².

To guide the effort in reducing radon-daughter backgrounds, the ${}^{210}\text{Pb}$ contamination on and around detectors from the previous generation experiment, SuperCDMS Soudan, is determined as a function of location and is described in Chapter 3. Radon-induced surface backgrounds may be reduced by limiting the exposure time to or the radon

concentration of environments where detectors are assembled and installed. Chapter 5 describes the SD Mines Radon-Reduction System (RRS) and the SD Mines low-radon cleanroom. The RRS has demonstrated a $4000\times$ reduction in the radon concentration of breathable air to the steady-state radon concentration of $\sim 25\text{ mBq/m}^3$. A close copy of the SD Mines RRS has been built and installed at the SNOLAB facility where SuperCDMS SNOLAB is being commissioned and is expected to surpass the SuperCDMS SNOLAB goal of a radon concentration of 100 mBq/m^3 during detector installation.

Chapter 3

Surface Contamination of SuperCDMS Soudan Detectors

The decays of radon daughters (specifically, those after ^{210}Pb , having a half-life of 22.3 y) represented the dominant background for SuperCDMS at Soudan [46]. Therefore, a better understanding of this important background may guide future fabrication of solid-state detectors and data analysis. Alphas emitted by the radioactive decay of ^{210}Po are easy to tag, as they have a large initial kinetic energy of 5.3 MeV, and provide position and timing information that can be used to infer other potentially dominant backgrounds: betas emitted from the decay of ^{210}Pb and ^{210}Bi and the recoiling ^{206}Pb nucleus after the ^{210}Po alpha decay. In addition, separating ^{210}Po alphas into the those originating from detector and line-of-sight surfaces and those buried in surrounding materials (such as the copper detector housing or readout cabling) may guide future detector and housing fabrication and material selection.

This chapter has six major parts: (1) selecting ^{210}Po alpha events that are used to infer the amount of ^{210}Pb contamination (Section 3.2), (2) correcting the estimated recoil energy and its dependence on z (Section 3.3), (3) simulating the recoil energy spectrum from ^{210}Po alphas buried in the copper housing that surrounds the detectors (Section 3.4), (4) exploring the spatial reconstruction of ^{210}Po events (Section 3.5 and Section 3.6), (5) analyzing the time dependence of ^{210}Po events, which is important for inferring the initial amounts of ^{210}Pb and ^{210}Po (Section 3.7), (6) and finally comparing inferred ^{210}Po contamination from this work with an assay using the high-sensitivity Alpha-Beta-radiation Assay CHamber (AlphaBACH) (Section 3.8 and Section 3.9).

3.1 SuperCDMS Soudan Science Runs and Data Processing

SuperCDMS Soudan had three science runs [53] that are used for this analysis:

- **Run 133** was the first science run, lasting from March 2012 to July 2013. The run was forced to end because a ^{133}Ba calibration source became trapped in the shield. Removing the source required a warm-up and partial shield deconstruction.
- **Run 134** lasted from July 2013 to July 2014, at which time the experiment was purposefully warmed-up to perform standard maintenance on the cryocooler.
- **Run 135** was the last run from September 2014 to November 2015, at which time the experiment was decommissioned. Though this science run had a similar length as the earlier two, the WIMP-search duration was comparatively much shorter.

3.1.1 Data Quality Cuts

The analysis described in this chapter takes advantage of pre-existing high-threshold (HT) data-quality cuts, as detailed in Table 3.1. Each quality cut is described beautifully in Chapter 3 of Brett Cornell’s thesis [70], where I refer the reader that is interested in greater detail than provided here. There are two types of quality cuts used for this analysis:

- **Time-Period-Quality Cuts** remove events occurring when detectors were not operating correctly or where in the CDMSlite (high-voltage) mode [70].
- **Event-Quality Cuts** remove events that did not pass event-reconstruction checks: the cut `!cRandom_133` removes random trigger events, `!cGlitch_133` removes events with phonon pulses with fall-times that are too short, `!cVTStrict_133` removes any event that is coincident with an event in the muon veto [70], and `!cNuMI_133` removes any event that is coincident with the NuMI Neutrino Beam [71] at Fermilab.

After applying these data-quality cuts, the total live-time varies between 173 to 409 days, depending on the detector. The total live-time for each detector analyzed

Science Run	Event-Quality Cuts	Time-Period-Quality Cuts
Runs 133 and 134	!cRandom_133 !cVTStrict_133 !cGlitch_133 !cNuMI_133	cBiasPM_133 cQstd_v53 cPstd_v53 cGoodDataPeriod_133 [†] cGoodDataPeriod_v53 [†] cDataPeriod_v53_HT [†]
Run 135	!cRandom_133 !cVTStrict_133 !cGlitch_133 !cNuMI_133	cBiasPM_133 cQstd_v53 cPstd_v53

Table 3.1: Quality cuts used for the Soudan Science runs used in this analysis.

is provided in Table 3.2 in Section 3.1.2. The efficiency for ^{210}Po alphas is expected to be 100% for these cuts.

3.1.2 Detector Selection

Table 3.2 tabulates the detectors that were used for this analysis. Detector numbers in **green** represent fully functional detectors (at least for this high-energy analysis), while those in **red** represent detectors that were dysfunctional (with a common issue being the charge channels being grounded to the chassis and thus not working correctly). Detector numbers in **blue** represent detectors with ^{210}Pb sources located near one face and are thus not included in estimations of ^{210}Pb contamination.

Throughout this chapter, the analysis will be developed using data from and showing plots for detector 1101. In terms of data quality, this detector is neither the best or the worst—but very similar to the other detectors analyzed, with important plots that result from this work presented in Appendix B.

3.2 ^{210}Po Event Selection

The decay of ^{210}Po results in an alpha particle with 5.3 MeV of kinetic energy and a ^{206}Pb atom recoiling with an energy of about 100 keV. A ^{210}Po decay on the surface of a detector or the material (usually copper) facing the detector has about a 50% chance to

Detector	Tower - Location	Total LT	Notes
1101	IT1 - top	373 days	
1102	IT1 - middle	—	QOS1, PAS2, and PBS1 shorted to chassis.
1103	IT1 - bottom	—	QIS1 and QOS1 both shorted to chassis. Both FETs disabled.
1104	IT2 - top	408 days	The only P-type crystal.
1105	IT2 - middle	409 days	
1106	IT2 - bottom	366 days	PBS1 and PDS1 shorted to chassis.
1107	IT3 - top	—	^{210}Pb calibration source was placed above side 1.
1108	IT3 - middle	393 days	
1109	IT3 - bottom	—	^{210}Pb calibration source was placed below side 2. Intermittent chassis short on QIS2. Pulse issue with PCS1.
1110	IT4 - top	—	Assayed by the AlphaBACH. QIS1 shorted to chasis. FET disabled.
1111	IT4 - middle	390 days	Assayed by the AlphaBACH
1112	IT4 - bottom	408 days	Assayed by the AlphaBACH
1113	IT5 - top	—	The only ion-implanted detector. QIS1 shorted to chassis. Large charge noise at low frequency. QIS1 FET disabled.
1114	IT5 - middle	173 days	
1115	IT5 - bottom	—	QOS1 and PCS2 shorted to chassis.

Table 3.2: Soudan detectors are color-coded into three groups: **green** represents fully functional detectors, **red** represents dysfunctional detectors (with some explanation given in the notes column), and **blue** represents detectors with ^{210}Pb sources located near one face (and are thus excluded from the analysis). The column labeled **Total LT** is the total live-time for each detector after data-quality cuts (see Section 3.1.1). Detectors 1110, 1111, and 1112 had their sides assayed for ^{210}Po with Dr. Juergen Reichenbacher's AlphaBACH (a high-sensitivity alpha-beta spectrometer).

pass into the detector where its energy is deposited. Alternatively, a ^{210}Po decay could occur within the copper housing that surrounds the detector; if this so-called buried alpha within the copper escapes and passes into the detector, the maximum energy that it can deposit will be reduced by the amount of energy lost to the copper (as will be discussed in Section 3.4). The distribution of deposited energy from these alphas is expected to

look like a Gaussian distribution centered at 5.3 MeV, representing the surface alphas, with a tail extending to zero energy that represents buried alphas that have lost some of their energy in the copper or the detector interface boards (DIBs) (according to the distance they traveled through the material).

In order to analyze the ^{210}Po alphas, they must be selected from all measured events. SuperCDMS Soudan has numerous data quantities that represent aspects of an event or the state of the detector. There are reduced quantities (RQs), such as the live-time, phonon pulse amplitude, or the detector bias voltage. There are also relational reduced quantities (RRQs), which are calibrated quantities built upon RQs, such as an event's ionization energy, prompt phonon energy, or the delay time between channels in prompt phonons. I will provide the SuperCDMS internal names for the RQs and RRQs used in this analysis to benefit my SuperCDMS readers.

As discussed in Chapter 2, the ionization yield $Y(E_r) \equiv E_Q/E_r$ and is equal to unity for an electron recoil (ER) event (such as gammas). This definition of the ionization yield suggests selecting alpha events (which will have $Y < 1$), from the phase space of Y and E_r . Rearranging Eq. 2.16 from Chapter 2 yields the recoil energy

$$E_r = E_t - \frac{e\Delta V_b}{\epsilon_{eh}} E_Q. \quad (3.1)$$

In terms of RRQ quantites, $E_Q = \text{qsummaxF5}$ and $E_r = \text{psumTFP} - \text{plukeqF5}$, and therefore $Y = \text{qsummaxF5} / (\text{psumTFP} - \text{plukeqF5})$.

Figure 3.1 shows the ionization yield versus the recoil energy. This phase space allows for alpha events to be selected from the gamma events. Above 3 MeV, the alpha separated (shown by the diagonal line with the gamma side hatched) has a nearly 100% passage fraction and 0% leakage of gammas (by inspection), as the highest energy gammas in these data have an energy of 2.6 MeV (emitted after the alpha decay of ^{212}Bi into ^{208}Tl [72]). Below 3 MeV, the passage fraction for alphas depends on energy and is $\sim 50\%$. For this analysis, as we use the alphas above 3 MeV, this alpha selection is sufficient.

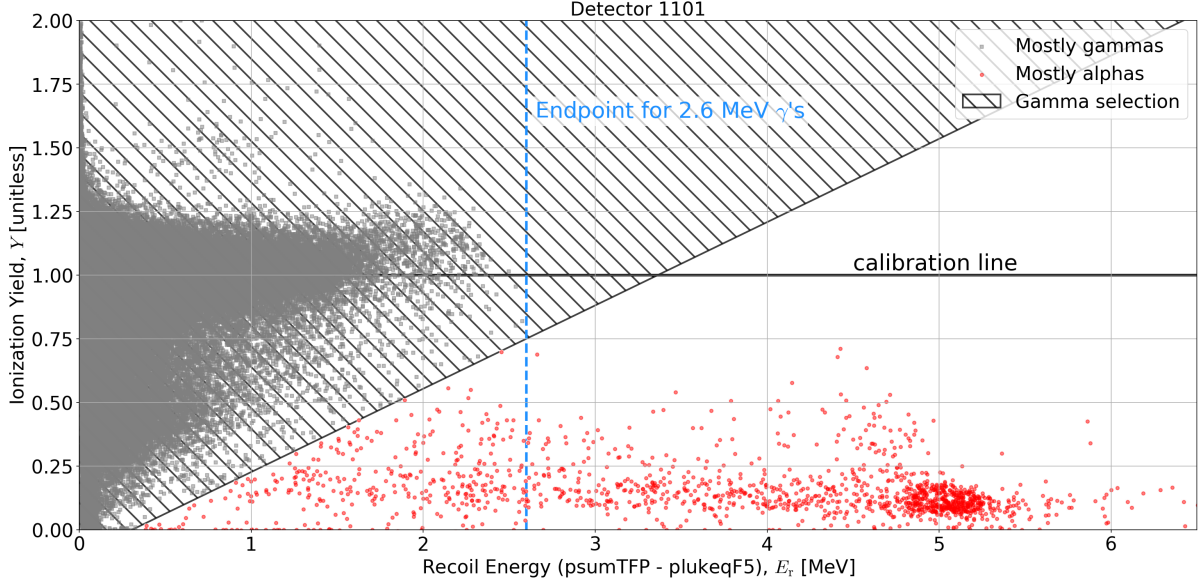


Figure 3.1: Ionization yield Y as a function of recoil energy E_r shows gammas below 2.6 MeV (dashed blue line) and primary along the $Y = 1$ (black) calibration line. The hatched region selects mostly gamma events (gray squares), and the open region selects mostly alpha events (red circles). The gammas don't quite reach their end point in recoil energy and the center of the 5.3-MeV alpha population is short of 5.3 MeV; this is believed to be caused by saturation of the phonons channels and is corrected later in Section 3.3.

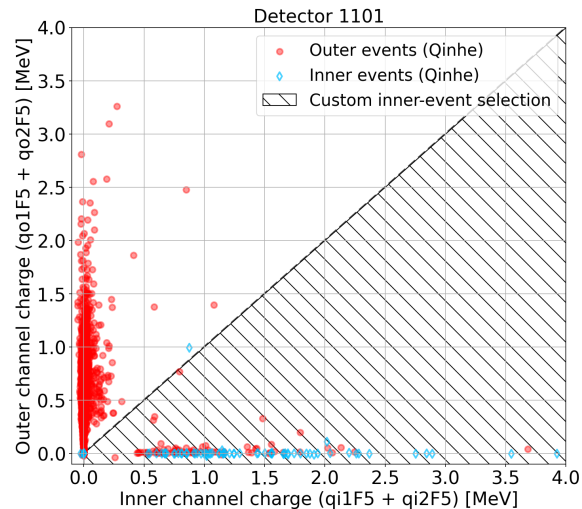


Figure 3.2: Total charge (from sides 1 and 2) from the outer channels versus the inner channels. The hatched region (defined by $y < x$) selects events that have more charge collected in the inner channels than in the outer channels. The SuperCDMS inner-outer selection (**Qinhe**) conservatively tags many inner events (blue diamonds) as outer events (black \times 's). For this analysis, such a conservative selection of inner events is not required.

Face (inner) and side (outer) events are discriminated according to the charge collected in the face and side channels. Figure 3.2 shows the total charge collected in the outer

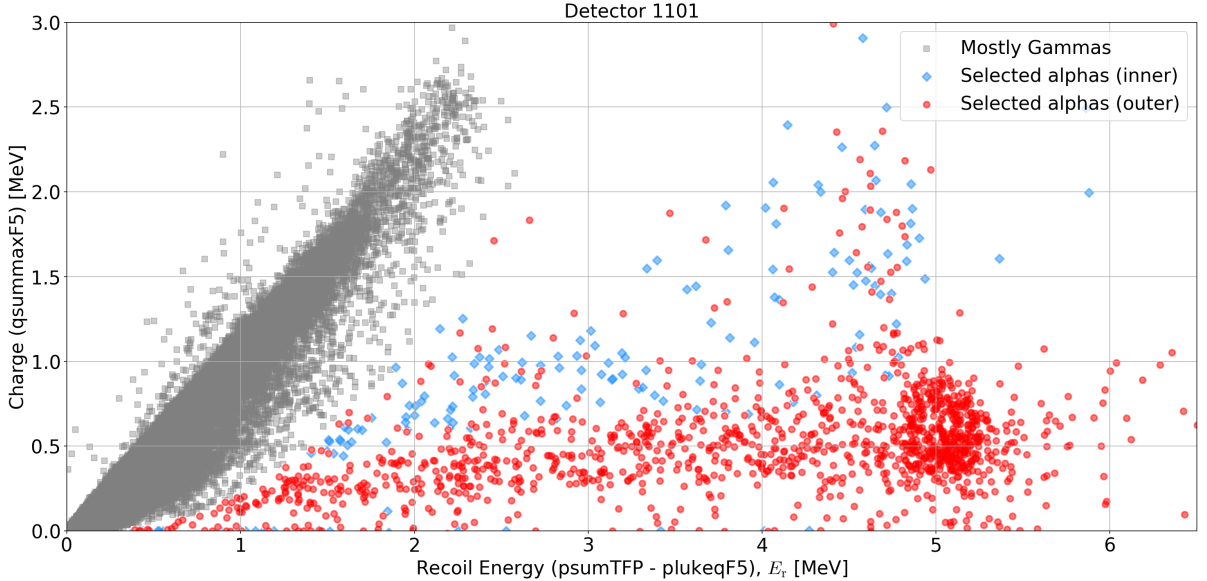


Figure 3.3: The charge versus (phonon) recoil-energy phase space for all events. Gamma events (gray squares) follow a one-to-one diagonal with an end-point energy of 2.6 MeV in both charge and recoil energy. Selected alpha events are grouped into inner events (blue diamonds) and outer events (red circles), with the vast majority of alpha events being in this latter group.

channels versus the total charge collected in the inner channels. For this work, *if the total charge (summed over sides 1 and 2) collected in the outer channels is greater than that collected in the inner channels, then the event is tagged as an outer event*. The hatched regions of the plots in Fig. 3.2 illustrate the selection for inner events. Because there are many more outer events than inner events independent of which inner-outer selection is used, the choice of selection method results in only a small change in the passage fraction. The Qinhe method tags 93% of all events to be outer events, while the custom selection tags 89% of all alpha events as outer events. From this point forward, inner and outer alphas are determined by the custom inner-outer selection developed in this section.

Because SuperCDMS Soudan measures charge and phonon energy, the charge versus recoil energy phase space is frequently a good way to inspect data. Figure 3.3 shows charge versus recoil energy for alphas passing (and not passing) the custom inner-outer selection. The custom inner-outer selection tags many alpha events with larger charge (> 0.5 MeV) as inner events. Most alphas are expected to be on the detector sidewalls, where they may suffer from incomplete charge collection (see Section 2.1.4). Alphas on

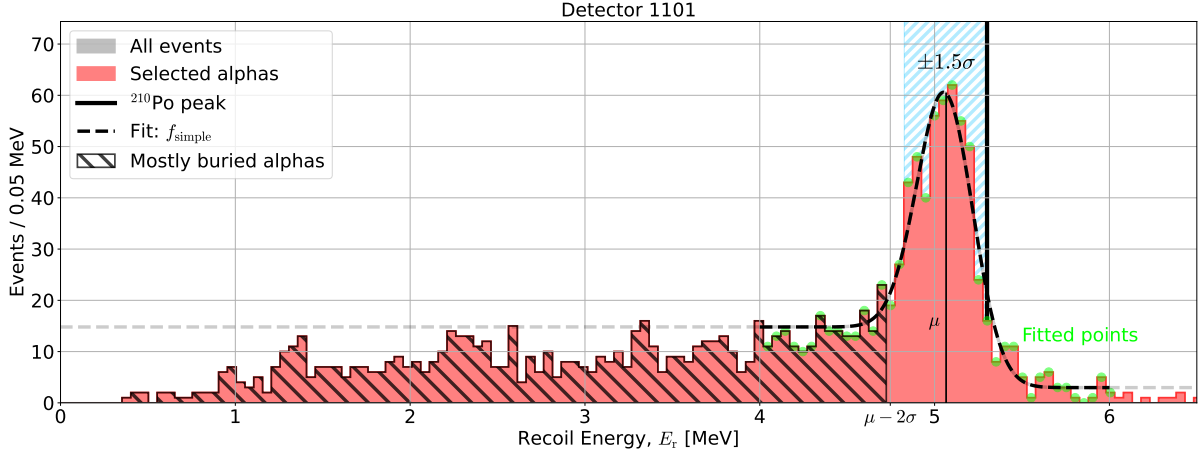


Figure 3.4: The recoil energy spectrum for selected alphas (red) is compared with the energy spectrum of all events (gray). The function f_{simple} (Eq. 3.2) is fit (dashed black line) to the Gaussian part of the selected alphas spectrum (fitted points highlighted with green circles), with the best-fit $\mu = 5.07 \pm 0.01$ MeV and $\sigma = 0.16 \pm 0.01$ MeV. The goodness-of-fit statistic $\chi^2/\text{ndf} = 39.31/35 = 1.12$ and p-value = 0.28. The low-energy tail below $\mu - 2\sigma$ (left-hatched region) is presumed to be from buried alphas, with most events above $\mu - 2\sigma$ representing decays occurring on the detector or copper surface. The $\pm 1.5\sigma$ (blue, right-hatched) region centered at μ is used for selecting events for fitting the ^{210}Po peak versus z later in this section (see Eq. 3.8). The thick black line at 5.3 MeV represents the expected energy of the ^{210}Po alphas.

detector faces are thus expected to deposit more charge than alphas on the sidewall. Therefore, the inner alphas having more charge may also be expected. Most of the outer events are observed to be in the population around $E_r = 5$ MeV, representing ^{210}Po decays occurring on either the detector sidewall or on the inner surface of the copper housing. As mentioned earlier, the lower-energy (outer) alphas are expected to be caused by alphas escaping the copper.

3.3 Event Energy Reconstruction and Estimates of ^{210}Po Contamination

The selected alpha events from the outer region of the detector are henceforth referred to simply as *selected alphas*, with inner events denoted explicitly when needed. These selected alphas may be further explored by studying their recoil energy spectrum. Figure 3.4 shows the event rate versus recoil energy and emphasizes two important features: (1) the ^{210}Po peak is less than the expected energy of 5.3 MeV and (2) the shape of the energy spectrum appears comprised of a Gaussian part and a roughly linear part. The

Gaussian part represents alpha decays on the *surface* of the detector or copper, while the roughly linear, low-energy tail represents alphas that were *buried* in the copper housing or surrounding materials. A simple model for the recoil energy spectrum (that is improved upon in Section 3.4) is a Gaussian function plus a step function that is convoluted with a Gaussian function:

$$f_{\text{simple}}(E_r) = G(E_r) + \int_{-\infty}^{+\infty} L(\eta) \bar{G}(E_r - \eta) d\eta, \quad (3.2)$$

where

$$L(E_r) \equiv (A - B)\Theta(\mu - E_r) + B \quad (3.3)$$

where A and B are fitted parameters representing the event rate below and above the value μ and Θ is the Heaviside function. The Gaussian function

$$G(E_r) \equiv C \exp \left[-\frac{(E_r - \mu)^2}{2\sigma^2} \right], \quad (3.4)$$

where the amplitude is C , the center of the peak is μ , and the standard deviation is σ , with all being fit parameters. The second G appearing in Eq. 3.2 is barred (as \bar{G}) to denote it being normalized to unity and given $E_{1/2}$, the center of the energy space, in place of μ (but using the same value of σ as G). The convolution of the step function with \bar{G} serves to smooth out the step function as if measured by the detector (which has a limited energy resolution, inferred from σ). The convolution is performed numerically using the Python library `scipy.signal.convolve` with the input argument `mode = 'same'`, such that the output array has the same dimension as $L(E_r)$.

The function f_{simple} is fit to the Gaussian part of the spectrum primarily, yielding the best-fit mean $\mu = 5.07 \pm 0.01$ MeV and standard deviation $\sigma = 0.16 \pm 0.01$ MeV. From here, a crude estimate of the surface and buried ${}^{210}\text{Pb}$ contamination can be made, though a more thoughtful estimate will be presented in Section 3.5. While some buried events are in the Gaussian (surface) part of the spectrum, some surface events are in the buried part. For now, a cut is placed at $\mu - 2\sigma$ to mostly separate the buried events from the surface events.

Adding up all of the counts in the buried and surface regions of the recoil energy spectrum yields $N_b = 750$ counts and $N_s = 574$ counts respectively. The recipe that converts N_s counts to the surface rate S is

$$S \equiv \frac{N_s}{At_{\text{LT}}\epsilon_s}, \quad (3.5)$$

where A is the surface area in cm^2 (for example, the detector sidewall or face area), t_{LT} is the detector live-time in seconds, and the detection efficiency for surface events $\epsilon_s = 0.5$ (an estimate that assumes only half of all alphas produced on a surface enter the detector). Referring to the overview on detector geometry presented in Section 2.1.5, the ^{210}Po contamination for the detector sides is estimated to be $S = 398 \pm 17 \text{nBq}/\text{cm}^2$ for the surface events. For buried events, contamination is quoted in units of activity per mass, presuming buried events originate from the copper housing:

$$B \equiv \frac{N_b}{m_{\text{Cu}}t_{\text{LT}}\epsilon_{\text{Cu}}}, \quad (3.6)$$

where $m_{\text{Cu}} = \rho_{\text{Cu}}V_{\text{skin}}$, with the copper density $\rho_{\text{Cu}} = 8.96 \times 10^{-3} \text{ kg}/\text{cm}^3$, the skin-depth volume $V_{\text{Cu}} = 3.77 \times 10^{-2} \text{ cm}^3$, and the detection efficiency for buried alphas $\epsilon_{\text{Cu}} = 17.37 \pm 0.02\%$ (with the latter two quantities discussed in Section 3.4). The bulk ^{210}Po contamination of the copper housing is thus estimated by the buried events as $B = 396 \pm 14 \text{ mBq}/\text{kg}$ (and may be compared to improved estimates shown in Table 3.3).

The ^{210}Po peak energy being lower than expected is believed to be caused by phonon pulses being saturated at high energy (above about 1 MeV). The gamma end-point energy is also less than 2.6 MeV, as further evidence. Dr. Daniel Jardin studied the saturation of phonon channels (see Appendix D of his thesis) and suggested improvements on how energy is estimated (though leaving room for further improvement) [73]. The amount of saturation observed depends on the phonon channel and detector. For this analysis, it is sufficient to infer that the measured ^{210}Po peak has a true energy of 5.3 MeV, with energy cuts then chosen accordingly. To make this assumption more transparent, an energy correction is made to the phonon recoil energy such that the ^{210}Po peak is at

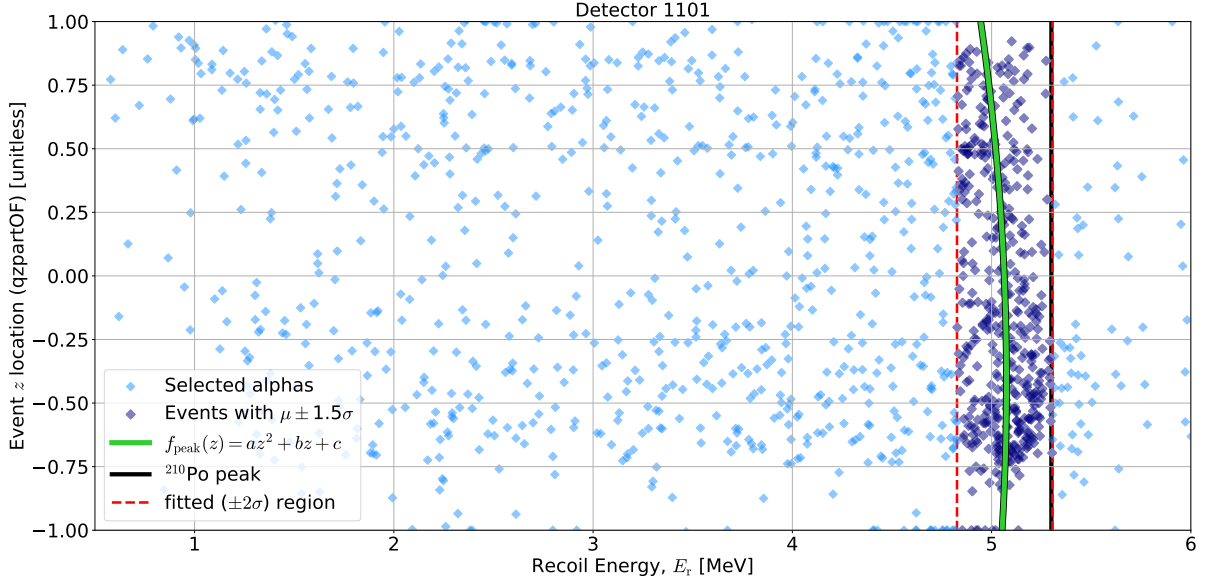


Figure 3.5: The z location of each event (as determined by Eq. 3.7) versus recoil energy (light blue diamonds) shows a slight z dependence on the ^{210}Po peak location. The quadratic function given by Eq. 3.8 is fit (green line) to a selection of these data (dark blue diamonds) within $\mu \pm 1.5\sigma$ (red dashed lines), with μ and σ determined by fitting Eq. 3.2 to the recoil energy spectrum by Fig. 3.4. The goodness-of-fit statistic $\chi^2/\text{ndf} = 1217/441 = 2.76$ and $p\text{-value} = 0$, clearly indicating that the quadratic function is not a great model of the data; however for this analysis, such a crude model will suffice, as its effect is less than one percent on the inferred σ .

5.3 MeV for each detector by a single multiplicative factor. In addition, it was found that the measured recoil energy has a slight z dependence, which, though not having a significant effect, is corrected at the same time that the recoil energy correction is applied.

Figure 3.5 shows the z location (between the detector faces) of events versus the recoil energy. The z location is provided by the RRQ `qzpartOF`, which infers the z location by

$$z = \frac{Q_{S1} - Q_{S2}}{Q_{S1} + Q_{S2}}, \quad (3.7)$$

where Q_{S1} and Q_{S2} is the total charge collected on side 1 and 2 respectively. Therefore, an event with $z = 1$ was on side 1, an event with $z = 0$ was between the sides (in the middle of the detector), and an event with $z = -1$ was on side 2.

Still referring to Fig. 3.5, a selection of events within $\mu \pm 1.5\sigma$ (found from fitting Eq. 3.2 to the energy spectrum shown by Fig. 3.4) of the measured ^{210}Po peak is fit by

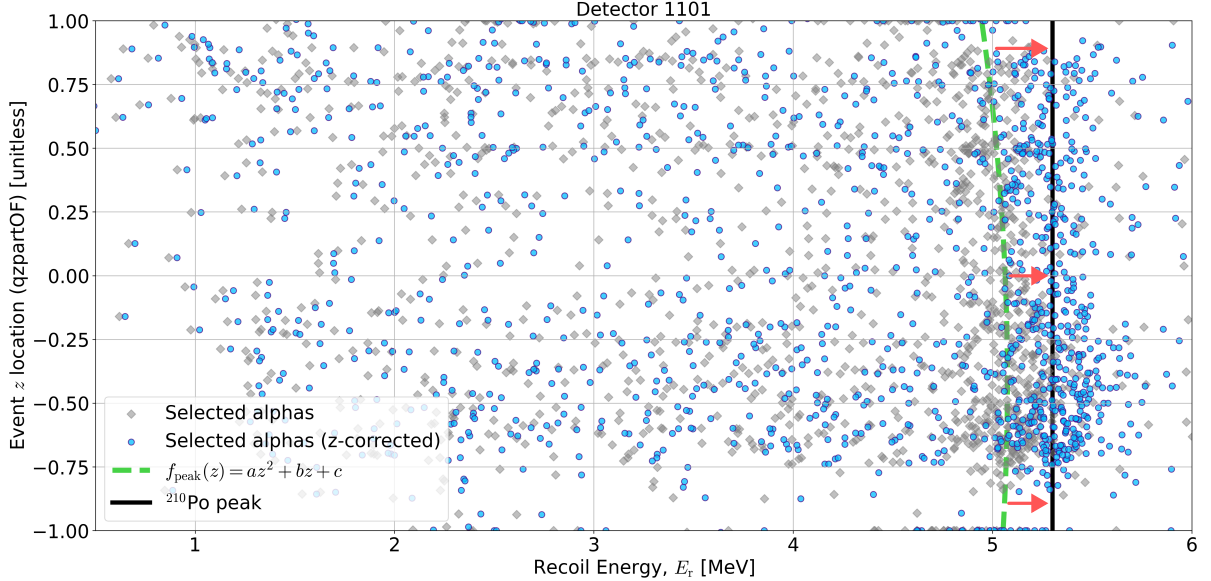


Figure 3.6: Similar to Fig. 3.5, the quadratic function given by Eq. 3.8 is fit to the ^{210}Po peak of the selected alphas (gray diamonds). The recoil energy of each event is scaled according Eq. 3.9 such that the ^{210}Po peaks inferred from the quadratic fit (green dashed line) aligns with the expected ^{210}Po decay energy of 5.3 MeV (black line).

the quadratic function (as empirically motivated):

$$f_{\text{peak}}(z) = az^2 + bz + c, \quad (3.8)$$

where a , b , and c are fitted parameters. The function $f_{\text{peak}}(z)$ shows how the ^{210}Po peak changes as a function of z . In order to force the ^{210}Po peak to be at 5.3 MeV at any location z , a z -dependent energy calibration is applied for each event i :

$$E_{r,i} \rightarrow E_{r,i} \times \frac{5.3 \text{ MeV}}{f_{\text{peak}}(z_i)}. \quad (3.9)$$

Figure 3.6 shows the result of this z -dependent energy correction.

Figure 3.7 shows the z -corrected recoil energy spectrum against the uncorrected spectrum. As we did before, a cut is made at $\mu - 2\sigma$ that separates buried events (below the cut) from the surface (above the cut); this leads to an estimate of the ^{210}Pb contamination (using Eq. 3.5 and Eq. 3.6) of $S = 402 \pm 17 \text{ nBq/cm}^2$ and $B = 393 \pm 14 \text{ mBq/kg}$ (with improved estimates presented in Table 3.3). As expected, these estimates differ from the uncorrected spectrum estimates by only about one percent. However, performing the

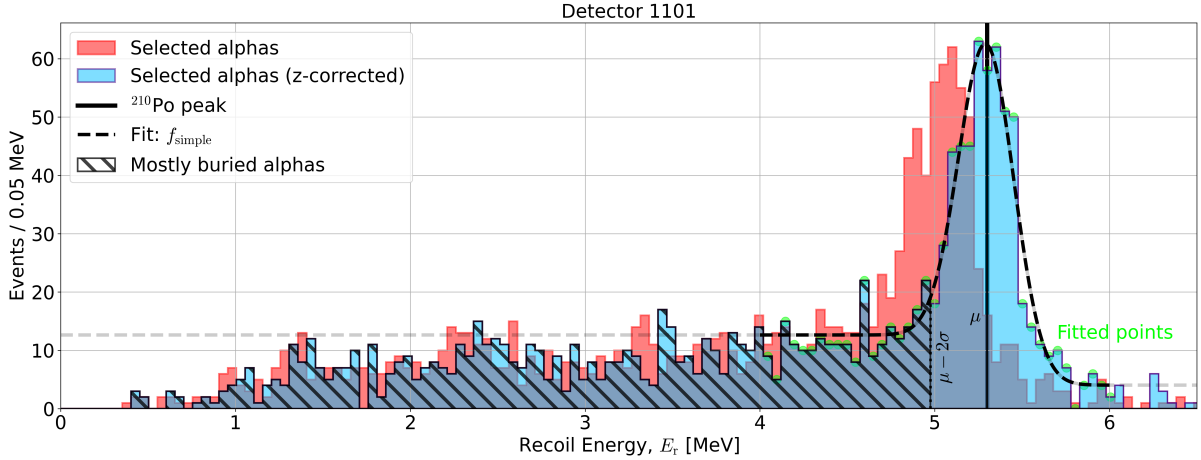


Figure 3.7: Similar to Fig. 3.4, but showing the z -corrected spectrum (blue) as it compares to the uncorrected spectrum (red). As before, the function f_{simple} (Eq. 3.2) is fit (dashed black line) to the Gaussian part of the selected alphas spectrum (fitted points highlighted with green circles), with the best-fit $\mu = 5.30 \pm 0.01$ MeV and $\sigma = 0.16 \pm 0.01$ MeV. The goodness-of-fit statistic $\chi^2/\text{ndf} = 42.72/35 = 1.22$ and p-value = 0.17. The low-energy tail below $\mu - 2\sigma$ (left-hatched region) represents buried alphas, with events above $\mu - 2\sigma$ representing decays occurring on the detector or copper surface.

z -dependent recoil energy correction provides a clear rationale for where and why energy cuts are made, and with the possible benefit (though admittedly slight) of improving the estimated recoil energy as a function of z .

3.4 Toy Monte Carlo Simulation for Buried ^{210}Po Alphas

Each SuperCDMS Soudan detector was encased in a copper housing (see the left side of Fig. 3.8). A detector tower consisted of three detectors, each inside their housing, stacked vertically (face-to-face) with no intervening material. Once assembled, the copper housings formed a closed volume around the detectors that are held at vacuum during operation. Measured ^{210}Po alphas that originate on the surface of the detector, or a line-of-sight surface of the copper housing, are expected to produce a recoil energy spectrum with the shape of a Gaussian distribution with a mean of 5.3 MeV, the kinetic energy of a ^{210}Po alpha. However, an alpha produced within the bulk of the copper housing will lose kinetic energy as it travels; therefore, the deposited energy of an alpha that escapes the copper and enters the detector could be anywhere between 0 and 5.3 MeV. The goal

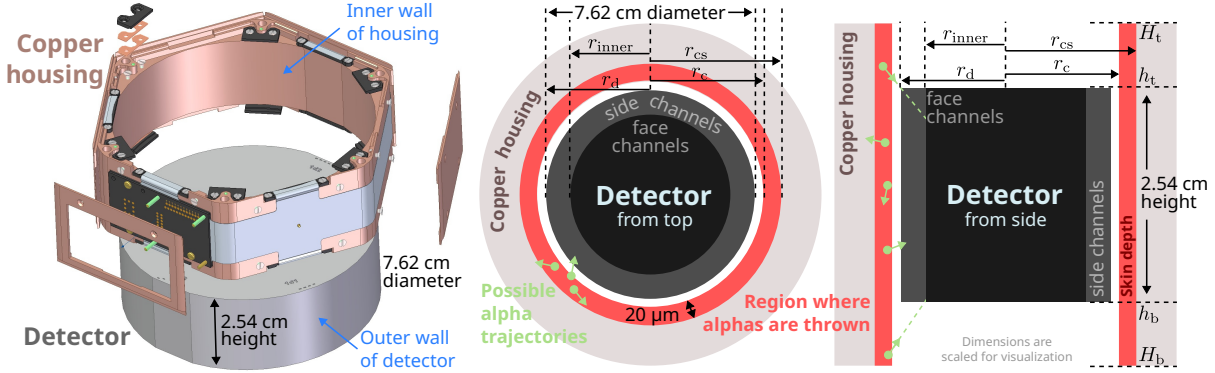


Figure 3.8: **Left:** An exploded-view rendering of a SuperCDMS SNOLAB detector within its copper housing, which is very similar to the Soudan detector and housing (with the inside surface of the Soudan housing being hexagonal instead of circular). The figure is reprinted from [69]. The Soudan detector is very nearly cylindrical, with a diameter of $2r_d = 7.62$ cm and height of 2.54 cm. **Middle:** Shown from the top down, the toy MC randomly places ^{210}Po alpha decays within $r_{\text{cs}} - r_c = 20 \mu\text{m}$ (red region) of the copper housing (light brown). Some of the trajectories of these alphas may be incident on the detector (black region). Three possible alpha trajectories are shown with initial and final locations denoted as a dot and arrow respectively. **Right:** Similar to the middle diagram, but shown from the side. Five possible alpha trajectories are shown.

of this section is to estimate the shape of the recoil energy spectrum produced by these buried alphas.

A toy Monte Carlo simulation (MC) is used to estimate the shape of the energy spectrum produced (in the outer charge channel) by ^{210}Po embedded in the copper housing bulk. The toy MC consists of five major parts: (1) generate random locations for ^{210}Po decays that are uniformly distributed within the copper housing, (2) assign an isotropically-random direction to the alpha produced by each decay, (3) calculate the trajectory of each alpha and determine whether it is incident on the detector, (4) calculate the distance each incident alpha traveled through the copper, (5) estimate the remaining kinetic energy of each incident alpha. Face events (*i.e.*, events impacting on the face of the detector) are predicted to be about 2% of the total incident events from this simulation and are thus ignored in this analysis.

Illustrated by the middle and right of Fig. 3.8, the detector and copper housing geometry can be closely approximated by an inner cylinder (the detector) enclosed in a cylindrical shell (the copper housing). The copper housing has a radius $r_c = 4.31$ cm,

and has been given a larger height ($H_t - H_b = 3.54\text{ cm}$) such that it extends both above and below the detector centered within it by 0.5 cm . This ensures that alphas that escape the copper housing just above the top of the detector (where they would have line-of-sight) have a chance to be counted. The detector is approximately a cylinder with radius $r_d = 7.62/2 = 3.81\text{ cm}$ and height of $h_t - h_b = 2.54\text{ cm}$. The region of the copper housing that will be populated by ^{210}Po decays has a skin depth (*i.e.*, the distance into the surface) starting at the inner surface of the housing r_c and extending into the copper to $r_{cs} \equiv r_c + 20\text{ }\mu\text{m}$; this skin depth is about twice the maximum distance that a 5.3 MeV alpha can travel in copper $R_{\max} \equiv 10.996\text{ }\mu\text{m}$.

An alpha particle created inside copper bulk with some initial kinetic energy has a maximum distance (or range) it can travel, as its energy is lost through nuclear and electronic scattering on copper nuclei. The amount of energy lost by an alpha is primarily through the electronic interaction and depends on its kinetic energy, though both types of energy loss are used in the Toy MC. With each collision (scattering event), the alpha's momentum changes, resulting in it slowing down and/or changing direction; these effects are often called *longitudinal* and *lateral straggling* respectively and depend on the alpha's kinetic energy. For a 5.3-MeV alpha, longitudinal and lateral straggling are both around 5% of the maximum range, increasing to about 100% as the initial kinetic energy approaches zero [74]. As an approximation, the toy MC ignores longitudinal and lateral straggling.

The deposited energy spectrum depends on the copper surface roughness (*i.e.*, the average deviation from a reference plane). If the surface is rough (having valleys and peaks with varying separation sizes similar to the maximum range of the alpha), an alpha may pass through a peak as it leaves the surface and lose additional energy. This effect creates a low-energy tail on the Gaussian distribution representing the reconstructed deposited energy spectrum of surface alphas [75, 76]. The surface roughness of milled copper $R \approx 0.66\text{ }\mu\text{m}$ [75]. The inner surface of the Soudan copper housing is expected

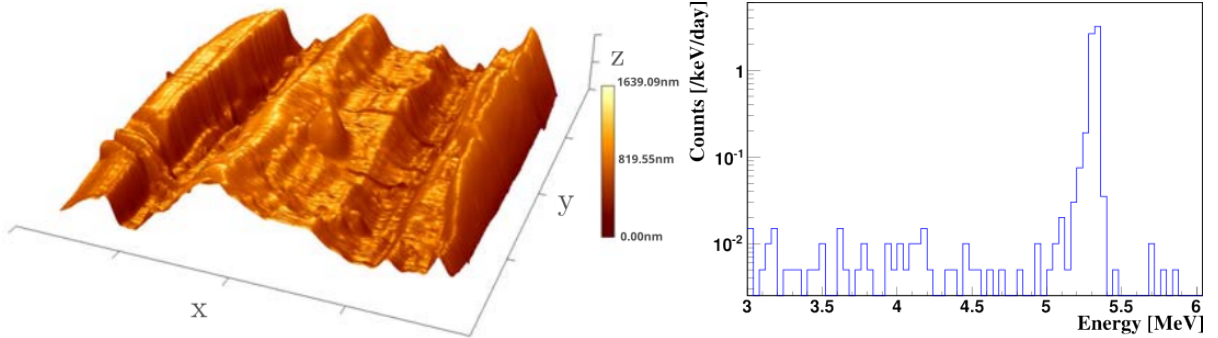


Figure 3.9: Simulated energy spectrum for ^{210}Po alphas originating on the surface of milled copper. This figure is reprinted from [75], with the permission of AIP Publishing. **Left:** Atomic force microscope (AFM) image showing the surface of milled copper with average roughness $R = 0.66 \mu\text{m}$. **Right:** The simulated energy spectrum of ^{210}Po alphas originally implanted (tens of nanometers) in the copper surface. Some alphas pass through copper hills and, in doing so, lose some of their kinetic energy; this results in a low-energy tail (between 0 and 5.3 MeV). The fraction of events in this tail region is only about 1% of those in the peak region centered at 5.3 MeV.

to have a surface roughness not worse than a milled finish (as indicated by Fig. 3.9, reprinted from [75]). Therefore, the fraction of events in the tail is expected to be only about 1% (small compared to that observed, implying that most events in the low-energy tail are from buried alphas) and is thus ignored in this work.

Three Soudan detectors were positioned face-to-face within each detector tower. This simulation is for a single detector, with the copper housing extending both above and below the detector (see the right side of Fig. 3.8); this approximation has only one effect: inner events may be slightly overestimated, as many of the line-of-sight, incident alphas would presumably have interacted with material above or below the detector, however this strengthens our reasoning for ignoring inner events. For outer events, having more line-of-sight alphas only increases the rate of incidence but does not impact the predicted shape of the deposited energy spectrum (the important result of the simulation), as will be shown later in this chapter.

Because vacuum is held within the copper housing, once an alpha with an incident trajectory leaves the copper it is not expected to interact and can travel any distance to the detector. The trajectory of each alpha is presumed to be linear, and its final location

\vec{x}_f is described by the vector

$$\vec{x}_f = \vec{x}_i + \ell \hat{u}, \quad (3.10)$$

where \vec{x}_i is the alpha's initial location (in the copper), the trajectory length is ℓ , and the alpha's direction is \hat{u} . A trajectory length of $\ell = r_{\text{cs}}$ is sufficiently long (and not too long) that any incident direction will have a final location within the detector radius; with this presumed trajectory length, a selection for possibly-incident events is made by checking whether \vec{x}_f is within the the detector radius r_d (with $x, y = 0$ at the center of the detector):

$$\sqrt{x_f^2 + y_f^2} \leq r_d. \quad (3.11)$$

A trajectory that terminates at the inner surface of the copper housing is described by the condition

$$\sqrt{(x_i + \ell u_x)^2 + (y_i + \ell u_y)^2} = r_c, \quad (3.12)$$

where ℓ is distance that an alpha would have to travel through the copper. Requiring that $\ell \leq R_{\text{max}}$ further reduces the selected events. The trajectory length is solved for as

$$\begin{aligned} (x_i + \ell u_x)^2 + (y_i + \ell u_y)^2 &= r_c^2 \\ (u_x^2 + u_y^2) \ell^2 + (2u_x x_i + 2u_y y_i) \ell + (x_i^2 + y_i^2 - r_c^2) &\equiv a\ell^2 + b\ell + c = 0 \\ \rightarrow \ell_{\pm} &= \frac{-b \pm \sqrt{b^2 - 4ac}}{2a}, \end{aligned}$$

where the physical solution is $\ell = \ell_-$ (the negative solution). A similar calculation is used to determine the length of trajectories terminating on the surface of cylindrical shells with other radii (described next).

The incidence criterion is that a trajectory must pass through either the outer sidewall of the detector or the cylindrical shell at r_{inner} , separating the side and face channels, and be within the bottom h_b and top h_t of the detector in the z direction. The incidence

criterion in mathematical terms is to require

$$h_b \leq z_f \leq h_t, \quad (3.13)$$

where

$$z_f = z_i + \ell u_z \quad (3.14)$$

with ℓ solved from

$$\sqrt{(x_i + \ell u_x)^2 + (y_i + \ell u_y)^2} = r_d, \quad (3.15)$$

the sidewall-intersection condition. Or, if the sidewall-intersection condition has no solution, the innerwall-intersection condition is checked:

$$\sqrt{(x_i + \ell u_x)^2 + (y_i + \ell u_y)^2} = r_{\text{inner}}. \quad (3.16)$$

In both cases, the negative solution of ℓ is the physical one. The sum of the number of incident events passing the sidewall- and innerwall-intersection conditions represent the total number of events having trajectories passing through the detector's side volume (and thus might be measured in the Soudan detector's outer channels).

Figure 3.10 shows a 3D scatter plot representation of the toy MC, but run with a reduced number of events ($N = 1000$) and with the skin depth increased from $20 \mu\text{m}$ to 1 cm and the maximum range R_{\max} increased from $10.996 \mu\text{m}$ to 0.5 cm to improve visibility. After running the toy MC with 10 million events and the correct geometry, the two histograms in Fig. 3.11 show the number of incident events (trajectories passing the incidence criterion, Eq. 3.13) is 953,778 (about 9.5% of those thrown). As a sanity check, the left-side histogram confirms that the rate of incident events is largest for alphas originating closest to the detector (that is, nearest to the copper housing's inner surface). An important result of the toy MC is the distribution of distance traveled through the copper housing by incident alphas (calculated by solving Eq. 3.12 for ℓ), as the distance traveled by an alpha particle through material is related to its remaining kinetic energy.

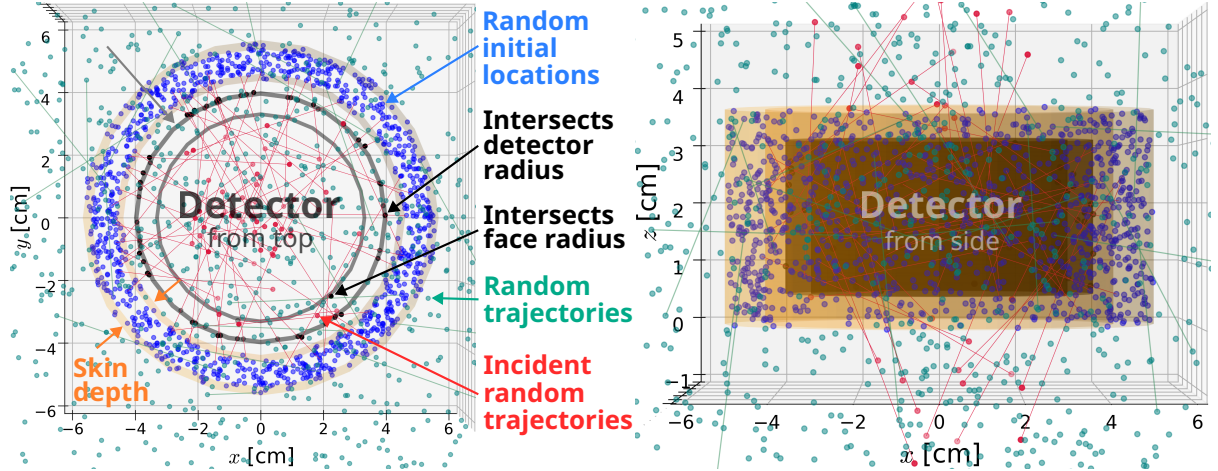


Figure 3.10: A 3D scatter plot viewed from the top (left) and side (right) representing the toy MC for buried ^{210}Po alphas is shown, but with $N = 1000$ and the skin depth and maximum range R_{\max} scaled to improve visibility. The initial location of each ^{210}Po decay is distributed randomly throughout the first $20 \mu\text{m}$ (twice the maximum range of a 5.3 MeV alpha) of the copper housing (blue dots). An isotropically-random direction is assigned to each initial location that produces a random trajectory (teal lines and dots, with only 20 lines drawn for clarity). Trajectories that intersect the cylindrical shells at the detector's radius r_d or the inner face radius r_{inner} , which separates the side and face channels, are called incident events (black circles); the termination points of these incident events given a trajectory length of r_{cs} are shown as red dots, with red lines connecting origins to corresponding ends.

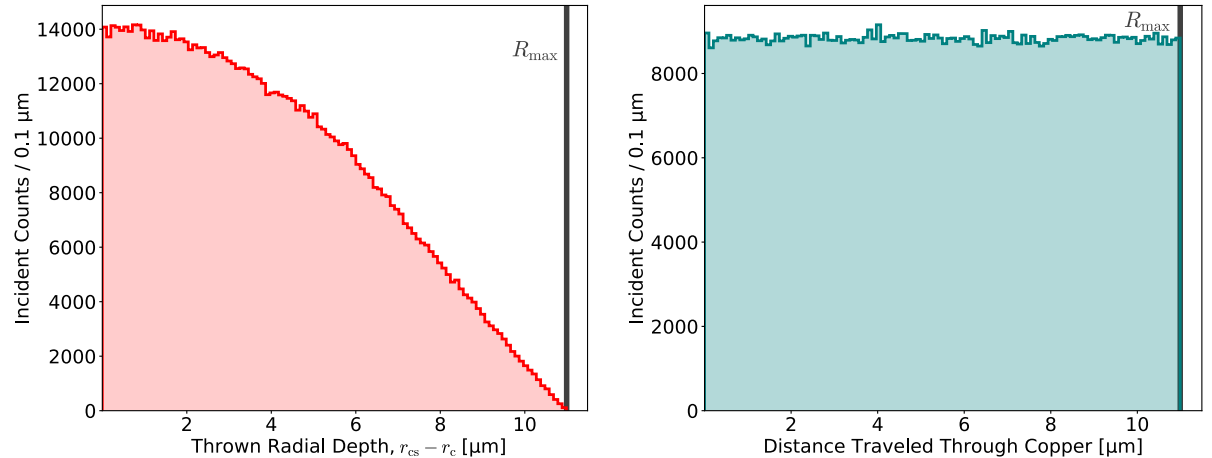


Figure 3.11: Left: For $N = 10^7$ randomly generated events, the number of incident trajectories is shown as a function of the initial depth $r_{\text{cs}} - r_c$ the alpha was located within the copper housing. As expected, the maximum initial depth of an incident alpha is the maximum range of a 5.3 MeV alpha in copper $R_{\max} = 10.996 \mu\text{m}$. **Right:** The distribution of distances that incident alphas travel through the copper is approximately flat; this is because the probability of an alpha decay in the copper is uniform over depth.

As expected, the distribution is essentially flat; for any incident trajectory, the probability is the same for any distance traveled not larger than R_{\max} , as the alphas are distributed

uniformly within the copper. The only exception is for trajectories originating close to the top or bottom of the copper housing, where the boundary of the copper volume restricts the possible implantation depth to be smaller than R_{\max} (shown to be negligible by this simulation).

The Soudan detection efficiency for alphas buried in the surrounding copper housing may now be estimated. From all thrown events (within the 20 μm copper skin depth), those with an initial depth $\leq R_{\max}$ are selected, representing the total number of events that *could* enter the detection volume, with their count denoted as N_{could} . The detection efficiency for buried alphas is calculated by dividing the total number of events that *did* enter the detector, N_{did} , by the number that could, N_{could} :

$$\epsilon_{\text{Cu}} = N_{\text{did}}/N_{\text{could}} = 954,746/5,496,486 = 0.1737 \pm 0.002 = 17.37 \pm 0.2\%, \quad (3.17)$$

where the quoted uncertainty is for 1σ . For this simulation, $N_{\text{could}} = 5,496,486$ and $N_{\text{did}} = 954,746$.

James F. Ziegler of the United States Navy Academy's Department of Physics has written software that describes the **S**topping and **R**ange of **I**ons in **M**atter (SRIM) [74]. Using SRIM, the projected range R of an alpha particle (*i.e.*, a helium ion) passing through copper is provided as a function of the alpha's energy E , as shown by Fig. 3.12. The projected range versus energy is interpolated (using `scipy.signal.interp1d` in Python with its cubic method) as the function f , yielding $R = f(E)$, which predicts the maximum distance an alpha will travel in the copper when starting with the energy E . Referring to the left plot of Fig. 3.12, a 5.3-MeV alpha has a maximum range R_{\max} . After the alpha travels the distance R_i in the copper, its remaining range is $R_{\max} - R_i$, which corresponds to the kinetic energy defined by $R_{\max} - R_i = f(E)$. Therefore, the remaining kinetic energy $E_{\text{rem},i}$ of an alpha that traveled the distance R_i is calculated by taking the inverse of the fitting function f :

$$E_{\text{rem},i} = f^{-1}(R_{\max} - R_i), \quad (3.18)$$

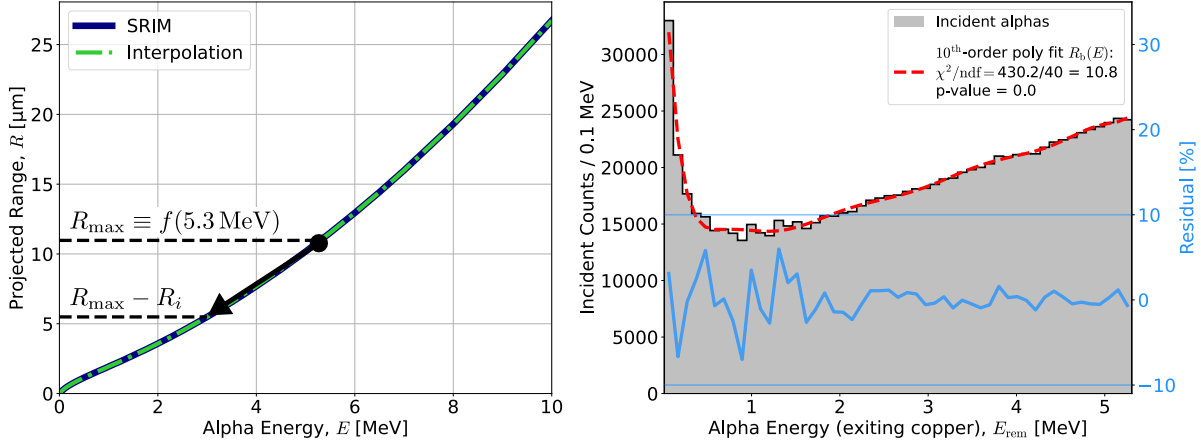


Figure 3.12: **Left:** The projected range R of an alpha particle in copper is a function of the alpha's kinetic energy E (thick, solid curve), as provided by the SRIM software [74] (containing 79 points, with a much higher density of points at low energy to better describe the Bragg peak). Producing an interpolation function f to the projected range yields a functional dependence $R = f(E)$, with $R_{\max} = f(5.3 \text{ MeV})$ being the maximum range that a 5.3-MeV alpha can travel through copper. **Right:** The remaining kinetic energy of an alpha E_{rem} after traveling a distance R_i through the copper is found by taking the inverse of f : $E_{\text{rem},i} = f^{-1}(R_{\max} - R_i)$. The remaining energy of alphas randomly-generated by the toy MC, based on their calculated distances R_i traveled through the copper housing, is shown as a histogram (shaded region)—this is the energy spectrum a detector is expected to measure due to alphas buried in the copper housing. A 10th-order polynomial $R_b(E)$ fit to the E_{rem} distribution agrees to within 10%, as shown by their residuals (right axis). Due to the histogram statistics, it is clear that the fit differs systematically from the data, with $\chi^2/\text{ndf} = 430.2/40 = 10.8$ and p-value of 0.0.

where the maximum range of a ^{210}Po alpha $R_{\max} = f(5.3 \text{ MeV})$. Because the SRIM curve in the left plot of Fig. 3.12 is a single-valued function, the inverse of f may be similarly inferred by interpolation, but with the axes switched: $x, y \rightarrow y, x$. The right side of Fig. 3.12 shows the rate of incident alphas as a function of their remaining kinetic energy E_{rem} ; the shape of this distribution is the expected recoil energy spectrum measured by the SuperCDMS Soudan detectors produced by alphas buried in the surrounding copper housing.

The shape of the energy spectrum produced by buried alphas shows a minimum event rate around 1 MeV, with the rate increasing sharply as the alpha energy approaches zero. This can be understood by looking more closely at the energy loss of an alpha particle traveling through material (referred to as the Bragg curve [77]). The left plot of Fig. 3.13 shows the remaining kinetic energy of an alpha (calculated by Eq. 3.18) as a function of

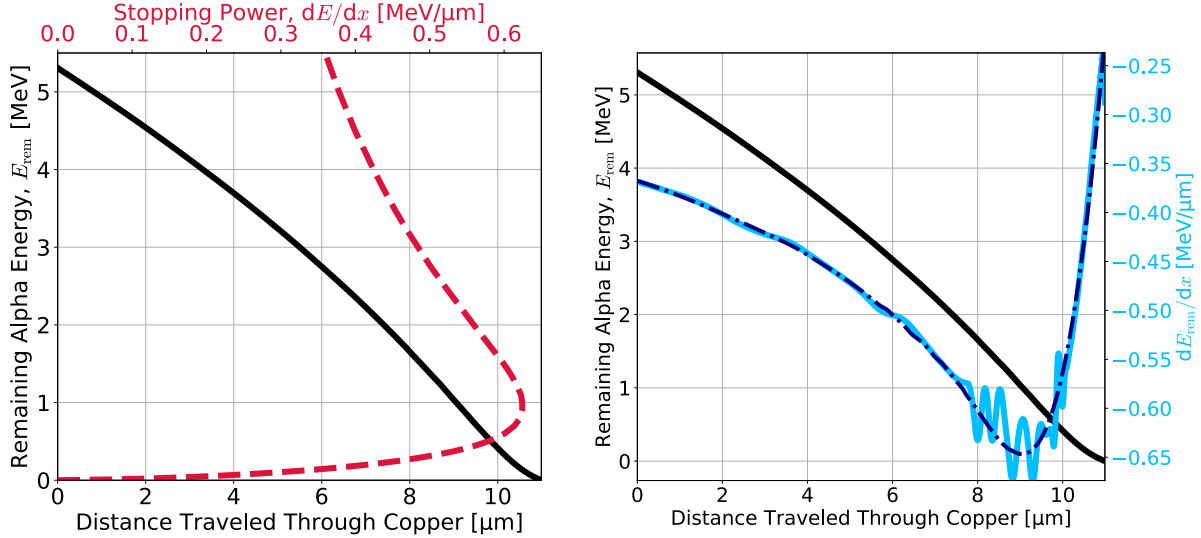


Figure 3.13: **Left:** The remaining kinetic energy of an alpha (calculated by Eq. 3.18) as a function of its distance traveled through copper (black curve) is compared with the electronic component of its stopping power (red curve), with the negligible nuclear component ignored. **Right:** Similar to the left plot, the remaining kinetic energy versus distance traveled (black curve) is compared with the change in the remaining energy over distance dE_{rem}/dx (blue curve), which has been smoothed out (dashed curve) to correct inaccuracies of the interpolation method employed in obtaining the inverse function of Eq. 3.18. The stopping power dE/dx is equivalent to dE_{rem}/dx , but plotted versus the kinetic energy of the alpha instead of the distance traveled (where it is called the Bragg curve, but usually with a minus sign: $-dE_{\text{rem}}/dx$); the latter may better inform an expectation for the energy spectrum of buried alphas, as it shows a maximum energy loss at around 9 μm, with a sharp decrease in lost energy for the last $\approx 2 \mu\text{m}$ of the maximum range R_{\max} .

its distance traveled through copper. Also drawn on this plot is the absolute energy loss dE/dx (referred to as the stopping power), which shows that an alpha will lose more energy per distance traveled for decreasing alpha energy until a maximum is reached at about 1 MeV; below 1 MeV, the change in energy dE/dx drops off sharply as the alpha's energy approaches zero. The right plot of Fig. 3.13 is similar to the left plot, but with the change in the remaining alpha energy over distance traveled dE_{rem}/dx drawn. From this plot, it may be more easily seen that the alpha particle increasingly loses energy until it has traveled about 9 μm through the copper. For the remaining $\approx 2 \mu\text{m}$, the energy loss in the material is increasingly reduced as the alpha approaches its projected range R_{\max} . Therefore, we may expect that the rate of alphas with about 1 MeV of remaining energy

should be minimal, with the rate increasing for those with smaller ($< 1 \text{ MeV}$) and larger ($> 1 \text{ MeV}$) energies.

Let the incident counts versus distance traveled through copper (right plot of Fig. 3.11) be denoted as $P(R)$ and the incident counts versus the alpha energy (right plot of Fig. 3.12) be denoted as $g(E)$. The alpha energy E is related to the distance traveled through the copper according to the interpolation of the SRIM data (left plot of Fig. 3.12), where $E = f^{-1}(R) \equiv h(R)$. Since the transformation $h(R)$ is one-to-one [78],

$$g(E)dE = P(R)dR. \quad (3.19)$$

With $dE/dR = h'(R)$,

$$g(E) = \frac{P(R)}{|h'(R)|}. \quad (3.20)$$

Because $P(R)$ is essentially constant for all R , this simplifies to

$$g(E) = \frac{c}{|h'(R)|} = \frac{c}{|\frac{d(f^{-1}(R))}{dR}|}, \quad (3.21)$$

where c is a constant. For this work, $g(E)$ has been determined by simply fitting the spectrum on the right side of Fig. 3.12, as the interpolation function $f^{-1}(R)$ has a somewhat noisy first derivative (seen in right plot of Fig. 3.13).

Fitting a 10th-order polynomial to the predicted detected energy spectrum of buried alphas yields an analytic form of the distribution's shape. The fitting function is defined for $E \leq 5.3 \text{ MeV}$ as

$$R_b(E) = a_{10}E^{10} + a_9E^9 + \cdots + a_1E + a_0, \quad (3.22)$$

where a_i for $i = 0, 1, \dots, 10$ are fitted parameters and have units of $1/(\text{MeV})^{(i+1)}$; with the function normalized to unity (dividing by 9.55×10^5), their values are:

$$\begin{aligned}
a_0 &= 0.0431 \pm 0.0003 & a_6 &= 0.126 \pm 0.008 \\
a_1 &= -0.182 \pm 0.004 & a_7 &= -0.029 \pm 0.002 \\
a_2 &= 0.49 \pm 0.02 & a_8 &= 0.0042 \pm 3 \times 10^{-4} \\
a_3 &= -0.72 \pm 0.03 & a_9 &= -3.4 \times 10^{-4} \pm 3 \times 10^{-5} \\
a_4 &= 0.63 \pm 0.03 & a_{10} &= 1.2 \times 10^{-5} \pm 10^{-6} \\
a_5 &= -0.35 \pm 0.02
\end{aligned}$$

This function will likely need to be scaled to match the absolute rate of the energy spectrum to which it is fit. The fit agrees to within 10%, as shown by their residuals (shown in Fig. 3.12). Due to the histogram statistics, it is clear that the fit differs systematically from the data, with $\chi^2/\text{ndf} = 430.2/40 = 10.8$ and p-value of 0.0. Nonetheless, this fit (Eq. 3.22) is expected to be sufficient for the purpose of predicting the shape of the energy spectrum due to detecting alphas initially buried within the copper housing to within $\sim 10\%$.

3.5 Improved Estimates of Buried and Surface ^{210}Pb Contamination

With the predicted shape of the energy spectrum for buried alphas (developed in Section 3.4), an improved fitting function is applied to the recoil energy spectrum of selected alphas. The Gaussian part $G(E_r)$, given by Eq. 3.4, still represents the ^{210}Po decays on the detector's surface, or the inner surface of the copper housing and/or other surrounding materials (such as the DIBs).

The predicted spectrum for buried alphas $B(E_r)$ has the shape given by $R_b(E_r)$ (Eq. 3.22), but with two important changes: (1) it is scaled by the constant A_b to match the event rate of the selected alpha spectrum and (2) it is convoluted with a normalized Gaussian distribution $\bar{G}(E_r)$ centered at $E_{1/2}$ (the middle of the energy space

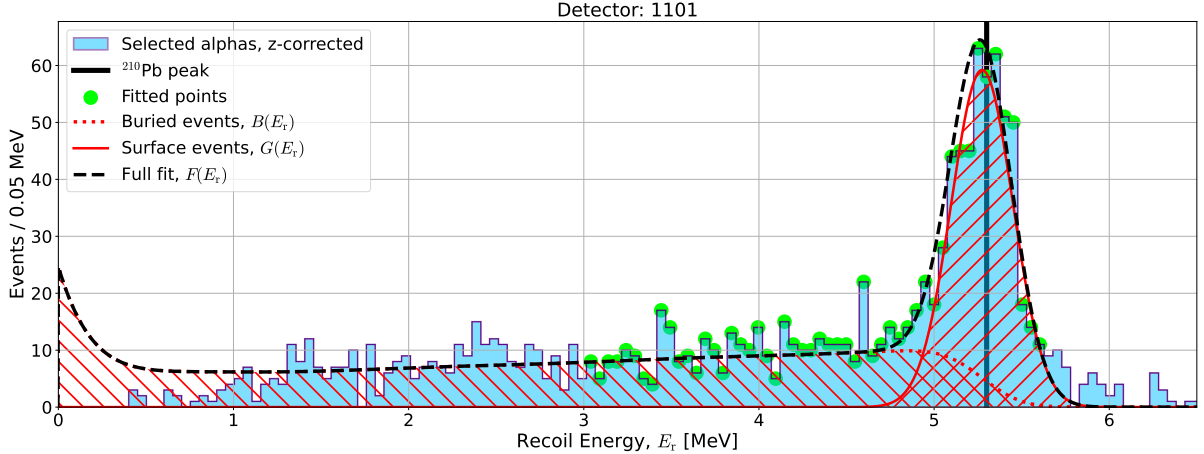


Figure 3.14: Similar to Fig. 3.7, the z -corrected energy spectrum for selected alphas is fit by the predicted spectrum model $F(E_r)$ (black, dashed curve) described by Eq. 3.23. The model is fit to the recoil energy spectrum above 3 MeV (green circles), yielding $\chi^2/\text{ndf} = 56.4/48 = 1.17$ and $p\text{-value} = 0.19$. The full fit is shown decomposed into its surface (right-hatched region) and buried (left-hatched region) parts.

being integrated over, as required by `scipy.signal.convolve`) and sharing the same σ as $G(E_r)$. Implementing each of these changes to $R_b(E_r)$ and adding in the Gaussian part yields

$$F(E_r; A, \mu, \sigma, A_b) = G(E_r; A, \mu, \sigma) + B(E_r; A_b), \quad (3.23)$$

where

$$B(E_r) = \int_{-\infty}^{+\infty} \tilde{R}_b(\eta) \overline{G}(E_r - \eta; E_{1/2}, \sigma) d\eta \quad (3.24)$$

and

$$\tilde{R}_b(E_r) = A_b \times R_b(E_r) \Theta(\mu - E_r), \quad (3.25)$$

where Θ is the Heaviside function. The arguments of \overline{G} have made explicit in Eq. 3.24 as a reminder that the normalized Gaussian shares σ with G but is centered at $\mu = E_{1/2}$, the middle of the energy space. The spectrum function Eq. 3.23 has units of counts per energy. Figure 3.14 shows the same recoil energy spectrum as Fig. 3.7, but now fit by the improved model $F(E_r)$ for surface and buried events. As discussed in Section 3.2, the selection of outer alphas has a passage fraction of nearly 100% with almost no leakage of

gammas beyond 3 MeV (due to their 2.6 MeV end point). Because the improved model describes buried and surface ^{210}Po alphas only, events with energies beyond the ^{210}Po peak distribution are excluded by a cut at $\mu + 2\sigma$, with μ and σ both obtained by Eq. 3.2 as done in Fig. 3.7. Therefore, the recoil energy spectrum is fit by $F(E_r)$ between 3 MeV and $\mu + 2\sigma$, with goodness-of-fit statistics $\chi^2/\text{ndf} = 56.4/48 = 1.17$ and p-value = 0.19.

The surface counts are inferred by

$$N_s = \sum_{i=0}^n G(E_i) \quad (3.26)$$

while the buried counts are inferred by

$$N_b = \sum_{i=0}^n B(E_i), \quad (3.27)$$

where the index $i = 0$ corresponds to a recoil energy $E = 0$ MeV, and the index $i = n$ corresponds to $E = 8$ MeV. The predicted spectrum Eq. 3.23 has the same number of bins as the measured spectrum during the fit. When calculated the number of counts from the best-fit predicted spectrum curve, a larger number of bins is used (to better represent the shape of the predicted spectrum); therefore, the fitting function Eq. 3.23 must have its units modified by the ratio of the predicted spectrum and measured spectrum (*i.e.*, the histogram) binsizes.

The inferred contamination using the improved spectrum model for buried and surface events is presented for detector 1101 in Table 3.3, where quoted values compared with those found earlier in this chapter (before and after the z -corrected energy calibration, and using a crude energy cut for buried and surface event selection). As expected, estimates of buried and surface contamination is within uncertainties before and after the z -corrected energy calibration. Estimates of the buried and surface contamination using the predicted spectrum model indicate a smaller surface contamination (by about 10%), and a larger buried contamination (by 15%).

Context	Location	Counts	Activity [μBq]	Contamination
Uncorrected energy	Faces	164 ± 13	10 ± 1	$164 \pm 13 \text{nBq/cm}^2$
	Sidewall	1324 ± 36	82 ± 9	$918 \pm 25 \text{nBq/cm}^2$
	→ Surface	574 ± 27	36 ± 1	$398 \pm 17 \text{nBq/cm}^2$
	→ Buried	750 ± 24	47 ± 2	$396 \pm 14 \text{mBq/kg}$
With z -dependent energy correction	Faces [†]	164 ± 13	10 ± 1	$164 \pm 13 \text{nBq/cm}^2$
	Sidewall [†]	1324 ± 36	82 ± 9	$918 \pm 25 \text{nBq/cm}^2$
	→ Surface	580 ± 27	36 ± 1	$402 \pm 17 \text{nBq/cm}^2$
	→ Buried	744 ± 24	46 ± 2	$393 \pm 14 \text{mBq/kg}$
Using the improved model [‡]	Sidewall	—	—	—
	→ Surface	521 ± 49	32 ± 3	$361 \pm 34 \text{nBq/cm}^2$
	→ Buried	874 ± 40	54 ± 2	$461 \pm 21 \text{mBq/kg}$

Table 3.3: Inferred ^{210}Po contamination for detector 1101. [†]These rows are identical to those for the uncorrected energy, but left here to show that the z -dependent energy correction did not change the inner-outer selection (as expected). [‡]This is the spectrum model predicted by toy Monte Carlo simulation, as discussed in Section 3.4. The surface areas of the Locations are provided in Table 2.1. The mass of copper within the skin-depth volume (from which ^{210}Po alphas may escape) is $3.38 \times 10^{-4} \text{ kg}$.

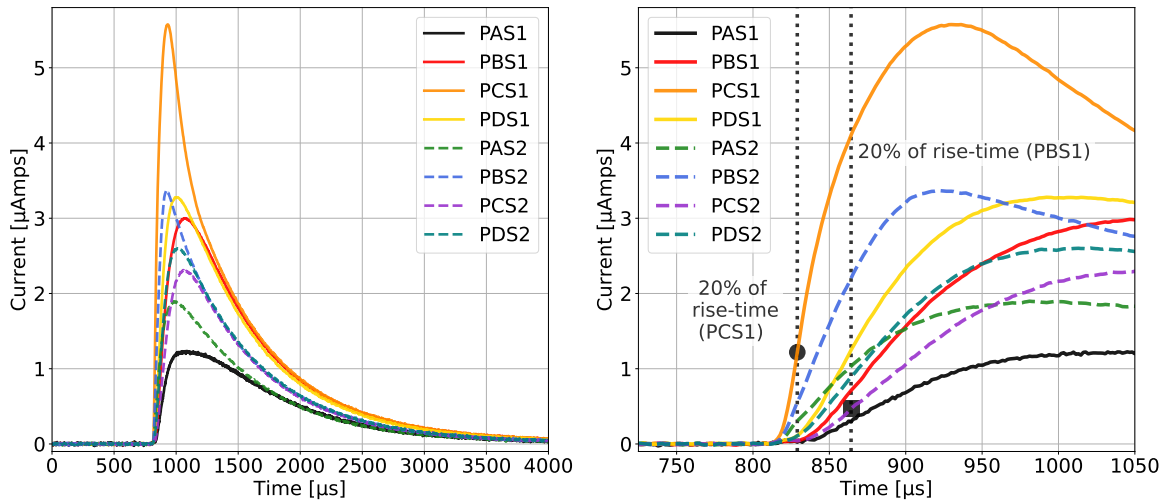


Figure 3.15: **Left:** Phonon pulses (S1: solid curves, S2: dashed curves) of an event in detector 1101 with an uncorrected recoil energy of 1.25 MeV. Phonon pulses are drawn for all eight channels (PAS1, PBS1, ..., PDS2); on each side, A is the outer channel and B, C, and D are the inner channels. **Right:** Similar to the left plot, but zoomed in to the rise-time region of the pulses. The rise-time at 20% of pulse maximum $t_{20\%}$ is used to obtain event position information. As examples, $t_{20\%}$ is shown for the PCS1 pulse (black circle) and the PCS2 pulse (black square).

3.6 Event Position Reconstruction from Phonons

Prompt phonons produced at the initial time of scattering are collected by phonon sensors on the detector faces. The rise-time of the measured phonon pulse in each channel depends on its proximity to the event location, as is illustrated by Fig. 3.15. As a measure of the time phonons reach the sensor, we use the time $t_{20\%}$ when the phonon pulse reaches 20% of its maximum value. For the inner channel C on side 1, the SuperCDMS RRQ for the 20% of rise-time is PCS1WKr20.

Using only the inner three phonon channels (as the outer phonon channel wraps completely around the detector face), the x and y positions on each side of the detector (S1 or S2) are reconstructed, for side 1, as T_x^{S1} and T_y^{S1} with units of μs :

$$T_x^{S1} \equiv -[\cos(150^\circ) \times \text{PBS1WKr20} + \cos(270^\circ) \times \text{PCS1WKr20} + \cos(30^\circ) \times \text{PDS1WKr20}] \times 10^6 \quad (3.28)$$

$$T_y^{S1} \equiv -[\sin(150^\circ) \times \text{PBS1WKr20} + \sin(270^\circ) \times \text{PCS1WKr20} + \sin(30^\circ) \times \text{PDS1WKr20}] \times 10^6 \quad (3.29)$$

Similarly, for side 2

$$T_x^{S2} \equiv -[\cos(330^\circ) \times \text{PBS2WKr20} + \cos(90^\circ) \times \text{PCS2WKr20} + \cos(210^\circ) \times \text{PDS2WKr20}] \times 10^6 \quad (3.30)$$

$$T_y^{S2} \equiv -[\sin(330^\circ) \times \text{PBS2WKr20} + \sin(90^\circ) \times \text{PCS2WKr20} + \sin(210^\circ) \times \text{PDS2WKr20}] \times 10^6. \quad (3.31)$$

The time reconstruction of position can be converted to distance by multiplying T_x^{S1} , for example, by the average speed of athermal phonons in Germanium (which is $\sim 0.1 \text{ cm}/\mu\text{s}$ by inspection). The angular positions θ_{S1} and θ_{S2} of an event can be obtained without any conversion, as follows:

$$\theta_{S1} \equiv \arctan(T_y^{S1}/T_x^{S1}) \quad (3.32)$$

$$\theta_{S2} \equiv \arctan(T_y^{S2}/T_x^{S2}), \quad (3.33)$$

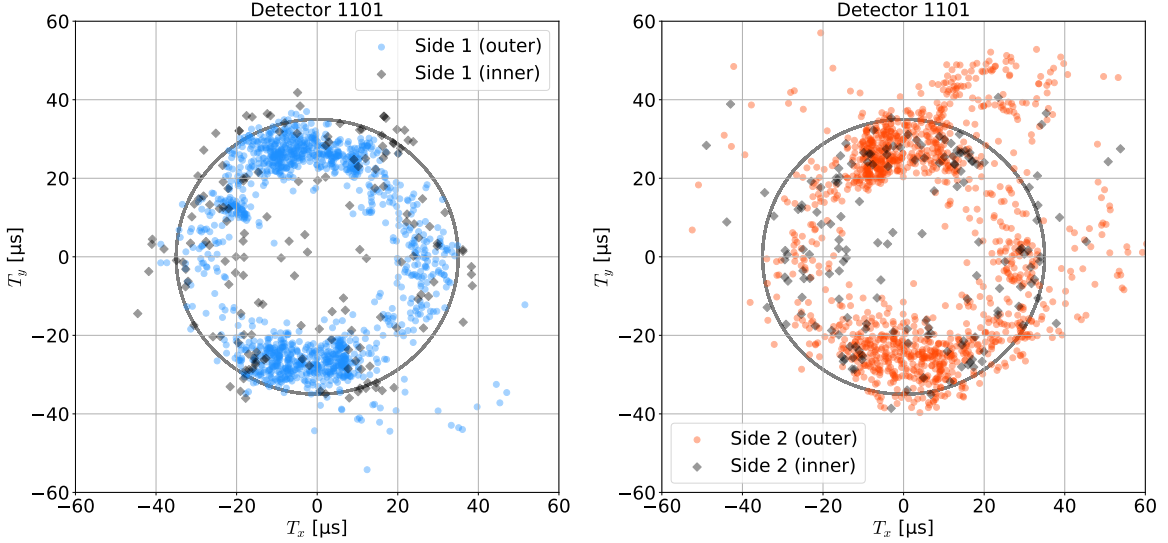


Figure 3.16: Position reconstruction (in units of microseconds) for inner (black squares) and outer (blue and orange circles) selected alphas for both side 1 (left) and side 2 (right), with the same events shown in both plots. A black ring roughly illustrates the outer shape of the Soudan detector, with outer events primarily near the ring and inner events more frequently near the center of the ring.

with the average angular position

$$\theta \equiv (\theta_{S1} + \theta_{S2})/2. \quad (3.34)$$

Figure 3.16 shows the reconstructed event positions (in time) for inner and outer alphas for both side 1 and 2. As expected, most outer event positions are reconstructed around an outer ring with a radius of about 35 μs, with more inner events within the middle of this ring. As is seen in the right plot of Fig. 3.16, the reconstruction is not perfect; this is expected to be due to saturation of some phonon channels resulting in the rise-time being miscalculated (as the pulse maximum is not correct, but lower due to saturation).

Figure 3.17 shows a diagram of the Soudan detector phonon channels (left) and the reconstructed event positions (in time) for only outer alphas for both side 1 and 2 (right). The phonon channel diagram emphasizes the fact that inner phonon channels on side 1 are rotated 180° with respect to the inner channels on the side 2, which improves the

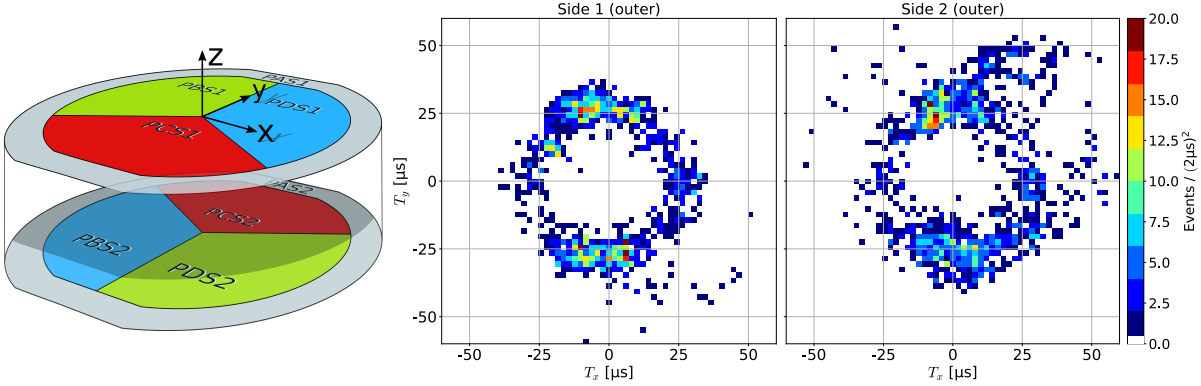


Figure 3.17: **Left:** This diagram of the Soudan iZIP phonon channels shows how the three inner channels on side 1 are rotated 180° with respect to those on side 2, providing robust event position reconstruction. **Right:** Event positions as a 2D histogram for the side 1 (left) and side 2 (right) face, showing an angular dependence on event rate when $|T_y| > 15 \mu\text{s}$.

position reconstruction. From the event position plots, one may observe a clear increase in event rate for two angular regions in particular.

As a brief review, the Soudan detector geometry is not quite cylindrical, as is described in Section 2.1.5. Each detector has two major flats, two minor flats, and one off-axis flat. The major and minor flats are regions where the detector sidewall was sheared off (and made flat). Both major flats are on opposite sides of the detector, with minor flats also on apposing sides but located at angles rotated by 90 degrees with respect to the major flats. As the names indicate, the major flats are larger than the minor flats, while the off-axis flat is similar in size to a minor flat.

Figure 3.18 shows event rate versus average event angle θ (as defined by Eq. 3.34). The major flat regions of the detector sidewall are bound between $\theta_1 = 70^\circ$ and $\theta_2 = 110^\circ$ and between $\theta_3 = -70^\circ$ and $\theta_4 = -110^\circ$. There are two important features in the angular event rate: (1) the event rate is roughly 4 times larger per bin in the major flat regions than otherwise and (2) the increase in the event rate in the major flat regions appears independent of detector side. In addition, there does not appear to be a significant increase in event rate at the minor flat regions (at $\theta = 0^\circ$ and $\theta = \pm 180^\circ$). The angular rate suggests that: (1) significant contamination exists at the locations of the major flat

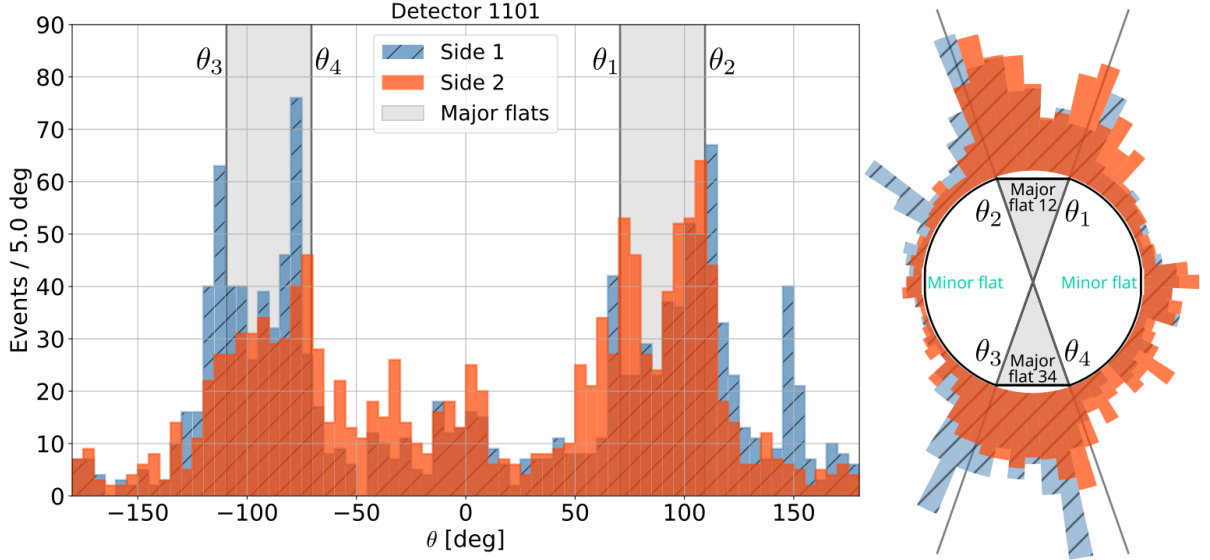


Figure 3.18: **Left:** The event rate for side 1 (orange) and side 2 (blue, hatched) strongly depends on the event angle θ (defined by Eq. 3.34), with around 4 times as many events per bin within the major flat regions as compared to outside those regions. **Right:** Similar to the left plot, the event rate versus angle θ is plotted around a cartoon of a Soudan detector (showing the two major flats). Agreement in the angular distribution between both sides suggests no nonlinearity in the position reconstruction due to the detectors having three (inner) phonon sensors (on each side).

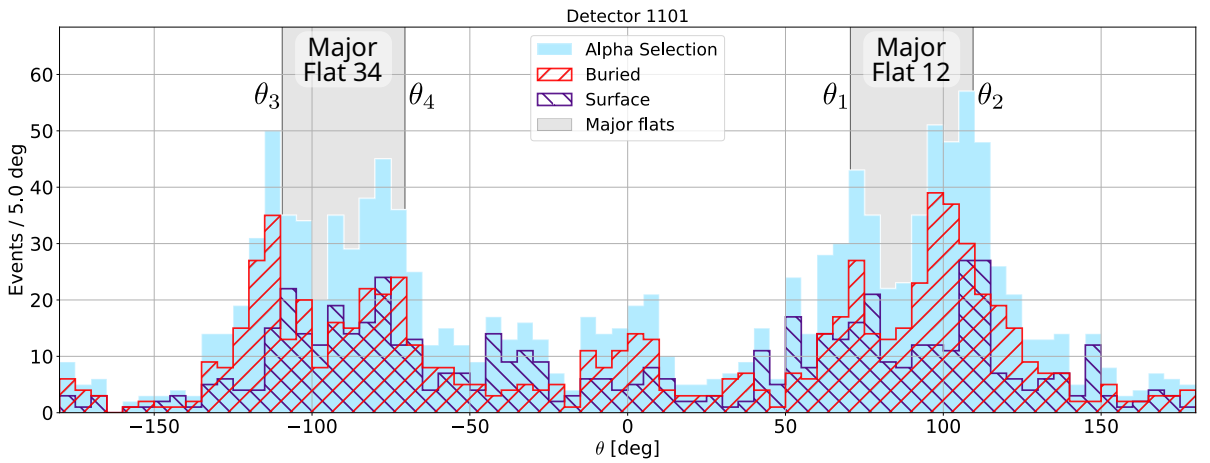


Figure 3.19: Event rate of outer selected alphas (blue filled region) versus angle θ . Both surface (red, right-hatched region) and buried (blue, left-hatched region) show an increased rate in the major flat regions.

regions and (2) the increased rate is unlikely from a source above or below the detector, as those events would be detected primarily on one side.

Figure 3.19 shows the event rate versus angle θ for both buried and surface events. The buried and surface events are selected by setting a cut on the recoil energy at $\mu - 2\sigma$,

Location	Counts	Activity [μBq]	Contamination
Major flat 12	—	—	—
→ Surface	88 ± 23	5 ± 1	$572 \pm 150 \text{nBq/cm}^2$
→ Buried	205 ± 19	13 ± 1	$1002 \pm 93 \text{mBq/kg}$
Major flat 34	—	—	—
→ Surface	113 ± 19	7 ± 1	$735 \pm 124 \text{nBq/cm}^2$
→ Buried	122 ± 16	8 ± 1	$596 \pm 78 \text{mBq/kg}$
Both major flats	—	—	—
→ Surface	221 ± 30	14 ± 2	$719 \pm 98 \text{nBq/cm}^2$
→ Buried	379 ± 27	24 ± 2	$926 \pm 66 \text{mBq/kg}$
Neither major flat	—	—	—
→ Surface	302 ± 31	19 ± 2	$209 \pm 21 \text{nBq/cm}^2$
→ Buried	336 ± 32	21 ± 2	$177 \pm 17 \text{mBq/kg}$

Table 3.4: Inferred ^{210}Po contamination on the sidewall of detector 1101 as a function of sidewall location using the improved spectrum model (see Eq. 3.23). Surface contamination is quoted with units of activity per area, while the buried (or bulk) contamination is quoted in activity per mass (in red for emphasis), presuming the contamination is in copper. The surface areas of the Locations are provided in Table 2.1. The mass of copper within the skin-depth volume (from which ^{210}Po alphas may escape) is $3.38 \times 10^{-4} \text{kg}$. The quoted uncertainties are obtained by evaluating the spectrum model with unique combinations of input parameters, with each parameter drawn from a normal distribution described by the best-fit value and standard deviation provided by fitting the spectrum model to the measured spectrum (as shown in Fig. 3.14).

with μ and σ defined by fitting Eq. 3.2 to the z -dependent, calibrated energy spectrum.

However, this selection method underestimates the number of buried events, as the alphas have a passage fraction of only about 50% below 3 MeV (as discussed in Section 3.2).

The buried and surface selections are improved upon using the improved spectrum model (see Eq. 3.23). First, alphas are selected according to the angle θ to form four groups:

- events between θ_1 and θ_2 , denoted **major flat 12**,
- events between θ_3 and θ_4 , denoted **major flat 34**,
- events in **both major flats**, and
- events in **neither major flat** (the detector sidewall, excluding the major flats).

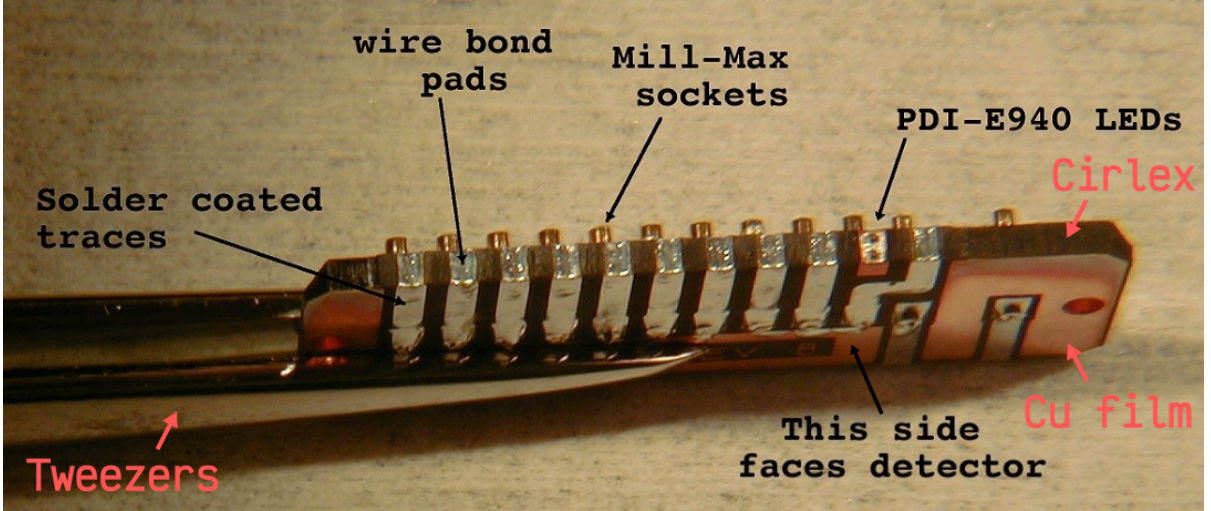


Figure 3.20: The detector interface board (DIB) is an electrical feed-through circuit used by SuperCDMS Soudan and are located between the detector and the detector housing at both major flat regions. Each DIB supports 12 connections: 8 for the bias and return lines, 2 for charge bias lines, and 2 for the DIB-mounted LEDs [79]. The DIB is made of 1.30 mm-thick CIRLEX with 0.036 mm-thick copper traces on each side [80]. Aluminum wire-bond pads are seen to extend along the detector-facing side. Figure courtesy of the SuperCDMS Collaboration.

Each group of events is fitted by the improved spectrum model (Eq. 3.23) to provide estimates of buried and surface events as a function of detector sidewall location; the results are presented in Table 3.4. An important subtlety is that there is significant increase in rate near (not only at) the major flat regions; this suggests that the counts inferred in the neither-major-flat region may overestimated (with some of those counts belonging to the major flat regions). The number of counts at regions of the detector sides far from the major flats appear to be $\sim 5\times$ lower than at regions close to the major flats (but not within them). The increased counts near the major flat regions is likely due to imperfect position reconstruction of events and is not expected to significantly impact the results of this analysis.

An important observation in the angular event rate is that the buried rate is similarly increased in the major flat regions as is the surface rate. It is suspected that the detector interface boards (DIBs) between the detector and the copper housing at the locations of the major flats were responsible for the increased rate. All detectors analyzed show an increased rate in the major flat regions.

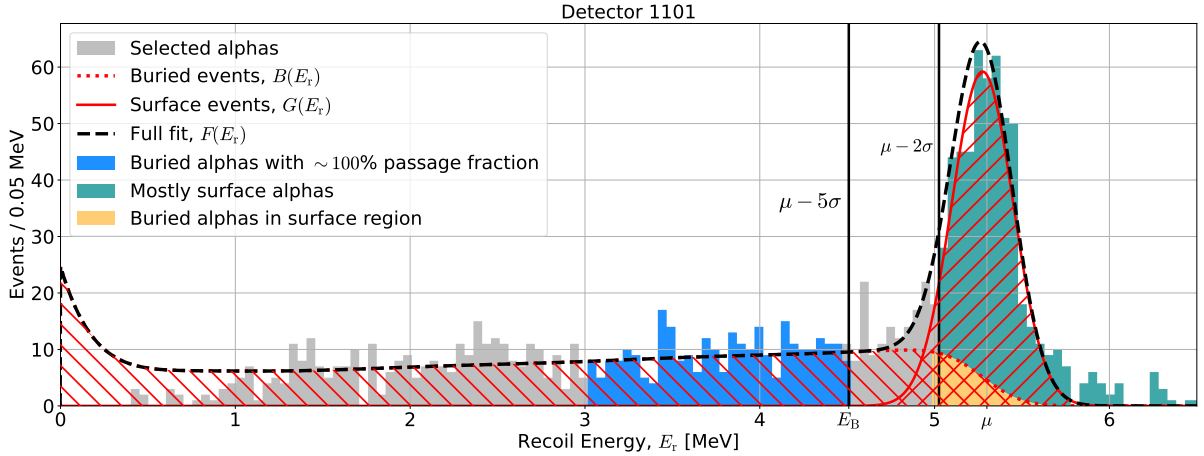


Figure 3.21: Similar to Fig. 3.14, but emphasizing the buried and surface event selection used for the time-series analysis. Buried events (blue region) are chosen by requiring $E_r \in [3, \mu - 5\sigma]$ MeV in order to minimize leakage of surface events and gammas and include only the part of the buried spectrum that has a 100% passage fraction. The surface events (green region) are chosen by requiring $E_r \geq \mu - 2\sigma$; buried events that leak in (yellow region) are subtracted out statistically later.

The spectrum model (developed in Section 3.4 and given functionally as Eq. 3.23) describes the deposited energy spectrum of alphas buried in the copper housing that encases the detectors. No attempt was made to account for the DIBs that exist at the major flat regions. As shown in Fig. 3.20, the DIBs are made from CIRLEX with a copper film on the detector-facing side (see [80]) and presumably have a surface roughness similar to a milled finish. The DIBs have 12 pads for wire bonding to the 8 phonon channels, 2 charge channels, and 2 for LEDs that are located on the DIBs. The energy spectrum expected from alphas buried in the DIBs will be different than assumed for copper. The low-energy tail could be partly caused by alphas on the surface of the DIBs, as described in Section 3.4. For this work, the DIBs are assumed to be made entirely of copper. The total rate (*i.e.*, from surface and buried alphas) at the location of the DIBs does not depend on the assumption that the DIBs are made of copper and can help guide the reduction of ^{210}Pb backgrounds for SuperCDMS SNOLAB (as discussed later in Section 3.9).

3.7 ^{210}Po Event Rate Versus Time

The time-series analysis of the ^{210}Po event rate provides an estimate of the initial ^{210}Pb and ^{210}Po on and around the detectors. Referring to Fig. 3.21, buried events are selected to have minimal leakage from surface events while maximizing the passage fraction; this is achieved by selecting buried events with recoil energy between 3 MeV and $\mu - 5\sigma$. The buried event selection has efficiency

$$\epsilon_B = \frac{\mu_{\text{sel}}^B}{\mu_{\text{tot}}^B}, \quad (3.35)$$

where the number of counts in the selected buried region is μ_{sel}^B . The total number of counts inferred from the buried part of the spectrum model

$$\mu_{\text{tot}}^B = \sum_{i=0}^n B(E_i), \quad (3.36)$$

where the index $i = 0$ corresponds to a recoil energy $E = 0$ MeV, and the index $i = n$ corresponds to $E = 8$ MeV. The fitting function $B(E)$ represents the buried events spectrum defined by Eq. 3.23.

Still referring to Fig. 3.21, the surface events are selected roughly to maximize their selection efficiency while minimizing leakage of buried events; this is done by requiring the recoil energy $E_r \geq \mu - 2\sigma$. The surface selection efficiency

$$\epsilon_S = \frac{\mu_{\text{sel}}^S}{\mu_{\text{tot}}^S}, \quad (3.37)$$

where the number of counts in the selected surface region is μ_{sel}^S . The total number of counts inferred from the surface part of the spectrum model

$$\mu_{\text{tot}}^S = \sum_{i=0}^n G(E_i), \quad (3.38)$$

where $G(E)$ is the Gaussian distribution representing the surface events defined by Eq. 3.23. The index $i = 0$ corresponds to a recoil energy $E = 0$ MeV, and the index $i = n$ corresponds to $E = 8$ MeV. The buried events that leak into the surface selection (yellow region in plot) are subtracted off; however, the explanation for how this is done

is better described after presenting the model for event rate versus time, which is now discussed.

If at time $t = 0$ (the start of data taking, with t called the *wall time* in reference to a wall clock) the number of ^{210}Pb atoms on the detector (or in nearby materials) is N_{grow} , then the number of ^{210}Po atoms N_{Po} resulting from the decay of ^{210}Pb is obtained as a function of time from the Bateman equations [81]:

$$N_{\text{grow}}(t) \equiv N_{\text{Pb}} \frac{\lambda_{\text{Pb}}}{\lambda_{\text{Po}} - \lambda_{\text{Pb}}} [e^{-\lambda_{\text{Pb}}t} - e^{-\lambda_{\text{Po}}t}], \quad (3.39)$$

where the decay constants for ^{210}Pb and ^{210}Po are $\lambda_{\text{Pb}} = 8.55 \times 10^{-5} \text{ days}^{-1}$ and $\lambda_{\text{Po}} = 5.02 \times 10^{-3} \text{ days}^{-1}$ respectively. The intermediate decay to ^{210}Bi is ignored, as its half-life is only 5 days. The subscript ‘grow’ refers to an isotope (^{210}Po) growing in from a radioactive parent (^{210}Pb).

If the initial number of ^{210}Po atoms (at $t = 0$) is N_{Po} , the number of ^{210}Po atoms as a function of time is described by an exponential decay:

$$N_{\text{decay}} \equiv N_{\text{Po}} e^{-\lambda_{\text{Po}} t}. \quad (3.40)$$

The total number of ^{210}Po atoms as a function of time is the sum $N_{\text{grow}}(t) + N_{\text{decay}}(t)$. However, because the Soudan detectors are not always live (and capable of measuring an event) the detector live-time is included to obtain the ^{210}Po decay rate. The wall time t is discretized into time bins with duration $\Delta t = 30$ days. The number of counts in each bin is divided by the total live-time in each bin. If a bin contains a live-time of zero, there will also be zero counts, and the bin is excluded. The resulting counts per live-time is the ^{210}Po rate and is fit to by

$$R_{\text{Po}}(t; N_{\text{Pb}}, N_{\text{Po}}) \equiv R_{\text{grow}}(t; N_{\text{Pb}}) + R_{\text{decay}}(t; N_{\text{Po}}) \equiv \lambda_{\text{Po}} N_{\text{grow}}(t) + \lambda_{\text{Po}} N_{\text{decay}}(t), \quad (3.41)$$

where the number of ^{210}Po atoms are converted to a decay rate by multiplying by λ_{Po} .

The issue where the surface event selection contains some buried events, is now addressed: the number of ^{210}Pb atoms from the buried spectrum that leaks into the surface

selection is the best-fit number of ^{210}Pb atoms from the time-series fit to the buried events multiplied by the fraction of buried counts in the surface selection over the total number of buried counts:

$$N_{\text{Pb}}^B \times \frac{\mu_{\text{peak}}^B}{\mu_{\text{tot}}^B}, \quad (3.42)$$

where the best-fit number of ^{210}Pb atoms from the time-series fit to the buried events is N_{Pb}^B and

$$\mu_{\text{peak}}^B = \sum_{i=0}^n B(E_i), \quad (3.43)$$

where the index $i = 0$ corresponds to a recoil energy $E = 0 \text{ MeV}$, and the index $i = n$ corresponds to $E = 8 \text{ MeV}$. Therefore, the best estimate of the number of initial ^{210}Pb atoms inferred from surface events

$$N_{\text{Pb}}^S = N_{\text{Pb}} - N_{\text{Pb}}^B \times \epsilon_S, \quad (3.44)$$

where the best-fit number of ^{210}Pb atoms from the time-series fit of the surface selection is N_{Pb} . Similarly, the best estimate of the number of ^{210}Po atoms in the surface selection

$$N_{\text{Po}}^S = N_{\text{Po}} - N_{\text{Po}}^B \times \epsilon_B. \quad (3.45)$$

Figure 3.22 shows the ^{210}Po rate equation (Eq. 3.41) fit to all selected alpha events, as well as the surface events, buried events, and the surface and buried events only within the major flat regions. The time-series data plotted for each selection has been scaled by dividing the estimated number of selected counts by the corresponding selection efficiency. For all selected events, the selection efficiency

$$\epsilon_{\text{all}} = \mu_{\text{sel}}^{\text{all}} / \mu_{\text{tot}}^{\text{all}}, \quad (3.46)$$

where the total counts in the selection $\mu_{\text{sel}}^{\text{all}}$ is divided by the total inferred counts from the predicted spectrum model (buried plus surface), as given by Eq. 3.23. Already described, the efficiency for buried and surface rates are ϵ_B and ϵ_S respectively (refer to Eq. 3.35 and

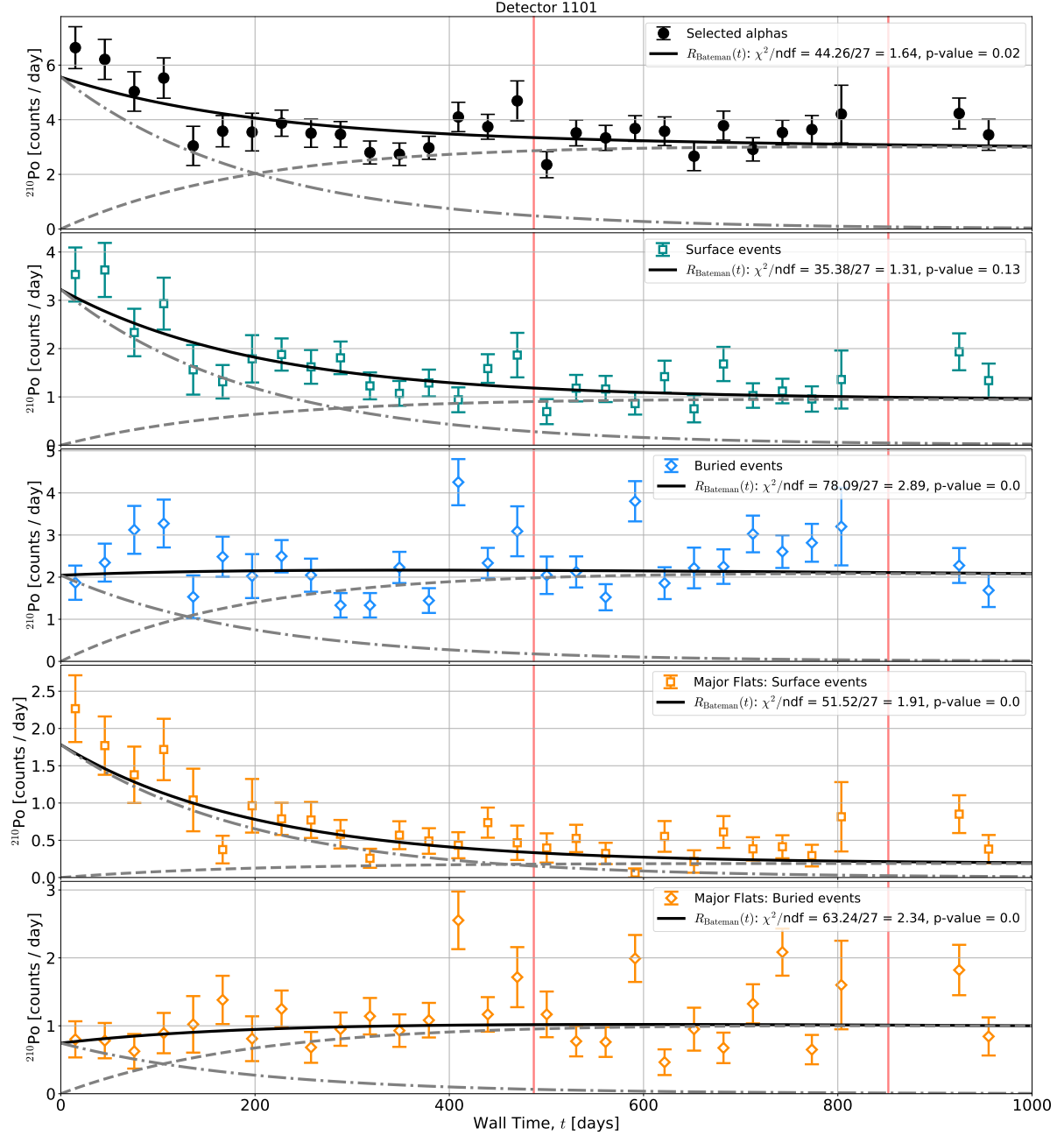


Figure 3.22: The inferred ^{210}Po rate (after correcting for data-selection cut inefficiencies) is shown (from top to bottom) for all selected alphas (black solid circles), surface (green open squares) and buried (blue open diamonds) alphas in the side region, and surface (orange open squares) and buried (orange open diamonds) alphas in the major flat regions (goodness-of-fit in the legends). These data have a binsize of 30 days, with red vertical lines separating science runs R133, R134, and R135.

Eq. 3.37). Similarly, Fig. 3.23 shows the event rate versus wall time for the sidewall region excluding both major flats (*i.e.*, the neither major flat region) and Fig. 3.24 for the inner

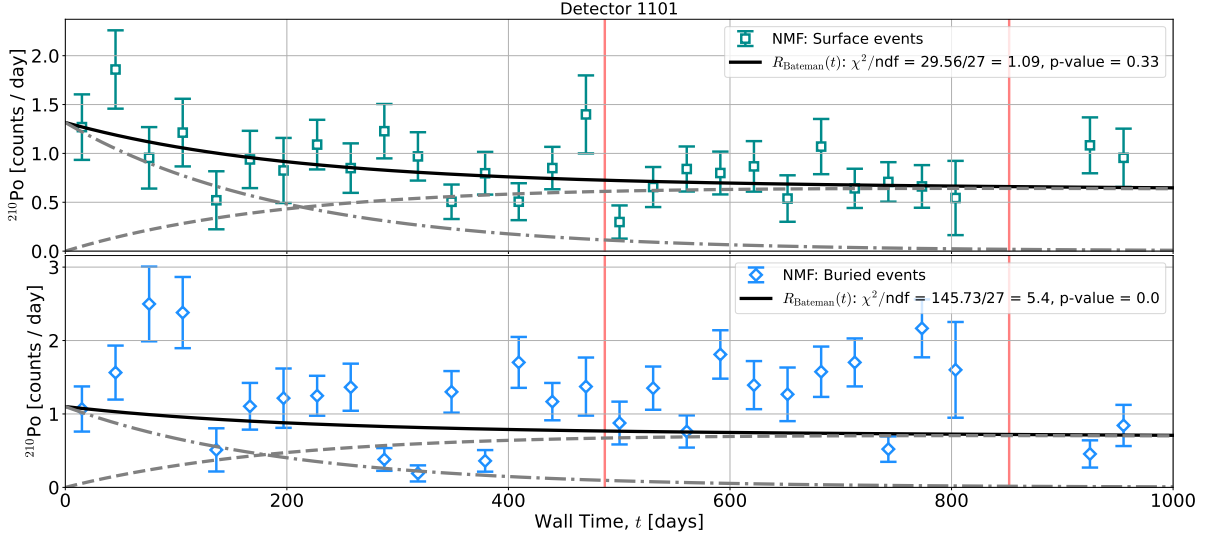


Figure 3.23: The inferred ^{210}Po rate (after correcting for data-selection cut inefficiencies) is shown for the sidewall regions, excluding both major flats, for both the surface (green squares) and buried (blue diamonds) events. The ^{210}Po rate equation (Eq. 3.41) is fit to these data (solid black curve), with the decay (dot-dashed curve) and growth (dashed curve) terms drawn as well. These data have a binsize of 30 days, with red vertical lines separating the three science runs (R133, R134, and R135).

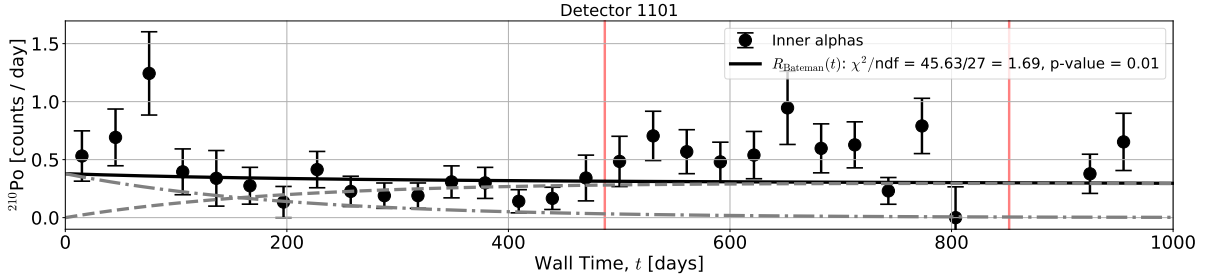


Figure 3.24: The inferred ^{210}Po rate (after correcting for data-selection cut inefficiencies) is shown for inner (face) events (black circles). The ^{210}Po rate equation (Eq. 3.41) is fit to these data (solid black curve), with the decay (dot-dashed curve) and growth (dashed curve) terms drawn as well. These data have a binsize of 30 days, with red vertical lines separating the three science runs (R133, R134, and R135). A system shift can be seen between science runs R133 and R134.

(face) events, as defined by the custom inner-event selection developed in Section 3.2 and shown in Fig. 3.3.

There are three features seen in the time-series data: (1) the surface selections have a decaying time-dependence (with detector 1111 being the one exception, shown in Appendix B); this indicates that initially more ^{210}Po was on the surface than ^{210}Pb , as is nominally expected from etching a surface to remove ^{210}Pb and ^{210}Po (as ^{210}Po can

redeposit [82]), (2) the buried rates indicate either secular equilibrium had been reached at the start of data taking (0 days) or that there was more ^{210}Pb than ^{210}Po (which is not yet understood), (3) the inner, face event rate shows little to no time-dependence; this may be expected, as great care was used in minimizing contamination on the faces, where the sensors are located.

Two possible systematics can also be seen in the time-series data presented in this section (for detector 1101), as well as for the other detectors analyzed (plots presented in Appendix B): (1) there appears to be several outlier events (for example, near 400 days and also 600 days in either buried event plots shown in Fig. 3.22); this is suspected to be caused by events (perhaps gammas) leaking into our alphas selection, though further investigation is needed. For this work, these outliers are not expected to significantly impact the inferred ^{210}Pb and ^{210}Po contamination. (2) there is a possible systematic in the measured rate of selected alphas between science runs, particularly between science runs R133 and R134 (shown by the first vertical line in the time-series plots) as can be seen in Fig. 3.24. While the cause of this shift in the measured rate needs further investigation, a possible impact is that the initial amount of ^{210}Po is underestimated (as the fit is pulled up at times beyond about 550 days). However, the results from this work are not expected to be significantly impacted, as the shift in rate is most pronounced for inner (face) events.

3.8 Assay of ^{210}Po on Detector Sidewalls by the AlphaBACH

The Alpha-Beta-radiation Assay CHamber (AlphaBACH) is a custom-built, high-sensitivity alpha and beta spectrometer [83]. The AlphaBACH boasts a large detection chamber that allows for surface radiation to be measured for samples of varying geometry (up to $W \times L \times H = 2 \text{ ft} \times 2 \text{ ft} \times 2 \text{ ft}$). Ultra-pure copper is used to limit the line-of-sight to one (or more) of the AlphaBACH's 52 mm Si detectors, such that a particular sized sample (or part of a sample) may be assayed, while minimizing backgrounds from the inner chamber walls.

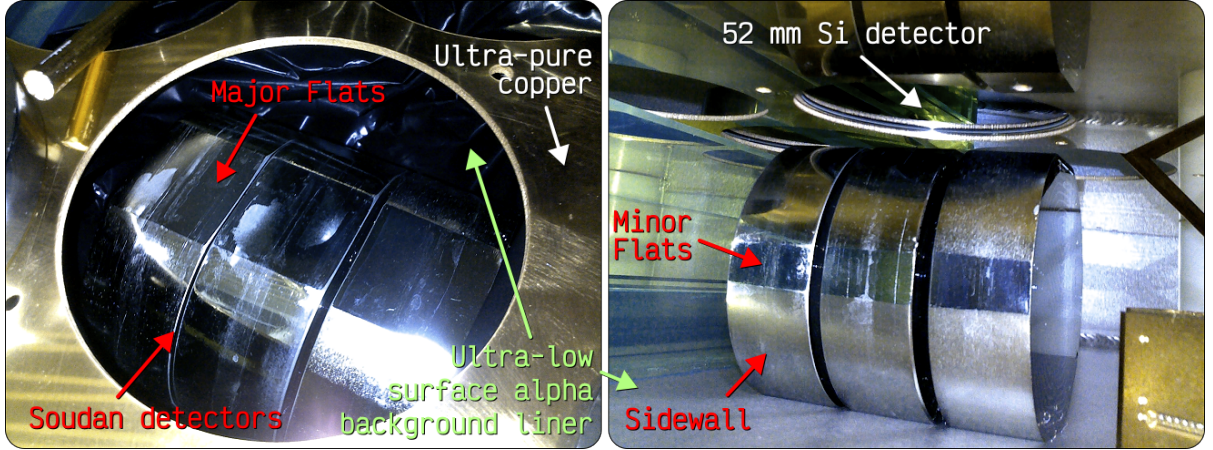


Figure 3.25: Soudan detector 1110, 1111, and 1112 are seen placed on their sides, face-to-face, with major flats facing up, toward the AlphaBACH's 52 mm Si detector. Ultra-pure copper shields radiation from the inner chamber walls reaching the Si detector. A black conductive Teflon foil with a ultra-low surface alpha background (courtesy of Dr. Cooley's group at SMU) is used as a liner of the chamber floor. These images are courtesy of Dr. Juergen Reichenbacher (with annotations added by me).

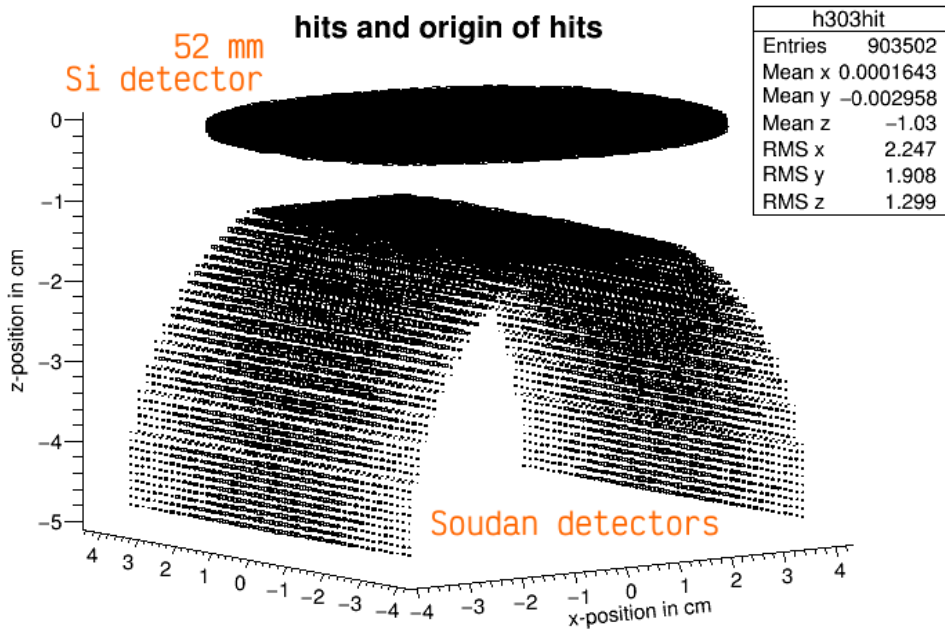


Figure 3.26: Detection efficiency for ^{210}Po decays on the surface of three Soudan detectors (placed on their sides, face-to-face, with their major flats facing up, toward the AlphaBACH detector) was estimated by Monte Carlo simulation. The hits are shown as black dots on the 52 mm Si detector with corresponding origins shown below (black dots) on the Soudan detector (with their surfaces made invisible). The estimated detection efficiency for ^{210}Po alpha decays on the surface of Soudan detectors was 22.59% averaged over all line-of-sight surfaces (the major flats and roughly half of the sidewalls) and 30.63% for the major flat regions only. This figure is courtesy of Dr. Juergen Reichenbacher (with orange annotations added by me).

Dr. Juergen Reichenbacher (the creator of the AlphaBACH), performed a ^{210}Po assay of Soudan detectors 1110, 1111, and 1112 for the SuperCDMS collaboration. All three Soudan detectors had their sidewalls assayed together, with the major flat regions facing the AlphaBACH Si detector. Figure 3.25 shows the Soudan detectors on their sides and face-to-face in the AlphaBACH detection chamber. As part of the conducted assay, Dr. Reichenbacher wrote a simulation to estimate the detection efficiency for ^{210}Po alpha decays on the Soudan detector surfaces to be 22.59% for all line-of-sight surfaces (the major flats and roughly half of the sidewalls) and 30.63% for the major flat regions only; this simulation is illustrated by Fig. 3.26.

Three letters were etched (or scored) into one of the major flats on each detector (for identification). For this reason, Dr. Reichenbacher performed two separate assays: one with the etched major flats facing up (toward the AlphaBACH detector) and one with the etched major flats facing down. His expectation was that the etched major flats might have an increased rate as compared to those without etching. The results of these assays are listed below:

- With the **etched major flats facing up**, the inferred ^{210}Po surface activity was $1040 \pm 380 \text{ nBq/cm}^2$; this presumes a uniform contamination throughout the entire line-of-sight surface. If the measured rate is presumed to originate only from the major flats, the inferred contamination increased to $3050 \pm 940 \text{ nBq/cm}^2$.
- With the **etched major flats facing down**, the inferred ^{210}Po surface activity was $710 \pm 370 \text{ nBq/cm}^2$.
- The **average ^{210}Po contamination** from both assays (presuming a uniform contamination throughout the entire line-of-sight surface) was $875 \pm 265 \text{ nBq/cm}^2$.

3.9 Inferred Contamination and Conclusions

Table 3.5 and Table 3.6 present best estimates of ^{210}Pb and ^{210}Po contamination at the start of data taking. All quoted surface (S) and buried (B) contamination values are

Det. Num.		Faces (S) [nBq/cm ²]	Total Sides (S) [nBq/cm ²]	Major Flats (S) [nBq/cm ²]	NMF (S) [nBq/cm ²]
1101	Pb	118 ± 16	224 ± 21	156 ± 52	210 ± 20
	Po	142 ± 47	798 ± 76	2102 ± 244	408 ± 65
1104	Pb	91 ± 16	142 ± 17	341 ± 53	119 ± 16
	Po	94 ± 49	401 ± 56	955 ± 180	135 ± 46
1105	Pb	26 ± 9	96 ± 16	199 ± 43	52 ± 12
	Po	52 ± 26	313 ± 48	590 ± 146	179 ± 42
1106	Pb	55 ± 13	226 ± 19	420 ± 55	150 ± 17
	Po	57 ± 38	399 ± 60	392 ± 148	389 ± 61
1108	Pb	42 ± 9	155 ± 17	311 ± 56	86 ± 13
	Po	16 ± 21	501 ± 58	1712 ± 218	170 ± 41
1111 assayed	Pb	56 ± 12	513 ± 26	1274 ± 91	276 ± 21
	Po	103 ± 38	300 ± 60	863 ± 214	130 ± 45
1112 assayed	Pb	51 ± 13	260 ± 19	625 ± 63	128 ± 15
	Po	243 ± 51	481 ± 57	979 ± 184	313 ± 49
1114 [†]	Pb	60 ± 18	229 ± 36	372 ± 109	172 ± 33
	Po	29 ± 24	683 ± 82	1883 ± 278	371 ± 70

Table 3.5: Inferred initial ^{210}Pb and ^{210}Po surface (S) contamination for all functional detectors (abbreviated ‘Det. Num.’) as a function of location. The column labeled **NMF** refers to the region of the detector sidewall between both major flats. Detector 1106 has been included, though the inner phonon channel (PBS1) was not functional: while Total Sides values likely still reliable, the Major Flats and NMF columns should be considered with caution (as the position reconstruction of events is pulled to a single side of the detector). As a courtesy to the reader: $100 \text{ nBq/cm}^2 = 1 \text{ mBq/m}^2$. [†]This detector had a short livetime (only 173 days) and thus fewer statistics; this resulted in larger uncertainties (as compared to the other detectors) on the number of initial ^{210}Pb and ^{210}Po atoms as inferred from the time-series fit.

inferred from the best-fit N_{Po} and N_{Pb} of the time-series analysis described in Section 3.7. The time-series analysis showed that there was more initial ^{210}Po on detector surfaces than initial ^{210}Pb ; this is not surprising, as ^{210}Po has been observed to redeposit on surfaces during a surface etch to remove ^{210}Pb contamination [82]. For buried events, either secular equilibrium between ^{210}Pb and ^{210}Po had been reached at the start of data taking or there was less ^{210}Po than ^{210}Pb ; this is not yet understood. The total buried contamination (for the total sides) of ^{210}Po was larger than the inferred ^{210}Pb (by $\geq 1\sigma$) for half of all examined detectors, with others having inferred ^{210}Pb and ^{210}Po within 1σ .

Det. Num.		Total Sides (B) [mBq/kg]	Major Flats (B) [mBq/kg]	NMF (B) [mBq/kg]
1101	Pb	440 ± 21	979 ± 64	190 ± 17
	Po	403 ± 54	680 ± 152	277 ± 52
1104	Pb	352 ± 18	470 ± 44	215 ± 17
	Po	342 ± 48	325 ± 106	256 ± 48
1105	Pb	312 ± 16	774 ± 57	169 ± 13
	Po	209 ± 40	518 ± 146	62 ± 25
1106	Pb	542 ± 22	1135 ± 67	285 ± 19
	Po	259 ± 54	199 ± 128	331 ± 56
1108	Pb	315 ± 17	888 ± 60	81 ± 10
	Po	135 ± 36	363 ± 127	96 ± 29
1111 assayed	Pb	274 ± 16	724 ± 54	122 ± 12
	Po	189 ± 35	291 ± 105	108 ± 27
1112 assayed	Pb	306 ± 16	659 ± 52	101 ± 12
	Po	269 ± 41	844 ± 141	95 ± 31
1114 [†]	Pb	234 ± 25	615 ± 93	90 ± 17
	Po	229 ± 43	828 ± 172	8 ± 21

Table 3.6: Inferred initial ^{210}Pb and ^{210}Po buried (B) contamination for all functional detectors (abbreviated ‘Det. Num.’) as a function of location. The column labeled **NMF** refers to the region of the detector sidewall between both major flats. Detector 1106 has been included, though the inner phonon channel (PBS1) was not functional: while Total Sides values likely still reliable, the Major Flats and NMF columns should be considered with caution (as the position reconstruction of events is pulled to a single side of the detector). [†]This detector had a short livetime (only 173 days) and thus fewer statistics; this resulted in larger uncertainties (as compared to the other detectors) on the number of initial ^{210}Pb and ^{210}Po atoms as inferred from the time-series fit.

As seen in Table 3.6, the contamination of ^{210}Po being larger than the ^{210}Pb is driven by the major flat regions for 3 out of the four detectors that show larger ^{210}Po contamination. It is surprising that the amount of ^{210}Po is larger in the copper (or, at the major flat region, the cabling) than ^{210}Pb , as this requires the bulk material to have been created in a way that preferentially removes ^{210}Po (leaving behind the ^{210}Pb) *and* not be older than about five months at the start of data taking (otherwise, secular equilibrium will have been mostly reached). While not clearly evident, there could be a time-dependent

leakage of gammas or a change between science run R133 and R134 that is influencing the time-series fit (but more investigation is needed).

The ^{210}Po rate was found to have a significant angular dependence, with the major flat regions having roughly four times the event rate of other regions of the detector sidewall. Interestingly, the event rate was increased in the major flat regions for both surface and buried selections. While the surface rate could be due to contamination on either the detector or surrounding materials, the increased buried rate can only be caused by bulk contamination of surrounding materials, as described in Section 3.4. Therefore, this study indicates that the increased rate (particularly the buried rate) was caused by the detector readout cabling that passes between the detector and copper housing at the location of the major flats. This important result was communicated to the SuperCDMS collaboration, where it helped guide fabrication of the SNOLAB cabling.

A surface assay of detectors 1110, 1111, and 1112 was conducted by Dr. Juergen Reichenbacher between January 2017 and January 2018 using the AlphaBACH alpha-beta spectrometer [83]. The results of two assays (with major flats facing the AlphaBACH Si detector) agree within 2σ of the inferred surface contamination quoted in Table 3.5. The AlphaBACH assay indicated an average surface ^{210}Po contamination of $875 \pm 265 \text{ nBq/cm}^2$.

A closer comparison of the inferred contamination from this work and the assay results is now presented. Because Soudan detector 1110 was not included in this chapter’s analysis, it will be presumed to have the same contamination detector as 1111 (which has the largest amount of ^{210}Pb). Because secular equilibrium will have been reached by the time of the assay, the measured ^{210}Po contamination from the assay will be compared with the inferred final ^{210}Pb rate at the time of assay:

$$N_{\text{Pb}}^f = N_{\text{Pb}} e^{-\lambda_{\text{Pb}} \Delta t}, \quad (3.47)$$

were the time between the start of data taking and Dr. Reichenbacher’s assay $\Delta t \approx 2000$ days, and the ^{210}Pb decay constant $\lambda_{\text{Pb}} = 8.55 \times 10^{-5}$ days. The fraction of the

initial ^{210}Pb that had decayed at the time of the assay was $1 - e^{-\lambda_{\text{Pb}}\Delta t} \approx 0.16$ or 16%. The uncertainties on the inferred values presented in Table 3.5 are ignored as they are small compared to those from the assay and because the contamination of detector 1111 is not known. Agreement between the assay and the inferred contamination is determined by comparing the total activities:

$$\begin{aligned} \text{inferred activity from this study} &\stackrel{?}{=} \text{activity from assay} \\ A_{\text{MF}}\epsilon_{\text{MF}}C_{\text{MF},i} + A_{\text{NMF}}\epsilon_{\text{NMF}}C_{\text{NMF},i} &\stackrel{?}{=} A_{\text{MF}}\epsilon_{\text{MF}}C_{\text{MF},a}, \end{aligned} \quad (3.48)$$

with each variable defined below:

$$A_{\text{MF}} \equiv \text{MF area} = 19.1 \text{ cm}^2$$

$$A_{\text{NMF}} \equiv \text{NMF area} = 70.4 \text{ cm}^2$$

$$\epsilon_{\text{MF}} \equiv \text{assay efficiency for MF} = 30.6$$

$$\epsilon_{\text{los}} \equiv \text{assay efficiency for all line-of-sight (los)} = 22.6$$

$$\epsilon_{\text{NMF}} \equiv \text{assay efficiency for NMF} = 20.5$$

$$C_{\text{MF},i} \equiv \text{MF contamination inferred from this work} = 891 \text{ nBq/cm}^2$$

$$C_{\text{NMF},i} \equiv \text{NMF contamination inferred from this work} = 191 \text{ nBq/cm}^2$$

$$C_{\text{los},a} \equiv \text{average contamination from assay for all line-of-sight} = 875 \pm 265 \text{ nBq/cm}^2$$

$$C_{\text{MF},a} \equiv \text{MF contamination from assay} = 3050 \pm 940 \text{ nBq/cm}^2,$$

where $C_{\text{MF},i}$ and $C_{\text{NMF},i}$ are determined as the average of contamination for detector 1111 taken twice and 1112. For example (and referring to Table 3.5, but reducing values by 16% to account for decay),

$$C_{\text{MF},i} = (1074 + 1074 + 527)/3 = 891 \text{ nBq/cm}^2. \quad (3.49)$$

The neither-major-flat (NMF) region efficiency ϵ_{NMF} for the assay is estimated algebraically:

$$(A_{\text{MF}}\epsilon_{\text{MF}} + A_{\text{NMF}}\epsilon_{\text{NMF}})C_{\text{los,a}} = A_{\text{MF}}\epsilon_{\text{MF}}C_{\text{MF,a}} \\ \rightarrow \epsilon_{\text{NMF}} = \frac{A_{\text{MF}}}{A_{\text{NMF}}C_{\text{los,a}}} (\epsilon_{\text{MF}}C_{\text{MF,a}} - \epsilon_{\text{MF}}C_{\text{los,a}}) = 20.5. \quad (3.50)$$

The left hand of the comparison equation (Eq. 3.48) is

$$A_{\text{MF}}\epsilon_{\text{MF}}C_{\text{MF,i}} + A_{\text{NMF}}\epsilon_{\text{NMF}}C_{\text{NMF,i}} = 798 \mu\text{Bq}, \quad (3.51)$$

where nBq is converted to μBq by dividing by 10^3 . The right hand side is

$$A_{\text{MF}}\epsilon_{\text{MF}}C_{\text{MF,a}} = 1782 \mu\text{Bq}. \quad (3.52)$$

The lower- 1σ and lower- 2σ values of the assay activity are

$$A_{\text{MF}}\epsilon_{\text{MF}}(C_{\text{MF,a}} - 1 \times 940 \text{nBq/cm}^2) = 1232 \mu\text{Bq} \quad (\text{lower}-1\sigma) \quad (3.53)$$

$$A_{\text{MF}}\epsilon_{\text{MF}}(C_{\text{MF,a}} - 2 \times 940 \text{nBq/cm}^2) = 683 \mu\text{Bq}, \quad (\text{lower}-2\sigma) \quad (3.54)$$

where the 940nBq/cm^2 is the uncertainty on $C_{\text{MF,a}}$. Therefore, the result of comparing the inferred activity given by Eq. 3.51 with the assay activity given by Eq. 3.54 agree within 2σ . The assays conducted with the AlphaBACH support this chapter's findings of large contamination on detector sides as compared with faces. The assay, however, does not require the contamination to have been primarily on the detector's major flats (as the sidewall region, excluding the major flats, was not exclusively assayed). If taken at face value, the assay does suggest that most of the contamination is on the detector sides and not on surrounding materials.

The estimate of the amount and location of ^{210}Pb contamination for SuperCDMS Soudan detectors and surrounding materials provide important guidance for its successor SuperCDMS SNOLAB. The important conclusions from this analysis are as follows:

1. The large bulk contamination in surrounding materials increase backgrounds from ^{210}Pb , ^{210}Bi , and ^{210}Po alphas that have lost sufficient energy to be mistaken as

signal events; these backgrounds may be reduced by using cleaner copper for the detector housing (has been done for SuperCDMS SNOLAB).

2. The significantly higher rate measured at the major flats indicates surface and bulk contamination of the detector interface boards (DIBs); these backgrounds can be reduced by taking care in selecting radio-pure materials for the DIBs (has been done for SuperCDMS SNOLAB) and limiting plate-out onto them.
3. The overall surface contamination (faces and sides) was found here to be high (hundreds of nBq/cm²); decreasing the time exposed to environmental radon and/or the radon concentration of such environments can reduce ²¹⁰Pb plate-out on detector surfaces. SuperCDMS SNOLAB has done this in order to meet a goal for the average surface contamination of < 50 nBq/cm².

Chapter 4

Radon Removal From Breathable Air

There are trace amounts of ^{238}U (having a half-life of 4.5 billion years) in most materials (*e.g.*, rock, dirt, metals, and plastics). After several decays, ^{226}Ra (radium) is produced, which has a half-life of 1600 years; due to its long lifetime, ^{226}Ra is also found in most materials. Figure 4.1 shows how radium decays to ^{222}Rn (radon)—a noble gas that easily diffuses through most materials (that are not metals). Radon also has a short half-life of only 3.8 days, decaying to ^{218}Po . A couple hours and several decays later, ^{210}Pb is produced, with the intermediate daughters ^{214}Pb , ^{214}Bi , and ^{214}Po often called the *fast daughters*. ^{210}Pb has a half-life of 22.3 years that is particularly long compared

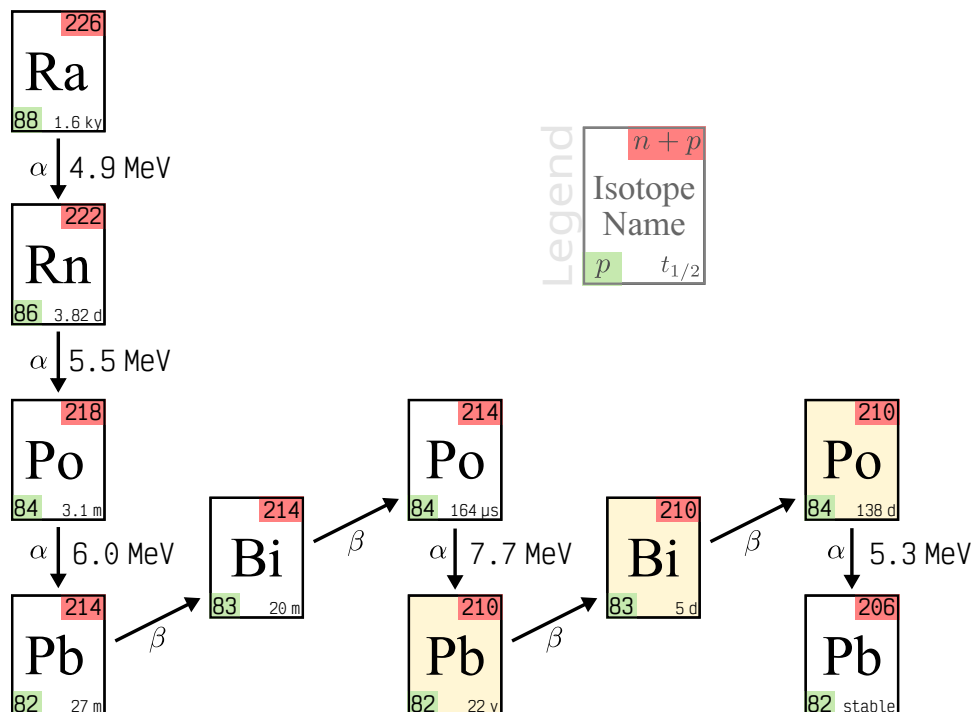


Figure 4.1: ^{222}Rn decay chain with legend shows the atomic number (the number of protons $Z = p$), mass number (the number of protons and neutrons $A = n + p$), and half-life $t_{1/2}$ of isotopes. Radon and its progeny prior to ^{210}Pb have relatively short half-lives. ^{210}Pb has a long half-life of 22.3 years from which ^{210}Po (having a half-life of 138 days) will grow into equilibrium over several months.

to the duration of many experiments (where waiting for it to decay away is often impractical). Eventually, ^{210}Pb undergoes two beta decays and one alpha decay to produce the stable ^{206}Pb atom.

Three important observations are made from the radon decay chain:

1. Radon emanates from most materials, is a noble gas, and is therefore in the air all around us. Because radon is a heavy gas (~ 15 times heavier than air), its concentration can be particularly high in low-elevation and poorly-ventilated regions of closed spaces (such as basements, underground caverns, and closets).
2. Radon decay is followed by several successive decays of the fast daughters over just a couple hours, depositing ~ 20 MeV of energy in surrounding materials (just from the kinetic energy of the alphas produced).
3. After radon decays, its fast daughters often settle on surfaces, with their subsequent decay having a 50% chance of embedding the long-lived ^{210}Pb atom into the surface by tens of nanometers, where it can remain for decades.

While there are many reasons one may desire to reduce the concentration of radon in air, perhaps the most familiar is case is for lower regions, such as basements, of residential dwellings. Depending on geography, the amount of radium in the earth can be abundant, leading to significant production of radon gas. The radon easily diffuses out of the rock and dirt and through basement walls. Because radon is heavier than air, it tends to stay in the lower regions of the house—particularly when ventilation is poor. Because people live in these homes, they must breath the high-radon air into their lungs. Some of the radon inside the lungs decays, emitting an alpha particle and the ^{218}Po daughter; the alpha particle will deposit all of its 5.3 MeV of energy into the surrounding lung tissue, while the ^{218}Po atom settles inside the lung, shortly followed by the decay of the three fast daughters—each producing radiation (two betas and one alpha) that is deposited in the lung tissue. The lung tissue suffers various types of damage, including

damage to its DNA, which might result in a cancerous cell being formed. There are many studies documenting the increase probability of lung cancer from exposure to high-radon environment (having a radon concentration above $\sim 100 \text{ Bq/m}^3$, a unit of decays per volume) [84, 85, 86].

The success of a rare-event search experiment is hinged on its ability to understand and control its backgrounds. A frequently dominant background for dark-matter search experiments is from radon daughters. During detector assembly radon will decay to its daughters and they may become embedded just within the surface of these devices and other line-of-sight materials. With increased exposure, the long-lived radon daughter ^{210}Pb can become further concentrated just under the surface. Further subsequent decays can mimic dark-matter events and thus reduce sensitivity, as discussed in Section 2.2.1.

Backgrounds from radon progeny can be reduced by either reducing the time that sensitive materials are exposed to high-radon environments or by reducing the radon concentration of these environments. Because people are needed to assemble detectors and their line-of-sight components, and people must breath air, sensitive components are removed from their protective enclosures and exposed to radon in breathable-air environments, having a typical radon concentration of 100 Bq/m^3 . A major focus of this thesis is in reducing the radon concentration in breathable air that is supplied to a low-radon cleanroom where detectors and associated components are assembled. Radon is removed from air by using a vacuum-swing-adsorption system, introduced in Section 4.4.

This chapter introduces the physics of adsorption (Section 4.1) and diffusion (Section 4.2) in order to develop a statistical description of the radon concentration within a column packed with a porous medium. The diffusion of atoms in a packed bed depends on the speed of the air passing through the bed. Therefore, an estimate of air speed is developed for both an empty (a trivial case) and packed column in Section 4.3. Finally, the two primary types of systems used for reducing radon from air are described (Section 4.4), with both leaning on concepts developed throughout this chapter.

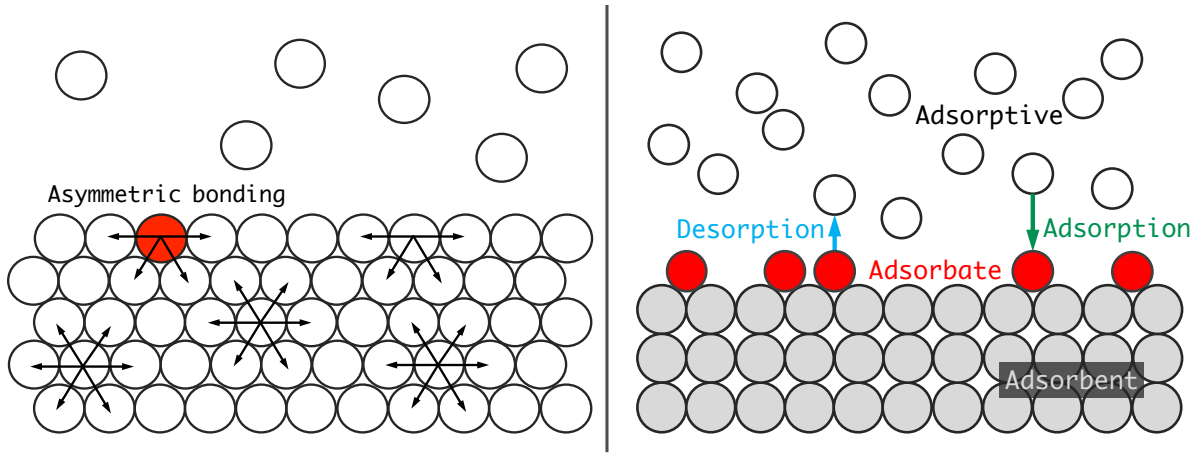


Figure 4.2: **Left:** Diagram of a surface. Interaction forces that define the bulk properties become asymmetric at this interface. Unused outer-most bonds enable surface reactions to take place. **Right:** Cartoon of adsorption illustrating common terminology.

4.1 Adsorption Physics

Before discussing the adsorption of atoms onto a surface, one should describe the different kinds of solids and what is meant by a “surface.” A surface is the interface between phases and denotes an end to bulk properties or behavior. Figure 4.2 shows a cartoon of a surface with asymmetric bonding at the interface (left). The nomenclature used in discussing adsorption is illustrated by Fig. 4.2 (right), and may be defined as follows: **Adsorption** describes an atom or molecule, the **adsorptive**, interacting and becoming bound (or attracted) to the surface of a material, the **adsorbent**. Once adsorbed, the atom or molecule is called the **adsorbate** and can leave the surface, which is called **desorption**. For this work, we primarily use the terms adsorption and desorption with respect to a surface.

There are two types of adsorption [87]:

1. **Physisorption** is described by the van der Waals interaction, sometimes called the dispersion force, and is shown in Fig. 4.3. All gases exhibit this induced-dipole adsorption and multilayers can form. This interaction is weak ($\sim 0.3 \text{ eV}$ or 30 kJ mol^{-1}) but becomes more stable at cooler (cryogenic) temperatures. The Lennard-Jones potential is a good approximation of physisorption [88, 89].

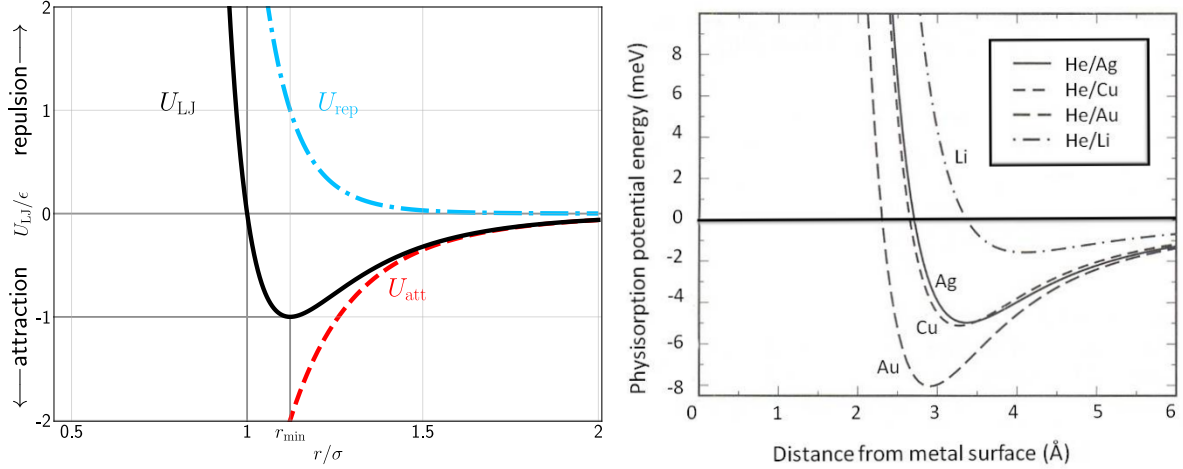


Figure 4.3: **Left:** The Lennard-Jones potential U_{LJ} is comprised of an attractive part U_{att} and a repulsive part U_{rep} ; their sum forms a potential well with depth ϵ at the distance r_{\min} from the adsorbent surface (at $r = 0$). **Right:** Examples of the Lennard-Jones potential is shown for helium adsorbing to silver (Ag), copper (Cu), gold (Au), and lithium (Li) [90].

2. **Chemisorption** is mediated by chemical reactions that may even dissociate the adsorbent. Electron exchange and chemical bonding produce a strong interaction ($> 1 \text{ eV}$ or 100 kJ mol^{-1}). The potential can be highly corrugated and a second phase can form under suitable temperatures and pressures.

For this work, radon is the adsorptive and activated carbon granules is the adsorbent. Radon (being a single, neutral atom) adsorbs via physisorption, where we will focus our attention for the rest of this chapter.

The *Lennard-Jones potential*, first proposed in 1924, approximates the interaction between two neutral atoms and is given as

$$U_{\text{LJ}} = 4\epsilon \left[\left(\frac{\sigma}{r} \right)^{12} - \left(\frac{\sigma}{r} \right)^6 \right], \quad (4.1)$$

where ϵ is the depth of the potential well, σ is the finite distance at which the inter-particle potential is zero, and r is the distance between the particles. As shown in Fig. 4.3, the r^{-12} term is repulsive and represents the Pauli repulsion at short distance due to the overlapping of electron orbitals. The r^{-6} term is attractive and represents the longer range dipole-induced or van der Waals interaction.

With this brief overview, we want to narrow our focus on the kind of adsorption interaction we expect for radon being adsorbed to activated carbon. Activated carbon is a kind of covalent solid (sometimes called a “network” solid) that has a very large surface area ($\sim 1000 \text{ m}^2/\text{g}$). Radon adsorbs to the activated carbon through an induced-dipole interaction (so, physisorption), meaning multiple layers of the adsorptive can form on the adsorbent. This type of adsorption was perhaps best described by Irving Langmuir in 1916 [91].

4.1.1 Langmuir Adsorption from the Kinetic Theory of Gases

Before using the Langmuir adsorption model to estimate the rates of adsorption and desorption, we will derive the rate at which particles strike a surface, that is, the so-called impingement rate. For the following derivation, I have roughly followed the excellent text by F. Reif called *Fundamentals of Statistical and Thermal Physics* [92].

Let us consider a cubic volume $V = L^3$ containing an ideal gas. An *ideal gas* consists of a large number N of molecules (or atoms), each with mass m , that interact only through perfectly elastic collisions. When a single molecule collides with one of the container’s walls (which will be presumed to have a single value in one axis while spanning the other two), its momentum p changes as

$$\Delta p \equiv p_{f,x} - p_{i,x} = p_{f,x} - (-p_{f,x}) = 2p_{f,x} = 2mv_x, \quad (4.2)$$

where i and f denote the initial and final states (before and after the collision) and v_x is the x -component of the molecule’s velocity. The time between collisions with a specific wall for this molecule is

$$\Delta t = \frac{2L}{v_x}. \quad (4.3)$$

Therefore the average force F exerted on this wall due to this one molecule is

$$F = \frac{\Delta p}{\Delta t} = \frac{2mv_x}{2L/v_x} = \frac{mv_x^2}{L}. \quad (4.4)$$

The total force on this wall due to all N of the molecules making up the gas is

$$F_T = NF = \frac{Nm v_x^2}{L}. \quad (4.5)$$

More conveniently, we may recast the total force in terms of the root-mean-square velocity in all dimensions v_{rms} . Courtesy of Pythagoras and since by symmetry $v_x = v_y = v_z$,

$$v_{\text{rms}}^2 = v_x^2 + v_y^2 + v_z^2 = 3v_x^2. \quad (4.6)$$

Substituting $v_x^2 = v_{\text{rms}}^2/3$ shows the total force to be

$$F_T = \frac{Nm v_{\text{rms}}^2/3}{L} = \frac{Nm v_{\text{rms}}^2}{3L}. \quad (4.7)$$

The pressure P exerted on any of the container's walls will then be

$$P = \frac{F_T}{L^2} = \frac{Nm v_{\text{rms}}^2}{3L^3} = \frac{Nm v_{\text{rms}}^2}{3V}. \quad (4.8)$$

The *ideal gas law*, first stated in 1834 by the French engineer and physicist Benoît Paul Émile Clapeyron, is the equation of state that describes the macroscopic properties (*i.e.*, the pressure and temperature) of an ideal gas and is given as

$$PV = Nk_B T, \quad (4.9)$$

where $k_B = 1.38 \times 10^{-23} \text{ J K}^{-1}$ is Boltzmann's constant and T is temperature in Kelvin. With insight from the ideal gas law, we arrive at an important result relating pressure and kinetic energy:

$$PV = \frac{Nm v_{\text{rms}}^2}{3} = \frac{2}{3} \left(\frac{1}{2} Nm v_{\text{rms}}^2 \right) = \frac{2}{3} K, \quad (4.10)$$

where K is the average translational kinetic energy of the gas. The skeptic is comforted by the fact that we have arrived at the macroscopic properties of the gas via microscopic ones (*i.e.*, the momenta of the molecules). Further comparison to the ideal gas law reveals that

$$\begin{aligned} PV &= \frac{Nm v_{\text{rms}}^2}{3} = Nk_B T \\ \frac{mv_{\text{rms}}^2}{3} &= k_B T, \end{aligned} \quad (4.11)$$

and thus we arrive at another important result relating temperature and kinetic energy:

$$T = \frac{k_B m v_{\text{rms}}^2}{3} = \frac{2}{3} \frac{K}{N k_B}. \quad (4.12)$$

Said another way, the translational kinetic energy per molecule per degree of freedom is

$$\frac{K}{3N} = \frac{k_B T}{2}. \quad (4.13)$$

To determine the frequency of molecules that collide with and adsorb to one wall, we need to know at what rate the molecules collide with the wall. From Eq. 4.11, we have an expression for the root-mean-square velocity

$$v_{\text{rms}}^2 = \frac{3k_B T}{m}, \quad (4.14)$$

but we really want the mean (or average) velocity \bar{v} . In 1860 James Clark Maxwell derived, heuristically, a probability distribution for the speed of particles in an ideal gas. Later, in the 1870s, Boltzmann further developed the theory on the basis of maximizing entropy. The resulting *Maxwellian velocity distribution* $f(v)$ is given as

$$f(v) d^3v = \left(\frac{m}{2\pi k_B T} \right)^{3/2} e^{-\frac{mv^2}{2k_B T}} d^3v. \quad (4.15)$$

The probability per unit speed of finding a particle with speed v is given by the probability distribution function (PDF), denoted as $\mathcal{P}(v)$, with

$$\mathcal{P}(v) dv = \int f(v) d^3v, \quad (4.16)$$

which is referred to as the *Maxwellian speed distribution* or *Maxwell-Boltzmann distribution*. In a spherical shell between v and $v + dv$, $d^3v = 4\pi v^2 dv$, so Eq. 4.15 becomes

$$\mathcal{P}(v) dv = \left(\frac{m}{2\pi k_B T} \right)^{3/2} 4\pi v^2 e^{-\frac{mv^2}{2k_B T}} dv. \quad (4.17)$$

With $a \equiv \sqrt{k_B T/m}$, we may write $\mathcal{P}(v)$ more concisely as

$$\mathcal{P}(v) = \sqrt{\frac{2}{\pi}} \frac{v^2 e^{-\frac{v^2}{2a^2}}}{a^3}, \quad (4.18)$$

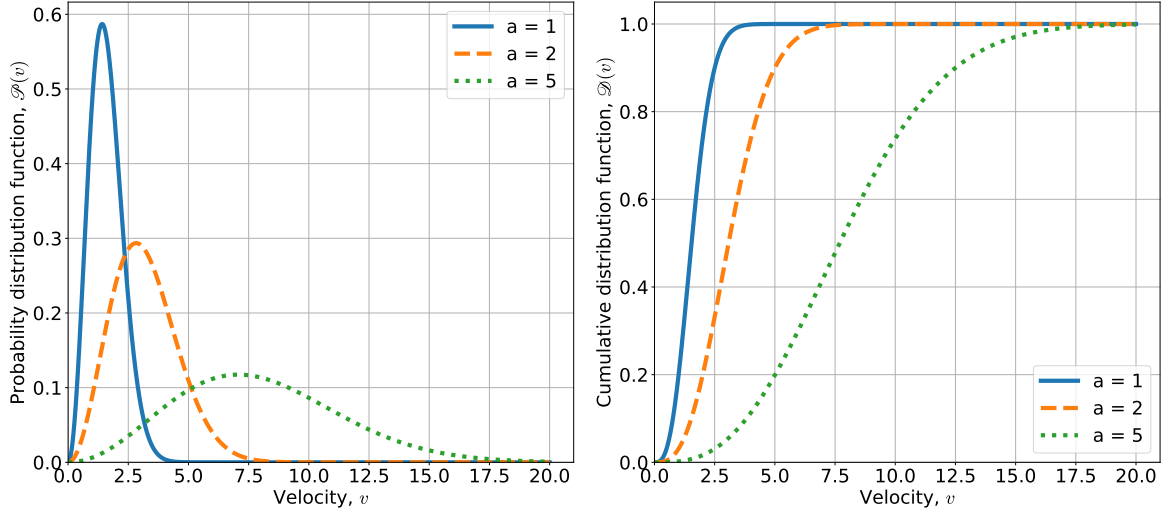


Figure 4.4: Probability and cumulative distribution functions for the Maxwellian speed distribution (refer to Eq. 4.18 and Eq. 4.19). **Left:** $P(v)$ describes the probably that a particle has the speed v . **Right:** $D(v)$ describes the probability that a particle has a speed $\leq v$. Recall that $a \equiv \sqrt{k_B T/m}$.

with examples curves shown in the left plot of Fig. 4.4.

The cumulative distribution function (CDF), denoted by $\mathcal{D}(v)$ is the the probability of a particle with a speed $\leq v$ and is found by integrating the PDF

$$\mathcal{D}(v) = \int_0^v P(v)dv = \operatorname{erf}\left(\frac{v}{\sqrt{2}a}\right) - \sqrt{\frac{2}{\pi}} \frac{ve^{-\frac{v^2}{2a^2}}}{a}, \quad (4.19)$$

where erf is the error function ($\operatorname{erf}(z) \equiv \frac{2}{\sqrt{\pi}} \int_0^z e^{-x^2} dx$). Examples curves for the CDF are shown in the right plot of Fig. 4.4.

Because we want to know the speed of molecules striking one surface, we must integrate Eq. 4.15 explicitly. Now, the volume V of our container is the area of one side A times L . Thus a differential volume element is $dV = dA \times dL$. With $dL = vdt \times \cos \theta$ in spherical coordinates, we have $dV = dA \times vdt \cos \theta$. Thus, we want to scale the Maxwellian speed distribution by the fraction of molecules that collide with the area dA as well as the number density $n = N/V$ (of course the rate must depend on the number of atoms within striking distance of the wall). Doing this, and converting to spherical coordinates with $d^3v = v^2 \sin \theta dv d\theta d\phi$, we get the differential number of molecules that

can adsorb to the wall dN_a :

$$dN_a = n (dA \times v dt \times \cos \theta) f(v) v^2 \sin \theta dv d\theta d\phi \quad (4.20)$$

$$= n (dA \times v dt \times \cos \theta) \left(\frac{m}{2\pi k_B T} \right)^{3/2} e^{-\frac{mv^2}{2k_B T}} v^2 \sin \theta dv d\theta d\phi. \quad (4.21)$$

By dividing by $dAdt$, we can get the impingement rate J_{imp} [$\text{m}^{-2} \text{s}^{-1}$]:

$$J_{\text{imp}} = \iiint n \cos \theta \left(\frac{m}{2\pi k_B T} \right)^{3/2} e^{-\frac{mv^2}{2k_B T}} v^3 \sin \theta dv d\theta d\phi. \quad (4.22)$$

To perform this integration we must choose our limits. Immediately we know we need $0 < v < \infty$. For angles, we want a full side and thus half of the total solid angle, *i.e.*, $0 < \theta < \pi/2$ and $0 < \phi < 2\pi$. Now

$$\begin{aligned} J_{\text{imp}} &= \int_0^{2\pi} \int_0^{\pi/2} \int_0^\infty n \cos \theta \left(\frac{m}{2\pi k_B T} \right)^{3/2} e^{-\frac{mv^2}{2k_B T}} v^3 \sin \theta dv d\theta d\phi \\ &= n \left(\frac{m}{2\pi k_B T} \right)^{3/2} \int_0^{2\pi} \int_0^{\pi/2} \int_0^\infty e^{-\frac{mv^2}{2k_B T}} v^3 \cos \theta \sin \theta dv d\theta d\phi. \end{aligned}$$

Substituting $2 \sin \theta \cos \theta = \sin 2\theta$ yields

$$\begin{aligned} J_{\text{imp}} &= n \left(\frac{m}{2\pi k_B T} \right)^{3/2} \int_0^{2\pi} \int_0^{\pi/2} \int_0^\infty e^{-\frac{mv^2}{2k_B T}} v^3 \left(\frac{1}{2} \sin 2\theta \right) dv d\theta d\phi \\ &= n \left(\frac{m}{2\pi k_B T} \right)^{3/2} \frac{1}{2} (2\pi) \int_0^{\pi/2} \int_0^\infty e^{-\frac{mv^2}{2k_B T}} v^3 \sin 2\theta dv d\theta. \end{aligned}$$

Noting that (with $u = 2\theta$ and $du = 2d\theta$)

$$\int_0^{\pi/2} \sin(2\theta) d\theta = \int_0^\pi \sin u \frac{du}{2} = -\frac{1}{2} \cos u \Big|_0^\pi = -\frac{1}{2} (\cos \pi - \cos 0) = -\frac{1}{2} (-1 - 1) = +1,$$

we have

$$J_{\text{imp}} = n\pi \left(\frac{m}{2\pi k_B T} \right)^{3/2} \int_0^\infty e^{-\frac{mv^2}{2k_B T}} v^3 dv.$$

Because $\int_0^\infty x^3 e^{-bx^2} dx = 1/(2b^2)$,

$$J_{\text{imp}} = n\pi \left(\frac{m}{2\pi k_B T} \right)^{3/2} \frac{1}{2} \left(\frac{2k_B T}{m} \right)^2 = \frac{n}{4} \sqrt{\frac{8k_B T}{\pi m}} = \frac{N}{V} \sqrt{\frac{k_B T}{2\pi m}}.$$

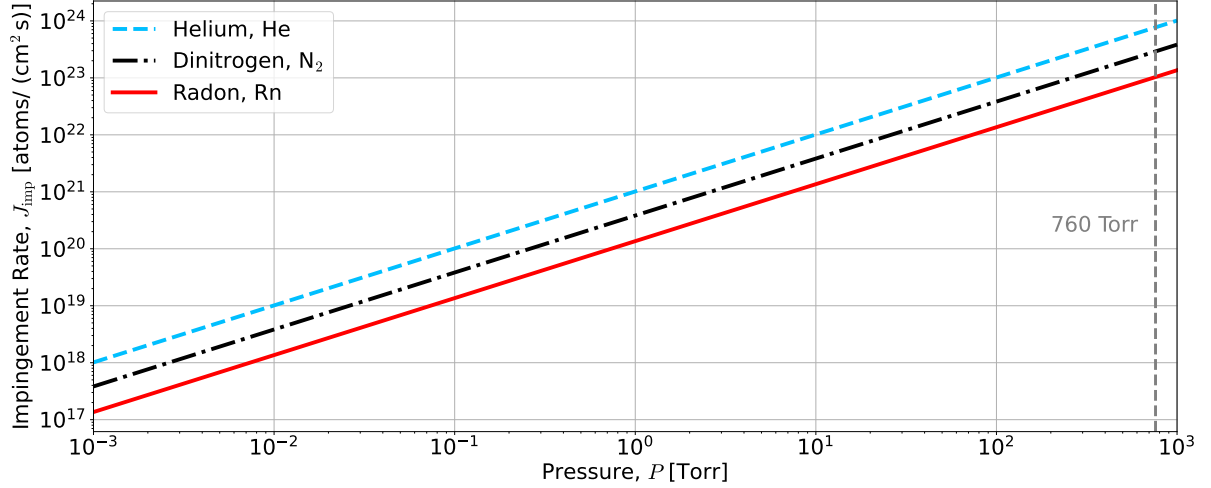


Figure 4.5: The impingement rate J_{imp} is shown as a function of pressure P for three different gasses: helium (blue, dashed curve), Dinitrogen (black, dot-dashed curve), and Radon (red solid curve).

Notice that the mean velocity $\bar{v} = \sqrt{\frac{8k_B T}{\pi m}}$. Making use of the ideal gas law (Eq. 4.9), we have what is often called the Hertz-Knudsen equation:

$$J_{\text{imp}} = \frac{P}{\sqrt{2\pi m k_B T}}, \quad [\text{m}^{-2} \text{s}^{-1}] \quad (4.23)$$

which describes the strikes per area per time, or the flux. Figure 4.5 shows the evaluation of Eq. 4.23 for helium, Dinitrogen, and Radon as a function of pressure. At atmospheric pressure (760 Torr), radon atoms strike a surface area of one square centimeter $\sim 10^{23}$ times per second.

Following the text *Adsorption Analysis: Equilibrium And Kinetics* by Duong D. Do [88], we may now write the *rate of adsorption*:

$$R_a = \alpha J_{\text{imp}} (1 - \varphi_a) = \frac{\alpha P}{\sqrt{2\pi m k_B T}} (1 - \varphi_a), \quad [\text{m}^{-2} \text{s}^{-1}] \quad (4.24)$$

where α is a proportionality constant that accounts for non-ideal striking angles that do not result in adsorption and φ_a is the fraction of the surface that is covered. The *Arrhenius equation*, proposed in 1889, describes the temperature dependence of reaction rate k as

$$k = k_0 e^{-\frac{E_d}{k_B T}}, \quad (4.25)$$

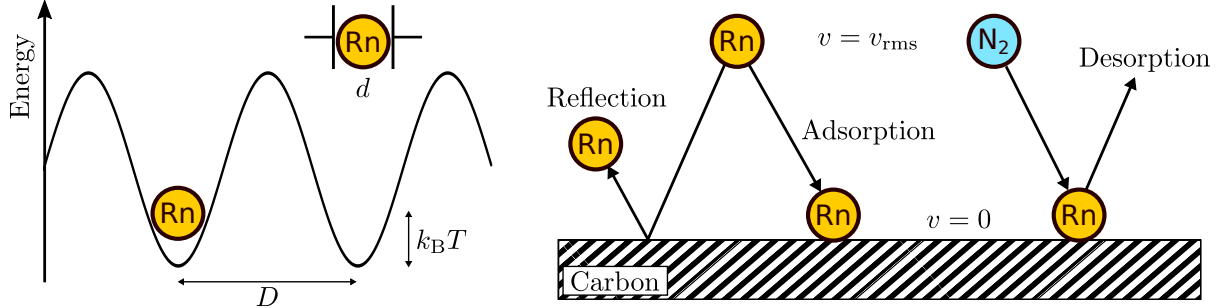


Figure 4.6: Left: A perfect surface can be characterized as a sinusoidal potential well. Each well is separated by the distance D , indicating that only one atom or molecule, with appropriate size d , may adsorb to a location. For an adsorbed radon atom to desorb, it must obtain enough energy $k_B T$ to escape the potential according to the Arrhenius equation (Eq. 4.25). **Right:** Radon, and other atoms and molecules, have a root-mean-square velocity v_{rms} according to the temperature of the gas. As illustrated, a radon atom may strike the surface (made, in this case, from carbon) and either be reflected or adsorbed. Once the radon atom is adsorbed (and is thus at zero velocity), it may become desorbed according to the impingement rate J_{imp} and whether energy transferred is more than the energy of desorption E_d . Figure adapted from [88].

where $k_0 \propto J_{\text{imp}}$ and E_d is the activation energy for desorption. The *rate of desorption*

$$R_d = AJ_{\text{imp}}e^{-\frac{E_d}{k_B T}}\varphi_a, \quad (4.26)$$

where A is a proportionality constant. The average residence time of adsorption is

$$\tau_a = \tau_0 e^{\frac{E_d}{k_B T}}, \quad (4.27)$$

where $\tau_0 = 1/(AJ_{\text{imp}})$. This formula means that if the potential well in which the radon atom, for example, resides is deeper (*i.e.*, E_d is larger), the atom will spend more time adsorbed, as illustrated by Fig. 4.6. A typical residence time for physical adsorption, or physisorption (the type we care about here, driven by van der Waals interaction), is between 10^{-13} and 10^{-9} seconds [88]. For chemisorption, the residence times can vary greatly from 10^{-6} (for weak chemisorption) to 10^9 seconds (for CO chemisorbed on Ni) [88].

Equating rates of adsorption and desorption (Eq. 4.24 and Eq. 4.26), we arrive at the famous Langmuir isotherm equation in terms of fractional loading:

$$\varphi_a = \frac{bP}{1 + bP}, \quad (4.28)$$

where

$$b = \frac{\alpha e^{Q/(k_B T)}}{A J_{\text{imp}} \sqrt{2\pi m k_B T}} = b_0 e^{Q/(k_B T)}. \quad (4.29)$$

The parameter b is the affinity or Langmuir constant. Q is the heat of adsorption, which is equal to the activation energy of desorption because there is no energy barrier for adsorption. The pre-exponential factor

$$b_0 = \frac{\alpha}{A J_{\text{imp}} \sqrt{2\pi m k_B T}}. \quad (4.30)$$

A possibly more useful form of the Langmuir isotherm is written in terms of the amount adsorbed:

$$C_a = C_0 \frac{b(T)P}{1 + b(T)P}, \quad (4.31)$$

where C_0 is a constant and $b = b(T)$ is made explicit.

Using the Langmuir model to improve our description of radon migrating through a carbon bed, we first characterize the mean velocity of radon atoms as

$$v_{\text{Rn}} = v_{\text{air}} f(T), \quad (4.32)$$

where $f(T)$ is a function that describes radon adsorption and desorption as it passes through the carbon bed (sometimes referred to as the sticking coefficient). The speed of air v_{air} (which is developed in Section 4.3) can be expressed in terms of the volumetric air flow F through the bed, which has a cross-sectional area A , at pressure P :

$$v_{\text{air}} = \frac{F}{\rho A} \frac{P_{\text{atm}}}{P}, \quad (4.33)$$

where ρ is the porosity of the activated charcoal (defined in Section 4.3) and P_{atm} is the local atmospheric pressure. The function $f(T)$ is defined qualitatively as the following ratio:

$$f(T) \equiv \frac{\text{time radon atoms are moving in air}}{\text{time spent on carbon surface and in air}}, \quad (4.34)$$

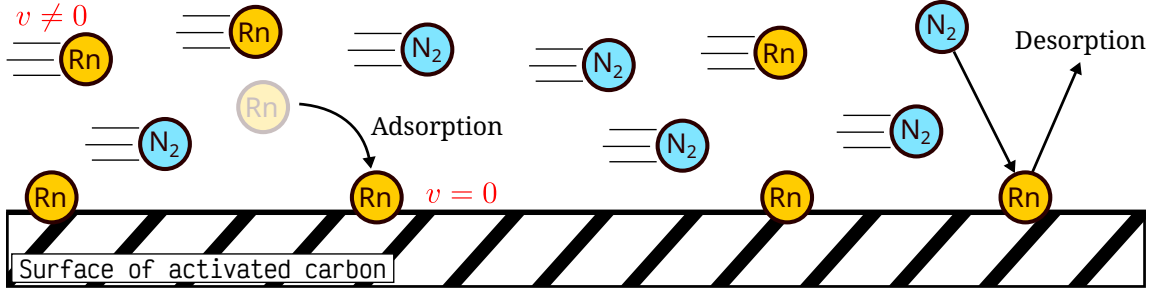


Figure 4.7: Cartoon of nitrogen and radon passing through a carbon bed, with radon spending more time than nitrogen on the carbon surface. Importantly, radon spends more time adsorbed to the carbon surface (with speed $v = 0$) than moving as a gas through the bed (with $v \neq 0$).

as illustrated by Fig. 4.7.

Let us now consider there being N radon atoms within the carbon bed at time t .

Over some Δt and carbon surface area ΔA , the number of radon atoms adsorbed to the carbon, thus not in the gas, is

$$N_a = R_a \Delta t \Delta A, \quad (4.35)$$

while the number of atoms in the gas is

$$N_d = R_d \Delta t \Delta A \quad (4.36)$$

The total number of atoms $N = N_a + N_d$, and therefore the fraction of radon atoms in the gas, for example, would be $N_d/(N_a + N_d) = N_d/N$. From this, one may see that the fraction of atoms desorbed over adsorbed is related to the average fraction of time atoms are moving in the gas. Therefore, we expand our description of $f(T)$:

$$f(T) = \frac{\text{time radon atoms are moving in air}}{\text{time spent on carbon surface and in air}} \approx \frac{N_d}{N_a} = \frac{R_d \Delta t \Delta A}{R_a \Delta t \Delta A} = \frac{R_d}{R_a}, \quad (4.37)$$

where we presume that $N_a \gg N_d$. Substituting in the adsorption and desorption rates (giving by Eq. 4.24 and Eq. 4.26 respectively) yields

$$f(T) = \frac{A J_{\text{imp}} \varphi_a e^{-E_d/(k_B T)}}{\alpha J_{\text{imp}} (1 - \varphi_a)} = \frac{A e^{-E_d/(k_B T)}}{\alpha} \frac{\varphi_a}{1 - \varphi_a} \approx \mathcal{A} e^{-E_d/(k_B T)}, \quad (4.38)$$

where $\mathcal{A} \equiv \frac{A}{\alpha} \frac{\varphi_a}{1 - \varphi_a} \approx \frac{A \varphi_a}{\alpha}$; this definition presumes that the coverage fraction φ_a is small and remains approximately constant while high-radon air passes through the carbon bed.

4.2 Diffusion Physics

In this chapter, a mathematical description for the diffusion of radon through a packed bed is developed for a discrete space. Starting from continuity and Fick's first law, Fick's second law is produced. The solution to Fick's second law describes the radon concentration in space and time according to a known diffusion coefficient D ; this solution is then modified to account for the radon within the column moving with a group velocity v_g . Finally, the error function is used to recast the solution into a form that can be used with a discrete space. This final form is then employed in creating operators that propagate radon through a packed bed in Section 7.2. The following derivations closely follow *The Mathematics of Diffusion* by J. Crank [93], which is arguably the best text on the subject.

The continuity equation describes the transport of a quantity (and expressed here for that quantity being conserved):

$$\frac{\partial \rho}{\partial t} = -\nabla \cdot (\rho \vec{v}) = -\nabla \cdot \vec{j}, \quad (4.39)$$

where ρ is an amount of substance per volume, t is time, \vec{v} is the velocity of the substance, and \vec{j} is the flux. The minus sign indicates that mass always moves toward lower concentrations.

Fick's first law is a mathematical theory of diffusion in isotropic media based on the hypothesis that the rate transfer of a substance through a unit-area section is proportional to the concentration gradient measured normal to the section [93]:

$$\vec{j} = -D\nabla\rho. \quad (4.40)$$

where D is the diffusion coefficient and has units of L^2/T . An isotropic medium has “structure and diffusion properties in the neighborhood of any point [that are] the same relative to all directions” [93]. A bed of activated carbon granules is a perfectly fine isotropic medium, and is used frequently in gas chromatography [87, 94, 93, 95].

Fick's second law is found from substituting Eq. 4.40 into Eq. 4.39, yielding

$$\frac{\partial \rho}{\partial t} = D \nabla^2 \rho = D \left(\frac{\partial^2 \rho}{\partial x^2} + \frac{\partial^2 \rho}{\partial y^2} + \frac{\partial^2 \rho}{\partial z^2} \right). \quad (4.41)$$

For this work particularly (and gas chromatography generally [94, 93, 95]), radon diffusion is reduced to a single dimension along the longitudinal axis of a packed column, which will be denoted here as the x axis. Though radon will be treated in terms of atoms by the simulation presented in Chapter 7, it is treated for the remainder of this chapter in terms of concentration; this is because radon in air is typically measured as a concentration, and the choice of units does not change the derivation or, therefore, the result. Substituting the density ρ for the radon concentration C (with units of Bq/m³), Eq. 4.41 simplifies to

$$\frac{\partial C}{\partial t} = D \frac{\partial^2 C}{\partial x^2}. \quad (4.42)$$

A solution to Fick's second law has the form of a Gaussian function:

$$C(x, t) = \frac{A}{\sqrt{t}} e^{-x^2/(4Dt)}, \quad (4.43)$$

where A is an arbitrary constant. The solution is a Gaussian function, which has the form $Ae^{-x^2/(2\sigma^2)}$; therefore, $4Dt = 2\sigma^2$, with σ the standard deviation. For now, radon decay will be ignored, as it is added back explicitly in Section 7.3 and in such a way that it may be turned ON or OFF in the simulation by the user. Therefore, the total amount M of radon cannot change, but can only diffuse:

$$\int_{-\infty}^{\infty} C(x, t) dx = M. \quad (4.44)$$

Performing the integration yields

$$\int_{-\infty}^{\infty} C(x, t) dx = \int_{-\infty}^{\infty} \frac{A}{\sqrt{t}} e^{-x^2/(4Dt)} dx = A \int_{-\infty}^{\infty} \frac{1}{\sqrt{t}} e^{-x^2/(4Dt)} dx. \quad (4.45)$$

Let us make the substitution $u = \frac{x}{2\sqrt{Dt}}$. Then $du = \frac{dx}{2\sqrt{Dt}}$ so $dx = 2\sqrt{Dt} du$, and

$$\int_{-\infty}^{\infty} C(x, t) dx = A \int_{-\infty}^{\infty} 2\sqrt{D} e^{-u^2} du = 2A\sqrt{D} \int_{-\infty}^{\infty} e^{-u^2} du = 2A\sqrt{D}\sqrt{\pi} = M \quad (4.46)$$

because $\int_{-\infty}^{\infty} e^{-u^2} du = \sqrt{\pi}$. Therefore,

$$A = \frac{M}{2\sqrt{\pi Dt}}, \quad (4.47)$$

and Eq. 4.43 becomes

$$C(x, t) = \frac{M}{2\sqrt{\pi Dt}} e^{-x^2/(4Dt)}. \quad (4.48)$$

We may check that this is indeed a solution to Eq. 4.42 directly (making use of the product rule). The LHS is

$$\begin{aligned} \frac{\partial C}{\partial t} &= \frac{\partial}{\partial t} \left[\frac{M}{2\sqrt{\pi Dt}} e^{-x^2/(4Dt)} \right] \\ &= \frac{M}{2\sqrt{\pi D}} \left[-\frac{1}{2} t^{-3/2} e^{-x^2/(4Dt)} + t^{-1/2} \frac{x^2}{4Dt^2} e^{-x^2/(4Dt)} \right] \\ &= \frac{M}{2\sqrt{\pi D}} e^{-x^2/(4Dt)} \left[-\frac{1}{2} t^{-3/2} + \frac{x^2}{4D} t^{-5/2} \right] \\ &= \frac{M}{4\sqrt{\pi D}} e^{-x^2/(4Dt)} \left[\frac{x^2}{2D} t^{-5/2} - t^{-3/2} \right] \end{aligned}$$

The RHS divided by D is

$$\begin{aligned} \frac{\partial^2 C}{\partial x^2} &= \frac{\partial}{\partial x} \left[\frac{\partial}{\partial x} \left[\frac{M}{2\sqrt{\pi Dt}} e^{-x^2/(4Dt)} \right] \right] \\ &= \frac{\partial}{\partial x} \left[\frac{M}{2\sqrt{\pi Dt}} \left(\frac{-2x}{4Dt} \right) e^{-x^2/(4Dt)} \right] \\ &= \frac{M}{2\sqrt{\pi Dt}} \left[-\frac{2}{4Dt} e^{-x^2/(4Dt)} + \left(\frac{-2x}{4Dt} \right)^2 e^{-x^2/(4Dt)} \right] \\ &= \frac{1}{D} \frac{M}{2\sqrt{\pi Dt}} e^{-x^2/(4Dt)} \left[-\frac{1}{2t} + \frac{x^2}{4Dt^2} \right] \\ &= \frac{1}{D} \frac{M}{2\sqrt{\pi D}} e^{-x^2/(4Dt)} \left[\frac{x^2}{4D} t^{-5/2} - \frac{1}{2} t^{-3/2} \right] \\ &= \frac{1}{D} \frac{M}{4\sqrt{\pi D}} e^{-x^2/(4Dt)} \left[\frac{x^2}{2D} t^{-5/2} - t^{-3/2} \right] = \frac{1}{D} \frac{\partial C}{\partial t} \checkmark \end{aligned}$$

If the radon in the air passing through the column has the group velocity v_g , the distribution is shifted by $v_g t$ (that is, $x \rightarrow x - v_g t$). Therefore, accounting for radon velocity and defining the initial concentration $C_0 \equiv M$, the solution to Fick's second law

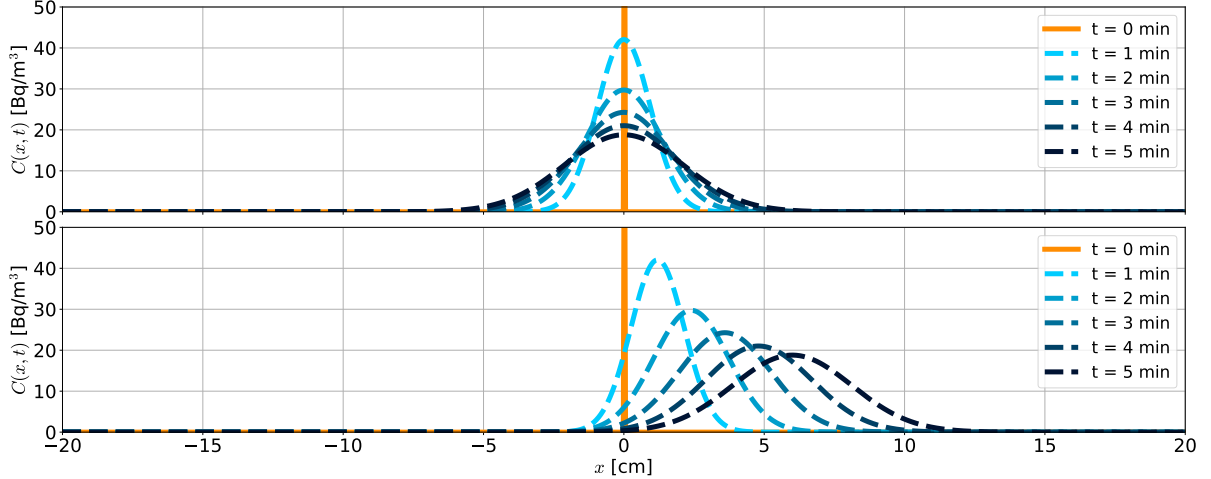


Figure 4.8: The solution to Fick's second law (Eq. 4.48) with initial radon spike at $x = 0$ of $C_0 = 100 \text{ Bq}/\text{m}^3$ (orange vertical line). The dashed curves represent the concentration as a function of x for $t = 1, 2, \dots, 5$ min for both $v_g = 0 \text{ cm/s}$ (top) and $v_g = 0.02 \text{ cm/s}$ (bottom).

becomes

$$C(x, t) = \frac{C_0}{2\sqrt{\pi Dt}} e^{-(x-v_g t)^2/(4Dt)}. \quad (4.49)$$

Figure 4.8 shows $C(x, t)$ for time $t \in \{0, 1, \dots, 5\}$ minutes. The initial condition, $C(x, 0)$, represents a radon spike at $x = 0$ with radon concentration $C_0 = 100 \text{ Bq}/\text{m}^3$ (shown as the orange vertical line). Curves in the top plot represent the case where $v_g = 0$, while those in the bottom plot represent $v_g = 0.02 \text{ cm/s}$.

More representative of a high-radon-air front passing through a column is a step in concentration (at $t = 0$):

$$C(x, 0) \equiv \begin{cases} C_0, & x \leq 0 \\ 0, & \text{otherwise} \end{cases} \quad (4.50)$$

For the case that $v_g = 0$, the step concentration diffuses throughout the column as illustrated by Fig. 4.9 (top). The contribution a distance ξ away from the substance in the region $\delta\xi$ at time t is

$$\frac{C_0 \delta\xi}{2\sqrt{\pi Dt}} e^{-(\xi-v_g t)^2/(4Dt)}. \quad (4.51)$$

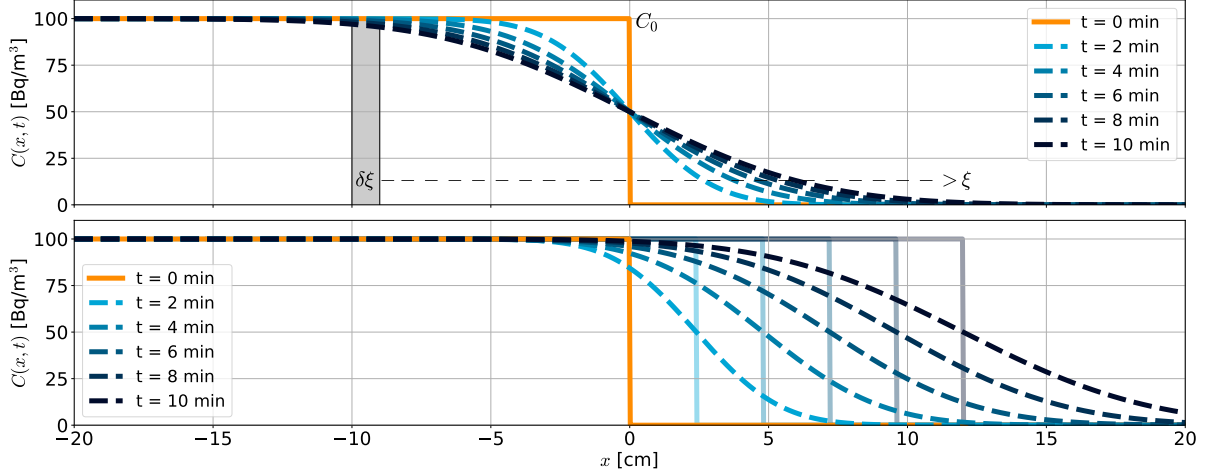


Figure 4.9: The solution to Fick’s second law (Eq. 4.48) with initial step radon concentration (orange line), as defined by Eq. 4.50. The dashed curves represent the concentration as a function of x for $t = 1, 2, \dots, 5$ min for both $v_g = 0 \text{ cm/s}$ (top) and $v_g = 0.02 \text{ cm/s}$ (bottom). Illustrated in the top plot, the amount of substance at any location in x is equal to the sum of contributions from substance within each differential element $\delta\xi$ with strength $C_0\delta\xi$ and a distance ξ away. The bottom plot shows in solid blue lines (that become darker for larger t) the initial step concentration shifted by $v_g t$ to illustrate a high-radon front moving through the column.

Thus for the condition given by Eq. 4.50, the concentration at the location x is the sum of contributions from each region $\delta\xi$ [93]:

$$C(x, t) = \frac{C_0}{2\sqrt{\pi Dt}} \int_x^\infty e^{-(\xi-v_g t)^2/(4Dt)} d\xi. \quad (4.52)$$

4.2.1 The error-function form of $C(x, t)$

Because the solution to Fick’s second law $C(x, t)$ (Eq. 4.48) is to be used in a numerical simulation, it is reformulated in terms of the error function, which allows for a finite and discrete spatial dimension to be used (as will now be shown). A standard mathematical function is the error function [93]:

$$\operatorname{erf}(z) \equiv \frac{2}{\sqrt{\pi}} \int_0^z \exp(-\eta^2) d\eta, \quad (4.53)$$

where $\eta \equiv x/(2\sqrt{Dt})$ and $d\eta = 1/(2\sqrt{Dt}) dx$, and with properties:

$$\operatorname{erf}(-z) = -\operatorname{erf}(z) \quad \operatorname{erf}(0) = 0 \quad \operatorname{erf}(\infty) = 1. \quad (4.54)$$

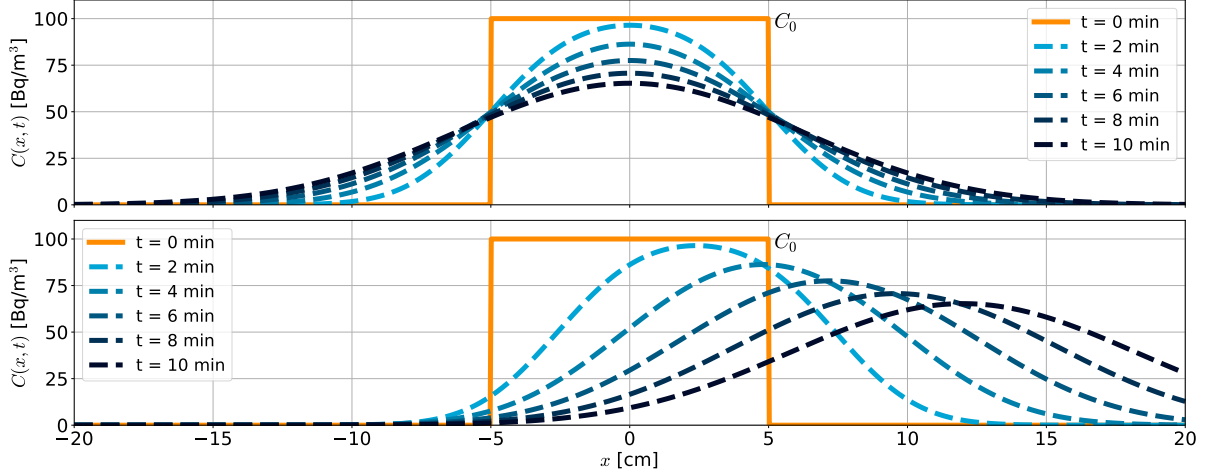


Figure 4.10: The solution to Fick’s second law (Eq. 4.48) with initial radon concentration $C_0 = 100 \text{ Bq}/\text{m}^3$ with $h = 5$ and centered at $x = 0$ (orange vertical line). The dashed curves represent the concentration as a function of x for $t = 1, 2, \dots, 5 \text{ min}$ for both $v_g = 0 \text{ cm/s}$ (top) and $v_g = 0.02 \text{ cm/s}$ (bottom).

The error-function complement $\text{erfc}(z)$ is defined by

$$\begin{aligned} \frac{2}{\sqrt{\pi}} \int_z^\infty \exp(-\eta^2) d\eta &= \frac{2}{\sqrt{\pi}} \int_0^\infty \exp(-\eta^2) d\eta - \frac{2}{\sqrt{\pi}} \int_0^z \exp(-\eta^2) d\eta \\ &= 1 - \text{erf}(z) = \text{erfc}(z). \end{aligned} \quad (4.55)$$

Therefore, the solution to Fick’s second law where all contributions are summed (Eq. 4.52) is rewritten as

$$C(x, t) = \frac{1}{2} C_0 \text{erfc} \left(\frac{x}{2\sqrt{Dt}} \right), \quad (4.56)$$

where C_0 is found at $x = 0, \forall t > 0$. J. Crank [93] (p.14) offers concisely that “The error function therefore enters into the solution of a diffusion problem as a consequence of summing the effect of a series of line sources, each yielding an exponential type of distribution.”

Therefore, if the substance is initially in the region $-h < x < +h$, the limits of integration of Eq. 4.52 become $x - h$ to $x + h$ instead of x to ∞ , leading to

$$C(x, t) = \frac{1}{2} C_0 \left[\text{erf} \left(\frac{h-x}{2\sqrt{Dt}} \right) + \text{erf} \left(\frac{h+x}{2\sqrt{Dt}} \right) \right]. \quad (4.57)$$

Figure 4.10 shows $C(x, t)$ with the concentration $C_0 = 100 \text{ Bq}/\text{m}^3$ and $h = 5$ (centered at $x = 0$). This result describes the amount of radon at the location x from cumulative

contributions from radon within a discrete bin of size $2h$ at location $x = 0$ —nearly exactly what we need for a simulation of radon diffusion!

4.2.2 The Diffusion Coefficient, D

For this work, the value of the coefficient D is inferred from elution (break-through) curve measurements (as shown in Section 7.13.3). The excellent text *Modern Practices of Gas Chromotography* by Robert Grob lists four types of diffusion [94]:

1. **Surface or Volmer Diffusion** takes place when pores are $\sim 100\text{\AA}$ [88]. The adsorbed molecules diffuse from the pore walls toward less densely coated areas. The diffusion coefficient $D < 10^{-3} \text{ cm}^2/\text{sec}$.
2. **Knudsen (or capillary) Diffusion** takes place when pores have diameters $< 0.1 \mu\text{m}$. Collisions with the walls are more frequent than intermolecular collisions. The diffusion coefficient $D \sim 10^{-2} \text{ cm}^2/\text{sec}$.
3. **Free or Molecular Diffusion** takes place between particles and in pores of diameters greater than $0.1 \mu\text{m}$. Here we encounter the largest values for the diffusion coefficient, with $D \sim 10^{-1} - 1.0 \text{ cm}^2/\text{sec}$.
4. **Solid Diffusion** takes place in pore diameters of about $0.001 \mu\text{m}$ (10 \AA). The diffusion coefficient $D \sim 10^{-5} \text{ cm}^2/\text{sec}$.

The activated carbon used in the SD Mines columns has a pore size of a few nanometers. Therefore, the expected diffusion coefficient is between 10^{-3} and $10^{-2} \text{ cm}^2/\text{s}$ (somewhere between Knudsen and Surface diffusion). As is discussed in Section 7.13.3, the diffusion coefficient that is inferred for the SD Mines Radon-Reduction System columns (introduced in Chapter 5) is between 10^{-3} and $10^{-2} \text{ cm}^2/\text{s}$, with the exact value depending on temperature, pressure, and the air speed through the column.

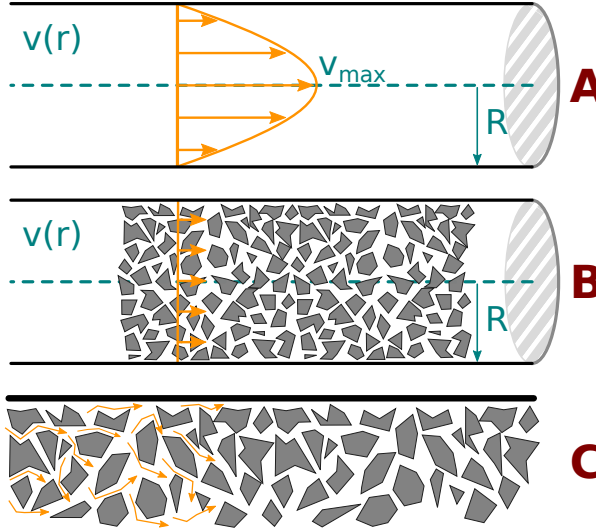


Figure 4.11: **A:** The velocity profile $v(r)$ within an empty pipe is parabolic. **B:** The velocity within a packed bed is a “plug” profile (constant in r). **C:** A zoomed-in view of the packed bed; the space between each granule is like a small pipe. Because the velocity is zero at any boundary, the velocity throughout the bed (having a radius much larger than the granule size) does not, on average, depend on r .

4.3 The Velocity Within Empty and Packed Columns

Consider a long empty pipe with length L and inner diameter D (and so a radius of $R = D/2$). *Not* near the ends of this pipe, the gas flow rate F is *laminar* (having constant streamlines) and is described by the Hagen-Poiseuille equation (introduced in the mid 18th century) [96]:

$$\Delta P = \frac{8\mu LF}{\pi R^4}, \quad (4.58)$$

where ΔP is the pressure difference between the input and output of the pipe (the pressure loss) and μ is the dynamic viscosity. The average air speed is called the *superficial velocity*:

$$u_s = \frac{F}{\pi R^2} = \bar{v}, \quad (4.59)$$

where $v = v(r)$, and r is distance in the radial direction. This expression holds for both gas and liquid. As described in [87], the velocity profile $v(r)$ within an empty pipe is parabolic in r (as illustrated by Fig. 4.11: **A**) and satisfies the boundary conditions: $v(R) = 0$ and $v(0) = v_{\max}$.

If we now consider a packed pipe or column (illustrated by Fig. 4.11: **B**, **C**), filled with, for example, granular carbon, the velocity u of air passing through is called “plug”

flow and is governed by Darcy's Law [94, 95, 97]:

$$u = -\frac{k'}{\mu} \frac{dP}{dz}, \quad (4.60)$$

where k' is the effective permeability, μ is still the dynamic viscosity, and dP/dz is the pressure drop over the column along its longitudinal axis z . This expression holds only for laminar flow conditions, which is almost always true of chromatographic flow [97].

4.3.1 For an Incompressible Fluid

If the fluid flowing through the column is a liquid (*i.e.*, incompressible), its velocity is constant; and therefore the change in pressure everywhere along z is constant, allowing for explicit integration:

$$\int_{P_0}^{P_1} dP = P_{\text{in}} - P_{\text{out}} = \Delta P \quad \int_0^L dz = L - 0 = L, \quad (4.61)$$

where P_{in} and P_{out} are the pressures measured at the input and output of the column.

Therefore

$$u = -\frac{k'}{\mu} \frac{\Delta P}{L}. \quad (4.62)$$

The dynamic viscosity may be estimated according to Sutherland's formula [98]:

$$\mu(T) = \mu_0 \left(\frac{T_0 + C}{T + C} \right) \left(\frac{T}{T_0} \right)^{3/2}, \quad (4.63)$$

where T and T_0 is temperature and reference temperature for which the viscosity is known in degrees Kelvin, μ_0 is the viscosity at T_0 , and C is the Sutherland's constant (with values found in Table 4.1).

The following effort in estimating the air velocity of a compressible gas through a packed bed leans heavily on the excellent paper by Carel A. Cramers [97]. To start our treatment, we need to introduce a few definitions. The porosity of the packed bed is characterized by the volume of empty space between flakes or granules, the space within the pores of these granules, and the volume of the solid flake or granules (the actual skeletal support structure). Below, we define useful fractions built from these volumes

Fluid	Sutherland's Constant, C [Kelvin]	μ_0 (for $T_0 = 20^\circ\text{C}$) [$\text{mPa s} = 10^{-3}\text{N s/m}^2$]
O ₂	140	0.02304
Air	110	0.01822
N ₂	120	0.01749
CO ₂	144	0.01473
CO	116	0.01745
SO ₂	349	0.01270
NH ₃	528	0.009945
H ₂	96	0.008804
Ar	157	0.02234
CH ₄	173	0.01103

Table 4.1: Viscosity for different gases taken from [98]. As noted there “The variation of viscosity with pressure is small for most gases. For gases on this page, the correction of viscosity for pressure is less than 10% for pressures up to 500 psia.”

that are referred to as the porosity (though there are different kinds!).

Skeletal fraction: The fraction of the skeletal carbon volume over the total outer volume

$$\epsilon_{\text{sk}} = \frac{V_{\text{sk}}}{V_{\text{total}}}. \quad (4.64)$$

Mobile-phase fraction: The fraction of volume between and around the carbon (*i.e.*, the interparticle volume), representing the *mobile phase* of the fluid within the bed, over the total volume:

$$\epsilon_{\text{m}} = \frac{V_{\text{m}}}{V_{\text{total}}}. \quad (4.65)$$

Stagnant-mobile-phase fraction: The fraction of volume within the pores of the carbon (*i.e.*, the intraparticle volume), representing the *stagnant mobile phase* of the fluid within the bed, over the total volume

$$\epsilon_{\text{s}} = \frac{V_{\text{s}}}{V_{\text{total}}}. \quad (4.66)$$

Total porosity: Finally, the total porosity is defined as the total void space over the total volume:

$$\epsilon_{\text{T}} = \frac{V_{\text{m}} + V_{\text{s}}}{V_{\text{total}}} = \epsilon_{\text{m}} + \epsilon_{\text{s}}. \quad (4.67)$$

For our activated carbon, $\epsilon_m \approx 0.4$, $\epsilon_s \approx 0.4$, and $\epsilon_{sk} \approx 0.2$ (according to the supplier, Calgon Carbon [99]). The total porosity is therefore $\epsilon_T \approx 0.8$. We then find the *mobile phase velocity* as:

$$u_m = \frac{u_s}{\epsilon_m} = \frac{F}{\epsilon_m \pi R^2}, \quad (4.68)$$

which describes the average effective speed of fluid moving through the carbon bed, but does *not* account for air passing into and spending time within the pores.

The velocity of fluid moving through the carbon bed, and within the pores, is called the *unretained component velocity* and is arrived at by

$$u_{ucv} = \frac{u_s}{\epsilon_m + \epsilon_s} = \frac{u_s}{\epsilon_T} = \frac{F}{\epsilon_T \pi R^2}. \quad (4.69)$$

In the case that $\epsilon_s = 0$ and $\epsilon_m = 1$, we have described an open pipe, and this form simplifies to the superficial velocity, as expected.

In terms of the permeability, pressure drop, dynamic viscosity, and the pipe or column length, we have (referring to Eq. 4.62)

$$u_{ucv} = -\frac{1}{\epsilon_T} \frac{k'}{\mu} \frac{\Delta P}{L}. \quad (4.70)$$

We obtain a slightly simplified expression by introducing the so-called *chromatographic permeability* [97]:

$$B_0 = \frac{k'}{\epsilon_m + \epsilon_s} = \frac{k'}{\epsilon_T}. \quad (4.71)$$

Substituting B_0 into Eq. 4.70, we arrive at the relation

$$u_{ucv} = -B_0 \frac{\Delta P}{\mu L}. \quad (4.72)$$

To make use of this expression, we still need to know how to estimate B_0 . In terms of the porosity fractions (ϵ 's), a shape factor ψ^2 , the column diameter d_c , and the particle diameter d_p , the chromatographic permeability is given by the Carman-Kozeny equa-

tion [97, 100] as

$$\begin{aligned} B_0 &= \frac{d_c^2}{32} && \text{(for an open pipe or column),} \\ B_0 &= \frac{d_p^2}{180\psi^2} \frac{\epsilon_m^3}{(1 - \epsilon_m)^2 (\epsilon_m + \epsilon_s)} && \text{(for a packed pipe or column).} \end{aligned} \quad (4.73)$$

The shape factor ψ^2 is found empirically for a specific medium, and Cramers quotes values of $\psi^2 = 1$ and $\psi^2 = 1.7$ for spherical glass beads and porous non-spherical support [97]. Though the shape factor is not known for our carbon, it appears that we can get by without it (as argued in the next section).

4.3.2 For a Compressible Fluid

For a compressible fluid (*i.e.*, a gas), dP/dz is not constant. Starting again with Darcy's Law (Eq. 4.60), but for a packed bed with total porosity ϵ_T , we have

$$u = -\frac{1}{\epsilon_T} \frac{k'}{\mu} \frac{dP}{dz}. \quad (4.74)$$

In terms of the chromatographic permeability B_0 , Darcy's Law becomes

$$u = -\frac{B_0}{\mu} \frac{dP}{dz}, \quad (4.75)$$

where B_0 is defined by Eq. 4.73.

Boyle's Law states, for ideal gases under isothermal conditions, that the product of pressure and velocity is conserved over all z . Therefore, we have

$$P(z) u(z) = P(L) u(L), \quad (4.76)$$

where $P(L) = P_{\text{out}}$ and $u(L) = u_{\text{out}}$, and u_{out} is the air velocity at the output. Rearranging and substituting this relation into Eq. 4.75 we get

$$u_{\text{out}} = \frac{P(z)}{P_{\text{out}}} u(z) = -\frac{B_0}{\mu} \frac{P(z)}{P_{\text{out}}} \frac{dP}{dz}. \quad (4.77)$$

After the separation of variables and integration

$$\int_{P(0)}^{P(L)} P dP = \frac{1}{2} P^2 \Big|_{P(0)}^{P(L)} = \frac{1}{2} (P(L)^2 - P(0)^2) = \frac{1}{2} (P_{\text{out}}^2 - P_{\text{in}}^2), \quad (4.78)$$

and, as before, $\int_0^L dz = L$, yielding

$$u_{\text{out}} = -\frac{B_0}{2\mu P_{\text{out}}} \frac{(P_{\text{out}}^2 - P_{\text{in}}^2)}{L}. \quad (4.79)$$

Continuing to follow [97], we define $P_r \equiv P_{\text{in}}/P_{\text{out}}$, and thus

$$u_{\text{out}} = \frac{B_0 P_{\text{out}}}{2\mu L} (P_r^2 - 1). \quad (4.80)$$

So far, however, we are only describing the output velocity, when we want the velocity of air passing through the carbon bed. As pointed out by Cramers [97], already in 1952 James and Martin [101] found a relation between the output velocity u_{out} and the time-averaged velocity \bar{u} :

$$\bar{u} = \gamma u_{\text{out}}, \quad (4.81)$$

where

$$\gamma = \frac{3}{2} \frac{P_r^2 - 1}{P_r^3 - 1}. \quad (4.82)$$

Finally, with this substitution, the time-averaged velocity may be expressed as

$$\bar{u} = B_0 \frac{3}{4} \frac{P_{\text{out}}}{\mu L} \frac{(P_r^2 - 1)^2}{P_r^3 - 1}. \quad (4.83)$$

We could stop here, if we knew with confidence the shape factor ψ^2 of our carbon medium. However, because we don't, let us test whether our gas-carbon system can be approximated as an incompressible fluid passing through a packed bed. That is, we want to compare the expressions for average speed of a incompressible Eq. 4.72 and compressible Eq. 4.83 fluid by taking the ratio

$$\left| \frac{\bar{u}}{u_{\text{ucv}}} \right| = \frac{B_0 \frac{3}{4} \frac{P_{\text{out}}}{\mu L} \frac{(P_r^2 - 1)^2}{P_r^3 - 1}}{B_0 \frac{\Delta P}{\mu L}} = \frac{\frac{3}{4} P_{\text{out}} \frac{(P_r^2 - 1)^2}{P_r^3 - 1}}{\Delta P} = \frac{3}{4} \frac{P_{\text{out}}}{\Delta P} \frac{(P_r^2 - 1)^2}{P_r^3 - 1}. \quad (4.84)$$

If this ratio is close to one, we may presume that the gas flowing through the carbon columns is not significantly compressing. As applied to the SD Mines Radon-Reduction

System that is introduced in Chapter 5, the relevant parameters are

$$P_{\text{in}} = 684 \text{ Torr} \approx 91192 \text{ Pa},$$

$$P_{\text{out}} = 680 \text{ Torr} \approx 90659 \text{ Pa},$$

$$\Delta P = P_{\text{in}} - P_{\text{out}} = 4 \text{ Torr} \approx 533 \text{ Pa},$$

$$P_r = P_{\text{in}}/P_{\text{out}} = 684/680 \approx 1.006,$$

yielding

$$\left| \frac{\bar{u}}{u_{\text{ucv}}} \right| \approx 0.999997; \text{ or, perhaps more clearly } 1 - \left| \frac{\bar{u}}{u_{\text{ucv}}} \right| \approx 3 \times 10^{-6}. \quad (4.85)$$

This indicates that we are likely safe to assume that our gas is behaving as an incompressible fluid in this system. This is due to the fact that the pressure drop across our carbon columns, having a very large cross-sectional area, is fairly small (a couple inches of water, or a few Torr). If the pressure drop were to increase, this assumption would become increasingly poor, as seen by Fig. 4.12.

Henceforth, the velocity of air v_{air} passing through the carbon columns will be taken, as it appears to be a reasonable approximation, in the form of the unretained component velocity (as introduced by Eq. 4.69):

$$v_{\text{air}} \equiv u_{\text{ucv}} = \frac{1}{\epsilon_T} \frac{F}{A}. \quad (4.86)$$

Plugging in typical values representative of the SD Mines RRS carbon columns, we find the superficial velocity to be

$$u_s = \frac{F}{A} = \frac{100 \text{ cfm}}{\pi(30 \text{ inches}/2)^2} \approx \frac{0.047 \text{ m}^3/\text{s}}{0.456 \text{ m}^2} \approx 0.10 \text{ m/s}. \quad (4.87)$$

Again, this would be the velocity of air passing through a column if it contained no carbon—it's just an empty pipe. The mobile-phase velocity comes to:

$$u_m = \frac{u_s}{\epsilon_m} = \frac{0.103 \text{ m/s}}{0.4} = 0.26 \text{ m/s}. \quad (4.88)$$

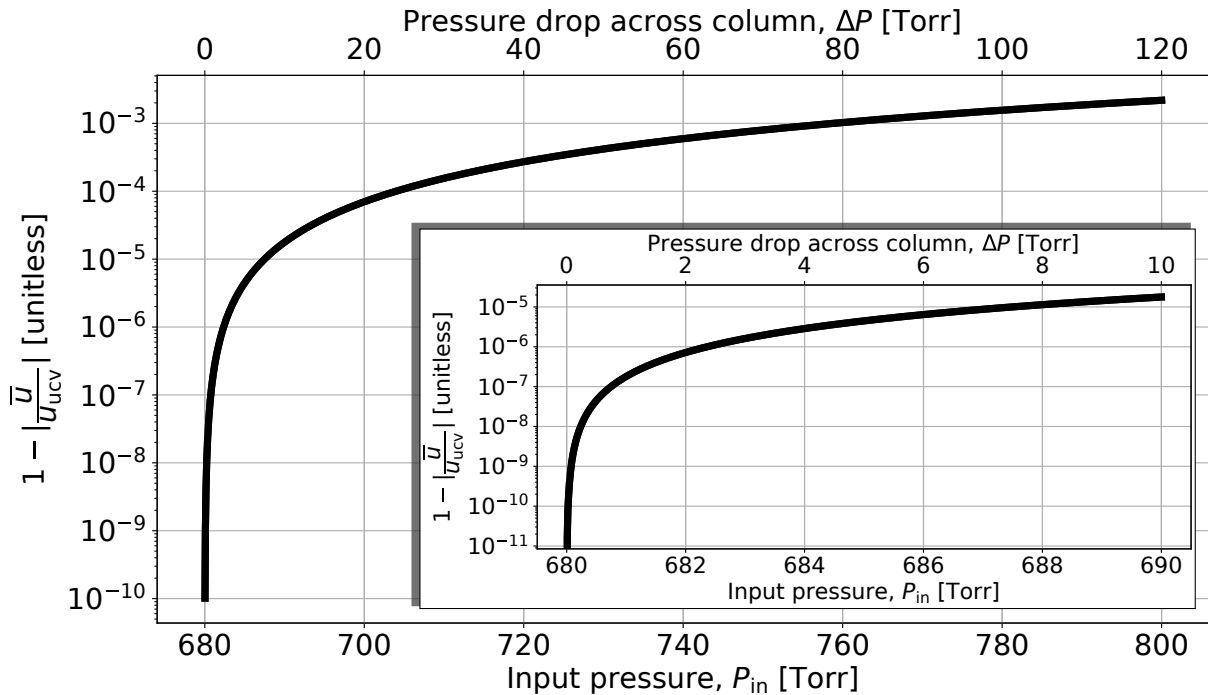


Figure 4.12: The assumption of the gas being incompressible, defined quantitatively by Eq. 4.85, is tested for varying input pressure P_{in} and, similarly, the pressure drop across the column, ΔP . For this plot, the only other parameter is held constant: $P_{\text{out}} = 680$ Torr, the nominal pressure in Rapid City, SD. **Inset:** Zoomed in view over a ΔP of only 10 Torr.

This would be the velocity of the air passing around and between the carbon granules, with the volumetric flow forced through, essentially, a smaller cross-sectional area. Thus the velocity of air is larger than the superficial velocity. The unretained component velocity, which we consider the air velocity, is (recalling that $\epsilon_T = \epsilon_m + \epsilon_s$):

$$v_{\text{air}} = \frac{1}{\epsilon_T} u_s = \frac{1}{0.4 + 0.4} \times 0.103 \approx 0.13 \text{ m/s.} \quad (4.89)$$

Here, the mobile-phase velocity is further weighted, so to speak, by the air that passes into, and spends some duration within the pores on the carbon surface (accounting for $\epsilon_s = 0.4$ of the total carbon volume). Therefore, this air velocity is less than the mobile phase velocity and larger than if the column was empty, as would be expected if one imagines that the effective cross-sectional area of the column becomes smaller by $\epsilon_m = 0.4$, but then less small when including the pores by $\epsilon_m + \epsilon_s = 0.8$. This estimate of the air speed is used to characterize the speed of radon passing through the carbon,

which is directly proportional to the air speed, and also inform the diffusion coefficient, which has been modeled to depend on air speed.

4.4 Types of Radon Mitigation Systems

Two classes of systems may create a radon-mitigated, breathable-air environment. One type flows continuously through a filtration column, while the second swings flow back and forth using two or more filtration columns. The filtration columns are usually filled with activated carbon due to its preferential adsorption of radon over oxygen or nitrogen [102]. The continuous-flow system (*e.g.*, [103, 104, 105]) operates on the basis that a considerable fraction of radon decays before exiting the column. The radon concentration leaving the outlet of the column $C_{\text{outlet}} = C_{\text{inlet}} \exp(-t_b/\tau_{\text{Rn}})$, where C_{inlet} is the radon concentration of the input air, t_b is the characteristic break-through time of the filter, and $\tau_{\text{Rn}} = 5.516$ days is the mean lifetime of radon. The break-through time is the mean-time it takes for radon to pass through the carbon filter. To increase the break-through time, and therefore make a continuous flow system practical, one must cool the carbon to reduce desorption of radon. Continuous systems are commercially available (from [106]) and typically achieve reduction factors of $\sim 1000\times$ at $\sim 100 \text{ m}^3/\text{hour}$.

In a swing-flow system, two or more filtration columns are used. While air is filtered through one column, the other is regenerated using either low pressure or high temperatures to allow radon to desorb and be exhausted efficiently. For a vacuum-swing-adsorption (VSA) system (*e.g.*, [107, 108, 109, 66]), high-radon input air is filtered through the first column while the second column is pumped down to ~ 20 Torr. Well before the break-through time, the path of the high-radon input air is switched so that it flows through the second column instead, allowing the first to regenerate. For an ideal column, no radon reaches the output. Swing-flow systems are more complicated both in operation and analysis. A VSA system can potentially outperform a continuous flow system even at a lower cost. Temperature-swing systems (*e.g.*, [110]) should provide best performance but at the highest cost and complexity.

While there are many applications for VSA systems other than removing radon from air, one particular example is included below, as it relates to Dark Matter detection. Argon is an excellent scintillator target for detectors searching for Dark Matter due to its excellent scintillation efficiency and transparency to its own light [111]. Atmospheric argon is mostly ^{40}Ar , but also contains cosmogenic ^{39}Ar (produced by $^{40}\text{Ar}(\text{n},2\text{n})^{39}\text{Ar}$ reactions) that corresponds to $> 1 \text{ Bq/kg}$ for atmospheric argon, which leads to an important background for Dark Matter experiments [112, 113]. In an effort to obtain Ar that is depleted in ^{39}Ar , a group at Princeton has used a VSA system—very similar to the design presented in Chapter 5—to extract argon from a CO_2 well found to contain 600 ppm of argon; deep underground, the ^{40}Ar had been largely shielded from cosmic rays and thus has less (by about $50\times$) ^{39}Ar than atmospheric argon [112, 113]. A VSA system was employed that trapped CO_2 , O_2 , H_2O , and CH_4 , but allowed He, Ar, and N_2 to pass through the filtering column, with the Ar later separated from He and N_2 by distillation. This example illustrates how VSA systems can be used in separating a variety of different gas species. However, removing radon from breathable air is the focus of this thesis.

Chapter 5

The SD Mines Demonstration Radon-Reduction System

The radon reduction system (RRS) commissioned at SD Mines (imaged by Fig. 5.1) is based closely on the design developed at Princeton [108, 107]. This system has been used as both a proof-of-concept (and is thus frequently referred to as the demonstration RRS) and to supply low-radon, breathable air to the SD Mines cleanroom (see Chapter 6). This system is built upon essentially two principles: (1) radon adsorbs to carbon and (2) air, and the radon in it, moves more quickly through carbon at lower pressure. The description of the SD Mines RRS below represents the current state of the system. That is, there are design strengths and weaknesses. Someone planning to build a similar system should be cautious to not incorporate weaknesses of this system (elaboration on system improvements may be found in Section 7.15).

Let us refer to Fig. 5.2 (with labels in **bold text** for the next few paragraphs). Nominally, high-radon air enters the system at the **input**. An inline **blower** forces air through the **box filter**, just before it, and then through an **air chiller**, a **dehumidifier**, and another **air chiller**. There are two circles containing the letter **G** representing a manual gate valve that physically connects the **input** and **output** ducting (which happens to be parallel and nearby, but not shown diagrammatically). This gate valve, when open, provides a pathway for air to bypass the RRS and be supplied to the clean room.

The dehumidifier works by passing (wet) air through a rotating cylindrical membrane that has a large surface area. The water in the air adsorbs to the surface of the membrane. As the membrane rotates, a heated stream of air, called the **reactivation air stream**, evaporates the water from the wheel and carries it out through an exhaust. The air then

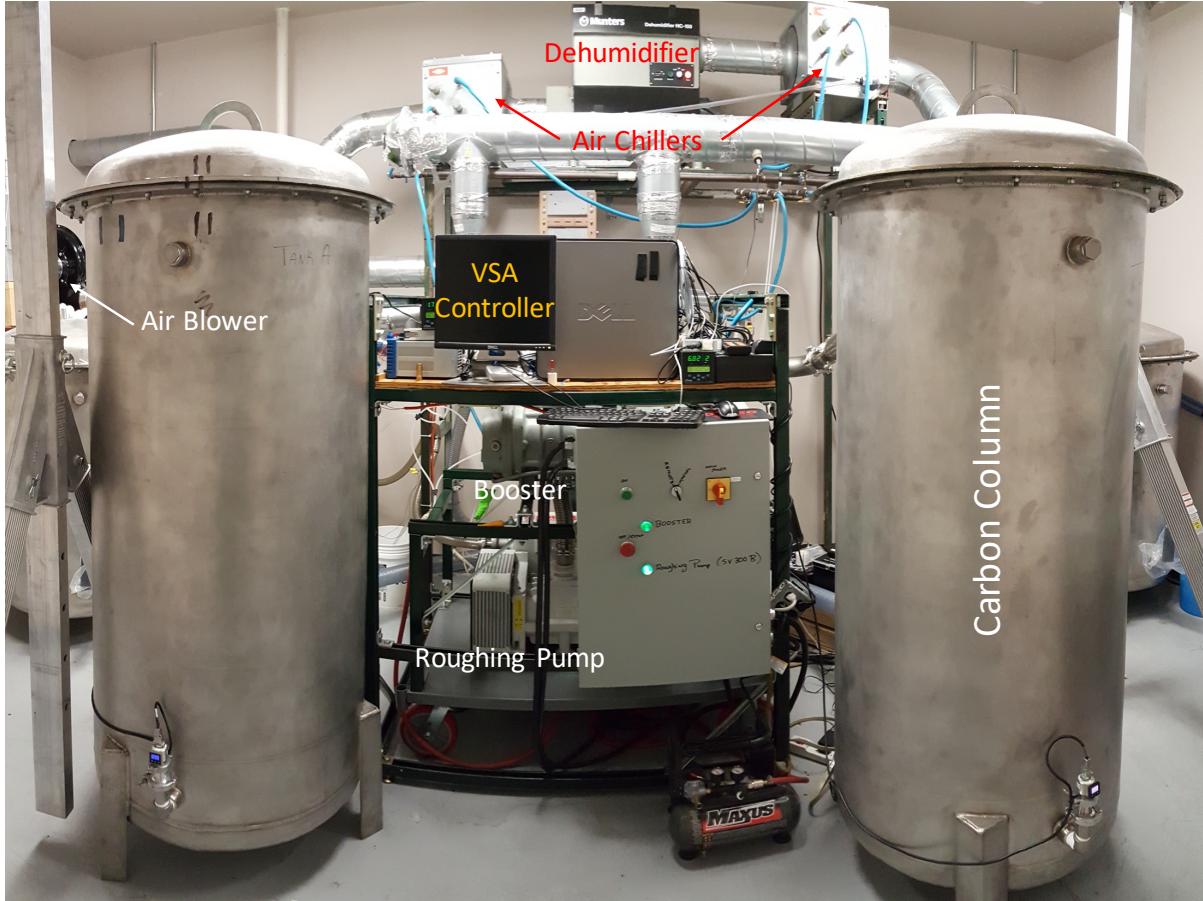


Figure 5.1: The SD Mines Radon-Reduction System

exits the dehumidifier with a lower relative humidity. For clarity, let the air passing from the **input** to the **output** be called the *process air*. The volumetric flow rate of the process air is measured by an inline anemometer denoted by the encircled **V**. The anemometer measures the linear velocity v of air passing through the duct with cross-sectional area A , while the volumetric flow is found by $F = v/A$.

As a byproduct of dehumidification, the process air is heated. To counter this, air chillers are added inline. Chilled water (held at about 12 °C) passes through radiators within the air chillers. Air passing through the air chillers give up heat to the radiator and thus exits at a cooler temperature. The temperature of the input air is nominally 22 °C (room temperature) and exits the **air processing** assembly with a temperature of around 22 °C. The relative humidity at the input is nominally 40% and exits the air

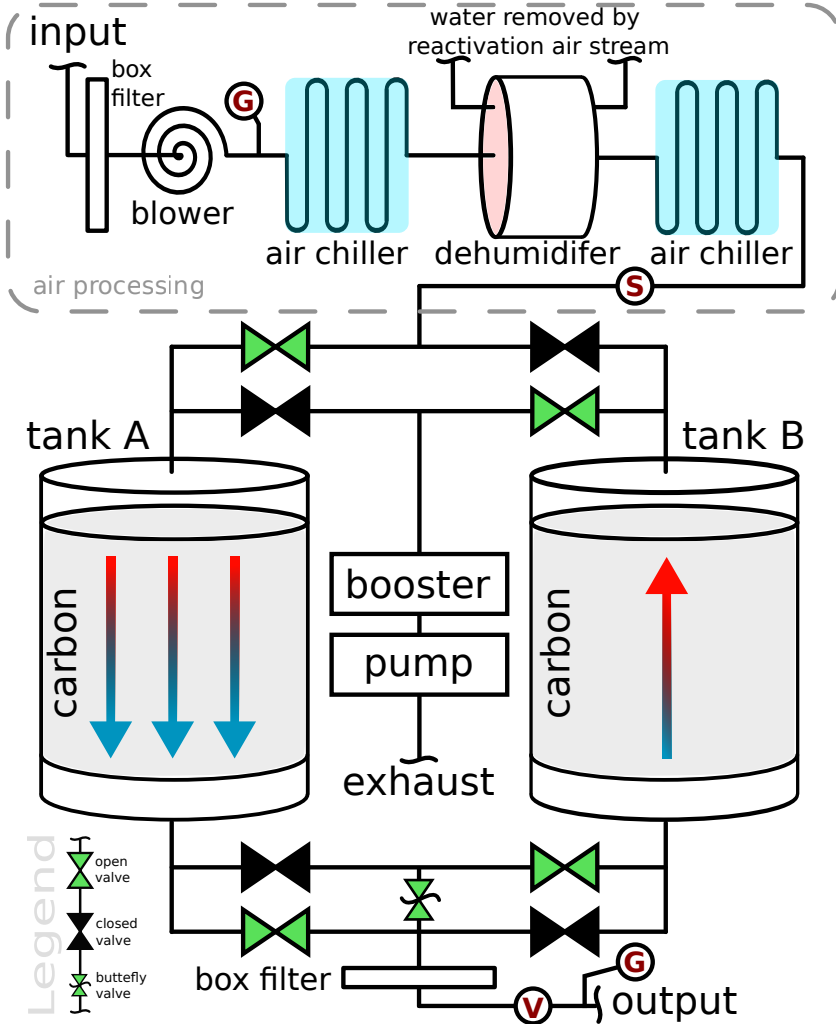


Figure 5.2: Schematic of Radon-Reduction System. A legend is found in the lower-left corner, while an in-depth description may be found in text. High radon air flows through the air processing assembly where it is dried, but not heated. This process air then flows, by use of valves, to one of the two columns. The radon in the air will move more slowly though the column than the air that carries it, such that the air leaving the column will, initially, have little radon in it. During this time, the other column is pumped on by the vacuum pumps, with a few cfm of purge-flow air provided from the other column. Radon will travel more quickly out of the column at low pressure such that this column can be regenerated, *i.e.*, purged of radon. Regeneration is achieved before radon substantially passes through the first column and is brought up to atmospheric pressure with the low-radon air being produced. At this point, the system begins filtering through the newly regenerated column and regenerates the other.

processing assembly at around 10%, and with a dew point of about -16°C (though these values can change depending on the input air and temperature of the chilled water). These measurements are made, penetrating the ducting, at the location of the encircled S.

After the air processing assembly, the high-radon, not-heated, dry process air passes through an **open valve** and into a stainless steel, vacuum-tight column (in this case, **tank A**) that contains ~ 225 kg of Calgon activated carbon (see Appendix A). As radon atoms move through the carbon bed, they adsorb to the surface of the carbon according to an induced dipole interaction (see Section 4.1). Radon atoms will stay adsorbed to the carbon until other atoms knock them off. This so-called desorption is therefore temperature dependent. As radon atoms spend some fraction of their time adsorbed to the carbon's surface, they will move more slowly through the carbon bed compared with the carrier gas, which is air (as N_2 and O_2 are polar and do not adsorb as easily to the carbon). Therefore, the air initially exiting the column is very low in radon.

While radon is being filtered (due to its moving slowly) through tank A, **tank B** is being regenerated. During regeneration a column is pumped on by the **booster** and roughing **pump**, but with a small amount (usually about 7 scfm) of low-radon air fed to the other end via the so-called purge flow valve (a **butterfly valve**). At low pressure, radon atoms move more quickly through the carbon (see Section 7.6). For this system, radon atoms move, on order, 10 to $1000\times$ faster during regeneration than when filtering. The reason there is a range here is due to the pressure gradient across the column. Before radon atoms break through the carbon in tank A, the carbon in tank B may be made mostly radon-free.

Before tank B is ready to be used as a filter, however, we must bring it up to atmospheric pressure. This is done by closing the valve that connects tank B to the pumps. The purge-flow (butterfly) valve remains open such that the pressure P in the tank will approach atmosphere P_{atm} after about $t = 15$ minutes:

$$P(t) \sim P_{\text{atm}} \frac{\varphi t}{V}, \quad (5.1)$$

where V is the tank air volume and φ is the purge flow rate, which, of course, determines how long it takes to bring the volume up to atmosphere. After reaching atmospheric pressure (or very nearly), tank B can be used as the radon filter. If the tank is not

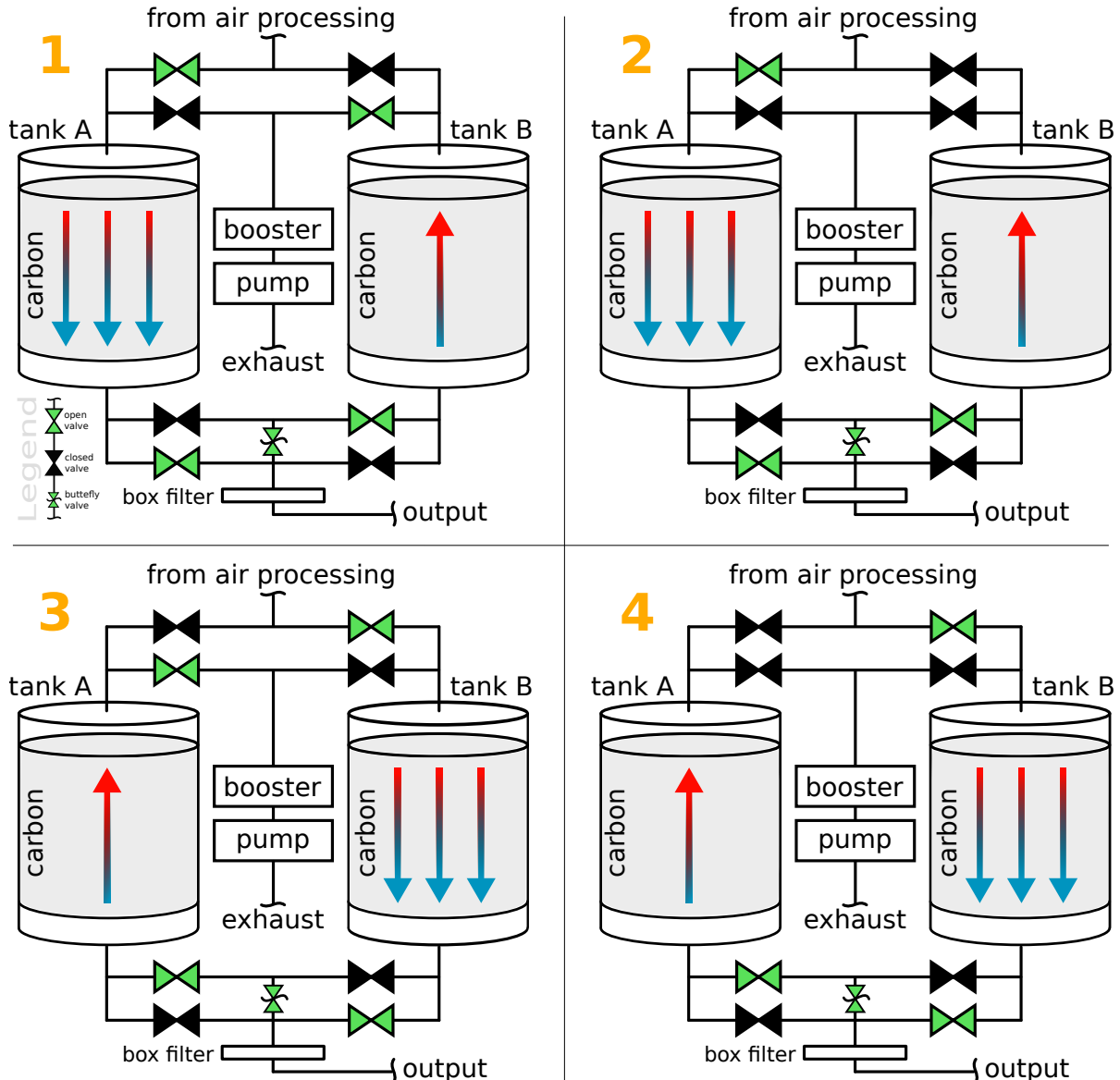


Figure 5.3: A full cycle of RRS operation is represented by four steps. In orange labels, step 1 (with legend found in lower-left corner) shows radon being filtered through tank A while tank B is regenerated. In step 2, the pumping system is closed off from tank B such that it can be brought up to atmospheric pressure by air continuing to be supplied by the purge flow valve (the so-called slow-fill mode). In step 3, filtering begins through tank B while tank A is regenerated. Finally in step 4, tank A is brought up to atmosphere. Going back to step 1, filtering begins through tank A while tank B is regenerated—beginning a second cycle.

brought up to atmosphere before filtering begins, the high-radon process air will be pushed into tank very quickly and therefore may compromise the recent regeneration. The continuous operation of the RRS is illustrated by Fig. 5.3.

The roughing pump and booster (along with their temperature monitoring sensors), valves, and pressure gauges are all controlled (or read out) by a custom LabView visual interface (VI) running on a local computer.

5.1 The SD Mines Radon Monitor

In order to measure the low-radon concentration produced by the SD Mines RRS (as described in Section 5.2) a sensitive radon detector is needed. The SD Mines Radon Monitor is a high-sensitivity radon detector (see diagram in Fig. 5.4) based on the design developed by K. Hosokawa *et al.* [116, 117] and built by Dr. Luke Corwin's group. By sampling boil-off liquid nitrogen, which is expected (but not measured) to have a radon concentration of $\sim 0.5 \text{ mBq/m}^3$, resulted in a radon concentration of $2.7 \pm 0.4 \text{ mBq/m}^3$

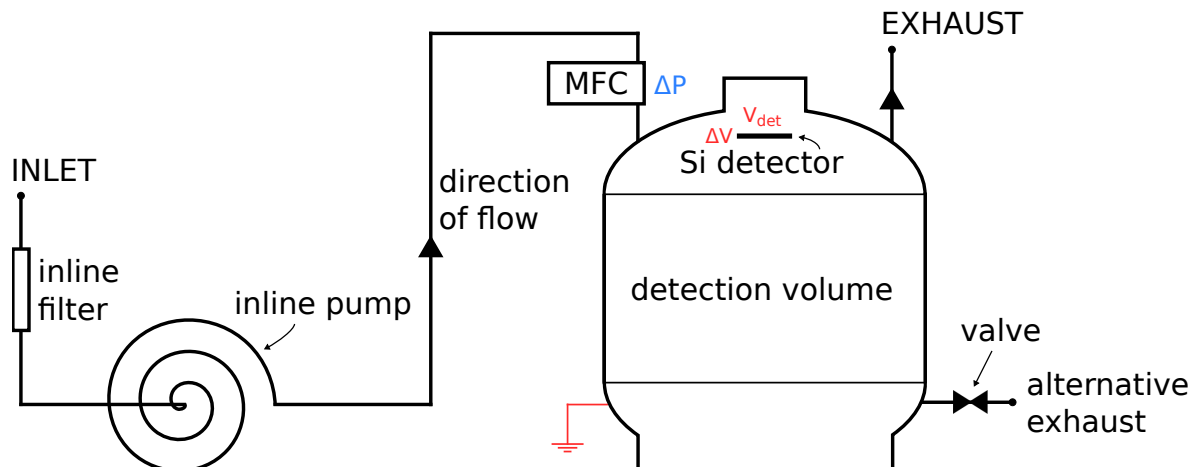


Figure 5.4: The SD Mines Radon Monitor measures the α -decay of the radon daughters ^{210}Po , ^{214}Po , and ^{218}Po . The system may be described as follows (with bold text referencing labels within the figure): air is sampled at the **INLET**, then passes through a 1/4-inch compression **inline filter** (capturing particles $> 1\mu\text{m}$ McMaster-Carr SKU: 9811K83) and reaches the low-pressure side of an **inline pump** (Enomoto Micro Pump Mfg. Co., Ltd., model MX-808ST-S), which provides the required pressure gradient ΔP of greater than $\sim 10 \text{ psig}$ across a Horiba Z500X mass-flow controller (**MFC**). The **MFC** sets and maintains the volumetric flow rate (of nominally 2 lpm) through the Radon Monitor **detection volume**. While sample air mixes within the **detection volume**, radon daughters may decay and, with a high probability of being positively charged, be collected by a **Si detector** having a voltage bias of $\Delta V = 25 \text{ V}$ and held at $V_{\text{det}} = -1.5 \text{ kV}$ below the grounded chamber. The air then leaves the Radon Monitor through the **EXHAUST**, or, for other configurations, the **alternative exhaust**, which is open or closed by an inline **valve**.

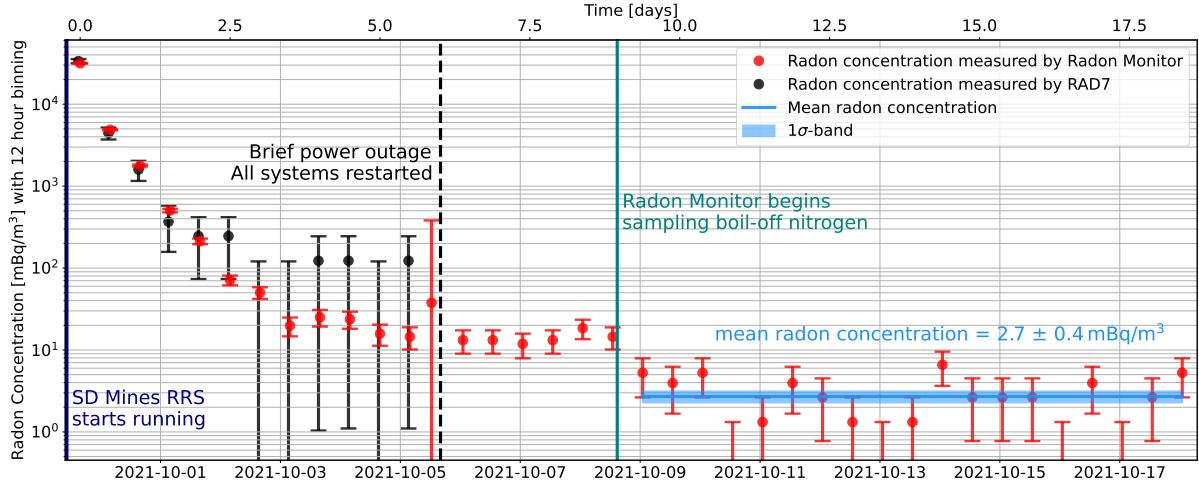


Figure 5.5: The SD Mines Radon Reduction System (RRS) starts swing operation at time = 0 days (top axis) and begins reducing the radon concentration measured by the Radon Monitor (red circles, inferred from ^{218}Po decays) and, simultaneously, a Durridge RAD7 set to a 20-min sampling period (black circles). Close agreement is seen between the Radon Monitor and RAD7, indicating that a delay in detection response (*e.g.*, from sample air mixing within the detection volume) is not significant. Just as the RRS output radon concentration approaches an equilibrium, a brief power outage (~ 2 hours) takes place (dashed line), but all relevant systems are restarted and measurement is resumed. After equilibrium is obtained at around 9 days, the Radon Monitor is made to sample boil-off nitrogen (solid teal line). After about one day, an equilibrium has been closely approached. Over the subsequent 9 days of steady-state counting, the mean radon concentration, and thus the Radon Monitor’s upper limit on its blank rate, is found to be 2.7 ± 0.4 mBq/m 3 . This is an upper limit because we do not know the boil-off nitrogen radon concentration (but expect it to be $\lesssim 0.5$ mBq/m 3 [114, 115]).

(see Fig. 5.5); the upper limit on the Radon Monitor’s blank rate for ^{222}Rn is therefore 3.5 mBq/m 3 at 95% C.L. (ignoring any contribution of the boil-off nitrogen).

The Radon Monitor was cross-calibrated with a Durridge RAD7 [118]. The radon concentration within the local lab space nominally ranges between 50 and 150 Bq/m 3 ; the swing in concentration can take place over just a few hours. This high-radon lab air is sampled by both the RAD7 and Radon Monitor over the course of many weeks (taken from a variety of runs over the course of a year). A single calibration constant, expected to be independent of the rate measured, is used to scale the inferred radon concentration of the Radon Monitor to closely agree with the RAD7 measurement. One weakness in this calibration is that the relative humidity of the sampled lab air changes over time, with a day-night variation of 20 to 40% (but much higher during storms),

with the relative humidity highest at night (when the temperature is cooler). The RAD7 is paired with a Durridge Drystik, which removes moisture from the air to ensure the sampled air has a relative humidity around 6%. The air sampled by the Radon Monitor is not typically dried (as for most applications the sample air will already be dry). The detection efficiency of the Radon Monitor is expected to be reduced with increased relative humidity. No attempt has been made to correct for relative humidity (in this work); the resulting systematic on the Radon Monitor measurement is expected to be smaller than 20% (but could be further investigated).

In order to understand the Radon Monitor’s detector response to a change in the radon concentration of the sample air, we first assume a perfect-mixing case: radon enters the detection volume V with flow rate F at a radon concentration C_{in} and mixes “perfectly” (*e.g.*, there at no time exists a concentration gradient within V) before being exhausted with the radon concentration $C(t)$. The differential equation describing this process is

$$\frac{\partial C}{\partial t} = \frac{F}{V}C_{\text{in}} - \lambda C - \frac{F}{V}C, \quad (5.2)$$

where λ is the radon decay constant. However, we will now ignore the decay term, as we expect the characteristic time of perfect mixing, V/F to be much shorter than the radon lifetime (of $1/\lambda$). For the Radon Monitor, $V = 68.7$ liters and $F = 2$ liters/minute, and so the characteristic time for perfect mixing would be $V/F = 34.4$ minutes. Therefore, we cut the second term and solve:

$$\begin{aligned} \frac{dC}{dt} &= \frac{F}{V}C_{\text{in}} - \lambda C \approx 0 - \frac{F}{V}C \\ &= \frac{F}{V}C_{\text{in}} - \frac{F}{V}C \\ &= \frac{F}{V}(C_{\text{in}} - C). \end{aligned}$$

We may now solve for C :

$$\begin{aligned}\frac{dC}{C_{\text{in}} - C} = \frac{F}{V} dt &\longrightarrow \int \frac{dC}{C_{\text{in}} - C} = \int \frac{F}{V} dt \\ -\ln |C_{\text{in}} - C| &= \frac{F}{V} t + k \\ C_{\text{in}} - C &= A e^{-\frac{Ft}{V}} \longrightarrow C = C_{\text{in}} - A e^{-\frac{Ft}{V}},\end{aligned}$$

where A is a constant (and captures the constant k). Using the boundary condition $C(0) = C_0$, the low-radon concentration of the RRS output air, provides the unique solution:

$$C(t) = (C_0 - C_{\text{in}}) e^{-Ft/V} + C_{\text{in}}. \quad (5.3)$$

Now, the assumption of perfect mixing *can* be wrong for two important reasons (though one can imagine other cases as well):

1. The input sample air travels, for example, along the outer wall of the detection chamber before being exhausted, does not mix perfectly, and leaves “old” air, so to speak, around (and with line-of-sight) to the detector.

This would result in the characteristic mixing time being **longer** than for perfect mixing.

2. The input air could circulate and efficiently replace air around the detector, leaving some spaces within the detection volume unmixed. This so-called dead-volume, if having poor line-of-sight to the detector, could act to reduce the volume the sample would need to replace.

This would result in the characteristic mixing time being **shorter** than for perfect mixing.

Fig. 5.6 shows the measured detector response to the following procedure: the Radon Monitor sampled low-radon air within the SD Mines cleanroom, as supplied by the SD Mines Radon Reduction System (RRS), until a steady state was achieved (around

10 mBq/m^3). At $t = -4.3$ hours, the Radon Monitor **began sampling high-radon lab air**. The radon concentration measured within the Radon Monitor increased and reached a nearly steady state. At time = 0 hours, the Radon Monitor **began sampling cleanroom air** again, resulting in a drop in the radon concentration measured. Both of these regions of the concentration (first increasing then decreasing) are fit to equation Eq. 5.3 in the following forms:

- Increasing concentration:

$$C(t) = A(1 - e^{-t/\tau}), \quad (5.4)$$

where A is fitting parameter describing C_{in} and τ , also a fitting parameter, is the characteristic mixing time which will be compared to V/F .

- Decreasing concentration:

$$C(t) = Ae^{-t/\tau} + B, \quad (5.5)$$

where A describes the high-radon lab air within the Radon Monitor that was previously sampled and B describes the low-radon cleanroom air now being sampled. The characteristic mixing time τ is fit and will similarly be compared to V/F .

From these two fits, we infer a characteristic mixing time of 30.6 ± 2.1 and 33.7 ± 0.4 minutes for increasing and decreasing regions respectively. Because the radon concentration of the lab air is not constant, the characteristic time obtained by fitting Eq. 5.4 to the increasing region of the data is less reliable as compared with that inferred from the decreasing region of the data, where the sampled radon concentration from the RRS output is much lower ($\sim 20 \text{ mBq/m}^3$). Therefore, the Radon Monitor characteristic time for mixing is taken as the latter value of 33.7 ± 0.4 minutes. Comparing this measured characteristic time to that of perfect mixing, we find that the two agree within 1σ .

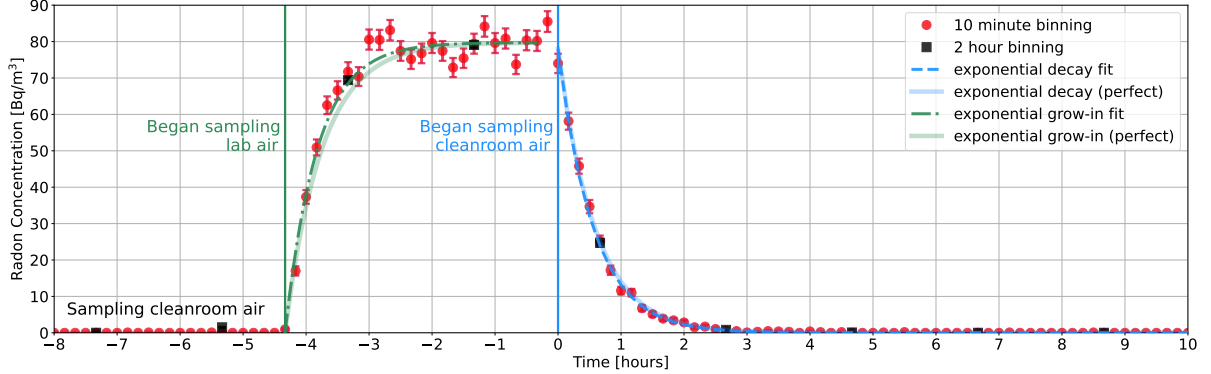


Figure 5.6: The Radon Monitor responds to a step-change in the sampled radon concentration with a characteristic time of 33.7 ± 0.4 minutes (with sample flow rate of 2 lpm). For both grow-in (-4.3 to 0 days) and decay (0 to 10 days) regions, best fits (of Eq. 5.4 and Eq. 5.5, for grow-in and decay, shown in dot-dash and dash, respectively) to measurement closely agree with the perfect-mixing case (thick transparent lines with matching colors), having the characteristic time of 34.4 minutes.

Flow Rate [lpm]	Time [minutes]	$C(t)/C_{in}$
1	60	0.576
1	120	0.820
1	240	0.968
2	60	0.820
2	120	0.968
2	240	0.998
3	60	0.923
3	120	0.994
3	240	1.000

Table 5.1: The mixing fraction $C(t)/C_{in}$, defined by Eq. 5.6, for varying flow rate and time sampled.

A natural next question is, “How long should we measure to reach, say, 99% of the true sample air concentration?” Here, we consider the fraction:

$$\frac{C(t)}{C_{in}} = 1 - e^{-t/(V/F)}, \quad (5.6)$$

which is a rearrangement of Eq. 5.3. The measurement time necessary to achieve a desired confidence is illustrated by Fig. 5.7, with numerical values provided in Table 5.1.

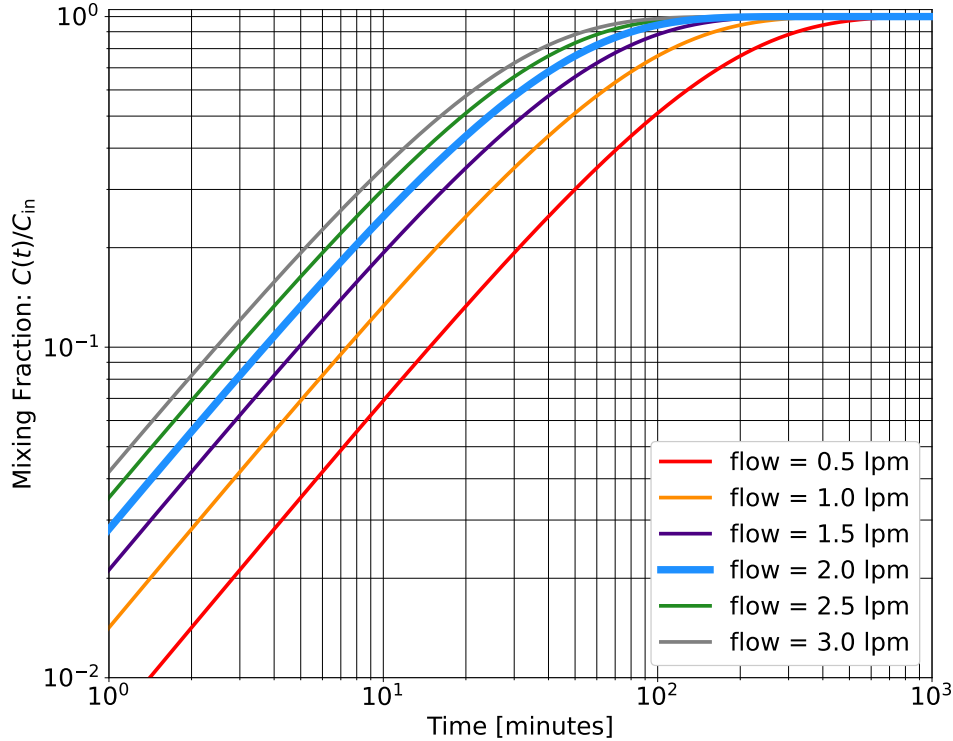


Figure 5.7: The mixing fraction $C(t)/C_{in}$, defined by Eq. 5.6, depends on the sample air flow rate (nominally 2 lpm) and time t . Table 5.1 provides the mixing fraction numerically for varying flow rate and time.

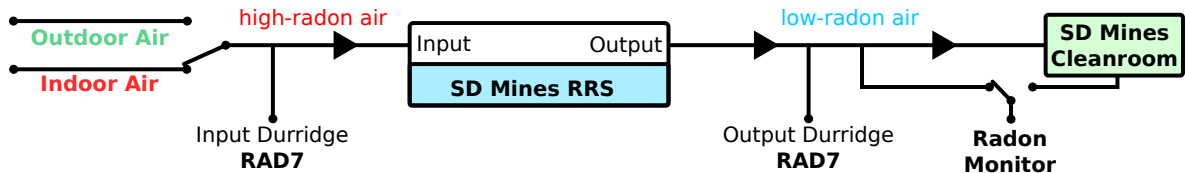


Figure 5.8: Indoor or outdoor air is supplied to the input of the SD Mines RRS. A Durridge RAD7 samples this high-radon input air with, typically, a 20 minute sampling period. The low-radon RRS output air supplies the SD Mines cleanroom, and along the way, is sampled by both a Durridge RAD7 and the SD Mines Radon Monitor (which may be configured to sample directly from the SD Mines cleanroom).

5.2 Performance of the SD Mines RRS

The performance of the SD Mines Radon Reduction System (RRS) is determined by its ability to reduce the radon content of the air passing through it. Referring to the diagram illustrated by Fig. 5.8, the input to the SD Mines RRS is supplied with indoor or “lab” air, which has a nominal radon concentration of $\sim 100 \text{ Bq/m}^3$, or, alternatively, outdoor air, which has a nominal radon concentration of $\sim 10 \text{ Bq/m}^3$. This high-radon

air is sampled by a Durridge RAD7, a reliable device with a well-suited sensitivity of $\sim 0.1 \text{ Bq/m}^3$. The SD Mines RRS output (typically low-radon) air then supplies and overpressures the SD Mines cleanroom. Before entering the cleanroom, the low-radon air is sampled by another Durridge RAD7 and the SD Mines Radon Monitor. The Radon Monitor provides an improved sensitivity over the RAD7 of $2.7 \pm 0.4 \text{ mBq/m}^3$, while the RAD7 provides a useful check on the Radon Monitor detection response and calibration (a description of the SD Mines Radon Monitor may be found in Section 5.1). Both the RAD7 and SD Mines Radon Monitor (shown explicitly in Fig. 5.8) may be configured to sample the SD Mines cleanroom, as this is useful in understanding, for example, radon emanation from the cleanroom's construction materials.

When the SD Mines RRS begins operating, air is filtered through one column while the second regenerates (as described earlier in Chapter 5). Because neither column starts in a regenerated state, the filtered air has approximately the radon concentration as the input air. Each full cycle regenerates both columns once, with each regeneration stage removing more radon from the column than is introduced during the filtering stage. Over time a steady state is reached, where the equilibrium output concentration is *mostly* determined by the radon concentration of the input air and the through-column flow F ; however, there are many configurations of the RRS that influences output equilibria, as discussed in RRS Simulation Predictions (Section 7.15).

Figure 5.9 shows the measured output radon concentration (*i.e.*, regeneration curves, or RCs) for several make-up air flows F_{cr} , with two at around 25 scfm, two at around 45 scfm, and two at just over 80 scfm. The input radon concentration was measured by a RAD7 and showed fluctuations between 12 and 178 Bq/m^3 with an average value (across all runs) of 76 Bq/m^3 ; not at all unusual for our lab space. The six curves are easily put into three groups (for low, medium and high flow) by observing the differences in the time to approach equilibrium, with equilibrium being reached within 3 days for all flows shown. As can be seen, the choice of flow rate impacts the time to reach equilibrium. For

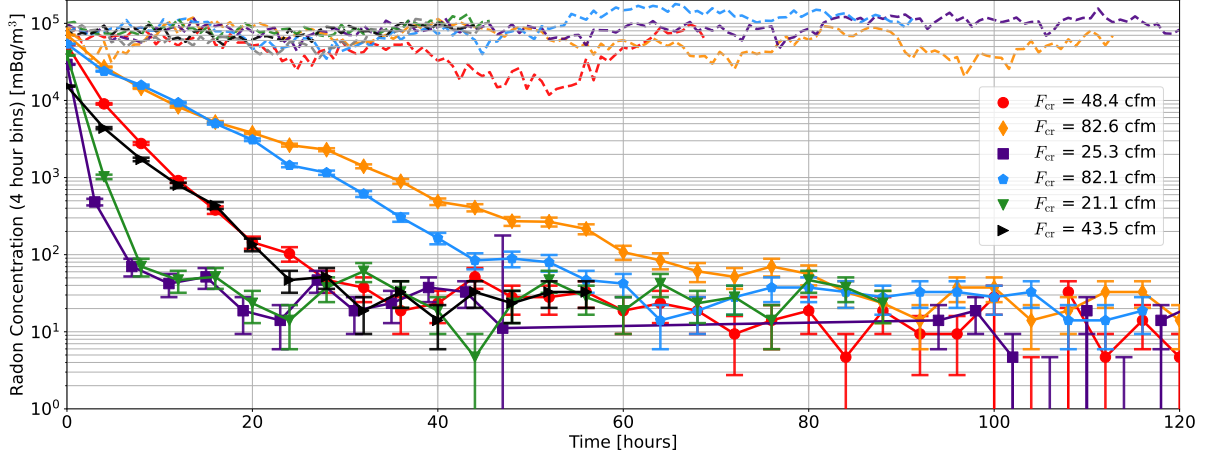


Figure 5.9: When the SD Mines RRS first starts, the output radon concentration (colored shapes) has a similar concentration as the input air (thin dashed lines with corresponding color). Each regeneration stage removes more radon from the column than was added during the preceding filtering stage, and thus the output concentration drops over time until, reaching a steady state within 1 to 3 days depending on the make-up air flow F_{cr} .

example, if power was lost to the RRS, one could start the system at a lower flow to more quickly reach equilibrium (by a day or two), but at the cost of cleanroom overpressure (perhaps reducing it by a factor of two).

Figure 5.10 shows the equilibrium radon concentration as a function of make-up air flow F_{cr} to the cleanroom. These data were measured by the SD Mines Radon Monitor sampling the RRS output (not the SD Mines cleanroom) and are compared to predicted equilibria by the RRS simulation (introduced in Chapter 7). For $F_{cr} < 70$ scfm, the average equilibrium concentration stays below 25 mBq/m³, but quickly increases for higher flow rates. All of these equilibrium concentrations are low enough to meet the SuperCDMS SNOLAB goal (of 100 mBq/m³) described in Section 2.2.1. A close copy of the SD Mines RRS has been built and installed at SNOLAB; this SNOLAB RRS will provide low-radon air to a cleanroom where the SuperCDMS detectors will be installed.

The performance of the SD Mines RRS may be compared to the (more expensive) continues-flow radon-reduction system available to order from the Czech Republic company ATEKO [106]. The ATEKO RRS can provide radon-reduced air at a flow rate between 120 and 300 m³/hour (70 and 177 scfm) with a radon reduction of $\sim 1000 \times$ [119].

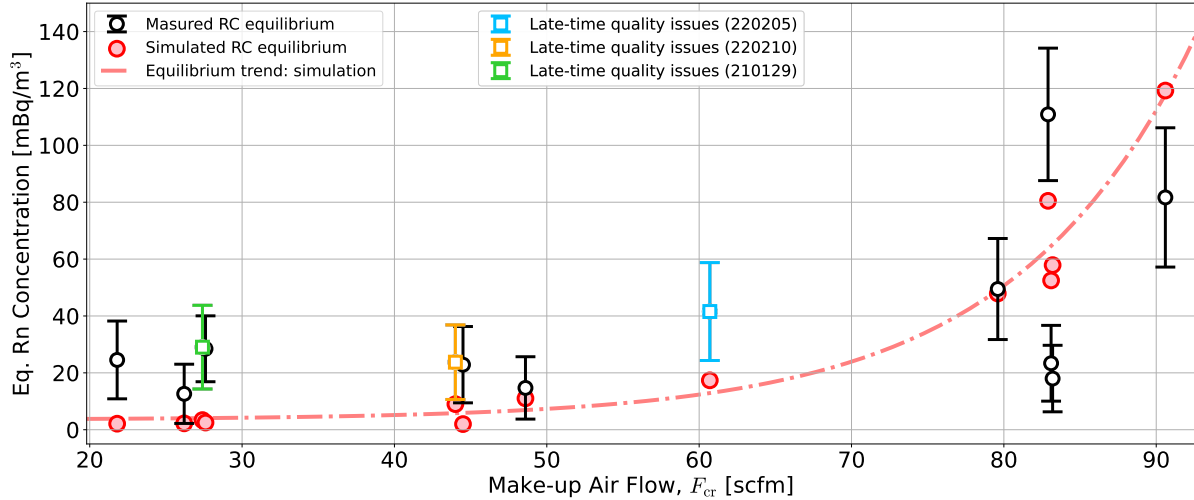


Figure 5.10: The equilibrium radon concentration of measured RCs (open black circles and colored squares) is compared with that of their corresponding simulated RCs (filled red circles); an exponential trend line (dot-dashed red curve) is drawn for the simulated equilibria. For all but three runs, equilibria are inferred from a time selection where both measured and simulated RCs have reached equilibrium. Each of the three exception runs (220205, 220210, and 210129 represented by colored squares) approached equilibrium but then presented several high-rate readings that are not understood; for this reason, equilibria were inferred by taking the mean of measured data between times different than those used to infer equilibria from their simulated counter-part. For more details on the simulated points, see Section 7.13.4.

As described in Section 7.15.2, the SD Mines RRS design could potentially outperform the ATEKO system at a lower cost.

5.3 Vacuum Pumps and Measured Pressure in Columns

The pressure within a column is monitored by pressure transducers (MKS, P/N 901P-21034) located at the top (just above the carbon bed) and bottom (just below the carbon bed) of a stainless steel column. The pressure is measured during both typical operation, and more specific tests, such as determining the pumping speed or leak rate in part of the system. These transducers employ both a micro-pirani sensor for low pressure (under 100 Torr) and a piezo-electric crystal sensor for high pressure (above 100 Torr). Though the accuracy depends on the the pressure and type of sensor in use, in this work the error on the measured pressure will be taken as $\pm 5\%$ of the recorded value. This uncertainty is taken from the micro-pirani sensor accuracy for the pressure range 10^{-3} to 100 Torr.

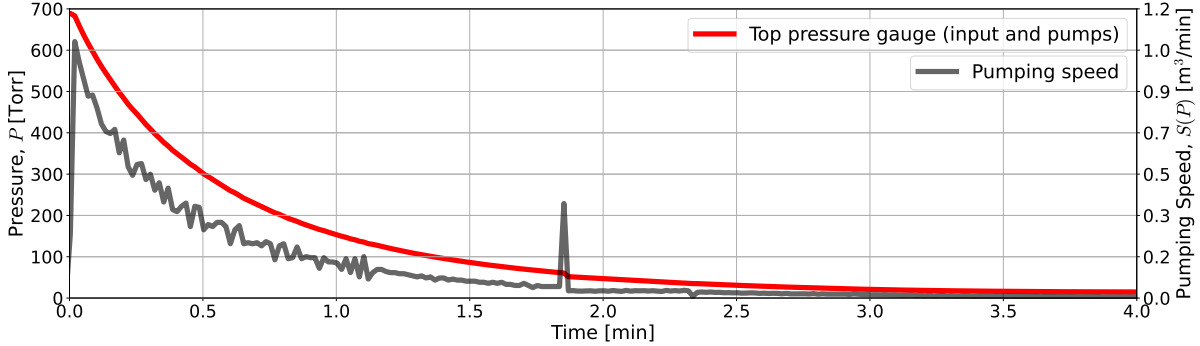


Figure 5.11: During the regeneration stage (or a test of the vacuum system), the valve connecting the column to the pumps is opened, and the pressure in the column (red curve) drops and approaches its base pressure (a function of the purge flow). The time derivative of the measured pressure (along with the column volume and starting pressure, typically P_{atm}) may be used to estimate the pumping speed (gray curve in units of volume at atmospheric pressure per time) according to Eq. 5.7. The sharp spike at around 1.8 minutes is caused by the pressure transducer switching between piezo-electric and micro-pirani sensors.

The RRS system may be configured with pressure transducers at both ends (top and bottom) of a single stainless-steel carbon column or at the bottom (purge end) of both columns. During typical operation, the pressure gauges are installed on each column such that the purge pressure may be monitored. During characterization, both pressure gauges are installed on a single column.

The SD Mines RRS vacuum system consists of a Sogevac SV300B roughing pump and Edwards EH1200 booster, which increases pumping speed under ~ 100 Torr. With a purge flow f_{purge} , the pumping speed

$$S(P) = \frac{V}{P_{\text{atm}}} \frac{dP}{dt} + f_{\text{purge}}, \quad (5.7)$$

where P is the measured pressure on the pump-side of the column, the volume of air within the column $V = 0.5 \text{ m}^3$, and atmospheric pressure $P_{\text{atm}} = 680 \text{ Torr}$. Figure 5.11 shows the resulting plot for $f_{\text{purge}} = 7.2 \text{ scfm}$. Though we account for the purge flow in this calculation, its contribution is negligible (as $10 \text{ scfm} = 0.0047 \text{ m}^3/\text{s}$).

Figure 5.12 shows the pressure as measured at the top (inlet) and bottom (outlet) of a single column during swing-mode operation. During the filtering stage, the top pressure is only slightly larger (by a couple Torr) than the bottom pressure (as seen by the right

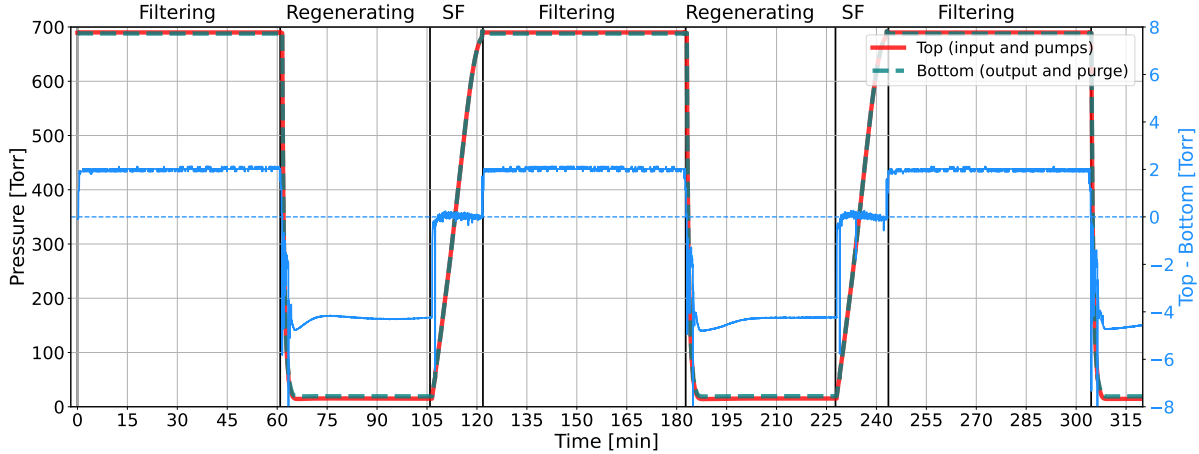


Figure 5.12: The measured pressure (left axis) at the Top (solid red line) and the Bottom (dashed teal line) of a column during swing mode shows periodicity over time (with uncertainties of 5% not shown). At the end of the slowfill (SF) stage, the pressure at the Top and Bottom locations should be equal, and this is used as a calibration between pressure gauges. Also in the slowfill stage, the pressure difference (right axis, blue line) is zero (within uncertainties) indicating that the pressure quickly relaxes throughout the carbon bed during this stage. During the filtering and regeneration stages respectively, we observe a positive and negative pressure gradient along the column axis, as expected.

axis). During the regeneration stage, the pressure within the column quickly approaches a base pressure of about 20 Torr, with the top pressure (nearest the pumps) about 4 Torr lower than the bottom pressure (at the column outlet, which is then being fed by the purge-flow line). During the slowfill stage, the pressure within the column quickly relaxes as air is slowly introduced to the otherwise-closed column through the purge-flow line at around 7 scfm, with the column reaching atmosphere in about 15 minutes (with the time determined by the purge-flow rate). After the slowfill stage, the filtering stage begins again and this pattern is repeated.

5.4 Temperature Measurements Within the Carbon Bed: Dependencies and Discussion

The SD Mines RRS has had one of the carbon columns outfitted with temperature monitoring. Resistive-temperature devices (RTDs, specifically **Platinum PT1000, 3-wire**) were installed within the column and externally on the outside of the stainless steel (the material the column is made from), with their respective locations indicated in

Fig. 5.13. Additional RTDs were installed within the 6" input ducting before (so, room temperature) and after the air is dried and cooled (usually $\sim 12^\circ\text{C}$); this is just before the air enters a carbon column. These RTDs are read out by a Raspberry Pi 4B mini computer, where the measurements are logged and a real-time plot of the readings is displayed. Of course, the RTD tells us how the resistance of a small mass of material changes, with the temperature of the mass then inferred. Illustrated by Fig. 5.14, the RTD mass can change temperature through a combination of conduction (where the RTD mass is in contact with carbon granules) and convection (where air passing through the carbon bed exchanges energy with the RTD).

The time radon spends on the carbon surface (adsorbed) depends on the carbon surface temperature (as described by Eq. 7.31). If we have good reason to suspect the RTDs are primarily measuring the temperature of the air passing through the column, we may be able to improve the simulation by treating the RTD data differently. Of course, even if the RTDs measure the temperature of the air, this measurement may also approximate the temperature of the carbon surface. Comparing the surface area of graphene, which is about $2630 \text{ m}^2/\text{g}$ [120], to the measured surface area of our activated carbon, which is between 1300 and $1500 \text{ m}^2/\text{g}$ (as inferred from a specific surface area assay given in Appendix A), suggests that outermost surface layer of the activated carbon represents about half of the total mass of the carbon bed; this combined with the input-side of the carbon bed changing temperature before the other (output) end suggests that the surface of the activated might indeed be represented by the measured temperature of the embedded RTDs.

In order to test whether conduction or convection might play a dominant role in influencing the RTD temperature measurements, we consider two historical cases. As part of a senior design project, an attempt was made to share heat between the filtering and regenerating columns (which should improve system performance by slowing radon moving through the filtering column while speeding up radon moving through the regenerating

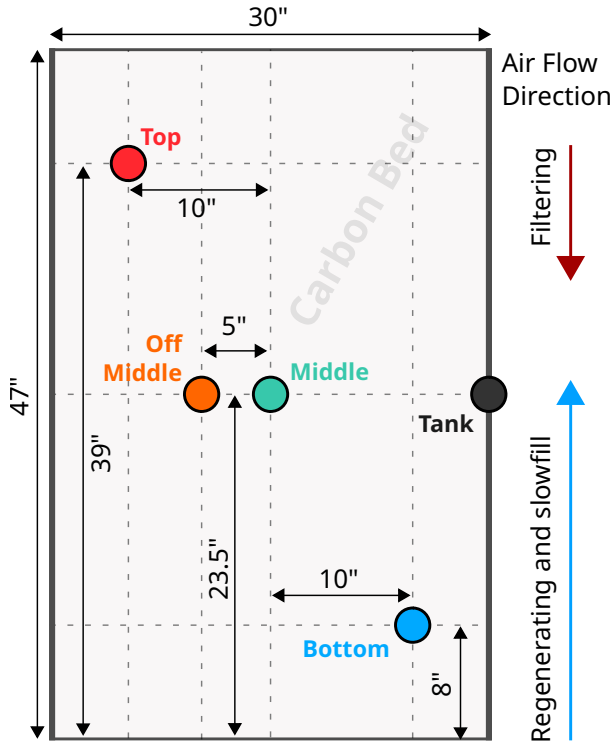


Figure 5.13: Resistive-temperature devices (RTDs) have been installed to monitor temperature at five locations within a single tank. The **Tank** RTD is located on the outer stainless steel vessel, placed externally on the middle height of the column. The **Top** and **Bottom** RTDs are both 8 inches within the carbon bed at a distance of 10 inches from the column's axis. The **Middle** RTD is located, per its name, at the center of the carbon bed, while the **Off Middle** RTD is located 5 inches in the radial direction from it.

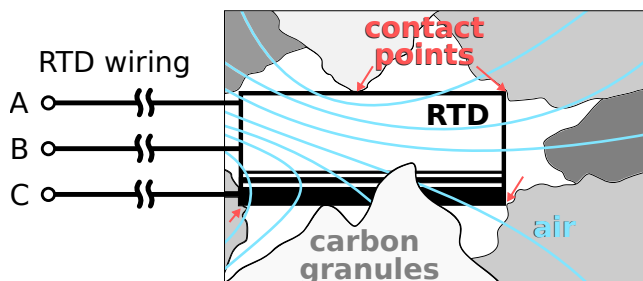


Figure 5.14: The RTDs that were installed within the carbon bed have points of contact (red arrows) between the RTD mass (black rectangle) and the carbon granules (chunks of gray). The majority of the RTD surface area is not in direct contact with the carbon granules, but bathed in the air (represented by blue lines) passing through the bed. The RTDs used have three leads labeled, here, as A, B, and C.

column). Plastic (polyvinyl chloride, or PVC) tubing was used to wrap each tank while forming a closed loop. Water was then pumped through the tubing in order to transfer heat between the two columns. This resulted in a change in temperature measured by

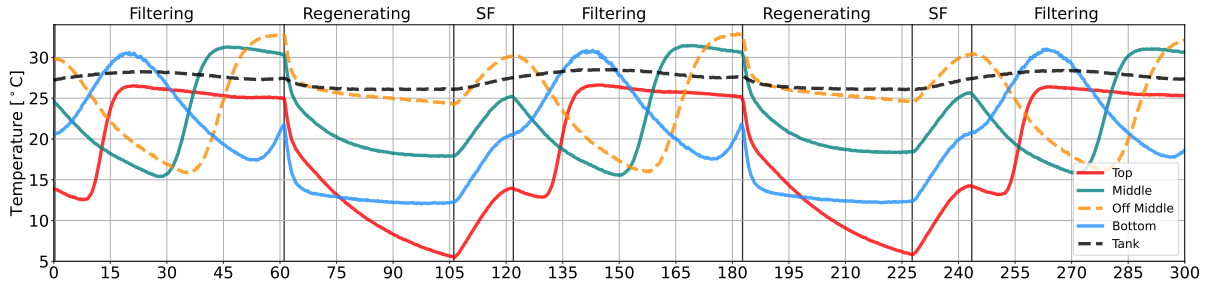


Figure 5.15: Temperature is measured by RTDs at four locations within one carbon column labeled Top, Middle, Off Middle, Bottom, and one location on the external side of the stainless steel vessel, labeled Tank. For more details on the RTD locations, see Fig. 5.13. During this 90.1 cfm swing-mode measurement, the measured temperature changes by as much as 10°C during the filtration stage, and in a way that appears nearly identical for each filtering stage. The temperature drops quickly during regeneration, reaching minima different than at low flow (see Fig. 5.16). The temperature steadily increases during slowfill (appearing to depend only on the starting temperature and the purge flow, though not seen in this plot). This segment of the data was taken after the RRS was producing a steady output radon concentration.

the RTDs, but small compared to what was expected, and appeared to indicate that conductive thermal transport between the tank and carbon was not dominant (as compared with that of convection by the air passing through the column). This seemed to indicate that the RTDs were either primarily measuring the air, and not really the carbon bed; or, the RTDs do measure the carbon temperature, and the heat transfer through the system was not calculated correctly. In either case, we could not demonstrate that this type of heat-exchange system is effective. On the other hand, we know that the input air is first cooled by air-chillers to $\sim 12^\circ\text{C}$ before entering the filtering column. The Top RTD (8 inches within the front of the carbon bed, as illustrated by Fig. 5.13) is frequently the warmest RTD reading and, more importantly, has a similar time dependence as the RTDs in the middle and bottom of the column (as shown by Fig. 5.15). This appears to indicate that either the air passing through the column efficiently exchanges heat with the carbon bed (even over just a few inches) or there are additional interactions influencing the temperature measured.

There are several important mechanisms that may change the temperature measured by the RTDs:

1. the input air, cooled by the air chillers, may remove heat from the carbon;

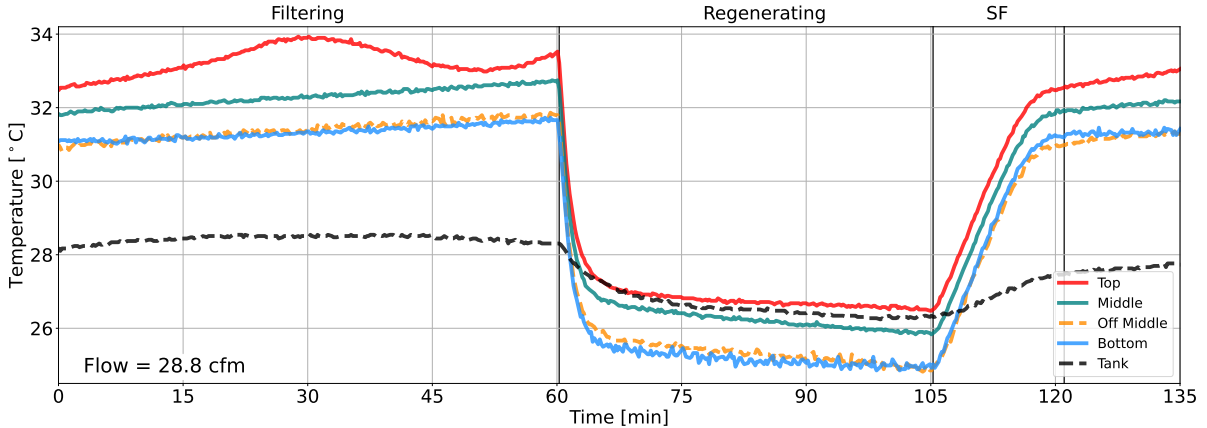


Figure 5.16: RTD temperature measurements (at $F = 28.8 \text{ cfm}$) are made at the Top, Middle, Off Middle, Bottom locations within the tank (shown in red, teal, orange, and blue curves respectively), while the Tank temperature is shown in black. Each location is illustrated by Fig. 5.13.

2. the regenerating column is cooled by purge-flow air expanding into the evacuated volume;
3. water may adsorb or desorb from the carbon surface;
4. water may change phase (for example, from gas to liquid);
5. heat may be lost or gained through the tank walls, which are surrounded by the warm ambient air (courtesy of the pumps!) contained within the small room that has been partitioned off from the general lab space to house the SD Mines RRS.

Each of these play a role, but some appear to drive the temperature changes, particularly during different stages and at lower or higher input flow rates. Figure 5.16 shows low-flow, swing-mode temperature data. In this plot, temperature is reasonably steady during the filtering stage, with the Top RTD showing the largest variations. During the regeneration stage, temperature at each location within the carbon appears to drop with pressure (which changes from 680 Torr to ~ 20 Torr within the first 3 min) and each by a similar amount, where the RTD measuring the highest temperature before pump down still measures the highest temperature. Similarly during the slowfill stage, the tempera-

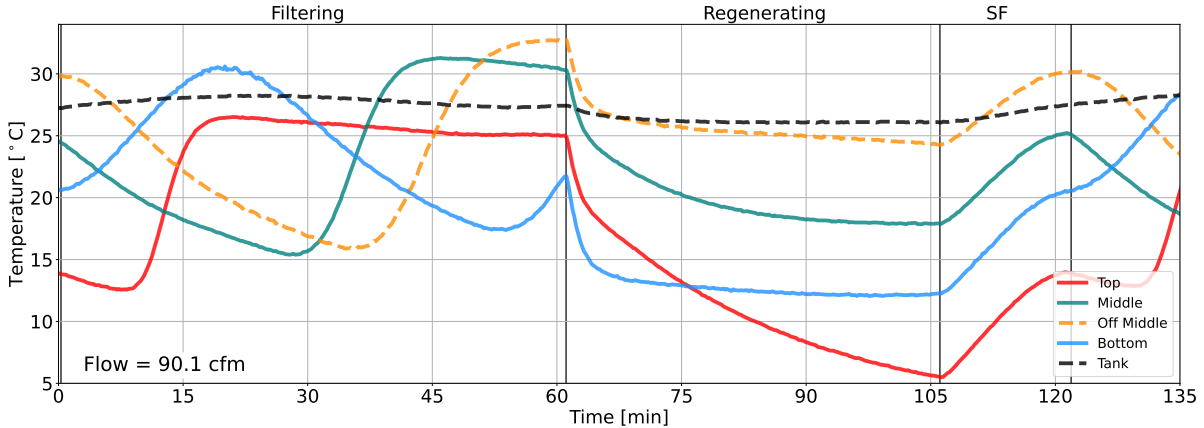


Figure 5.17: RTD temperature measurements (at $F = 90.1 \text{ cfm}$) are made at the Top, Middle, Off Middle, Bottom locations within the tank (shown in red, teal, orange, and blue curves respectively), while the Tank temperature is shown in black. Each location is illustrated by Fig. 5.13.

ture appears closely connected with pressure, which increases linearly from $\sim 20 \text{ Torr}$ to atmospheric pressure (680 Torr) over 15 minutes.

Figure 5.17 shows high-flow, swing-mode temperature data. The most noticeable difference at higher flow is the variations in temperature during the filtering stage. The changes in temperature appear consistent during each filtering stage, but with the exact shape depending on flow, with increasing flow producing larger changes in temperature (see Appendix C for more examples of RC temperature data).

While there are many features in the temperature data that would benefit from further study, the remainder of this section provides some explanation for the temperature drop during regeneration, and discusses the possibility that water introduced to the column during the filtering stage may contribute to changes in temperature through adsorption/desorption and changes of phase.

5.4.1 Cooling During Regeneration

The largest change in temperature comes when a column switches between filtering and regenerating (item 1 from above). During regeneration (illustrated by Fig. 5.18), the column is connected to vacuum pumps on one end and to the purge-flow valve on the other end, which supplies a controlled $\sim 10 \text{ scfm}$ through the column. Pressure in the

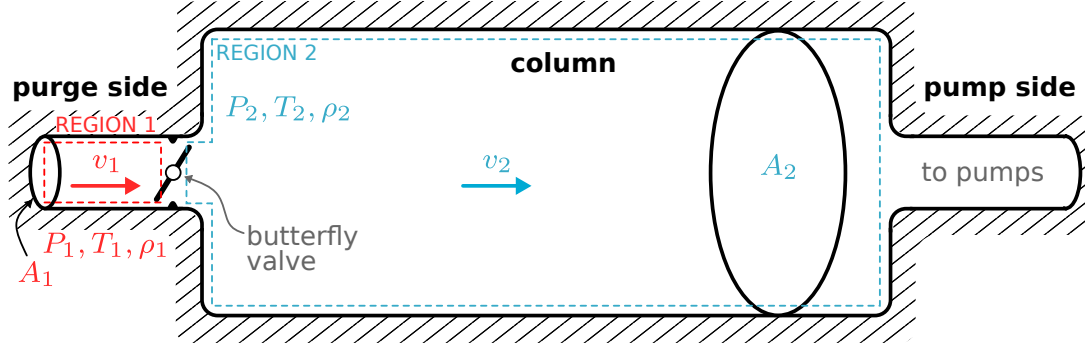


Figure 5.18: During the regeneration stage, a **butterfly valve** allows a constant flow of air F from the **purge side** through both **region 1** (the purge-flow piping before the valve) and **region 2** (the stainless steel **column**, which is filled with carbon granules), before being exhausted out of the **pump side**. The measured pressure and temperature in region 1, P_1 and T_1 , allow for an estimate of the air density ρ_1 . Vacuum pumps at the pump side hold region 2 at the pressure P_2 (we ignore the gradient of a few Torr that exists across the column's length). The temperature in region 2 is measured by RTDs in the carbon bed. The air velocity in region 1, v_1 , and region 2, v_2 , are found by continuity, along with their respective cross-sectional areas A_1 and A_2 .

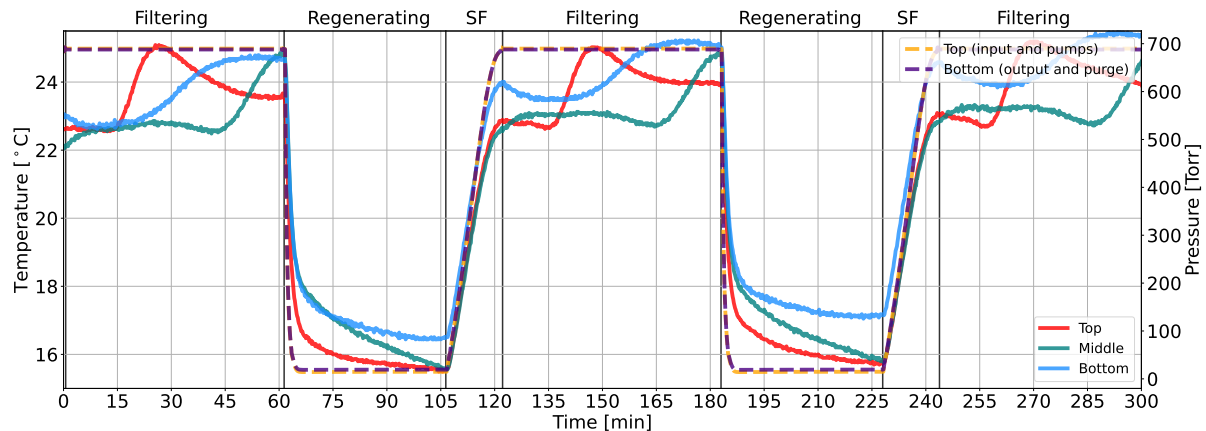


Figure 5.19: The RTD temperature measured at the **Top**, **Middle**, and **Bottom** locations (red, teal, and blue solid lines) of a column (with $F = 63 \text{ cfm}$) changes with the measured pressure at the **Top** (orange dashed line) and **Bottom** (indigo dashed line).

column drops quickly over the first couple minutes until an equilibrium pressure (of about 20 Torr) is reached, at which point the pumping speed is equal to the purge flow. The change in temperature appears proportional to the change in pressure (see Fig. 5.19).

We may estimate the change in temperature as air passes into the evacuated column by starting with the principle of continuity:

$$\frac{\partial \rho}{\partial t} - \nabla \cdot (\rho \mathbf{v}) = 0, \quad (5.8)$$

where ρ is the density of air and \mathbf{v} is the air velocity. For this system, air enters and leaves the system along the column axis, and so we may drop the other two dimensions, yielding

$$\frac{\partial \rho}{\partial t} - \frac{\partial}{\partial x}(\rho v) = 0, \quad (5.9)$$

where v is the air velocity along the column axis. Here, we are interested in the steady-state solution (where $\partial \rho / \partial t = 0$), because the regenerating column reaches an equilibrium pressure within just a few minutes (out of a nominal 45 min). Because air is compressible (*i.e.*, ρ is not constant throughout the system), we have that

$$\frac{d}{dx}(\rho v) = \frac{\rho_2 v_2 - \rho_1 v_1}{x_2 - x_1} \rightarrow \rho_2 v_2 - \rho_1 v_1 = 0. \quad (5.10)$$

The continuity equation is then simplified to

$$\rho_1 v_1 = \rho_2 v_2, \quad (5.11)$$

where ρ and v are the density of air and velocity of air within the regions 1 and 2. After integrating both sides over the cross-sectional areas A_1 and A_2 , we have an expression of conservation of mass [121]

$$\rho_1 v_1 A_1 = \rho_2 v_2 A_2. \quad (5.12)$$

Estimates of velocity in the two regions can be made by observing continuity and applying the ideal gas law, which works well enough for this application. The flow of air F passes through both regions with cross-sectional areas A_1 and A_2 respectively. As described in Section 4.3, the porosity factor ϵ_T accounts for the fact that the column is filled with carbon granules; therefore we have

$$v_1 = \frac{F}{A_1} \quad \text{and} \quad v_2 = \frac{F}{\epsilon_T A_2} \frac{P_1}{P_2} \frac{T_2}{T_1} \frac{Z_2}{Z_1} \approx \frac{F}{\epsilon_T A_2} \frac{P_1}{P_2}, \quad (5.13)$$

where $T_2/T_1 \approx 1$ and the ratio of compressibility factors Z_2/Z_1 is also approximately unity for air at 300 K (see the generalized compressibility chart, Fig. 3.12, in [122]).

The cooling measured during regeneration cannot be explained if the gas is assumed to be ideal. We can see this from energy conservation, where

$$\Delta U = Q - W. \quad (5.14)$$

In steady state, the change in energy $\Delta U = 0$. The change in work $W \propto \Delta(PAv) = 0$ from continuity, where P is pressure, A cross-sectional area, and v and velocity. Therefore, the change in heat added or removed from the system $Q = 0 \rightarrow \Delta T = 0$. That is, for an ideal gas, the internal energy is related only to the kinetic energy of the point-like particles that are assumed to describe the gas; therefore, for this system, there would be no predicted change in the temperature between the two regions—contrary to the measurement.

By accounting for molecular forces described by the Lennard-Jones potential, the molecular physicist van der Waals suggested in 1873 an equation of state (EOS) for real gases that can be expressed as

$$\left(P + \frac{aN^2}{V^2} \right) (V - bN) = Nk_B T, \quad (5.15)$$

where P , V , N , k_B , and T are the usual pressure, volume, number of atoms, Boltzmann constant, and temperature [122, 123, 124]. When the so-called van der Waals coefficients a and b are set to zero, the EOS becomes the familiar ideal gas law. Solving van der Waals EOS for P , we have

$$P = \frac{Nk_B T}{V - bN} - \frac{aN^2}{V^2}. \quad (5.16)$$

The first term is what we would expect for an ideal gas, with the modification that the volume V is made smaller by bN , where the van der Waals coefficient b describes how much of the volume is not accessible due to the finite size of the molecules. The second term reduces pressure due to the attraction between molecules at large distances, with the van der Waals coefficient a scaling this effect for the particular gas. Both coefficients a and b are found empirically, and are sometimes described in terms of the

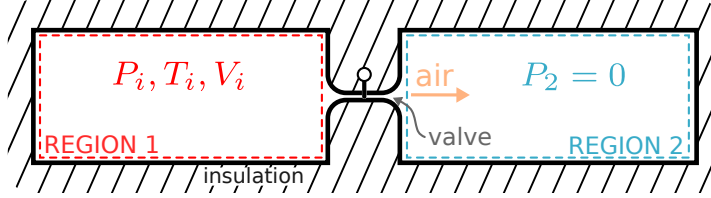


Figure 5.20: Two insulated volumes (regions 1 and 2) are initially isolated by the valve connecting them being closed. Initially, region 1 has pressure, temperature, and volume of P_i , T_i , and V_i . Region 2 is a perfect vacuum with $P_2 = 0$. Once the valve opens, air moves from region 1 to region 2 until equilibrium is reached.

critical temperature T_c and pressure P_c of a particular gas.

$$a = \frac{27}{64} \frac{R^2 T_c}{P_c} = \frac{27}{64} \frac{N_A^2 k_B^2 T_c}{P_c} \quad \text{and} \quad b = \frac{1}{8} \frac{RT_c}{P_c} = \frac{1}{8} \frac{N_A k_B T_c}{P_c}, \quad (5.17)$$

where N_A is Avogadro's number.

Before using Joule-Thomson expansion to estimate temperature during regeneration, I describe *Joule expansion* to avoid confusion between the two similar processes. Illustrated by Fig. 5.20, an example of Joule expansion (sometimes called *free expansion*) is presented. Air within region 1 occupies the volume V_i at the pressure P_i and temperature T_i , and is isolated from region 2 by the valve being closed. Region 2 is a perfect vacuum. Once the valve opens, air flows into region 2 but does no work as there is no gas to displace. That is

$$W = \int P_2 dV = \int 0 dV = 0. \quad (5.18)$$

No heat is added to or removed from the gas because the system is insulated (*i.e.*, the process is adiabatic and $Q = 0$). And finally, because the internal energy U only depends on temperature (*i.e.*, kinetic energy), $\Delta U = 0$ implies $\Delta T = 0$.

For a real gas, however, the temperature *can* change according to the *Joule coefficient*

$$\mu_J \equiv \left(\frac{\partial T}{\partial V} \right)_U. \quad (5.19)$$

To make use of it, however, it will need to be expressed in measurable variables (not energy, for example). The reciprocal relation for partial derivatives (see Eq. 11.16 in [122])

implies

$$\left(\frac{\partial T}{\partial V}\right)_U \left(\frac{\partial U}{\partial T}\right)_V \left(\frac{\partial V}{\partial U}\right)_T = -1. \quad (5.20)$$

The definition of the heat capacity at constant volume

$$c_v \equiv \left(\frac{\partial U}{\partial T}\right)_V. \quad (5.21)$$

Substitution of c_V into Eq. 5.20 yields

$$\left(\frac{\partial T}{\partial V}\right)_U c_v \left(\frac{\partial V}{\partial U}\right)_T = -1. \quad (5.22)$$

Rearranging to solve for the Joule coefficient (Eq. 5.19) yields

$$\mu_J = \left(\frac{\partial T}{\partial V}\right)_U = -\frac{1}{c_V} \left(\frac{\partial U}{\partial V}\right)_T. \quad (5.23)$$

The first law of thermodynamics (*e.g.*, [92, 52, 125])

$$dU = TdS - PdV, \quad (5.24)$$

leads to

$$\mu_J = -\frac{1}{c_V} \left[T \left(\frac{\partial S}{\partial V}\right)_T - P \right]. \quad (5.25)$$

Maxwell's second relation, $(\partial S/\partial V)_T = (\partial P/\partial T)_V$, provides the last ingredient for a usable expression of the Joule coefficient

$$\mu_J = -\frac{1}{c_V} \left[T \left(\frac{\partial P}{\partial T}\right)_V - P \right]. \quad (5.26)$$

The change in temperature is obtained by integrating the Joule coefficient:

$$\Delta T = \int_{V_i}^{V_f} \mu_J dV = - \int_{V_i}^{V_f} \frac{1}{c_V} \left[T \left(\frac{\partial P}{\partial T}\right)_V - P \right] dV. \quad (5.27)$$

If we plug in the EOS for an ideal gas, we first find

$$\left(\frac{\partial P}{\partial T}\right)_V = \frac{\partial}{\partial T} \left(\frac{Nk_B T}{V}\right) = \frac{Nk_B}{V}, \quad (5.28)$$

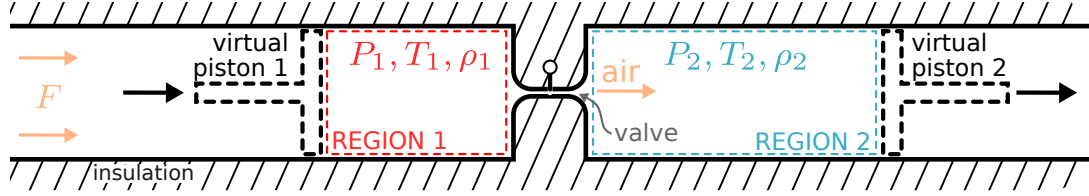


Figure 5.21: Air flows continuously through a pipe-type system where two regions, 1 and 2, are separated by a valve. The valve controls the flow rate F and, therefore, the pressure drop of P_1 to $P_2 < P_1$. The pressure and temperature, T_1 , in the region 1 are assumed to be known (and therefore ρ_1 is known). The pressure in region 2 is assumed to be known, but not the temperature T_2 , and therefore we don't know ρ_2 either. The flow of gas from region 1 to region 2 can be represented as a volume in region 1 that is pushed by virtual piston 1, while virtual piston 2 opens; thus moving this physical volume from the region with P_1 to the region with P_2 . The system is drawn to be insulated, as represented by the diagonal lines. This diagram was inspired by a similar figure from [124].

and then the temperature change

$$\Delta T = - \int_{V_i}^{V_f} \frac{1}{c_V} \left[T \frac{Nk_B}{V} - P \right] = - \int_{V_i}^{V_f} \frac{1}{c_V} [0] = 0, \quad (5.29)$$

as expected. For the van der Waals EOS

$$\left(\frac{\partial P}{\partial T} \right)_V = \frac{Nk_B}{V - bN}, \quad (5.30)$$

which leads to the temperature change

$$\begin{aligned} \Delta T &= - \int_{V_i}^{V_f} \frac{1}{c_V} \left[T \frac{Nk_B}{V - bN} - P \right] = - \int_{V_i}^{V_f} \frac{1}{c_V} \left[T \frac{Nk_B}{V - bN} - \left(\frac{Nk_B T}{V - bN} - \frac{aN^2}{V^2} \right) \right] \\ &= - \int_{V_i}^{V_f} \frac{1}{c_V} \left[\frac{aN^2}{V^2} \right] \\ &= - \frac{aN^2}{c_V} \left(\frac{1}{V_i} - \frac{1}{V_f} \right) < 0, \end{aligned}$$

and therefore the gas will cool as it expands, as observed in real life [124].

Similar to Joule expansion, but for a system where gas flows continuously through it (just like ours), we employ *Joule-Thomson expansion* to estimate the temperature of the air during regeneration. Figure 5.21 builds upon Fig. 5.18 to illustrate the similarity between our physical system and that of Joule-Thomson expansion. In this example, virtual (or imaginary) pistons are drawn to emphasize that a volume of air in region 1 moves to region 2, where the pressure has dropped from P_1 to P_2 . The size of the volume

considered is arbitrary; indeed, one may consider the volume: $V = F\rho_1\Delta t$, where F is air flow, ρ_1 is the air density in region 1, and Δt is some duration, say, 5 min—or just set $V = 1 \text{ m}^3$. This choice ultimately falls out, as we will see shortly.

The *Joule-Thomson coefficient*

$$\mu_{JK} \equiv \left(\frac{\partial T}{\partial P} \right)_U = \frac{1}{c_P} \left[T \left(\frac{\partial V}{\partial T} \right)_P - V \right], \quad (5.31)$$

where c_P is the heat capacity at constant pressure. Because it is challenging to obtain $(\partial V/\partial T)_P$ by direct differentiation of the van der Waals EOS, we instead make use of the relation:

$$\left(\frac{\partial V}{\partial T} \right)_P = 1 / \left(\frac{\partial T}{\partial V} \right)_P. \quad (5.32)$$

Alternatively, one may use the chain rule as

$$\left(\frac{\partial V}{\partial T} \right)_P = \left(\frac{\partial P}{\partial T} \right)_V / \left(\frac{\partial P}{\partial V} \right)_T, \quad (5.33)$$

but the first way seems easier. To start, we solve the van der Waals EOS for T , yielding

$$\begin{aligned} T &= \frac{1}{Nk_B} \left[\left(P + \frac{aN^2}{V^2} \right) (V - bN) \right] \\ &= \frac{1}{Nk_B} \left[PV + \frac{aN^2}{V} - bNP - \frac{abN^3}{V^2} \right]. \end{aligned} \quad (5.34)$$

Differentiating T with respect to V yields

$$\begin{aligned} \left(\frac{\partial T}{\partial V} \right)_P &= \frac{1}{Nk_B} \frac{\partial}{\partial V} \left[PV + \frac{aN^2}{V} - bNP - \frac{abN^3}{V^2} \right] \\ &= \frac{1}{Nk_B} [P + aN^2(-V^{-2}) - abN^3(-2V^{-3})] \\ &= \frac{1}{Nk_B} \left[P - \frac{aN^2}{V^2} + \frac{2abN^3}{V^3} \right] \\ &= \frac{1}{Nk_B} \left[P - \frac{aN^2}{V^2} \left(1 - \frac{2bN}{V} \right) \right]. \end{aligned}$$

Upon taking the inverse, we have

$$\left(\frac{\partial V}{\partial T} \right)_P = \frac{Nk_B}{P - \frac{aN^2}{V^2} \left(1 - \frac{2bN}{V} \right)}. \quad (5.35)$$

The change in temperature is obtained by the following integration:

$$\begin{aligned}\Delta T &= \int_{P_i}^{P_f} \mu_{JK} dP = \int_{P_i}^{P_f} \frac{1}{c_P} \left[T \left(\frac{\partial V}{\partial T} \right)_P - V \right] dP \\ &= \int_{P_i}^{P_f} \frac{T}{c_P} \left(\frac{\partial V}{\partial T} \right)_P dP - \int_{P_i}^{P_f} \frac{V}{c_P} dP.\end{aligned}\quad (5.36)$$

The heat capacity should have units of J/K, and so $c_P = c_o V \rho_1 = 1058 \text{ J/K}$, with $V = 1 \text{ m}^3$. As eluded to earlier, the choice of volume drops out because

$$N = V \rho_1 N_A / M, \quad (5.37)$$

where N_A is Avogadro's number and M is the molar mass of air, and so

$$\frac{N}{c_P} = \frac{V \rho_1 N_A / M}{c_o V \rho_1} = \frac{N_A k_B T}{c_o M}. \quad (5.38)$$

Similarly,

$$\frac{N}{V} = \frac{V \rho_1 N_A / M}{V} = \rho_1 N_A / M, \quad (5.39)$$

and

$$\frac{V}{c_P} = \frac{V}{c_o \rho_1 V} = \frac{1}{c_o \rho_1}. \quad (5.40)$$

Therefore, we may express the first term of Eq. 5.36 as

$$\begin{aligned}\int_{P_i}^{P_f} \frac{T}{c_P} \left(\frac{\partial V}{\partial T} \right)_P dP &= \int_{P_i}^{P_f} \frac{N k_B T / c_P}{P - \frac{aN^2}{V^2} \left(1 - \frac{2bN}{V} \right)} dP \\ &= \int_{P_i}^{P_f} \frac{N_A k_B T / (M c_o)}{P - a \left(\frac{\rho_1 N_A}{M} \right)^2 \left(1 - \frac{2b\rho_1 N_A}{M} \right)} dP.\end{aligned}\quad (5.41)$$

With the definitions

$$\alpha \equiv \frac{N k_B T}{c_P} = \frac{N_A k_B T}{M c_o} \quad (5.42)$$

and

$$\beta \equiv \frac{aN^2}{V^2} \left(1 - \frac{2bN}{V} \right) = a \left(\frac{\rho_1 N_A}{M} \right)^2 \left(1 - 2b\rho_1 N_A / M \right), \quad (5.43)$$

we complete the integration as

$$\int_{P_i}^{P_f} \frac{\alpha}{P - \beta} dP = \alpha \ln(P - \beta) \Big|_{P_i}^{P_f} = \alpha \ln \left(\frac{P_i - \beta}{P_f - \beta} \right). \quad (5.44)$$

The second term of Eq. 5.36 may be found directly as

$$\int_{P_i}^{P_f} \frac{V}{c_P} dP = \frac{V}{c_P} (P_f - P_i) = \frac{1}{c_o \rho_1} (P_f - P_i). \quad (5.45)$$

The change in temperature of air passing from region 1 into region 2

$$\Delta T = \alpha \ln \left(\frac{P_i - \beta}{P_f - \beta} \right) - \frac{1}{c_o \rho_1} (P_f - P_i), \quad (5.46)$$

which indicates that temperature T_2 of air within the regenerating column is

$$T_2 = T_1 + \Delta T. \quad (5.47)$$

Using the values from Table 5.2, we find $\alpha = 85.7 \text{ m}^6 \text{ Pa/atoms}^2$ and $\beta = 175.9 \text{ m}^3/\text{atoms}$.

The first and second term of Eq. 5.46 yield -308 and 83 K respectively, and thus $\Delta T = -225 \text{ K}$. Assuming a conservative $3 \text{ }^\circ\text{C}$ uncertainty on T_1 , which is expected to dominate, the temperature of air in the regenerating column $T_2 = -198 \pm 2 \text{ }^\circ\text{C}$: much colder than the temperature measured by any RTD in the column, but also ignoring the fact that the carbon exchanges heat with the air through forced convection. Therefore next, we estimate the energy that was required to cool the air passing into the regenerating column from T_1 to T_2 , and then apply it to cool the carbon (as the mass of air will be negligible).

The energy E needed to change the temperature of an object with mass m and specific heat c_V (at constant volume and with units of $\text{kJ kg}^{-1} \text{K}^{-1}$) from T_i to T_f is

$$E = \int_{T_i}^{T_f} mc_V dT. \quad (5.48)$$

The energy removed to cool the air is then

$$E_{\text{air}} = m_o c_o (T_2 - T_1), \quad (5.49)$$

where the specific heat of air is c_o and the mass of air is obtained by

$$m_o = \int_0^{t_{eq}} f_{\text{purge}} \rho_1 dt = f_{\text{purge}} \rho_1 t_{eq}, \quad (5.50)$$

where f_{purge} is the purge flow rate, t_{eq} is the time for the regenerating column to reach a steady-state temperature (about 5 min), and ρ_1 is the air density at P_1 and T_1 . If we now presume all of this energy is used to heat the carbon, we would expect the temperature of the carbon to change by

$$\Delta T_\bullet = \frac{E_{\text{air}}}{c_\bullet m_\bullet}, \quad (5.51)$$

where the carbon bed has the mass m_\bullet and specific heat capacity c_\bullet . The air can be safely ignored, as $(m_o c_o) / (c_\bullet m_\bullet) = 0.007$. We could make this estimate more conservative by

Description	Symbol	Value	Units
van der Waals coefficient	a	85.70	$\text{m}^6 \text{ Pa/atoms}^2$
van der Waals coefficient	b	175.89	$\text{m}^3/\text{atoms}^2$
Mass of the carbon bed [‡]	m_\bullet	200 ± 25	kg
Mass of the stainless-steel tanks	m_{ss}	~ 200	kg
Pressure in purge-flow pipe (in region 1)	P_1	680	Torr
Pressure in column (in region 2)	P_2	20	Torr
Temperature of purge-flow air (in region 1) [‡]	T_1	300 ± 3	K
Cross-sectional area of purge-flow pipe (in region 1)	A_1	0.005	m^2
Cross-sectional area of column (in region 2)	A_2	0.46	m^2
Carbon porosity factor (introduced in Section 4.3)	ϵ_T	0.8	unitless
Flow rate through purge valve	f_{purge}	0.28	m^3/s
Density of air [†] in region 1	ρ_1	1.19	kg/m^3
Specific heat capacity of activated carbon [126]	c_\bullet	0.8	$\text{kJ}/(\text{kg.K})$
Specific heat capacity of air at constant pressure [127]	c_o	1.005	$\text{kJ}/(\text{kg.K})$
Time until steady state	t_{eq}	300	s

Table 5.2: Numerical values of relevant system parameters for estimating the temperature measured by an RTD within the carbon bed during the regeneration stage. [†]One may calculate the air density (in g/m³) as $\rho = MP/(RT)$, where the molecular weight $M = 29.86 \text{ g/mol}$, P is pressure in Pascals, the real gas constant $R = 8.3145 \text{ J/mol/K}$, and T is temperature in Kelvin. Calculated values agree with those tabulated at the Engineering Toolbox website [128].

[‡]For these estimates, the dominant uncertainties are expected to be in the measurement of the purge-flow air temperature T_1 and the carbon mass m_\bullet .

requiring the stainless steel tank to be heated as well, but this probably isn't warranted as the tank temperature changes by only a small fraction of that inferred from the RTD's in the carbon (see Fig. 5.15 for example).

Again using values from Table 5.2, Eq. 5.49 provides the required energy change for the temperature of the air entering the regenerating column over $t_{\text{eq}} = 5 \text{ min}$ to drop from T_1 to T_2 to be $E_{\text{air}} = -240 \text{ kJ}$. For this estimate, the dominant uncertainty is in the carbon mass, which can vary due to its water content when measured. Because the column in the real system contains carbon, we assume the energy removed from the air is replaced by heat from the carbon bed (and the RTD's within it) and, by Eq. 5.51, estimate the change in the carbon's temperature (from filtering to regeneration) to be $\Delta T_{\bullet} = -1.5 \pm 0.2^\circ\text{C}$; this temperature drop is not large enough to explain the observed (absolute) drop of $\Delta T_{\text{obs}} \sim 6^\circ\text{C}$. One possibility is that not all of the carbon is cooled, but perhaps only by the fraction φ . That is, if we demand

$$\Delta T_{\text{obs}} = \frac{|E_{\text{air}}|}{c_{\bullet} m_{\bullet} \varphi + m_{\circ} c_{\circ}}, \quad (5.52)$$

we find that $\varphi = 0.24$, which seems reasonable enough to not be rejected outright. Alternatively, the RTDs may essentially be measuring the air passing through the carbon bed, warmed by convective heat transfer with the carbon, and not the temperature of the carbon surface, let alone its bulk.

As a check, we compare (at equilibrium) the rate of heat added to the carbon bed Q_{added} (in Watts) from the warm room where the column sits and the rate heat removed from the carbon bed Q_{rem} (also in Watts) by warming the air passing through it. We already estimated the rate of heat removed from the carbon by the air to be

$$Q_{\text{rem}} = E_{\text{air}}/t_{\text{eq}} = 801.5 \text{ Watts}, \quad (5.53)$$

where the integral performed by Eq. 5.50 is undone to keep units of energy per time. The rate of heat added to the carbon is given by

$$Q_{\text{added}} = UA\Delta T, \quad (5.54)$$

where A is the surface area of the column (the tank) and $\Delta T = T_1 - T_2$, which we have estimated. The overall heat transfer coefficient U is defined as

$$\frac{1}{UA} = \frac{1}{h_{ci}A_c} + \frac{1}{A} \sum_n \frac{\Delta x_n}{k_n} + \frac{1}{h_{co}A}, \quad (5.55)$$

where h_{ci} and h_{co} are the convection heat transfer coefficients for air moving inside the column and around the outside of the column respectively, while Δx_n and k_n are the thickness and heat conductivity of each layer (*i.e.*, the walls stainless steel tank and carbon itself) [129]. The effective surface area [130] of the packed carbon bed

$$A_c = \frac{6(1 - \epsilon_T)V_c}{d} \approx 100 \text{ m}^2, \quad (5.56)$$

where the average particle diameter $d = 6 \pm 1 \text{ mm} = 0.006 \pm 0.001 \text{ m}$ and the carbon bed volume $V_c \approx 0.5 \text{ m}^3$. If our estimate of the equilibrium temperature, T_2 , is good, then we should find

$$Q_{\text{added}} - Q_{\text{rem}} = 0. \quad (5.57)$$

That is, once the system reaches equilibrium the rate of heat being added and removed from the carbon are the same. In order to prepare for evaluation, the overall heat transfer coefficient for our system may be expressed as

$$\frac{1}{UA} = \frac{1}{h_{ci}A_c} + \frac{\Delta x_{ss}}{k_{ss}A} + \frac{\Delta x_{\text{carbon}}}{k_{\text{carbon}}A} + \frac{1}{h_{co}A}, \quad (5.58)$$

where the convective heat transfer coefficients are taken from the Engineering Toolbox [131] according to estimates of air velocity within the room and passing through the column as $h_{co} = 1.6 \text{ W/m}^2/\text{K}$ and $h_{ci} = 10 \text{ W/m}^2/\text{K}$ respectively; the value of h_{co} was chosen such that Q 's agree (as the value is not known for our system and ranges from 0.5 to 1000 $\text{W/m}^2/\text{K}$), while the value of h_{ci} does not significantly change U beyond the minimum value of its typical range (of 10 to 1000 $\text{W/m}^2/\text{K}$), as $1/(h_{ci}A_c) \approx 0$ due to $A_c \gg A$. The thickness of the walls of the stainless steel tank $\Delta x_{ss} = 3/16 \text{ in}$ (0.005 m), while the thickness of the carbon layer is taken to be the radius of the carbon bed, $\Delta x_{\text{carbon}} = 15 \text{ in}$

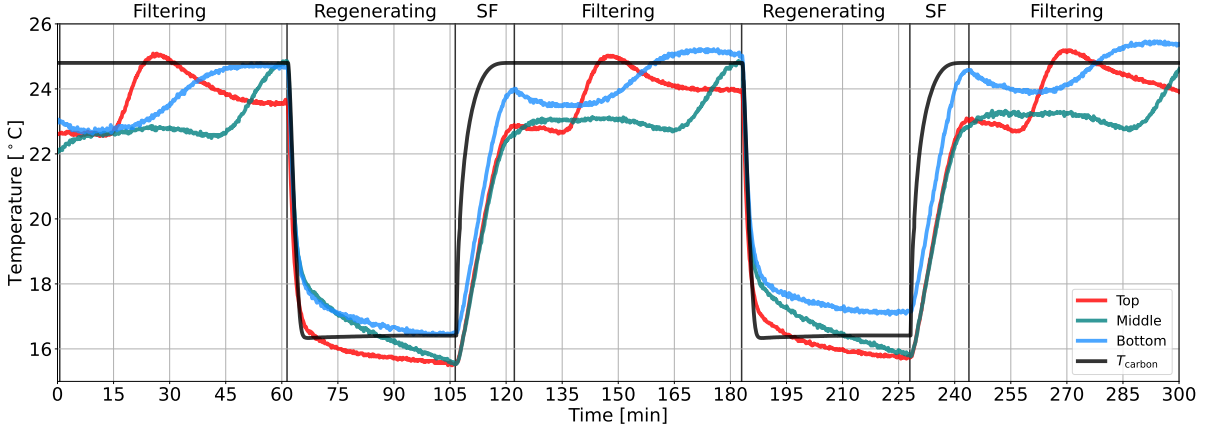


Figure 5.22: The RTD temperature measured at the **Top**, **Middle**, and **Bottom** locations (red, teal, and blue lines) of a column (with $F = 63 \text{ cfm}$) are compared with the predicted temperature T_{\bullet} (denoted as T_{carbon} for clarity in this figure) of the carbon bed (black line).

(0.38 m). The thermal conductivity for stainless steel $k_{ss} = 14 \text{ W/m/K}$ [132] and for carbon $k_{\text{carbon}} = 0.63 \text{ W/m/K}$ [133]. Therefore, the rate of heat removed $Q_{\text{rem}} \sim 800 \text{ Watts}$ and the rate of heat added $Q_{\text{added}} \sim 800 \text{ Watts}$. While this result does not confirm that T_2 has been estimated correctly, it also does not reject the estimate. A better understanding of the convective heat transfer coefficients h_{co} and h_{ci} would improve the constraint of T_2 .

As a practical test, the measured pressure in the column (*i.e.*, P_2 versus time) has been fed into our model (Eq. 5.47) to predict the temperature of the carbon, $T_{\bullet} = T_1 + \Delta T_{\bullet}$. Figure 5.22 shows the result, with the temperature of the inlet air T_1 chosen to agree with the temperature at the Bottom location of the column. However, in order to obtain the measured temperature drop, at the Bottom location, by the end of the regeneration stage, the fraction of carbon cooled was set to $\varphi = 0.175$. From this, we may say that Joule-Thomson expansion does appear to drive temperature. However, there are other effects clearly not captured by this model. For example, the pressure becomes steady within a couple minutes, while the temperature continues to drop throughout the regeneration stage, and more so at some locations. During the slow-fill stage, pressure rises more quickly than temperature, which may be explained by the heat capacity of the carbon bed (*i.e.*, how quickly heat can be transferred from the increasingly warm air entering

the column to RTD). This last point implies that the RTDs installed within the carbon bed may very well be measuring the carbon, or at least the surface of the carbon, and not just the air passing through it. This is an important outcome, as the desorption rate follows the Arrhenius equation, which depends on the adsorbent's temperature (*i.e.*, the temperature of the carbon's surface).

5.4.2 Temperature Change due to Water Vapor in the Input Air

The RRS input air is dried by a dehumidifier and cooled by air chillers (that remove some moisture as well) to a dew point of around -18°C (with $T = 12^{\circ}\text{C}$ and relative humidity $H \sim 11\%$). Though this air is fairly dry, the water it contains is added to the carbon bed during the filtering stage. We estimate the amount (in grams) that is added per second as

$$\dot{m}_w = F\rho_{\text{vd}}, \quad (5.59)$$

where F is the flow of air passing through the column and ρ_{vd} is the vapor density of water, which is found by

$$\rho_{\text{vd}} = \rho_{\text{svd}}H, \quad (5.60)$$

where ρ_{svd} is the saturation vapor density, which is the maximum amount of water vapor per unit volume at temperature T (any more water vapor that is added will condense to a liquid). Below 200°C , the vapor density can be estimated with the ideal-gas law, but with pressure set to the saturation vapor pressure P_{svp} , which follows an empirical relationship that depends on temperature [134]:

$$P_{\text{svp}} = \exp(77.3450 + 0.0057T - 7235/T)/T^{8.2}. \quad (5.61)$$

Rearranging the ideal-gas law for density yields

$$PV = nRT \rightarrow \frac{n}{V} = \frac{P}{RT}, \quad (5.62)$$

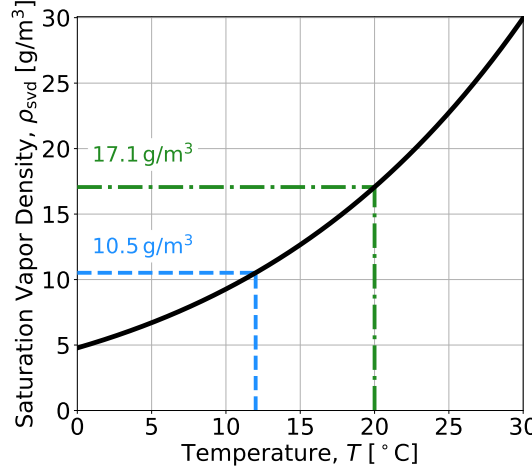


Figure 5.23: Saturation vapor density calculated by Eq. 5.63 (solid black line). At $T = 12^\circ\text{C}$ (blue, dashed lines) and $T = 20^\circ\text{C}$ (green, dot-dashed lines), evaluation yields the saturation vapor density of 10.5 g/m^3 and 17.1 g/m^3 respectively.

where V is volume, R is the ideal-gas constant (of 8.324 J/mol/K), and T is temperature in Kelvin. The number of moles $n = m/M$, where m is the mass of the water vapor (grams) and M is the molar mass (g/mol). Therefore, after setting $P = P_{\text{svp}}$, the saturation vapor density (in units of g/m^3) becomes

$$\rho_{\text{svd}} = \frac{m}{V} = \frac{MP_{\text{svp}}}{RT}, \quad (5.63)$$

where the molar mass of water $M = 18 \text{ g/mol}$. The saturation vapor density calculated in this way (for specific temperatures) agrees with literature values [135], and is plotted in Fig. 5.23. The amount of water added to the carbon bed per second is then

$$\dot{m}_w = F\rho_{\text{svd}}H = \left(0.05 \frac{\text{m}^3}{\text{s}}\right) \left(10.5 \frac{\text{g}}{\text{m}^3}\right) (0.11) = 5.5 \text{ g/s}, \quad (5.64)$$

for $F = 100 \text{ cfm}$, $T = 12^\circ\text{C}$, and relative humidity $H = 11\%$.

When water adsorbs to a surface, the surface is heated according to the enthalpy of adsorption. Similarly, when water condenses, energy is released in heating the surrounding materials according to the enthalpy of condensation. In order to estimate the change in temperature ΔT of an object with a mass m and specific heat capacity c_v , at constant volume, for some change in energy ΔE , we rearrange Eq. 5.48 as

$$\Delta T = \frac{\Delta E}{mc_v}. \quad (5.65)$$

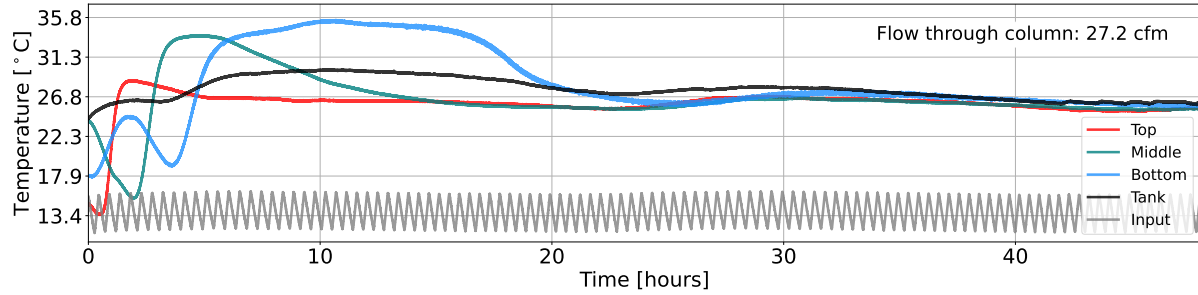


Figure 5.24: The RTD temperature measured during a break-through curve run at the **Top**, **Middle**, and **Bottom** locations (red, teal, and blue lines respectively) of a column (with $F = 27.2 \text{ cfm}$). The input temperature (gray line) appears as a triangle wave due the water chiller (which chills the water passing through the air chillers) turning ON and OFF between two temperature trip points.

The enthalpy of adsorption for water $\Delta H_{\text{ads}} = 40 - 45 \text{ kJ/mol}$ [136, 137], while the enthalpy of vaporization $\Delta H_{\text{vap}} = 45 \text{ kJ/mol}$ [138], with the enthalpy of condensation $\Delta H_{\text{con}} = -\Delta H_{\text{vap}}$. The mass to be heated is the carbon bed ($m_{\bullet} = 200 \text{ kg}$) and the mass of air that has entered the column after time t , which is

$$m_{\text{air}} = F\rho_{\text{air}}t, \quad (5.66)$$

where F is the flow of air through the column and ρ_{air} is the density of air. Evaluation with $F = 100 \text{ cfm}$, $\rho_{\text{air}} = 1.05 \text{ kg/m}^3$, and $t = 5 \text{ min}$ yields $m_{\text{air}} = 15 \text{ kg}$. If we first assume that water is adsorbed and its energy is used exclusively for heating the air, we would expect a change in temperature of $\Delta T_{\text{air}} = 3.8^\circ\text{C}$. Similarly, the temperature rise of the entire carbon bed in $t = 5 \text{ min}$ comes to $\Delta T_{\bullet} = 0.26^\circ\text{C}$ (with $\varphi = 1$). This cannot explain the quick jump of $\sim 11^\circ\text{C}$ over 5 min observed in the RTD temperature data during filtering at high-flow (see Fig. 5.17). It is expected that more work is needed to better understand the detailed temperature dependence, and water adsorption to the carbon surface still appears to provide the best explanation for the observed temperature jumps during the filtering stage. The SD Mines Table-top System (see Chapter 8) has the potential to further examine the temperature dependence of the carbon bed on air flow and its water content.

Similarly, the BTC temperature data in Fig. 5.24 shows a jump that then continues for \sim 10-20 hours before dropping and becoming steady, with future changes in temperature appearing to be driven by ambient room conditions.

In addition to water vapor, the input air also contains other gases, such as CO₂ and Ar. A typical composition of not-dry air is 74% N₂, 20% O₂, 5% H₂O, and 1% Ar [139]. N₂ (or O₂) represents the largest fraction of air but is not expected to significantly contribute to the measured changes in the carbon surface temperature during the filtering stage. During the previous slowfill stage, purge air fills the carbon column until atmospheric pressure is reached; during this stage, N₂ will have adsorbed to the surface of the carbon and reached a steady state (where the pressure within the closed column does not change, suggesting that N₂ is not continuing to adsorb). Therefore, flowing air through the column during the subsequent filtering stage is similarly not expected to change the amount of N₂ on the surface (and thus does not contribute to changes in the measured temperature by adsorption).

Similar to radon, Ar (or CO₂) is expected to move more slowly through the carbon bed as compared with air and thus may not be present in the purge-flow air; this suggests that after the slowfill stage, the carbon surface will be occupied by nitrogen and oxygen, but perhaps very little Ar (or H₂O, CO₂), as these molecules are not expected to have passed through the carbon bed within a typical 45-min filtering stage. Therefore, during subsequent filtering, water, Ar, and CO₂ may adsorb to free sites on the carbon surface, with each contributing to the measured increase in temperature. However, the enthalpy of adsorption of argon to carbon is about 10 kJ/mol [140] (so about 4 times less than for water) while representing about 5 times less of the air than water. Argon adsorbing to the carbon surface is thus expected to increase the surface temperature by about one twentieth of that due to water adsorbing, and has therefore been ignored in estimating the change in surface temperature caused by adsorption. Similarly, CO₂ has not been included in estimating the change in the carbon temperature because it represents only

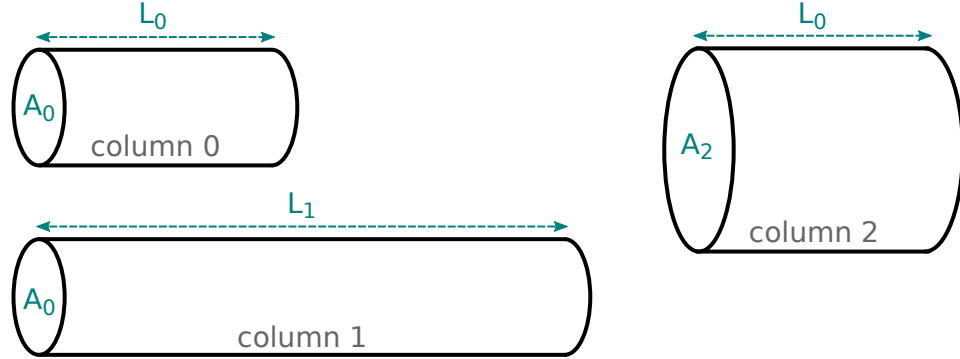


Figure 5.25: A column is a vacuum vessel that has been filled with an adsorbent such as activated carbon. Column 0 will act as a reference geometry that column 1 and 2 will be compared against.

0.04% of air, while water represents between 3 and 5% (depending on relatively humidity), with 7% representative of air having 100% relative humidity (at 104°F) [139].

5.5 Long or Short Columns?

We would like to consider how changing the length or diameter of a carbon column will influence the standard deviation (or spread, denoted as \$\sigma_t\$, where the \$t\$ indicates time) in a measured break-through curve (BTC). This discussion presumes that the speed of radon passing through the column is proportional to the air speed though the column. Also, porosity of the carbon bed is ignored (see Section 4.3), as it drops out.

Referring to Fig. 5.25, let us take a column with length \$L_0\$ and cross-sectional area \$A_0\$ to be our reference column. If the flow rate through this column is \$F_0\$, then the speed of air passing through the column is \$v_0 = F_0/A_0\$. The speed of radon atoms moving though the column (adsorbing and desorbing to the carbon's surface along the way) is proportional to the air speed: \$v_{Rn,0} \propto v_0\$. The break-through time \$\tau\$ represents the mean time it takes for a radon atom to move completely through the column.

The solution (in terms of radon concentration) to the diffusion equation (Fick's 2nd law) is (with details provided in Chapter 4 and [93]):

$$C(x, t) = \frac{M}{2\sqrt{\pi Dt}} e^{-x^2/(4Dt)}, \quad (5.67)$$

where M is the total amount of substance, D is the diffusion coefficient, x is distance along the longitudinal axis of a column, and t is time. The standard deviation in space (equal to half of the base of the distribution) and the variance are:

$$\sigma_x = \sqrt{2Dt} \quad \sigma_x^2 = 2Dt \quad (5.68)$$

From *Modern Practice of Gas Chromatography*, we have that the diffusion coefficient D depends on the speed of gas moving through the column:

$$D = D_a + \gamma D_g, \quad (5.69)$$

where D_a is the so-called apparent longitudinal diffusivity, γ accounts for irregular diffusion patterns and is usually less than unity (as molecular diffusion is small in a packed column), and D_g is the true molecular diffusivity (which would dominate over D_a in an empty column). Dependence on air speed v comes from:

$$D_a = \lambda v d_p, \quad (5.70)$$

where λ describes the packing of the carbon (for regular packing, $\lambda < 1$, while non-uniform packing with channels has $\lambda > 1$) and d_p is the diameter of the particle moving through the carbon.

Let us now compare the diffusion characteristics of **column 1 with column 0** (from Fig. 5.25) with the requirement that the break-through time of both columns are the same: $\tau_0 = \tau_1 = \tau$. Using this requirement, we find:

$$\tau \propto L_0/v_0 = L_1/v_1 \longrightarrow v_1 = \frac{L_1}{L_0} v_0. \quad (5.71)$$

And therefore,

$$F_1 = A_0 v_1 = A_0 \frac{L_1}{L_0} v_0 = \frac{L_1}{L_0} A_0 v_0 = \frac{L_1}{L_0} F_0. \quad (5.72)$$

Because $L_1/L_0 > 1$, we know $F_1 > F_0$. The standard deviation for column 0 (in space) is then:

$$\sigma_{x,0} = \sqrt{2Dt} = \sqrt{2(\lambda v_0 d_p + \gamma D_g)t} = \sqrt{2\lambda v_0 d_p t} + \sqrt{2\gamma D_g t}, \quad (5.73)$$

If we assume γD_g is small (emphasizing the case where the velocity-dependent term is dominant, and thus considering the strongest influence the velocity can have), then we get the relation:

$$\sigma_{x,0} \propto \sqrt{v_0}. \quad (5.74)$$

The standard deviation in time σ_t (as observed during a BTC), is then:

$$\sigma_{t,0} = \sigma_{x,0}/v_0 \propto \sqrt{v_0}/v_0 = 1/\sqrt{v_0}. \quad (5.75)$$

And thus the standard deviation (in space and time) compared between column 0 and 1, yield:

$$\sigma_{x,1} > \sigma_{x,0} \quad \sigma_{t,1} < \sigma_{t,0}. \quad (5.76)$$

By this reasoning, we would expect that a BTC performed through a longer column, at a higher flow, but with the same break-through time, would have a smaller spread (standard deviation σ_t) in the measured elution curve.

Let us now compare the diffusion characteristics of **column 2 with column 0** (from Fig. 5.25). Again, we require that the break-through time of both columns are the same $\tau_0 = \tau_2 = \tau = L/v_{Rn}$, and thus $v_2 = v_0$. Therefore, helping ourselves to the previous comparison, we find immediately that:

$$\sigma_{x,2} = \sigma_{x,0} \quad \sigma_{t,2} = \sigma_{t,0}. \quad (5.77)$$

From this result, the BTC we would measure would have the same standard deviation σ_t for both columns, even though the volumetric flow through column 2 will be larger than through column 0:

$$F_2 = A_2 v_2 > F_0 = A_0 v_0, \quad (5.78)$$

as $A_2 > A_0$.

Both a longer column and a column with a larger diameter can provide a larger flow rate for the same break-through time. However, one may prefer to choose the

longer column over the squatter (larger diameter) column as this will produce a smaller standard deviation σ_t in the measured elution curve for the same increased flow (see the simulated output radon concentration curves for changing column length at constant column volume in Section 7.15.2). Nonetheless, one might still prefer shorter columns as they can more easily fit within a typical room or lab space.

Chapter 6

The SD Mines Low-Radon Cleanroom

A low-radon environment can be crucial in reducing the amount of long-lived ^{210}Pb that embeds itself in the surface of sensitive materials. If the sensitive materials are only being stored, a nitrogen over-pressured glove box or air-tight bagging can serve as a practical solutions. However if work is still being conducted on the sensitive materials, a breathable-air environment, having the required low-radon concentration, is desired. A machine that removes radon from air, while leaving its oxygen and nitrogen content unchanged, fulfills this demand. A cleanroom supplied by this low-radon, breathable air provides a practical solution to minimizing ^{210}Pb contamination while facilitating ongoing work by personnel.



Figure 6.1: The SD Mines low-radon cleanroom was fabricated from aluminum with doors and windows made from polycarbonate. The cleanroom overpressure is measured by pressure gauges that penetrate both the anteroom and main walls. The HVAC located inside the cleanroom (right image) recirculates air (at $\sim 1000 \text{ scfm}$) through four HEPA filters, removing particles larger than $0.6 \mu\text{m}$ and slightly overpressuring the main room as compared with the anteroom. The cleanroom is supplied low-radon make-up air (at 20-100 scfm) by the SD Mines Radon-Reduction System.

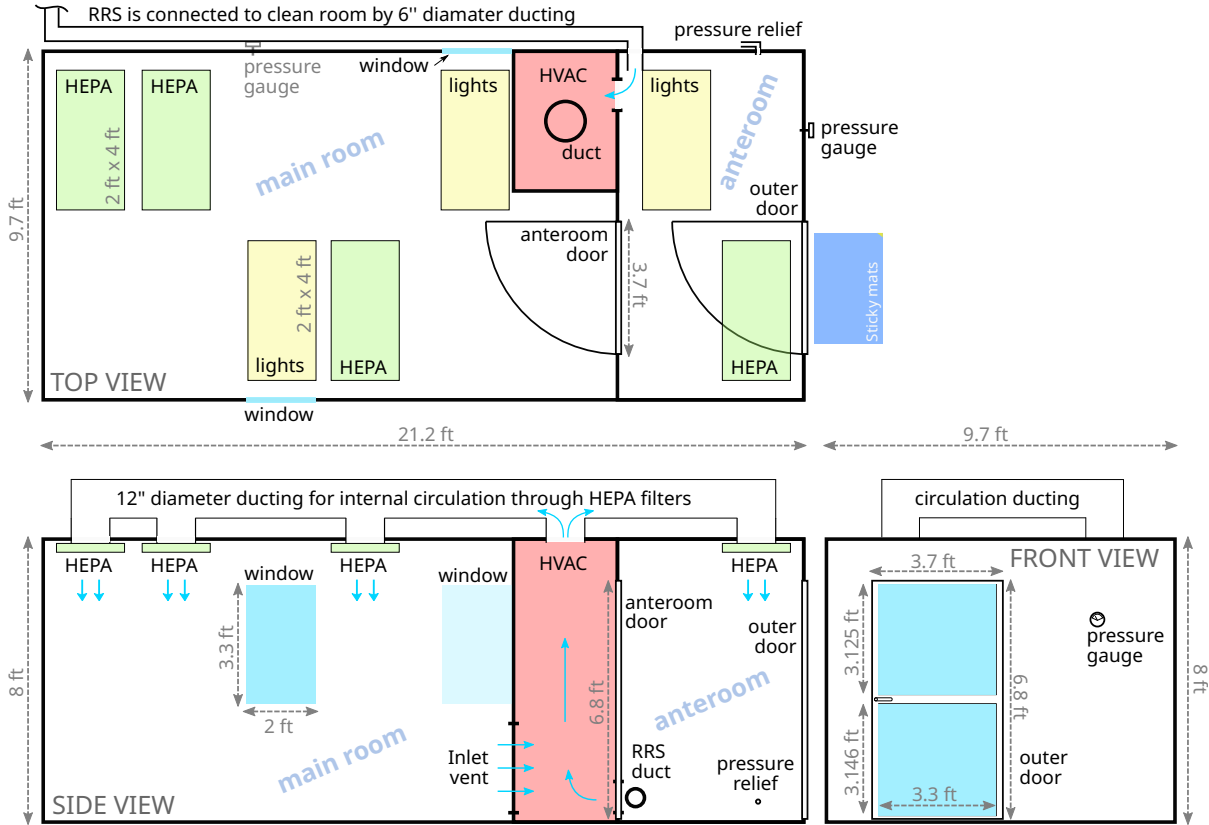


Figure 6.2: This schematic of the SD Mines cleanroom illustrates the location and approximate size (± 1 inch) of important components. Blue arrows show, roughly, how low-radon air enters the clean room and is pushed into the low-pressure region of the HVAC. The HVAC then circulates the air up through ducting above the clean room and down through HEPA filter (that remove particles larger than $0.6 \mu\text{m}$). The circulation rate can be chosen between 0 and 2000 cfm, and is nominally set to 1500 cfm for noise reasons (larger flow creates a hum that is apparently not enjoyed by cleanroom personnel).

The SD Mines cleanroom (imaged in Fig. 6.1) is constructed primarily of aluminum, in which radon has a very small coefficient of diffusion (further described in Section 6.1). As illustrated by the cleanroom schematic that is Fig. 6.2, an outer door opens to an anteroom, and the anteroom door then opens into the larger inner room. Both doors have large polycarbonate windows that are 3.175 mm (1/8 inch) in thickness, while the larger room has two polycarbonate windows that are 6.4 mm (1/4 inch) in thickness. The flooring consists of stamped aluminum sheets of thickness 1.59 mm (1/16 inch) that help shield radon that diffuses out of the concrete floor beneath it. Seams between wall sections, for example, were sealed by butyl-backed aluminum tape. Where this tape could

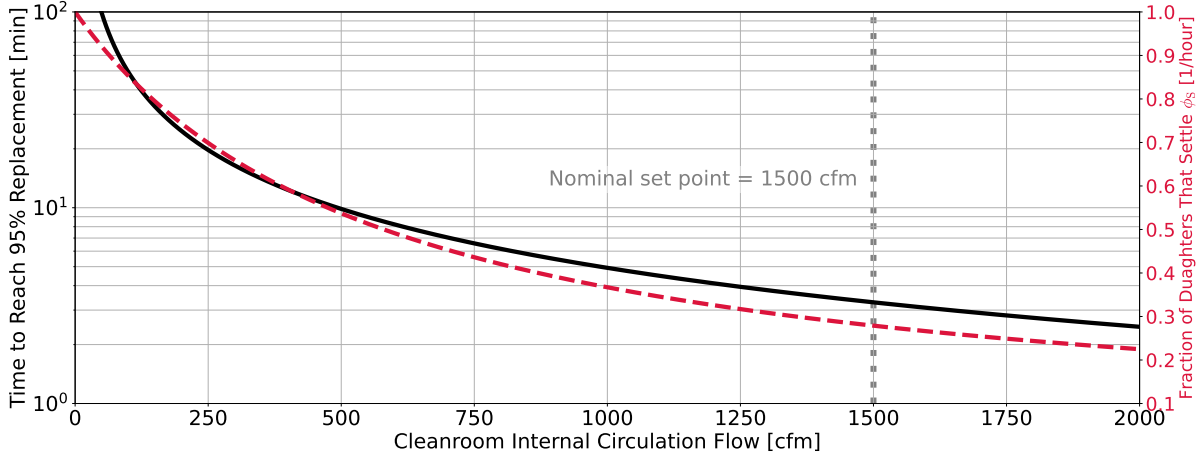


Figure 6.3: The time to reach 95% replacement of the SD Mines cleanroom due only to internal circulation by the HVAC (black curve) is inversely proportional to the circulation flow F . Circulated air passes through HEPA filters in the cleanroom ceiling, where radon daughters in the air are removed, reducing the fraction ϕ_s of daughters that will deposit on surfaces within the cleanroom (red dashed curve).

not be used, butyl caulking was applied (for example, around the electrical outlet boxes that are embedded in the walls). Details regarding the diffusion and emanation of radon from the materials used in this cleanroom may be found in Section 6.1.

A heating, ventilation, and air conditioning (HVAC) unit was installed just within the larger main room. With chilled gas from an external chiller accompanied by an internal heating element, the HVAC increases or reduces the cleanroom air temperature according to a user's set point. The water content (relative humidity) of the cleanroom air is similarly controlled by evaporating water sourced externally (see Section 6.3.2) or draining water off the internal gas-chilled condenser. By its internal blower, the HVAC circulates air within the cleanroom, up through ducting above the cleanroom and then back down through HEPA filters in the cleanroom ceiling (as shown in Fig. 6.2). The air circulation speed can be set by the user within the range 0 – 2000 cfm.

The volume replacement as a function of time t for a internal volume V_0 is described by an exponential decay (where perfect mixing is assumed):

$$V(t) = V_0 \left[1 - \exp \left(-\frac{t}{V_0/F} \right) \right], \quad (6.1)$$

where F is the air flow rate. For the SD Mines cleanroom, $V_0 = 46.6 \text{ m}^3 = 1645 \text{ cf}$. The time to reach 95% volume replacement is found by setting $V(t)/V_0 = 0.95$, and solving for t :

$$V(t)/V_0 = 0.95 = 1 - \exp\left(-\frac{t}{V_0/F}\right) \quad (6.2)$$

$$\begin{aligned} \exp\left(-\frac{t}{V_0/F}\right) &= 0.05 \\ \rightarrow t &= -\frac{V_0}{F} \ln(0.05). \end{aligned} \quad (6.3)$$

Figure 6.3 shows the time to reach 95% volume replacement as a function of flow for the SD Mines cleanroom. Nominally, we set the internal circulation to be 1500 cfm, which results in 95% of the volume being replaced in about 3 minutes. While the circulation of internal air does not filter out radon (as it easily migrates through HEPA filters), it does reduce the radon daughters in the air, and thus the fraction of daughters that will settle on surfaces. The first radon daughter ^{218}Po is of particular interest because it has a half-life of only 3.1 minutes (while its daughter, ^{214}Pb , has a half-life of 27 minutes). When radon decays, the ^{218}Po daughter will either settle on a nearby surface, decay to ^{214}Pb in air, or remain in the air long enough (a couple minutes) to be captured by a HEPA filter (and the same story for any other daughter). Following an internal note (built on the Jacobi model [84]) presented by Richard Schnee for the LZ experiment [141], the plate-out deposition rate (assumed to be the same for all daughters)

$$\lambda_d = vS/V_0 \approx 21 \text{ hour}^{-1}, \quad (6.4)$$

where the diffusion velocity $v = \sqrt{D_a \lambda_{Rn}} \approx 10 \pm 5 \text{ m/hour}$, with the radon diffusion constant in air D_a and decay constant λ_{Rn} , and the total internal surface area $S \sim 100 \text{ m}^2$. Internal ventilation by the HVAC moves air through the HEPA filters, which are presumed to have a 100% capture efficiency). Therefore, the ventilation deposition rate

$$\lambda_v = F/V_0. \quad (6.5)$$

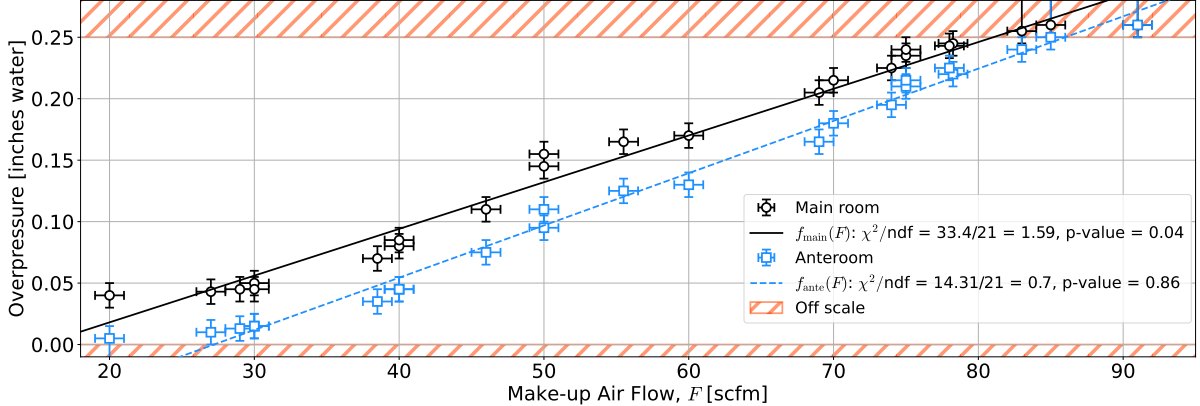


Figure 6.4: The cleanroom overpressure is measured for both the main room (black circles) and anteroom (blue squares) as a function of make-up air flow F by differential-pressure meters (with pressure displayed in inches of water, with 1 inch of water = 1.87 Torr). Due to the internal circulation of air by the HVAC through the ceiling-mounted HEPA filters, the main room is always (when doors are closed) about 0.04 inches of water higher overpressure than the anteroom. Linear trends are drawn for both anteroom and main room pressures. All points at each location are fit, though the lowest- and highest-pressure data points likely suffer from inaccuracies in the meter, with values below zero and greater than 0.25 inches of water being off-scale (hatched region).

The fraction of radon daughters that settle on nearby surfaces

$$\phi_s \equiv \frac{\lambda_d}{\lambda_v + \lambda_d} \quad (6.6)$$

and, as shown by the right axis of Fig. 6.3, decreases with increased internal circulation (as expected).

While placing the HVAC outside of the cleanroom to increase the usable space within it may seem like a good choice, we have intentionally not done so. The reason is that the internal blower creates, necessarily, a pressure differential; that is, it creates a low-pressure region within the HVAC unit. If the HVAC were placed outside the cleanroom, high-radon air could be pushed into it following the pressure gradient. One would then be tasked with making the HVAC unit sufficiently leak tight, which in the past has been, a formidable job depending on the specific HVAC unit; and limited success can easily compromise the low-radon state otherwise achieved. With the HVAC located inside the low-radon cleanroom (as shown in the inset of Fig. 6.1), this potential challenge was circumvented.

Low-radon make-up air supplied by the SD Mines RRS (between about 10-100 cfm, as determined by the RRS blower) enters the cleanroom anteroom via 6" diameter ducting. The air is then pushed into an opening in the HVAC that leads to the low-pressure side of the HVAC's internal blower, which then circulates the cleanroom air as described previously. The make-up air that enters the cleanroom must also leak out, with the cleanroom overpressure determined by how leak-tight the cleanroom has been made. Figure 6.4 shows the SD Mines cleanroom overpressure as a function of make-up air flow. The overpressure was measured by (**Dwyer Magnehelic**) differential-pressure meters that penetrate both the anteroom and main room walls, with the internal circulation by the HVAC set to 75% (or about 1500 scfm). Because the HVAC forces more air through HEPA filters in the main room, the main room overpressure is always slightly larger than that of the anteroom (by about 0.04 inches of water). Linear trends are fit to both anteroom and main room pressures; for the main room,

$$f_{\text{main}}(F) = \left(0.0038 \pm 0.0001 \frac{\text{inches water}}{\text{scfm}} \right) F - (0.058 \pm 0.007 \text{ inches water}), \quad (6.7)$$

and for the anteroom

$$f_{\text{ante}}(F) = \left(0.0043 \pm 0.0001 \frac{\text{inches water}}{\text{scfm}} \right) F - (0.116 \pm 0.005 \text{ inches water}), \quad (6.8)$$

where F is the cleanroom make-up air flow in standard cubic feet per minute (scfm). All points at each location are fit, though the lowest- and highest-pressure data points likely suffer from inaccuracies in the meter, with values below zero and greater than 0.25 inches of water being off-scale. Originally, the cleanroom was so leak tight that a pressure relief port was installed such that make-up air flow above ~ 30 cfm could be supplied without creating an overpressure that was off scale (> 0.25 inches of water). Section 6.2 presents a measurement indicating that back-diffusion of radon through the pressure relief pipe is not observed with sufficient overpressure.

Similar to internal circulation by the internal HVAC, the make-up air supplied by the RRS replaces the air within the cleanroom according to Eq. 6.1. Figure 6.5 shows both

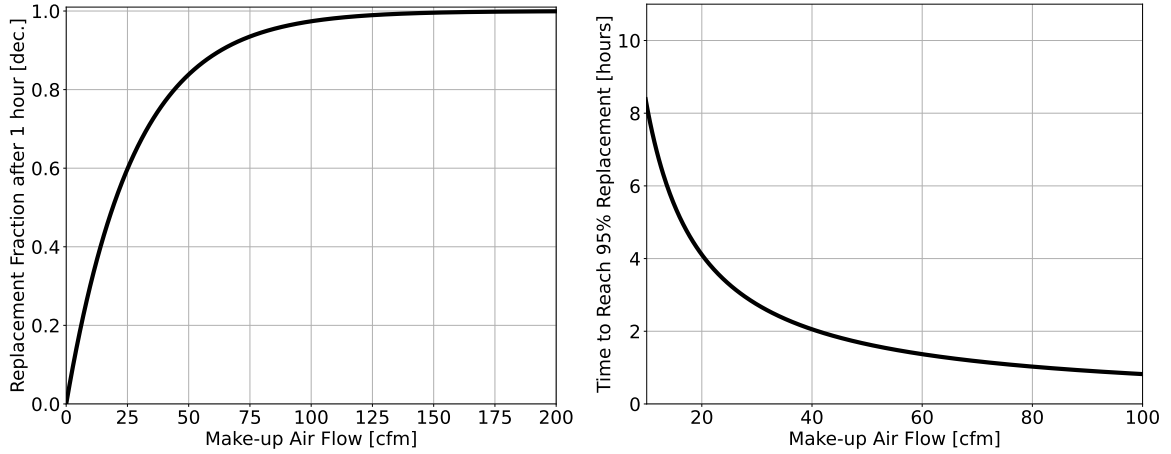


Figure 6.5: **Left:** The fraction of the cleanroom volume that replaced in one hour depends on the make-up air flow F according to Eq. 6.1. **Right:** The time to reach 95% replacement depends on the make-up air flow F according to Eq. 6.3. At $F = 50$ scfm it takes about 2 hours to reach 95% replacement.

the replacement fraction $V(t)/V_0$ after $t = 1$ hour (left plot) and the time to reach 95% volume replacement (right plot). By inspection, 95% of the internal volume is replaced with low-radon air within about 2 hours at 50 scfm. The radon concentration within the cleanroom also depends on the make-up air flow, as is described in Section 6.1.

6.1 Sources of Radon Within the SD Mines Cleanroom

When constructing a low-radon cleanroom, it is important to understand the sources of radon that might increase the radon concentration within the space. There are four ways radon might enter the cleanroom: (1) radon in the make-up air supplied to the cleanroom, (2) radon back-diffusing through cracks or other openings, (3) radon emanating out of materials constructing or contained within the cleanroom, and (4) radon diffusing through materials constructing the cleanroom.

Ignoring all sources of radon except radon entering through the make-up air supplied at a volumetric flow rate F at a radon concentration C_{RRS} , we can start building an equation of the radon concentration C within the cleanroom:

$$\frac{\partial C}{\partial t} = \frac{F}{V} C_{RRS} - \frac{F}{V} C - C/\tau, \quad (6.9)$$

where τ is the radon mean lifetime of 5.52 days, V is the cleanroom volume. The last term represents radon decaying within the cleanroom as

$$C(t) = C_0 e^{-t/\tau} \longrightarrow \frac{\partial C}{\partial t} = -\frac{1}{\tau} C_0 e^{-t/\tau} = -\frac{1}{\tau} C(t) = -C/\tau, \quad (6.10)$$

where C_0 is the concentration of radon at $t = 0$.

When the flow rate F is sufficiently reduced, thus reducing the overpressure, radon can back-diffuse through openings into the cleanroom. The back-diffusion rate B_s , having units of Bq/s, is easily added to our previous equation:

$$\frac{\partial C}{\partial t} = \frac{F}{V} C_{\text{RRS}} - \frac{F}{V} C + \frac{B_s}{V} - C/\tau. \quad (6.11)$$

Radon that diffuses out of a material's bulk is referred to as emanation. The emanation rate E_s , with units of Bq, is particularly large for materials rich in ^{226}Ra and where radon has a long mean path length (allowing it to more easily escape). Similarly, radon outside the cleanroom can diffuse through materials that are sufficiently thin and/or have a sufficiently large coefficient of diffusion (such as many plastics). Adding these two contributions to our previous equation, and denoting the rate of diffusion as D_s , with units of Bq, we have an expression that accounts for each possible radon source:

$$\frac{\partial C}{\partial t} = \frac{F}{V} C_{\text{RRS}} - \frac{F}{V} C + \frac{B_s}{V} + \frac{E_s}{V\tau} + \frac{D_s}{V\tau} - C/\tau. \quad (6.12)$$

Because we are interested in the equilibrium radon concentration within the cleanroom, it is sufficient to take the steady-state case:

$$\frac{\partial C}{\partial t} = 0 = \frac{F}{V} C_{\text{RRS}} - \frac{F}{V} C + \frac{B_s}{V} + \frac{E_s}{V\tau} + \frac{D_s}{V\tau} - C/\tau. \quad (6.13)$$

Solving for C , we find a frequently useful expression:

$$\begin{aligned} C &= \frac{1}{F/V + 1/\tau} \left[\frac{F}{V} C_{\text{RRS}} + \frac{1}{V} (B_s + E_s/\tau + D_s/\tau) \right] \\ &= (F C_{\text{RRS}} + B_s + E_s/\tau + D_s/\tau) / (F + V/\tau). \end{aligned} \quad (6.14)$$

The back-diffusion term is negligible (with the outer door is closed) when $F \gtrsim 20$ cfm (as indicated by work described in Section 6.2). Therefore, we estimate the total source as the sum of contributions from emanation and diffusion, that is $S \equiv E_s + D_s$, and solve:

$$\begin{aligned} S &= V\tau \left[\left(\frac{F}{V} + \frac{1}{\tau} \right) C - \frac{F}{V} C_{RRS} \right] \\ &= F\tau (C - C_{RRS}) + CV, \end{aligned} \quad (6.15)$$

where we set $B_s = 0$. We know the cleanroom volume $V = 46.6 \text{ m}^3$, and F is easily measured.

6.2 Radon Concentration During Entry/Exit and Back Diffusion

There are two ways high-radon air can enter the SD Mines cleanroom: (1) during cleanroom entry and exit, high-radon air from the surrounding lab space can enter the cleanroom, as the overpressure drops significantly; this is particularly the case when large objects are being brought into the cleanroom, requiring the outer door to remain open for tens of minutes or longer. (2) Depending on the cleanroom overpressure, high-radon air can diffuse against air leaking out from cracks or other openings in the cleanroom outer walls (such as at the outer door seem or through pressure relief ports).

6.2.1 Radon Concentration During Entry and Exit

Figure 6.6 shows the radon concentration within the SD Mines cleanroom as measured by the SD Mines Radon Monitor (see Section 5.1) with the internal HVAC recirculation flow set at about 1500 scfm. The radon concentration was sampled in the cleanroom's main room (not the anteroom), but with the door between the anteroom and main room left completely open (refer to Fig. 6.2); this represents a worst-case scenario, as the main room loses its relative overpressure compared to the anteroom. The cleanroom was supplied by 40 scfm of low-radon make-up air, resulting in a main-room and anteroom overpressure of ≈ 0.05 inches of water. The outer cleanroom door was opened by about 45° (where an angle of zero represents the door being fully closed) at $t = 0$ hours. Once the

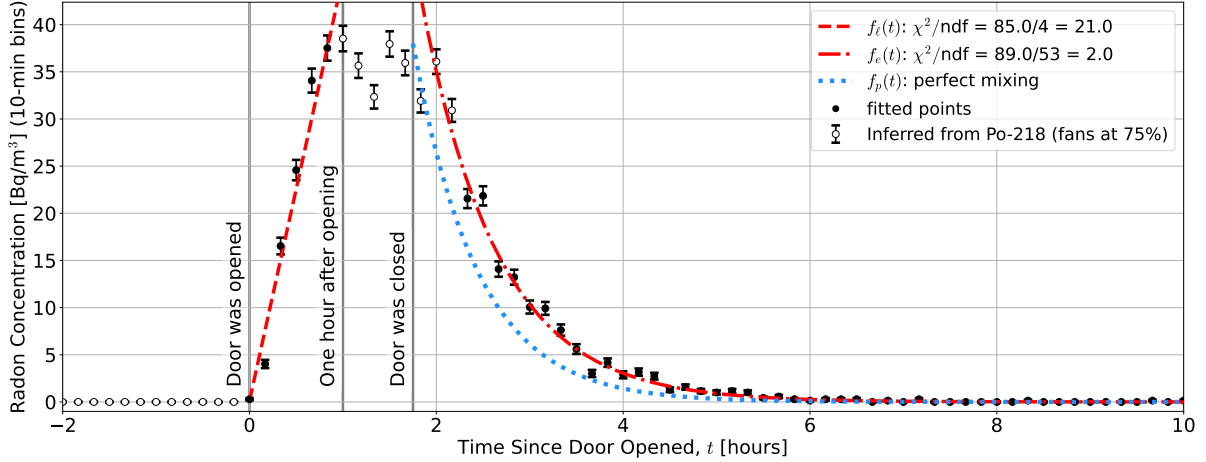


Figure 6.6: Radon concentration (open circles, with fitted points filled) within the SD Mines cleanroom during an entry-exit test with **internal recirculation set to 75%** (corresponding to recirculation flow of 1500 scfm). When the outer door is opened (by 45°), high-radon air enters the anteroom and quickly mixes with the main-room air by the HVAC recirculating air through the HEPA filters. The radon concentration during the first hour after the outer door is opened is fit (red dashed curve) by a linear function $f_\ell(t)$ given by Eq. 6.16. The reduction in the radon concentration starting when the outer door is closed is fit (red dot-dashed curve) by an exponential function $f_e(t)$ given by Eq. 6.17; the characteristic time of this exponential decay can be compared to the perfect-mixing case $f_p(t)$, where $\tau_{\text{perfect}} = V/F = 0.69$. The best-fit parameters are presented in Table 6.1.

outer door is opened, the ingress of radon is expected to follow an exponential function with form $a(1 - e^{-t/b})$, provided that the radon concentration in the surrounding lab space is constant in time; because it is not, only the first hour of the ingress region is fit, where the increase is approximately linear. Once the door is again closed, air within the cleanroom is replaced with the low-radon air supplied by the SD Mines RRS; as described earlier (see Eq. 6.1), the radon concentration is expected to approach the concentration of the supply air exponentially (and the fit is started 30 minutes after closing the door to minimize the effect of the time dependence of the lab radon concentration). Therefore, the ingress region is fit by the linear function

$$f_\ell(t) = mt + b, \quad (6.16)$$

where a and b are fitted parameters. The decay region is fit by the exponential function

$$f_e(t) = Ae^{-t/\tau} + B, \quad (6.17)$$

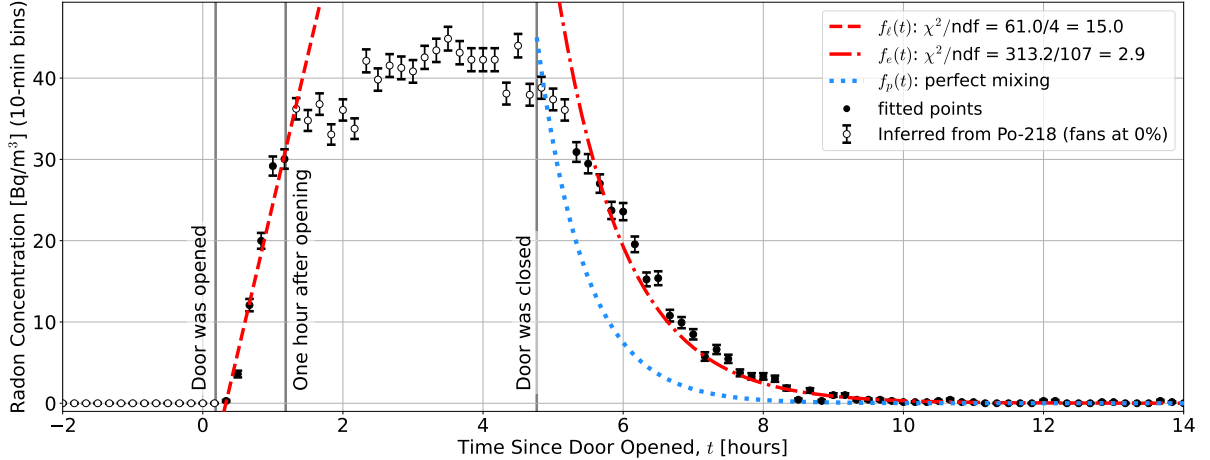


Figure 6.7: Radon concentration (open circles, with fitted points filled) within the SD Mines cleanroom during an entry-exit test with **internal recirculation set to zero**. When the outer door is opened, high-radon air enters the anteroom and slowly mixes with the main-room air (without help from the HVAC recirculation air, which has been turned OFF). The radon concentration during the first hour after the outer door is opened is fit (red dashed curve) by a linear function $f_\ell(t)$ given by Eq. 6.16. The reduction in the radon concentration starting when the outer door is closed is fit (red dot-dashed curve) by an exponential function $f_e(t)$ given by Eq. 6.17; the characteristic time of this exponential decay can be compared to the perfect-mixing case $f_p(t)$, where $\tau_{\text{perfect}} = V/F = 0.69$. The best-fit parameters are presented in Table 6.1.

where A , τ , and B are fitted parameters. The best-fit values of these parameters are presented in Table 6.1. The characteristic time for a perfect-mixing scenario $\tau_{\text{perfect}} = V/F = 0.69$ hours. During the ingress region, the slope m of the linear fit indicates how quickly the radon concentration increases with time t ; therefore, a smaller value is better, as less radon enters the cleanroom per unit time. During the decay region, the characteristic time τ of the exponential fit represents how quickly high-radon air within the cleanroom is replaced with low-radon air supplied by the RRS; therefore, a smaller value is better, as radon within the cleanroom is more quickly reduced to a minimum concentration.

Similarly, Fig. 6.7 shows the radon concentration within the SD Mines cleanroom, but with the HVAC fan speed set to zero. Comparing the rate of radon entering the cleanroom (the slopes m) for the HVAC fan speed set to either 75% or zero shows that if the outer cleanroom door was required to be open for 10's of minutes, it would be

HVAC Fan Speed	Ingress or Decay	$m \left[\frac{\text{Bq}}{\text{m}^3 \text{hour}} \right]$	$b \left[\frac{\text{Bq}}{\text{m}^3} \right]$	$A \left[\frac{\text{Bq}}{\text{m}^3} \right]$	$\tau \text{ [hours]}$	$B \left[\frac{\text{Bq}}{\text{m}^3} \right]$
75% (1500 scfm)	Ingress	45 ± 4	0.1 ± 0.5	—	—	—
	Decay	—	—	403 ± 43	0.8 ± 0.02	0 ± 0.02
0% (0 scfm)	Ingress	37 ± 3	-12 ± 1	—	—	—
	Decay	—	—	9436 ± 1398	0.97 ± 0.02	0 ± 0.01

Table 6.1: Best-fit parameters for the linear and exponential functions fit to the increase and decrease in radon concentration due to opening and closing the outer cleanroom door respectively. During the ingress region, a linear function (Eq. 6.16) is fit to the radon concentration during the first hour. The slope m indicates how quickly the radon concentration increases with time t . During the decay region, an exponential function (Eq. 6.17) is fit to the radon concentration. The characteristic time τ represents high-radon air being replaced with low-radon air supplied by the RRS. Preferred values are highlighted in blue, while the values that are expected to result in a higher radon concentration within the cleanroom are highlighted in red.

better to turn the HVAC recirculation fan OFF, such that high-radon air is not mixed throughout the cleanroom as efficiently. Similarly, comparing the characteristic times τ determined by fitting the decay regions shows that once the outer door is closed a high-fan speed mixes the low-radon air introduced to the anteroom more efficiently with the main-room air, reducing its radon concentration more quickly.

6.2.2 Back Diffusion

Particularly in cases where the cleanroom overpressure is very low, radon might enter the cleanroom through gaps in doors or seams in the cleanroom walls that were not sufficiently sealed. The SD Mines cleanroom was originally made to be so leak-tight that only 30 scfm of make-up air flow would result in the overpressure being off scale (>0.25 inches of water). Because the SD Mines RRS would frequently be configured to produce close to 100 scfm (for demonstration purposes), a pressure relief port was installed in the cleanroom anteroom wall. This relief port consisted of a steel pipe with a 2 inch diameter and 14 inches in length (consisting of a 12 inch straight pipe that was connected to a 2 inch right angle union that penetrated the anteroom outer wall).

To ensure radon from the lab space was not diffusing against the air stream leaving the pipe, the radon concentration was measured by a Durridge RAD7 [118] at three locations

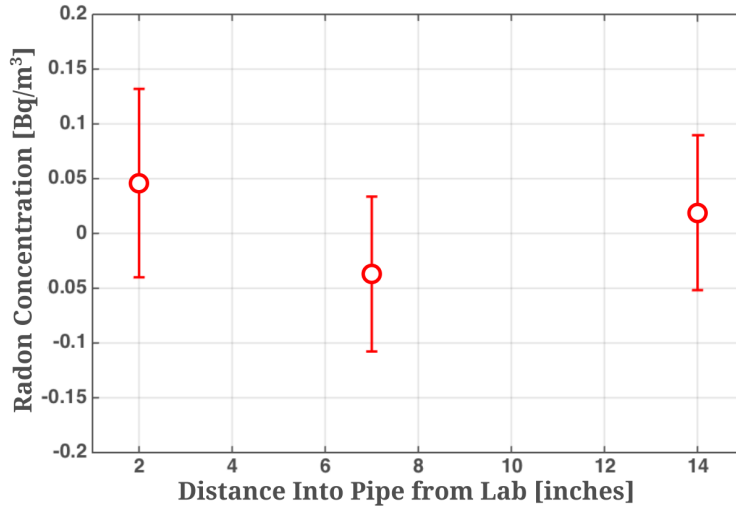


Figure 6.8: The radon concentration as a function of distance within SD Mines cleanroom pressure relief pipe measured by a Durridge RAD7. The cleanroom had an overpressure of 0.01 ± 0.01 inches of water (very low and nearly off scale) during each measurement. The distance of zero represents the high-radon lab-air side, while 14 inches represents the outer anteroom wall. The measured concentration at each location (2, 7, and 14 inches) is consistent with the RAD7 background, indicating no significant back diffusion of radon into the cleanroom (against flow) through the pipe.

within the pipe: 2 inches inside the pipe as measured from the lab side, 7 inches, and 14 inches inside—all the way to the outer wall. The make-up air supplied to the cleanroom was set to 16.7 ± 1 scfm and, by inspecting Fig. 6.4, the inferred cleanroom overpressure was ~ 0.01 inches of water (potentially off scale, as the gauge displays readings from 0 to 0.25 inches of water). The average radon concentration in the lab space during the in-pipe measurements was ~ 75 Bq/m³.

Figure 6.8 shows the background-subtracted radon concentration as a function of sample location inside of the pressure relief pipe. All measurements were consistent with the RAD7 background, indicating that back diffusion of radon is likely negligible even with minimal overpressure.

6.3 Low-radon Water Source for Cleanroom Humidification

The air supplied by the SD Mines Radon-Reduction System (RRS) tends to be very dry (about 5% relative humidity). This is for two reasons: input air to the RRS is

intentionally dried before passing through a column and is then further dried as water adsorbs to the significant surface area of the carbon within the column. The result is that the air supplied to the SD Mines low-radon cleanroom is exceedingly dry (again, about 5%), requiring water to be introduced through the HVAC from an external source.

Dry air is a better insulator than moist air, thus allowing more charge to build up on surfaces; particularly when high voltage is in use, this can result in electrical discharge that can damage equipment or injure personnel. Dry environments are also uncomfortable to cleanroom occupants.

Though water can be added to the cleanroom air via its internal HVAC, doing so can also introduce radon to the degree that radium-226 was present in the sourced water. The amount of radon produced by water varies by location and, in our case specifically, can be quite high. Therefore, the water used by the SD Mines cleanroom is passed through the so-called *Radon Bubbler* (described in Section 6.3.2) that reduces the radon concentration in the water before it is introduced to the cleanroom.

6.3.1 Water Consumption

The amount of water in the air is referred to as the *vapor density* and will henceforth be denoted as ρ_v , with units of g/m³. The maximum amount of water as a vapor that can exist per unit volume is called the *vapor density at saturation*, ρ_{vs} , and is a function of the dry-bulb temperature T_{db} [142], with $\rho_{vs} = 17.3 \text{ g/m}^3$ at $T_{db} = 20^\circ\text{C}$ [143].

The relative humidity ϕ is defined as the vapor density divided by the vapor density at saturation:

$$\phi \equiv \rho_v / \rho_{vs}, \quad (6.18)$$

where it is often multiplied by 100% and quoted as a percentage.

The SD Mines cleanroom is supplied with make-up air flow F having a relative humidity of 5%. The rate water enters the cleanroom (in units of kg/s)

$$Q_{in} = \rho_{v,in} F = \phi_{in} \rho_{vs} F, \quad (6.19)$$

where the make-up air has the relative humidity of $\phi_{\text{in}} = 5\%$ and $\rho_{v,\text{in}} \equiv \phi_{\text{in}}\rho_{\text{vs}}$.

To increase the relative humidity of the cleanroom, water must be added. Air leaks out of the cleanroom with flow F_{out} and relative humidity ϕ_{out} . Therefore, the rate water leaves the cleanroom

$$Q_{\text{out}} = \rho_{v,\text{out}}F = \phi_{\text{out}}\rho_{\text{vs}}F, \quad (6.20)$$

where Q_{out} has units of kg/s. Notice that the volumetric flow rate $F = F_{\text{out}}$ by continuity (though the water content can be different, as water can be added to or taken away from the cleanroom via its HVAC).

Presuming that air within the cleanroom is perfectly mixed (which it nearly is due to internal recirculation), the desired humidity ϕ_{desired} is achieved by adding water at the rate Q_{added} to satisfy $\phi_{\text{out}} = \phi_{\text{desired}}$:

$$\begin{aligned} Q_{\text{added}} &= Q_{\text{out}} - Q_{\text{in}} \\ &= \phi_{\text{desired}}\rho_{\text{vs}}F - \phi_{\text{in}}\rho_{\text{vs}}F \\ &= [\phi_{\text{desired}} - \phi_{\text{in}}]\rho_{\text{vs}}F, \end{aligned} \quad (6.21)$$

where Q_{added} has units of kg/s. Figure 6.9 illustrates the dependence of Q_{added} on the make-up air supplied to the cleanroom (at $\phi_{\text{in}} = 5\%$) and desired relative humidity of the cleanroom air.

When water is added to the cleanroom for humidification, any radon contained in that water contributes to the radon concentration within the space by the amount:

$$\Delta C = \frac{A_w m_w}{V} = A_w \rho_v = A_w \phi_{\text{out}} \rho_{\text{vs}}, \quad (6.22)$$

where A_w is the radon activity of the sourced water (in units of Bq/kg) and is found by measuring the radon concentration of the water, where $A_w = C_w/\rho_w$ with the density of water $\rho_w = 1000 \text{ kg/m}^3$. The mass of the water in the air within the cleanroom is $m_w = \rho_v V$, where V is the cleanroom volume.

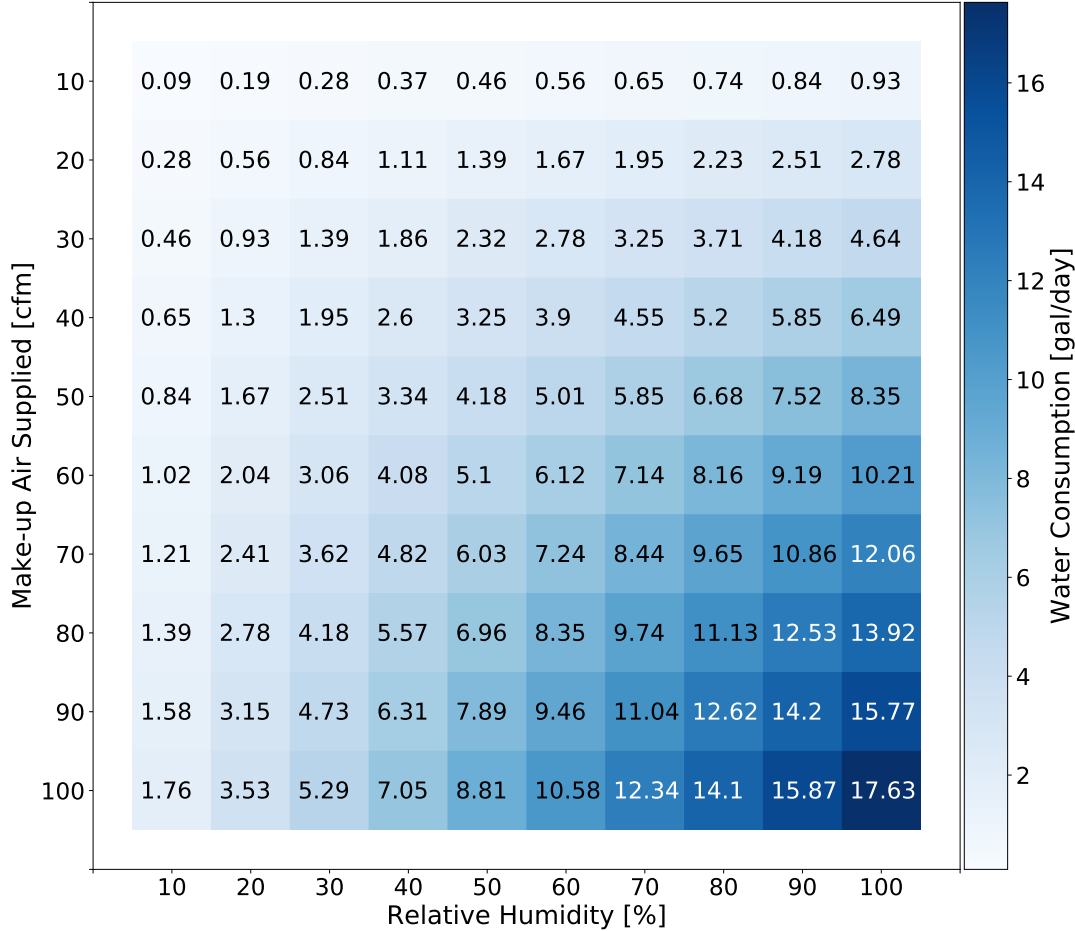


Figure 6.9: The amount of water that must be added (shown as a heat map) to achieve some relative humidity, ϕ_{out} , given the make-up air supplied, F . The units have been converted to those more commonly used in the United States. For the Reader's convenience, 1 Gallon \approx 3.8 Liters.

For example, requiring $\phi_{\text{desired}} = \phi_{\text{out}} = 0.40$ and presuming that the sourced water has an activity $A_w = 0.1 \text{ Bq/kg}$ increases the radon concentration within the cleanroom by

$$\Delta C = 0.1 \frac{\text{Bq}}{\text{kg}} \times 0.40 \times 17.3 \frac{\text{g}}{\text{m}^3} \times \frac{1 \text{ kg}}{1000 \text{ g}} \times \frac{1000 \text{ mBq}}{1 \text{ Bq}} \approx 0.7 \text{ mBq/m}^3. \quad (6.23)$$

This increase in the radon concentration is about an order of magnitude smaller than the sensitivity of the device we use to measure the radon concentration within the cleanroom (see Section 5.1) and is subdominant to other sources (such as radon emanation from construction materials), and would thus be acceptable.

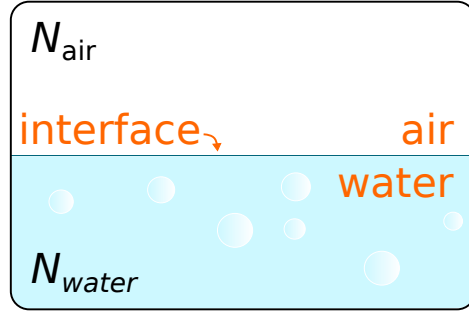


Figure 6.10: A water volume shares an interface with an air volume. Radon atoms may diffuse through the interface until equilibrium is reached. The number of radon atoms at equilibrium in the air volume is denoted by N_{air} , while the same for water is denoted as N_{water} .

6.3.2 The Radon Bubbler

In 1978, Fritz Weigel observed the diffusion of radon through the liquid-gas system presented in Fig. 6.10. Ignoring radon decay, let the total number of radon atoms in the system be N . These atoms could be placed, originally, in the water volume, the air volume, or with some fraction in both. In any event, these atoms will diffuse throughout the water or air volume, and also through the air-water interface. For equal volumes of air and water, an atom will spend more time in the air than in the water. These observations led to the so-called *Fritz Weigel equation* [144]:

$$a = 0.105 + 0.405 \exp(-0.0502T), \quad (6.24)$$

where a is the partition coefficient and T is temperature in degrees Celsius. The partition coefficient a describes the amount of radon atoms in each volume at equilibrium. In words, a partition coefficient of $a = 0.25$ means that there is four times as much radon in the air as in the water [145]. Returning to our example, and with reference to Fig. 6.10, we have that N radon atoms are added to the system, which is held at temperature $T = 20^\circ\text{C}$. At equilibrium, we are given that

$$N_{\text{water}} = aN_{\text{air}}, \quad (6.25)$$

where a is found according to Eq. 6.24. After some algebra (but ignoring radon decay), we have

$$N = N_{\text{air}} + N_{\text{water}} = (a + 1)N_{\text{air}}. \quad (6.26)$$

And so

$$N_{\text{air}} = \frac{N}{a + 1} \quad \text{and} \quad N_{\text{water}} = \frac{aN}{a + 1}. \quad (6.27)$$

If radon decay is not ignored, and we waited Δt to reach equilibrium, we need only multiply by the factor $\exp(-\Delta t/\tau_{\text{Rn}})$ (for equations depending on N):

$$N_{\text{air}} = \frac{N \exp(-\Delta t/\tau_{\text{Rn}})}{a + 1} \quad \text{and} \quad N_{\text{water}} = \frac{aN \exp(-\Delta t/\tau_{\text{Rn}})}{a + 1}. \quad (6.28)$$

Leveraging the Fritz Weigel equation, the so-called *Radon Bubbler* (illustrated by Fig. 6.11) is a device that reduces the radon concentration in water that is supplied to the SD Mines cleanroom. As shown in Fig. 6.11, with figure labels in **bold**, water, supplied by a reverse-osmosis system (not shown), passes through an **electric valve** that is either open or closed according to the **water level sensor**. Water fills the **main column** while simultaneously filling the **reservoir** by passing through the **transfer tube**. Water leaves the system through the **water outlet**, where it is then pumped (not shown) to the SD Mines cleanroom. If the **water level sensor** were to fail, water can also pass through the **overflow port**, which leads to a nearby drain.

Supplied by a standard **air pump** used in ponds (having a factory flow rate of 571 gallons/hour), air from the lab enters the system through the **air inlet**. Immediately afterward, the air passes through a **check valve**, such that water does not escape through the **air inlet** in the event that the pump fails, and then a **manual valve**, which is used during maintenance and experimentation. The air then flows up through the **main column**, according to the Bernoulli principle, in the form of bubbles (hence the device's name), and is exhausted through the **air outlet**.

It is in the **main column** that the Fritz Weigel equation is applied. At any time, there is a volume of air and water that share an interface. Radon will diffuse from the

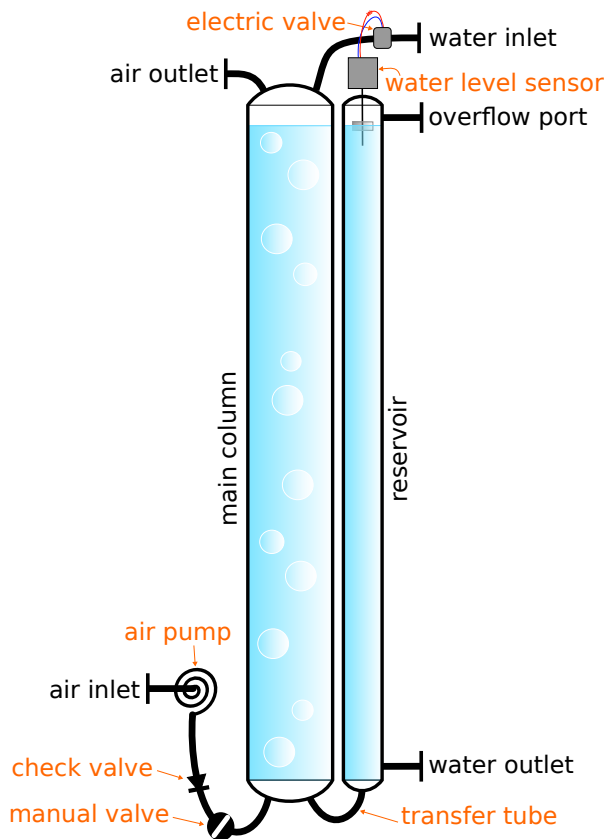


Figure 6.11: Lab air (with a radon concentration of 30-150 Bq/m³) is pumped from the air inlet, up through the main water column, and finally exhausted through the air outlet. Potentially-high-radon water from the water inlet passes through the electric valve and fills the main column. Air bubbles move through the water within the main column, capturing radon along the way. The water then leaves the reservoir through the water outlet, where it is supplied to the SD Mines cleanroom. Both the water level sensor and the water outlet benefit from the reservoir column being free of air bubbles.

air into the water and vice versa—but will spend most of its time in the air. The result is a net transfer of radon atoms from the water volume into the air volume (providing the air does not already contain a significant amount of radon, which does not tend to be the case).

In order to test whether the Radon Bubbler does indeed reduce the radon activity of water passing through it, the Durridge RAD AQUE device was employed (see Fig. 6.12). The RAD AQUA device works by the same principle as the Radon Bubbler. Water from the **water outlet** of Fig. 6.11 flows through the **water in** tube shown in Fig. 6.12. As shown in Fig. 6.12, the water fills the Durridge RAD AQUA up to a designated height

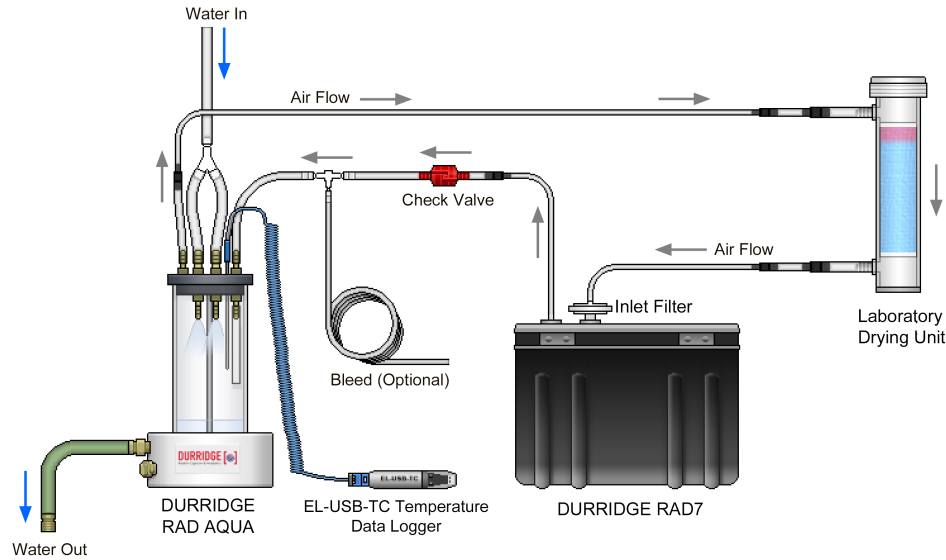


Figure 6.12: The Durridge RAD AQUA device allows the radon concentration of water, that shares an interface with a closed air volume, to be inferred. The Durridge RAD7 counts the decays of radon daughters in the closed air volume and, making use of the Fritz Weigel equation, the radon activity of the water is then estimated. This figure was taken from the Durridge RAD AQUA manual [145].

where it is then drained through the **water out** tube. The air volume above the water within the RAD AQUA is circulated in a closed loop through an inline **Laboratory Drying Unit** and then a Durridge RAD7, where decays of radon daughters are counted. The temperature of the air volume is also measured (shown here as a **Temperature Data Logger**). As water flows through the RAD AQUA, radon in it can diffuse into the closed air volume, which is being sampled by the RAD7. Approximate equilibrium appears to be achieved within perhaps tens of minutes, as indicated by Fig. 6.13.

Figure 6.13 shows the observed reduction in the radon concentration of the water leaving by the Radon Bubbler. Initially, the air pump was set to OFF and the RAD AQUA device sampled the outlet water. After one day, the air pump was turned ON. A reduction of the radon concentration in the outlet water was observed, reaching an ultimate reduction of $R_{ab} = C_a/C_b = 5.6 \pm 0.4$. The air pump was then turned OFF and then ON again, to check reproducibility, and produced the reduction of $R_{cd} = C_c/C_d = 5.8 \pm 0.3$. Both reductions observed agree within statistical uncertainties.

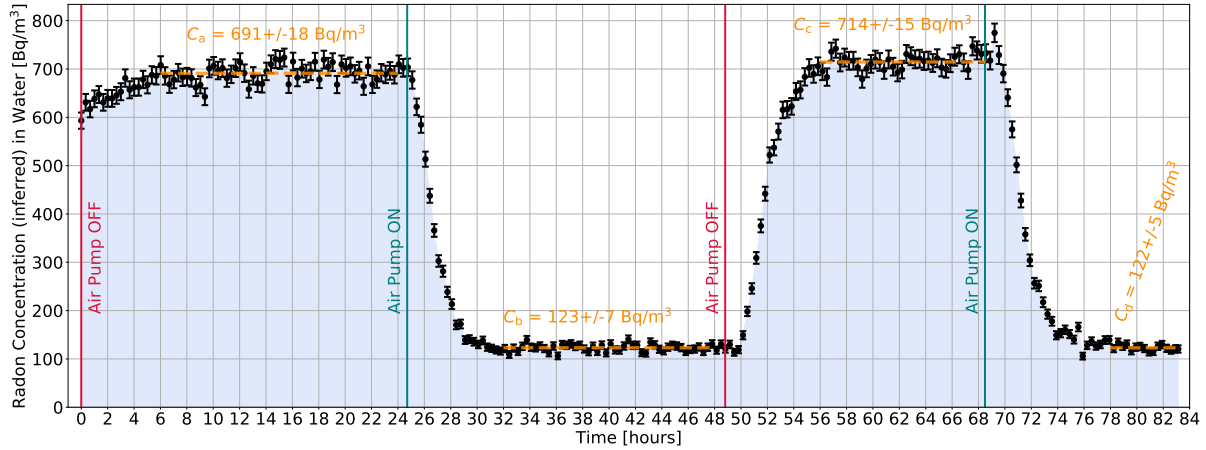


Figure 6.13: As the Radon Bubbler air pump changes from OFF to on, a measured reduction of the outlet water is observed by the RAD AQUA device. Performing this OFF then ON test twice, we find consistent reductions of $R_{ab} = C_a/C_b = 5.6 \pm 0.4$ and then, afterward, $R_{cd} = C_c/C_d = 5.8 \pm 0.3$.

Radon introduced through humidification has the potential, depending on the initial activity of the water, to be the dominant source of radon in the SD Mines cleanroom. The amount of radon in water can vary widely and ranges between 0.1 and 100 Bq/kg (for example, [146, 147]). According to the calculation shown by Eq. 6.23, a water radon concentration of 100 Bq/kg leads to a change in the cleanroom radon concentration $\Delta C = 700 \text{ mBq/m}^3$, many times larger than the radon concentration of the SD Mines RRS output air (that is between 10-100 mBq/m³). The SD Mines Radon Bubbler has the capacity to make a potentially dominant source of radon as measured in within the cleanroom subdominant.

6.4 SD Mines Cleanroom Environmental Monitoring

Environmental monitoring of the SD Mines cleanroom is performed by the Cleanroom Monitoring System (CMS). The CMS provides measurements of temperature, relative humidity, pressure, and concentration of total volatile-organic compounds (VOCs), carbon dioxide (CO₂), and particles larger than 0.3 μm and 0.5 μm. The sensors chosen provide redundancy in temperature and relatively humidity; though useful in checking for self-consistency, absolute readings are checked against other instruments in our lab (having

Sensor Name	Quantity Measured [units]
DHT22	Temperature [$^{\circ}\text{C}$] and relative humidity [%]
MS8607	Temperature [$^{\circ}\text{C}$], pressure [Torr], and relative humidity [%]
SGP30	Total volatile-organic compounds (VOCs) [ppb] and carbon-dioxide [ppb]
PMSA003I	Particle counter [particles/L]

Table 6.2: The CMS uses sensors sourced from Adafruit, an education-focused electronics supplier (www.adafruit.com). The units listed here (and seen by the end-user) have already undergone unit conversion (e.g., Pa to Torr).

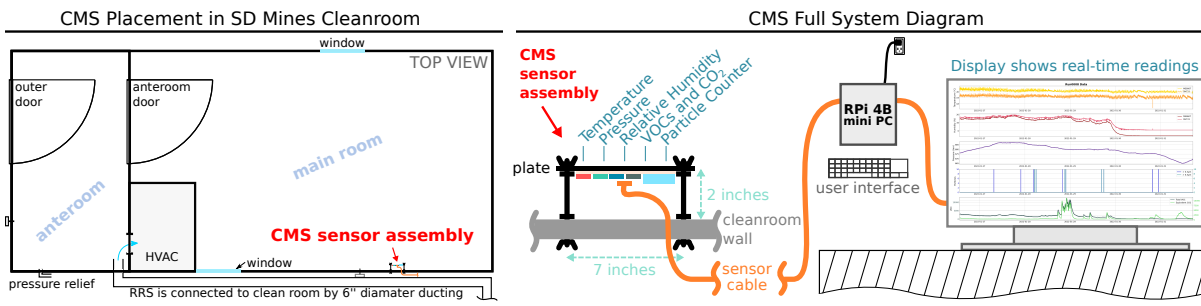


Figure 6.14: **Left:** The CMS sensor assembly is mounted at eye-level within the main room of the SD Mines cleanroom. The sensors themselves are located on the inner side of an aluminum plate 2 inches from the wall, which offers protection without largely obstructing air flow. **Right:** Sensors in the CMS sensor assembly measure temperature, relative humidity, pressure, VOCs, CO₂, and particles larger than 0.3 μm and 0.5 μm . These sensors are read out and recorded by a mini PC, which may also provide the user with real-time plots of measurements.

known accuracy); that is, with the exception of the VOCs and CO₂ sensors, which are *not* calibrated, but still provide a differential reading, which is sufficient for our purposes (e.g., to check for *new* contaminants within the clean space). For a complete listing of sensors and what they measure, refer to Table 6.2.

As shown by Fig. 6.14, an assembly of these sensors is mounted to an exterior wall panel within the cleanroom's main room. The sensor assembly is 6.5 ft from the floor, with the sensors themselves mounted to the inside of an aluminum plate, with the plate standing 2 inches away from the wall by use of a custom-built standoff (but consisting of common, locally-sourced hardware). This aspect of the sensor assembly design affords protection to the delicate sensors (hidden behind the plate), while still allowing cleanroom air to easily wash over them. With, presumably, the largely-unmodified speed and

smoothness of air passing over the sensors, measurements are expected to represent that of the room in general.

There was a concern that the particle count measured by the CMS while mounted to the cleanroom wall may not represent that of the cleanroom in general. Using a Dylos particle counter for reference, measurements were made with the CMS particle counter at varying distance from a wall. At distances of 2 feet to 2 inches, no significant difference in particle count (compared to the reference) was observed; this indicates sufficient air flow from the general space passes through the CMS particle counter, even mounted only 2 inches from a wall.

Each sensor in the CMS sensor assembly is connected via a single 22 awg (*i.e.*, American wire gauge), 8 conductor, shielded cable to a Raspberry Pi 4B (RPi 4B) mini computer where it is read out. A software suite (written in Python) reads in all the sensors, performs basic processing (*e.g.*, unit conversion), saves measurements to disk, and, optionally, displays “real-time” measurements once every 4 seconds (as set by the user) on a connected PC monitor. This sampling rate is more than sufficient for our purposes, as we don’t intend to track events on a timescale quicker than the SD Mines volume-replacement time of tens of minutes.

Chapter 7

The RRS Simulation

The Radon-Reduction System (RRS) Simulation is a physics model of the SD Mines RRS. It is a computer program that describes the transport of radon through a packed bed of carbon. The form of this physics description is that of a matrix (referred to as an operator) that may be applied to (made to operate on) a vector containing elements that represent the amount of radon atoms at each location within that carbon bed, or column. This simulation, frequently referred to as *the RRS simulation*, *the RRS sim*, or even, when context permits, just *the simulation* or *the sim*, defines algorithms for operators to be applied such that radon may be made to move forward or backward, diffusing as it does, in a way that closely approximates typical operation of the SD Mines RRS. Radon atoms that pass completely through a column are counted and the output radon concentration may be compared to the measured radon concentration of the SD Mines RRS. Both the physical RRS and, even more so, the RRS simulation behave according to user-set configurations that potentially modify the output radon concentration; the comparison of measured and simulated quantities (such as the output radon concentration) may serve the following major purposes:

1. **Improve physics understanding:** By attempting to describe all relevant physics of the SD Mines RRS, one's understanding of the underlying physics and the machine's operating logic is tested and, very likely (as it was for me!), improved upon.
2. **Optimize a current RRS:** A better understanding of system behavior provides a pathway for improving an already-built (physical) RRS in many ways, including improved reduction of the output radon concentration and access to higher process-air flow rates by optimizing user-defined configurations (*e.g.*, the cycle period of

the filtering and regenerating stages). The simulation predictions inform system specifications (required leak rate, for example) and good practices in operating the system for different applications.

3. **Inform future RRS builds:** Simulation parameters, limited mostly by one's imagination, can be explored in order to guide the hardware changes to an already-built RRS or a more-ambitious future build, or perhaps a smaller system with more modest performance requirements.

The RRS simulation describes radon atoms at some location at some time. As simulations tend to go, both time and space are discrete; therefore, the domain in which behavior is described is restricted. The movement of radon atoms is driven by an operator (a matrix) acting on a column (an array) and producing the state of that column but evolved by Δt , the minimum time step of the simulation. Each operation may move radon atoms from one location to another within the column, but with the location of these atoms specified only to the accuracy of the spatial step size, Δx .

In choosing Δt and Δx , we want to maximize descriptive ability while still allowing the simulation to be run quickly on available computers; this way, the results can be evaluated and put to use on an acceptable timescale (determined by applications of interest and, no doubt, a strong desire to graduate). For this work, Δt is nominally 5 min and Δx is 1 cm, with discussion provided in Section 7.2.

The i 'th element of the simulated column is the number of radon atoms at the i 'th centimeter within the carbon bed (*i.e.*, the column). Similarly, every operation (by an operator) evolves the column acted on by Δt . Therefore, if we operate twice the column shall be evolved by $2\Delta t$; operating n times evolves the column by $n\Delta t$. When describing successive operations by different operators, it is both more intuitive and more descriptive of underlying code to resist referring to the evolution of a column "after some time t ," but instead, "after some number of operations n ." When needed, one may quickly convert between operations n to time t by the relation: $t = n\Delta t$.

While the RRS simulation will generally be described at a high level, some topics, where useful, are described in substantial detail. Code snippets are included in-text where it is particularly helpful, while other code is only referenced. An effort has been made to keep the description of physics principles in Chapter 4; however, some will be restated for the convenience of the reader. The RRS simulation code can be made available upon request. Communication is highly encouraged and can be directed to the dedicated email: rrs.simulation.author@gmail.com

7.1 Brief Overview of RRS Simulation Modules

The RRS simulation consists of several code modules (described in Table 7.1) that are called by a master script. Each master script usually produces a single deliverable, such as a plot (a prediction!) of the equilibrium radon concentration versus air flow supplied to a cleanroom. These master scripts perform no calculations (or as few as possible)—even plotting methods are defined in a dependency. Benefits of this modular design include reducing the amount of code written (which usually reduces the opportunities for making errors) and making the program more intuitive. Figure 7.1 illustrates how the master script calls these modules and shows each module’s dependencies in the form of a flow chart.

As a best practice, the end user should not modify any master script that is already correctly producing a deliverable. If a different deliverable is needed, a separate master script should be created. The user should not (with one exception) modify a dependency unless there is reason to believe physics is not being described sufficiently by it (and thus a change is made, followed by validation tests); the exception is for the configuration dependency (a configuration file named `hConfig.py`), which is modified to suit the user’s specific application.

The configuration script defines values for the filtering flow rate, the input radon concentration, the mass of the carbon, the size of each carbon column, and so on. Many of these parameters will not change frequently (such as the mass of the carbon in a

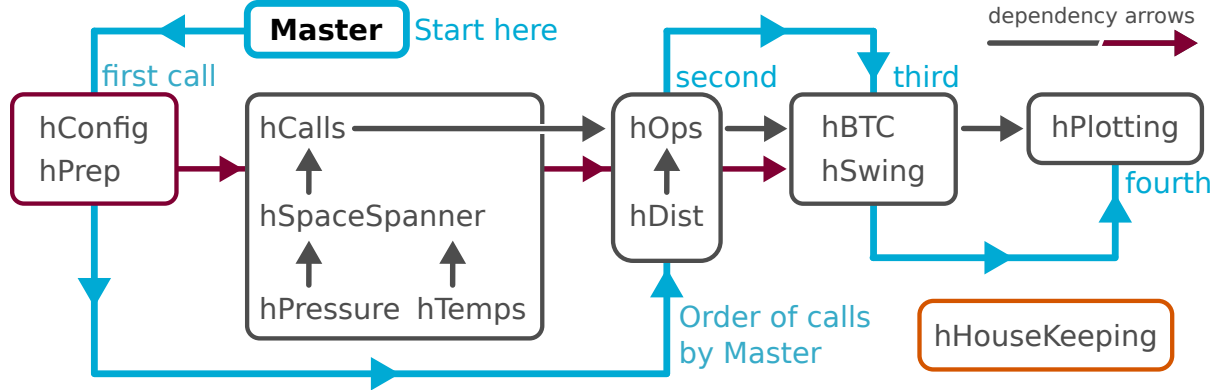


Figure 7.1: The **Master** script calls simulation modules and produces a user-defined output (such as a break-through or regeneration curve, as discussed in Section 7.4). The thick blue line illustrates the order of calls made by **Master**. The thin gray and maroon arrows show the direction of dependence (*e.g.*, $A \rightarrow B$ reads “ B depends on A ”), with the maroon arrow emphasizing that **hConfig** and **hPrep** are dependencies for most modules. The module **hHouseKeeping** performs a variety of duties, such as loading and processing input radon concentration data (real or otherwise) or rebinning a simulated output; drawing in its dependencies would greatly confuse this flowchart.

column), but others (such as the filtering flow rate or input concentration) will change frequently or may even, for radon concentration as example, be given as a time series. The user may modify this script, prior to running a master script, to configure the simulation as desired. The configuration is saved as part of the deliverable produced by the master script.

7.2 The Generator: A Distribution Function Governing the Translation and Diffusion of Radon Atoms

As described in Section 4.2, the motion of radon within a medium, such as a bed of carbon granules, is characterized by translation: the group velocity, which can be negative, positive, or zero; and diffusion: the random spreading out of the radon atoms due to temperature and/or the turbulent flow of the carrier gas. Let us denote x to be the longitudinal distance and D the diffusion coefficient of radon within a long column packed with this carbon. According to Eq. 4.57 from Section 4.2, an initial radon concentration C_0 within the region $[-h, h]$ diffuses, after a time t , to any location x within the column

Module Name	Brief Description
hConfig.py	Configuration file that contains parameters from the length and diameter of the columns, and the air flow through them, to booleans that turn ON or OFF radon decay or even regeneration (where the regeneration operator is set to the identity matrix). This script is meant to be modified as needed by the user (or by the Master script when iterating through a set of parameter values, such as flow rate). No calculations are made in this script.
hPrep.py	Performs simple calculations (unit conversions, etc.) to prepare the configuration parameters provided in hConfig.py for further use (in operator building, etc.).
hSpaceScanner.py	Creates radon-velocity and diffusion-coefficient vectors. These will be used when building operators and can be time-dependent. Pressure and temperature corrections are applied here as well.
hPressure.py	Provides the pressure in a column as a function of longitudinal distance and time (during slow-fill, for example). Also, defines methods for applying the pressure corrections.
hTemps.py	Loads raw temperature data for a chosen run and processes it for use by hSpaceScanner.py.
hCalls.py	Calls hSpaceScanner.py to build radon-velocity and diffusion-coefficient vectors with the most recent configurations (hConfig.py and hPrep.py).
hDist.py	Defines Diffusion and translation as the so-called Generator function, which is used for building operators (see Section 7.2).
hOps.py	Methods for building the filtering, regenerating, and slow-fill operators.
buildOps.cpp	C++ code alternative to hDist.py providing a substantial computational speedup. The compiled binary is called by hOps.py, and hDist.py is not used.
hHouseKeeping.py	Methods for loading input radon concentration data, saving intermediate data, basic rebinning methods, etc.
hBTC.py	Methods for performing simulated break-through curves (BTCs).
hSwing.py	Method that applies operators in a way that emulates the radon-mitigation system vacuum-swing behavior. This script provides the simulation's predictions of radon concentration as a function of flow rate, and/or other parameters.
hPlotting.py	Useful methods for plotting common deliverables.

Table 7.1: Simulation modules with high-level descriptions.

according to the equation:

$$C(x, t) = \frac{1}{2} C_0 \left[\operatorname{erf} \left(\frac{h - x}{2\sqrt{Dt}} \right) + \operatorname{erf} \left(\frac{h + x}{2\sqrt{Dt}} \right) \right]. \quad (7.1)$$

Recalling that space, for our simulation, is quantized (one may say “binned”), we substitute h by the step size Δx , the minimum spatial separation of our x space:

$$2h = \Delta x \longrightarrow h = \Delta x/2. \quad (7.2)$$

This substitution yields

$$C(x, t) = \frac{1}{2} C_0 \left[\operatorname{erf} \left(\frac{\Delta x/2 - x}{2\sqrt{Dt}} \right) + \operatorname{erf} \left(\frac{\Delta x/2 + x}{2\sqrt{Dt}} \right) \right]. \quad (7.3)$$

This expression tells us what fraction of the radon atoms initially within the bin centered at $x = 0$ move to any other x location. In order to consider radon initially at some other location, say, ξ , we make the additional substitution $x \rightarrow x - \xi$. Before substituting this in, we make one more change: the velocity of the radon atoms is v_{Rn} , and, when multiplied by t , acts as an additional offset. These two substitutions come together as:

$$\frac{\Delta x}{2} - x \longrightarrow \frac{\Delta x}{2} - (x - \xi - v_{Rn}t) = \frac{\Delta x}{2} + \xi - (x - v_{Rn}t) \quad (\text{for the left error function}) \quad (7.4)$$

$$\frac{\Delta x}{2} + x \longrightarrow \frac{\Delta x}{2} + (x - \xi - v_{Rn}t) = \frac{\Delta x}{2} - \xi + (x - v_{Rn}t) \quad (\text{for the right error function}) \quad (7.5)$$

Because each operation is performed over the time step Δt , yet another substitution is made: $t \rightarrow \Delta t$. Bringing this all together, with C now a function only of x , we have:

$$C(x) = \frac{1}{2} C_0 \left[\operatorname{erf} \left(\frac{\frac{\Delta x}{2} + \xi - (x - v_{Rn}\Delta t)}{2\sqrt{D\Delta t}} \right) + \operatorname{erf} \left(\frac{\frac{\Delta x}{2} - \xi + (x - v_{Rn}\Delta t)}{2\sqrt{D\Delta t}} \right) \right]. \quad (7.6)$$

So far, this expression translates and diffuses the radon concentration C_0 , within the bin of width Δx , at the location ξ to any other location x , according to the radon velocity v_{Rn} and diffusion coefficient D , both functions of ξ .

Our last task is to normalize this expression such that it may be used in the construction of a matrix, which we will call an operator. Henceforth referred to as the *Generator*, we have:

$$G(x, \xi, v_{Rn}, D, \Delta x, \Delta t) = \frac{1}{2} \left[\operatorname{erf} \left(\frac{\frac{\Delta x}{2} + \xi - (x - v_{Rn}\Delta t)}{2\sqrt{D\Delta t}} \right) + \operatorname{erf} \left(\frac{\frac{\Delta x}{2} - \xi + (x - v_{Rn}\Delta t)}{2\sqrt{D\Delta t}} \right) \right]. \quad (7.7)$$

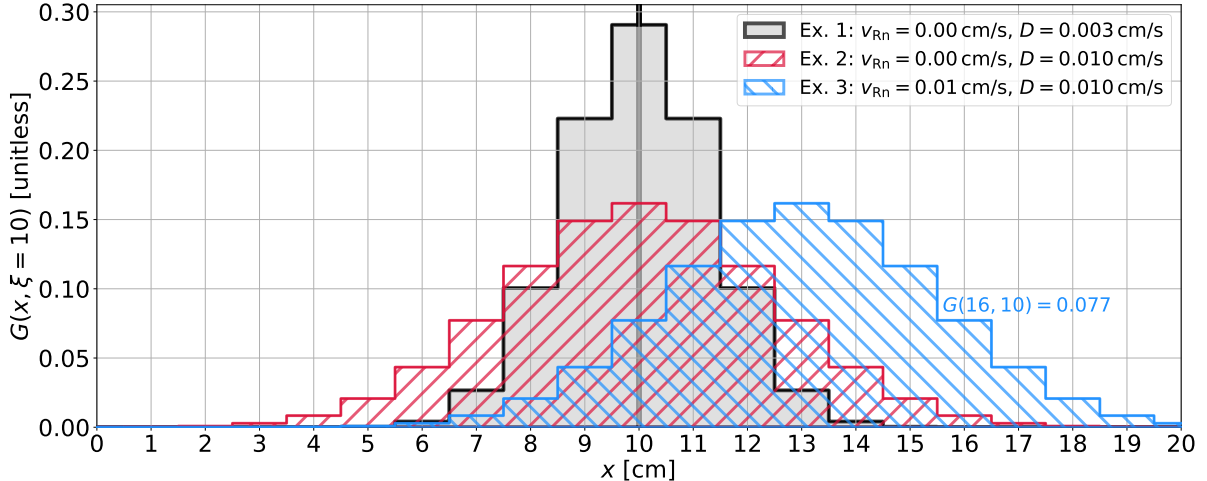


Figure 7.2: The Generator described by Eq. 7.7 was evaluated for choices of v_{Rn} and D , as printed in the legend, and with a time step of $\Delta t = 300$ seconds ($= 5$ min). For **Ex. 1** (black-gray curve) from the legend, we have: $G(x, \xi, v_{Rn}, D, \Delta t) \rightarrow G(x, 10 \text{ cm}, 0.00 \text{ cm/s}, 0.003 \text{ cm}^2/\text{s}, 300 \text{ s})$. For **Ex. 1** and **Ex. 2** (red with forward hatching), the radon velocity is zero everywhere and we observe only diffusion, but with **Ex. 2** diffusing more, as expected due to its larger diffusion coefficient. In **Ex. 3** (blue with backward hatching), the radon velocity is nonzero and positive, so we observe the peak of the distribution has moved to the right by $v_{Rn}\Delta t = 0.01 \text{ cm/s} \times 300 \text{ s} = 3 \text{ cm}$. Each curve produced by the Generator integrates to unity (within the error-function precision of $\sim 10^{-7}$).

Before building our first operator, a demonstration is in order: imagine radon atoms at the location $\xi = 10 \text{ cm}$ within a column. Upon evaluation, the Generator, Eq. 7.7, describes what fraction of the radon atoms at $\xi = 10 \text{ cm}$ will move to any location x . The radon velocity and diffusion coefficient, v_{Rn} and D , are both constants at any ξ . Figure 7.2 illustrates the evaluation of the Generator for three different radon velocities and diffusion coefficients combinations.

Going a step further, let there be $N(n, \xi) = 10^8$ radon atoms at the location ξ after n operations (*i.e.*, at time $t = n\Delta t$). We may calculate the number of radon atoms at the location $x = 16 \text{ cm}$ after $n + 1$ operations (so, $t + \Delta t$), with choices of variables made explicit below, but taken from **Ex. 3** of Fig. 7.2, as:

$$N(n + 1, x) = G(x, \xi, v_{Rn}, D, \Delta t)N(n, \xi). \quad (7.8)$$

Or, specifically for our example:

$$\begin{aligned} N(n+1, 16 \text{ cm}) &= G(16 \text{ m}, 10 \text{ cm}, 0.01 \text{ cm/s}, 0.01 \text{ cm}^2/\text{s}, 300 \text{ s})N(n, 10 \text{ cm}) \\ &\approx 0.077 \times 10^8 = 7.72 \times 10^6 \text{ atoms}. \end{aligned}$$

We see that Eq. 7.8 provides the number of radon atoms at the location x that were at location ξ in the column one Δt earlier in time. The total number of radon atoms at the location x from atoms originally at, for example, two locations ξ_1 and ξ_2 , is found simply as the sum:

$$N(n+1, x) = G(x, \xi_1, v_{\text{Rn}}, D, \Delta t)N(n, \xi_1) + G(x, \xi_2, v_{\text{Rn}}, D, \Delta t)N(n, \xi_2). \quad (7.9)$$

Generalizing this to account for radon atoms contributing to the location x from everywhere in the column (so, $\forall \xi \in [0, 1, \dots, L]$), we have:

$$N(n+1, x) = \sum_{\xi=0}^L G(x, \xi, v_{\text{Rn}}, D, \Delta t)N(n, \xi). \quad (7.10)$$

At this point, we are ready for the construction of an operator: a matrix that provides the number of radon atoms, after one Δt , at all locations x due to radon atoms diffusing and/or translating from all locations ξ in the column.

7.3 Operators

What we want from an operator can be expressed by the following matrix equation:

$$\mathbf{M} \cdot \mathbf{c}(n) = \mathbf{c}(n+1), \quad (7.11)$$

where \mathbf{M} , the operator, is a square matrix with dimensions $L \times L$, $\mathbf{c}(n)$ is a vector of the radon atoms after n operations in a “column” of length L , and $\mathbf{c}(n+1)$ represents the radon atoms in the column after they have diffused and translated by one Δt , according to the elements of the operator. To be clear, I avoid writing $\mathbf{c}(n, x)$ because \mathbf{c} is not a function of x , but contains elements spanning x ; \mathbf{c} is, however, a function of number of operations. The number of atoms after n operations and at the location x will be denoted as $N(n, x)$.

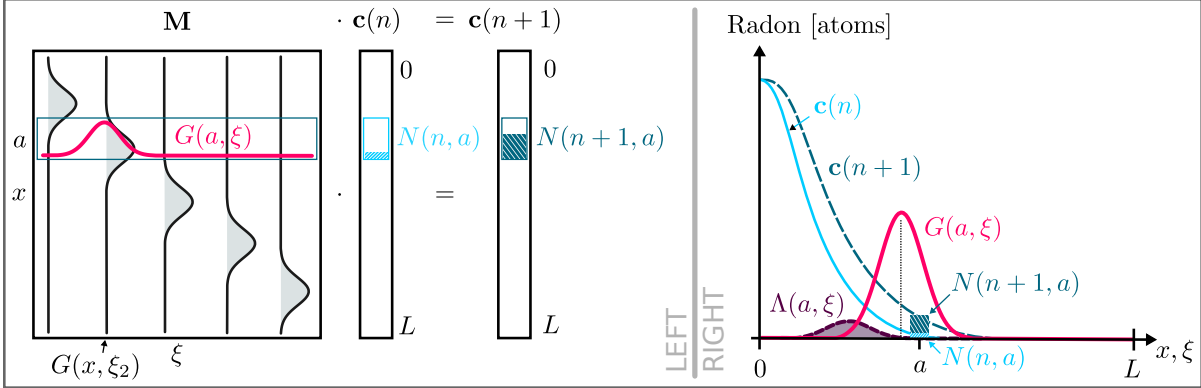


Figure 7.3: Left: The columns of the operator \mathbf{M} are described by the Generator (see Eq. 7.7). As noted in the figure, the ξ_2 column is populated by $G(x, \xi_2)$, and describes the fraction of radon that will move from the location ξ_2 to each location x . The rows of this matrix are similarly populated by the Generator, but spanning ξ . As shown in the figure (thick, red line), the row at $x = a$ is made from $G(a, \xi)$, and represents the fraction of radon that will move from any location ξ in the column (the carbon bed) to the location a . The dot product of the a 'th row with $\mathbf{c}(n)$ provides the a 'th element of $\mathbf{c}(n + 1)$. The a 'th element of vectors $\mathbf{c}(n)$ and $\mathbf{c}(n + 1)$ contain partially filled hatched regions to help illustrate the number of atoms, which may be compared to the plot on the right. **Right:** The initial radon atoms, shown qualitatively, is described by $\mathbf{c}(n)$ (light blue line), while the radon atoms in the column after operation is $\mathbf{c}(n + 1)$ (dashed, dark blue line). The Generator evaluated at $x = a$ over ξ (thick, red line) overlaps $\mathbf{c}(n)$; their element-wise product $\Lambda(a, \xi)$ (maroon, close-dashed filled curve), as defined by Eq. 7.13, represents the fraction of radon atoms that will move to the location a , after Δt , according to the dot product of $G(a, \xi)$ with $\mathbf{c}(n)$, as shown by Eq. 7.14. The number of radon atoms $N(n, a)$ and $N(n + 1, a)$ are illustrated by light blue right-hatched and dark blue left-hatched regions respectively.

Comparing the matrix operation Eq. 7.11 with Eq. 7.10 indicates that

$$M_{x,\xi} = G(x, \xi, v_{Rn}(n, \xi), D(n, \xi), \Delta t), \quad (7.12)$$

where the radon velocity and the radon diffusion coefficient are made explicit functions of both space ξ and time bin n . In words (and illustrated by the cartoon that is Fig. 7.3), the column index of the matrix \mathbf{M} represents a location ξ of radon atoms initially in the column (the carbon bed). The ξ 'th column spans x and, for each x , describes what fraction of the initial radon atoms move there after Δt . The row index corresponds to locations x in the column (the carbon bed). The x 'th row spans ξ , and when dotted with $\mathbf{c}(n)$, yields the number of radon atoms at x as contributed by every location ξ within the column (the carbon bed). For convenience, the following definition is made:

$$\Lambda(x, \xi) \equiv G(x, \xi, v_{Rn}, D, \Delta x, \Delta t)N(n, x), \quad (7.13)$$

so that Eq. 7.10 can be expressed as

$$N(n+1, x) = \sum_{\xi=0}^L \Lambda(x, \xi). \quad (7.14)$$

So far, radon decay has been ignored; it is included by modifying the operator matrix such that in each time step Δt , radon in the column decays by

$$\exp(-\Delta t/\tau_{Rn}), \quad (7.15)$$

where the radon's mean lifetime $\tau_{Rn} = 5.52$ days. Therefore, when radon decay is turned ON by the user-set boolean within the simulation, Eq. 7.14 becomes

$$N(n+1, x) = \sum_{\xi=0}^L \Lambda(x, \xi) \exp(-\Delta t/\tau_{Rn}). \quad (7.16)$$

Having described the matrix operator, the choice of Δt and Δx may more easily be discussed. Larger values of Δx and Δt reduce computation time (good!). However, if Δx becomes too large the distribution $G(x, \xi)$ may not be well described (as it may only be represented by a couple non-zero points); this can lead to non-physical movement of the simulated radon atoms within the column. If Δt is too large, the simulation suffers from the lack of time resolution, making comparisons to data and predictions more difficult. For this work, Δt is nominally 5 min and Δx is 1 cm.

There are three types of operators used by the RRS simulation: a *filtering* operator, a *regenerating* operator, and a *slowfill* operator. Though the construction of each operator is the same (defined by Eq. 7.12), this naming convention signals to the user that the radon velocity and diffusion-coefficient arrays, that are input arguments to operator construction, are suited for one of the three modes, or stages, in which a carbon column is used, or exists in:

Filtering: This mode describes the radon moving through a carbon column in what will be called the forward direction (positive velocity), from the system input to its output (*e.g.*, to the SD Mines cleanroom). This is referred to as the filtering mode, or stage,

because the time radon takes to exit the column is much longer than that for air, and so the outgoing air tends to be low radon (we may say radon was filtered out of the air).

Regenerating: This mode describes the purging of radon from a column that was recently used for filtration. For the physical system, the regenerating column is pumped down to ~ 20 Torr (about a 30'th of an atmosphere) which increases both the radon velocity and its diffusion coefficient (as described in Section 7.7). With radon moving more quickly backwards through the column during regeneration than it does moving forward through the column during filtering, the column can be purged of radon before it is again used for filtering.

Slowfill: This mode describes the case when regeneration has finished, but the column needs to be brought back up to atmospheric pressure before the filtering mode can begin. The time needed to raise the column sufficiently close to atmosphere depends on the flow of air (that is, the purgeflow air, described in Chapter 5) entering the column. For a purgeflow of ~ 7.2 scfm, the slowfill mode, or stage, is set to last 15 min (which brings the column to within a percent or so of atmospheric pressure, P_{atm}). The radon velocity array, during this stage, represents radon moving quickly as it enters the column (moving backwards, with negative velocity), but respecting the boundary condition at the back of the column ($x = \xi = 0$, where the valve to the pumps is closed), which demands that $v_{\text{Rn}}(0) = 0$ m/s. The pressure in the column $P(x, t)$ rises over the 15 minutes with the radon velocity similarly reducing until it approaches zero, as $P(x, t) \rightarrow P_{\text{atm}}$.

The first operator we will build will be a filtering operator (so, for example, velocity will be positive). For now, the velocity of radon and its diffusion coefficient throughout the column will be assumed constant. In python, the code (somewhat simplified) to build the operator looks like:

```

1 import numpy as np
2 dt = 300 # simulation time step [s]
```

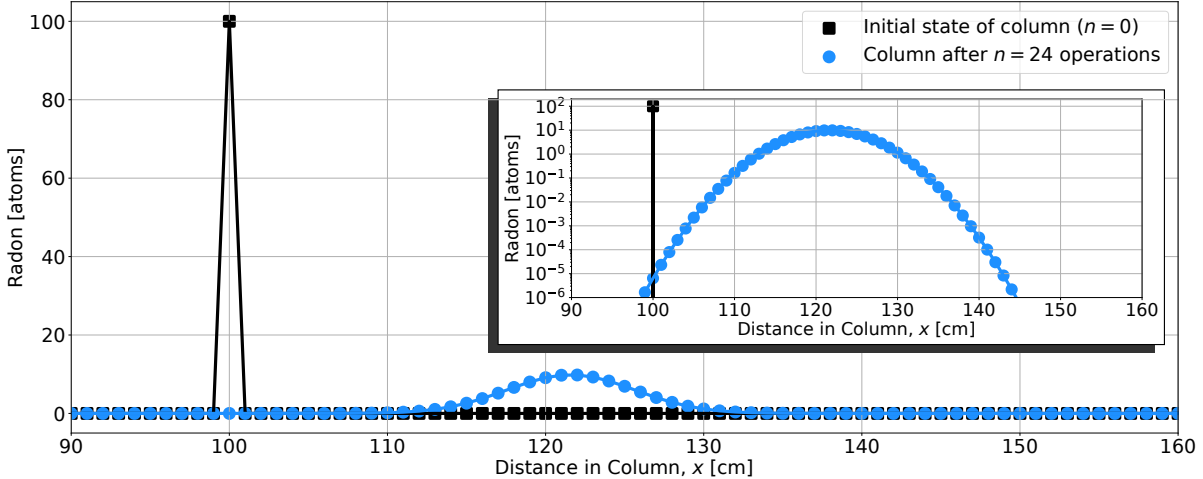


Figure 7.4: Radon atoms are initially (at $n = 0$ operations) at the location $x = 100$ cm (black squares). After operating $n = 24$ times, the radon atoms have translated to the right according to the radon velocity of 0.003 cm/s and have diffused according to the diffusion coefficient of 0.001 cm 2 /s (both defined by the python code that created the operator \mathbf{M}), resulting in the distribution of radon atoms at $n = 24$ operations (blue circles). The **inset** shows the same plot, but in semi-log space,

```

3  dx = 1      # spatial step size [cm]
4  L = 500     # length of carbon column (which sets the size of M) [units of
               # dx, cm]
5
6  # Preallocate the matrix M
7  M = np.zeros([L,L])
8
9  # Define radon velocity and diffusion coefficient arrays
10 v = np.zeros(L)+0.003 # [cm/s]
11 D = np.zeros(L)+0.001 # [cm^2/s]
12
13 # Build operator
14 for xi in range(0,L): # choose position in carbon column
15   for x in range(0,L): # build distribution over x
16     M[x, xi] = G(x, xi, v[xi], D[xi], dt, dx) # M[rows, cols]
```

Let us again denote the number of radon atoms in a carbon column, after n operations, to be the column vector $\mathbf{c}(n)$, which has elements located (indexed) at every integer $x \in [0, L]$. For this demonstration the initial number of radon atoms (at $n = 0$) in the column, represented as $\mathbf{c}(0)$, will be zero everywhere—except at $x = 100$, where we have placed 100 radon atoms. Next, we will operate until the radon atoms in the column have been evolved by $t = 120$ minutes. Each operation of \mathbf{M} on $\mathbf{c}(0)$ will evolve the column by one Δt , translating and diffusing atoms according to the elements of the

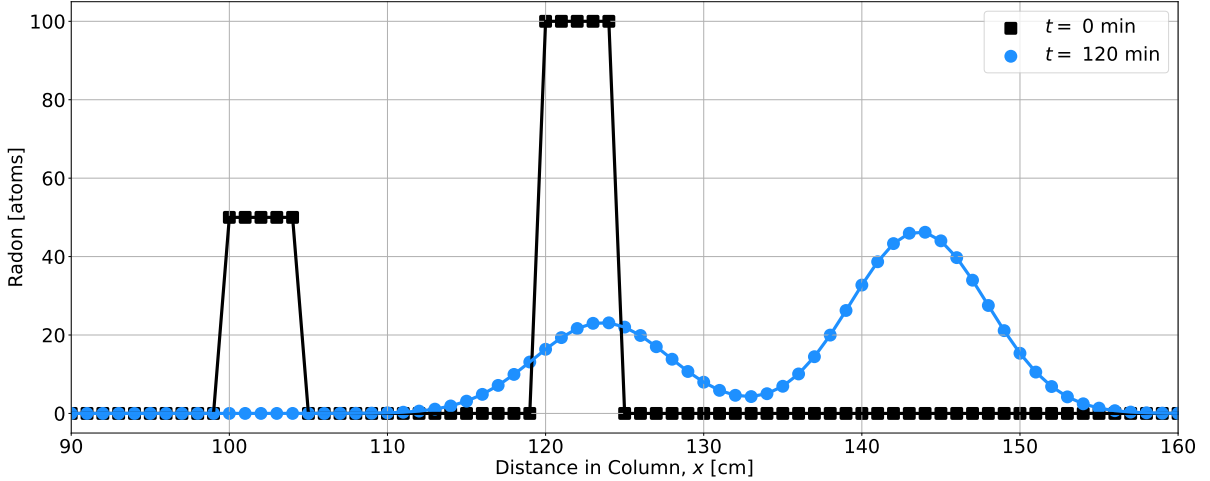


Figure 7.5: 50 radon atoms (at $n = 0$ operations) are placed at each location $x \in [100, \dots, 104]$, and 100 radon atoms (at $n = 0$ operations) are place at the locations $x \in [120, \dots, 124]$. After operating $n = 24$ times, the column is evolved by $t = n\Delta t = 24 \times 5 \text{ min} = 120 \text{ min}$, with radon atoms from both initial groups contributing to the distribution of radon throughout the column. Each bin of radon atoms $\in [100, 104]$ are evolved (by $n = 24$ operations) separately to produce five distributions of radon atoms; these distributions are represented by indigo-to-light orange lines, with color-matched triangles pointing to the bins of atoms, at $n = 0$, that were evolved; and these distributions, when summed, result in the total contribution of radon atoms from the bins $\in [100, 104]$ (thick, indigo line).

operator. Because the time step, Δt , was chosen to be 300 s (5 min), we must operate $n = t/\Delta t = 120/5 = 24$ times:

$$\mathbf{c}(24) = \mathbf{M}^{24} \cdot \mathbf{c}(0) \quad (7.17)$$

Figure 7.4 shows the result of these operations, with the inset showing the same plot, but with the vertical axis set to log scale. This illustrates how far the tails of diffused radon atoms extend, an important behavior to keep track of in order to defend against the possible unintentional loss of atoms (as will be discussed in Section 7.12).

Perhaps not only for fun, we consider the case where we have placed 50 radon atoms in $\mathbf{c}(0)$ at each $x \in [100, \dots, 104]$ and 100 radon atoms at each $x \in [120, \dots, 124]$. The result of the exact same operation on this column produces Fig. 7.5, where we may observe that radon atoms at different locations within the column, translating and diffusing, contribute to the radon atoms that are later (after $t = 120 \text{ min}$ or $n = 24$ operations) observed at each location in the column, as expected.

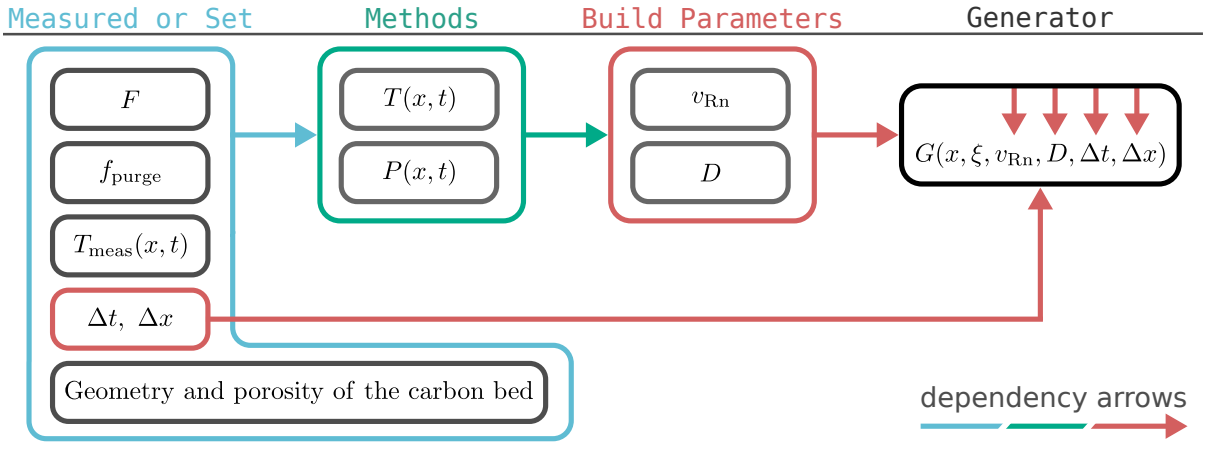


Figure 7.6: The dependencies of the operator’s build parameters are illustrated by this flow chart. Starting on the left, the **Measured or Set** column lists both measured quantities and configuration choices set by the user. The item labeled “Geometry and porosity of the carbon bed” refers to both the length L and diameter of the carbon bed, as well as the porosity of the bulk carbon granules, which modify the air speed passing through it (discussed in Section 4.3). These quantities, moving to the right, inform **Methods** that are used to modify the radon velocity and/or diffusion coefficient arrays. The **Build Parameters** include the results of these methods, along with the user-set configuration of the simulation time step Δt and spatial step size Δx . The **Generator** takes as inputs the build parameters (red arrows) and populates, over x , each column ξ of the operator being built.

In summary, each operator, no matter what mode it will be used for, is built according to five input, or build, parameters: (1) the length of the column L that will be operated on, (2) the time step Δt , (3) the spatial step size Δx , (4) the radon velocity v_{Rn} , and (5) the radon diffusion coefficient D . These last two parameters (v_{Rn} and D) are arrays with elements that may be different at each location $\xi \in \mathbf{x}$, where \mathbf{x} denotes the x space that spans the column. Figure 7.6 provides a somewhat simplified flow chart to help illustrate the dependencies of each of the operator’s build parameters. Further description and discussion of radon velocity and diffusion parameters are found in Section 7.6 and Section 7.7, while Section 7.8 and Section 7.9 treats temperature and pressure within the columns.

7.3.1 More on the Matrix Operator

Let us now examine the operator itself (refer to Fig. 7.7). This operator, simply denoted as \mathbf{M} , has been built with a size of $L = 100$ (so the dimension of \mathbf{M} is $L \times L$).

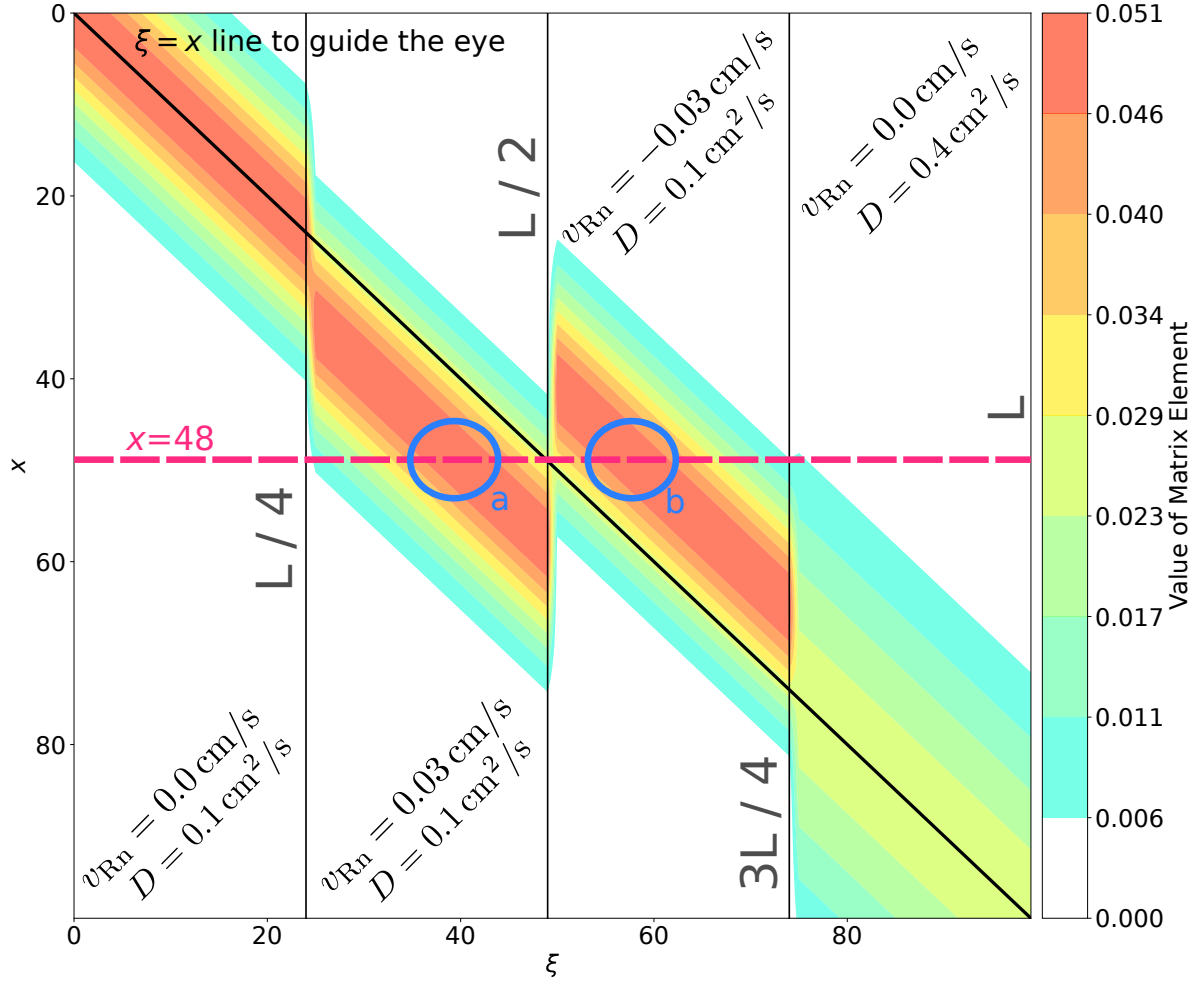


Figure 7.7: A heatmap of a matrix operator (see text for description).

To emphasize the key features, the velocity and diffusion coefficients have been chosen to be an order of magnitude or more larger than what would be typical of the SD Mines RRS. Furthermore, and easily the aspect most unrepresentative of a real system, the direction of the radon velocity has been chosen to change sign throughout the column: zero in the first region, positive in the second, negative in the third, and then again positive in the last. While impractical to achieve in real life, this choice of radon velocity makes for a strong example—and the simulation doesn't mind at all!

Shown as a heatmap by Fig. 7.7, the matrix operator illustrates several important qualities. Symmetry is observed about the $\xi = x$ when the radon velocity is zero: the gradient about this diagonal line is equivalent on either side; and, when the diffusion

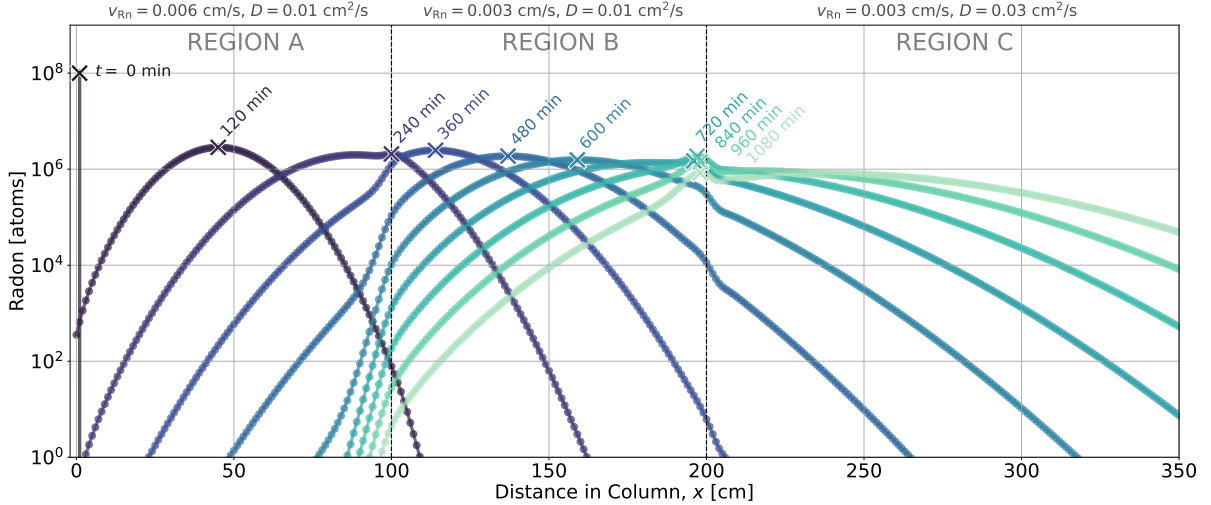


Figure 7.8: Radon atoms initially at $x = 1\text{ cm}$ within the column move quickly through the column in the high-velocity REGION A, as seen by following the \times 's that mark the maximum of each curve, and labeled by the time evolved ($t = n\Delta t$, with $\Delta t = 5\text{ min}$). In REGION B, the radon atoms move more slowly under the reduced velocity in this region. In REGION C, radon atoms continue to move with the same group speed as the previous region, but now spread out more per operation according to the $(3\times)$ larger diffusion coefficient.

coefficient tends to zero, the operator approaches the identity matrix. While the first $([0, L/4])$ and last $([3L/4, L])$ regions have a radon velocity of zero, the second $([L/4, L/2])$ and third $([L/2, 3L/4])$ regions have positive $(+0.03\text{ cm/s})$ and negative (-0.03 cm/s) velocities respectively. This would mean that radon atoms in those regions are both moving toward the center of the column. If we consider the row of \mathbf{M} at $x = 48$ (dashed, red line) we observe it passing through two “hot” spots as indicated by circles (blue) labeled **a** and **b**. This row, $\mathbf{M}_{48,\xi}$, tells us what fraction (the value of the matrix element) of radon at locations ξ in the column will contribute to the location $x = 48$ in the column. The number of atoms at this location $N(n + 1, a)$, after Δt , would be found by the dot product of the row with a column $\mathbf{c}(n)$ of radon atoms (of correct length): $\mathbf{M}_{48,\xi} \cdot \mathbf{c}(n) = N(n + 1, a)$. Unlike the first three regions, the last region $([3L/4, L])$ has a diffusion coefficient that is $4\times$ larger than the other regions. This can be seen by the far weaker gradient about the $\xi = x$ line.

Taking an example that is more subtle (but no less interesting), we consider a column that initially contains no radon, except at $x = 1\text{ cm}$, where we have placed 10^8 radon

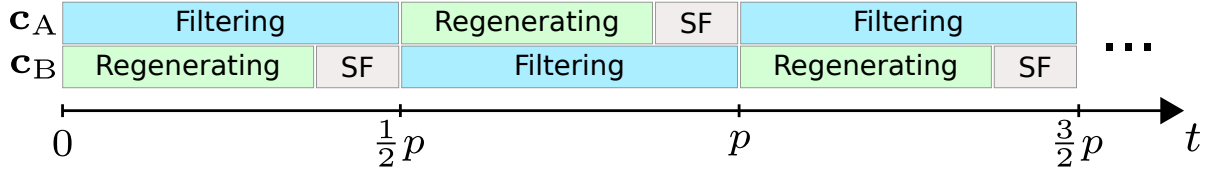


Figure 7.9: During swing operation, the RRS simulation cycles between filtering, regenerating, and slowfill (SF) in order to approximate the cycling, sometimes called swinging, (typically symmetric) behavior of the SD Mines RRS. Along the time axis, p denotes one full period.

atoms. The velocity and diffusion coefficient arrays have been made to depend on the location ξ within the column (referring to Fig. 7.8):

$$\text{REGION A: } v_{\text{Rn}}(\xi) = 0.006 \text{ cm/s and } D(\xi) = 0.01 \text{ cm}^2/\text{s } \forall \xi \in [0, 99]$$

$$\text{REGION B: } v_{\text{Rn}}(\xi) = 0.003 \text{ cm/s and } D(\xi) = 0.01 \text{ cm}^2/\text{s } \forall \xi \in [100, 199]$$

$$\text{REGION C: } v_{\text{Rn}}(\xi) = 0.003 \text{ cm/s and } D(\xi) = 0.03 \text{ cm}^2/\text{s } \forall \xi \in [200, 399]$$

In this example, radon atoms are observed to become slightly concentrated as they pass quickly through the first region, but must slow down in the second. Radon atoms then pass from region B to region C, where they are subject to increased diffusion; this results in an apparent drop in the number of atoms per bin as atoms diffuse to neighboring bins. Some of these neighboring bins are in region B, where atoms are again subject to the smaller amount of diffusion; as this asymmetric exchange of atoms, driven by diffusion, is repeated every operation, one may observe an apparent pile-up, so to speak, of radon atoms just before the boundary of regions B and C (around $x \sim 195$ cm).

7.4 RRS Simulation: Modes of Operation

This section describes ways of running the simulation to produce deliverables (usually the output radon concentration versus time) under conditions/configurations that closely represent those used with the SD Mines RRS. There are two categories of modes:

- **Swing operation:** This is the operational mode we use to provide low-radon air to the SD Mines cleanroom. It is frequently referred to as the “swing” mode, as it describes filtering through a column while the second column is regenerated.

According to a user-set cycle period p , each column (\mathbf{c}_A or \mathbf{c}_B) will spend some time t_F in the filtering stage, then t_R in the regenerating stage, and then t_S in the slowfill stage (with, typically, the relationship $t_F = t_R + t_S$), at which point the cycle repeats (as illustrated by Fig. 7.9).

- **Characterization:** This mode is used to learn something specific about the SD Mines RRS and/or the RRS Simulation. For example, this mode may refer to intentionally configuring the SD Mines RRS to perform very poorly in order to test the dependence on some parameter, which the simulation attempts to describe. The most common mode of this type is called a break-through curve (BTC) measurement, which is described in Section 7.4.1.

The following sections expand on both the swing mode and the break-through curve (BTC) mode, providing additional explanations and examples. The BTC mode is treated first, as it is simpler to describe and lays the foundation for describing the swing mode.

7.4.1 The Break-through Curve

Perhaps the most important characterization mode involves making a measurement we call a **break-through curve (BTC)** (sometimes called an elution curve in gas chromatography, *e.g.*, [94]). For our application, a BTC is performed by flowing high-radon air through a carbon column, that has very little radon initially in it, and measuring the radon activity of the air coming out the other end as a function of time (see Fig. 7.10). The radon adsorbs to the carbon and thus moves more slowly through the column than the air (*i.e.*, the carrier gas). The measured radon concentration versus time ideally has the form of a sigmoid or S-curve. The inflection point of this curve (where the second derivative changes sign) is defined as the break-through time t_b and the spread in the sigmoid relates to the diffusion coefficient D of radon spreading throughout the carbon per unit time.

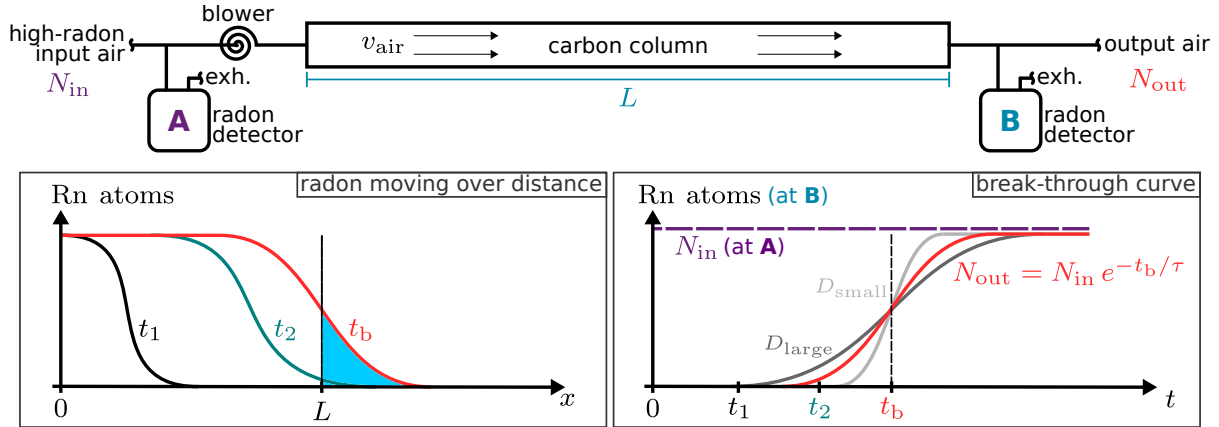


Figure 7.10: The top diagram provide a setup for measuring a break-through curve. Using an inline blower to provide the pressure gradient, high-radon air is passed through a carbon column (or bed) that is initially free of radon. Radon will adsorb to the carbon surface and take longer to move through the column than the air that carries it. Radon detectors at both the inlet and the outlet measure the amount of radon in the air stream. The lower left plot shows radon, in atoms, translating and diffusing through a column of length L , with snapshots at three different times: at t_1 (black line), essentially no radon has exited the column; at t_2 (teal line), just the tail of the radon distribution has exited; and at t_b (red line), the break-through time, the number of radon atoms exiting the column is half of the number entering the column. The blue shaded region indicates radon that has exited the column. The lower right plot shows the number of radon atoms entering the column is N_{in} (purple dashed line) while the number exiting is N_{out} (red solid line, and modified by radon decay). The break-through time t_b passes through the inflection point of the curve that shows the measured radon concentration at the output as a function of time. The light and dark gray curves represent smaller (D_{small}) and larger (D_{large}) values for diffusion compared to the red curve.

The break-through curve measurement provides the numerical value of two important (even sufficient, for our applications) characteristics of radon moving and diffusing through the carbon bed. The aforementioned break-through time t_b describes how fast radon is moving through the column (*i.e.*, its group velocity) according to:

$$v_{\text{Rn}} = L/t_b, \quad (7.18)$$

where the column has length L , and holds for a constant radon velocity over both space and time (with the simulation being much more accommodating on this point). The diffusion coefficient comes directly from the spread in the BTC; that is, the BTC is the cumulative distribution function of the Gaussian distribution, and therefore the diffusion coefficient relates to the standard deviation:

$$\sigma_t = \sigma_x/v_{\text{Rn}} = \sqrt{2Dt}/v_{\text{Rn}}, \quad (7.19)$$

where the standard deviation of radon spreading over space and time are denoted with the subscripts x and t .

If the number of radon atoms entering the column per unit time is constant, one may fit a measured BTC to an analytic form of a sigmoid to infer the break-through time and diffusion coefficient:

$$N(t) = \frac{N(\infty)}{2} \left[1 - \operatorname{erf} \left(\frac{v_{\text{Rn}} (t_b - t)}{\sqrt{4Dt}} \right) \right] + N(0), \quad (7.20)$$

where $N(t)$ is the number of radon atoms measured exiting the column, $N(\infty)$ is the number of radon atoms exiting the column as $t \rightarrow \infty$ (or, at least, $t \gg t_b$) and $N(0)$ is the number of radon atoms that were exiting the column at time $t = 0$. The radon velocity is assumed constant throughout the column of length L , and is therefore defined as $v_{\text{Rn}} = L/t_b$. Because radon decays, $N(\infty) = N_{\text{in}} \exp(-t/\tau_{\text{Rn}})$, where N_{in} is the number of radon atoms entering the column (assumed constant in time) and $\tau_{\text{Rn}} = 5.52$ days and is radon's mean lifetime. Equation 7.20 can be slightly improved by substituting in the standard deviation σ_t defined by Eq. 7.19:

$$N(t) = \frac{N(\infty)}{2} \left[1 - \operatorname{erf} \left(\frac{t_b - t}{\sigma_t} \right) \right] + N(0). \quad (7.21)$$

In practice, we tend to measure the radon concentration (in decays per second per cubic meter, Bq/m^3) not the number of radon atoms, as a radon concentration is independent of the sampling time and flow rate of the detector employed. The simulation, however, treats only radon atoms—that is, until a deliverable, such as a BTC, is provided, which will be given units of radon concentration, which are easily compared with in-lab measurements.

Coming back to our example, an ideal BTC measurement (*i.e.*, having a constant input rate of radon atoms and a uniform velocity and diffusion coefficient over both the length of the column and time) is illustrated by Fig. 7.11. For this example, both the data and fit are based upon Eq. 7.20, but with its units converted from atoms to radon concentration (Bq/m^3).

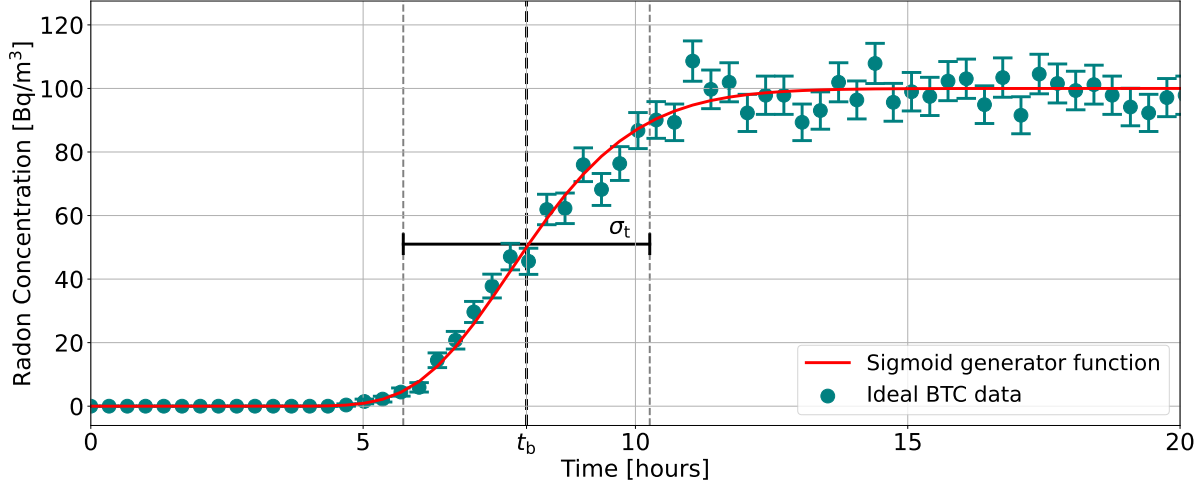


Figure 7.11: An idealized break-through curve (BTC) has been randomly generated (teal circles) about the function labeled “Sigmoid function” (solid red curve). The error bars are also fabricated, but based upon Poisson statistics and a reasonable collection efficiency. For this example, Eq. 7.20 has been converted to units of Bq/m^3 and given the arguments: $D = 0.01 \text{ cm}^2/\text{s}$, $v_{\text{Rn}} \approx 0.0042 \text{ cm/s}$, with $L = 120 \text{ cm}$ and $t_b = 8 \text{ hours}$ (thick dashed line). The standard deviation from Eq. 7.19 is also shown (black, horizontal line), with $\sigma_t = 2.27 \text{ hours}$

More often is the case, however, that the input radon concentration *does* depend on time. For the SD Mines RRS, the input air has the radon concentration of the local lab space, which tends to be around $80 \text{ Bq}/\text{m}^3$ and can easily fluctuate by 50% or more within several hours. In this real-life case, a simple sigmoid fit won’t capture the changing input concentration (let alone changes in the radon speed due to changes in air temperature, for example). Although it is not practical to modify the analytic form of the BTC to correctly model such a non-ideal BTC measurement, the simulation can easily produce BTCs given a time-dependent input radon concentration (and/or time dependence of temperature or other parameters). All of the important characterizing parameters can then be optimized in order to reach agreement between simulation and measurement.

A BTC can be simulated by repeating several lines of logic. Starting with a column (an array) \mathbf{c}_0 that *may* be considered to contain no radon atoms, the first line applies the filtering operator \mathbf{F} :

$$\mathbf{c} \equiv \mathbf{F} \cdot \mathbf{c}_0, \quad (7.22)$$

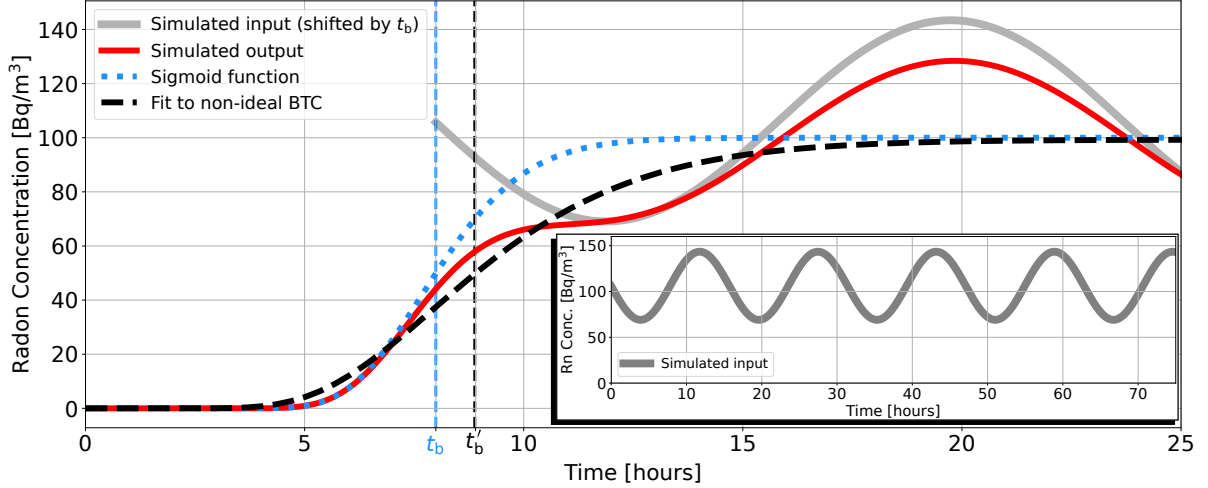


Figure 7.12: A simulated break-through curve (BTC) (solid red line) is produced for an (realistic!) oscillating input radon concentration (solid gray line, **inset**), with this input (solid gray line) in main plot shifted by the true break-through time t_b (thin blue dashed line) so its influence on the BTC can be seen. All parameters except the input radon concentration are the same as in the example shown in Fig. 7.11; the simulation was performed with $D = 0.01 \text{ cm}^2/\text{s}$, $v_{\text{Rn}} \approx 0.0042 \text{ cm/s}$, $L = 120 \text{ cm}$, and $t_b = 8 \text{ hours}$ (blue dotted line). Fitting a sigmoid function to the non-ideal BTC results in a best-fit curve (thick dashed line) with best-fit break-through time $t'_b = 8.89 \pm 0.17 \text{ hours}$ and diffusion coefficient $D' = 0.025 \pm 0.004 \text{ cm}^2/\text{s}$; while t_b is different than actual by only $\sim 10\%$, D is off by $\sim 250\%$. This emphasizes that a taking proper account of any time-variation in the input concentration (*e.g.*, via its simulation) is important to obtain a good estimation of t_b and especially σ_t (*i.e.*, D).

where \mathbf{c} is the evolved state of \mathbf{c}_0 . Next, any radon atoms that have passed completely through the physical column (having a length of L) during this operation are counted:

$$N_{\text{exited}} = \sum_{x=L}^{x_{\text{end}}} \mathbf{c}[x], \quad (7.23)$$

where I have denoted x_{end} to be the end of the padded region (a region that extends beyond L for radon atoms to pass into and not be lost; this is further described in Section 7.12) after the physical column region. Here, I'm using square brackets to denote index selection of an element of \mathbf{c} . The atoms N_{exited} are recorded for every Δt . *Plotting N_{exited} versus time is the simulated break-through curve.*

Returning to the lines of logic, now that all radon atoms in the padded region have been counted, all atoms in the region are removed to avoid double counting:

$$\mathbf{c}[x > L] \equiv 0, \quad (7.24)$$

where all elements at $x > L$ are set to zero. The next Δt of radon atoms, denoted as N_{in} , are injected into the $x = 0$ element of \mathbf{c} :

$$\mathbf{c}[0] \equiv N_{\text{in}}. \quad (7.25)$$

Finally, we redefine \mathbf{c} as \mathbf{c}_0 , and return to Eq. 7.22, where each line is repeated for the next Δt until the desired break-through curve simulation time is reached (after some $n\Delta t$). In python, this looks like:

```

1 def performBTC(op, Num_dt_ToEvolve):
2     """
3         Inputs: the operator (op) to be used to evolve C for Num_dt_ToEvolve
4         Returns:
5
6             (1) list of arrays that represent the number of radon atoms
7                 in column at each operation n,
8             (2) array of number of atoms that have exited the column
9                 at each dt.
10
11    Notice: hConfig and hPrep are imported (as cfg and hp) and used as
12                inputs,
13    though they are not explicit inputs (or arguments) of this method.
14
15    # import configuration dictionaries cfg and hp
16    cfg, hp = reload_config()
17
18    C = np.ones(hp.Lext)*hp.initialRnAtoms # radon atoms in column at t =
19                                0
20    matrixC = [] # empty list to contain columns states for each dt
21    atomsExited = [] # place to store all atoms exiting column each dt
22
23    # repeat operations until Num_dt_ToEvolve is reached
24    for n in range(0,Num_dt_ToEvolve):
25
26        # get the next operator index (used for multiple operators)
27        op_index = getOpIndex(n, op, cfg, hp)
28
29        # evolve column and add radon atoms from emanation
30        C = evolveColumn(C, op[op_index], cfg, hp)
31
32        # append column state for each dt
33        matrixC.append(C)
34
35        # add up all atoms that exit column
36        atomsExited.append(sum(C[cfg.Lpad+hp.L+1:])))
37
38        # remove counted atoms
39        C[cfg.Lpad+hp.L+1:] = 0

```

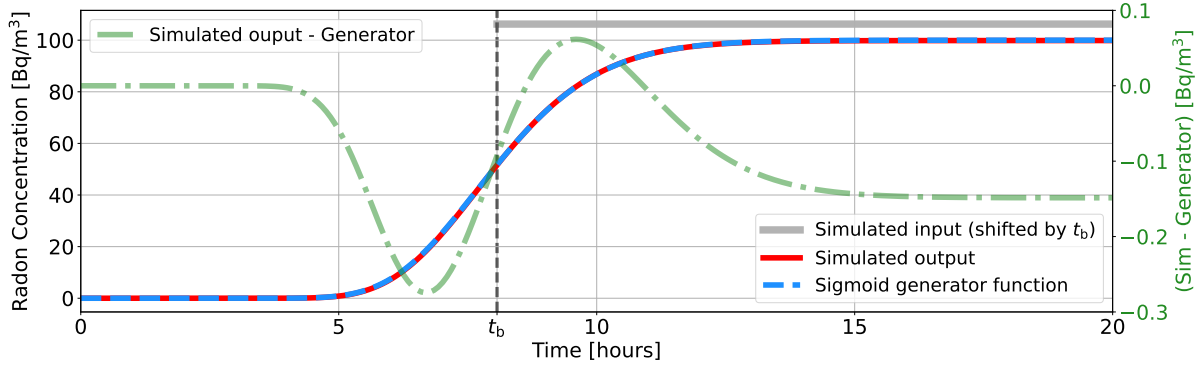


Figure 7.13: Building upon the example resulting in Fig. 7.11, a constant input radon concentration is passed to the RRS simulation producing a simulated BTC (solid red line). With all parameters matched, the simulated BTC is compared to the ideal BTC given by Eq. 7.20 (blue, dashed line). The difference between the simulated and ideal BTCs (green, dot-dashed line) shows only small disagreement, suggesting that the simulation is doing a good job of meeting expectations.

```

40     # add radon from next time step
41     C = injectRadonIntoColumn(n, C, hp.inputRnAtoms_per_dt, hp.Ls, op
42                               [op_index], cfg, hp)
43
44     atomsExited = np.array(atomsExited) # make atomsExited an array
45
46     return matrixC, atomsExited

```

The return `atomsExited` contains elements that are the sum of all radon atoms exiting the column at each Δt . Plotting this array versus time $[0, \Delta t, \dots, (n - 1)\Delta t]$ will produce the simulated BTC. Figure 7.12 shows such a simulated BTC with a custom input radon concentration that, for this demonstration, oscillates in time. For more discussion of BTC measurements and their comparison simulation, see Section 7.13.1.

Figure 7.13 shows that the simulation reproduces the ideal BTC predicted by Eq. 7.20 when fed a constant input radon concentration, as well matching all other parameters used in creating the BTC in Fig. 7.11.

7.4.2 The “Swing” Mode

Perhaps the mode of greatest interest is the **swing mode**. This mode represents the standard operation of the RRS used to produce low-radon air. One column is used to filter radon from the input air while the other is regenerated. Before radon breaks through

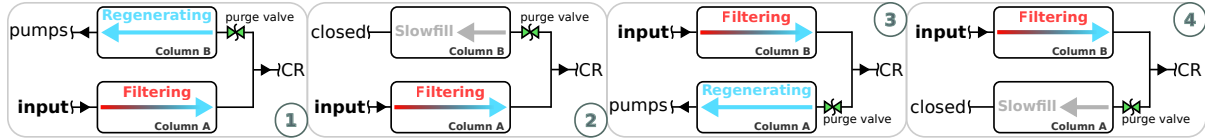


Figure 7.14: One full period of swing mode can be represented by four states (with labels found in the lower and upper right corners): ① column A is in the filtering mode while column B regenerates, ② column A continues filtering while column B slowfills, ③ after one half period the system “swings” and column B begins filtering while column A regenerates, ④ column B continues filtering while column A slowfills, and then the system swings back to ① having completed a full period.

the filtering column, the system “swings” such that the newly regenerated column is used for filtering, and the other column is regenerated (see Fig. 7.14, similar to Fig. 7.9).

An important distinction between the swing mode and the BTC mode is that the swing mode includes regeneration. While one can make a direct measurement of the speed and diffusion of radon passing through a column during a BTC measurement (*i.e.*, during the filtering stage), such a measurement has not been practical for the regeneration stage due to the low pressure. During swing mode, each stage (filtering, regeneration, and slowfill) influences the amount of radon exiting the system. As discussed in Section 7.13, which covers simulation parameter determination, simulation design has involved characterizing radon movement through a column during the filtering mode (a BTC) mathematically and then modifying this description to account for the pressure and temperature during the other modes. The result is tested by comparing simulation to measured regeneration curves (henceforth denoted as RCs) that are produced by running the SD Mines RRS in swing mode.

Unlike the treatment of break-through curves, here, because there are so many steps, the important lines of logic are captured by a sentence or two, with the details found in the only-slightly-simplified python code that follows. In describing swing mode, the two carbon columns will be referred to as column A and column B. Referring to block (1) of Fig. 7.14, the following lines of logic are performed for a single Δt :

Column A filters while column B regenerates:

1. Column A is evolved (operated on) by the filtering operator.
2. Any atoms that pass completely through column A are counted (and recorded). Those that have been counted are then removed to avoid double counting.
3. According to the purge flow, a fraction of the atoms that passed completely through column A are injected¹ into column B (which is being regenerated). The rest are considered to have passed to the cleanroom.
4. Column B is evolved by the regenerating operator.
5. Any atoms that pass completely through column B (moving with negative velocity during regeneration) are counted (and recorded). These atoms represent those exhausted out of the vacuum pumps, and, after being counted, are then removed to avoid double counting.
6. Atoms are then injected² into column A.

This logic block, I will call it, is repeated n times until $n\Delta t$ reaches the user-set regeneration time, which is nominally 45 min for the SD Mines RRS. After this regeneration time, we may refer to block (2) of Fig. 7.14:

Column A filters while column B slowfills:

1. Column A is evolved by the filtering operator.
2. Any atoms that pass completely through column A are counted (and recorded). Those that have been counted are then removed to avoid double counting.

¹The tail of the distribution of radon atoms leaving column A is mirrored (flipped about the space axis), scaled according to the fraction of air passing into column B, and added to the back (purge side) of column B.

²Radon atoms that enter the filtering column per Δt are introduced as a distribution created by placing all of these new radon atoms in the first bin of an empty array (a dummy column) and then evolving them according to the filtering operator. The resulting distribution is then added to the filtering column. This form of injection is imperfect but makes no significant difference.

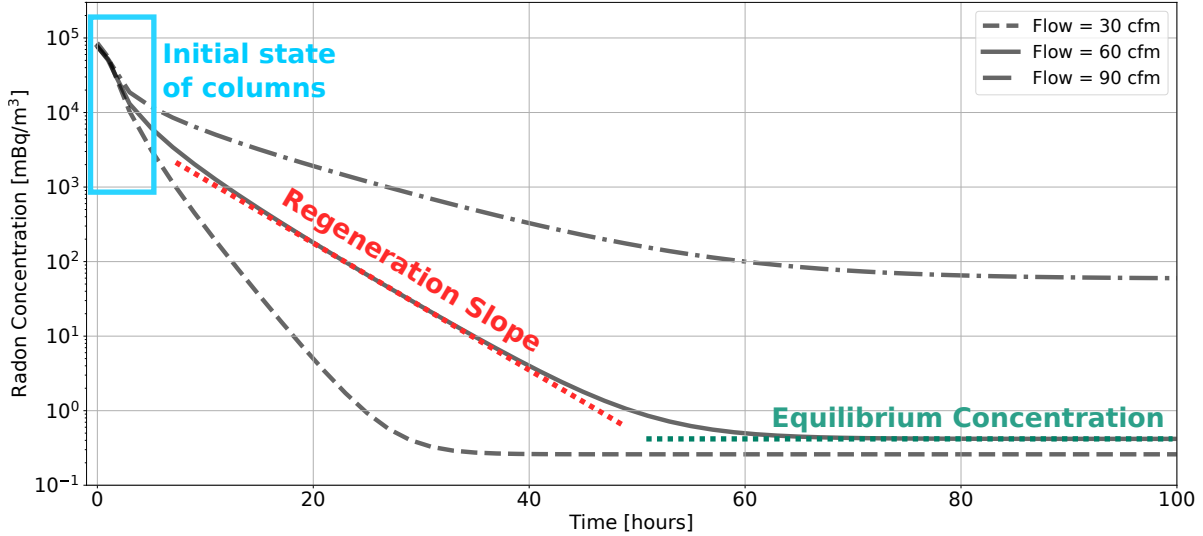


Figure 7.15: Three regeneration curves were created with input air flow set to 30, 60, and 90 cfm (dashed, solid, and dot-dashed respectively), but with all other configurations unchanged. Two important features can be seen by any one of these curves: (1) the middle region of the curve shows a so-called **regeneration slope** that is determined by relative amounts of radon passing into the filtering column and being purged from the regenerating column, and (2) after a steady state is achieved, the same amount of radon exits the filtering column each cycle period, resulting in an observed **equilibrium concentration**. The very first part of a curve is determined by the **initial state of the columns** (*i.e.*, how much radon is in the columns at the beginning of the swing mode).

3. According to the purge flow, a fraction of the atoms that passed completely through column A are injected¹ into column B (which is being slowfilled). The rest are considered to have passed to the cleanroom.
4. Column B is evolved by the slowfill operator. Atoms pass into the column, but never exit the other side (as we have closed the imaginary valve leading to the pumps).
5. Atoms are then injected² into column A.

This logic block is repeated n times until $n\Delta t$ reaches the user-set slowfill time, which is nominally 15 min. The total time filtering though a column is the regeneration time + the slowfill time, which, here, would be 60 min. For the second half of the swing period (blocks ③ and ④), columns A and B are switched, but with all other logic preserved.

Figure 7.15 shows examples of simulated regeneration curves (RCs), with each curve generated in the same way—except the input air flow was set to 30, 60, and then 90 cfm.

From each of these curves (and similar ones with different parameters), there are three typical features (with bold text referencing labels in Fig. 7.15):

1. The early-time region of a RC is influenced by the **initial state of the columns**.

During the very first cycle, high-radon air is supplied to the filtering column, and the amount of radon already in the column will determine how much radon will exit the column in the first minutes and, until a steady-state is reached, over many hours. For these three curves, the initial state was made to be the same, and so no difference can be seen.

2. After the early-time region, the radon exiting the filtering column is determined by

the relative amount of radon moving (according to its mean velocity and also from diffusion) through the filtering column as compared to the amount of radon that is purged from the regenerating column. This behavior, which could be described as a kind of “gain”, results in the output radon concentration being reduced by a similar fractional amount each full period. With the y-axis in log scale, the RC has what is henceforth called the **regeneration slope**.

3. In order for the output radon concentration to be reduced (the whole point of the RRS), more radon must be removed during regeneration than is added during filtering.

Because the carbon emanates radon and some non-zero fraction of the tail of the distribution of radon (spread out within the column) exits the column each filtering cycle (of, say, 60 min), the radon reduction per cycle equilibrates; that is, the radon added and removed from a column per cycle approaches a constant; consequently, the radon exiting the column per cycle becomes constant. This results in a **equilibrium concentration** after some number of swings (full periods), determined by the system’s configuration.

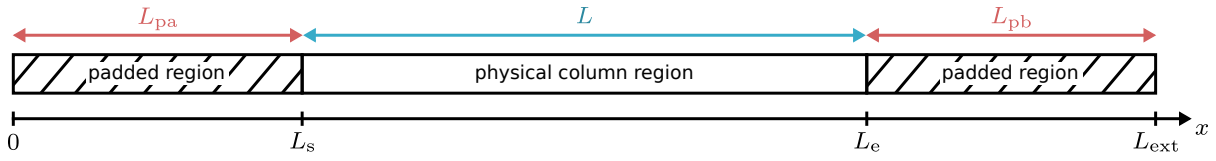


Figure 7.16: The column (or array) \mathbf{c} used by the simulation stores the estimated number of radon atoms after some number of operations n . This diagram shows padded regions before and after a physical column region. Along the x axis the beginning of the physical column starts at L_s and ends at L_e . The padded region before the physical column region has a length of L_{pa} , while the padded region after the physical region has a length L_{pb} . The total space has a length of $L_{\text{ext}} = L_{\text{pa}} + L + L_{\text{pb}}$.

7.5 Padded Columns

The RRS simulation attempts to describe the number of radon atoms at each location within each of two arrays. Each array, denoted as \mathbf{c} , must at least represent what is called the “physical column region”—the region that represents one carbon column from the SD Mines RRS. For practical reasons (that will be discussed shortly), this array is extended (made longer) by an additional padded region L_{pa} before and L_{pb} after the physical column region, so the length of the extended column $L_{\text{ext}} \equiv L + L_{\text{pa}} + L_{\text{pb}}$ (diagram shown by Fig. 7.16).

The purpose of the padded regions is to improve estimates of radon atoms in the physical region, as well as to provide a space for radon atoms to pass into before they are counted; therefore, we frequently benefit in showing plots that ignore these padded regions, and may refer to them only when it is useful. That is, the axis label “Distance in Column, x [cm]” will nearly always mean $x \rightarrow x - L_s$; and then, plotting from $x = 0$ to $x = L$ shows only the physical column region, and hides the padded regions.

Placing aside the practical advantage of using the padded regions as a place to temporarily store radon atoms, there is a more fundamental reason for having them: the padded regions provide a means to account for (keep track of) every radon atom; because no atoms are lost by leaving a column through, for example, the pumps, may not pose any concern; these atoms may be destroyed (lost as we say) and the number of

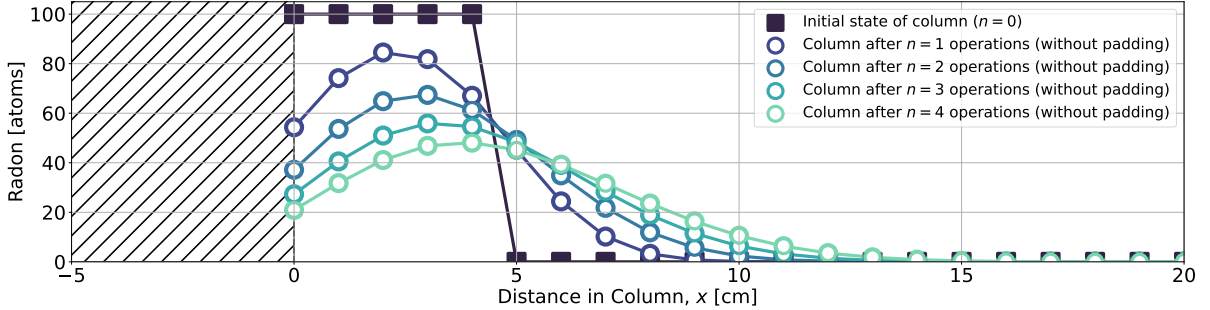


Figure 7.17: The initial ($n = 0$) distribution of radon atoms is shown as black squares, with the distance x defined such that $x = 0$ indicates the input-side boundary of the physical column. After each operation, the resulting distribution is plotted as open circles (with color ranging from dark to light as n increases). The hatched region (for $x < 0$) emphasizes that *padding is not present* in this example. In this example, the simulation was configured with $v_{Rn} = 0.001 \text{ cm/s}$, $D = 0.005 \text{ cm}^2/\text{s}$, and the time step $\Delta t = 5 \text{ min}$.

radon atoms that pass to the cleanroom (the atoms we care about!) remain unchanged.

The issue with a simulation that leaks atoms is that one must ensure that all atoms lost were alright to have been lost; therefore, one is burdened with the likely impossible task of proving non-existence. Alternatively, we choose to keep track of every radon atom. Those that enter the system (*i.e.*, the columns) do so at the time and in the amount that we intend, and those that exit the system also do so exactly as we intend, with some exhausted through the pumps, others being counted as entering the cleanroom, and still others being destroyed through radioactive decay.

To illustrate (and further motivate) a padded region that extends the array \mathbf{c} before the physical column by the length L_{pa} , we consider an example: let us denote the number of radon atoms in the column, after n operations, to be $\mathbf{c}(n)$. Each location x corresponds to an index i of \mathbf{c} (that is, we have chosen $\Delta x = 1 \text{ cm}$ so that $x = i\Delta x$). At $t = 0$ (and thus $n = t/\Delta t = 0$), 100 radon atoms are placed at each $x \in [0, 4]$, but none anywhere else. For this example, there is *no* padding before the physical column region. As shown by Fig. 7.17, the column is evolved (acted on) by the filtering operator (with $v_{Rn} = 0.001 \text{ cm/s}$ and $D = 0.005 \text{ cm}^2/\text{s}$, both constant in x and n) 4 times, with the resulting distribution plotted after each operation.

After the first operation ($n = 1$) shown in Fig. 7.17, atoms from every location in the $n = 0$ column (that is, $\mathbf{c}(0)$) are evolved correctly (padding or no padding). Upon the second operation ($n = 2$), atoms in $\mathbf{c}(1)$ that *would* have been at the location of, say, $x = -3$, where there is currently no padding, *could* have contributed to atoms at, say, $x = 2$. However, any radon atoms that had moved to locations $x < 0$ have been destroyed. This loss of radon atoms is revealed in two ways:

1. Adding up all of the atoms in the entire column (with radon decay turned OFF) yields: 500, 445, 411, 386, 368 atoms for $n = 0, 1, 2, 3, 4$. This unintentional loss of atoms could, potentially, seriously compromise the predictive power of the simulation and should thus be avoided. A more detailed treatment and discussion of atom counting is found in Section 7.12.
2. Less quantitatively (but possibly more intuitively), we compare the evolved distributions with and without the padded region, as shown by Fig. 7.18. For $n > 1$, a loss in atoms is seen (as a gap or drop between curves with equal n), primarily near the column boundary (at $x = 0$). This drop is due to radon atoms moving outside the column (when no padding is present) and, being lost, are unable to move back to the physical column region upon further operations.

While edge effects are likely to always require approximations, such removal (*i.e.*, loss) may correspond to reality only if a pump is at this end of the column; for most cases, the atoms would be able to move back later. Furthermore, a system that provides accurate counting of atoms allows testing that the approximations are sufficiently accurate.

As was alluded to previously, the padded region is also used as an overflow region. During filtering, any atoms that make it all the way through the column contribute to the output radon concentration supplied to the cleanroom. Therefore, the padded region of length L_{pb} after the physical column must be sufficiently long such that, for a single Δt , all non-zero bins are contained. The reason we require this be true for *only one* Δt is

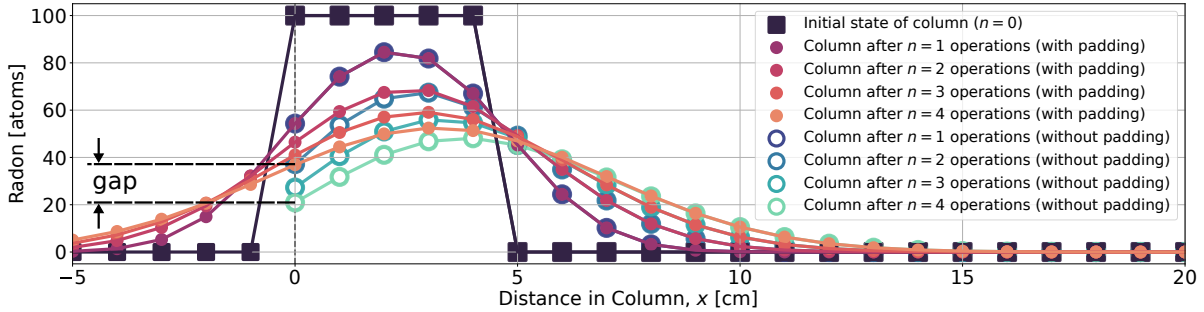


Figure 7.18: The initial distribution of radon atoms $\mathbf{c}(0)$ is subject to $n = 0, 1, 2, 3, 4$ operations, with resulting distributions plotted as circles (with color ranging from dark to light as n increases). The filled circles represent the case where the physical column has a padded region directly before it ($x < 0$), while the open circles represent the case where there is no padding. A **gap** is indicated between the $n = 4$ curves at the first spatial bin. Disagreement between curves with and without padding (but with the same n) becomes increasingly small for x increasingly far from the physical column boundary (at $x = 0$), as the expected contribution of radon atoms from $x < 0$ becomes smaller.

because the radon atoms in the padded regions are either: (1) put back into the physical column region, such that the padded region need not grow in size to continue to perform its duty, or (2) counted, recorded (as, for example, in a list or array named N_{exited}), and then deleted (such that they are not counted twice). This last point makes sense from a practical standpoint, as the narrow plumbing after a column makes back-diffusion of radon atoms negligible (see section Section 6.2).

The break-through curve (BTC) example discussed in Section 7.4.1 (on page 187) provides a clear demonstration of using a padded region after the physical column region. Figure 7.10 shows a simplified BTC setup and provides cartoons of BTCs, at different times, in x ; the shaded blue region under the t_b curve shows how a padded region after the physical column would fill with radon atoms, be counted, recorded, and cleared, all without influencing the shape of the distribution (due to being near a boundary).

7.6 The Radon Velocity Within a Column

The performance of the radon reduction system is essentially determined by how quickly radon atoms move through a carbon column during filtering, regeneration, and, perhaps less so, the slow-fill mode. Though diffusion plays an important role in the

movement of atoms (and will be treated in Section 7.7), here we describe the linear velocity of radon atoms as a function of temperature and pressure (parameters that change during different operation modes, as described in Section 7.8 and Section 7.9 respectively).

The superficial velocity, u_s , of air moving through an empty column with cross-sectional area πR^2 is

$$u_s = \frac{F}{\pi R^2}, \quad (7.26)$$

where F is the volumetric flow through the column. By measuring the RRS output air flow, F_{out} , with an inline, hot-wire anemometer (**Omega**, model: HHF1001R) and the purge air flow, f_{purge} , from an inline, vertically mounted flow meter (King Instrument Company, S/N: 32530112001, 1-8 scfm), the through-column air flow is determined as:

$$F = f_{\text{purge}} + F_{\text{out}}. \quad (7.27)$$

Because the RRS columns contain a large (packed) bed of activated carbon, the speed of air is different than if the columns were empty. As described in Section 4.3, the velocity through a packed column can be, for our system (having a particularly low pressure drop across the carbon bed, resulting in insignificant gas compression), expressed as the superficial velocity modified by the porosity of the carbon:

$$v_{\text{STP}} = \frac{u_s}{\epsilon_T} = \frac{1}{\epsilon_T} \frac{F}{\pi R^2}, \quad (7.28)$$

where ϵ_T is the *total porosity* and is the sum of the interparticle (between carbon granules) and intraparticle (within granules, *i.e.*, pores) volume fractions of the carbon, as defined in Section 4.3. For the SD Mines RRS carbon, $\epsilon_T \approx 0.8$.

Continuity demands that the mass (in this case, of the air) is conserved. Therefore, the velocity of air passing through a column changes according to the pressure in the column such that the volume (at STP) per unit time, passing through the column, is

conserved. That is, the velocity within a column at some pressure P would be

$$v_{\text{air}}(P) = \frac{1}{\epsilon_T} \frac{F}{\pi R^2} \frac{P_{\text{atm}}}{P}, \quad (7.29)$$

where P_{atm} is atmospheric pressure and $v_{\text{air}}(P)$ is shown explicitly as a function of pressure, though we will frequently just write v_{air} . The pressure P during filtering is within a couple Torr of P_{atm} , and so the ratio P_{atm}/P is close to unity. During regeneration and the beginning of slowfill, however, the pressure $P \sim 20$ Torr $\ll P_{\text{atm}}$ with a pressure gradient along the longitudinal axis of the column, as described in Section 7.9. This variation motivates expressing v_{Rn} as an array spanning \mathbf{x} , for each time t , according to the pressure gradient $P(x, t)$.

During regeneration, the pressure gradient is constant (due to the constant pumping speed and purgeflow set point), so the pressure depends only on x : $P = P(x)$. During slowfill, the pressure in the column starts in the same state as regeneration, but then the pump is closed off, which results in the pressure profile relaxing and raising to atmospheric pressure (P_{atm}). Therefore, during slowfill, the time dependence of the pressure profile $P(x, t)$ cannot be ignored. The velocity of air v_{purge} during regeneration and slowfill has the form

$$v_{\text{purge}} = \frac{1}{\epsilon_T} \frac{f_{\text{purge}}}{\pi R^2} \frac{P_{\text{atm}}}{P(x, t)}, \quad (7.30)$$

where F has been substituted by f_{purge} , the volumetric air flow passing to the regenerating or slowfill column, and, for regeneration, time-dependence can be ignored.

According to work conducted by Strong and Levins [102] and, later, by Aksel Hallin [110], the velocity of radon atoms moving through a carbon bed depends on temperature with the form:

$$v_{\text{Rn}} = v_{\text{air}} f_A e^{-T_{\circ}/T}, \quad (7.31)$$

where f_A is a fitting parameter specific to the material (the absorbent), and goes inversely with the absorbent's surface area; $T_{\circ} = 3500$ K and is the critical temperature

of adsorption of radon to activated carbon (with discussion on its uncertainties given in Section 7.13.3); and T is the column temperature in Kelvin. The exponential term $e^{-T_0/T}$ is related to the time a radon atom spends on the surface of the adsorbent, which reduces with increasing temperature (as discussed in Section 4.1). The RRS simulation passes the temperature T to v_{Rn} , and finally to the operator, as an array that can depend on both space and time; that is, $T \rightarrow T(x, t)$ (and is described in Section 7.8).

The radon velocity during each of the three modes are denoted as v_F , v_R , and v_S for filtering, regeneration, and the slowfill mode respectively:

$$v_F = v_{air} f_A e^{-T_0/T_F} \quad (7.32)$$

$$v_R = v_{purge} f_A e^{-T_0/T_R} \quad (7.33)$$

$$v_S = v_{purge}(t) f_A e^{-T_0/T_S}, \quad (7.34)$$

where $v_{purge}(t)$ has been made a function of time to emphasize that $v_{purge} \rightarrow 0$ as the slowfill column approaches atmospheric pressure. Temperature during each stage is denoted by the same subscript (F, R, or S) and can be a function of both space and time. The value of f_A is expected to be a constant within our domain of application, but dependence on pressure, temperature, or air speed (as explored in Section 7.13.3) could exist.

In principle, v_{Rn} may also depend on relative humidity, but we have not yet observed clear evidence that suggests it is significant, outside of modifying temperature through phase transitions and adsorption/desorption on the carbon surface (see Section 7.8). According to Strong and Levins [102], the adsorption factor f_A increased by just over a factor of three when the relative humidity was increased from 0 to 100% (in their work, they used the dynamic adsorption coefficient $k_a \propto 1/f_A$). The authors go on to say that once the bed is completely saturated (by air with 100% relative humidity), the column is no longer practical to use in slowing the speed of radon passing through it.

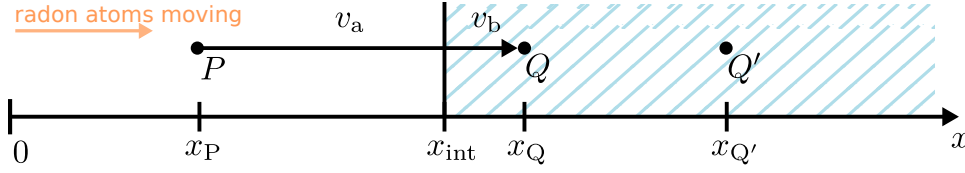


Figure 7.19: A radon atom starts at position P . Between $x = 0$ and $x = x_{\text{int}}$, the radon velocity is v_0 . After x_{int} , in the hatched region, the radon velocity is $v_b < v_a$. The radon atom will stop after Δt at position Q' , according to Eq. 7.35. If, however, a time-averaged velocity is used, the atom will stop at the position Q , as it should.

7.6.1 An Optional Correction: The Time-averaged Velocity

Though we may state with confidence the radon velocity within the carbon column, there are still corrections that *can be important* when the radon velocity varies abruptly, as compared with Δx and Δt . Let us refer to Fig. 7.19 where the initial position of the radon atom is at the location P and will be given the velocity v_0 . For example, let's say that after evolving the atom's position by Δt , the new position of the atom is

$$x = x_P + v_a \Delta t = x_{Q'}. \quad (7.35)$$

If $x > x_{\text{int}}$, then the atom will have continued to move into and through the region with velocity v_a instead of v_b , and thus stop at $x_{Q'}$ instead of x_Q . One way around this issue is to have our simulation make Δt very small, but this adds significant computation time and is thus impractical. What we want is the position of the radon atom to be correct after some Δt , even when it passes through an interface. For this example, the time-averaged velocity V that the radon atom should be given at position P to stop at the position Q (and not Q') is

$$V = \frac{v_a \Delta t_a + v_b \Delta t_b}{\Delta t}, \quad (7.36)$$

where Δt_a and Δt_b are the times the atom spends in each region.

In obtaining a more general solution to this problem, we build an array of time-averaged velocities that considers the instantaneous velocity and time spent in each spatial bin (nominally 1 cm). The distance in a column is represented by \vec{x} , where $\vec{x}(1) = 1 \text{ cm}$, $\vec{x}(2) = 2 \text{ cm}$, etc. The instantaneous velocity \vec{v} is given by equations

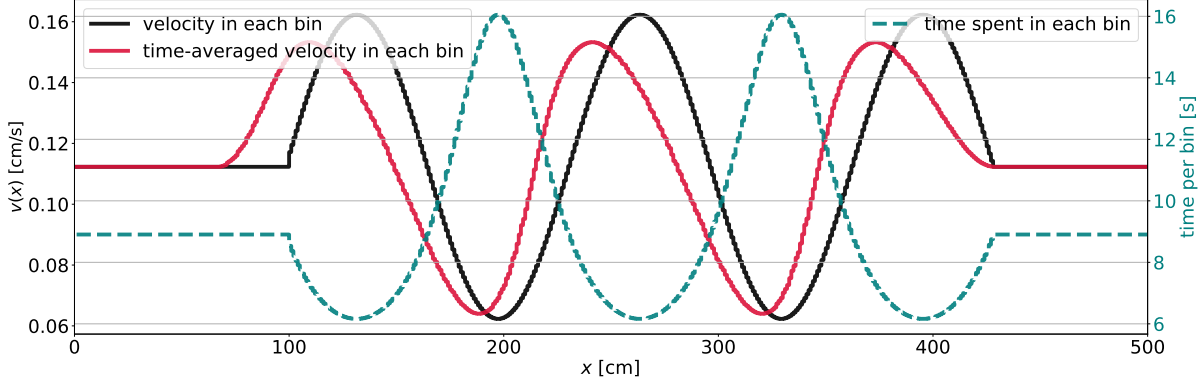


Figure 7.20: As an example of using this time-averaged velocity method, an arbitrary profile of the instantaneous velocity (black curve) is created (and denoted as the “velocity in each bin”). The “time spent in each bin” (teal, dashed curve) is then found according to Eq. 7.37. Finally, the time-averaged velocity of a radon atom starting in a given bin (crimson curve) is found according to Eq. 7.38 and Eq. 7.39.

Eq. 7.32, Eq. 7.33, or Eq. 7.34. The time an atom spends in the i 'th location of \vec{x}

$$T_i = \frac{x_{i+1} - x_i}{v_i}. \quad (7.37)$$

The time-averaged velocity, denoted as \vec{V} , is found by

$$V_i = \frac{1}{\Delta t} \sum_{j=i}^{n_i} v_j T_j, \quad (7.38)$$

where n_i is defined by the smallest n_i that satisfies

$$\sum_{j=i}^{n_i} T_j \geq \Delta t. \quad (7.39)$$

The application of this method is demonstrated by Fig. 7.20. The radon velocity in this example has been chosen to be of order 0.1 cm/s (100× larger than what is typical for this system) to emphasize the method. That being said, as the radon velocity approaches ~ 0.004 cm/s, which is representative for this system, the (uncorrected) radon velocity and time-averaged radon velocity become indistinguishable. By using the time-averaged radon velocity (by default in the sim), either no change is made or a change *is* made (for the better), due to some unusual or as-yet-unrecognized circumstance (*e.g.*, an abrupt jump in temperature, resulting in a jump in the radon velocity).

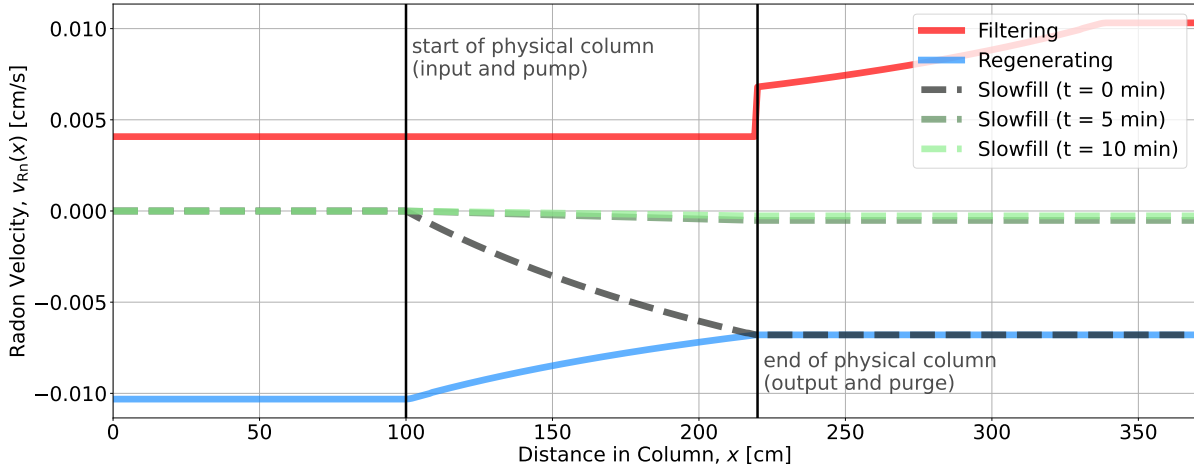


Figure 7.21: Radon velocity profiles (at $F = 90 \text{ scfm}$ and $f_{\text{purge}} = 7.2 \text{ scfm}$) for the three modes of operation (F, R, and S). During the filtering mode, the velocity is positive (red curve); while during regenerating (blue curve) and slowfill (dark-to-light green, dashed), the velocity is negative, as radon is moving backwards through the column (toward the pump). With a simulation time step of $\Delta t = 5 \text{ min}$ and slowfill duration of 15 min (to bring the column up to atmospheric pressure), the number of temperature profiles generated agree with the number of slowfill operators that are built: $15 \text{ min}/5 \text{ min} = 3$.

The RRS simulation builds instantaneous velocity profiles for filtering (F), regenerating (R), and the slow-fill mode (S). Applying this time-averaged velocity method to these velocity profiles results in Fig. 7.21. Though the time-averaged velocity method is used by default, it would require unconventional configuration parameters for it to change the velocity profiles significantly.

7.7 The Diffusion Coefficient Within a Column

In addition to radon atoms moving through a carbon column at the group velocity, v_{Rn} , these atoms may diffuse throughout the column, both forward (with the group velocity) and backward (or any other direction, even though they are ignored for reasons of symmetry). A larger diffusion coefficient gives the radon distribution a larger tail along the column's longitudinal axis; that is, the front of the radon concentration moving through the column (as described previous as an “S-curve”, and shown by Fig. 7.10) has a larger standard deviation, which means radon atoms are spreading out more per unit time, moving both forward and backward within the column. The radon atoms moving

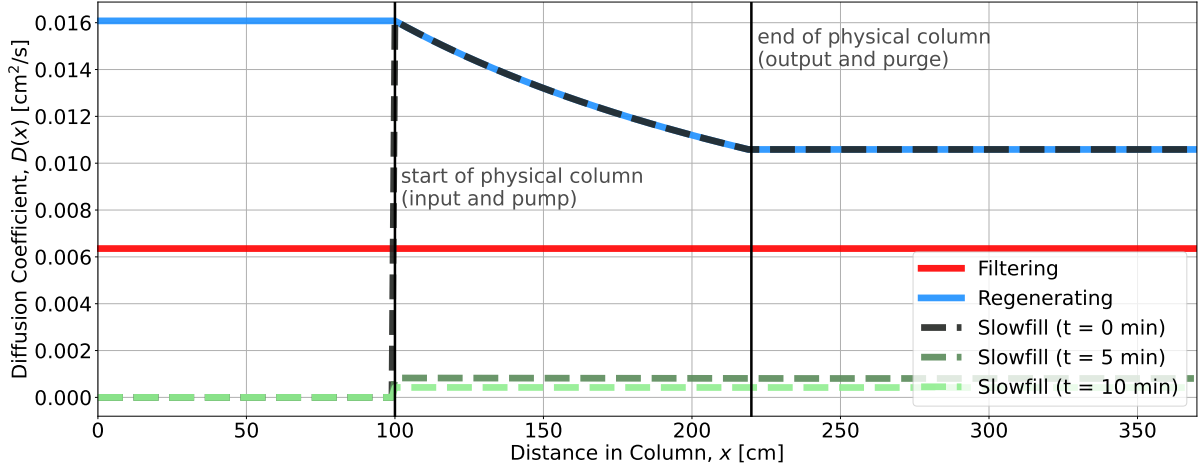


Figure 7.22: The diffusion coefficient during filtering (red, solid) is essentially horizontal, as the pressure drop across the column during filtering is nearly zero. For regeneration (blue, solid), the diffusion coefficient increases from $x = 120$ down to $x = 100$, where the physical column ends at the vacuum pumps, where the pressure reduces to a minimum. The diffusion coefficient during slowfill is represented by three curves (dark to light green, dashed): initially (at $t = 0$) the curve has the same values across the column as during regeneration; after one Δt (of 5 min), the pressure gradient across the column has relaxed, the diffusion coefficient is reduced according to Eq. 7.44; as the column approaches atmospheric pressure, over 15 min, the diffusion coefficient becomes minimal, both because the pressure ratio approaches unity, and, perhaps more importantly, the velocity term vanishes.

forward will exit the column sooner than expected from the group velocity. Here, a mathematical description of the diffusion coefficient is developed, for use by the RRS simulation, with typical diffusion coefficient (arrays) presented.

According to the *Physics at Surfaces* [87] by Andrew Zangwill and the 1979 paper on radon adsorption to activated carbon by Strong and Levins [102], the diffusion coefficient depends on temperature T following the Arrhenius equation:

$$D(T) = f_D(v)e^{-T_0/T}, \quad (7.40)$$

where $f_D(v)$ expressed by

$$f_D(v) = av + b, \quad (7.41)$$

where v is the air velocity (a function of pressure) and a and b are constants, which are found empirically from BTC data (see Section 7.13.3). The characteristic temperature of adsorption $T_0 = 3500$ K [110]. The first term, av , describes longitudinal diffusion and

depends on pressure P through the air speed:

$$v = v_{\text{atm}} \frac{P_{\text{atm}}}{P}, \quad (7.42)$$

where v_{atm} is the air speed inferred by measuring the volumetric flow during the filtration stage or, where pressure has the strongest influence, the regeneration or slowfill stages. The second term, b , describes molecular diffusion (*i.e.*, temperature-driven diffusion). Following the argument presented in Section 4.1, the adsorption and desorption rates both depend on pressure, but their ratio does not; therefore, the mean-free velocity of radon (due to molecular diffusion) is not expected to depend on pressure through the influence of radon adsorbing to or desorbing from the carbon surface. However, the diffusion of gases has been found to depend inversely on pressure, at low pressure (where this work is conducted) [148, 149]. Implementing this dependence into our description of diffusion, along with the substitutions of Eq. 7.41 and Eq. 7.42 yields

$$D(T, P) = \left(av_{\text{atm}} \frac{P_{\text{atm}}}{P} + b \frac{P_{\text{atm}}}{P} \right) e^{-T_{\circ}/T}, \quad (7.43)$$

where the pressure ratio $P_{\text{atm}}/P(x, t)$ works in two ways: (1) converts v_{atm} , as inferred by a measurement of flow at atmospheric pressure, to the true air speed passing through the column (according to continuity), and (2) modifies the parameter b to reflect the expected behavior of molecular diffusion at varying pressure. A slight rearrangement leads to

$$D(x, t) = f_D(v_{\text{atm}}) \exp \left[\frac{-T_{\circ}}{T(x, t)} \right] \frac{P_{\text{atm}}}{P(x, t)}, \quad (7.44)$$

where $D(x, t)$ spans x ; the time t emphasizes that we may have different diffusion coefficients throughout the column at different times (*i.e.*, for different operators created), while T and P have been dropped for brevity. Figure 7.22 shows typical diffusion coefficient arrays for filtering, regenerating, and slowfill.

7.8 The Temperature Within a Column

The SD Mines RRS has had one of the carbon columns outfitted with temperature monitoring. Resistive-temperature devices (RTDs, specifically Platinum PT1000,

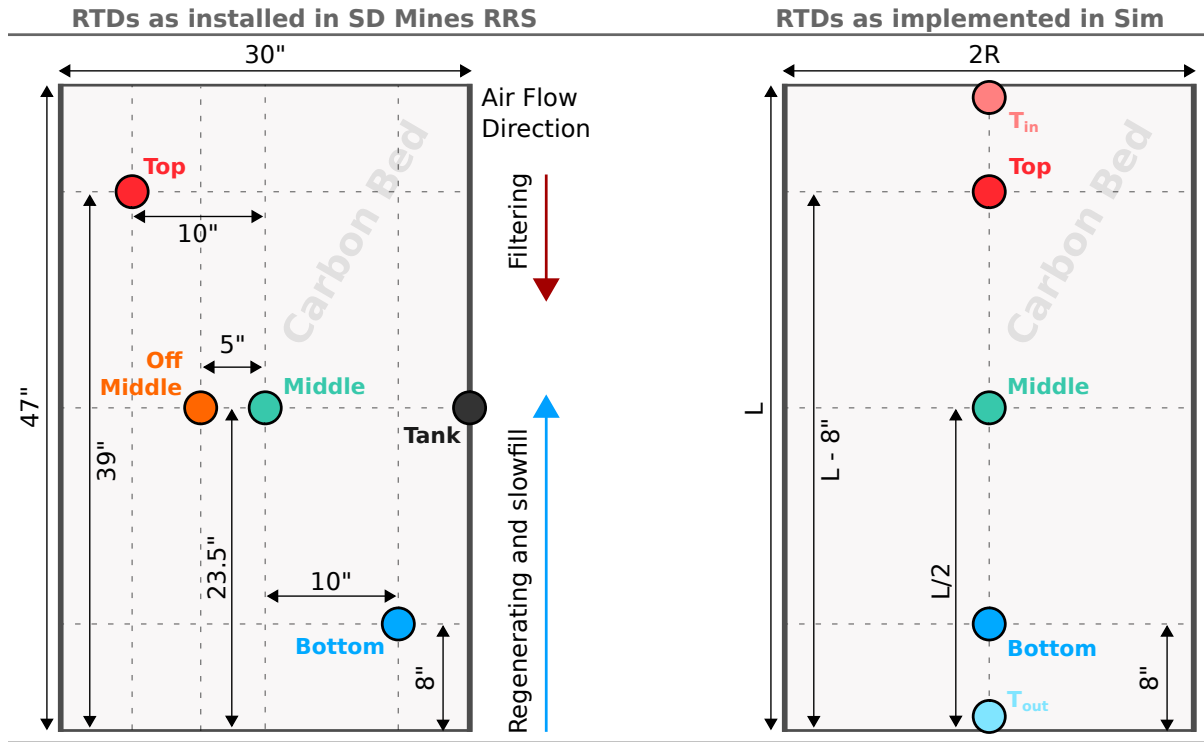


Figure 7.23: Left Diagram: Resistive-temperature devices (RTDs) have been installed to monitor temperature at five locations within a single tank. The **Tank** RTD is located on the outer stainless steel vessel, placed externally on the middle height of the column. The **Top** and **Bottom** RTDs are both 8 inches within the carbon bed at a distance of 10 inches from the column's axis. The **Middle** RTD is located, per its name, at the center of the carbon bed, while the **Off Middle** RTD is located 5 inches in the radial direction from it. **Right Diagram:** For the simulation, the **Top**, **Middle**, and **Bottom** RTDs are assumed representative of the complete tank cross-section at that distance in the column. The top boundary of the carbon bed has a temperature T_{in} and is assumed to be the input air temperature as measured in the 6-inch input ducting after the last air chiller, while the bottom boundary temperature T_{out} is assumed equivalent to the **Bottom** RTD reading (which is supported by direct measurement of the output air temperature.)

3-wire) were installed within the column and externally on the outside of the stainless steel (the material the column is made from), with their respective locations indicated in Fig. 7.23. Additional RTDs were installed within the 6" input ducting before (so, room temperature) and after the air is dried and cooled (usually $\sim 12^{\circ}\text{C}$); this is just before the air enters a carbon column.

The RRS simulation corrects the radon velocity and diffusion coefficient by the air temperature within the column, according to Eqs. 7.32-7.34. The number of velocity and diffusion coefficient arrays, therefore, will have the same length as the temperature data

provided. Though the RTD data is collected with a user-set frequency of ~ 1 Hz, it is averaged into enough bins that changes in the temperature are captured (and may be passed on to the velocity and diffusion coefficient arrays), but no more; this is because the time to build each temperature bin's operator (maybe 0.05 s), quickly adds up when running the simulation repeatedly while exploring varying configurations. Said another way, while we improve the realism of the radon velocity and diffusion coefficient arrays (which are fundamental to the simulation) by accounting for temperature changes, we gain nothing in making the temperature bins any shorter than the simulation time step Δt .

From Eq. 7.31, the radon velocity

$$v_{\text{Rn}}(T) \propto \exp(-T_{\circ}/T). \quad (7.45)$$

The fractional change of the radon velocity v_{Rn} for a change in temperature from T_1 to T_2

$$\frac{v_{\text{Rn}}(T_2)}{v_{\text{Rn}}(T_1)} \sim \frac{\exp(-T_{\circ}/T_2)}{\exp(-T_{\circ}/T_1)}, \quad (7.46)$$

where $T_{\circ} = 3500$ K and is the critical temperature of adsorption (for radon adsorbing to activated carbon) [102]. If we now consider a very reasonable temperature jump (say, between filtering and regeneration) of 10 to 30°C, we have the fractional change:

$$\frac{v_{\text{Rn}}(T_2)}{v_{\text{Rn}}(T_1)} = \frac{\exp(-3500 \text{ K}/283 \text{ K})}{\exp(-3500 \text{ K}/303 \text{ K})} = 2.26. \quad (7.47)$$

Figure 7.24 illustrates the expected change in the radon velocity (or, similarly, radon diffusion) for the column temperature T (in Kelvin) and temperature jumps $T_J \in \{2, 10, 20, 30\}$ °C. That is, the fractional change:

$$\mathfrak{F}(T, T_J) \equiv \exp\left[\frac{-T_{\circ}}{T + T_J}\right] / \exp\left[\frac{-T_{\circ}}{T}\right]. \quad (7.48)$$

For example, then, if the column is measured to be 20 °C and then the temperature increases (jumps) to 40 °C (perhaps due to an increase in the ambient room temperature),

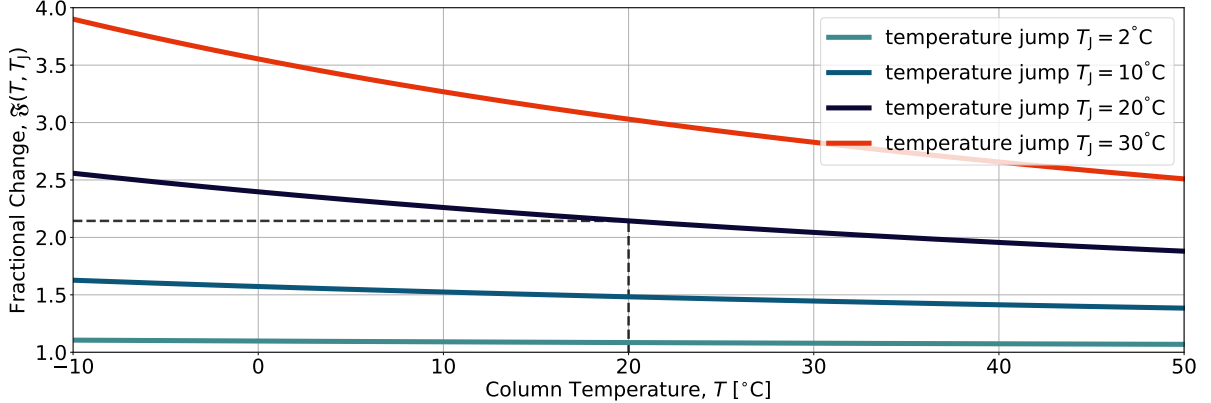


Figure 7.24: The expected change in the radon velocity and diffusion coefficient \mathfrak{F} depends on temperature T and the change (or jump) in the temperature T_J . The vertical and horizontal dashed lines emphasize the fractional change (of 2.2) for $T = 20\text{ }^\circ\text{C}$ and $T_J = 20\text{ }^\circ\text{C}$.

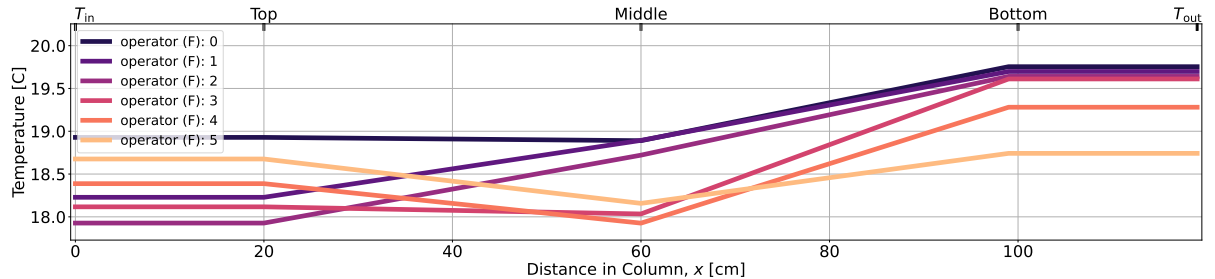


Figure 7.25: Based on measured temperature data, the temperature profiles shown are used to build 6 filtration operators. Here, the temperature was rebinned to 10 min intervals and the filtering stage was set to 60 min. With the simulation time step of $\Delta t = 5\text{ min}$, each operator is applied (or operates) twice, so that 12 operations by 6 operators evolves the column by 60 min.

we expect that the radon velocity would increase by a factor of 2.14. The fractional change in the radon velocity is nearly linear, but not quite. This may be seen by the Taylor series expansion of Eq. 7.48 to 2nd order:

$$\exp\left[\frac{-T_\circ}{T + T_J}\right] / \exp\left[\frac{-T_\circ}{T}\right] = \exp\left[\frac{T_\circ T_J}{T(T + T_J)}\right] \approx 1 + \frac{T_\circ T_J}{T^2} \left(1 - \frac{T_J}{T}\right) + \frac{T_\circ^2 T_J^2}{2T^4}, \quad (7.49)$$

where a few lines of algebra and the approximation that $T_J/T \ll 1$ have not been shown.

As shown in the right pane of Fig. 7.23, the simulation takes either a measured or user-set temperature at three locations within the 120 cm physical column: 20 cm, 60 cm, and 100 cm along the longitudinal axis. The temperature at these three locations, representing the top (input during filter or pump side during regeneration), middle, and bottom of a column, are then linearly interpolated in order to provide a temperature at

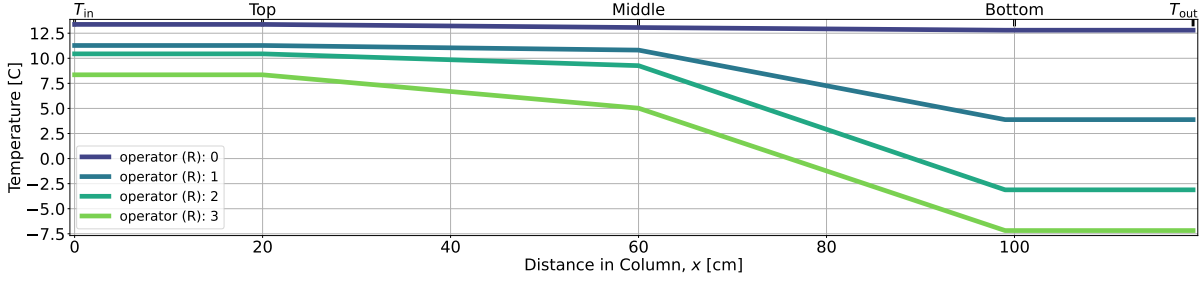


Figure 7.26: Based on measured temperature data, the temperature profiles shown are used to build 4 regeneration operators. Here, the temperature was rebinned to 10 min intervals and the regenerating stage was set to 45 min. With the simulation time step of $\Delta t = 5$ min, each operator is applied twice, with the exception of the final operator being applied three times. This is because the last 5 minutes of the regenerating stage is averaged into the last temperature bin (and is thus an average of the last 15 minutes of the stage).

each location x within the column, with a temperature profile for each operator built (as shown by Fig. 7.25 and Fig. 7.26 for filtering and regeneration respectively). In addition, the simulation allows for user-set temperatures at the input and output, denoted T_{in} and T_{out} . When the input and output temperature is known, these may be set to improve the temperature information passed to the simulation; when not set, each default to the value of their nearest neighbor (so $T_{\text{in}} = T_{\text{Top}}$).

For example, let us build filtering operators for the 6 temperature profiles shown in Fig. 7.25, denoted by $\eta = 0, 1, \dots, 5$. Each temperature profile would inform the radon velocity as:

$$v_{\text{Rn}}(\eta, x) = v_{\text{air}} f_A e^{-T_o/T_F(\eta, x)}, \quad (7.50)$$

where x still denotes location in the column. The reason we use η here, and not n , is because the number of operations n is not in general equal to the number of operators; that is, we do not necessarily have a unique operator for each operation applied.

7.8.1 The SD Mines RRS Column Temperature During BTCs

The temperature during BTCs varies significantly due to the input air temperature and/or physical effects (see Section 5.4), and is therefore incorporated into the simulation. For example, the temperature within the sound-proof room that contains the SD Mines RRS can increase by $\sim 10^\circ\text{C}$ when the door is shut, due to further limiting the air

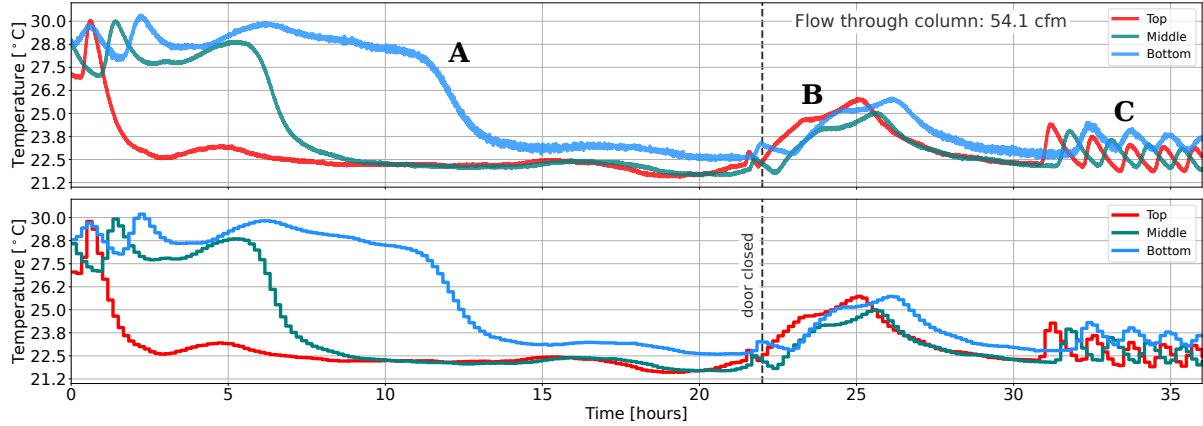


Figure 7.27: **Upper plot:** Temperature is measured by RTD during a 54.1 cfm break-through curve run at the Top, Middle, and Bottom locations within a carbon column. There are three major features in this data set: **(A)** is due to water content being added to the carbon bed, **(B)** is presumably due to the RRS room door being shut (with the dashed line showing approximate time) and then later opened, and **(C)** is due to a gas heater turning on and off (within temperature set points) in the general lab area. Further details on temperature dependencies are discussed in Section 5.4. **Lower plot:** The same RTD data, but rebinned for use by the RRS simulation.

exchange rate, and thus increases the input air temperature (when the input air is sampled from within this room). During the first couple hours, or even the first 15 hours for the Bottom RTD, there is a temporary increase of 10-15°C that we suspect is caused by water content introduced in the input air adsorbing to carbon surface, and possibly condensing as well (with further discussion in Section 5.4). We observe that temperature changes with time and, therefore, have incorporated the measurement into the parameters, v_{Rn} and D , with which operators are built.

As a practical consideration (mentioned in Section 7.8), we don't want to build more operators than necessary, and so we re-sample the BTC temperature data in bins just small enough to capture most changes in temperature. Figure 7.27 shows column temperature data before and after rebinning. For this example, the bin size is 10 minutes and appears to be sufficiently small such that the measured temperature is well approximated. If the simulation time step $\Delta t = 5$ min (as usual), each operator will act twice per temperature bin (that is, twice for each v_{Rn} and D array created, with these arrays created for each temperature bin).

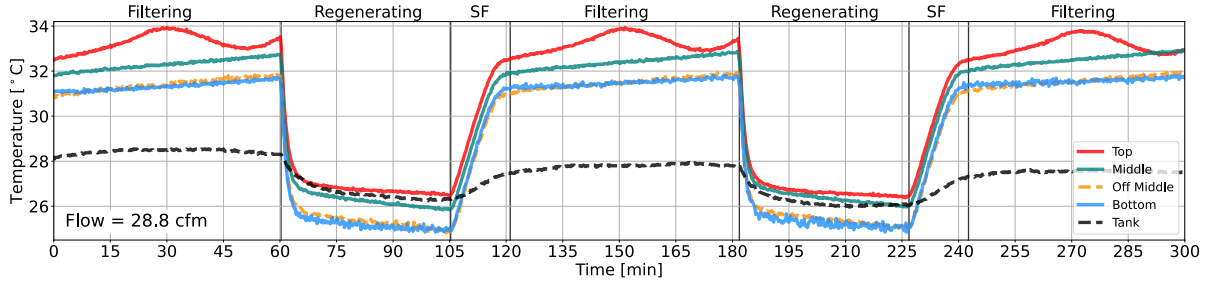


Figure 7.28: Temperature is measured by RTDs at four locations within one carbon column labeled Top, Middle, Off Middle, Bottom, and one location on the external side of the stainless steel vessel, labeled Tank. The data shown here was taken after the RRS reached equilibrium (after ~ 3 days). During this 28.8 cfm (through column) swing-mode measurement, the measured temperature slightly rises during filtration, drops quickly during regeneration, and slowly, but steadily, increases during slowfill. This segment of the data was taken after the RRS was producing a steady output radon concentration (*i.e.*, equilibrium had been reached) and appears roughly periodic.

7.8.2 The SD Mines RRS Column Temperature During Swing Mode

While the temperature within a column changes during a break-through curve by $\sim 10^\circ\text{C}$, particularly at early time, the change in temperature during swing can be even greater, with swings from -10°C to 30°C from regeneration to filtering (see Fig. C.2 in Section 5.4). Therefore, the column temperature is crucial to understand and account for within the simulation in order to make improved predictions and for real-data comparisons (as discussed in the validation studies in Section 7.13.4).

The measured temperature during typical swing operation has periodic behavior, but with additional features that depend on the flow rate of air passing through the filtering column. Illustrated by Fig. 7.28, at low input air flow (say, 30 cfm), the temperature during both the filtering and regenerating stages is roughly flat (changing by only a couple degrees).

Shown by Fig. 7.29 (top plot), during high flow (of, say, 90 cfm), the filtering stage, particularly, has significant time dependence and large changes in temperature. The regenerating stage does not behave much differently than at low flow, except for the **Top** RTD measuring the input side of the column. The temperature measured during the slowfill stage appears to be driven by pressure (as the column is raised to atmospheric

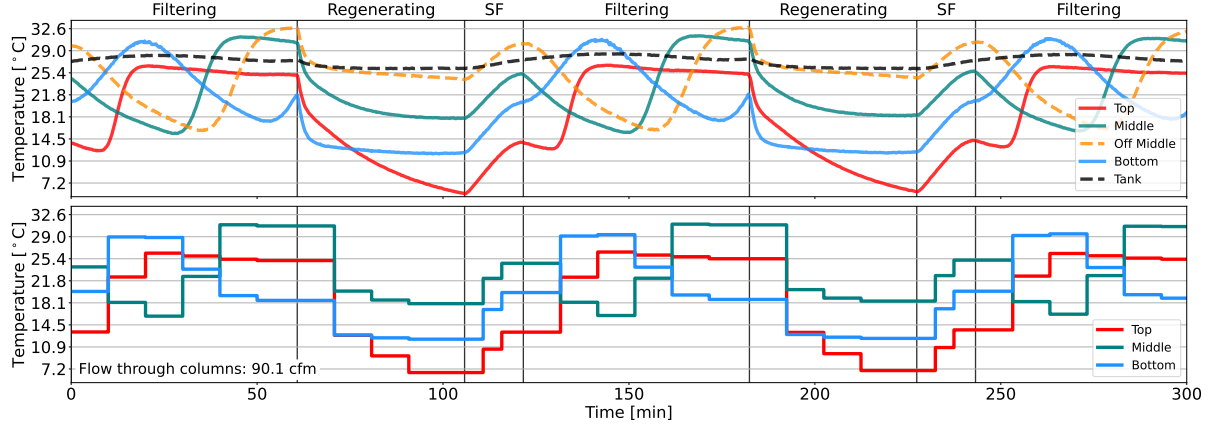


Figure 7.29: **Top:** Temperature data from RTDs within one column during swing mode at $\sim 90 \text{ cfm}$. With locations described by Fig. 7.23, the solid curves (red, green, blue) are used by the RRS simulation, while the dashed (orange and black) curves are used for improving general knowledge of column temperature (and put to use in Section 5.4). During this swing-mode measurement, the temperature changes by as much as 10°C during the filtration stage, in a way that appears nearly identical for each filtering stage. The temperature drops quickly during regeneration, reaching minima lower than at low flow (see Fig. 7.28). The temperature steadily increases during slowfill (appearing to depend only on the starting temperature and the purge flow, though not seen in this plot). This segment of the data was taken after the RRS was producing a steady output radon concentration. **Bottom:** Temperature data from the top plot, but rebinned with 10 min sampling during the filtering and regeneration stages and 5 min sampling during the usually-shorter slowfill stage (to still capture the temperature change over this short 15 min stage).

pressure by the air introduced through the purge-flow valve). Particularly in high-flow cases, sampling the temperature several times during each stage improves the accuracy of the radon velocity used to build operators in the RRS simulation. Figure 7.29 shows temperature data (top plot) converted to 10-min sampling during the filtering and regenerating stages and 5-min sampling during the usually-shorter slowfill stage (bottom plot).

7.9 The Pressure Within a Column

The pressure within each column depends on what stage it's in (where a BTC is essentially an extended filtering stage). Figure 7.30 shows the measured pressure for swing-mode operation (which captures the break-through curve mode as well). During the filtering stage, the average pressure throughout the column is approximately one atmosphere. The inlet pressure is a couple Torr above the outlet pressure, as required for

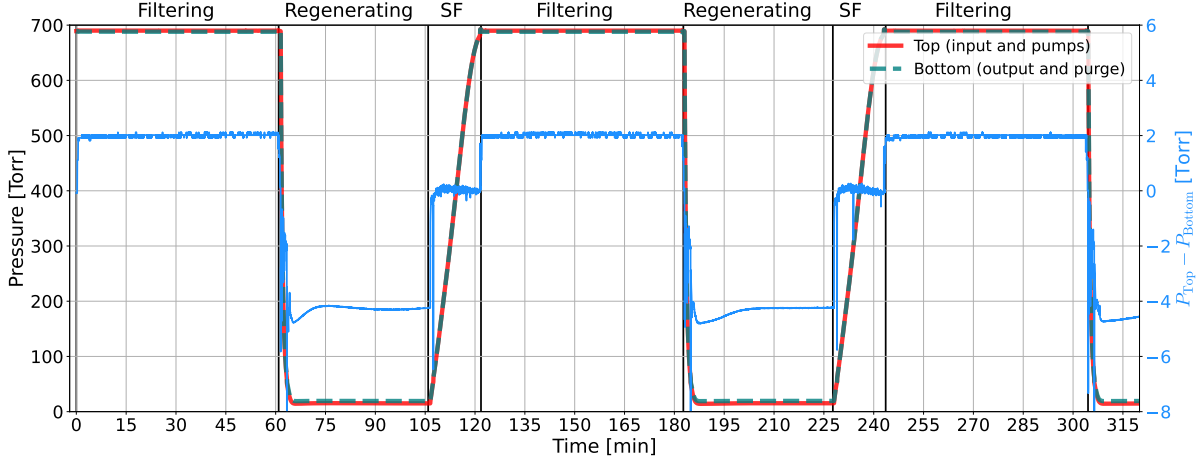


Figure 7.30: The measured pressure (left axis) at the Top (solid red line) and the Bottom (dashed teal line) of a column during swing mode shows periodicity over time (with uncertainties of 5% of reading, not shown). At the end of the slowfill (SF) stage, the pressure at the Top and Bottom locations should be equal, and this is used as a calibration between pressure gauges. Also in the slowfill stage, the pressure difference (right axis, blue line) is zero (within uncertainties) indicating that the pressure quickly relaxes throughout the carbon bed during this stage. During the filtering and regeneration stages respectively, we observe a positive and negative pressure gradient $\Delta P/\Delta x = (P_{\text{top}} - P_{\text{Bottom}})/L$ along the column axis, as expected.

positive flow through the column, with a linear pressure gradient (dP/dx) throughout the carbon bed. Steady state (where the pressure gradient does not change with time) is reached within seconds; therefore pressure within the column during this stage can be considered time-independent. With the pressure drop over the filtering column being small compared to atmospheric pressure, P_{atm} , it is not modeled in the RRS simulation—though it could be easily implemented for a system with, for example, slower pumps, higher-impedance carbon, or larger columns. Because the pressure along the column axis $P(x)$ is close to P_{atm} , its impact on the air speed for a given flow is negligible (*i.e.*, $P_{\text{atm}}/P(x) \approx 1$). If the measured pressure drop was indeed accounted for by the simulation, it would improve our estimate of the air velocity within the column by $\sim 680/682$ or about 0.3%.

During the regeneration stage, the pressure within a column becomes significantly less than atmospheric pressure, with a pressure gradient of ≈ 4.5 Torr (see the right axis of Fig. 7.30). During this stage, the purge-flow valve provides air (usually 7 scfm) to one

side of the column, while the vacuum pumps remove air from the other. The pressure, therefore, is determined by the purge flow setting and the pumping speed of the pumps. The slope of the pressure gradient also depends on the pressure, and therefore on the choice of purge flow (seen in Fig. 7.31).

A column is able to be pumped down to its minimum pressure (*i.e.*, its base pressure for a given purge flow) within a couple minutes. The pressure gradient along the column axis appears to reach a steady state within seconds after reaching the base pressure. The caveat here is that the pressure transducers used switch between sensor type around 50 Torr, adding a delay to the recorded pressure. Therefore, the pressure gradient likely changes with pressure as seen by Fig. 7.31, but perhaps to as much as inferred from the right axis of Fig. 5.12. Nonetheless, with a simulation time step of 5 min, this stage may be treated as time-independent. With the purge flow determining both the average column pressure and the gradient, it is useful to model the pressure by the simulation for this stage.

During the slowfill stage, the pressure within the column is brought up to atmospheric pressure in preparation of filtering. The pressure therefore increases linearly with time due to the fixed¹ flow of air passing into the column through the purge-flow valve. The pressure gradient during this stage is essentially zero, as air within the column moves quickly compared to the rate at which air is being added. Therefore, while it is important to model pressure versus time during this stage, the spatial dependence can be ignored (though the simulation can be configured to account for x as well).

To model pressure accurately, the simulation needs the following measured data:

1. the pump and purge pressure at equilibrium as a function of purge flow and

¹The purge-flow valve (a butterfly valve) sets the purge flow to a constant rate provided that the pressure drop across the valve is more than ~ 80 Torr. Therefore, the increase of pressure with time slows near the end of the slowfill stage, as the flow is instead determined by ΔP across the valve and drops below the valve's set point.

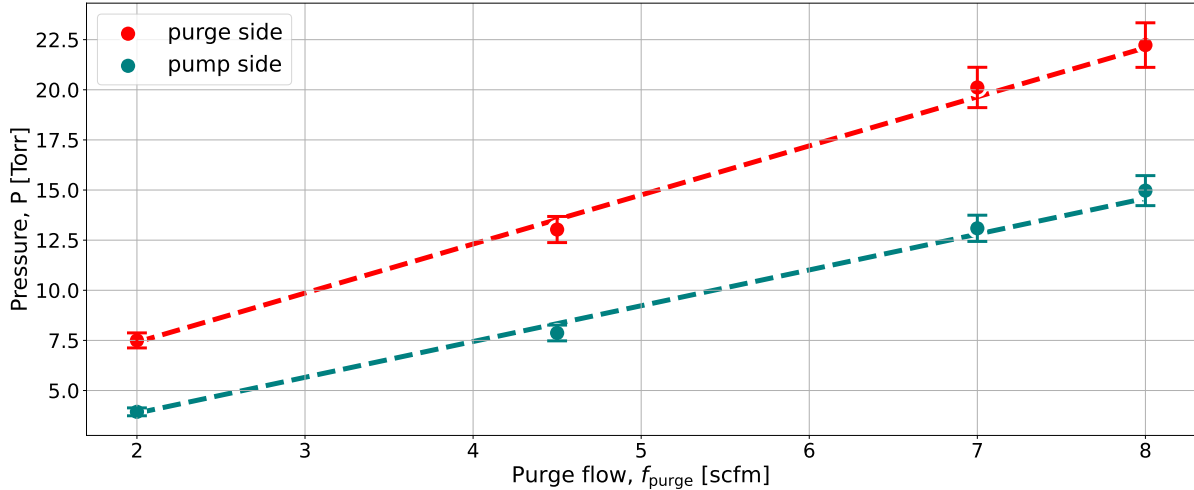


Figure 7.31: The pressure during regeneration at the pump side and purge side of a column is measured as a function of the purge flow (after waiting a couple minutes to reach equilibrium). The error bars are conservatively found by taking 5% of the recorded value (discussed in Section 5.3). A linear trend (dashed lines, given by Eq. 7.51) appears reasonable in this flow range, and has best-fit parameters: $m = 2.5 \pm 0.1$ Torr/scfm and $b = 2.3 \pm 0.5$ Torr on the purge side and $m = 1.9 \pm 0.1$ Torr/scfm and $b = 0.0 \pm 0.5$ Torr, on the pump side. The goodness-of-fit was $\chi^2/\text{ndf} \approx 0.44$ with p-value = 0.65 for the purge side and $\chi^2/\text{ndf} \approx 0.99$ with p-value = 0.37 on the pump side, where $\text{ndf} = 2$.

2. the pump and purge pressure as a function of time for a given purge flow during the slowfill stage.

To obtain this data for several choices of purge flow f_{purge} , a column is pumped on until equilibrium is reached (usually within a couple minutes). The base pressure P_{base} is recorded at each end of the column (the pump and purge sides). Figure 7.31 shows the result, with the function

$$P_{\text{base}} = m f_{\text{purge}} + b \quad (7.51)$$

fit to the data for both the purge- and pump-side readings. We observe that the pump-side pressure is always lower than on the purge side, as expected.

In order to measure the rate-of-rise of pressure during the slowfill stage for a given choice of purge flow, a column is pumped down to its base pressure (at this time, only connected to the pumps). Next, the purge flow is set, the valve connecting the column to the pumps is closed, and the valve connecting the column to the (purge-flow) butterfly

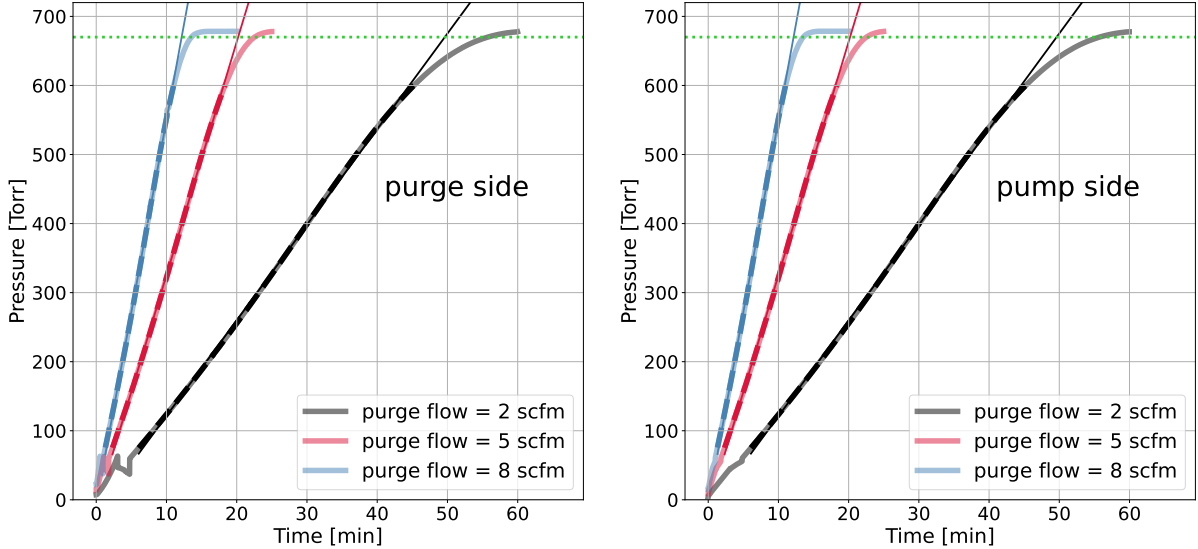


Figure 7.32: Pressure measured on the purge-flow (left plot) and pump (right plot) sides of the column (solid curves) versus time during slow-fill mode with varying values of the purge flow ($f_{\text{purge}} \in [2, 5, 8] \text{ scfm}$). The slope ($a = \Delta P / \Delta t$) is found by fitting (skinny, solid curves) the linear region of the data (dashed curves). The best-fit values are provided in Table 7.2. From smallest purge flow to largest, goodness-of-fit was $\chi^2/\text{ndf} = 0.19$, with $\text{ndf} = 2345$, $\chi^2/\text{ndf} = 0.24$, with $\text{ndf} = 960$, and $\chi^2/\text{ndf} = 0.26$, with $\text{ndf} = 569$. The green dotted line is drawn at 670 Torr and is used in estimating the time needed to raise a column from the base pressure to atmospheric pressure (see Fig. 7.34).

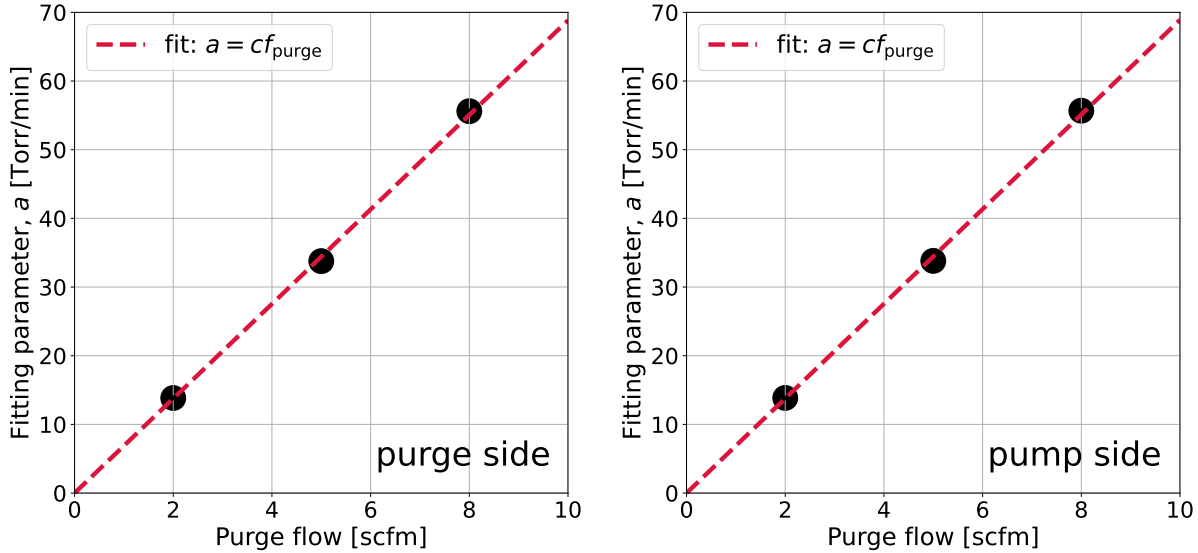


Figure 7.33: The slope a (black dots) found from the fits in Fig. 7.32 appears to depend linearly on the value of the purge flow f_{purge} . Equation 7.53 is fit to these three points and the best-fit value of c is found to be $6.9 \pm 0.1 \text{ Torr min}^{-1} \text{ scfm}^{-1}$ for both the purge-flow (left plot) and pump (right plot) side. The error bars for these points are smaller than the dots and are therefore not shown.

valve is opened. The pressure in the column begins to rise steadily, as the butterfly valve constricts flow, such that $dP/dt \sim \text{constant}$ for most of the pressure range. These steps are then repeated for a few choices of purge flow, with the result shown by Fig. 7.32. A line is fit to the linear part of the pressure rise curve with the form

$$P = at + P_{\text{base}}, \quad (7.52)$$

where a is a fitting parameter, the base pressure P_{base} is defined by Eq. 7.51, and t is time. As expected, for increasing purge flow, the parameter a becomes larger (so it takes less time to fill the evacuated volume). The values of the fitting parameter a are plotted in Fig. 7.33. A fit to these points provide a clear relationship between the fitting parameter a and the purge flow:

$$a = cf_{\text{purge}}, \quad (7.53)$$

where c is a fitting parameter. There is no constant offset because the change in pressure $\Delta P/\Delta t = a = 0$ when $f_{\text{purge}} = 0$ (as can be seen in Fig. 7.33).

With the above descriptions of pressure, we are prepared to build a model for pressure within a column during each stage. Substituting Eq. 7.51 and Eq. 7.53 into Eq. 7.52 yields

$$P(t, f_{\text{purge}}) = (ct + m) f_{\text{purge}} + b. \quad (7.54)$$

If we denote the purge-flow side with index 1 and the pump side with index 2, we may describe the pressure on either end of the column as

$$P_1(t, f_{\text{purge}}) = (ct + m_1) f_{\text{purge}} + b_1 \quad (7.55a)$$

$$P_2(t, f_{\text{purge}}) = (ct + m_2) f_{\text{purge}} + b_2, \quad (7.55b)$$

where the parameter c is not indexed because it was found to be the same (within uncertainties) for both purge and pump sides. The complete fitting results are found in Table 7.2.

Fitted parameter	m_1 [Torr/scfm]	b_1 [Torr]	m_2 [Torr/scfm]	b_2 [Torr]	c [Torr/(min scfm)]
Best-fit value	2.4 ± 0.1	2.5 ± 0.4	1.8 ± 0.1	0.3 ± 0.3	6.9 ± 0.1

Table 7.2: Best-fit values of parameters m and b from Eq. 7.51 and c from Eq. 7.53, with 1 and 2 denoting the purge and pump sides of the column respectively.

The slowfill stage exists to bring the regenerating column back up to atmospheric pressure; therefore the length of the stage depends on the purge flow. By setting Eq. 7.54 equal to P_{atm} and solving for time t , we obtain an estimate of the required time t_{req} needed to raise the column from its base pressure to atmospheric pressure. That is,

$$t_{\text{req}} = \frac{1}{c} \left(\frac{P_{\text{atm}} - b}{f_{\text{purge}}} - m \right). \quad (7.56)$$

The butterfly valve restricts the purge flow from being no larger than the set value. However, once the pressure drop across the valve becomes $\lesssim 10$ Torr, the flow through the valve drops and the time required to raise the column to approximately atmospheric pressure is increased. Comparing to Fig. 7.32, we add an empirical factor that accounts for the behavior of the butterfly valve, yielding an improved estimate of the time required

$$t_{\text{req}} = \frac{1}{c} \left(\frac{P_{\text{atm}} - b}{f_{\text{purge}}} - m \right) + \frac{16 \text{ scfm min}}{f_{\text{purge}}}, \quad (7.57)$$

with the result shown by Fig. 7.34 (Left). This relationship is built into the RRS simulation in order to improve estimates of performance for different choices of purge flow. The required time to raise a column to atmospheric pressure is estimated by the pump-side pressure transducer. This gauge was chosen arbitrarily. Figure 7.34 (Right) shows that the pressure within a column quickly relaxes (*i.e.*, the pressure profile along the column axis becomes flat), and therefore the choice of gauge does not change the result during the slowfill mode.

In order to describe the pressure at the location x along the column axis, we consider an example illustrated by Fig. 7.35. We pump down a carbon column to P_{low} , the base pressure. The purge-flow valve is initially closed, and the pressure within the column $P(x, 0) = P_{\text{low}}$. Just after the purge-flow valve is opened, a fixed amount of air moves

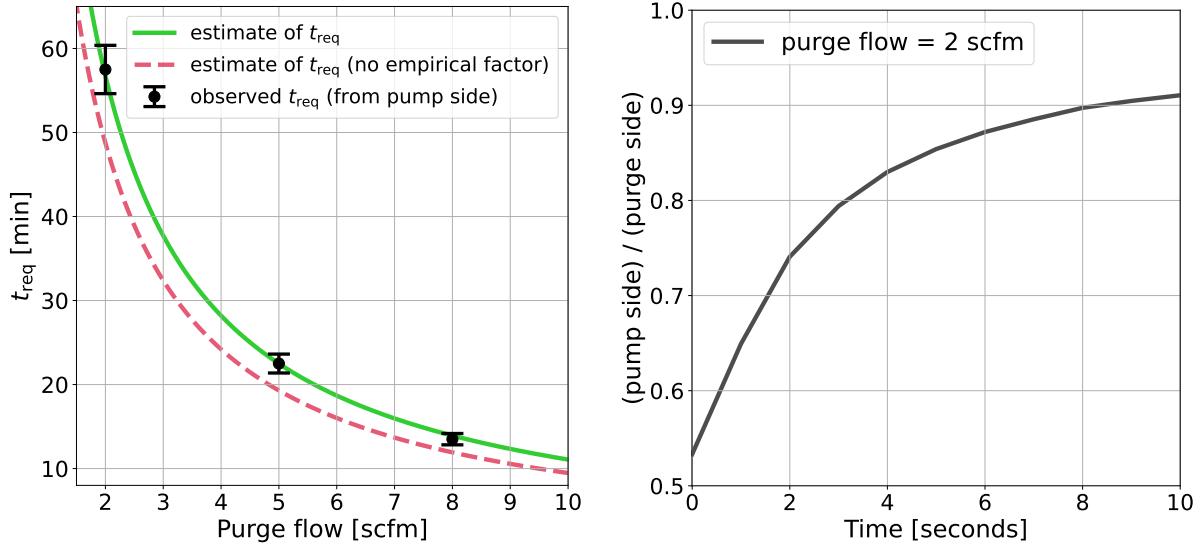


Figure 7.34: **Left:** The time needed to raise a column from its base pressure back up to atmospheric pressure is modeled by the RRS simulation according to Eq. 7.57 (green line), and this empirical model is made to agree with the observed need time (black dots). Each observed time represents how long it takes to raise a column from the base pressure to 670 Torr (see the green dotted line of Fig. 7.32), and the uncertainty is 5% (and is the worst-case accuracy of the gauge). Equation 7.56 (dashed line) does not include the empirical factor $16/f_{\text{purge}}$ and is seen to underestimate the time needed to approach atmospheric pressure. **Right:** The ratio of pressure measured at the pump and purge sides of a column approaches unity during the slowfill stage on order 10 seconds. The caveat with this plot is that the pressure transducer switches between its micro-pirani and piezo-electric sensors around 50 Torr, and thus lowers, so to speak, the right end of this curve down for a minute or so before settling at unity (not seen in this plot). This transitioning blip is easily seen at early times in Fig. 7.32, and is worse for the purge-side pressure gauge.

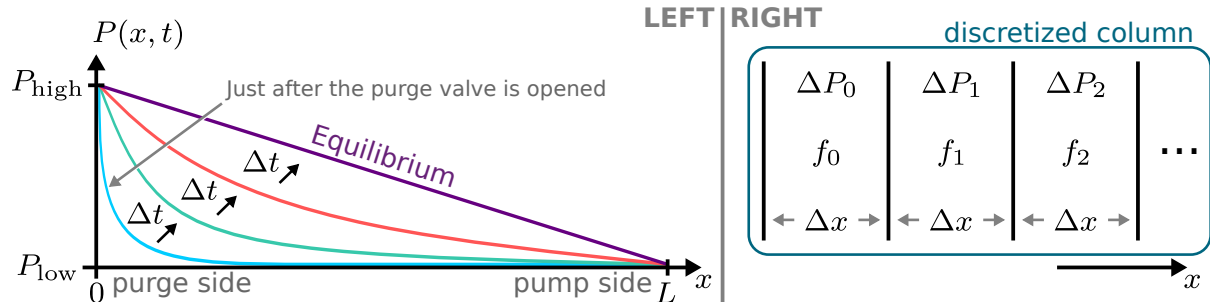


Figure 7.35: **Left:** Let the initial pressure at any location x in a column be held at P_{low} , but with $P(L) = P_{\text{low}} \forall t$. Just after the purge valve is opened, the pressure increases at $x = 0$ from P_{low} to P_{high} (blue line). After each time interval Δt , the pressure profile further approaches the equilibrium profile (indigo line), described by a line connecting the pressures at the column boundaries. The time needed to reach equilibrium is determined by the impedance of the medium. **Right:** Imagining the column in discrete segments: the i 'th segment has a length along the column axis of Δx , a pressure drop ΔP_i , and air flow f_i .

into the column per unit time. The pressure at the purge side increases to P_{high} (see Fig. 7.35: (Left), but the pump side doesn't learn about this until L/v_{sound} seconds later, where v_{sound} is the speed of sound in this medium (*i.e.*, the air in the carbon bed at P_{low}) and L is the length of the column. If we assume in this example that the purge and pump-side pressures remain fixed at P_{high} and P_{low} respectively, the pressure profile within the column eventually approaches an equilibrium. This equilibrium pressure profile will be linear, as is now described. Consider a discretized, homogeneous column (or medium) where the i 'th segment of the column has width Δx , pressure drop ΔP_i , and air flow f_i . Referring to Fig. 7.35: (Right), imagine that

$$\Delta P_0 > \Delta P_1. \quad (7.58)$$

Because $f \propto \Delta P$,

$$f_0 > f_1. \quad (7.59)$$

This means that more air is passing into segment 1 than is leaving—this must increase ΔP_1 , therefore increasing f_1 . This will continue until $\Delta P_1 = \Delta P_0$. Similarly, if

$$\begin{aligned} \Delta P_0 < \Delta P_1, &\rightarrow f_0 < f_1 \\ &\rightarrow \Delta P_1 \text{ decreases} \\ &\rightarrow f_1 \text{ decreases.} \end{aligned} \quad (7.60)$$

This again continues until $\Delta P_1 = \Delta P_0$. Therefore, no matter the initial conditions, the equilibrium pressure profile is described by

$$\Delta P_i = \Delta P_j \quad \forall i, j, \quad (7.61)$$

where i and j are any two locations along the column axis. Therefore, the pressure profile along the column axis will be linear (provided the carbon bed is homogeneous, and it should be). Because the impedance of the carbon is small, air moves quickly through it. The pressure profile within the column reaches equilibrium quickly—on order 10 seconds,

as indicated by Fig. 7.34:(Right). Therefore, during the regeneration stage the pressure between the purge and pump side is linear, with the form

$$P(x, f_{\text{purge}}) = \left(\frac{P_2(0, f_{\text{purge}}) - P_1(0, f_{\text{purge}})}{L} \right) x + P_2(0, f_{\text{purge}}), \quad (7.62)$$

where x is the distance along the column axis and P_1 and P_2 are the estimates of pressure at the purge and pump sides respectively, and given by Eq. 7.55a and Eq. 7.55b, with time t set to zero because we are regenerating (therefore the pressure at the column boundaries is constant in time).

We may now model the pressure in each stage for reasonable choices of simulation parameters (*e.g.*, duration of the regeneration stage or choice of purge flow). To summarize:

1. During the filtering stage, the pressure throughout the column is assumed to be P_{atm} .
2. During the regenerating stage, the pressure at each end of the column is determined by Eq. 7.55a and Eq. 7.55b, but evaluated at time $t = 0$ (reducing the expression to our empirical model of the base pressure at each end of the column, Eq. 7.51). The pressure at a location x along the column axis is described by a linear function connecting the pressure at the column boundaries, and given by Eq. 7.62.
3. During the slowfill stage, the pressure within the column does not depend on x , but does depend on time, and is given by Eq. 7.54.

Figure 7.36 shows the result of this pressure model for a typical purge flow $f_{\text{purge}} = 7 \text{ scfm}$. For the purpose of informing future RRS design and operation, the precision of this pressure model appears sufficient.

Figure 7.37 compares the simulated pressure to the measured pressure, where largest difference is seen during the regeneration stage. The measured pressure drops from 680 Torr to the base pressure (~ 20 Torr) in about 4 minutes, while the simulated pressure

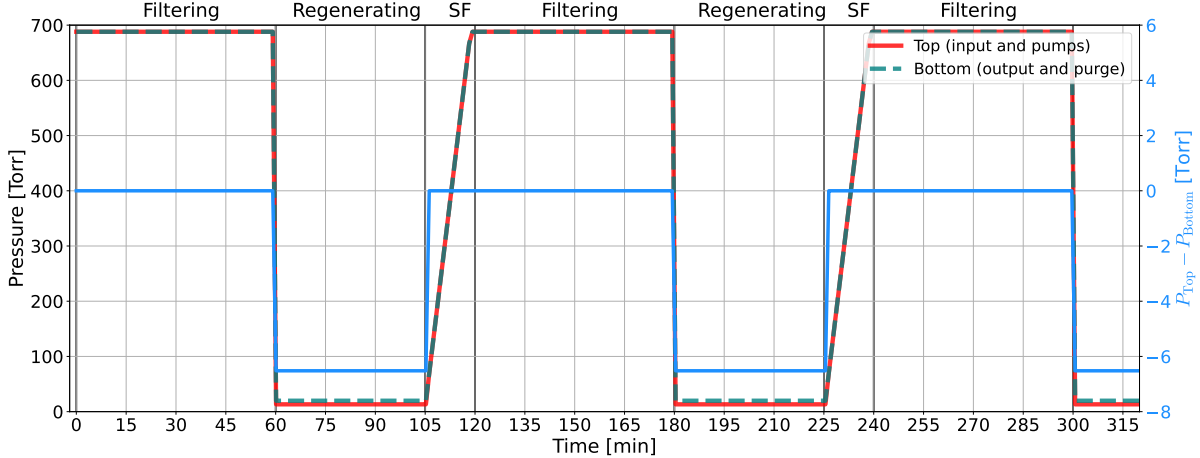


Figure 7.36: The simulation models pressure during the swing mode for each stage: filtering, regenerating, and slowfill (SF). The simulated pressure at the Top of the column (red line) represents the input pressure during filtering and the pump-side pressure during regeneration. The simulated pressure at the Bottom of the column (teal, dashed line) represents the output pressure during filtering (which is equal to the input pressure) and the purge-side pressure during regeneration. During the slowfill stage, the Top and Bottom pressures are equal. The pressure difference between the Top and Bottom (right axis, blue line) shows the pressure gradient along the column axis.

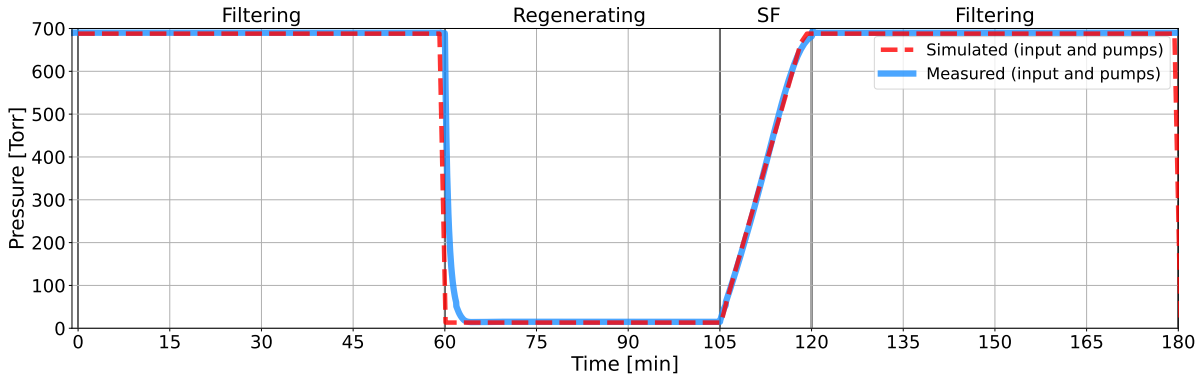


Figure 7.37: Comparison between simulated pressure (dashed line) and the measured pressure (solid line). The simulated pressure captures the general features and provides sufficiently accurate pressure information for the simulation.

drops to the base pressure instantly. The radon velocity $v_{\text{Rn}} \propto P_{\text{atm}}/P(t)$. By not accounting for the exponential drop in pressure, the flat-pressure radon velocity v_{flat} moves faster than the inferred radon velocity v_{meas} from the measured pressure by

$$\frac{v_{\text{flat}}}{v_{\text{meas}}} \propto \frac{1/P_{\text{flat}}}{\langle 1/P_{\text{meas}}(t) \rangle} = 1.06, \quad (7.63)$$

where angle brackets denote a mean and P_{flat} is the base pressure reached by $P_{\text{meas}}(t)$. This agreement is acceptable for this work (and is not obviously the dominant imprecision of the simulation).

The second-largest difference is during the slowfill stage. The measured pressure increases linearly until it reaches about 600 Torr. With the pressure drop over the butterfly valve being insufficient to provide the set flow, the pressure increases more slowly, and appears to follow a $1 - \exp(-t/t_0)$ form. Because this behavior is not modeled, the simulated pressure continues linearly until reaches atmospheric pressure—a few minutes earlier than the measured pressure would have. This has a negligible impact on the radon velocity for two reasons: (1) the purge-flow rate begins to drop to zero at the end of the slowfill stage (where this behavior occurs) and (2) the radon velocity decreases as the pressure increases, and therefore the radon velocity is at its smallest during the end of the slowfill stage (again, where this behavior occurs).

If one compares the simulated pressure gradient across a column during regeneration (right axis of Fig. 7.37) to the measured pressure gradient as seen by the right axis of Fig. 5.12, there is a disagreement of about $7.5 - 4.5 = 2$ Torr. This because the base pressure reached during different runs can be slightly different depending on environmental factors (*e.g.*, moisture in the column outgassing and the ambient temperature slightly changing pump performance). The pressure model was created using pressure data was taken while the columns were in a particular state (that appeared not unusual). The pressure data during swing mode (shown by Fig. 5.12) is likely in a difference state, as the column was used prior for a BTC measurement (which tends to add water content to the carbon bed that takes a few days of swing mode to mostly remove).

7.10 Radon Emanation from Carbon Beds

Activated carbon, like most things, emanates radon. Direct measurement of our carbon indicates an emanation rate of ~ 80 mBq/kg, within a factor of two of the 53.6 ± 1.3 mBq/kg found in literature for the same type of carbon [150]. For this work, the

carbon emanation rate is assumed to be 100 mBq/kg (as the direct measurement was not available until after most analysis had been finished). Let us consider a radon source that is like a thin wafer exactly occupying the cross section of a pipe (see Fig. 7.38: **left**). Air flows at a rate F through the pipe and, we declare, easily through the thin wafer. Radon atoms emanate from the wafer source according to its activity A (in units of Bq) and are carried in the air through the pipe. The number of radon atoms N produced by the source in the time Δt , is

$$N = A\Delta t. \quad (7.64)$$

The volume of air passing through the wafer $V = F\Delta t$ (assuming the pressure is nearly the same everywhere). Therefore, the number of radon atoms exiting the pipe per volume is

$$\frac{N}{V} = \frac{A\Delta t}{F\Delta t} = \frac{A}{F}. \quad (7.65)$$

The radon concentration C (in units of Bq/m³) at the pipe outlet is

$$C = \frac{N/\tau}{V} = \frac{A}{F\tau}, \quad (7.66)$$

where the mean lifetime of radon $\tau = 5.52$ days. This expression makes the assumption that all radon atoms that are produced exit the wafer instantly (*i.e.*, none decay before exiting). For a small radon source, this assumption is very reasonable, as the time for an atom to diffuse out of the source material is typically much smaller than τ .

Similar to our imagined source wafer, the RRS carbon beds allow air to easily pass them. Furthermore, a carbon bed emanates radon atoms that may be carried by the air until they exit the column. However unlike the thin wafer source, radon atoms produced near the input side of a carbon bed might take many hours traveling with the air and spending significant time on the carbon's surface before exiting. Therefore, we must improve our estimate of the outlet radon concentration to capture this behavior.

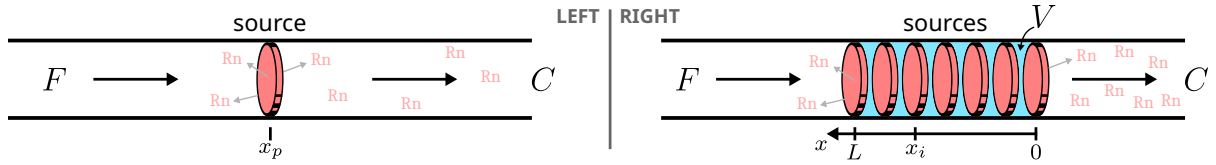


Figure 7.38: **Left:** Air flowing with rate F through a pipe passes through a thin wafer of material that emanates radon. These radon atoms are carried with the air and contribute to the radon concentration C at the pipe outlet. **Right:** Air flowing with rate F through a pipe passes through a column of porous material drawn here as many thin wafers. Each wafer emanates radon atoms that move more slowly through the wafers than through the open pipe. These radon atoms contribute to the radon concentration C at the pipe outlet, but in an amount dependent on the distance they traveled through the many-wafer column (where some decay before exiting). The air volume V within the porous column (the wafers) is small compared to the volume passing through the source $F\tau$, and may be safely ignored.

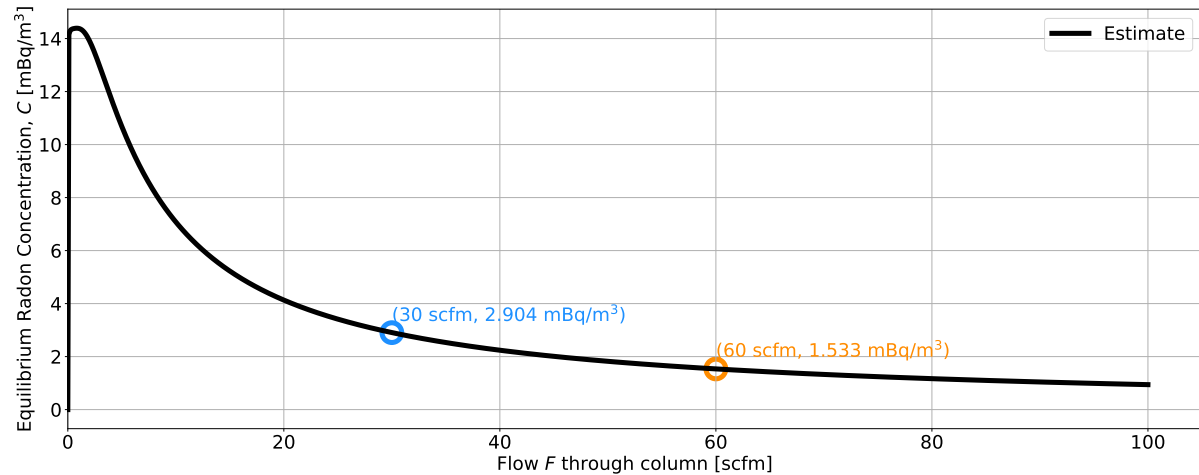


Figure 7.39: After flowing zero-radon air through a carbon bed for a time much greater than the break-through time (the average time for radon to pass through the column), the output radon concentration due *only* to radon emanating from the carbon bed (black curve) is estimated from Eq. 7.70. Numerical values of the radon concentration are printed explicitly for 30 and 60 scfm, as these will be referred to by Fig. 7.40.

Radon atoms move with a velocity v_{Rn} through the carbon bed proportional to air flow F (as described in Section 7.6). The time t a radon atom needs to pass through a distance Δx of a carbon bed is

$$t = \Delta x / v_{Rn}. \quad (7.67)$$

The expected fraction of atoms remaining after this time is

$$\frac{N(t)}{N_x} = \exp(-t/\tau), \quad (7.68)$$

where N_x was the initial number of radon atoms produced at the distance x within the carbon bed and $N(t)$ is the number of atoms at the time t . Figure 7.38: **right** illustrates the carbon bed as a series of thin source wafers, with the i 'th wafer at the distance x_i along the column axis. Radon atoms emanated from the source wafer at $x = 0$ need not travel through any carbon, as this is the outlet side of the carbon column. Radon atoms emanated from the source wafer at $x = L$ must travel through the entire length of the carbon bed, with some radon decaying along the way. We may estimate the radon concentration C at the outlet by adding up contributions from each infinitesimal wafer source along the column axis, yielding

$$C = \frac{1}{F\tau} \int_0^L \frac{A}{L} \exp\left(-\frac{x}{v_{Rn}\tau}\right) dx, \quad (7.69)$$

where A/L is the radon activity per length of the carbon (in Bq/cm). Solving the integral yields an improved estimate for the equilibrium radon concentration at the column outlet due *only* to radon emanating from the carbon bed:

$$C = \frac{Av_{Rn}}{FL} \left[1 - \exp\left(-\frac{L}{v_{Rn}\tau}\right) \right]. \quad (7.70)$$

For the SD Mines RRS carbon columns, the radon activity from emanation $A = A_{kg}M$, where the activity per kilogram $A_{kg} = 100 \text{ mBq/kg}$ and the mass of the carbon bed $M = 219 \text{ kg}$. The air volume within the carbon bed my be ignored because $V \ll F\tau$ (with $V = 0.44 \text{ m}^3$ and $F\tau = 13489 \text{ m}^3$ at $F = 60 \text{ scfm}$)². Figure 7.39 shows the result of this estimate for a practical domain of flow through a column for these parameters.

The simulation accounts for radon emanating from the carbon by adding the number of radon atoms emanated from the carbon per Δt and per Δx (*i.e.*, the simulation time and spatial step size):

$$N_{em} = \frac{A_{kg}M\tau\Delta x}{L} (1 - e^{-\Delta t/\tau}), \quad (7.71)$$

²If we did need to include the air volume V within the porous column source, the expression for the outlet radon concentration becomes: $C = \frac{1}{F\tau+V} \int_0^L \frac{A}{L} \exp\left(-\frac{x}{v_{Rn}\tau}\right) dx$.

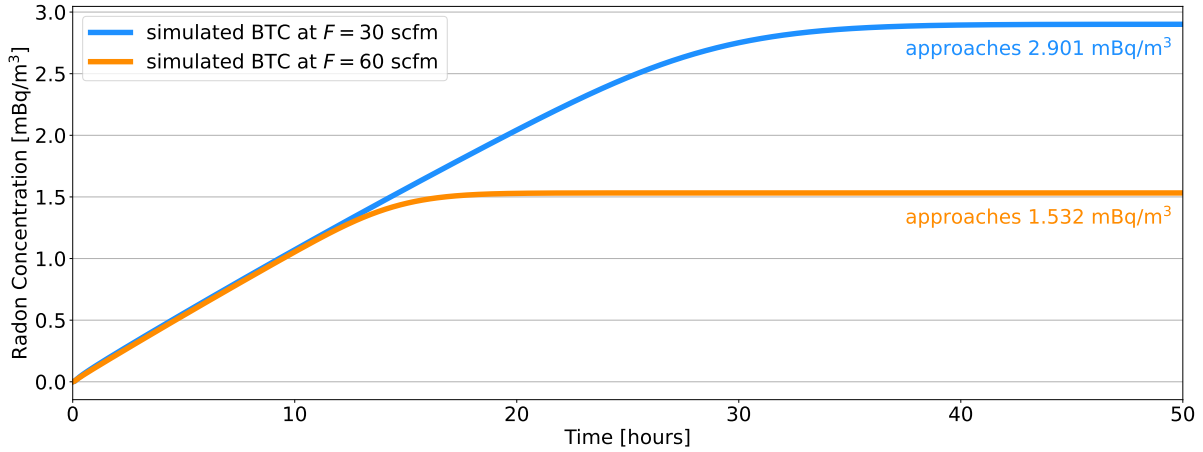


Figure 7.40: Break-through curves are simulated for flow rates of 30 and 60 scfm, but with the input radon concentration set to zero. The equilibrium output radon concentration predicted by the simulation agrees with the radon concentration predicted by Eq. 7.70. Specifically, at $F = 30$ scfm, the equilibrium radon concentration is simulated to be $2.901 \text{ mBq}/\text{m}^3$, which agrees very well with the estimated value of $2.904 \text{ mBq}/\text{m}^3$ from Eq. 7.70. Similarly, at $F = 60$ cfm, the simulation predicts $1.532 \text{ mBq}/\text{m}^3$ while the estimate predicts $1.533 \text{ mBq}/\text{m}^3$.

where L is the length of the carbon bed. This number of radon atoms is added for each Δt to the simulation column arrays (that keep track of how much radon is where, and introduced in Section 7.3) in the region that represents the carbon bed (not in the padded regions, introduced in Section 7.5).

To check the accuracy of the simulation for radon emanation, a column is made to initially have no radon atoms inside, and the input air is given a radon concentration of zero. The air flow through the column is set to either 30 or 60 scfm, and a BTC is simulated until equilibrium has been reached to obtain Fig. 7.40. The equilibrium radon concentration is then compared with the equilibrium radon concentration predicted by Fig. 7.39. This comparison shows that radon emanation from the carbon has been implemented in the simulation correctly. Of course, the calculation used in the simulation to treat radon emanation from the carbon is essentially the same as Eq. 7.70, but we may take comfort in observing that no oddities occur after implementation.

During the swing mode, radon emanates from the carbon and moves a distance $d = v_{Rn}t_F$, where v_{Rn} is the radon velocity and t_F is the duration of the filtering stage. Radon atoms emanating from a carbon bed of length L at location $x < L - d$ will not exit

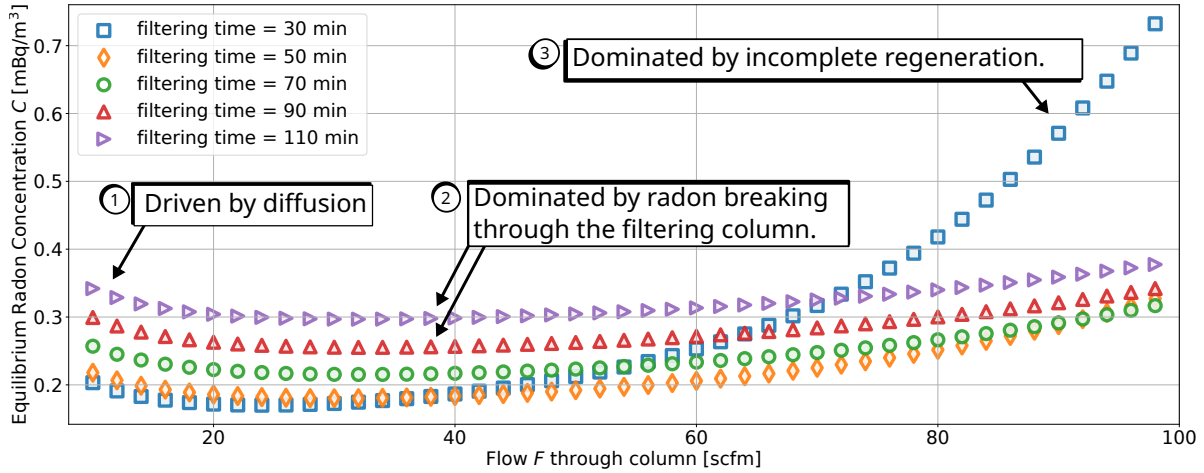


Figure 7.41: The equilibrium radon concentration is simulated versus air flow rate for several choices of filtering time (as indicated in the figure legend). These data were generated with the input radon concentration set to zero. Radon atoms are *only* created by the simulation according to emanation from the carbon beds. Outside of the flow and filtering time, all other simulation parameters (*e.g.*, purge flow or temperature during regeneration) are held constant. There are three features of interest (labeled by circled numbers) that are described in the paragraph that introduces this figure. For these predictions, the simulation was configured with a constant purge flow of 7.2 scfm and slowfill time $t_S = 15$ min.

the column during the filtering stage (with $x = 0$ being the input-side of the column). During the regeneration stage, these atoms may be purged from the column. Therefore, during the swing mode, we should expect a lower equilibrium radon concentration than for the BTC mode due to emanation alone.

Figure 7.41 shows the equilibrium radon concentration during swing mode versus air flow through a column. These data have been produced for several choices of filtering time t_F , but all with the slowfill time $t_S = 15$ min (and recall that $t_F = t_R + t_S$, where F, R, and S denote filtering, regenerating, and slowfill stages respectively). There appear to be three major features: ① at low flow ($F \lesssim 30$ scfm), the radon concentration appears to be dominated by radon diffusing out of the carbon bed (as determined by changing the diffusion coefficient used by the simulation—though not seen here), ② for larger filtering times, radon emanating from deeper within the carbon may escape during the filtering stage thus increasing the outlet radon concentration by the same proportion, and ③ at high flow ($F \gtrsim 40$ scfm) and small filtering time the radon concentration appears to be

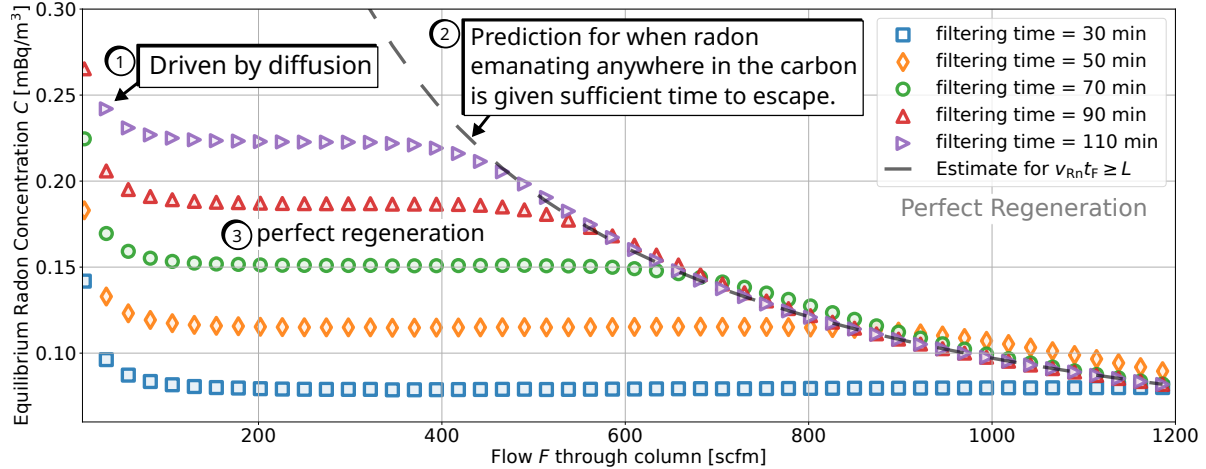


Figure 7.42: These equilibrium output radon concentration points (shapes) were generated similar to those in Fig. 7.41, but with the simulation set to perfect regeneration and over a larger flow domain. Equation 7.70 (gray, dashed line) shows the prediction of the equilibrium radon concentration when radon emanating anywhere in the carbon bed is given enough time t_F to escape, and thus goes like $1/F$. Curves with smaller, insufficient filtering time will overshoot the dashed-line prediction, but will eventually approach it when the flow is sufficiently higher (for example, see the green circles around $F = 1000$ scfm). There are three features of interest (labeled by circled numbers) that are described in the paragraph that introduces this figure. For these predictions, the simulation was configured with a constant purge flow of 7.2 scfm and slowfill time $t_S = 15$ min.

dominated by the incomplete regeneration of the regenerating column (where at higher flow, radon moves farther forward to the outlet of the filtering column so is less likely to be removed during the regeneration stage).

Figure 7.42 shows equilibrium output radon concentration (shapes) versus flow generated similar to those shown in Fig. 7.41, but with *perfect regeneration* (where the regeneration operator is a matrix of zeros) and for a larger domain of flow through the filtering column. These curves have three major features: ① the low-flow region has a tail that may be made smaller or larger depending on the size of the diffusion coefficient set in the simulation, ② when $v_{Rn}t_F > L$, radon emanating from even the input side of the column may escape the carbon bed (and thus further increasing the flow only reduces the outlet radon concentration, as described by Eq. 7.70), and ③ unlike Fig. 7.41, the perfect-regeneration operator has eliminated the increase in the outlet radon concentration when $F \gtrsim 40$ scfm.

7.11 Radon Distribution Within a Column After Break-through Curve Completion

During a break-through curve measurement (a long filtering stage), radon atoms move slowly through the carbon bed as compared to the air that carries them. For an input flow F and input radon concentration C_{in} , the total number of radon atoms that enter the column is

$$N_{\text{in}} = C_{\text{in}} \tau_{\text{Rn}} F \int_0^t dt', \quad (7.72)$$

where the radon mean lifetime $\tau_{\text{Rn}} = 5.52$ days and t is the time flowing. The output radon concentration C_{out} depends on time in that, initially, no radon leaves the column (if the column was initially free of radon). As time goes on, C_{out} increases according to the mean speed v_{Rn} of radon passing through the column of length L , described by the break-through time t_b , with $v_{\text{Rn}} = L/t_b$. The diffusion coefficient D is related to the standard deviation $\sigma = \sqrt{2Dt}$. When C_{in} has no time dependence (as will be presumed here), the output radon concentration has the form

$$C_{\text{out}}(t) = \frac{C_{\text{in}} e^{-t_b/\tau_{\text{Rn}}}}{2} \left[1 + \operatorname{erf} \left(\frac{v_{\text{Rn}} t - L}{\sqrt{4Dt}} \right) \right], \quad (7.73)$$

as described in Section 7.4.1. Similarly, the total number of radon atoms that exit the column is

$$N_{\text{out}} = \frac{C_{\text{in}} \tau_{\text{Rn}} F e^{-t_b/\tau_{\text{Rn}}}}{2} \int_0^t \left[1 + \operatorname{erf} \left(\frac{v_{\text{Rn}} t' - L}{\sqrt{4Dt'}} \right) \right] dt'. \quad (7.74)$$

So that it is easier to interpret the following estimates, we will henceforth ignore radon decay, as its effect is small when $t_b \ll \tau_{\text{Rn}}$, so $e^{-t_b/\tau_{\text{Rn}}} \approx 1$. As a practical convenience, the total number of atoms leaving the column N_{out} is calculated discretely

$$N_{\text{out}}(n) = \frac{C_{\text{in}} \tau_{\text{Rn}} F}{2} \sum_{i=0}^n \left[1 + \operatorname{erf} \left(\frac{v_{\text{Rn}} t_i - L}{\sqrt{4Dt_i}} \right) \right] \Delta t, \quad (7.75)$$

where $t = n\Delta t$. The number of radon atoms that stay within a carbon column during a BTC run (a long filtering stage) is

$$N_{\text{added}} \equiv N_{\text{in}} - N_{\text{out}}. \quad (7.76)$$

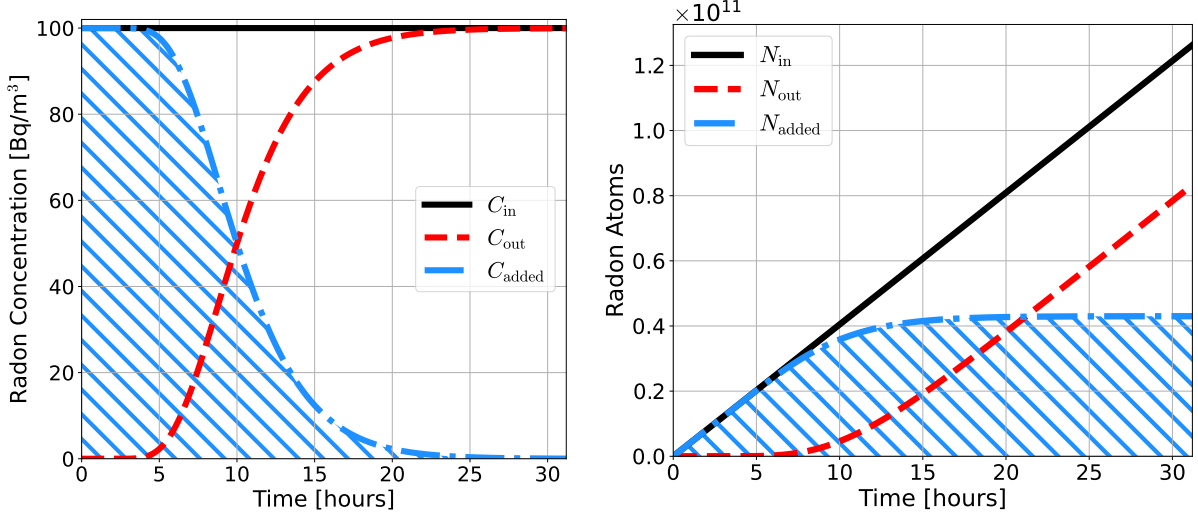


Figure 7.43: **Left:** The radon concentration of the input air C_{in} (black curve) slowly moves through the carbon column and exits, denoted by C_{out} , with the form of an S-curve (dashed red curve). The radon concentration added to the column $C_{added} = C_{in} - C_{out}$ (blue dot-dashed curve with hatching). **Right:** After converting radon concentration to radon atoms, every atom is counted entering the column as N_{in} (black curve) and exiting the column N_{out} (dashed red curve). The radon atoms N_{added} within the column increases with time until the number of atoms entering the column equals the number exiting (blue dot-dashed curve with hatching).

Combining Eq. 7.72, Eq. 7.74 and Eq. 7.76 indicates the total radon atoms remaining within a column may be expressed as

$$N_{\text{added}}(t) = C_{\text{in}} \tau_{\text{Rn}} F \int_0^t \left(1 - \frac{1}{2} \left[1 + \operatorname{erf} \left(\frac{v_{\text{Rn}} t' - L}{\sqrt{4 D t'}} \right) \right] \right) dt' \quad (7.77)$$

and discretely as

$$N_{\text{added}}(n) = \frac{C_{\text{in}} \tau_{\text{Rn}} F}{2} \sum_{i=0}^n \left[1 - \operatorname{erf} \left(\frac{v_{\text{Rn}} t_i - L}{\sqrt{4 D t_i}} \right) \right] \Delta t. \quad (7.78)$$

Figure 7.43 illustrates that for an input flow $F = 50 \text{ scfm}$ and input radon concentration $C = 100 \text{ Bq/m}^3$, we estimate that $N_{\text{added}} \approx 43$ billion radon atoms with $N_{\text{added}} \approx 8.6 \times 10^6 C_{\text{in}} F$ (where the units of F are scfm and time is long compared to t_b). For this example, the break-through time $t_b = 10$ hours and the diffusion coefficient $D = 0.025 \text{ cm}^2/\text{s}$.

After completing a BTC run, allowing for sufficient time to reach equilibrium (where the output concentration is not changing with time), the distribution of radon along the longitudinal axis of the column primarily depends on the radon decay rate. At

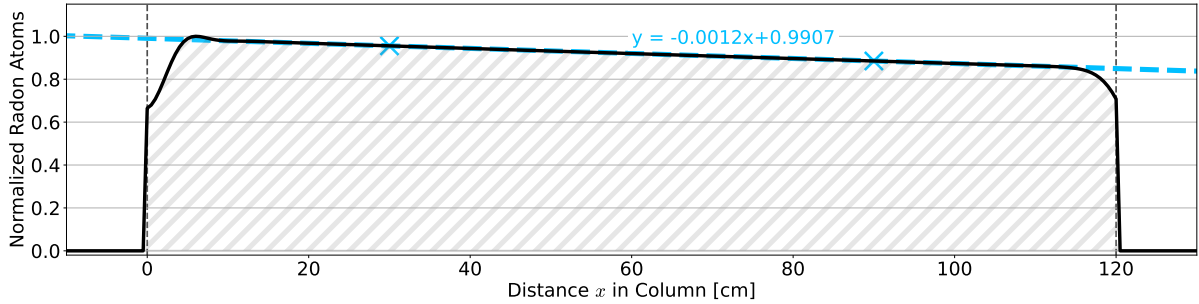


Figure 7.44: The distribution of radon in a column after a BTC has completed (black curves with hatching) has been normalized by its maximum value. A line drawn along the top of the distribution (blue dashed curve) is determined algebraically from the two points denoted by \times 's, far enough away from the edges that edge effects from diffusion can be neglected; the line's equation is provided in the typical way: $y = mx + b$, where the slope $m = -0.0012$ atoms/cm and the offset $b = 0.9907$ atoms.

equilibrium, the radon atoms at a location x along the column axis will have traveled for a time x/v_{Rn} , where v_{Rn} is the radon velocity. Therefore, the fraction of radon atoms expected to decay depends on the location x :

$$\frac{N(x)}{N(0)} = \exp\left(-\frac{x/v_{\text{Rn}}}{\tau}\right) \approx 1 - \frac{x}{v_{\text{Rn}}\tau}, \quad (7.79)$$

where $N(x)$ is the number of radon atoms at the location x , $N(0)$ is the number of radon atoms at the column input ($x = 0$ cm), the radon mean lifetime is τ , and we have used the fact that $x/v_{\text{Rn}} \ll \tau$ for a reasonable flow domain. Therefore, the radon distribution along the column axis is expected to have a shape that is approximately linear, with its negative slope inversely proportional to v_{Rn} .

Figure 7.44 shows the radon distribution produced by simulating a BTC at $F = 50$ scfm for 120 hours (long enough so that equilibrium is ensured). A linear function, represented by a dashed line, is determined algebraically by two points in the distribution: one at $x = 30$ cm and another at $x = 90$ cm, with locations illustrated by \times 's. While much of the middle of the distribution is linear, the distribution shape near the edges (at 0 and 120 cm) is strongly influenced by radon diffusing out of the “physical” column (between 0 and 120 cm) and into the padded regions (everywhere else) where it is counted and deleted by the simulation; therefore, the deviation from linearity at the edges reflects how the simulation functions, not what is expected in reality.

Upon performing the same routine over the flow domain from 20 to 120 scfm, the inferred slopes of each equilibrium radon distribution are estimated (by the aforementioned two-point, line-creation protocol). The left side of Fig. 7.45 shows that the inferred slopes closely match the expected trend:

$$m \approx -\frac{1/v_{Rn}}{\tau} \propto 1/F, \quad (7.80)$$

where we recall that $v_{Rn} \propto F$ (approximately). The proportionality constant may be calculated explicitly according to simulation parameters, but here it is estimated by demanding that the trend pass through the inferred slope at 60 scfm (far from the ends of the flow domain).

The right side of Fig. 7.45 shows how the total number of atoms within a column changes with through-column flow. For $F \leq 40$ scfm, the amount of radon in the column appears dominated by the fraction of atoms that decay in the column, which increases for decreasing flow. Above 40 scfm, the dominant effect is from the fact that the radon velocity v_{Rn} and diffusion coefficient depend quadratically on the air speed v_{air} (see Sec-

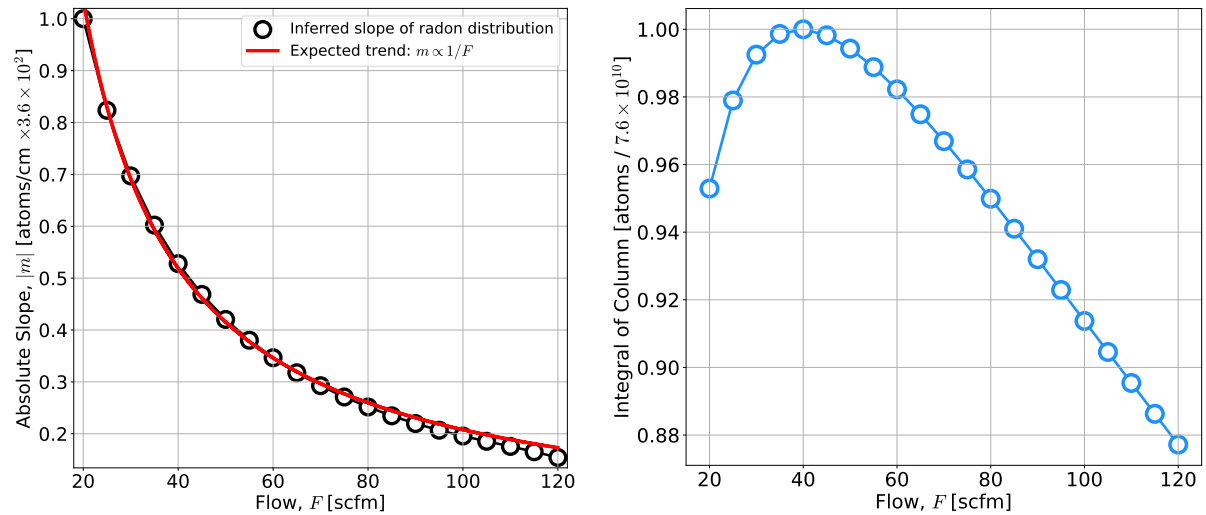


Figure 7.45: Left: The inferred slope from the simulated radon distribution within a column after BTC completion (black circles) is shown to decrease approximately as $1/F$ with increasing flow F , as expected from radon decaying during travel (red curve). **Right:** The total radon within a column is largest at 40 scfm. For lower flows, radon decay dominates, resulting in less radon within the column for decreasing flow. For higher flows, the quadratic form of the radon velocity and diffusion coefficient result in radon exiting the column at an increasing fraction with increasing flow F .

tion 7.13.3); this results in radon exiting the filtering column more quickly (with a larger fraction of the air speed) for increasing flow, thus reducing the total number of radon atoms within the column, as compared with the number expected for a linear dependence (*i.e.*, $v_{Rn} \propto v_{air}$).

When the input radon changes, of course, the radon distribution within the column can vary greatly from the linear approximation. While the initial radon distribution within the column is expected to influence the output radon concentration at early times for both BTC and RC simulations, only a flat initial distribution has been employed in the simulation. Measured BTC data can provide a strong indication of whether the BTC column was initially fully regenerated (containing essentially no radon), allowing the initial column state to then be set (to zero) for the BTC simulation (see Section 7.13.1). While simulating an RC, the flat distribution is simply scaled such that the simulated and measured output concentration during the first filtering stage match (as discussed in Section 7.13.4). This simplification of the initial column state is for two reasons: (1) the initial column state during swing mode is not expected to influence the RC equilibrium and (2) sufficient data is often not available to simulate the state of a column (and even less so both columns) just prior to the start of a simulated run of interest (such as an RC run).

7.12 Checking Simulation Consistency by Counting Atoms

This section describes work conducted in validating the Radon-Reduction System (RRS) simulation. The simulation is passed measured or user-defined inputs (for example, the input radon concentration and flow rate) and produces a predicted output radon concentration as a function of time. Similar to the physical RRS, the simulation may be configured to operate in break-through curve (BTC) or swing mode (see Section 7.4 for their descriptions), with a variety of parameter configurations (*e.g.*, the duration of the filtering stage or the purge-flow rate). Simulation predictions may then be compared to measurements made in the lab in order to test how well the simulation works.

It is convenient to the end user for simulation parameters (such as column length, flow rate, or input radon concentration) and deliverables (such as the output radon concentration) to have human-friendly units, such as centimeters, cfm, or Bq/m³. However, the simulation is internally parametrized in terms of the simulation step sizes Δt (in seconds) Δx (in centimeters), and radon atoms (along with a few other parameters, such as temperature in degrees Kelvin). Simulation development, therefore, is primarily concerned with the creation, destruction, and evolution of radon atoms over one-dimensional space and time.

On a qualitative level, much is gained by simulation sanity checks, such as passing the simulation an oscillatory input concentration and checking that the predicted output agrees with expectation, as discussed in Section 7.4.1. Another way to check whether the simulation is functioning as desired is to count all of the radon atoms created by the simulation and keep track of them until they are destroyed. This test of logical consistency allows us to find bugs (*i.e.*, physically-impossible program logic or incorrect physics descriptions) and correct them. Because the simulation is performed in a discrete, finite space and uses numerical approximations of, for example, the error function, we may expect some losses related to precision and rounding; this type of test provides an important statement on the simulation precision in terms of losses and gains of radon atoms over time.

The first task in validating the RRS simulation is to ensure atoms are not being created or destroyed without explicit intention from the user. Radon atoms should be “created” by the simulation under the following circumstances:

1. when radon is introduced at the RRS input according to the radon concentration and volumetric flow rate of the input source (*e.g.*, lab air),
2. when radon emanates from the activated carbon within each column (which has an emanation rate of ~ 100 mBq/kg),

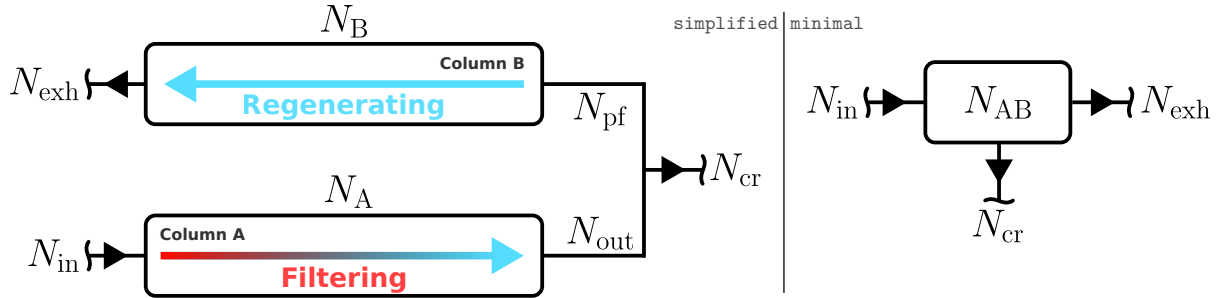


Figure 7.46: Left: Simplified Radon-Reduction System diagram emphasizing the number of atoms entering (N_{in}), exiting (N_{exh} and N_{cr}), staying within the system (N_A and N_B), and passing a checkpoint, so to speak, within the system (N_{out} and N_{pf}). Right: Minimal diagram illustrating the radon atoms entering, exiting, and staying within the system (N_{AB}).

3. when radon is introduced for exploratory reasons. For example, one may presume that there is a leak in the purge-flow plumbing and would like to see how it may influence simulation predictions.

Though radon atoms should not be destroyed unintentionally, they should be “destroyed” in well-defined circumstances:

1. when radon is exhausted by the vacuum system during the regeneration stage,
2. when radon within the system decays according to its mean lifetime.

Here, we count every atom entering or exiting the simulated system and determine if there is an excess or a loss. The number of radon atoms that enter the simulation per Δt is:

$$N_{in} = CF\Delta t\tau, \quad (7.81)$$

where C is the radon decay rate per volume (in Bq/m^3), the input air has volumetric flow rate F , the simulation time step is Δt , and the radon mean lifetime $\tau = 5.52$ days. Once we have N_{in} , the simulation will propagate these atoms according to physics descriptions.

For the rest of this section, the simulation will be run with the following configuration: through-column air flow $F = 90 \text{ scfm}$, input radon concentration $C = 100 \text{ Bq}/\text{m}^3$, purge flow $f_{\text{purge}} = 7 \text{ scfm}$, both columns initially contain radon (as if one just finished

flowing high-radon air through the columns), the filtering stage duration is 60 min (with regeneration and slowfill stages lasting 45 and 15 minutes respectively), and the simulation step sizes $\Delta t = 5$ min and $\Delta x = 0.5$ cm respectively. Radon decay and radon emanation from the carbon will be turned OFF within the simulation; this way, we need not disentangle their respective losses and gains from other causes (as both radon decay and radon emanation have been studied in Section 7.10).

Radon atoms are counted at different locations within the simulation's representation of the SD Mines RRS, as illustrated by Fig. 7.46. The radon atoms N_{in} are introduced to the sim at each time step Δt ; they then pass through the filtering column with perhaps some exciting and counted at the column's output as N_{out} . Any atoms that remain in the column are represented as N_A . From here (N_{out}), some of these atoms (about 10%) move to the regenerating column within the purge-flow air stream and are counted as N_{pf} . The remainder, in this example, pass to a low-radon cleanroom and are counted as N_{cr} . The purge-flow atoms N_{pf} pass through the regenerating column with ones exhausted counted as N_{exh} . Similar to as we had before, any atoms remaining in the regeneration column are represented as N_B . Because we have set radon decay and radon emanation from the carbon to OFF in the sim for this analysis, the following relation holds:

$$N_{\text{in}} = \Delta N_{AB} + N_{\text{exh}} + N_{\text{cr}}, \quad (7.82)$$

where the change in the sum of all atoms in both column $\Delta N_{AB} \equiv \Delta N_{AB}(t) = N_{AB}(t) - N_{AB}(t-\Delta t)$ and Δt is the simulation time step. The time $t \in [0, \Delta t, 2\Delta t, \dots, n\Delta t]$, where n is determined by the end user, perhaps by an equilibrium condition on the output radon concentration being met.

Figure 7.47 shows the number of radon atoms (or their change over one Δt) at each location illustrated by right side of Fig. 7.46 and also the change in the number of atoms in columns A and B. During the slowfill stages (shown by the hatched regions), it appears that the the value of, for example, ΔN_B is equal to zero, but this is not the case. The values of the three 5 minute bins between 0.75 and 1 hour (the slowfill stage of column

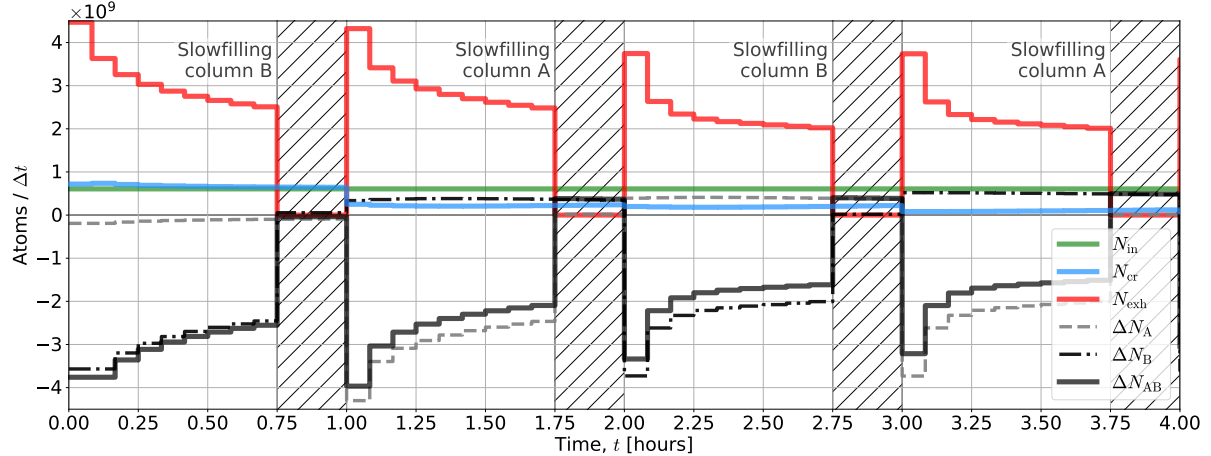


Figure 7.47: The number of atoms introduced at time t to the RRS simulation per Δt is $N_{in}(t)$ (green solid curve). Similarly, the atoms passed to the cleanroom or exhausted (therefore exiting the simulated system) is shown by the blue and red curves respectively. The change in the number of atoms within each column is represented by ΔN_A (dashed curve) and ΔN_B (dot-dashed curve), for columns A and B respectively. The total change in atoms between both columns is denoted as ΔN_{AB} (solid black curve). The slowfill stage of each column is represented by black, right-hatched regions.

B) are: 6.28×10^8 , 6.26×10^8 , and 6.24×10^8 . As expected, the change in atoms during slowfill is positive, as atoms are being supplied by the purge-flow line. At equilibrium these same bins have values of 1.39×10^8 , 1.48×10^8 , and 1.55×10^8 , showing an increasing trend as radon slowly breaks through the filtering column and is then in part passed to the slowfill column. The change in radon atoms introduced to the slowfill column should in fact become smaller as the slowfill column approaches atmospheric pressure; however because the purge flow f_{purge} only begins to reduce from its set value when the pressure drop over the purge-flow valve becomes less than about 10 Torr, this effect is expected to be negligible. The additional radon atoms passed to the slowfill column during the last (five-minute) operation accounts for only a small fractional excess in radon, and therefore this nonphysical effect is left uncorrected.

Figure 7.48 again shows the number of radon atoms (or their change over one Δt) at each location illustrated by Fig. 7.46: **Right**, but over a larger time scale, where a few trends become apparent. The number of atoms being passed to the cleanroom (blue curve) is reducing over time (but only clearly seen until maybe 8 hours in). Similarly,

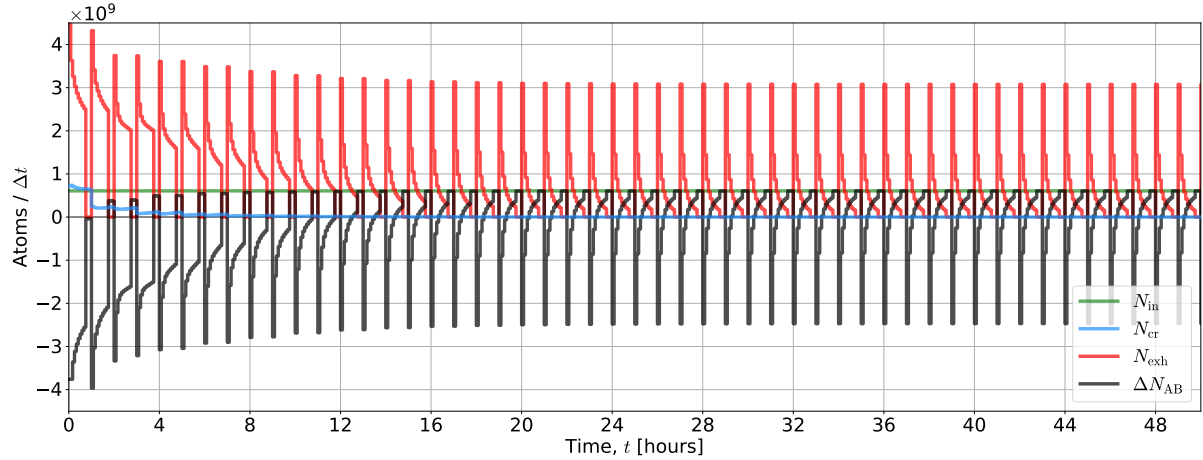


Figure 7.48: Similar to Fig. 7.47, but on a larger time scale (and excluding the curves representing N_A and N_B). The number of radon atoms (black curve) in the columns can be seen to reduce, with the number of radon atoms exhausted (red curve) or entering the cleanroom (blue curve) following the same trend. A steady-state condition is reached at about 50 hours (which may be seen more clearly in Fig. 7.50).

the number of radon atoms being exhausted per hour (red curve) is reducing as the total number of atoms in both columns reduces, as indicated by ΔN_{AB} coming closer to zero. After 40 hours or so, we see only sharp negative peaks in ΔN_{AB} , complemented by sharp positive peaks in N_{exh} , representing the relatively quick regeneration of the column, where radon is primarily concentrated at the input side (which is the low-pressure pump side during regeneration).

Figure 7.49 again shows the same quantities as in Fig. 7.47, but at equilibrium (between 50 and 54 hours). The first thing to notice is that each two-hour period appears identical. As a check on equilibrium, we may compare the integrals of radon atoms per hour during filtering (F) and the following regeneration and slowfill (RS) stages, where

$$I_F = \int_{51}^{52} \Delta N_B dt \quad \text{and} \quad I_{RS} = \int_{52}^{53} \Delta N_B dt. \quad (7.83)$$

At equilibrium, the change in the number of radon atoms in the filtering column is equal to the negative change in radon atoms in the regenerating column (when the same column used for filtering is regenerated one half cycle later). Therefore, to determine how close we are to equilibrium at 53 hours (rounding to the next filtering stage), we compute: $(I_F + I_{RS})/I_F = -7.0 \times 10^{-5}$. As expected, the sign is negative (because we are slowly

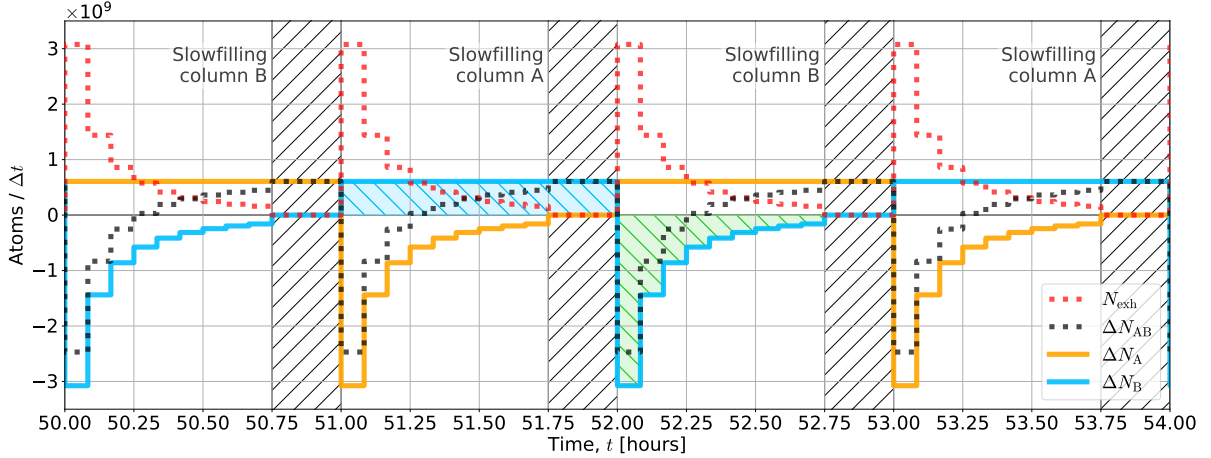


Figure 7.49: Similar to Fig. 7.47, but at late time (between 50 and 54 hours) and excluding N_{in} and N_{cr} , as they are both constants at this time. The colors and line styles have been changed to emphasize ΔN_A (orange) and ΔN_B (blue), while N_{exh} (red dotted curve) and ΔB_{AB} (black dotted curve) have been de-emphasized. Equilibrium is checked by comparing the integral of the atoms per hour during the filtering stage (blue, left-hatched region) with the atoms per hour during the following regeneration and slowfill stages (green left-hatched region).

removing more atoms during regeneration than we are adding during filtering) and the absolute value of the number is much less than unity, indicating that we are close to equilibrium. Performing this check earlier at 41 hours, yields -6.1×10^{-4} , while much later at 73 hours yields -9.3×10^{-7} .

Similarly, the number of radon atoms exiting the filtering column

$$N_{\text{out}} \equiv N_{\text{cr}} + N_{\text{pf}}, \quad (7.84)$$

where the fraction of atoms that pass to the regenerating column is determined by the ratio of air flow through the filtering column and through the purge-flow line f_{purge}/F , which in this example is $7/90 \approx 0.08$; therefore, the remaining $(1 - 7/90) \times 100 = 92\%$ of the radon atoms are passed to the cleanroom.

Figure 7.50 shows N_{out} , N_{cr} , and N_{pf} for the same swing-mode example we have been exploring. As expected in a semi-log plot, the curve representing the number of radon atoms per hour exiting the filtering column N_{out} appears almost on top of the curve representing the atoms passing to the cleanroom N_{cr} . After about 50 hours, a steady state is nearly reached, where the number of atoms entering the regenerating column via

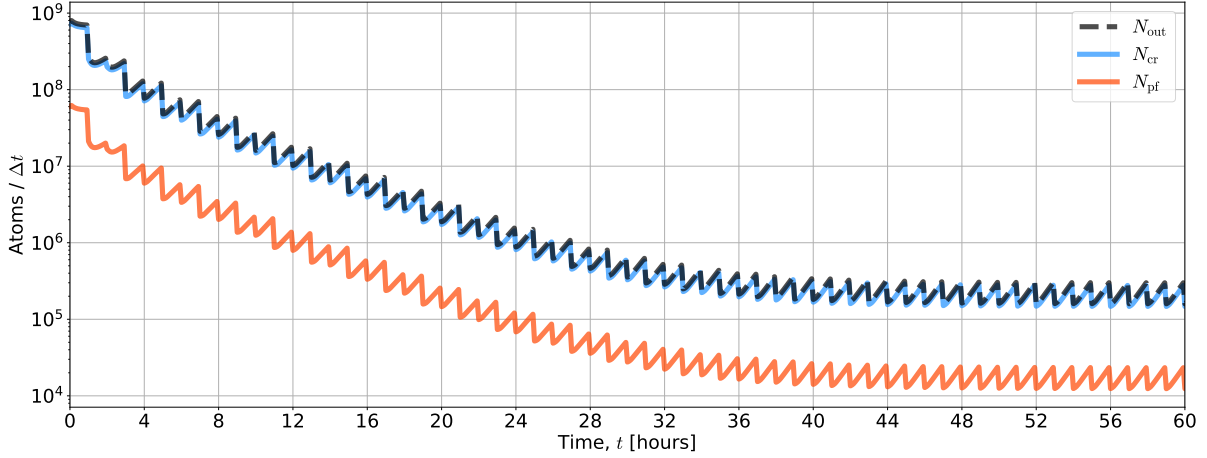


Figure 7.50: At time $t = 0$, both columns contain radon. During the filtering stage, all radon passing out of the filtering column N_{out} (black dashed curve) then passes to either the cleanroom N_{cr} (blue curve) or the regenerating column via the purge-flow N_{pf} (orange curve). In this example, the fraction that passes to the cleanroom is about 0.92 of the all radon atom that left the filtering column. A steady-state condition appears to be reached at around 50 hours.

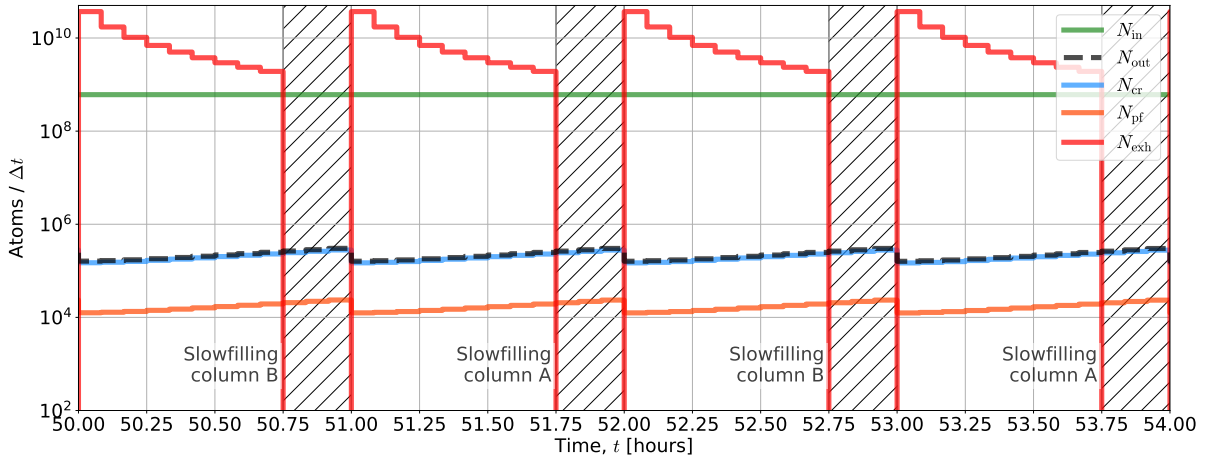


Figure 7.51: Similar to Fig. 7.50, but at late time near equilibrium (between 50 and 54). Also included is the number of radon atoms per Δt exhausted by the vacuum pumps during the regeneration stage (red curve) which may be compared to those introduced to the filtering column N_{in} (green curve), a constant rate in this example of 6.1×10^8 atoms per Δt . The slowfill stage of each column is represented by black, right-hatched regions.

the purge-flow line N_{pf} approaches its minimum (along with the other two curves). At this time, the number of radon atoms purged during the regeneration stage is dominated not by those entering the column via the purge-flow line N_{pf} , but the atoms from the input air passing into the filtering column and not passing completely through it (as seen in Fig. 7.51).

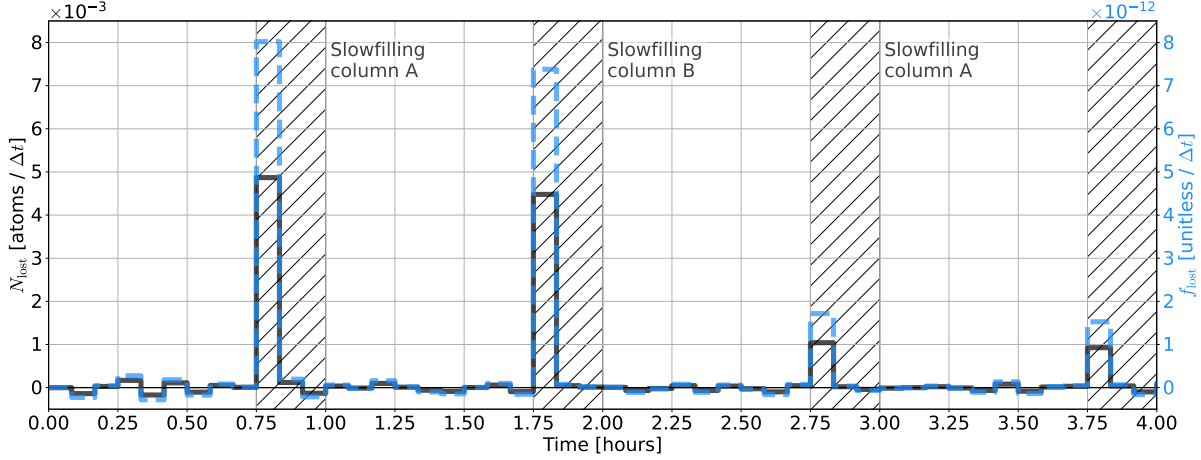


Figure 7.52: **Left axis:** The number of radon atoms lost per $\Delta t = 5 \text{ min}$ during typical swing operation, as defined by Eq. 7.87. **Right axis:** the fraction of radon atoms lost per Δt , as defined by Eq. 7.88. The slowfill stage of each column is represented by black, right-hatched regions. The initial radon placed in each column produces a huge change (order 10^{10}) in ΔN_{AB} over the first Δt and has been excluded from this plot.

If we require that all atoms are conserved at any time t (as we expect in this example), we may write the expression:

$$0 = N_{\text{in}}(t) - \Delta N_A(t) - \Delta N_B(t) - N_{\text{exh}}(t) - N_{\text{cr}}(t) \quad (7.85)$$

$$= N_{\text{in}}(t) - \Delta N_{AB}(t) - N_{\text{exh}}(t) - N_{\text{cr}}(t), \quad (7.86)$$

If the LHS of Eq. 7.86 is greater than zero, atoms are being unintentionally created somewhere; while if its less than zero, atoms are being unintentionally destroyed. Therefore, we make the definition of the atoms lost per Δt

$$N_{\text{lost}} \equiv N_{\text{in}}(t) - \Delta N_{AB}(t) - N_{\text{exh}}(t) - N_{\text{cr}}(t), \quad (7.87)$$

where N_{lost} is defined as the RHS of Eq. 7.86. The fractional loss of atoms per Δt may be expressed as the ratio

$$f_{\text{lost}} \equiv \frac{N_{\text{in}}(t)}{\Delta N_{AB}(t) + N_{\text{exh}}(t) + N_{\text{cr}}(t)} - 1. \quad (7.88)$$

Figure 7.52 shows N_{lost} and f_{lost} for this swing-mode example. Before one Δt , there is a change in radon in the columns equal to the radon that we initially gave them (a huge amount); however, because this change does not represent an unintentional loss or gain

of atoms, it has been excluded from this plot. From one Δt onward, we see no larger loss or gain than about 4/1000 atoms per Δt (or slightly more than 1 atom per day). This plot also shows that, particularly at early times when there is still lots of radon in the column from the initialization, atoms are primarily lost at the start of the slowfill stage. This is likely caused by the boundary control method used to ensure radon does not escape the rear (pump-side) end of the slowfill column, and is being exacerbated by the large amount of radon in the column. The discrepancy is about 10^8 times too small to be a simple indexing issue, but could be due to a rounding error at the tail end of the radon distribution that is put back into the slowfill column. Because this discrepancy is so small, its cause will not be further pursued.

From this analysis of counting atoms during swing mode (which uses each stage type), we find that the number of atoms lost or gained is roughly consistent with the expected computer precision. In Python, floating point arithmetic values appear to be rounded to the 17th decimal place [151]. Therefore, we may expect that the order 10^{10} atoms evolved per Δt by a square matrix with size ~ 1000 may suffer a loss or gain of 0.0001 atoms/ Δt . Here, we are seeing about 30 times this number. Along with a possible coding issue during the slowfill stage, it may be presumed that the many additional lines of calculation within the simulation contribute to larger discrepancies. In any case, the inferred gain or loss of ~ 1 atom per day is a very small fraction of nominal 10^8 radon atoms that enter the simulated RRS per minute and represents an uncertainty that is dwarfed by those of any radon detector currently being used for these measurements.

We therefore expect that disagreement between the simulation and measured data is dominated by, at best, statistical or systematic uncertainties in measured data and, at worst, insufficient descriptions of the relevant physics used by the simulation to make predictions; somewhere between these two, lives programming bugs. The following sections test simulation predictions against measured data for the purpose of constraining some

simulation parameters and providing a statement on simulation accuracy in modeling a physical Radon Reduction System.

7.13 Determination of Simulation Parameters

A simulation parameter that is considered to be exactly known would be, for example, the length of the carbon column or the mass of the carbon. Simulation parameters that cannot be directly (or easily) measured are considered unknown, such as the adsorption factor. Although we might have some educated guess of their value, these unknown parameters are found empirically by comparing simulation predictions (that rely upon perhaps a theoretical model of the unknown parameter) to measured data.

For example, a model describing the diffusion coefficient of radon during the filtering mode is determined by comparing the simulated BTC predictions to corresponding BTC measurements. The diffusion model is then extended to the domain of the regeneration or slowfill stages, where it is more difficult to directly measure the diffusion coefficient. If all relevant influences of radon diffusion are captured by the diffusion model, simulation prediction may agree well with measurement (providing that no other simulation issue undermines the predictions). If the model isn't sufficiently descriptive of the relevant physics, it is improved.

We may describe a model of the diffusion coefficient as a function of other parameters (such as air flow or temperature) and then have the simulation make predictions that are compared to data, thus allowing the model coefficients to be inferred. Next, we use knowledge gained during the filtering stage to predict the radon diffusion coefficient during regeneration (where the pressure, for example, is very different). If our model captures everything important, the simulation predictions will agree with data, and we might stop here. However, often is the case that the model isn't completely descriptive and additional parameter freedom may be needed (or even modified model).

Starting in Section 7.13.1, simulated break-through curves (BTCs) are compared with those measured in order to determine the diffusion and adsorption factors during

the filtering stage, resulting in a functional model for each parameter. Extending these models to the regeneration and slowfill stages, the simulation is run in swing mode to produce regeneration curves (RCs) that are compared to those measured (see Section 7.13.4). At this point, these models may be modified to capture important influences of, for example, the lower pressure during the regeneration stage—or a different (but probably similar) model may need crafted.

7.13.1 Break-through Curves: Simulation versus Measurement

An important validation data set is a break-through curve (BTC). A BTC is performed by flowing high-radon air through a carbon column, having very little radon already in it, and measuring the radon activity of the air coming out the other end. Spending time adsorbed to the carbon surface, radon atoms will move more slowly through the carbon bed than the air does. The measured outlet radon concentration will initially be close to zero, with only radon that was not fully purged from the column, or that emanates from the carbon, escaping. Radon will eventually pass from the inlet to the outlet of the column in the break-through time

$$t_b = L/v_{Rn}, \quad (7.89)$$

where L is the column length and v_{Rn} is the radon speed described in Section 7.6. Because radon atoms diffuse, particularly in the axial direction when flow is non-zero, the outlet radon concentration measured has the form of a sigmoid (see Section 7.4.1) [94]. After approximately $2t_b$ the outlet radon concentration will be equal to the input concentration—but reduced by the fraction of radon that has decayed over t_b .

There are two ways of crudely estimating the break-through time: (1) the input measurement may be shifted until features, such as peaks for example, line up or (2) the input measurement may be shifted until the break-through time is sufficient to reduce the input concentration to the value of the output concentration (useful for particularly time-independent input radon concentrations). The weakness of either of these methods

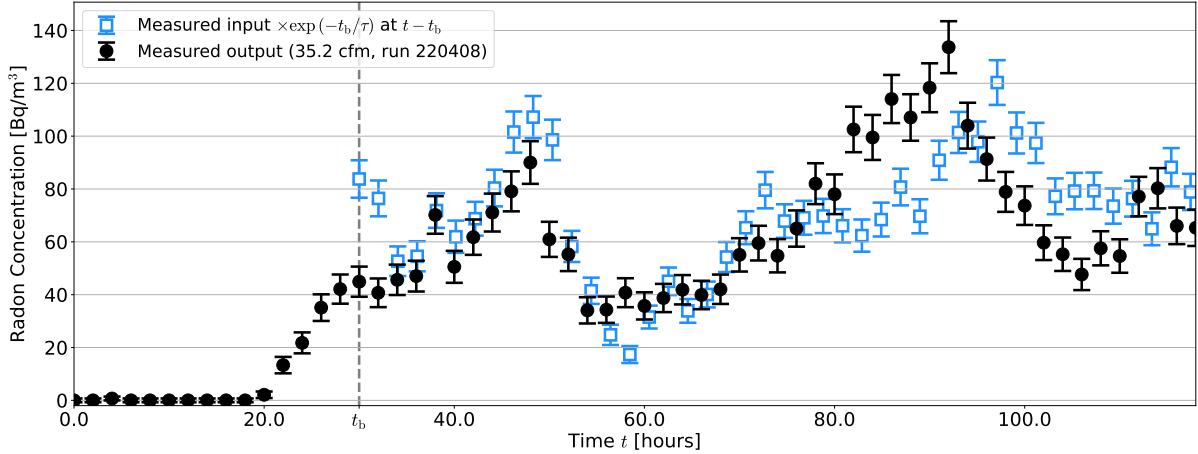


Figure 7.53: High-radon input air sampled from the SD Mines lab space (blue squares) is supplied at 35.2 cfm to the inlet of a newly-purged carbon column. The radon concentration at the column outlet (black circles) is consistent with the device background for almost 20 hours before radon is observed breaking through the column. Informed by shared features of the inlet and outlet radon concentrations, the inlet radon concentration is shifted by an estimate of the break-through time $t_b = 29$ hours (gray dashed line) since start of flow and multiplied by $\exp(-t_b/\tau)$, where τ is the radon mean lifetime, to account for radon decay. These data have been resampled in 2 hours binning.

is that they may fail, for example, if the temperature has a strong time dependence, which may move or flatten a peak. Figure 7.53 shows an example of a measured BTC. The measured input radon concentration has been shifted (to the vertical dashed line) by an estimate of the break-through time ($t_b = 29$ hours) obtained by comparing the peaks and amplitude of the input and output radon concentrations (as the output should be reduced by a fraction due to radon decay).

For the purpose of determining simulation parameters, we want to learn how quickly radon moves through the column (which relates to the break-through time) and how much radon diffuses per unit time. As shown in Section 7.6 and Section 7.7, the radon velocity has the form

$$v_{\text{Rn}} = f_A v_{\text{air}} \exp \left[-\frac{T_\circ}{T(t, x)} \right], \quad (7.90)$$

and the diffusion coefficient has the form

$$D = f_D \exp \left[-\frac{T_\circ}{T(t, x)} \right] \frac{P_{\text{atm}}}{P(t, x)}, \quad (7.91)$$

where f_A and f_D are presumed to depend on the air speed v . However for this discussion, we look at a single BTC at a constant flow, and therefore both f_A and f_D are considered constant. During a BTC measurement, the pressure ratio $P_{\text{atm}}/P(t, x) \approx 1$.

When comparing a simulated BTC to a measured BTC, a goodness-of-fit is provided using the χ^2 -test along with its corresponding p-value. For the χ^2 -test, we evaluate

$$\chi^2 \equiv \sum_i \frac{(y_i - s_i)^2}{\sigma_i^2}, \quad (7.92)$$

where y is an array indexed by i representing the measured BTC (*i.e.*, the output radon concentration) with measured uncertainty of σ , and s is the radon concentration of the simulated BTC [152]. The p-value (a one-sided tail test) is determined by evaluating the cumulative χ^2 distribution as

$$p \equiv 1 - \frac{1}{\Gamma(\nu/2)} \gamma\left(\frac{\nu}{2}, \frac{x}{2}\right), \quad (7.93)$$

where Γ is the gamma function and γ is the lower incomplete gamma function [153, 154, 155]. The location x is our calculated χ^2 and the shape factor ν is the number of degrees of freedom

$$\nu = n - n_p, \quad (7.94)$$

where n is the number of data, and the number of free parameters $n_p = 2$ [152, 155]. In Python, the p-value can be calculated by the lines:

```
1 from scipy import stats
2 p = 1 - stats.chi2.cdf(chisquared, len(y)-n_p) # p-value
```

where `chisquared` is the calculated χ^2 from Eq. 7.92. With this definition, a p-value close to unity is too-good of a fit, close to zero is a bad fit, and above about 0.1 the null hypothesis cannot be rejected.

Figure 7.54 shows that simulated output radon concentration (green) with the input radon concentration set to a constant value equal to the average of the measured input and the flow set to the measured flow of 35.2 cfm. The simulated BTC shows poor

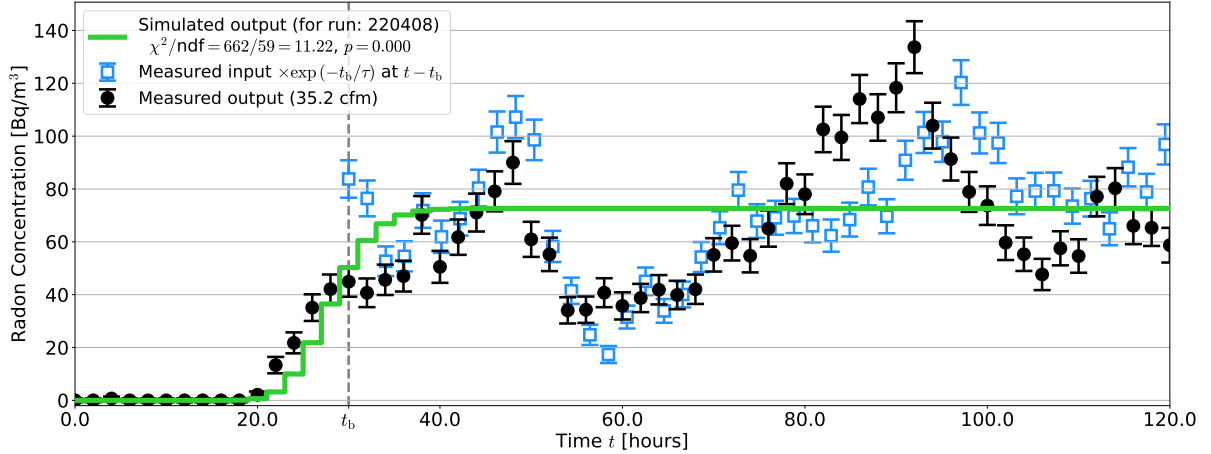


Figure 7.54: Similar to Fig. 7.53, but with a simulated output radon concentration (green) produced assuming a constant input radon concentration = 80 Bq/m³, t_b = 29 hours, and air flow F = 35.2 cfm.

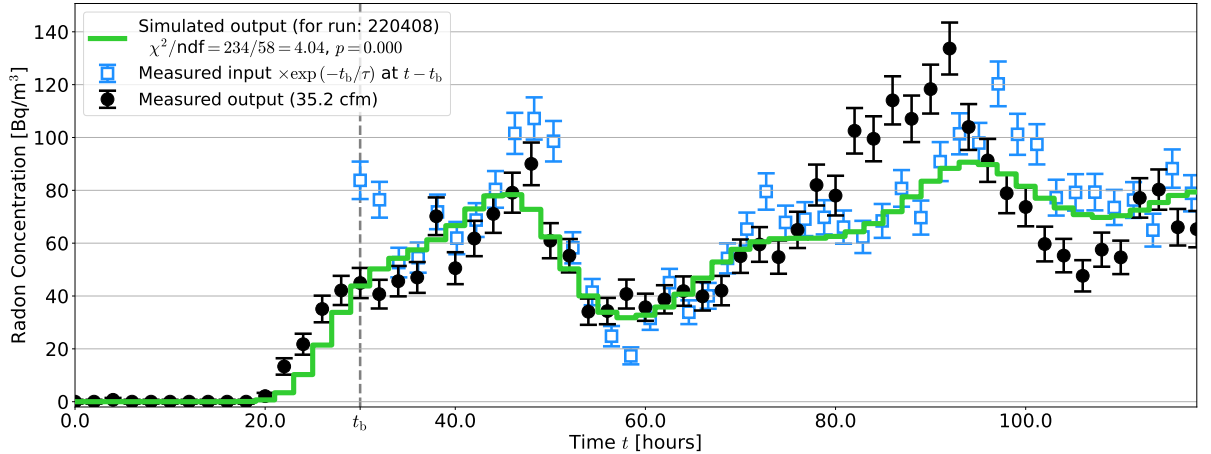


Figure 7.55: Similar to Fig. 7.53 with the measured BTC in black circles, but with the simulated output radon concentration (green) produced with the measured input radon concentration (blue squares) as a simulation input parameter.

agreement with the output data, with the largest differences clearly due to the variation of the input radon concentration over time.

The simulated output radon concentration better represents the measured concentration when the measured input radon concentration (the blue squares) is passed through the simulation. Figure 7.55 shows how most of the time-dependent features in these data are due to the input radon concentration changing with time. Some features, however, are still not captured. The simulation appears to underestimate the concentration be-

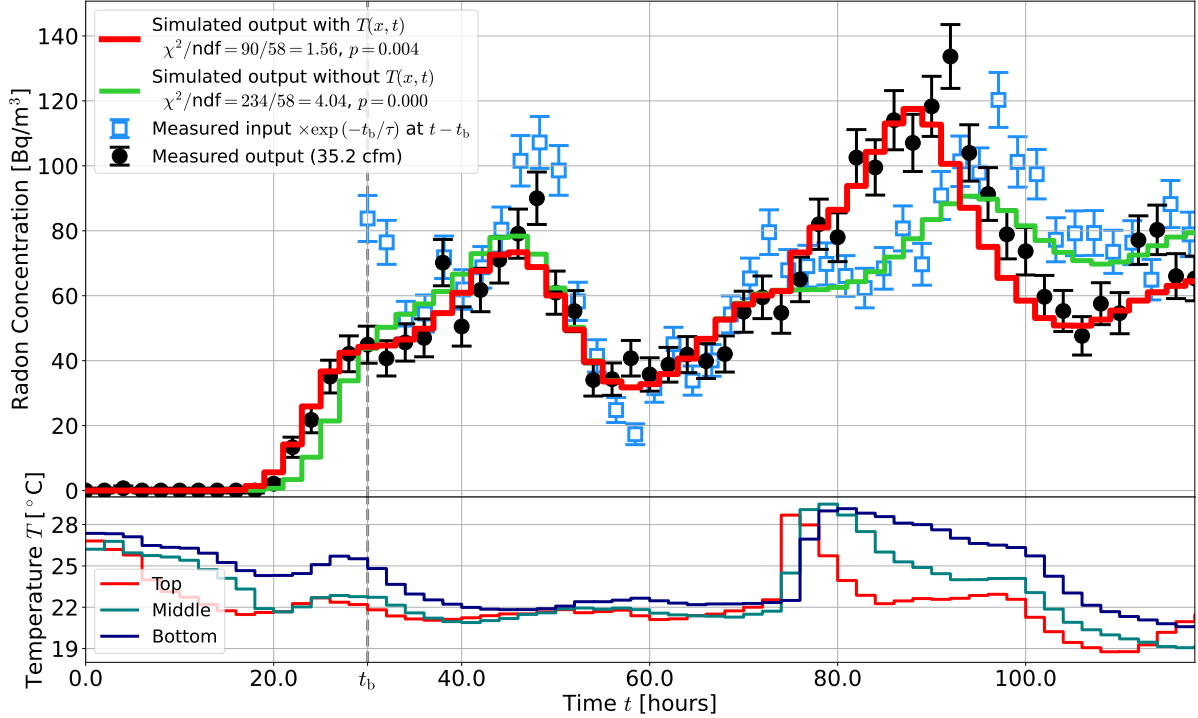


Figure 7.56: This plot is built on Fig. 7.55. By including the measured temperature within the column, the simulation (red) shows improved agreement with the measured output concentration (black) as compared to the simulated curve that does not include temperature data (green). The simulation underestimates the radon concentration between about 90 and 110 hours. **The lower plot** shows the measured temperature during this BTC run at the Top, Middle, and Bottom locations within the column, as described in Section 7.8.

tween 20 and about 30 hours, while overestimating the concentration between 30 and about 45 hours. Between 75 and 100 hours, the simulation underestimates the measured concentration significantly, while then overestimating the concentration after about 90 hours.

Passing the measured temperature during this BTC run to the simulation further improves agreement between simulation and measurement. Figure 7.56 shows the simulated output concentration with (red) and without (green) the measured column temperature (as described in Section 7.8). In the lower plot of Fig. 7.56, we observe a large increase in the measured temperature (around 75 hours) that causes radon to move more quickly through the column and thus increases the measured output radon concentration. The increase in temperature was created by reducing ventilation of the room housing the

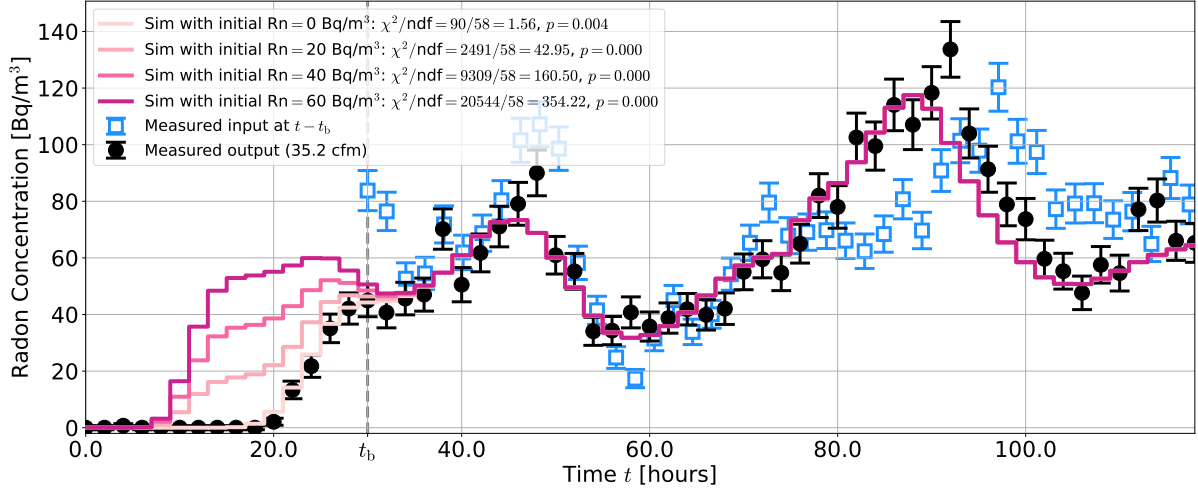


Figure 7.57: This plot is built on Fig. 7.56, but excluding the simulated BTC without $T(x, t)$ and the bottom temperature plot. By adding radon atoms to the input-side half of the column just before starting the simulated BTC, we observe an increase in the radon concentration at times earlier than t_b (light to dark purple curves), which would drive a fit to infer a t_b that is smaller than actual. Put another way, the column is essentially being made shorter by filling the first half of the column with radon atoms.

RRS. Following this increase in temperature, ventilation was restored, bringing the temperature back to a lower value.

While passing measured temperature to the simulation improves agreement between the measured and simulated BTC, there are still regions that disagree; however our goal here is to show the influence of different simulation parameters which may then inform a formal optimization, such as that described in Section 7.13.3. For example, Fig. 7.57 shows how the simulated output changes when varying the initial radon concentration within the front half (from the input side to the middle) of the column. By presuming that the column was *not* fully regenerated before the BTC run began, we observe an increase in the radon concentration at times earlier than t_b , as may be expected. Directly comparing the simulated curves with the measured BTC, the presumption that the column was indeed fully regenerated appears to hold; this conclusion is mirrored by the χ^2 and p-value calculated for each curve, as found in the figure's legend.

The simulated BTCs in this discussion have been produced with f_A and f_D having default values obtained by the optimization routine (over many runs) described in

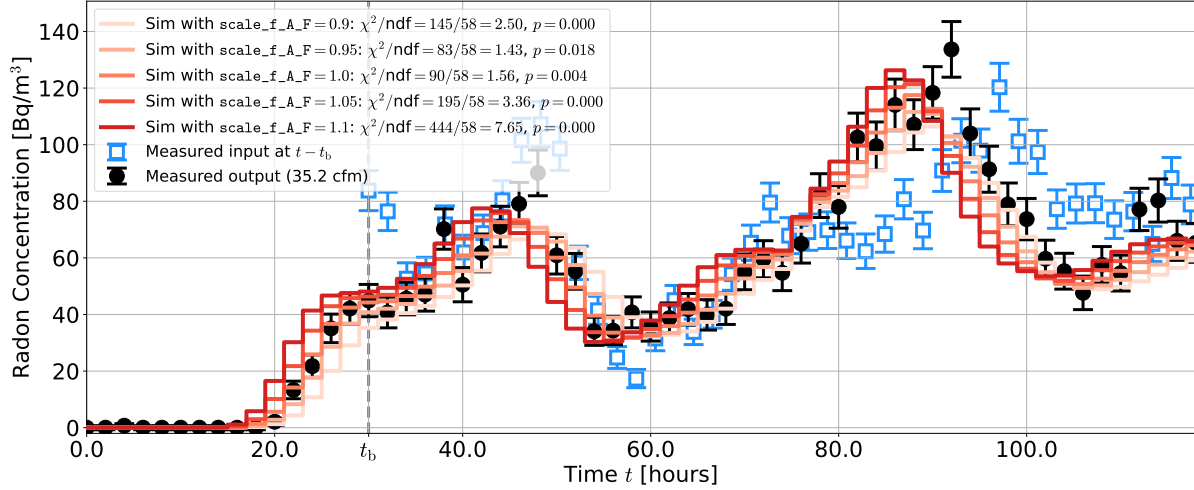


Figure 7.58: The simulated output radon concentrations (solid curves) show that for a smaller adsorption factor f_A radon spends more time in the column, thus exiting the column later in time.

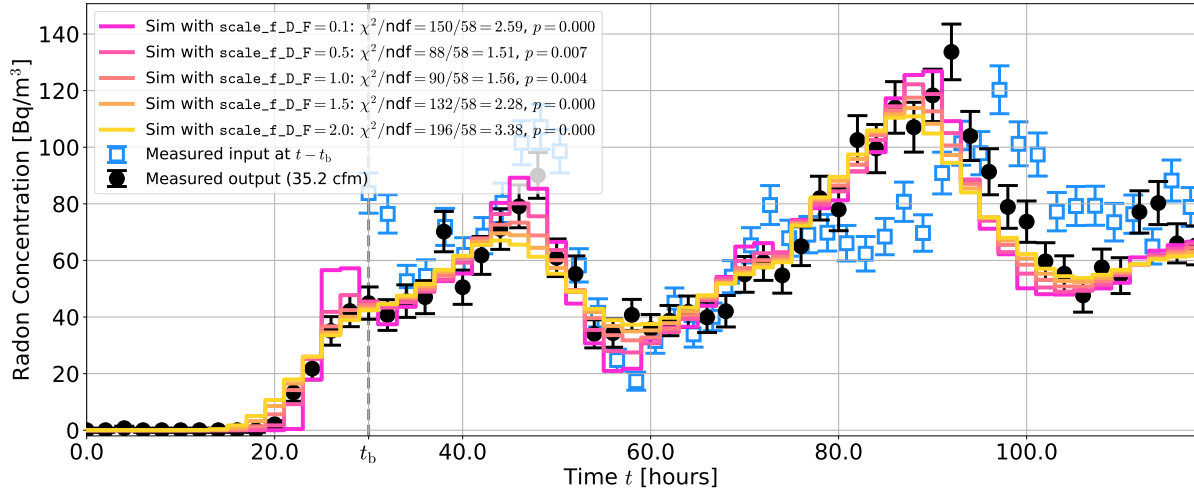


Figure 7.59: The simulated output radon concentration (solid curves) show that smaller diffusion coefficients preserve features while larger diffusion coefficients spread them over longer times.

Section 7.13.3. Nonetheless, Fig. 7.58 shows how scaling the adsorption factor f_A by a simulation parameter called `scale_f_A_F`, where the `f_A` means we are scaling f_A , and the `F` at the end denotes that we are scaling f_A only during the filtering stage. Figure 7.58 shows how decreasing or increasing the speed of radon by scaling f_A influences the simulated BTC. In this example, a scaling value different than unity leads to worse agreement, as shown by the goodness-of-fit displayed in the figure's legend, as expected.

Similar to the exploration above where we scaled f_A , we may vary the diffusion coefficient factor f_D . The simulation parameter `scale_f_D_F` allows the end user to scale f_D , the diffusion factor f_D , during F , that is, the filtering stage. Our expectation is that features will become more pronounced with a smaller diffusion coefficient. Figure 7.59 shows that the simulated BTCs support this presumption. As f_D has already been optimized, as discussed in Section 7.13.3, a value of `scale_f_D_F` different than unity worsens agreement between simulation and measurement, as indicated by the goodness-of-fit for each of the simulated curves found in the figure's legend.

The region between 90 and 110 hours shows the simulation underestimating the radon concentration. One possibility is that the critical temperature of adsorption T_\circ of our particular carbon has not been determined correctly (that is, differs from the literature value of 3500 K [102]). Figure 7.60 shows that upon varying T_\circ within the simulation, there may be a preference for a smaller value of T_\circ closer to 3000 K, as it produces a slightly better goodness-of-fit. With this development, it seems reasonable to perform an optimization where T_\circ is included as one of the free parameters (see the end of Section 7.13.3). However, because the prefactors f_A and f_D are determined for a particular T_\circ and at a particular temperature T , if we want to change T_\circ to T_\bullet , but without having to again determine, for example, f_A , we must satisfy the relation

$$v_{\text{Rn}} = f_A v_{\text{air}} \exp\left(\frac{-T_\circ}{T}\right) = \lambda f_A v_{\text{air}} \exp\left(\frac{-T_\bullet}{T}\right), \quad (7.95)$$

where we recall that $f_A = f_A(v_{\text{air}})$, the speed of air is v_{air} , and λ is the factor that we need to find. Taking a ratio and solving for λ yields

$$\lambda = \exp\left(\frac{-T_\circ}{T}\right) / \exp\left(\frac{-T_\bullet}{T}\right). \quad (7.96)$$

The subtlety here is that f_A was determined with T_\circ and a time-dependent $T(t)$. What I've done here, is set $T = 295$ K, which I presume to be approximately the time-average temperature $\langle T(t) \rangle$. Because T is not constant, f_A and f_D need to be found again and

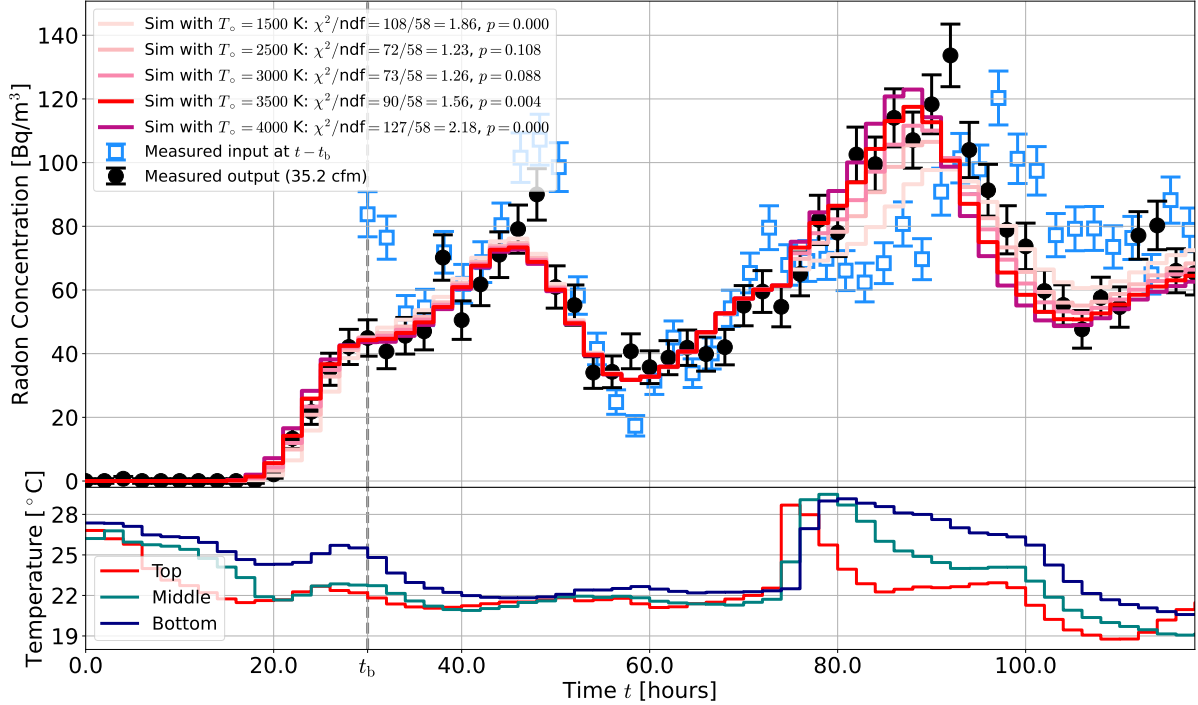


Figure 7.60: By varying values of T_0 (ranging from 1500 K to 4000 K, with the literature value of 3500 K drawn in red), the simulated BTC (solid curves) response to changes in temperature is more pronounced for larger values of T_0 (darker curves). **The lower plot** shows the measured temperature during this BTC run at the Top, Middle, and Bottom locations within the column, as described in Section 7.8.

is done so in Section 7.13.3; however, using this approximation allows us to gain some intuition on how T_0 influences the simulated BTC response to changing temperature.

7.13.2 Possible Simulation Shortcomings

Water in the air passing through a carbon bed, like radon, moves more slowly than the air that carries it (measurement shown in Chapter 8). As the water slowly migrates through the carbon column, it adsorbs to the carbon's surface where it may condense. It is expected that water molecules occupying sites on the carbon surface reduce the carbon's ability to adsorb radon atoms [102, 110]. An intriguing future measurement using the SD Mines Table-top System is to measure radon break-through curves while varying the relative humidity of the input air.

Whether the initial state of the filtering column at the beginning of a BTC measurement is completely free of radon, or, as is likely in real life, has some small amount

of radon, is not expected to have an important influence on a BTC. The first 10 hours, or much longer, of a measured BTC presents a radon concentration consistent with the Durridge RAD7 background rate ($\sim 100 \text{ mBq/m}^3$). At the end of the regenerating and slowfill stages, the radon distribution is expected to be concentrated near the output side (during filtering). This is because during regeneration, vacuum pumps produce a pressure gradient across the column length with the pressure lowest at the input side, where the pumps are connected. Radon is introduced to the outlet side of the regenerating column via the purge-flow line. These atoms move quickly in the low-pressure environment, moving more quickly still as they approach the input side of the column, where the pressure is lowest. During the slowfill stage following regeneration, radon continues to be introduced to the column as the pressure within the column approaches one atmosphere. During both regeneration and slowfill, the concentration of radon at the input side of a filtering column is expected to be lower than on the outlet side.

If the presumption that there is always more radon in the outlet side of the filtering column is true, we expect to see an increase in the radon concentration at very early times of a BTC (in the first couple hours). The radon concentration may then reduce and gain increase as radon begins breaking completely through the column. If, however, the presumption is false, and so much so that, in fact, there is a considerable concentration of radon confined to the input-side of the column, we would expect the radon concentration before t_b to increase. Depending on the distribution of radon initially in the input side of the column, the inferred diffusion coefficient and break-through time are expected to change; the diffusion coefficient may appear larger when radon originating within the column exits *too early*, and thus increases the tail of the S-curve; the break-through time may appear *too small*, as radon did not have to pass completely through the column before exiting, essentially making the column seem shorter (as shown in Fig. 7.57). Therefore, a simulated BTC is routinely compared to the measured BTC to check for two conditions:

1. Does radon appear to exit the column in the first few hours?

2. Does the simulated BTC appear to underestimate the measured BTC at early times?

This last condition is a bit tricky, as a fitting routine could find a value of f_A that would improve agreement at early times, and therefore we may also look for underestimate at later times (essentially suffering from the unexpected radon at early times). In the end, these sanity-type checks may be informative but do not substitute for collecting additional high-quality data.

Another important aspect of the BTC data is whether the temperature profile passed to the simulation does indeed represent the surface temperature of the carbon within the column. Section 5.4 discusses how the carbon's surface temperature is inferred from the measured RTDs that are embedded within the carbon bed. An improved temperature monitoring system, using infrared sensors installed throughout both columns, for example, could be used to collect higher-quality temperature data for future simulation validations (if this topic is a sticking point), or for other exploration.

Measurements have been conducted that suggest that the Durridge RAD7 radon detectors, which are used to measure the input and output radon concentration of the SD Mines RRS, may be sensitive to the large swings in ambient temperature. The sound-proof room that contains the SD Mines RRS, when closed, becomes rather warm ($> 30^\circ\text{C}$). When a RAD7 is transferred from the comparatively cool lab space into this warm room at the start of a BTC measurement, the RAD7 may take several hours or more to reach a steady-state temperature. During this time, disagreement (by as much as 20%) has been observed between such a device (initially cold) and two other similar devices that had already spent a couple days in the warm room. If such a case occurred while measuring a BTC, the first day or two of the input measurement would be lower than actual; this would present itself as a strange disagreement when shifted by t_b and compared with the BTC measured at the output (as if radon was being created within the RRS). While this is a practical issue in setting up the measurement, it illustrates

how a simple aspect of the BTC measurement can introduce confounding factors that are difficult to identify and challenge the simulation in ways that are not usually useful.

7.13.3 Using Break-through Curve Data to Constrain Simulation Parameters

Of the many parameters that may possibly influence the form of a simulated break-through curve (BTC), there are two that stand out: the adsorption factor f_A and the radon diffusion coefficient factor f_D . The adsorption factor was introduced in Section 7.6 and describes how long a radon atom remains adsorbed to the surface of the carbon as compared to in the carrier gas (the air) at infinite temperature. Though the expectation is that f_A does not depend on the air velocity v_{air} flowing through the column, BTC measurements suggest that there is linear dependence of the form

$$f_A(v_{\text{air}}) = av_{\text{air}} + b, \quad (7.97)$$

where a and b are fitted parameters. Introduced in Section 7.7, the diffusion coefficient factor f_D is expected to be a linear function of the air velocity v_{air} through the carbon bed with the form

$$f_D^{\text{exp}}(v_{\text{air}}) = cv_{\text{air}} + d, \quad (7.98)$$

where c and d are fitted parameters. The superscript `exp` is used to set the expected linear form apart from the quadratic expression that is a better model of the measured data:

$$f_D(v_{\text{air}}) = q_1 v_{\text{air}}^2 + q_2 v_{\text{air}} + q_3, \quad (7.99)$$

where q_i for $i = 1, 2, 3$ are fitted parameters. This quadratic form is used as the default model by the simulation. In both cases, the velocity dependence may be inferred by the best-fit values of f_A and f_D obtained from BTC runs at varying flow rates.

Another reasonable parameter that could be made free is the critical temperature of adsorption T_c . It has a literature value of 3500 K [102], but may differ for our specific

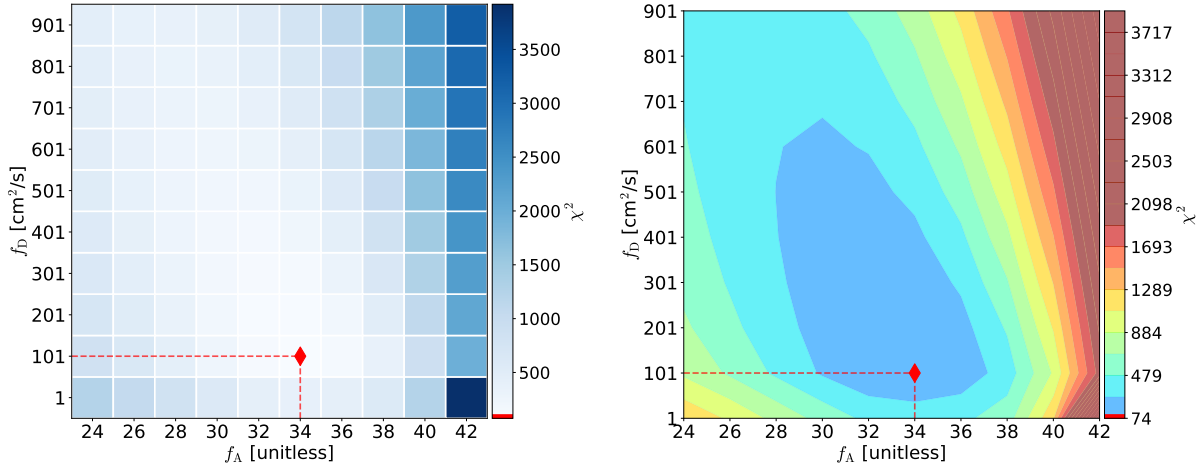


Figure 7.61: **Left:** The calculated χ^2 from Eq. 7.92 for guessed values of f_A and f_D with step size $\Delta f_A = 2$ and $\Delta f_D = 100 \text{ cm}^2/\text{s}$. This meshplot uses no interpolation. The red dashed lines point to the best-fit value pair expressed as a red diamond. **Right:** Similar to the plot on the left, but with interpolation (described in Python's matplotlib source code³).

carbon, and perhaps also due the circumstances specific to our measurements (such as moisture in the carrier gas). The following minimization routine constrains the free parameters f_A and f_D with T_\circ fixed. The routine is then performed again with all three as free parameters, with the literature value of T_\circ a suitable initial value for the minimizer.

In order to choose an appropriate minimization routine and initialize it with reasonable estimates of the free parameters, a simulated BTC has been produced for each pair of f_A and f_D values within a coarse grid. Each simulated BTC is then compared to measurement where a χ^2 is calculated (as described in Section 7.13.1). Figure 7.61 shows the resulting χ^2 map for the same BTC we had explored in Section 7.13.1. The best-fit value pair is represented by a red diamond at the intersection of the red dashed lines. Even from this coarse sampling, the χ^2 -minimizing pair of f_A and f_D produce reasonable agreement to measurement, as shown by Fig. 7.66. The obtained χ^2 -minimizing pair certainly should provide a satisfactory initial guess of the parameters as required by a minimization routine.

³Matplotlib source code: https://github.com/matplotlib/matplotlib/blob/main/lib/matplotlib/axes/_axes.py

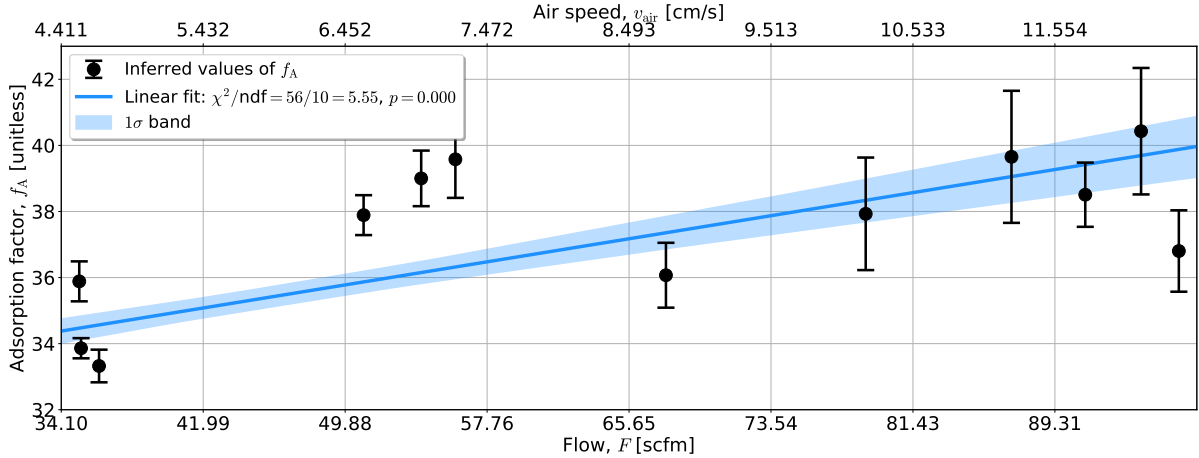


Figure 7.62: Best-fit values of the adsorption factor f_A (black dots) found from the minimization routine are plotted for several BTC runs that were performed at differing air flow rates F through the column. The linear functional form of f_A defined by Eq. 7.97 (blue line) is fit to these data, yielding the following best-fit parameters: $a = 0.68 \pm 0.09 \text{ s/cm}$ and $b = 31.4 \pm 0.5$ (unitless). The light blue band shows the 1σ -uncertainty interval.

The minimizer used is the Python module `scipy.optimize.curve_fit` [156], but configured to call the `scipy.optimize.leastsq` module, which is a wrapper for the FORTRAN subroutine MINPACK where the LMDIF and LMDER algorithms are employed [157]. If we let $y(t)$ be a measured BTC, with uncertainties $\sigma_y(t)$, and $f(t, \text{params})$ represents a simulated BTC produced with parameters denoted as `params`, the expression

$$\sum_t \frac{[y(t) - f(t, \text{params})]^2}{\sigma_y^2} \quad (7.100)$$

is minimized for a particular choice of parameters, where t is time (the array's index). This minimizer is run for each measured BTC yielding best-fit parameters, while their 1σ uncertainties are obtained from the estimated covariance of the parameters.

By using the aforementioned minimization routine on all measured BTC data, we obtained the best-fit values of the adsorption and diffusion factors f_A and f_D . Figure 7.63 shows the best-fit values of f_A . The linear fit to these data provide the best-fit parameters for the adsorption model given by Eq. 7.97, which the simulation uses by default to obtain the values of f_A . The 1σ -uncertainty band was produced by toy Monte Carlo. The poor goodness-of-fit indicates that our model does not capture all relevant influences on the adsorption factor (such as water vapor), or there are important systematics that are not

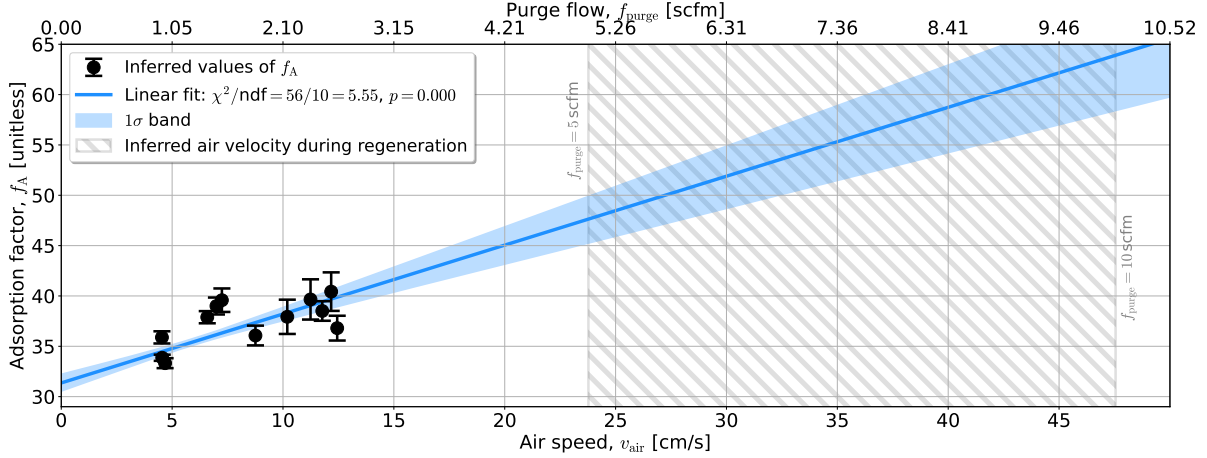


Figure 7.63: Similar to Fig. 7.62, but extended to the larger air velocity typical during the regeneration stage, illustrated by the gray hatched region between the purge flow f_{purge} of 5 and 10 scfm.

being accounted for correctly (possibly the inferred column temperature) or at all. With a more dedicated measurement of this relationship (possibly using the SD Mines Table-top System, introduced in Chapter 8), one may not be surprised if f_A is in fact independent of air speed; though these data do not support this hypothesis. A possible explanation for apparent dependencies of f_A on flow could be from flow-dependent channeling (*i.e.*, the preferential flow of gas through certain pathways within the bed); this systematic effect has not been explored, but could be inferred by a careful measure of the pressure drop across the column [158].

Because we do not currently make BTC-like measurements during regeneration, our model of f_A is extended to the air velocities that are typical during regeneration (keeping in mind that regeneration is performed at $\sim 1/30$ the pressure during filtering), with the model prediction shown by Fig. 7.63.

Figure 7.64 shows best-fit values of f_D as obtained by minimization. To ensure that a fit does not predict a negative diffusion coefficient, a value of $f_D = 0 \pm 26 \text{ cm}^2/\text{s}$ is appended at $F = 0 \text{ scfm}$, with the uncertainty of this point set equal to the smallest uncertainty of any other measured point. The quadratic form f_D (red curve) describes these data much better than the linear form (dashed cyan curve), as indicated by the

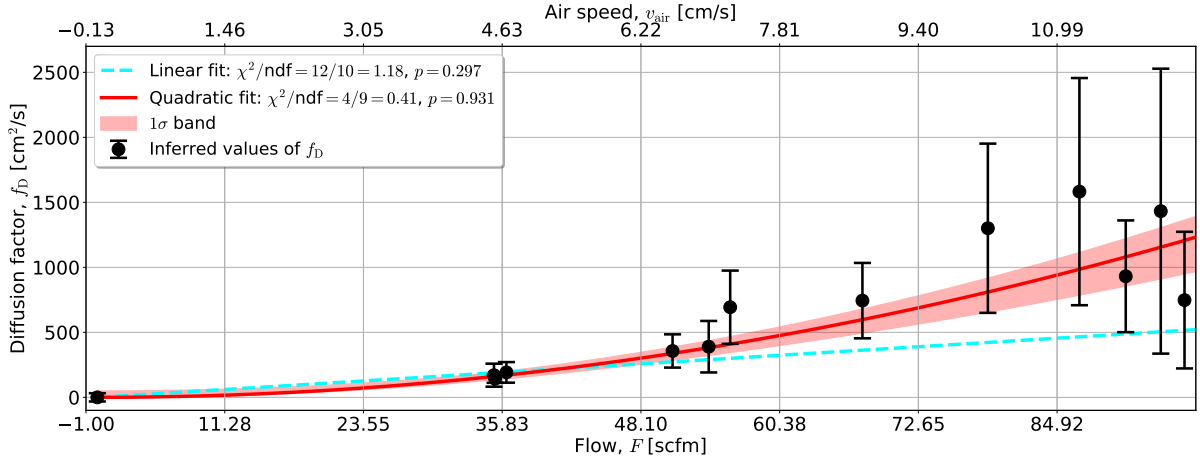


Figure 7.64: Best-fit values of the diffusion factor f_D (black dots) are plotted for several BTC runs that were performed at differing air flow rates F through the column. The linear functional form of f_D defined by Eq. 7.98 (dashed cyan curve) is fit to these data, yielding the following best-fit parameters: $c = 41 \pm 8$ cm and $d = 0.0 \pm 31$ cm²/s. The quadratic model of f_D (red curve with 1 σ band) given by Eq. 7.99 is also fit to these data, having best-fit parameters: $q_1 = 7.8 \pm 3$ s, $q_2 = 0 \pm 20$ cm, and $q_3 = 0.0 \pm 32$ cm²/s.

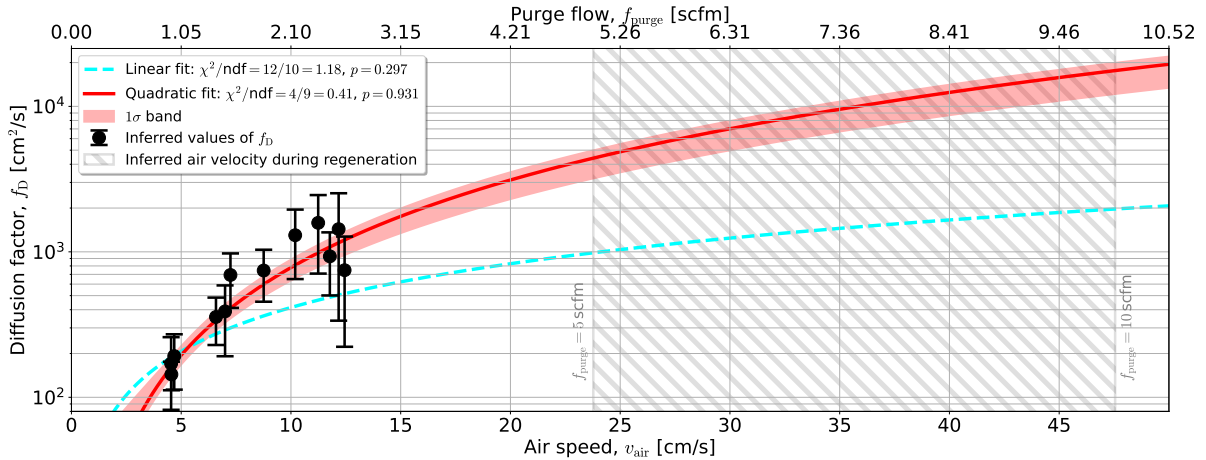


Figure 7.65: Similar to Fig. 7.64, but extended to the larger air velocity typical during the regeneration stage, illustrated by the gray hatched region between the purge flow f_{purge} of 5 and 10 scfm.

goodness-of-fit found in the figure's legend. The 1 σ -uncertainty band was produced by toy Monte Carlo and constrained primarily by the low-flow data points (< 40 scfm) having fairly small uncertainties. Figure 7.65 shows the diffusion models extended to the larger velocities during regeneration.

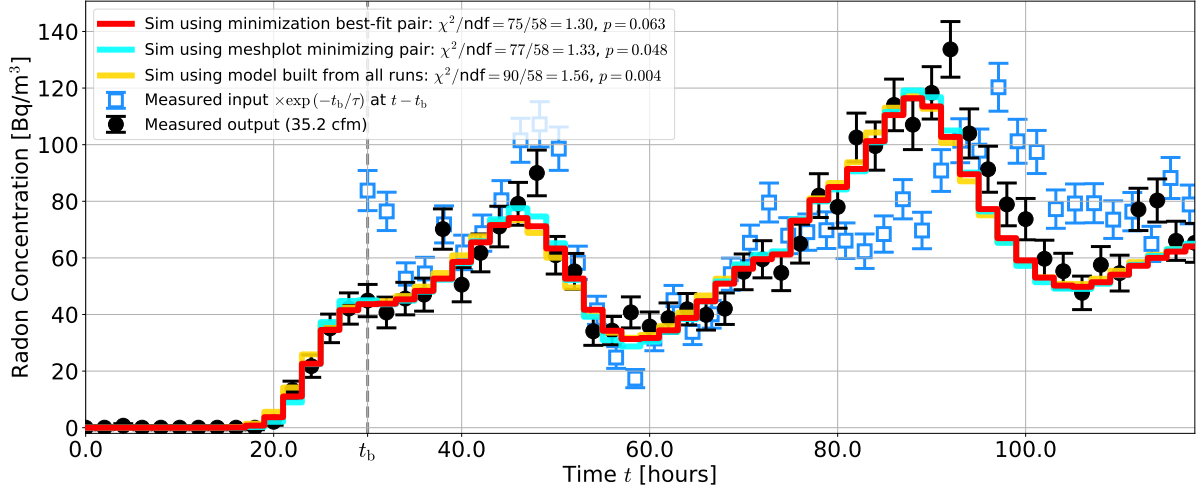


Figure 7.66: Built on the BTC measured shown by Fig. 7.53 in Section 7.13.1, the measured input radon concentration (blue squares) is multiplied by the decay fraction $\exp(-t_b/\tau)$, shifted by the inferred break-through time $t_b = 29$ hours, and may be compared to the measured output radon concentration (black circles); both input and output measurements are shown with 1σ uncertainty bars. Simulated BTCs use the best-fit pair of f_A and f_D obtained by the minimization routine (red curve), those taken directly from the meshplot that is the left plot of Fig. 7.61 (cyan curve), and the values provided by respective adsorption and diffusion factor models as described by Eq. 7.97 and Eq. 7.99 (gold curve).

The diffusion coefficient D that is inferred from the diffusion factor f_D depends on temperature and air speed. if we presume $T = 300$ K and $P = P_{\text{atm}}$, then

$$D = f_D(v_{\text{air}}) e^{-T_0/T} \frac{P_{\text{atm}}}{P} = f_D(v_{\text{air}}) e^{-3500/300} \approx f_D(v_{\text{air}}) \times 8.6 \times 10^{-6}. \quad (7.101)$$

Using the data plotted in Fig. 7.64, the diffusion coefficient D ranges between 1.2×10^{-3} and 1.4×10^{-2} cm²/s. The range of diffusion coefficient values is consistent with the expected diffusion coefficient for activated carbon, which has a pore size of a few nanometers (see Section 4.2.2).

Figure 7.66 shows the same simulated BTC that we explored in Section 7.13.1, but using different values of f_A and f_D . The minimization routine provides the best fit of the simulation (red curve) against the measured BTC (black circles). As expected, the best-fit parameters obtained by the minimizer is only slightly better than simply using the χ^2 -minimizing pair from the meshplot (cyan). One clear advantage of the minimizer is that it returns the covariance of the fit parameters which is used to estimate

parameter uncertainties, while the meshplot must be interpolated and may suffer from insufficient resolution (as has been experienced). Upon using the minimization routine on all measured BTC data, coefficients to the linear model for f_A and both the linear and quadratic models for f_D are obtained. Producing the same simulated BTC using these models yields slightly worse agreement (gold curve) than the other two solutions. This is not a surprise because the models are characterized by all runs and not this particular run. Aside from the statistical differences between measured data, there are likely other real-world differences that are not accounted for by these models, or otherwise by the simulation (relative humidity of the input air comes to mind, which can vary greatly when, for example, it rains where the measurements are conducted in typically-arid Rapid City, SD).

The critical temperature of adsorption for radon adsorbing to the surface of activated carbon $T_\circ \approx 3500\text{ K}$ [102, 110]. No uncertainties were quoted in [102, 110], but the value is within uncertainties of other measurements of T_\circ (also for radon adsorbing to activated carbon): $T_\circ = 3670 \pm 782\text{ K}$ [159] and $T_\circ = 3790 \pm 253\text{ K}$ [160]. The value is expected to depend on the properties of the carbon surface, with no known mechanism for T_\circ to depend on air flow. For this work, T_\circ has been assumed to be 3500 K, with the value checked by comparing simulated and measured BTCs, as is now described.

By repeating the minimization routine with T_\circ included as a free parameter, along with f_A and f_D , we obtain the results shown by Fig. 7.67, Fig. 7.68, and Fig. 7.69. The factors f_A and f_D are divided by

$$\lambda = \exp\left(\frac{-T_\circ}{T}\right) / \exp\left(\frac{-T_\bullet}{T}\right), \quad (7.102)$$

where T_\circ is the critical temperature of adsorption being varied and $T_\bullet = 3500\text{ K}$. This scalar was introduced in Section 7.13.1 (defined by Eq. 7.95) and serves two purposes: (1) to make the minimization routine robust against f_A and f_D changing many orders of magnitude for differing values of T_\circ and (2) to allow quoted values of, for example,

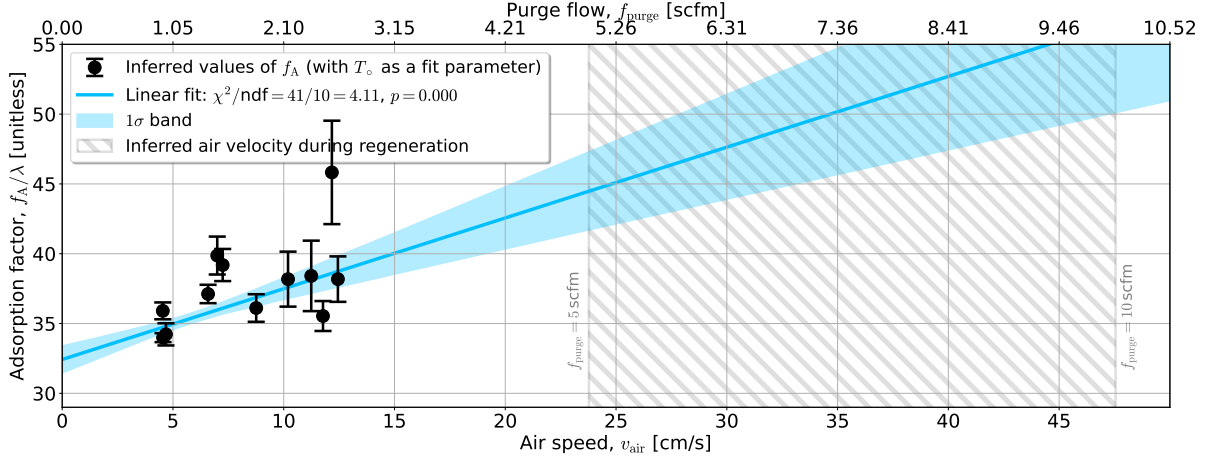


Figure 7.67: Best-fit values of the adsorption factor f_A (black dots) found from the 3-parameter minimization routine are plotted for several BTC runs that were performed at differing air flow rates F through the column. The linear functional form of f_A defined by Eq. 7.97 (blue line) is fit to these data, yielding the following best-fit parameters: $a = 0.51 \pm 0.10 \text{ s/cm}$ and $b = 32.4 \pm 0.6$ (unitless). The light blue band shows the 1σ -uncertainty interval.

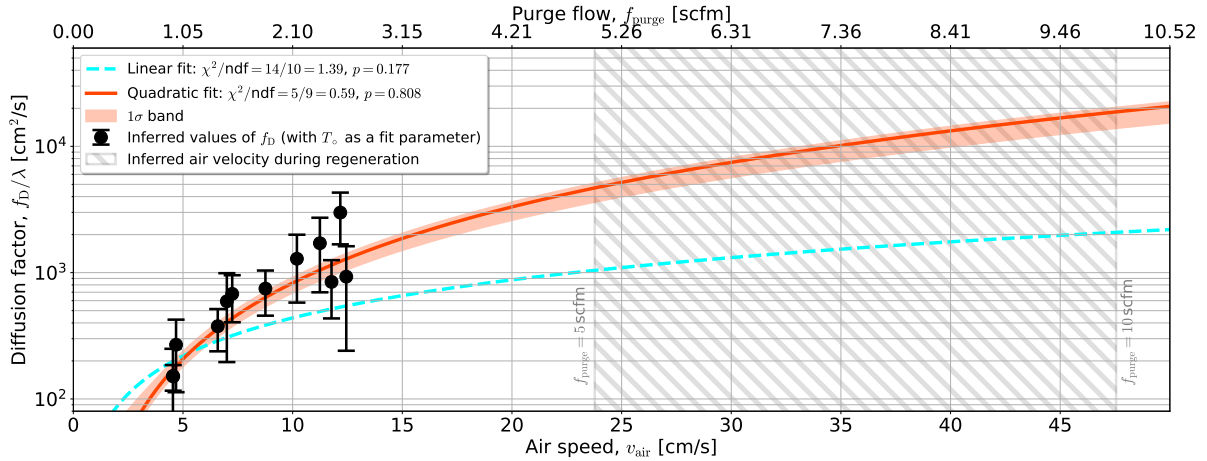


Figure 7.68: Best-fit values of the diffusion factor f_D (black dots) found from the 3-parameter minimization routine are plotted for several BTC runs that were performed at differing air flow rates F through the column. The linear functional form of f_D defined by Eq. 7.98 (dashed cyan curve) is fit to these data, yielding the following best-fit parameters: $c = 44 \pm 9 \text{ cm}$ and $d = 0.0 \pm 34 \text{ cm}^2/\text{s}$. The quadratic model of f_D (red curve with 1σ band) given by Eq. 7.99 is also fit to these data, having best-fit parameters: $q_1 = 8.3 \pm 3.4 \text{ s}$, $q_2 = 0 \pm 22 \text{ cm}$, and $q_3 = 0.0 \pm 34 \text{ cm}^2/\text{s}$.

f_A/λ (found when $T_o \neq 3500 \text{ K}$) to be of similar order of magnitude as f_A (found when $T_o = 3500 \text{ K}$).

The change in T_o could be due to, for example, water in the air stream adsorbing to the carbon and thus changing the surface properties. The observed progressive change

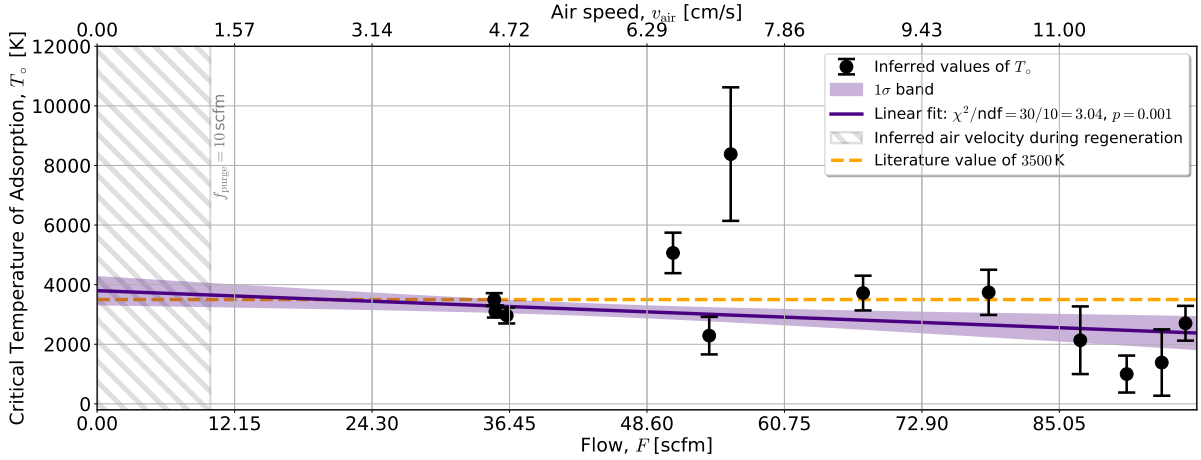


Figure 7.69: Best-fit values of the critical temperature of adsorption T_o (black dots) found from the 3-parameter minimization routine are plotted for several BTC runs that were performed at differing air flow rates F through the column. The linear functional form of f_{T_o} defined by Eq. 7.104 (indigo line) is fit to these data, yielding the following best-fit parameters: $c = -15 \pm 6 \text{ K s/cm}$ and $d = 3799 \pm 297 \text{ K}$. The light indigo band shows the 1σ -uncertainty interval. This linear fit may be compared to the literature value of $T_o = 3500 \text{ K}$ (dashed orange line). The purge flow f_{purge} at STP during the regeneration stage is between 0 and 10 scfm (gray hatched region).

could be related to the coverage fraction of the carbon by a layer of water molecules, or to the amount condensed (perhaps the adsorption potential is being shielded?). Similarly, water vapor may condense into the pores of the activated carbon (referred to as capillary condensation, for example [161, 162]) and reduce the adsorption capacity of the carbon, possibly, in effect, modifying the enthalpy of adsorption (*i.e.*, T_o). In either case, the mass of water m_w added to a column in time Δt

$$m_w \propto FH\Delta t, \quad (7.103)$$

where F is the through-column air flow at atmospheric pressure P_{atm} and H is the relative humidity of the air, which is directly proportional to the density of water in the air. If water vapor is indeed influencing T_o , this reasoning implies that T_o , should depend on air flow F (at P_{atm}) and *not* the air speed v_{air} . Based on data observed, T_o appears to have a functional form that depends on the air flow F

$$T_o(F) = cF + d, \quad (7.104)$$

BTC Run	Flow	2 free parameters: f_A and f_D				3 free parameters: f_A , f_D , and T_\circ			
		χ^2	ν	χ^2/ν	p	χ^2	ν	χ^2/ν	p
220408	35.2	137	119	1.15	0.125	131	118	1.11	0.189
220316	86.9	58	44	1.33	0.073	57	43	1.32	0.078
220224	91.0	122	64	1.91	0.000	118	63	1.88	0.000
220217	78.8	31	45	0.69	0.942	31	44	0.71	0.928
220212	67.7	103	69	1.50	0.005	103	68	1.52	0.004
220207	50.9	74	70	1.06	0.338	71	69	1.03	0.418
211111	56.0	119	81	1.47	0.004	115	80	1.44	0.006
210926	96.2	80	44	1.81	0.001	77	43	1.79	0.001
210910	36.2	136	97	1.40	0.006	130	96	1.36	0.011
210830	94.1	100	52	1.92	0.000	91	51	1.79	0.000
210819	54.1	112	90	1.25	0.056	108	89	1.21	0.086
210805	35.1	136	92	1.48	0.002	137	91	1.51	0.001

Table 7.3: The goodness-of-fit statistics for each BTC run used to infer models for f_A , f_D , and T_\circ . The quoted flow has units of cubic feet per minute (cfm). BTC run 220408 has been used to illustrate aspects of the BTC analysis in this section (blue row). The BTC run 211111 (orange) draws attention to the point in Fig. 7.69 with an inferred T_\circ of ~ 8300 K.

where c and d are fitted parameters.

It must be mentioned that the overall agreement between simulated and measured BTCs is not very good. Table 7.3 tabulates the goodness-of-fit for each BTC run using either the two or three parameter minimization routine. Only a couple of the simulated runs agree well (according to their goodness-of-fit) with their measured counter part, suggesting the simulation does not very well describe the data. Including T_\circ as a free parameter results in only slightly better goodness-of-fits as compared to the two-parameter minimization, as may be seen from the reduced χ^2 and p-values of the two- and three-parameters goodness-of-fits in Table 7.3. For this reason, we will keep $T_\circ = 3500$ K throughout future sections (as it has been in previous sections) unless explicitly stated. Further development of the simulation, should greatly benefit from collecting additional BTC data to validate/optimize against, especially if additional parameters and models are explored.

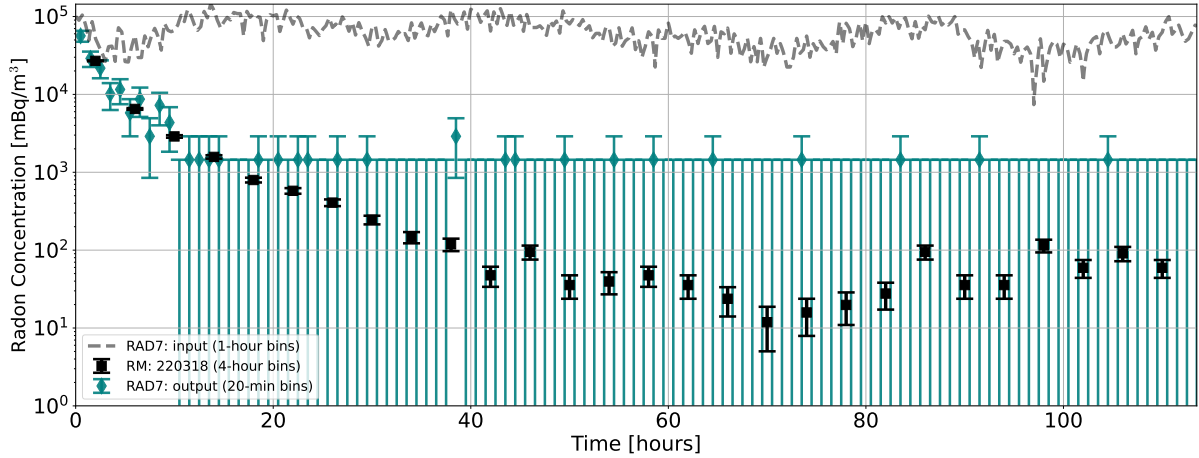


Figure 7.70: High-radon input air is supplied to the SD Mines RRS operating in swing mode, with input radon concentration measured by a Durridge RAD7 (gray dashed line). No changes are made to the input data (such as delaying by the expected through-system time). The output radon concentration is measured by two devices: the SD Mines Radon Monitor (abbreviated as RM and shown in black squares) and a Durridge RAD7 (teal diamonds).

7.13.4 Regeneration Curves: Simulation versus Measurement

After both carbon columns have been flushed with high-radon air, the radon-reduction system is started with some configuration (*i.e.*, flow rate, cycling period, purge flow, etc.). The output radon concentration versus time is called a regeneration curve (RC), and was introduced in Section 7.4.2. By comparing simulated RCs with those measured, aspects of the simulation not easily constrained by comparisons with measured BTCs may be tested and, where needed, modified. Similar to when comparing to BTC runs, in order for a simulated RC to agree well with measurement the adsorption and diffusion factors (the free parameters of this analysis) must be accurate for not just the filtering stage (the BTC stage, if you like) but also the regenerating and slow-fill stages.

Figure 7.70 shows an example RC produced by the SD Mines RRS with a through-column air flow rate of 86.6 cfm, regeneration and slowfill stage durations of 45 min and 15 min respectively, and thus a filtering duration of $45 + 15 = 60$ min. The purge flow rate was 7.2 scfm. The output radon concentration was measured using the SD Mines Radon Monitor (see Section 5.1) inferred from the decays of radon's fast daughter ^{218}Po . A less-sensitive Durridge RAD7 radon detector [118] is used to measure the RRS's input

radon concentration, and another is used to measure the RRS output as a redundancy to the Radon Monitor. While a RAD7 does not have the sensitivity to place more than an upper limit on the output radon concentration after regeneration, it does provide an additional check on the Radon Monitor response time (as the latter device has a detection volume of ~ 70 L, compared with the RAD7's ~ 800 mL detection volume).

The simulation predicts periodic, saw-tooth-like features during the early time (first 10 hours or so) of a RC, with the exact shape of the features depending on simulation parameters. As a brief review, a RC represents radon exiting the simulated (or physical) RRS during the filtering stages; this radon may have passed completely through the filtering column during the filtering stage duration or was originally somewhere in the filtering column, due to incomplete regeneration for example. The shape of the radon distribution within a filtering column at the start of filtering strongly influence the time dependence of radon exiting the column. With both columns initially full of radon, the simulation predicts that the radon exiting the column during the first filtering stage is roughly constant in time. During each successive filtering stage (that is, while filtering through the second column that was just regenerated partially and so contains a slightly reduced distribution of radon near its output), the radon concentration is expected to drop substantially initially, but then slowly increase over time; therefore, we may expect saw-tooth-like behavior where the radon concentration initially drops and then begins to increase, repeating every half cycle (or $45 + 15 = 60$ min).

A subtlety about the RC plots is that when the physical RRS is configured for one hour filtering time (with 45 min of regeneration, as in this example), there is an additional 0.75 min required per half cycle (*i.e.*, per hour) reserved for valves opening and closing. This additional time is not built into the simulation, and though it is not expected to have an important influence on predicted performance, it does make comparing measured RC data to simulation less intuitive by producing increasing discrepancies of the timing features. Therefore, I slightly stretch the simulated RC predictions by 60.75/60

so that features such as crests are in alignment. This “hack” should allow us to more quickly compare the major features between simulation and data as we investigate the simulation’s strengths and weaknesses.

Commonly a RC run is performed by the SD Mines RRS directly after performing a BTC through a regenerated column. When the BTC measurement has finished (*i.e.*, the measurement has lasted longer than a few times the expected break-through time t_b), one may then flush high-radon lab air through both columns such that each has a similar state at the start of the RC (that is, when starting swing mode). Alternatively, one may save a few days by simply starting the RC measurement at the end of the BTC measurement. In this case, one column contains a high concentration of radon (as described in Section 7.11) while the other column, when left regenerating, contains less than 1% of that concentration.

The regenerating column is supplied by the purge flow f_{purge} that is typically about 10% of the flow F (at STP) through the filtering column, as determined by the ratio f_{purge}/F . The regenerating column is maintained at ~ 20 Torr, which is $20/680 \approx 3\%$ of one local atmosphere. By continuity, the total radon flux though the purge-flow valve and regeneration column is conserved, and therefore the radon density during regeneration

$$\rho_R = \frac{P}{P_{\text{atm}}} \rho_{\text{pf}}, \quad (7.105)$$

where local atmospheric pressure $P_{\text{atm}} = 680$ Torr, the average pressure in the column $P = 20$ Torr, and ρ_{pf} is the radon density of the purge-flow air at STP (fed from the output of the filtering column, and so $\rho_{\text{pf}} \approx \rho_F$, the radon density during filtering). The number of radon atoms entering the regenerating column

$$\dot{N}_{\text{pf}} \propto \frac{f_{\text{purge}}}{F} \dot{N}_{\text{out}}, \quad (7.106)$$

where \dot{N}_{out} is the number of radon atoms exiting the filtering column per unit time. Because the radon density within the regenerating column $\rho_R \propto N_{\text{pf}}$, the ratio of radon

densities within the filtering and regenerating columns

$$\frac{\rho_F}{\rho_R} = \frac{f_{\text{purge}}}{F} \frac{P}{P_{\text{atm}}}. \quad (7.107)$$

Therefore, at the end of a regeneration stage that was *sufficiently long such that equilibrium had been reached* we may presume that the amount of radon in the regenerating column is about 0.003 of that in the filtering column (upon evaluating Eq. 7.107 with $F = 100 \text{ scfm}$ and $f_{\text{purge}} = 10 \text{ scfm}$). However, after regenerating, we must perform slowfill to raise the column to atmospheric pressure before using it for filtering. When the valve connecting the regenerating column to the vacuum pumps is closed the regenerating column becomes the slowfill column, and air is supplied from the filtering column to the slowfill column via the purge-flow line. The number of radon atoms that are passed to the slowfill column as we raise it from approximately perfect vacuum to one atmosphere is

$$N_{\text{sf}} = V_{\text{col}} C \tau, \quad (7.108)$$

where the air volume of a column $V_{\text{col}} \approx 0.5 \text{ m}^3$, the radon concentration of air exiting the filtering column $C = 100 \text{ Bq/m}^3$, and the mean lifetime of a radon atom $\tau = 5.52 \text{ days}$. Evaluation yields $N_{\text{sf}} = 24 \times 10^6$ radon atoms. Discussed in Section 7.11, the number of radon atoms expected to be in the filtering column after a long BTC run is

$$N_{\text{added}} = 8.6 \times 10^6 F C, \quad (7.109)$$

where C is the input radon concentration (in Bq/m^3) and F is the air flow (in scfm) during the BTC run. Plugging in typical values for a BTC yields $8.6 \times 10^6 F C = 8.6 \times 10^6 (50)(100) = 4.3 \times 10^{10}$ radon atoms. The total number of radon atoms in the column that was left regenerating at the beginning of swing mode (the RC run) is roughly estimated as the number of atoms at the end of regeneration (lasting long enough to reach an equilibrium state) plus the number of atoms at the end of slowfill: $0.003 \times N_{\text{added}} + 24 \times 10^6 = (129 + 24) \times 10^6$. Therefore, number of radon atoms in the regenerating

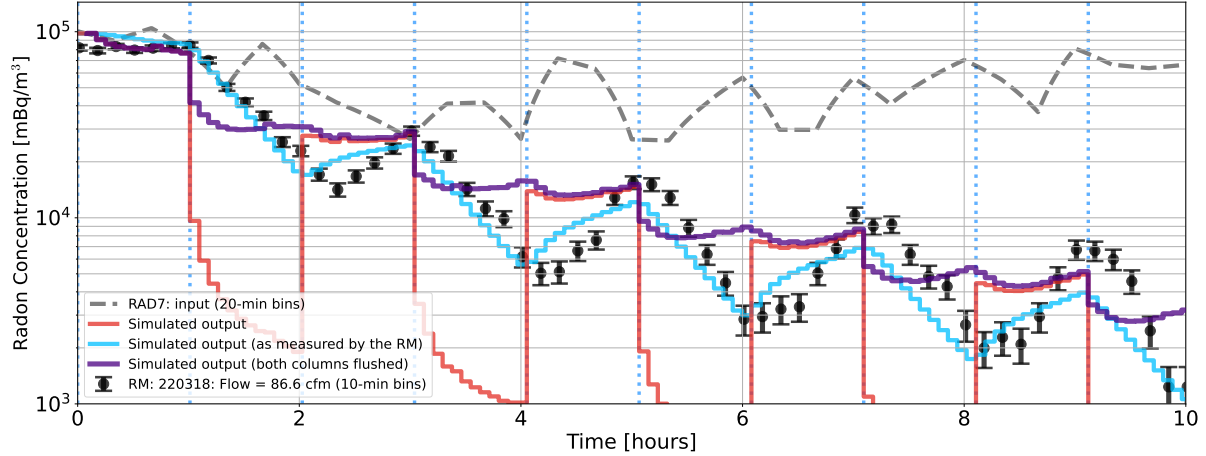


Figure 7.71: By zooming in on the first 10 hours of the regeneration curve (RC) shown in Fig. 7.70, periodic features in the output radon concentration produced by SD Mines RRS RRS operating in swing mode may be seen (black circles with 1σ uncertainties). While the SD Mines Radon Monitor sampled the RRS output, a Durridge RAD7 sampled the RRS input (gray dashed line), which is fed to the RRS simulation to produce a predicted RC (red curve). The simulated RC shows radon exiting the filtering column during even hours (0 to 1, 2 to 3, etc.), while very little radon exits during odd hours (1 to 2, 3 to 4, etc.). If *both* columns had been flushed with high-radon air, the simulated saw-tooth features (indigo curve) show similar amounts of radon exiting each column with drops each filtering stage determined by how many times the column has been regenerated. The simulated RC is passed through the differential equation describing the air-volume replacement within the SD Mines Radon Monitor (discussed later in this section and given by Eq. 7.110), thus providing the inferred radon concentration (blue curve) as expected to be measured by the Radon Monitor. By accounting for the response characteristic of the Radon Monitor, improved agreement between the simulated RC and the measured RC is observed.

column is about 281 times lower than in the filtering. From this, we are likely safe to presume that the column left regenerating has no radon in it at the start of the RC.

Figure 7.71 shows the same RC measurement as Fig. 7.70, but zoomed in to the first 10 hours (black circles). Presuming that one column was flushed with high-radon lab air, while the other remained in a regenerating state during the previously conducted BTC run, the simulated RC (**red curve**) shows radon exiting the filtering column as if still in a BTC mode during the first hour. At the start of the first hour, we begin filtering through the freshly regenerated column that was set to contain no radon initially; the result is that the outlet radon concentration drops significantly, with the shape shown by the simulated output between hours 1 and 2 of Fig. 7.70 and believed to be descriptive of the distribution of radon as introduced to the outlet side of the column from the purge-flow

line. At the start of the second hour, we are again filtering through the first column (that was used during the first hour); a drop in the output radon concentration relative to that during the first hour is seen due to the fact that the column has been regenerated once. This pattern continues and, more generally, shows a drop in the *simulated* output radon concentration when the *measured* RC begins to drop and a increase in the simulated output when (or just before, at early times) the measured RC begins increase (thus showing agreement between simulation and measurement at least in the sign of their derivatives).

To serve as a comparison (or, if you like, a sanity check), the simulation is made to predict a RC, but where both columns are presumed to be flushed with high-radon air (**indigo curve**), as apposed to only one. Similar as before, the output concentration appears flat for the first hour. At the start of the first hour, we begin filtering through the freshly regenerated second column that was set to initially contain lots of radon; the result is that we see a drop due to the column having been regenerated once, but as not all radon was removed, significantly more radon leaves the column as compared to the previous example where the column was initialized with no radon in it. At the start of the second hour, we are again filtering through the first column, and the output concentration appears very similar to that seen after the start of the first hour. This is expected and is because each column started with the same amount of radon and have been regenerated (and slowfilled) exactly once. At the start of the third hour, we again see a drop as the second column has been regenerated twice, and the pattern continues.

By inspecting the peak-to-peak drop in the output radon concentration of the measured RC in Fig. 7.71, a reduction in the output per regeneration stage appears to be about 2 (which appears consistent for both of the simulated curves). This should not be confused with our previous estimate of the relative amount of radon in the regeneration and filtering columns at the end of a long BTC run, as that estimate presumed equilibrium had been reached in both columns. During swing mode, the regeneration stage

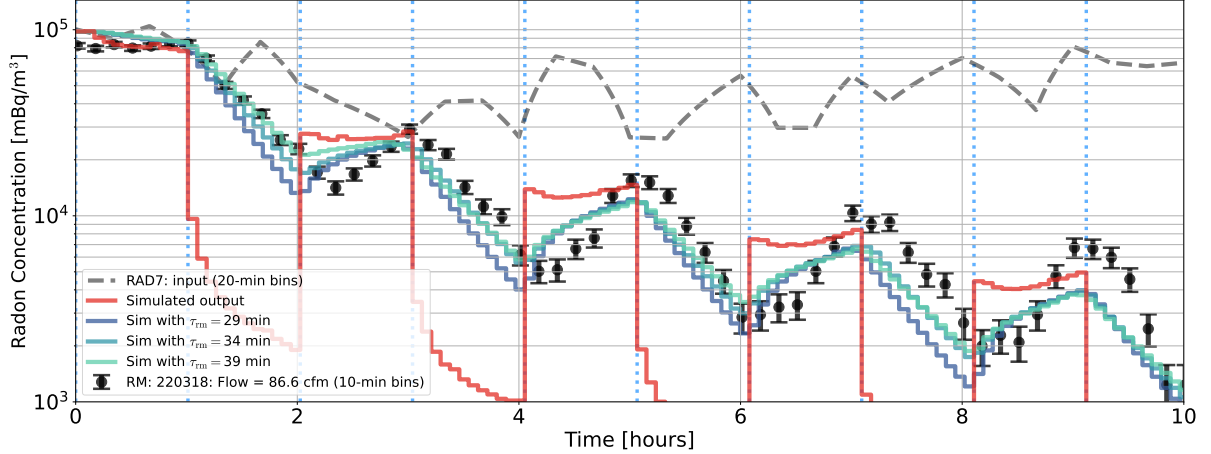


Figure 7.72: Built upon Fig. 7.71, the characteristic time for air-volume replacement within the SD Mines Radon Monitor is varied by ± 5 min (blue-to-teal curves), showing the influence of this empirically-found parameter (that has a best-fit value of 33.7 ± 0.4 min).

lasts typically 45 minutes; this is *not* expected to provide enough time for the amount of radon in the regenerating column to reach its minimum, where the number of radon atoms introduced via the purge-flow line is equal to those decayed or purged through the vacuum pumps.

An important difference between simulation and measurement can be explained by describing how the SD Mines Radon Monitor responds to changes in the radon concentration of sample air. The Radon Monitor (RM) has a detection volume of $V \approx 70$ L and samples air with radon concentration $y_{\text{rrs}}(t)$ at a flow rate $F = 2$ slpm. The radon concentration measured by the radon monitor y due to a step change in the sample radon concentration will be observed not as a sharp step but an exponential approach to the new value. This deviation from a step change is due to the sample air needing to replace the air already present in the detection volume, and is described by the differential equation:

$$\frac{dy}{dt} = -\frac{1}{\tau} [y_{\text{rrs}}(t) - y], \quad (7.110)$$

where $\tau = 33.7 \pm 0.4$ min as found in Section 5.1, while in a perfect-mixing scenario $\tau = V/F = 34.4$ min. Because $y_{\text{rrs}}(t)$ is not described by an analytic function (as it represents the simulated output radon concentration), this differential equation is solved

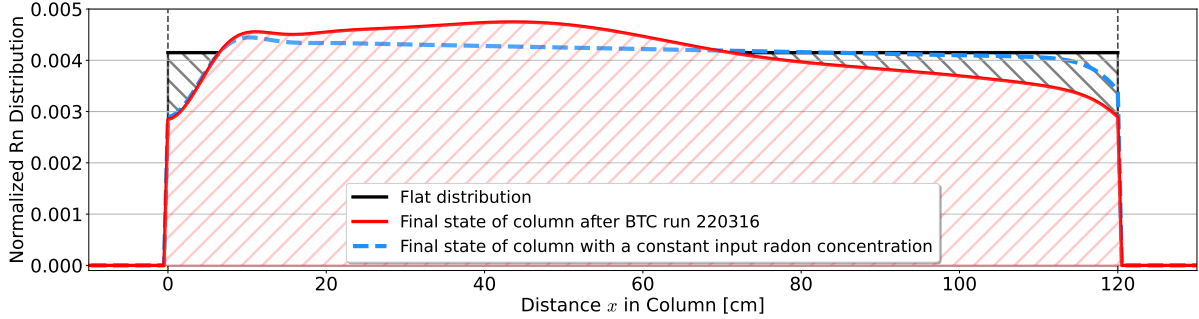


Figure 7.73: The number of radon atoms throughout a column along the axial direction is presumed to be a flat distribution (black curve) for the analyses in this section, with the amplitude of each scaled such that radon exiting the simulation during the first filtering stage matches that from measurement. However, the (normalized) shape of the distribution predicted from simulation after a BTC can vary depending on whether the input radon concentration during the BTC was constant (blue dashed curve) or changing with time (red curve with hatching). This time-dependent input used here is that from the BTC measurement that preceded the RC measurement that is being explored in this section; therefore, this radon distribution is expected to represent the initial state of the filtering column of RC run 220318.

numerically. Specifically, I have employed the python ODE solver `scipy.integrate.solve_ivp`. The blue curve in Fig. 7.71 shows the result of passing the simulated RC prediction y_{rrs} through Eq. 7.110 where we solve for y , the inferred radon concentration expected to be observed if measured by the SD Mines Radon Monitor. Figure 7.72 shows the effect of the characteristic time τ on the simulated RC as measured by the RM.

We may expect that the shape of the initial distribution of radon atoms within each column would also have an influence on the periodic features during the first few cycles. The reason that the distribution shape is expected to primarily influence the first several hours of a RC is that each regeneration stage reduces the total number of atoms by about a factor of 2, with the atoms diffusing significantly according to our diffusion model given by Eq. 7.99. From observed reduction alone, we would expect the initial distribution to be reduced by 2^n , where n is the number of regeneration stages completed. Each cycle, then, effectively overrides the original distribution, with each iteration bringing the distribution closer to that caused by the introduction of radon from the purge-flow line and the pressure gradient sustained during the regeneration stage.

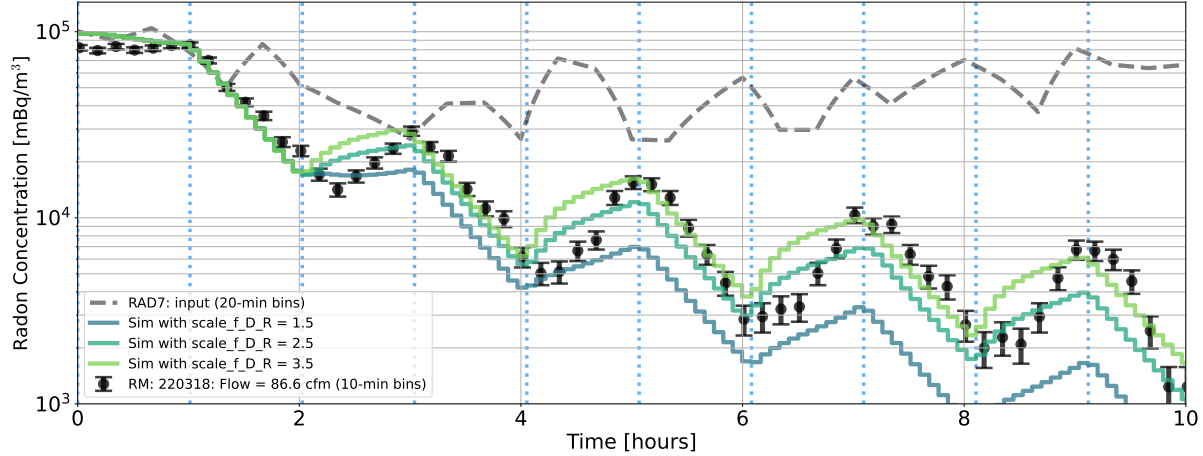


Figure 7.74: Similar to Fig. 7.71 but excluding the unmodified simulated RC (not passed through Eq. 7.110), the influence of scaling the radon diffusion coefficient during regeneration may be seen (green-spectrum curves). By comparing the simulated curves to the measured RC data (black circles), we may reject values of the diffusion factor f_D that have been scaled by values very different than 2.5 or 3.5 (if no other parameters are changed).

While this analysis presumes that the initial state of a column that contains radon is represented by a flat distribution throughout the longitudinal axis of the column, we could set the initial radon distribution for a simulated RC run to be that inferred at the end of a preceding simulated BTC, where the measured input radon concentration from that BTC is passed to the simulation. Figure 7.73 shows radon distributions at equilibrium (after 48 hours) produced by simulated BTCs; these may be compared to the flat radon distribution (black line in figure) used as the initial column state(s) for the simulated RCs in this analysis. In the case of the flat distribution and final state produced by a constant input radon concentration (dashed blue line in figure), the normalized shape of the radon distribution is scaled such that the output radon concentration exiting the first filtering stage (during the first hour of Fig. 7.71) matches the measured concentration. That is, the amount of radon exiting the simulation and the physical RRS in the first filtering stage is expected to be the same, and therefore the amount of radon in the column (which is not exactly known) is scaled to match. To the extent that the radon distribution within the columns does not approximate a flat distribution, the first few cycles could be less representative of the measured radon concentration.

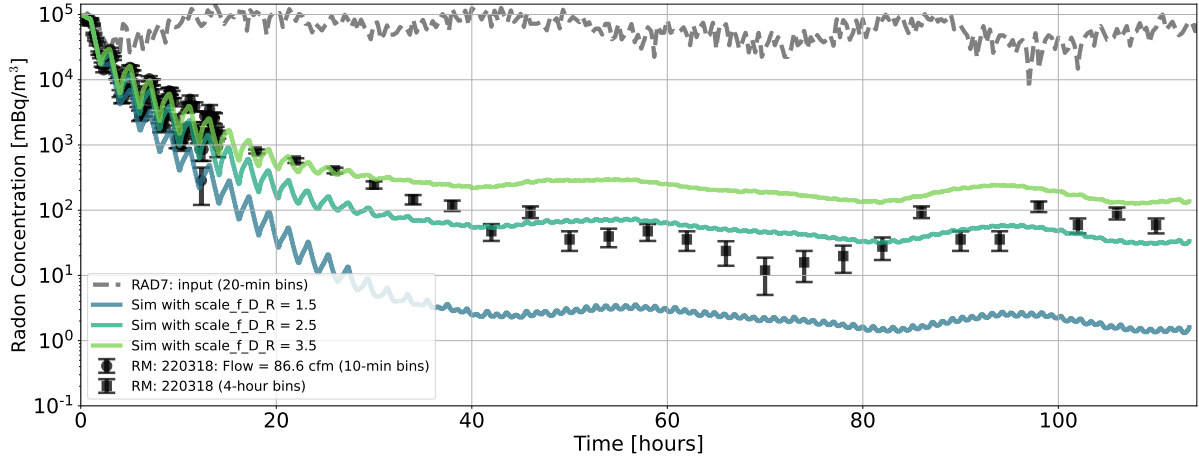


Figure 7.75: Repeat of Fig. 7.74, but showing a larger time scale. At equilibrium, a scaling value of about 2.5 appears preferred over the smaller and larger values.

While agreement is not within uncertainties, Fig. 7.71 indicates that the values of f_A and f_D are reasonably accurate as obtained from BTC runs, but with f_D increased by a factor of two. We may vary each to see if and how we may achieve better agreement particularly during regeneration, as the models have only been informed by the filtering stages. The least-constrained simulation parameter considered in this analysis is the diffusion coefficient factor f_D , as discussed in Section 7.13.3. Here, we make use of a simulation parameter that allows for f_D to be scaled by a multiplicative factor during any stage during swing mode. Figure 7.74 shows results from scaling the diffusion coefficient during regeneration by `scale_f_D_R` (where the “R” stands for regeneration). The diffusion model informed by BTC data appears to underestimate the diffusion coefficient factor during regeneration by a factor of about 2.5 or even 3.5. Figure 7.75 shows the same simulation predictions, but at larger time, allowing simulation and measurement to be compared at equilibrium. We observe better agreement with measurement when the value predicted by the quadratic model (Eq. 7.99) is scaled up by a factor of 2.5. For this entire section, the default value of `scale_f_D_R` has been set to the value of 2.5. Further scaling up the diffusion factor to, say, 3.5, appears to worsen agreement at large time (at least for this run). The reason for changing the diffusion factor value instead of the adsorption factor value (recognizing that a similar effect may be obtained from either) is

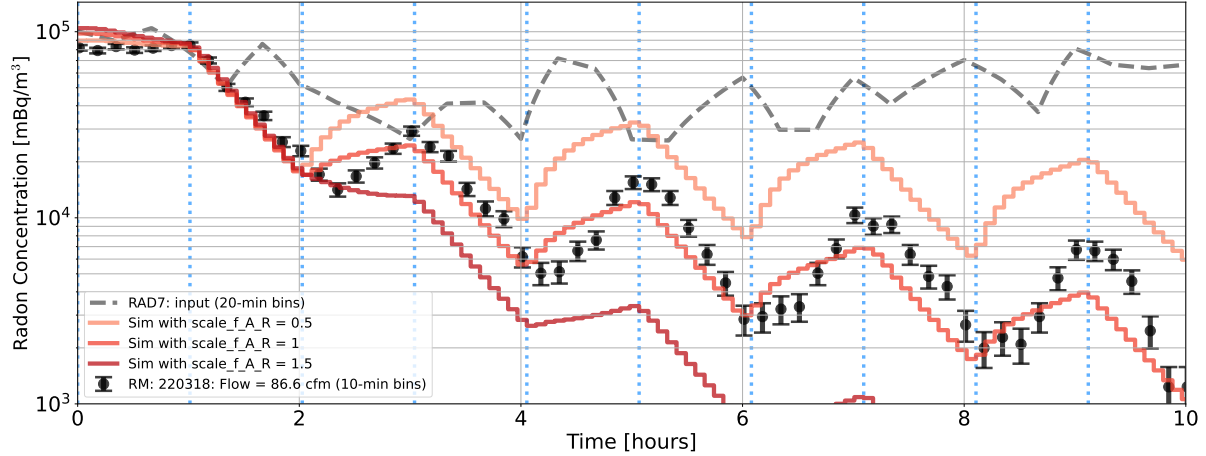


Figure 7.76: Similar to Fig. 7.71 but excluding the unmodified simulated RC (not passed through Eq. 7.110), the influence of scaling radon adsorption during regeneration may be seen (red-spectrum curves). By comparing the simulated curves to the measured RC data (black circles), we may reject values of the adsorption factor f_A that has been scaled by values very different than 1.

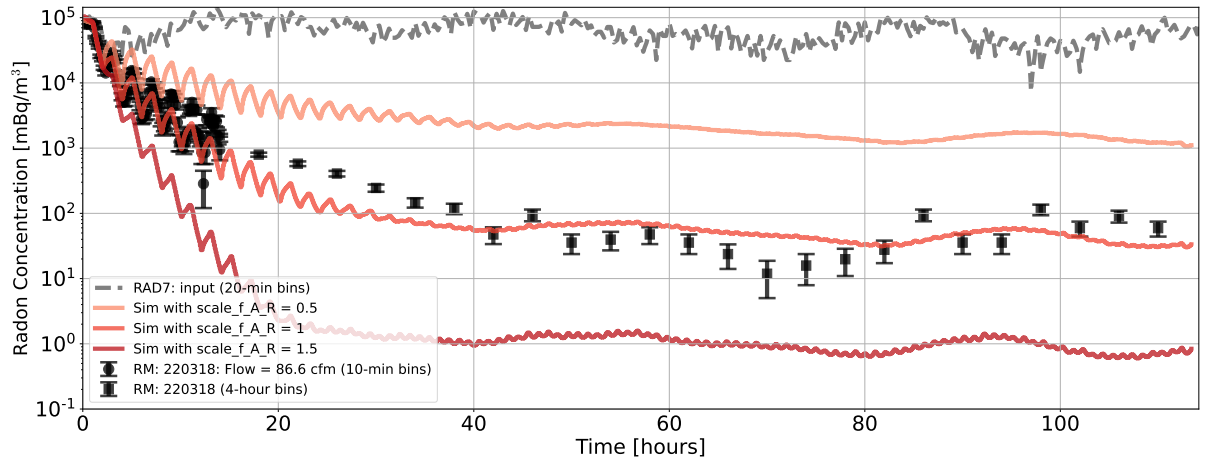


Figure 7.77:]

Repeat of Fig. 7.74, but showing a larger time scale. At equilibrium, a scaling value of about 1 appears preferred over the smaller and larger values.

that the diffusion model does not constrain the diffusion factor during regeneration very much (as compared to the adsorption factor).

Similarly, we may scale the adsorption factor f_A (also discussed in Section 7.13.3) during regeneration by the simulation parameter `scale_f_A_R`. We would not expect scaling values different than unity to improve agreement with measurement much, as f_A appears not to vary greatly with air speed. Therefore, when extrapolating to larger air

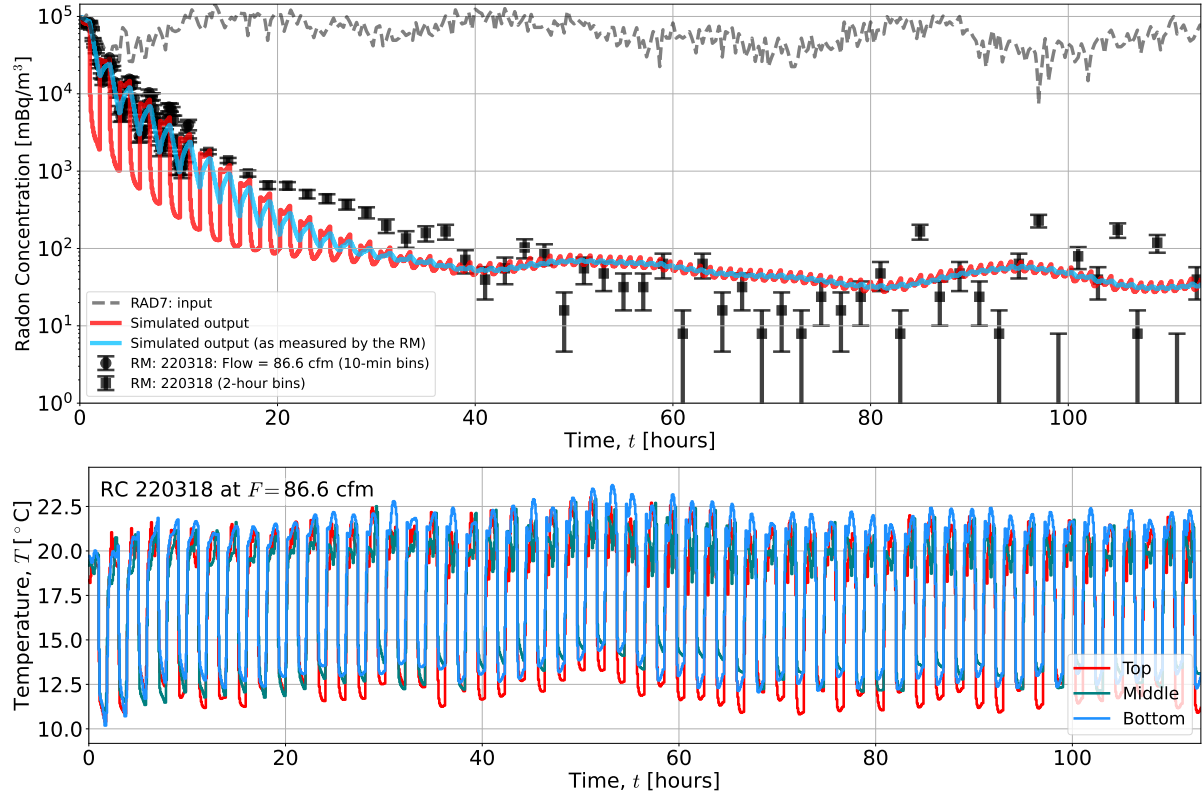


Figure 7.78: Top: The measured RC (black circles and squares denoting 10-minute and 2-hour bin sizes respectively) as produced by the SD Mines RRS provided with input air drawn from the local lab space (gray, dashed curve). The simulated RC (red curve) is passed through the mixing equation (Eq. 7.110) to produce the expected output radon concentration as measured by the RM (blue curve). **Bottom:** The temperature within one column is inferred by resistive-temperature devices (RTDs) located at the Top, Middle, and Bottom locations within the column, as described by Fig. 7.23.

speed, such as that during regeneration, we expect a more reliable prediction as compared with our diffusion model. Figure 7.76 shows the first 10 hours of the same RC run we have been exploring in this section. By scaling the adsorption factor to be smaller or larger by 50%, we observe worsened agreement than when set to unity (the default value). Figure 7.77 also shows some preference for the default value after equilibrium has been reached.

The simulated RC for run 220318, that we have explored thus far, shows reasonable (though not great) agreement with its measured counterpart. However, general agreement among all runs is worse, with particularly poor agreement at the lower flow rates (around 30 scfm) and somewhat better agreement at around 50 scfm. One important

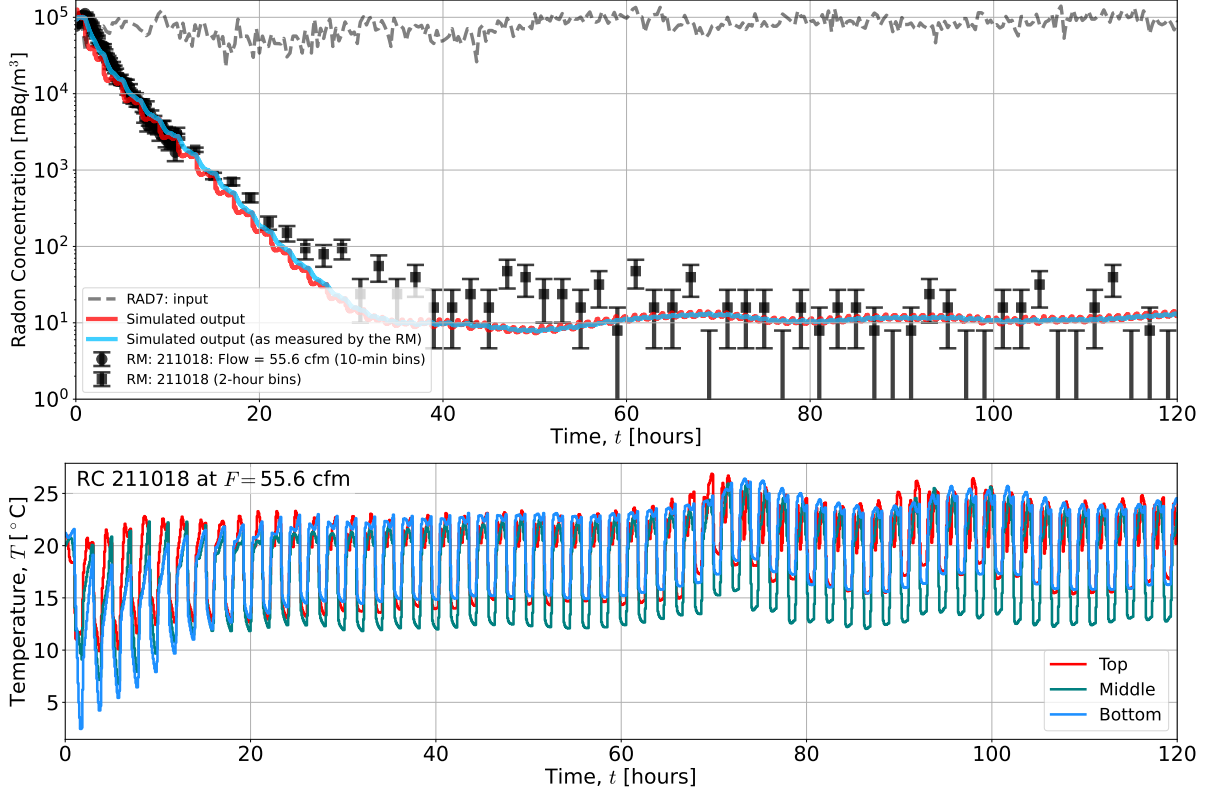


Figure 7.79: Top: Similar to Fig. 7.79, the measured RC (black circles and squares denoting 10-minute and 2-hour bin sizes respectively) as produced by the SD Mines RRS provided with input air drawn from the local lab space (gray, dashed curve). The simulated RC (red curve) is passed through the mixing equation (Eq. 7.110) to produce the expected output radon concentration as measured by the RM (blue curve). **Bottom:** The temperature within one column is inferred by resistive-temperature devices (RTDs) located at the Top, Middle, and Bottom locations within the column, as described by Fig. 7.23.

difference between low- and high-flow runs is that low-flow runs show more pronounced time dependence at early times (in the first 20 hours or so). We presume that the change in column temperature is due to changes in the amount of moisture within the column (as water is removed each regeneration stage). It is expected that as the amount of moisture in the carbon changes, so will the adsorption factor, and thus the speed of radon moving through the column. Figure 7.78 (Top) shows once again run 220318 while Fig. 7.78 (Bottom) shows its associated temperature profile measured within one of the two columns. At the relatively high flow of 86.6 scfm, the temperature profile shows large swings between temperature during regeneration and filtering stages; but otherwise, the average temperature during each stage is similar, with deviations of only a couple degrees.

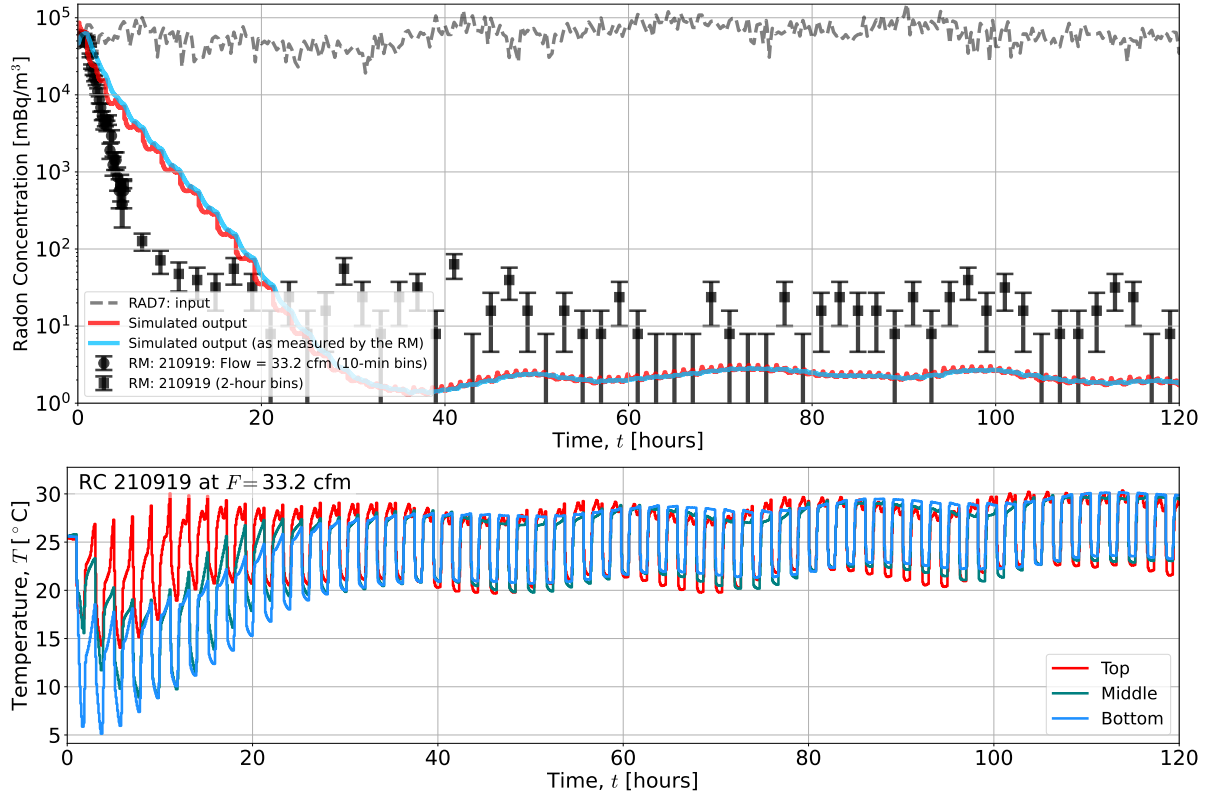


Figure 7.80: Top: Similar to Fig. 7.79, the measured RC (black circles and squares denoting 10-minute and 2-hour bin sizes respectively) as produced by the SD Mines RRS provided with input air drawn from the local lab space (gray, dashed curve). The simulated RC (red curve) is passed through the mixing equation (Eq. 7.110) to produce the expected output radon concentration as measured by the RM (blue curve). **Bottom:** The temperature within one column is inferred by resistive-temperature devices (RTDs) located at the Top, Middle, and Bottom locations within the column, as described by Fig. 7.23.

In order to further study the differences between simulated and measured RCs, we need to look at a couple other representative runs. Figure 7.79 shows RC run 211018 which was performed with the same configuration as 220318, but at a lower flow of 55.6 scfm and with both columns originally flushed with high-radon lab air (so the sawtooth features at early times are less pronounced). This run shows the best agreement of any of the runs; though this is not purely due to the flow rate, as there is another run around 50 scfm that shows more disagreement at both early and late times, indicating that there is at least another important variable at play.

Figure 7.80 shows RC run 210919 which also was performed with the same configuration as 220318, but at a low flow of 33.2 scfm and with both columns flushed with

high radon lab air. At this relatively low flow rate, we observe the largest time dependence in the temperature profiles, as seen in the first 30 hours of the run. The simulated RC for this run shows significant disagreement at both early and later times. Low-flow RC runs are particularly instructive for the following reason: the measured reduction in the output concentration over time is larger than predicted by the simulation (*i.e.*, equilibrium is reached more quickly), while the steady-state concentration is larger than predicted. This presents the simulation with an impossible task, as changes to either radon adsorption or diffusion factors may improve agreement in one region, but at the cost of worsened agreement in the other. One possible explanation comes from the time dependence observed in the associated temperatures measured within the columns.

The temperature within a column appears to depend significantly on the moisture in the input air and any water already in the carbon bed at the start of swing mode. When water adsorbs to the carbon or condenses (from a gas to a liquid), energy is given up to the environment (an exothermic reaction, which *heats* the surrounding air and carbon). Similarly, desorption and vaporization requires bonds to be broken, which requires energy from the environment (an endothermic reaction, which *cools* the surrounding air and carbon bed). Unfortunately, neither the relative humidity of the input air or the moisture content of the carbon beds is actively monitored such that we may implement a robust model for how relative humidity might influence the adsorption and diffusion coefficients of radon. Though we do have hand-recorded values of the relative humidity and temperature (and therefore dew point) of the post-chillers input air (just before the columns), they serve to indicate only that the amount of moisture in the input air does change over time according to ambient lab conditions. Perhaps fortunately, the relative humidity can vary significantly in the lab space that we occupy, often ranging from 20% to 60% over a day-night cycle, and well over 80% during storms. The SD Mines RRS dehumidifier and air chillers do remove some of this moisture, but with a modest efficiency

(such that storms, for example, have a notice influence on the achieved radon reduction by the RRS).

If the humidity of the input air is always the same, the amount of water introduced to the filtering column is proportional to the flow rate. During swing mode, at equilibrium, the amount of water added to a column each filtering stage is equal to the amount of water purged during the regeneration stage (ignoring the very small amount that exits the filtering column). From these two statements, we may expect that at higher flow rates the average amount of water in the columns is larger. As indicated by the temperature profiles at decreasing flow rates (for example, bottom plot of Fig. 7.79, Fig. 7.79, and finally Fig. 7.80), it appears to take longer to reach an equilibrium state (of water being added and removed) at smaller flow (as the time until a steady-state temperature profile is reached for 90, 50, and 30 scfm appear to be *roughly* 1, 15, and 30 hours respectively).

This relationship between how quickly equilibrium (of the temperature profiles) is approached and flow suggest that at high flow the amount of water added each filtering stage is nearly the same as that removed during each regeneration stage as soon as after the second cycle (depending on how much water was originally in the column, of course). At low flow, the amount of water added each filtering stage appears relatively small compared with that removed each regeneration stage, and so equilibrium is only reached after many cycles (perhaps 15 for RC run 210919). Because it is expected that humidity in the input air will increase the speed at which radon passes through the carbon bed [102, 110], an important inference is that, at low flow, we may expect a time dependence on the radon adsorption and possibly also diffusion factors.

At late times (once equilibrium has been reached), the temperature measured during the filtering stage is due to the temperature of the input air and any adsorption/desorption or phase changes of the water within the column, which depends on the moisture content of the input air. Similarly, the late-time temperature within the regeneration column is due to the initial temperature of the column (at the end of filtering), the

pressure drop within the column, and how much water is available to be desorbed or vaporized (both endothermic reactions). By comparing the late-time (after equilibrium) to the early-time temperature (the first 20 hours of the bottom plot of Fig. 7.80), we may infer that the much lower regeneration temperatures observed at early times for low-flows must be due only to the excess water (*i.e.*, more than is added each filtering stage) in the column being removed (as all other parameters are presumed to be the same). The time dependence on the regeneration temperatures, then, indicates the removal of water over time, reaching a steady state after about 30 hours (where the water added during filtering is equal to the water removed during regeneration). Therefore, the lower temperatures at early times indicate a large initial amount of water in the columns that is vaporizing or desorbing and then purged each regeneration stage; the presumed coverage fraction of water molecules on the carbon surface is thus reduced, making available additional radon adsorption sites, resulting in radon moving more slowly during both regeneration and filtering stages at late times.

Intriguingly, we may expect improved regeneration when a column contains more water, provided that the reduced temperature during that stage is subdominant to the depletion of radon adsorption sites. If one tried to exploit this effect, one would, of course, have to ensure that the similarly increased speed of radon during the filtering stage does not compromise the net effect on system performance.

Though we can't take this line of explanation for the disagreement between simulated and measured RCs much further without at least time-series data of the relative humidity of the input air, we may still propose a toy model, which may aid in guiding future work (and act as a weak test of the humidity hypothesis). We have good evidence for there being more water in the columns at early time as compared to later time, with the difference being most significant at low flow. A result is that the adsorption factor f_A is larger at early times than at later times (recall that a larger adsorption factor f_A means that radon adsorbs less and travels more quickly). The proposed toy model will be a

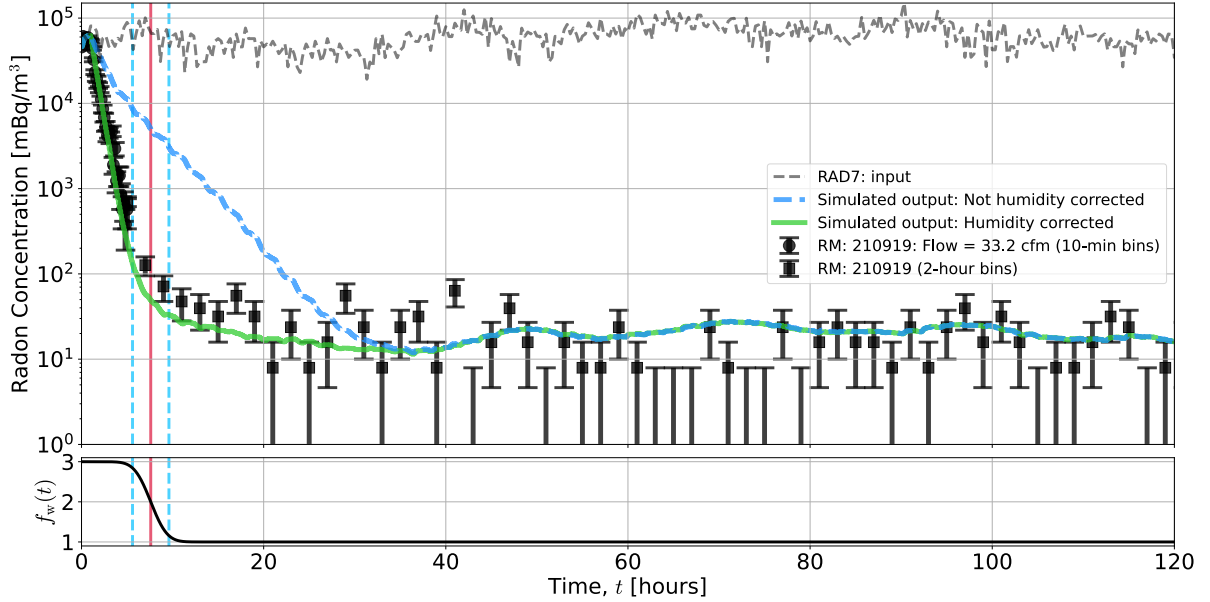


Figure 7.81: **Top:** The measured RC (black circles and squares denoting 10-min and 2-hour binning respectively) is represented far better by the simulated RC with the relative humidity correction (green curve), as compared to that without the correction (thick blue dashed curve). **Bottom:** Relative humidity correction factor $f_w(t)$ with $t_{1/2} = 7.4$ hours (vertical red line) and width $\sigma_t = 1.5$ hours (vertical blue dashed lines) (refer to Eq. 7.112).

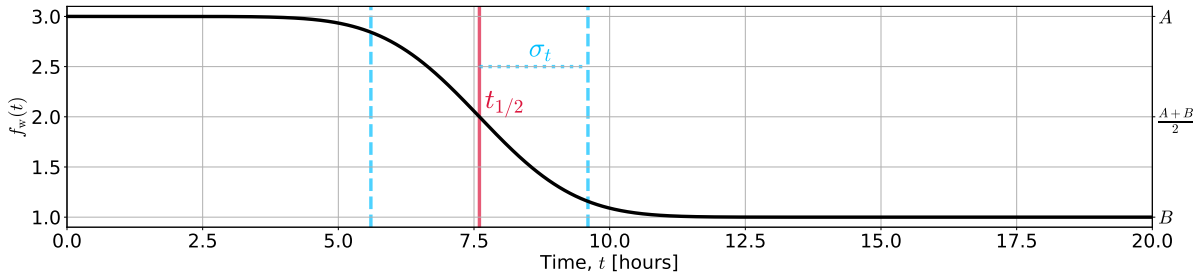


Figure 7.82: Initially, the column contains moisture that is expected to increase the adsorption factor f_A . As time t increases, moisture is removed from the column, eventually reaching an equilibrium (where the amount of water in a column at the end of each cycle is not changing). The adsorption factor is scaled by f_w (Eq. 7.112) as a function of time t . At early times, radon moves more quickly through the column by the factor $f_w(0) = 3$. At late times, the radon speed is unchanged as $f_w(\infty) = 1$. The inflection point time $t_{1/2} = 7.4$ hours and the standard deviation in the sigmoid $\sigma_t = 1.5$ hours, with both inferred from the time dependence of the measured RC.

factor $f_w(t)$ related to the coverage fraction of water in a column, which depends on time t , and will modify the existing adsorption model so that it is a function of time:

$$f_A(v, t) = f_A(v)f_w(t), \quad (7.111)$$

where v is the speed of air passing through the column. Because water vapor passes through a carbon bed in a similar way as radon (moving more slowly than the air that carries it and diffusing along the way), the distribution of water remaining in a column as a function of time will be taken as

$$f_w(t) = \frac{A - B}{2} \left[1 - \operatorname{erf} \left(\frac{t - t_{1/2}}{\sigma_t} \right) \right] + B, \quad (7.112)$$

where $\lim_{t \rightarrow -\infty} f_w(t) = A$, $\lim_{t \rightarrow \infty} f_w(t) = B$, the inflection point $t_{1/2}$ is where $f_w(t_{1/2}) = (A+B)/2$, and the width of the sigmoid is σ_t , with Fig. 7.82 showing the time dependence of $f_w(t)$. Figure 7.81 shows the result of this humidity correction implemented in the simulation for the low-flow run (RC 210919), with empirically found parameters: $A = 3$, $B = 1$, $t_{1/2} = 7.5$ hours, and $\sigma_t = 1.5$ hours. I have also slightly increased the diffusion scaling parameter `scaling_f_D_R` from 2.5 to 3.5, as the value of 2.5 is preferred by some runs while others prefer this larger value. The humidity-corrected simulated RC now agrees reasonably well with this run's data at both early and late times, but the empirical parameters of the humidity model are particular to this run only. A more general humidity model would require measurements of humidity over time.

Comparing simulated RCs with those measured indicates that there is another parameter (suspected to be the humidity of the input air) that is not being accounted for by the simulation. Because the relative humidity of the input air varies widely in our lab space, it is impractical to account for this additional variable without making additional measurements of the relative humidity of the input air, perhaps combined with measurements of the moisture within the columns. Of course, the adsorption and diffusion models used by the simulation for the regeneration stage could be further tweaked; however, this is not necessarily productive in light of the significant effect that water vapor appears to have on at least one (the adsorption factor) of these two parameters (f_A and f_D).

A simulated RC has been produced for each measured RC, using the adsorption and diffusion models found in Section 7.13.3 (parametrized against all measured BTCs). An important comparison between simulated and measured RCs is their respective equilib-

rium radon concentrations (at late time). While the early-time region of a RC can vary significantly between runs due to environmental factors such as humidity and the history of the columns, the equilibrium is not expected to depend on these early-state conditions. Though variability in the measured equilibria is expected due to varying input humidity (not accounted for by the simulation), it is still useful to compare the measured and predicted equilibrium values to obtain a rough sense of the simulation's predictive ability.

Figure 7.83 (Top) shows the result of running the simulation in swing mode with the configurations and measured inputs (such as the input radon concentration and column temperatures) corresponding to each measured RC. The diffusion factor f_D during regeneration has continued to be scaled by $\text{scale_f_D_R} = 2.5$ for all runs; however, it may be recognized that this scaling choice is expected to be driven by input humidity and thus would be particular to a run, and thus not necessarily optimal for any other run. Of the measured runs, three (denoted by squares) showed a sudden increase in the output radon concentration that was sustained over many hours after appearing to approach equilibrium, with logs taken during the run unable to provide any explanation; this increase in the output concentration could, for example, be due to a sudden increase in environmental humidity (perhaps a storm came through the region).

For these three exception runs, equilibria was inferred by taking the mean of measured data between times different than those used to infer equilibria from their simulated counter-part. The usual method is used to infer equilibria from the average of the late-time part (where equilibrium has confidently been reached) of measured and simulated RCs, with the regions averaged starting at a particular time and extending until the end of the run. For these three exception runs, the measured equilibria is inferred from only a portion of the averaged region used for the simulated runs; therefore, time dependence in the input radon concentration and column temperature can influence the inferred equilibria of the two selected regions (that are of different length). The simulated equilibria are

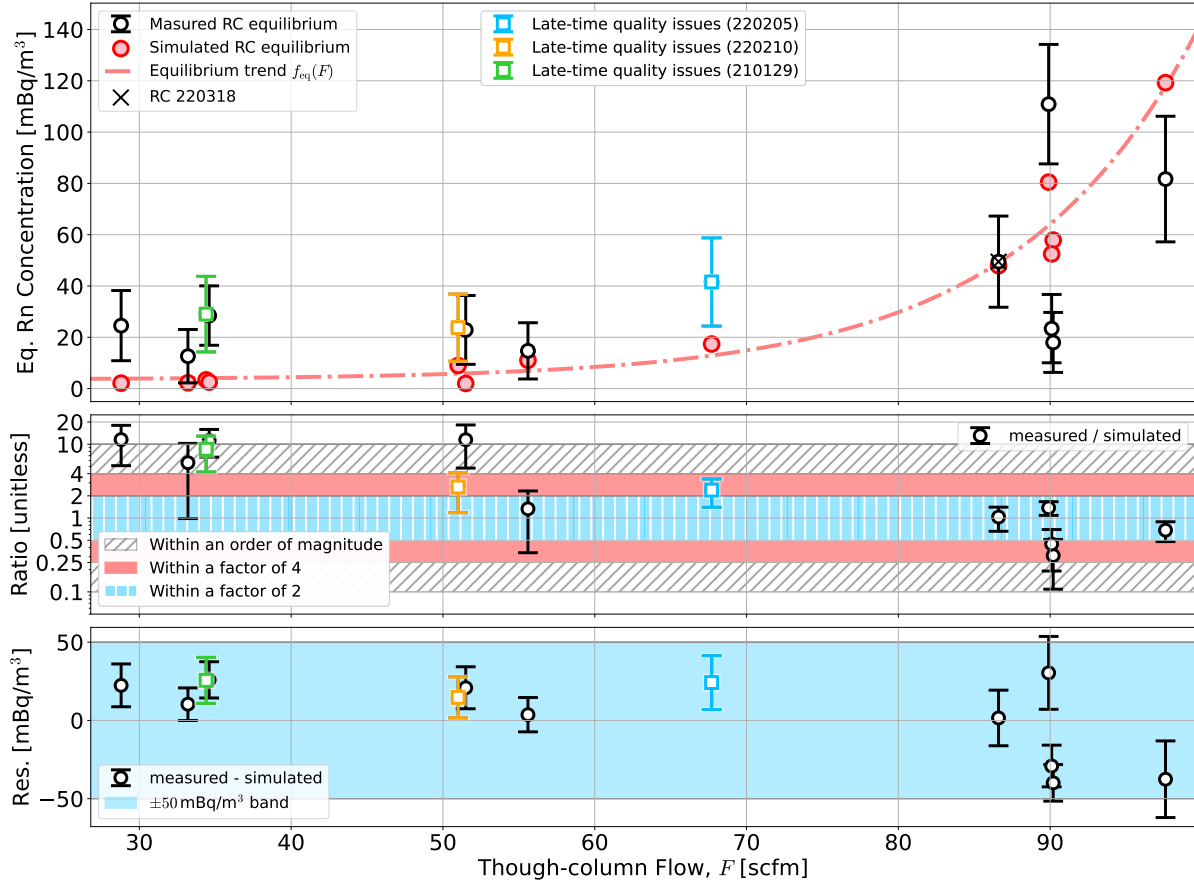


Figure 7.83: Top: The equilibrium radon concentration of measured RCs (open black circles and colored squares) is compared with that of their corresponding simulated RCs (filled red circles); an exponential trend line is drawn (dot-dashed red curve) simulated equilibria. For all but three runs, equilibria is inferred from a time selection where both measured and simulated RCs have reached equilibrium. Each of the three exception runs (220205, 220210, and 210129 represented by colored squares) approached equilibrium but then presented several high-rate readings that are not understood; for this reason, equilibria was inferred by taking the mean of measured data between times different than those used to infer equilibria from their simulated counter-part. RC run 220318, primarily explored in this section, is denoted by the black \times . **Middle:** Filled bands illustrate where the ratio of measured over simulated equilibria is within a factor of 2 (vertically-hatched blue region), a factor of 4 (light red region), and a factor of 10 (forward-hatched gray region). **Bottom:** The residual is calculated by subtracting simulated equilibria from corresponding measured equilibria. All points are within the ± 50 mBq/m³ band (blue region).

still inferred from a particular time until the end of the run to obtain a better estimate of the equilibrium concentration. The slight difference in methodology between these three exception runs and the rest of the runs might suffer from both differences in the inferred equilibria due to time dependence and/or selection bias in the region of the measured RC used to infer equilibrium.

No attempt to account for input relative humidity has been made in these predictions. The general trend in simulated equilibria is represented well by an exponential function depending on the through-column flow F :

$$f_{\text{eq}}(F) = A \exp\left(\frac{F}{B}\right) + C, \quad (7.113)$$

where the fitted parameters $A = 0.03 \pm 0.04 \text{ mBq/m}^3$, $B = 12 \pm 1.7 \text{ scfm}$, and $C = 3.5 \pm 3.1 \text{ mBq/m}^3$. The trend passes through the measured equilibrium of RC 220318, as expected since `scale_f_D_R` was chosen specifically for this run. The middle plot of Fig. 7.83 shows that simulation predicts equilibria systematically $\sim 5\text{-}10\times$ lower than data at low flow ($< 55 \text{ scfm}$); at high flow ($> 80 \text{ scfm}$), agreement is frequently within a factor of two, and not worse than a factor of 4. The bottom plot of Fig. 7.83 shows that the residual between predicted and measured equilibria are always within 50 mBq/m^3 . While this is not a high bar to meet at low flow, as all equilibria are below 50 mBq/m^3 , it is encouraging at higher flow where equilibria increases. Therefore, it is reasonable to take simulated predictions at low flow somewhat less seriously than at high flow, where agreement is rather encouraging.

While the RRS simulation appears to describe many important observations, there are still mysteries that need to be solved. The simulation appears to provide reasonable agreement to BTC data (considering the simplicity of the model). Simulated RCs are also compared to their measured counterpart by the tweaking of only two free parameters (f_A and f_D during the regeneration stage, starting from what is inferred from BTC data). For the simulated RCs, we find poor agreement with measurement, particularly for low-flow runs, with the disagreement believed to be caused by the time dependence of water vapor, not accounted for in the simulation. Because the humidity is not sufficiently monitored, presumptions on how humidity affects radon transport cannot be directly tested. Alternatively, the systematic underestimate of the simulation at low flow could be caused by ambient radon being introduced into either the RRS (perhaps via a leak or from construction material that has an unexpectedly high rate of radon emanation) or

the SD Mines Radon Monitor (see Section 5.1. perhaps at the (low-pressure) input side of the Radon Monitor pump (though no leak has been identified); these types explanations are particularly intriguing, as they can be flow independent (as the measured equilibria at low flow appears to be). At high flow ($> 80 \text{ scfm}$), measured and simulated equilibria often agree within a factor 2 (and always 4). At all flows, predicted equilibria are within 50 mBq/m^3 of that measured. The next steps in simulation development are discussed in Section 7.14.

7.14 Future Work on the Simulation

There is much future work that could possibly improve the RRS simulation's ability to more accurately predict the performance of a physical RRS that uses vacuum (and possibly temperature)-swing adsorption. While there are some specific improvements that could be made to the simulation in the way it is constructed (such as writing faster code for slow modules), most of the tasks listed below require taking additional data with the SD Mines RRS (and/or the SD Mines Table-top System) and then using that data to inform our physics descriptions within the simulation.

Perhaps the most significant roadblock to making further progress in tuning (and otherwise making corrections to) the simulation is not knowing the relative humidity of the input air and, somewhat related, how much moisture is in each carbon bed at any time. By installing humidity sensors at the SD Mines RRS input and output that are read out by a computer, where readings are recorded at standard intervals, we may construct a model for how humidity influences radon adsorption and diffusion. By implementing a model of humidity and column moisture into the simulation, we may obtain improved agreement between simulation and measurement, particularly in swing mode, where the predictions most important are made. Monitoring the moisture content of the carbon beds is expected to improve the simulation's predictive ability in the early times of swing mode, though getting this right is not expected to change predictions of the radon

concentration at equilibrium. Relative humidity sensors are inexpensive, easy to use, and could be installed alongside additional temperature sensors.

While resistive-temperature devices (RTDs) have already been installed at various locations within one column and in the input air stream, there is some concern as to whether their readings are representative of the carbon surface or the air stream passing through the carbon (and thus not necessarily representative of the carbon surface). To determine what the RTD measurements best represent (such as the temperature of the carbon surface or that of the air stream), infrared (IR) sensors may be installed alongside (or possibly in place of) the RTDs within each column. The IR sensors are sensitive to radiative losses from material surfaces and should provide a direct measure of the carbon's surface temperature (about which we are most concerned). Installing additional RTDs and/or IR sensors within both columns (as apposed to just one) provides the necessary temperature data needed to construct evolution operators for both columns individually. Improved temperature data should allow the temperature model implemented in the simulation to be further tested and improved, thus improving the accuracy of simulation predictions.

Currently, each column within the simulation is presumed to be identical with one set of operators used to evolve radon atoms within them. For example, operators representing the first 60 minutes of filtering for one column are then used by the second column during its first filtering stage, and so on. This method reduces computation time, but lacks representation of both columns. Treating both columns equally is specifically problematic when the histories of both columns is not the same, as is often the case after performing long BTC measurements through one column while the other is kept in a regenerating state. Therefore, the simulation is expected to make more accurate predictions when each column has its own set of operators built for each stage during a run. This means double the operators will be created.

While the the module used for building operators is already written in C++, the simulation may greatly benefit from more modules being rewritten from Python to a lower-level, faster language (*e.g.*, C++, Golang, etc.). Alternatively, one may consider using the Numba Python library, which compiles Python code to optimized machine code (using the LLVM standard compiler [163]), which can increase algorithms to speeds approaching that of C or FORTRAN [164].

7.15 RRS Simulation Predictions

Though the simulation is far from perfect (as was discussed in the last several sections), it may still serve to guide exploration of future research and development on similar radon reduction systems. As discussed at the end of Section 7.13.4, predictions of the output radon concentration at equilibrium are expected to be more reliable at high flow ($> 55 \text{ scfm}$) than at low flow ($< 55 \text{ scfm}$). Trends produced by changing simulation variables are expected to be of particular interest in system design and optimization and are thus explored extensively in this section.

Because water in the input air, and in the column at the start of a run, appears to have a significant influence on the shape and equilibrium reached during swing mode, it is presumed that the input air is sufficiently dry such that any influence of water can be neglected (and moisture in the columns at the beginning of swing mode is eventually removed as equilibrium is approached). This presumption that the air is dry, is expected to affect predicted equilibria by factor of four (and more often two), which is small compared to the many orders of magnitude spanned by predicted equilibria.

The equilibrium output concentration is the most important performance characteristic of a radon reduction system. The time required to approach equilibrium tends to correlate with equilibrium performance, and therefore is not explored in detail here. For these predictions, however, one might expect that equilibrium is likely reached well within a week of starting swing mode operation. The following prediction plots were generated

with the simulation configured in the same way, but with one parameter varied (unless noted otherwise). The most relevant simulation parameters are listed in Table 7.4.

In practice, we are often interested in the flow rate F_{cr} of low-radon air that may be provided to a low-radon cleanroom. This flow rate, sometimes called the *make-up air*, is defined as

$$F_{\text{cr}} = F - f_{\text{purge}}, \quad (7.114)$$

where F is the through-column flow rate and f_{purge} is the purge-flow rate (all with units of scfm).

Often when describing the performance of a RRS, it is useful to refer to the *radon reduction*, defined as

$$\text{RR} \equiv C_{\text{in}}/C_{\text{eq}}, \quad (7.115)$$

Parameter Description	Symbol	Default Value	Units
Through-column flow	F	varied	scfm
Purge flow	f_{purge}	7	scfm
Input radon concentration	C_{in}	100	Bq/m ³
Regeneration time	t_R	45	min
Slowfill time	t_S	15	min
Column length	L	120	cm
Column diameter	d_{\odot}	76.2	cm
Filtering temperature	T_F	22	°C
Regenerating temperature	T_R	13	°C
Slowfill temperature	T_S	13	°C
Carbon emanation rate	E_{\bullet}	0.1	mBq/kg
Faster vacuum pumps*	\tilde{S}	1	unitless
Leak rate during filtration	f_{leak}^F	0	scfm
Leak rate during regeneration	f_{leak}^R	0	scfm
Leak rate during slowfill	f_{leak}^S	0	scfm
Low-emanation carbon†	φ	0	unitless

Table 7.4: The default simulation parameter values are listed in the *Default Value* column. While this list is not exhaustive, it includes the most relevant parameters that are varied within this section. *The simulation modifies the pressure within the regenerating column to emulate vacuum pumps with higher pumping speeds. †A fraction φ of the carbon within a column (as measured from the output side during filtering) is replaced with carbon having a lower radon emanation rate.

where C_{in} represents the input radon concentration (nominally 100 Bq/m³) and C_{eq} is the equilibrium output radon concentration.

The following predictions are sorted into three categories: operation, modifications, and leak-tightness criteria. Depending on particular details of a RRS (*e.g.*, column geometry and pumping speed), there likely exists a preferred set of basic **operational parameters** (such as the regeneration time and purge-flow rate) that produces, for example, the largest radon reduction when supplying 100 scfm to a cleanroom (or other application). Further improvements in system performance may be obtained through **hardware changes**. For example, one might consider longer carbon columns or active heating of the purge-flow air. Several intriguing and practical hardware changes of this type are explored, with plots showing predictions of how system performance may be affected. Finally, during commissioning, after modifying some aspect of the system or performing certain maintenance work, one often has the troubleshooting task of finding and minimizing the rate that high-radon lab air is leaking into the low-pressure regions of the RRS. The simulation can provide insight into **leak-tightness criteria** for particular regions of the system in order to achieve a required radon reduction. Of course, the simulation can be used to help troubleshoot other issues as they arise.

A baseline in RRS performance is illustrated by Fig. 7.84, where only the input radon concentration C_{in} is varied. The general trend is that an increase in the input concentration results in an increase in the output concentration. Similarly, as the through-column flow increases, more radon exits the filtering column, thus increasing the equilibrium radon concentration. The nominal input concentration for the SD Mines RRS is ~ 100 Bq/m³ (red curve). When the through-column flow $F > 55$ scfm, the predicted output concentrations are often within about a factor of two of equilibria measured (though agreement isn't necessarily expected as water is not being accounted for).

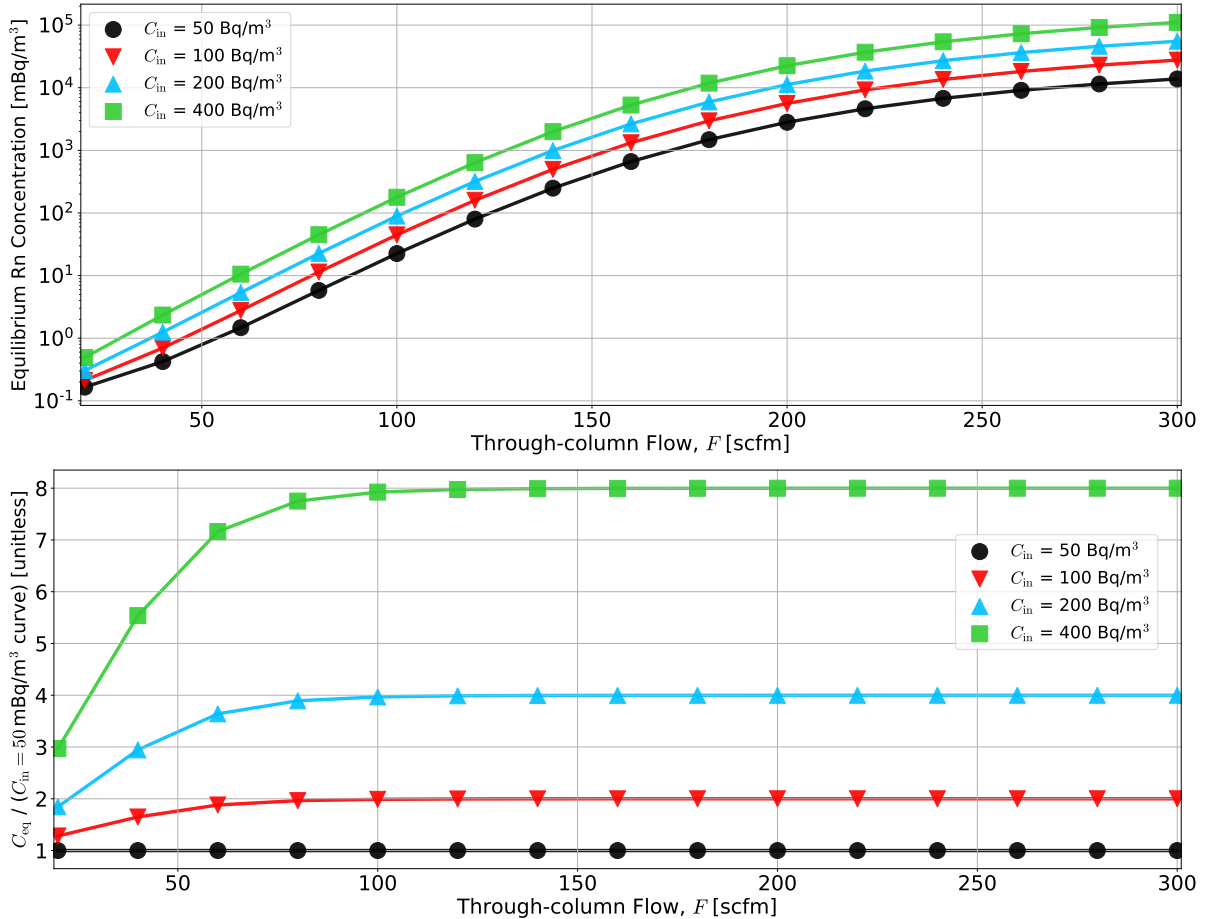


Figure 7.84: **Top:** The equilibrium radon concentration (colored shapes) depends on the flow F passed through the filtering column. Here, the input concentration is varied from 50 to 400 Bq/m^3 , with each increase a doubling of the previous value. Increasing the input radon concentration increases the amount of radon that breaks through the filtering columns, thus increasing the equilibrium radon concentration. **Bottom:** Each curve from the top plot (denoted as C_{eq}) is divided by the $C_{in} = 50 \text{ mBq/m}^3$ curve; this shows that the equilibrium concentration is proportional to the input concentration (for $F \geq 100 \text{ scfm}$). For $F \leq 100 \text{ scfm}$, radon emanation from the carbon brings curves closer together.

7.15.1 Improving RRS Performance by Optimizing Operational Parameters

Swing mode operation requires setting two important parameters: (1) the time spent regenerating t_R before switching to the slowfill stage and (2) the purge-flow rate f_{purge} . Figure 7.85 shows that there is an optimal regeneration time for this particular system. When the regeneration time is small (15 min), we spend 30 min filtering, as the default slowfill time is 15 min. This means that only half of the time filtering is spent regenerating. System performance improves when t_R/t_S becomes large, but only in the limit

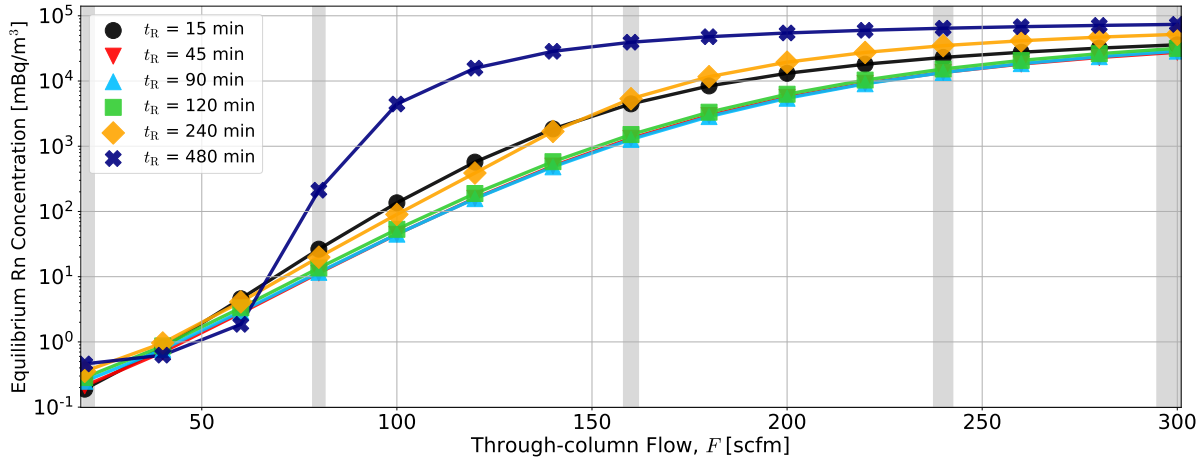


Figure 7.85: Dependence on regeneration time t_R of the equilibrium radon concentration (colored shapes) versus the flow F passed through the filtering column. As t_R increases, radon reduction improves until about 120 min; further increasing the regeneration time then begins to reduce performance as radon breaking through the filtering column increases with the increased filtering time $t_F = t_R + t_S$. The vertical gray lines with thickness increasing with increasing flow are referenced by Fig. 7.86, where equilibria versus t_R at particular through-column flows F are shown.

that we are not being dominated by radon breaking through the filtering column. As the regeneration time is increased to more than 120 min, we observe a larger output concentration (illustrated by the left plot of Fig. 7.86), particularly at higher flows (where we would expect more break through). The SD Mines RRS operates with the default regeneration time of 45 min to balance these two competing effects, while a regeneration time of 90 min would have also been a slightly better choice.

We also show the effects of changing the slowfill time t_S . Because the filtering time $t_F = t_R + t_S$, increasing t_S always comes at the cost of increased time filtering per cycle or reduces the fraction of time per cycle spent regenerating. Figure 7.87 shows that the slowfill time t_S should always be minimized to the time required to raise the regenerating column to atmospheric pressure (so that it is ready to be used for the filtering stage).

The required slowfill time t_S is inversely proportional to the purge flow f_{purge} . While the purge flow could be chosen to reduce t_S , by increasing the purge flow we increase the base pressure during regeneration, reducing the speed of radon being purged, and thus reducing the efficiency of the regeneration stage. Another drawback to increasing the

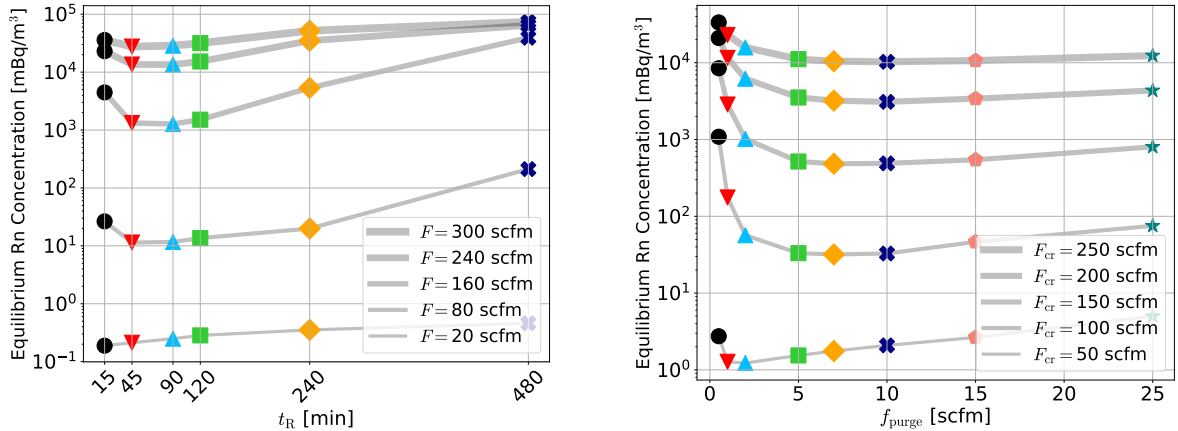


Figure 7.86: **Left:** Built from the prediction curves shown in Fig. 7.85, at increasing flow F (gray lines of varying thickness), the equilibrium radon concentration (colored shapes) is minimized by setting the regeneration time t_R between 45 and 90 minutes (with the exception of the very lowest flow where $t_R = 15$ min is optimal). **Right:** Similar to the left plot, but when varying the purge flow. Increasing the purge flow improves radon reduction only until about $f_{\text{purge}} \approx 5$ scfm, but at the cost of make-up air F_{cr} (please refer to Fig. 7.88); further increasing the purge flow worsens radon reduction as the pressure within the regenerating column increases.

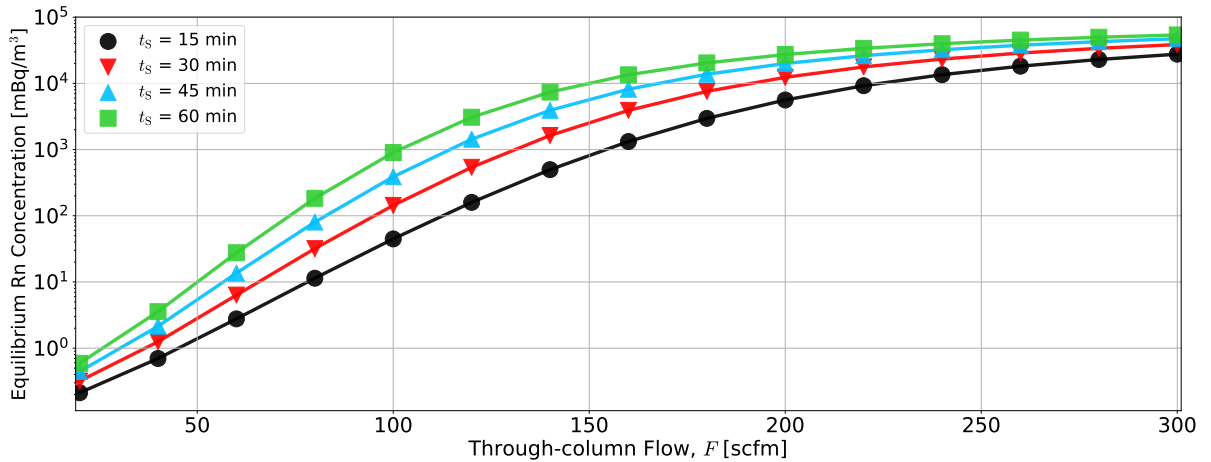


Figure 7.87: While the slowfill stage (of at least 15 min for this system) is required to raise a regenerated column to atmospheric pressure, increasing its duration always reduces system performance, as it comes at the cost of regeneration and increases the time filtering per cycle.

purge flow is that, for a fixed through-column flow, it is subtracted from the make-up air that can be supplied (to a cleanroom, for example), and thus reduces the radon reduction per scfm supplied. Therefore, once again it is difficult to determine an optimal value for the purge flow without a simulation or more measurements. Figure 7.88 shows the equilibrium radon concentration versus make-up air provided to a cleanroom. Unlike the

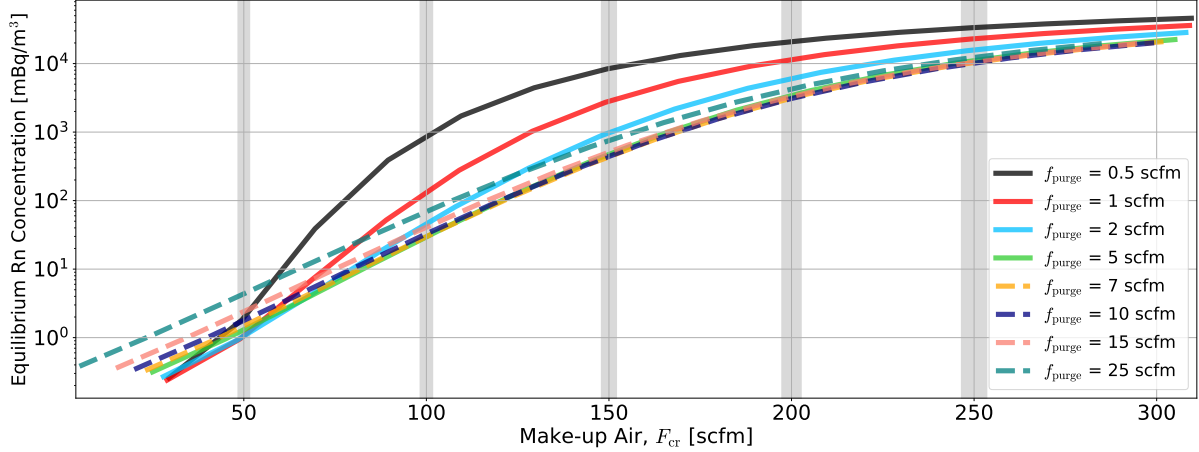


Figure 7.88: The equilibrium radon concentration (colored lines) are plotted against the clean-room make-up air flow $F_{\text{cr}} = F - f_{\text{purge}}$, with increasing values of f_{purge} . For each f_{purge} chosen, the slowfill time is set by the time required to raise the regenerating column to atmospheric pressure. The vertical gray lines, having thickness increasing with flow, are referenced by the right plot of Fig. 7.86, where equilibria versus f_{purge} at particular make-up air flows F_{cr} are shown. Increasing the purge flow improves radon reduction for this system up to about 5–10 scfm; further increasing the purge flow worsens reduction as the pressure during regeneration increases. All increases in the purge flow come at the cost of the make-up air flow F_{cr} .

through-column flow F used in other prediction plots, using the make-up air flow F_{cr} as the domain shows more clearly that at higher purge flow the reduction per scfm decreases as the curve is shifted left (to smaller make-up flow). If make-up air flow requirements are low (~ 30 scfm), a small purge flow of less than 5 scfm appears preferred. If a large make-up air flow is required, setting the purge flow between 5 and 10 scfm appears to provide the best radon reduction for this system; while further increasing the purge flow does not predict improved radon reduction. A purge flow off by 50% from the most optimal value causes about a 10% difference in the predicted radon reduction. The SD Mines RRS allows for the purge flow to be chosen between 1 and 8 scfm (on-scale) and is nominally set to 7 scfm.

In the simulation, the slowfill time t_S must be sufficient to raise the slowfill column to the fraction $\alpha = 0.95$ of atmospheric pressure P_{atm} , but not any longer; therefore, it is calculated according to the set value of the purge flow f_{purge} :

$$t_S \equiv \frac{\alpha P_{\text{atm}} - P_{\text{base}}}{c f_{\text{purge}}} + \frac{16 \text{ scfm min}}{f_{\text{purge}}} \quad (7.116)$$

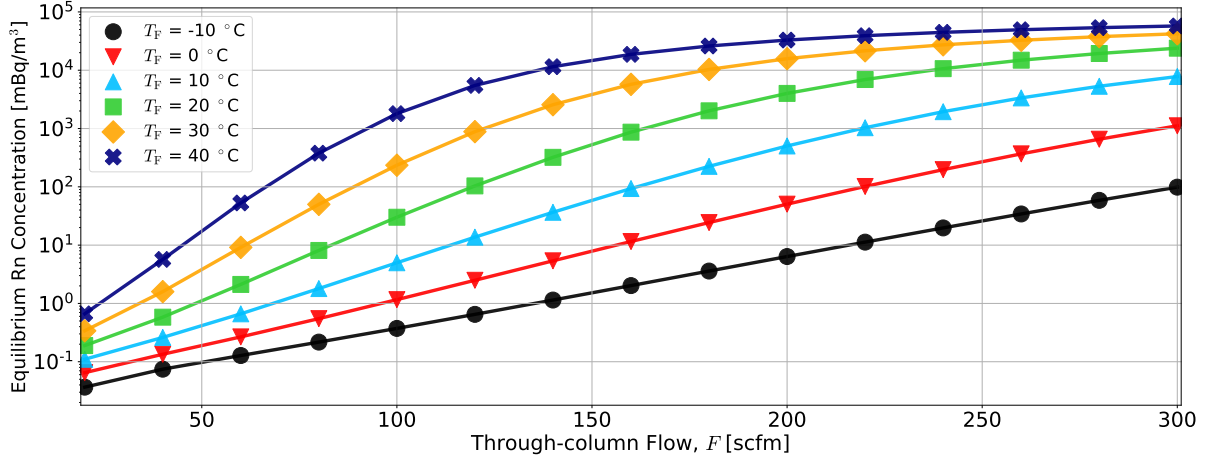


Figure 7.89: Dependence on filtering temperature T_F of the equilibrium radon concentration (colored shapes) versus the flow F passed through the filtering column. The speed of radon passing through the filtering column depends exponentially on the surface temperature T_F of the carbon during the filtering stage. When T_F increases, radon breaks through the column sooner and thus increases the amount of radon exiting the system at equilibrium.

with

$$P_{\text{base}} = m f_{\text{purge}} + b, \quad (7.117)$$

where c , m , b and the factor $16/f_{\text{purge}}$ are found empirically from the SD Mines RRS (and discussed in Section 7.9). The fraction α of atmospheric pressure is empirically motivated by the requirement that the air flow pushed into a column at the start of the filtering stage, due to the column being slightly underpressured, should be small compared to the through column flow F . In this way, prediction curves in Fig. 7.88 account for the relationship $t_S \propto 1/f_{\text{purge}}$ and its affect on system performance.

7.15.2 Improving RRS Performance Through Hardware Changes

The most useful function of the simulation is to guide hardware changes to a physical RRS. Here, several approaches are considered that are expected to be both practical and effective. Along the way, we will also explore hardware changes that might be effective for certain applications, but otherwise do not provide improve reduction in the outlet radon concentration in general (*i.e.*, over the entire flow domain).

Because the mean speed at which radon travels through carbon depends on the temperature of the carbon's surface, a natural approach to improving system performance is to control the temperature of the columns; this may be done by changing the temperature of the air passing into a column or by heating or cooling the carbon bed directly (via electrical induction, a water jacket, or similar). Cooling helps during filtering, while heating helps during regenerating. Figure 7.89 shows how reducing the temperature during the filtering stage, T_F (nominally 22°C), can improve reduction in the output concentration by slowing the speed of radon during this stage, essentially lengthening the filtering column.

Cost Analysis for Active Cooling

One practical approach to cool the filtering column is to further cool the input air by increasing the number of air chillers. One might even substitute dehumidifier units with additional air chillers, as air chillers tend to also remove water from the air stream. Reducing the input air temperature by $\sim 10^\circ\text{C}$ (from 20 to 10°C) at 100 scfm is expected to cost around 5,000 USD (presuming a sufficient chilled-water supply is available), which may result in an additional factor of ten in radon reduction (by moving from the green curve to the blue curve in Fig. 7.89).

A consequence of cooling the filtering column is that the saturation vapor pressure is reduced. Unless the water content in the input air is very low (as presumed here), water vapor may condense within the column, occupying adsorption sites on the carbon surface (reducing the average time radon atoms spend passing through the carbon bed). However, if the input air is cooled by air chillers (as opposed to cooling the columns with, for example, a cooling jacket), the water may be extracted from the air stream before it enters the carbon bed, thus circumventing the issue.

Similarly, heating the regeneration column makes radon move more quickly through the bed and thus be purged more efficiently. Figure 7.90 shows predictions for heating the regeneration column, where the nominal temperature is 13°C (but appears to depend heavily on water content, which is ignored in these predictions). The regeneration stage,

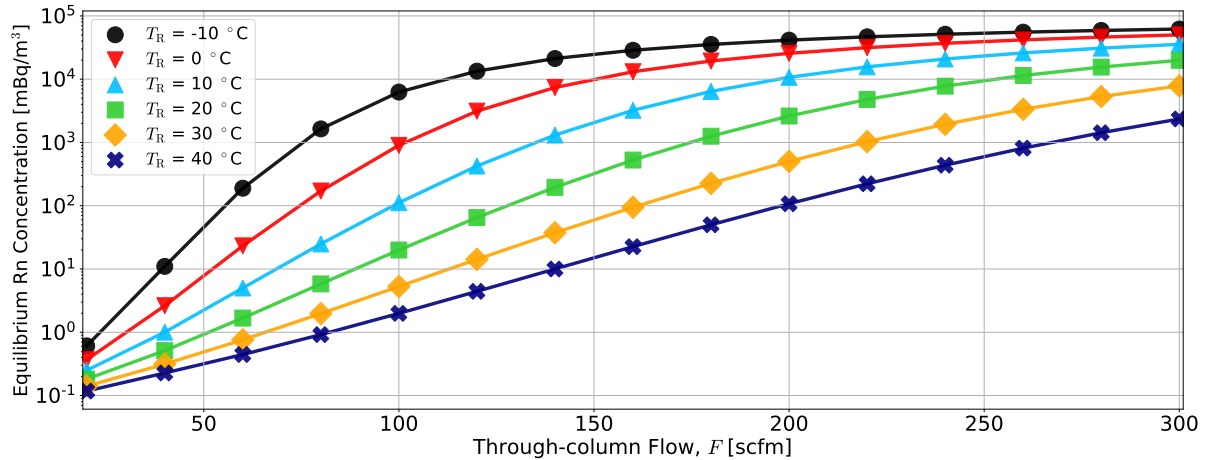


Figure 7.90: Dependence on regeneration temperature T_R of the equilibrium radon concentration (colored shapes) versus the flow F passed through the filtering column. When T_R increases, radon is purged from the regenerating column sooner, reducing the amount of radon that can exit during the filtering stage, and thus reduces the radon concentration at equilibrium (colored shapes).

which we would like to heat, will, after the slowfill stage, be used as the filtering column, which we would like to keep cold; this presents a slight challenge in timing. The slowfill stage could be used to cool the column after regeneration, such that the column is not heated during the filtering stage. Raising the column temperature for regeneration by electrical induction or a heating jacket, however, would need to take place at either the end of the filtering stage or the beginning of the regeneration stage (or partially spanning the two).

Cost Analysis for Active Heating

One practical approach to heating the regenerating column is by using an inline heater directly before the purge-flow valve (but downstream from the purge-flow meter); this heater would be active when either column is regenerating and powered off during the preceding slowfill stage. Raising the temperature of the purge air by $\sim 10^\circ\text{C}$ (from 10 to 20°C) at 7 scfm is expected to cost around 10,000 USD and provide an additional factor of ten in radon reduction (and a factor of about 50 if the temperature could be increased to 30°C). To achieve a 10°C change in the carbon temperature, the purge-flow air will likely need to be much warmer within the purge-flow line, as heat will be lost to surrounding materials.

A particular challenge in this approach is the fact that the purge flow is determined by the total pressure drop from the filtering column to the regenerating column, which is as much as one atmosphere. In practice, the impedance of the

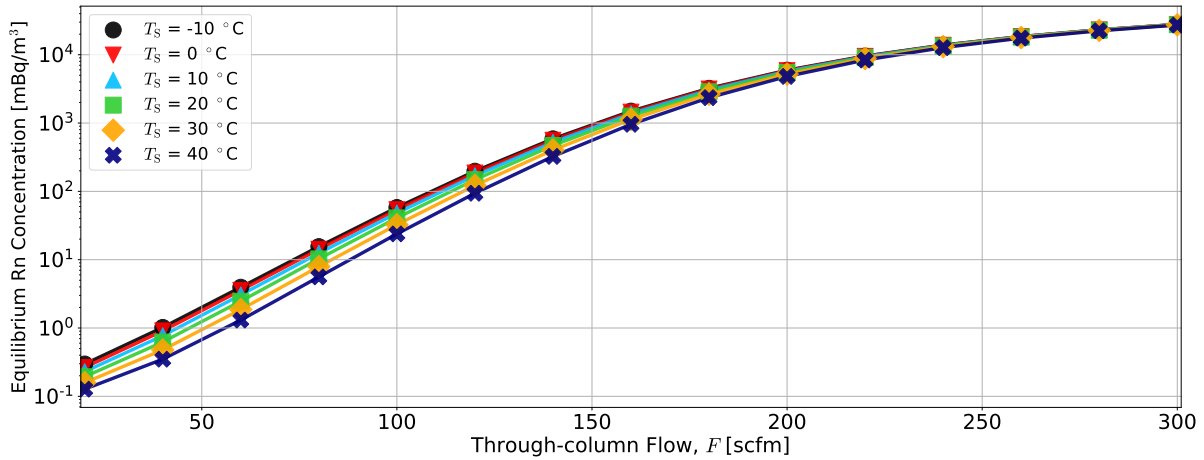


Figure 7.91: Dependence on slowfill temperature T_S of the equilibrium radon concentration (colored shapes) versus the flow F passed through the filtering column. When T_S increases, radon moves further into the slowfill column, reducing the amount of radon near the output of the column during its subsequent filtering stage, and thus slightly reduces the radon concentration at equilibrium (colored shapes), particularly at low flow.

purge-line plumbing (excluding the purge-flow valve) can easily limit the purge-flow rate. For this reason, it is important for the heater to have a very low impedance (perhaps using several in parallel) as well as any required fittings and other connections. Alternatively, one might place an inline blower before the heater in order to offset the heater's impedance, resulting in a net-zero change in the total impedance of the purge line (and thus no change in the purge flow). The risk in using a blower, however, is that it introduces a low-pressure region to the purge-flow line (directly before the blower), and therefore one must ensure that high-radon lab air is not introduced as a result (see the Section 7.15.3). Another practical challenge is that water vapor introduced to the regeneration column via the purge-flow line appears to significantly reduce the temperature during regeneration. For the inline heating solution to be most effective, the purge-flow air should be very dry ($\lesssim 5\%$ relative humidity).

Unlike the filtering and regenerating stages, changing the column temperature during the slowfill stage does not appear to significantly improve system performance. As radon is not purged during this stage, the best-case scenario is that radon atoms that are introduced via the purge-flow line move throughout the column under the increased temperatures (mostly by diffusion). When the column begins its subsequent filtering stage, radon atoms will have diffused throughout the column as apposed to being concentrated on the output side, where they are more likely to exit the column and thus increase the

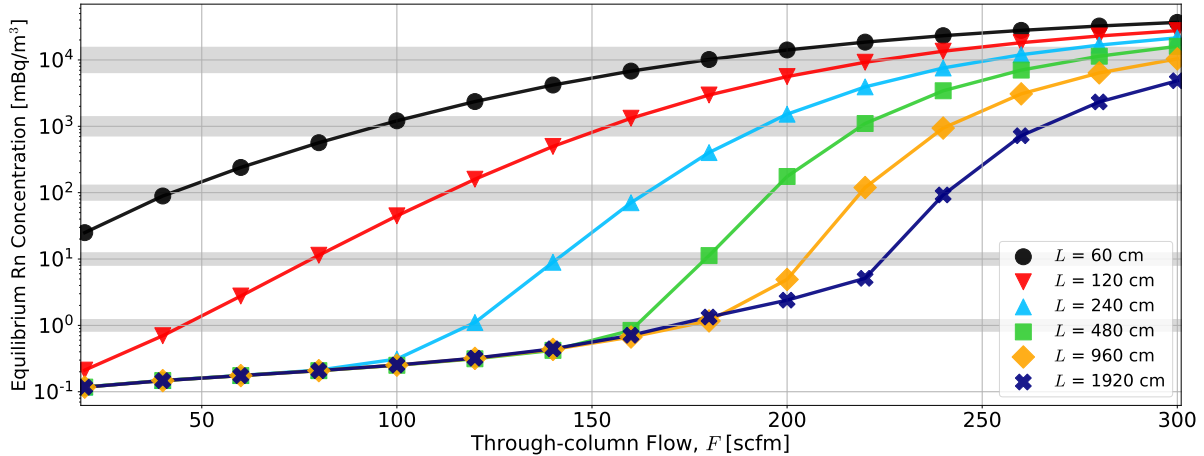


Figure 7.92: Dependence on column length L of the equilibrium radon concentration (colored shapes) versus the flow F passed through the filtering column. Each curve represents an increase in the column length L , while keeping the column diameter fixed. As L increases, the average time required for radon to pass through the column increases. The radon reduction at equilibrium is therefore increased as less radon exits the filtering column each cycle. The shape of the floor of these curves (traced by the $L = 1920$ cm curve until about 225 cm) is due to radon emanation (setting the value of the floor at low flow) and diffusion, which is assumed to be proportional to F^2 . The gray lines of varying thickness are referenced by Fig. 7.94, where the ratio of flow over equilibrium versus L is shown.

output concentration. Figure 7.91 shows predicted curves for increasing T_S that appear to support this logic. Because changing the column temperature during slowfill alone does not appear to provide significant benefit in system performance, it is likely better to use the stage to cool the column before filtering begins.

While controlling column temperature can provide significant gains in performance, a similarly effective approach is to increase the volume and/or geometry of the carbon columns. By increasing the column length L , a smaller fraction of the radon distribution moving through the column during each filtering stage will contribute to the output concentration. Figure 7.92 shows how longer columns provide similar radon reduction for increased flow. In the case that regeneration is perfect (*i.e.*, all radon atoms are purged each regeneration stage), we might expect that columns with twice the length provide the same radon reduction at twice the flow (explored in Fig. 7.94). The predicted curves, however, show diminishing returns on reduction with increasing length, indicating

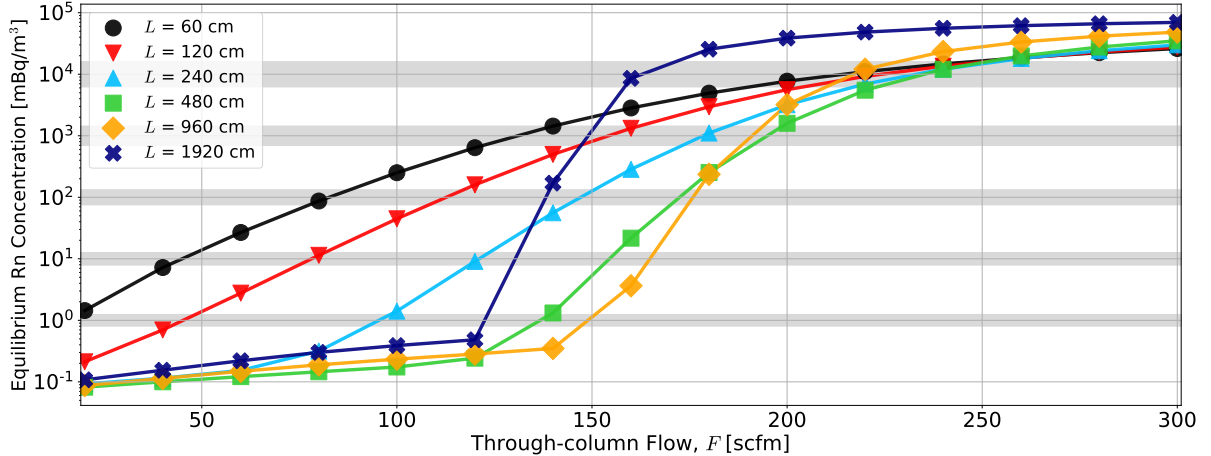


Figure 7.93: Similar to Fig. 7.92, but keeping the total column volume fixed (and thus reducing the column diameter as L increases). As discussed in the text body, the break-through time t_b depends inversely on L . Lengthening a column (with a fixed volume) first improves system performance by minimizing the width of the radon distribution σ_t , but then reduces performance as radon breaks through the filtering column more quickly (due to the decrease in adsorption at high flow). The gray lines of varying thickness are referenced by Fig. 7.94, where the ratio of flow over equilibrium versus L is shown.

that regeneration efficiency becomes a bottleneck for a system with columns triple or quadruple the length of the SD Mines system.

Because the diffusion coefficient of radon within carbon depends on the air speed v , lengthening a column is expected to provide improved performance even when the column volume V is kept the same, as shown by Fig. 7.93. For constant V , the column diameter d_\odot depends on L as

$$d_\odot = 2\sqrt{\frac{V}{\pi L}}. \quad (7.118)$$

As discussed in Section 5.5, the width σ_t of the radon distribution passing through the column in time is

$$\sigma_t \propto \sqrt{f_D/v_{Rn}}, \quad (7.119)$$

The diffusion factor is restated here from Eq. 7.99 for convenience:

$$f_D(v_{air}) = q_1 v_{air}^2 + q_2 v_{air} + q_3, \quad (7.120)$$

where q_i for $i = 1, 2, 3$ are fitted parameters. Because the second-order coefficient q_1 is much larger than the other two coefficients (as discussed in Section 7.13.3), the diffusion

factor may be further simplified as

$$f_D(v_{\text{air}}) \propto v_{\text{air}}^2. \quad (7.121)$$

The average radon velocity (for $v_{\text{air}} \gtrsim 60 \text{ cm/s}$ or similarly $F \gtrsim 10 \text{ scfm}$)

$$v_{\text{Rn}} = f_A(v_{\text{air}})v_{\text{air}} \propto v_{\text{air}}^2, \quad (7.122)$$

where the adsorption factor

$$f_A(v_{\text{air}}) = av_{\text{air}} + b, \quad (7.123)$$

where a and b are fitted parameters, as discussed in Section 7.13.1 and Section 7.13.3.

Substituting Eq. 7.121 and Eq. 7.122 into Eq. 7.119 yields

$$\sigma_t \propto 1/v_{\text{air}}. \quad (7.124)$$

Variables denoted with primes (A' , v'_{air} , etc.) will henceforth refer to a primed column that has its geometry modified while volume is held constant. For the same flow, the air velocity within the primed column is related to the air velocity within the unmodified column according to their respective cross-sections A' and A :

$$v'_{\text{air}}A' = v_{\text{air}}A. \quad (7.125)$$

Because $V' = V$, $A'L' = AL$, and therefore

$$v'_{\text{air}} = v_{\text{air}} \frac{L'}{L}. \quad (7.126)$$

Therefore, by increasing the length of a column while keeping its volume constant, we are exploiting the fact that reducing σ_t allows for higher flow (or longer filtering times) at the same radon reduction. That is, the S-curve distribution of radon passing through the filtering column is becoming more like a step function; thus an integral of its output-heading tail is smaller, even while integrating a larger fraction of the tail. The change in

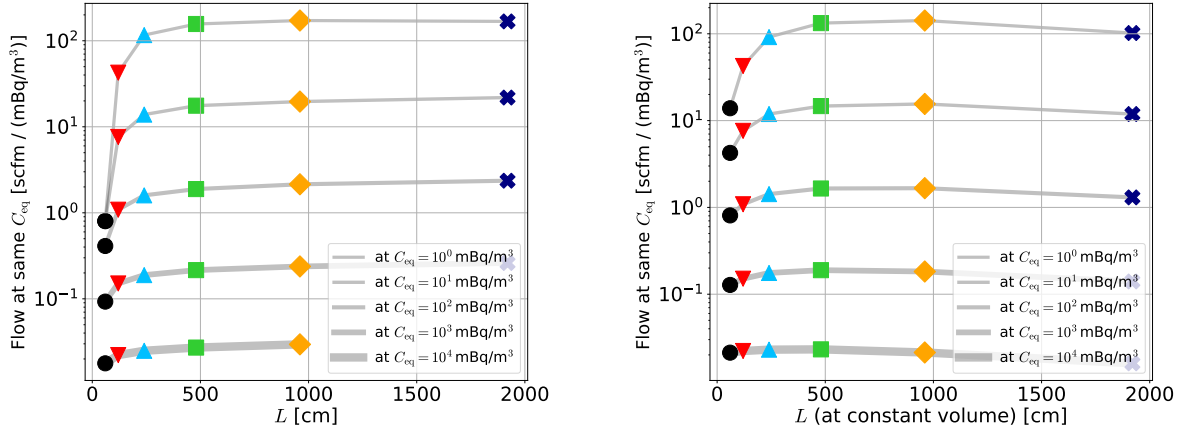


Figure 7.94: The ratio of the maximum flow F for which a specified equilibrium radon concentration (gray lines of varying thickness) is achieved referred to as flow at same equilibrium (larger is better). **Left:** For increasing values of L (with fixed column diameter), the flow at same equilibrium increases with diminished gains each increase in L (refer to Fig. 7.92). **Right:** Similar to the left plot, but with the column volume held constant (refer to Fig. 7.93). As the column length L increases, gains in radon reduction are initially only progressively diminishing; as the column is further lengthened (and the diameter further reduced), initial gains are lost as regeneration efficiency suffers.

σ_t for increasing L' is found using the chain rule:

$$\begin{aligned} \frac{d\sigma_t}{dL'} &= \frac{d\sigma_t}{dv'_{air}} \frac{dv'_{air}}{dL'} \propto - (v'_{air})^{-2} \frac{dv'_{air}}{dL'} = - \left(v_{air} \frac{L'}{L} \right)^{-2} \frac{v_{air}}{L} \\ &= - \frac{L}{v_{air}} \left(\frac{1}{L'} \right)^2 \propto - \left(\frac{1}{L'} \right)^2. \end{aligned} \quad (7.127)$$

There are two points to mention: (1) the sign is negative, as expected (as L' increases, the width of the distribution is reduced) and (2) the amount that the width is reduced decreases with increasing L' . Therefore, as $d\sigma_t/dL' \rightarrow 0$ for increasing L' , improvement in performance approaches zero. This inferred reduction in radon breaking through the filtering column, of course, ignores the eventual case where the column cross-section becomes so small that the carbon bed within it can no longer be characterized by its bulk properties (perhaps when the diameter is only order 10 times the average length of a carbon granule).

An important consequence of $v_{Rn} \propto v_{air}^2$ (Eq. 7.122) is that the break-through time of radon passing through a column of a given volume at a given air flow is not independent

of its length, as is the case for air. That is,

$$t'_b = \frac{L'}{v'_{\text{Rn}}} \propto L' \left(\frac{1}{v'_{\text{air}}} \right)^2 \propto \frac{1}{L'}. \quad (7.128)$$

From the break-through time becoming shorter with increased column length, the improvement in radon reduction is expected to reach a maximum; further increasing the column will then reduce the radon reduction, particularly at high flow, though the shape of the distribution will continue to approach that of a step function (as appears to be seen by the $L = 1920$ cm curve). The ratio of the maximum flow F for which a specified equilibrium radon concentration (gray lines of varying thickness) is achieved is a useful proxy for performance, henceforth referred to as flow at same equilibrium, and illustrates this behavior, as seen in Fig. 7.94. It should be appreciated, however, that if additional BTC data reveals that f_A does not actually depend on flow, this effect would not exist (*i.e.*, increasing length would provide diminishing returns on reduction, but would not eventually *worsen* reduction—though perhaps it would for other reasons).

Not surprisingly, a larger volume column will require more time to reach equilibrium during swing mode than one smaller (for the same pumping speed). Figure 7.95 illustrates how changing column geometry, input radon concentration, and purge flow may effect the time required to reach equilibrium. However, for the varying parameters discussed in this section, the simulation has typically required around 70 cycles (about 6 days) to reach equilibrium.

By increasing the column diameter d_\circlearrowleft (while keeping the column length L fixed), the radon velocity is reduced for a given flow, and we again expect improved radon reduction throughout nearly the entire flow domain F . Figure 7.96 shows prediction curves for varying column diameters around the SD Mines column diameter of 76.2 cm. As was the case for column length, for increasing column diameter we expect reduced gains as we become more limited by imperfect regeneration.

Again referring to Fig. 7.96, regions of curves below 0.1 mBq/m³ have been excluded because the chosen simulation spatial step size Δx was not large enough for some com-

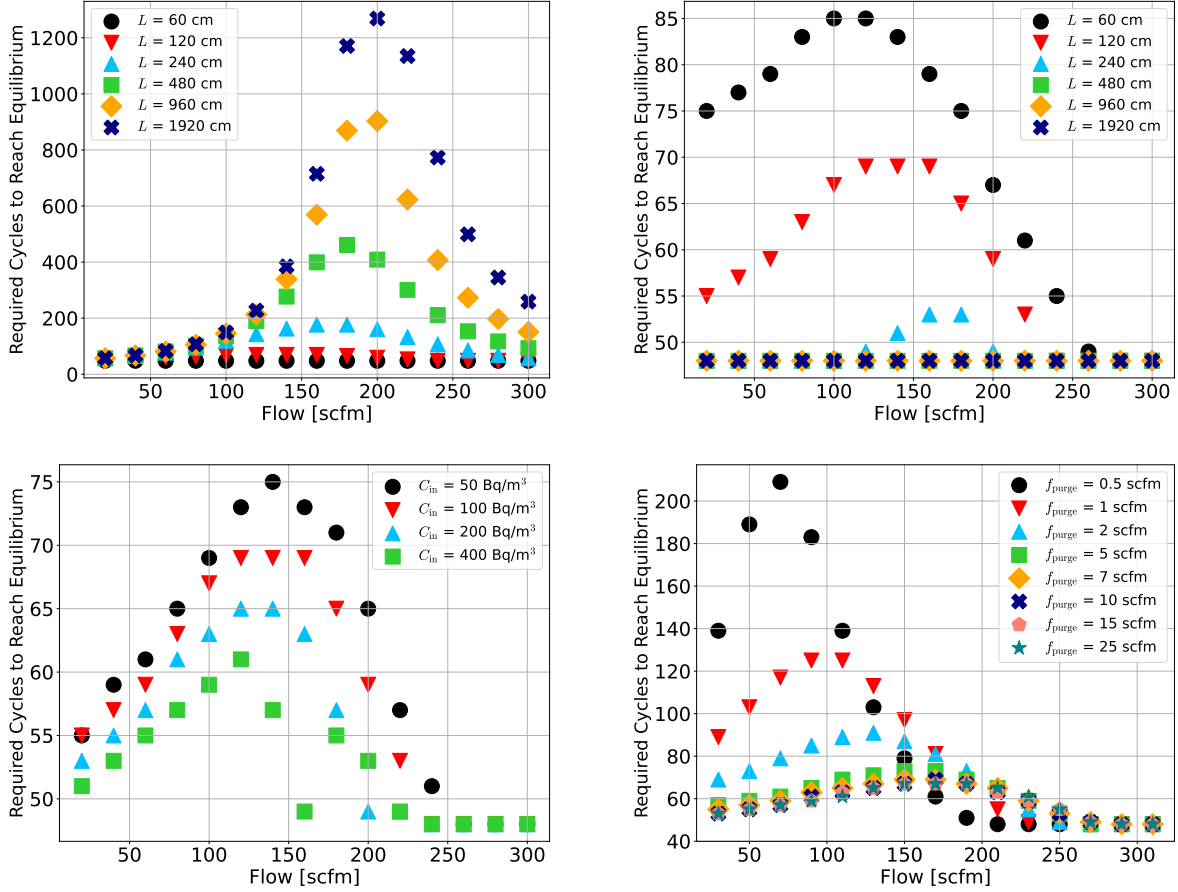


Figure 7.95: The number of cycles required before equilibrium is reached in swing mode can vary depending column geometry. The simulation is required to perform no less than 20 cycles before checking whether the equilibrium condition has been achieved. The symbols here are consistent with those used respective equilibrium concentration versus flow plots (as referenced in the descriptions below). **Top Left:** For increasing values of L (with fixed column diameter, refer to Fig. 7.92), the number of cycles required to reach equilibrium becomes large due to the increased time required to regenerated a column that was initially flushed with high-radon air. Here, 1000 cycles is equal to 2000 hours or about 83 days—probably too long for practical applications. **Top Right:** Similar to the left plot, but with the column volume held constant (refer to Fig. 7.93). The number of cycles required to reach equilibrium reduces as the column lengthens (with the diameter reducing), as the regeneration stage becomes more efficient. **Bottom Left:** For varying input radon concentration (refer to Fig. 7.84), the number of cycles required to reach equilibrium reaches a maximum around 130 scfm, revealing a condition where radon is both being exhausted during regeneration and breaking through during filtering minimally each cycle. **Bottom Right:** Similar to the left plot, but for varying purge flow (refer to Fig. 7.88). The number of cycles required to reach equilibrium generally reduces with increasing purge flow.

binations of flow and diameter. If we consider a through-column flow F , then

$$v_{Rn} \propto F/d_\odot^2. \quad (7.129)$$

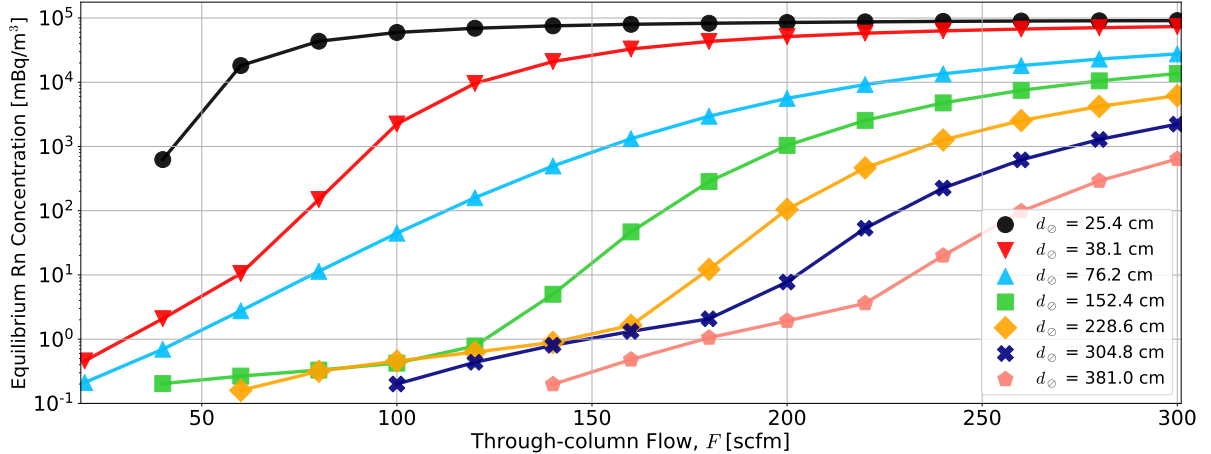


Figure 7.96: Dependence on column diameter d_\circ of the equilibrium radon concentration (colored shapes) versus the flow F passed through the filtering column. As d_\circ increases, while keeping the column length L fixed, the break-through time increases, reducing the amount of radon contributing to the equilibrium radon concentration of each cycle. During regeneration, the radon velocity is also slower, resulting in reduced gains in performance due to imperfect regeneration for the same increase in column diameter. The values of the column diameter are $1/3$, $1/2$, 1 , 2 , 3 , 4 , and 5 times the diameter of the SD Mines RRS columns. The lowest values of some of the predicted curves are excluded for accuracy (as the chosen spatial step size Δx was not sufficient for the lowest radon velocities).

The simulation predictions for a chosen step size Δx become poor when we approach the condition

$$v_{\text{Rn}} \Delta t \ll \Delta x, \quad (7.130)$$

where Δt is the simulation time step size. This condition is due to the simulation's discrete handling of radon propagation (where the tail of the radon distribution is essentially truncated by the values too close to zero in the spatial bin).

There is an important caveat to predictions where the column geometry is significantly modified. There is no attempt to account for the added impedance of, for example, a longer, skinnier column. During filtering, increased impedance can be overcome by a larger inline air blower. During regeneration, more powerful pumps could be employed; however, the pressure differential across the regenerating column is limited by the pump-side pressure, P_{pump} , which could be close to zero for the fastest pumps, and the impedance of the carbon, which has (for the SD Mines RRS) a pressure drop of a few Torr. In the best case (with perfect pumps), the pressure gradient at equilibrium is

linear with a pump pressure $P_{\text{pump}} = 0$ Torr and a purge pressure P_{purge} of a few Torr, as determined by the impedance within the column. Therefore, increasing pumping speed can only account for the added impedance of a longer column to a point. If we let the required pressure differential to achieve the desired purge flow be ΔP_{req} , then

$$\Delta P_{\text{req}} \geq P_{\text{atm}} - P_{\text{purge}} = P_{\text{atm}} - P_{\text{pump}} - \Delta P_L - \Delta P_{\text{line}}, \quad (7.131)$$

where the pressure drop across the column is ΔP_L and the pressure drop across the purge line (with the purge valve completely open) is ΔP_{line} . If an inline blower was installed in the purge line, we make the substitution $P_{\text{atm}} \rightarrow P_{\text{blower}} > P_{\text{atm}}$.

Cost Analysis for Changing Column Geometry

The cost of a column can depend significantly on where the system will operate as determined, for example, by the space available and required certifications for the column, which is a vacuum vessel. If a column is fabricated from stainless steel and certified to withstand a pressure differential of one atmosphere, the cost per column can exceed 10,000 USD (particularly if the pressure differential between the inside and outside of the column is greater than 760 Torr). Using longer columns may result in increased shipping costs and placement difficulties within one's lab; the latter could be circumvented by orienting the columns on their sides (with their long axis made horizontal).

A more important challenge is that longer columns result in larger impedance. Even with perfect pumps (creating a perfect vacuum at the pump side of the column), the impedance of a column can be made large enough to limit the maximum purge-flow rate (due to the increased purge-side pressure). The added impedance from lengthening the carbon bed from 120 to 240 cm can be addressed in two ways: (1) the pumping speed can be doubled or (2) a two-column compound column can be used instead of each single 240 cm column. The idea of a compound column is discussed later in this section, but for this example the 240 cm columns are replaced by two shorter columns with carbon length 120 cm. During filtering, the two 120 cm columns are used in series, with a larger input blower providing the required pressure head. During regeneration, the two columns are used in parallel along with a second pump, such that the pumping speed is doubled to provide the required pump-side pressure of about 15 Torr. The impedance of the two 120 cm columns in parallel is half that of a single 120 cm column (just like adding resistors in parallel). The reduced impedance during regeneration is expected to further increase radon reduction due to the improved effective pumping speed, but this will not be considered for this example.

Because the columns have only been lengthened by a factor of two, we are not *required* to use a compound column, but can presume that we have purchased only

two columns with carbon beds of length $L = 240\text{ cm}$. The pumping speed must be increased by a factor of two to account for the doubling in column impedance, so we will need to add a pump (and once the pump pressure is near zero, the impedance of the column can limit the maximum purge flow).

For this example, two large columns (with a carbon bed length of 240 cm), one extra pump (at 10,000 USD), and a few extra valves, is expected to increase radon reduction by $> 100\times$ at a 100 scfm through-column flow for the additional cost of 30,000 USD. Because there are many things that can change this estimate (for example, a requirement that the pumps be oil-free), the true cost could be much higher, but likely well within a factor of five. Though using compound columns is likely the better choice, and is well motivated (later in this section), the compound column is not yet a feature implemented in the simulation.

Figure 7.97 shows predictions for a case where the regenerating column is able to achieve a lower pressure than that achieved by the SD Mines RRS. The pressure throughout the regenerating column $P_{\text{SDMines}}(x)$ is modified to become

$$P(x) = P_{\text{SDMines}}(x)/\tilde{S}, \quad (7.132)$$

where \tilde{S} uniformly scales the pressure profile discussed in Section 7.9. With the SD Mines configuration, this effect is likely not practical for values of \tilde{S} larger than 5 due to the column's impedance limiting the air speed through the column. However, the purpose of these predictions is to provide insight into how performance might change *if* a variable, such as the pressure during regeneration, *could* be modified as such.

Referring to the top plot of Fig. 7.97, the curves produced with $\tilde{S} \in [1, 2]$ all cross at around 50 scfm. This is expected to be caused by the radon diffusion's quadratic dependence on air speed, which increases with reduced pressure. The front-leading tail of the radon distribution within a column exits a column during the filtering stage and contributes to the predicted equilibrium. When radon passes slowly through the filtering column (when $F < 50\text{ scfm}$) the fraction of the front-leading tail that escapes represents a small number of radon atoms. By reducing the pressure during regeneration, radon diffuses more throughout the column. While increased diffusion does increase the amount of radon that is exhausted, it also increases the amount of radon at the front-leading tail

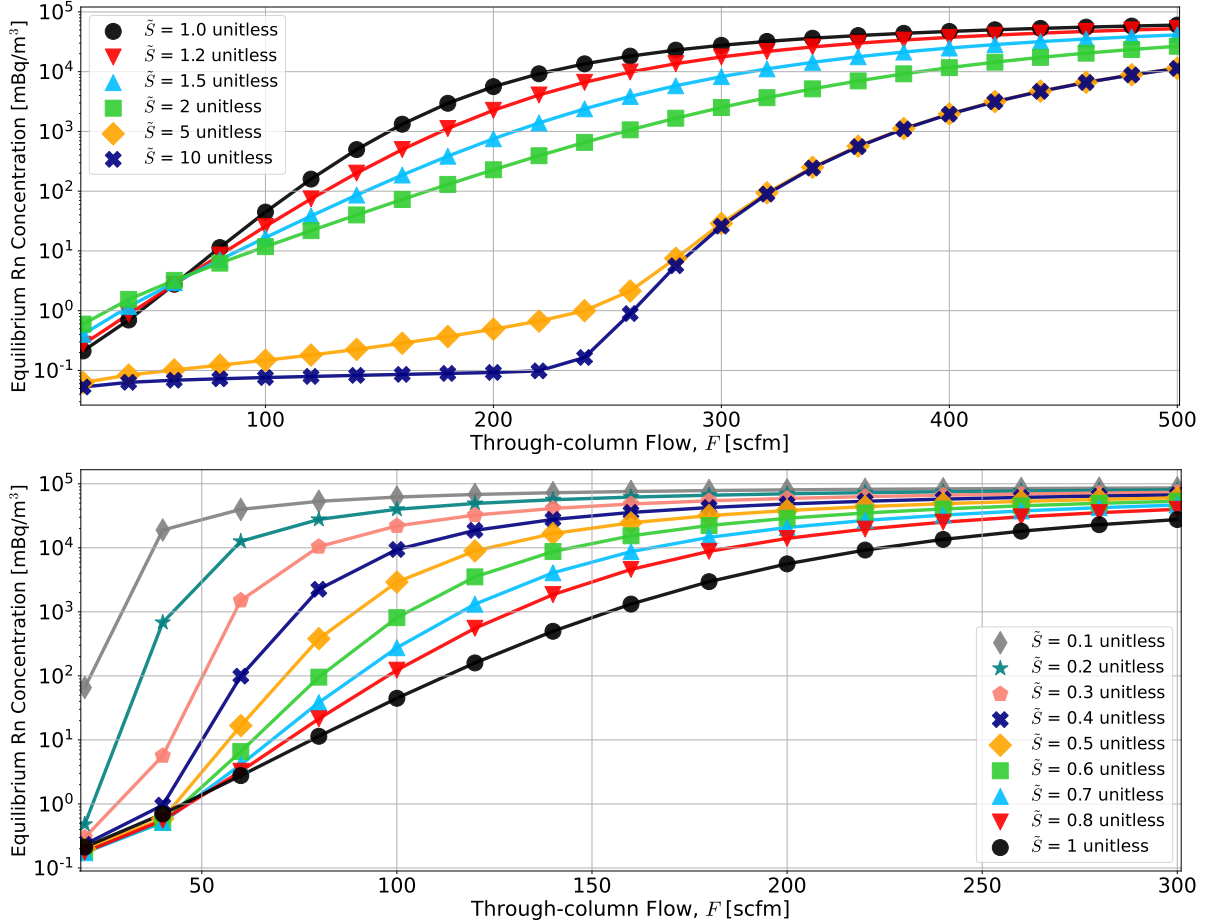


Figure 7.97: Top: As the pressure throughout the regeneration column is reduced by the scalar \tilde{S} , the equilibrium radon concentration (colored shapes) increases until the limit where regeneration is essentially perfect is reached (at about $\tilde{S} = 10$). The curve for $\tilde{S} = 1$ (black circles) is drawn on both top and bottom plots for reference. **Bottom:** Similar to the top plot, but here considering values of $\tilde{S} \leq 1$ (and notice the flow domain extends to only 300 scfm). As the pressure throughout the regeneration column increases by the scalar \tilde{S} , the equilibrium radon concentration generally increases throughout the flow domain as regeneration becomes less efficient.

of the radon distribution; that is, if the radon distribution is represented as an S-curve, increasing diffusion increases the standard deviation (the width) of the curve, resulting in more radon exiting during the subsequent filtering stage. This indicates that at low flow there may be an optimal pressure (and from these simulations based on the SD Mines RRS it appears to be at $\tilde{S} \approx 0.7$). At high flow ($F > 50$ scfm), a larger fraction of the front-leading tail exits during the filtering stage. By reducing the pressure during regeneration, radon does diffuse further out from the mean but the increase in radon

exhausted appears to be the dominant effect. For example, when F is sufficiently large such that much of the radon already within a column exits during filtering, reducing the pressure during regeneration must reduce the equilibrium output concentration, as more radon is exhausted during the regeneration stage (and thus subtracts from what can be exhausted during filtering). Therefore, when the through-column flow is larger than about 50 scfm, reducing the pressure during regeneration is expected to always improve radon reduction.

Cost Analysis for Increasing Pumping Speed

One might increase pumping speed simply by adding an additional pump, making appropriate adjustments to associated vacuum connections. In this discussion, pump refers to the pumping system that will likely consist of a roughing pump and booster (that increases pumping speed below 100 Torr). While the cost of a pump can easily vary by a factor of five (for example, if it must be oil-free), for this discussion an appropriate pump (roughing pump and booster) will be assumed to cost 10,000 USD. In addition, no attempt to account for increases in the cost of maintenance has been made (but may be presumed to be around 10% of the pump cost per year). Depending on pump options available, it may also be more efficient and cost effective to purchase a single larger pump as apposed to two smaller pumps, but this subtlety is not explored here. With these assumptions, adding an additional pump doubles the pumping speed and reduces the pressure throughout the regenerating column by a factor of two. Figure 7.97 shows that for a make-up air flow of 100 scfm ($F = 107$ scfm), radon reduction is expected to improve by a factor of about 6 at a cost of 10,000 USD.

As illustrated by Fig. 7.98, one possible hardware change that follows from the predictions of improved performance for longer columns and lower pressure, while addressing the concern of increased impedance, is to replace each large column with a *compound column* consisting of several skinnier columns. During filtering, air flows through each small column in series, where we benefit from the longer column (keeping in mind that a larger air blower will be needed to overcome the increased impedance). During regeneration, purge air passes through all columns in parallel and is exhausted by the pumps at the other end. The impedance of the compound column during filtering (with skinny

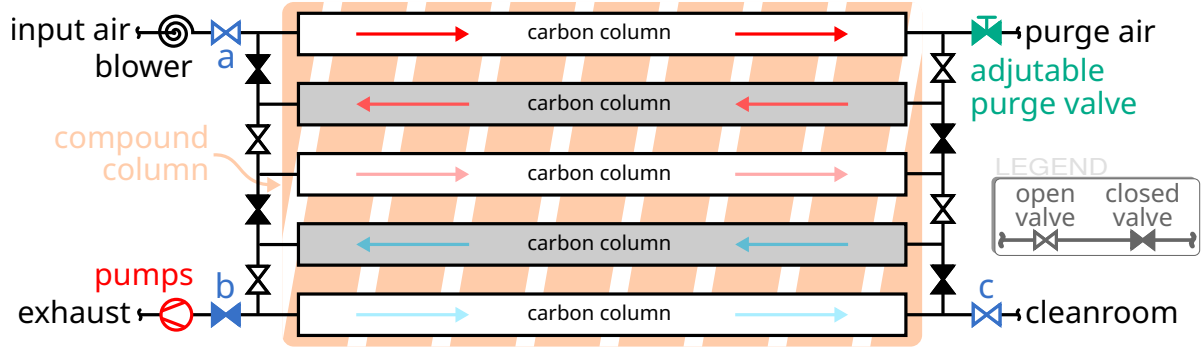


Figure 7.98: A **compound column** has the same length as a large column from the SD Mines RRS, but is composed of several smaller-diameter columns. In the filtering configuration shown in this figure, high-radon **input air** is drawn by the **blower** and passes through the open valve labeled **a**. The air then passes though each column in *series* until passing through the valve labeled **c**, which leads to the **cleanroom**. Arrows within the columns change from red to blue to illustrate the relative amount of radon in the later columns. In the regeneration configuration, **purge air** supplied by the secondary column (not shown) passes through the **adjustable purge valve**. The air then passes through all of the columns in *parallel*, with all of the valves between the columns (in black) opened. In addition, the valves labeled **a** and **c** are closed, while the valve labeled **b** is open, leading to the vacuum **pumps** and finally the **exhaust**. Please note, every other column is shaded gray to help guide the human eye, not because there is any difference between them.

columns in series)

$$Z_F = N Z_o, \quad (7.133)$$

where $N = L/L_o$; L is the cumulative length of all skinny columns within the compound column, with each skinny column having length $L_o = 120\text{ cm}$ and impedance Z_o (a few Torr in terms of pressure drop). The impedance of the compound column during regeneration (with skinny columns in parallel)

$$Z_R = \left[\sum_{i=1}^N \frac{1}{Z_o} \right]^{-1}. \quad (7.134)$$

The pumping speed sets the base pressure at the pump side of each column. The purge flow and impedance of each carbon bed sets the purge pressure at the purge-flow side. When pressure throughout the regenerating column reaches equilibrium (nominally a few minutes after the start of regeneration), the pressure gradient along the column axes is linear between the pump- and purge-side pressures at the two ends. By purging the columns in parallel, the purge pressure will be lower than if purged in series. With the

average pressure within each column lower than if configured in series, radon atoms move more quickly and, only needing to travel the length of a single column as apposed to all in series, are exhausted more quickly.

Cost Analysis for Material and/or Part Substitution

Particularly in the case of a compound column, the cost per column might be drastically reduced if fabricated from plastic instead of the traditional stainless steel. Because a column must withstand a pressure differential of only about one atmosphere, PVC pipe, for example, is suitable. Westlake Pipe and Fittings (which used to be LASCO Fittings), states [165]: “All sizes of Schedule 80 PVC pipe are suitable for vacuum service up to 140 degrees Fahrenheit and 30 inches of mercury vacuum [one atmosphere]. Solvent-cemented joints are recommended for vacuum applications.” Therefore, upon passing mechanical requirements and safe considerations for one’s application, fabricating columns from PVC (or similar) may reduce the cost per column to under 1,000 USD.

On a similar note, many (if not all) valves used throughout the RRS do not need to be rated for low vacuum (which cost upwards of 2,000 USD per unit), when wafer-style pneumatic butterfly valves are sufficient (at under 300 USD per unit, see PRM Filtration, SKU:BBVBNADAN500S0300). Using the compound column shown by Fig. 7.98 as an example, each valve shown in black needs to be leak tight only during the filtering stage (with columns used in series); both sides of each valve are near atmospheric pressure, with the pressure drop across them very small (< 10 Torr). During regeneration, the column is at vacuum (around 20 Torr) but all of the black valves are open and thus leak tightness across the valves is irrelevant. However, the leak tightness between the lab space and the inside of a valve is important (as discussed in Section 7.15.3), but is likely better than required. This same line of reasoning could also be used to motivate the substitution of other valves throughout the RRS with less costly alternatives (that even allow for larger pipe diameters, as compared to their low-vacuum counter parts).

Particularly in the case that larger columns are employed, if there existed a lower-cost, but higher radon emanation, carbon than used in the SD Mines system, we might choose to fill the columns with it. With each column containing ~ 200 kg of activated carbon, the rate radon emanates from the carbon E_{\bullet} can limit radon reduction, particularly at low flows. Figure 7.99 shows predicted equilibrium concentrations versus flow F for several radon emanation rates E_{\bullet} , having units of Bq/kg. There are two conclusions one may draw from these predictions with changing radon emanation: (1) radon reduction is not

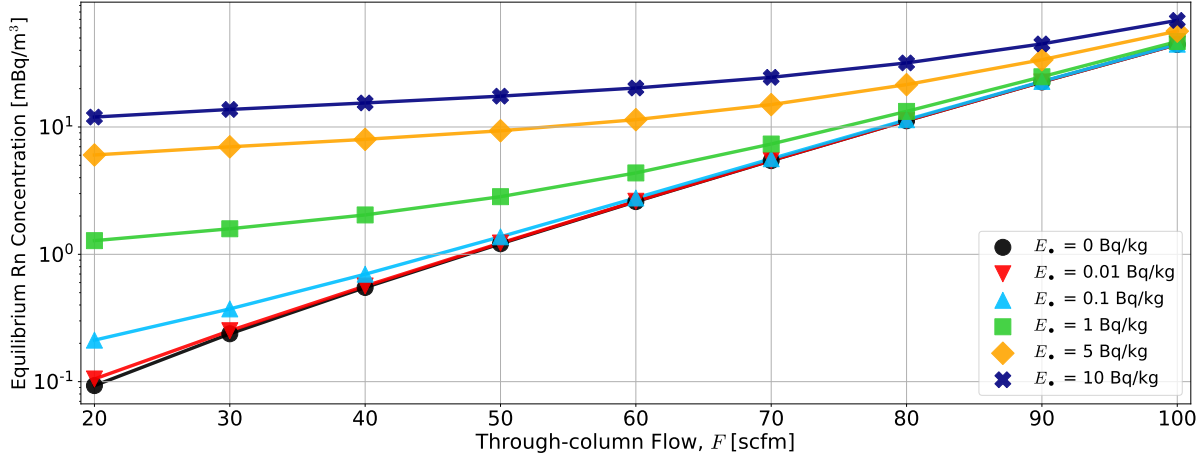


Figure 7.99: Each equilibrium radon concentration curve (colored shapes) represents a presumed value of the radon emanation rate E_{\bullet} of the carbon, with $E_{\bullet} = 0.1 \text{ Bq/kg}$ being the default for the SD Mines RRS. As E_{\bullet} increases, it can become the dominant cause of increased radon at equilibrium, while being essentially negligible for $E_{\bullet} \lesssim 0.1 \text{ Bq/kg}$.

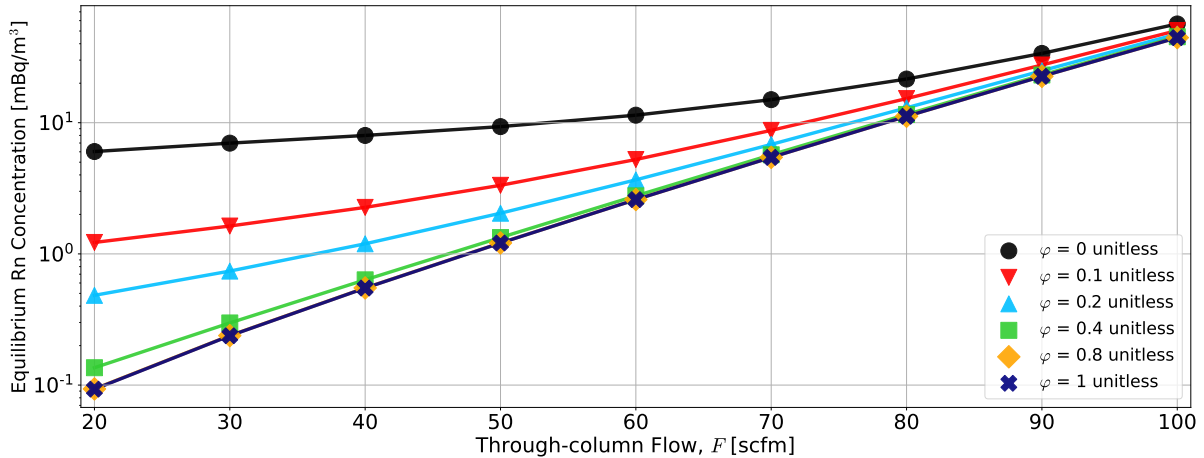


Figure 7.100: By replacing a fraction φ (as measured from the output side) of each carbon bed having an emanation rate of 5 Bq/kg with carbon having a emanation rate of zero can reduce the equilibrium radon concentration (colored shapes), particularly at lower flow. For example, the $\varphi = 0.2$ curve (in blue pentagons) shows about an order of magnitude improvement in radon reduction at 30 scfm as compared to the $\varphi = 0$ curve (in black triangles).

significantly improved even at low flow for emanation rates lower than about 0.1 Bq/kg (the SD Mines RRS value) and (2) radon reduction dependence on the carbon emanation rate decreases as flow increases, as break-through during filtering and/or imperfect regeneration becomes dominant.

If carbon in the columns has a particularly high radon-emanation rate of 5 Bq/kg ($50\times$ higher than in the SD Mines RRS), a fraction φ of the carbon bed (as measured

Hardware Change	Cost [USD]	Total Radon Reduction (RR) at		
		50 scfm	100 scfm	200 scfm
Do nothing	\$0	4.1×10^4	1.2×10^3	14.5
Cool input air by 10°C	\$5,000	1.7×10^5	1.2×10^4	145
Heat purge air by 10°C	\$10,000	6.7×10^4	2.8×10^3	30
Heat purge air by 20°C	\$15,000	1.4×10^5	1.2×10^4	146
Lengthen columns by 2×	\$30,000	5.8×10^5	1.7×10^4	42
Add a pump ($\tilde{S} = 2$)	\$10,000	3.3×10^4	6.5×10^3	350
Add more pumps ($\tilde{S} = 5$)	\$50,000	1×10^6	6.3×10^5	1.8×10^5

Table 7.5: The total radon reduction (RR) (defined by Eq. 7.115) is determined at 50, 100, and 200 scfm from simulation predictions explored in this section for a specific hardware change (such as heating the purge-flow air). The cost estimate for each hardware change is discussed at the relevant locations within this section (appearing within highlighted boxes). The regions highlighted in green emphasize hardware changes that are expected to provide improved radon reduction at a minimal cost, while regions highlighted in blue emphasize hardware changes that provide slightly better radon reduction though at a higher cost. Regions highlighted in orange emphasizes the single hardware change that is expected to provide the best radon reduction but at a high cost (and potentially complexity).

from the output side) could be replaced with carbon having a much lower emanation rate (that we presume to be zero). For example, $\varphi = 0.4$ means that 40% of the carbon bed as measured from the output side during filtering has been replaced with carbon having $E_\bullet = 0$ Bq/kg. Figure 7.100 shows predictions for varying φ . Particularly below 50 scfm, replacing even just the last 20% of high-emanation carbon with lower emanation carbon could provide significant improvement in radon reduction.

The above simulations suggest that radon emanation is not expected to be a dominant parameter, as even low-cost activated carbon tends to have radon emanation of not more than about 100 mBq/kg. Nonetheless, it is useful to know the effect of higher rates of emanation in the event that a different media (*e.g.*, molecular sieves) are used that might emanate more radon while providing some other advantage. The simulations in this section suggest that active temperature control, larger columns, or faster pumps are the most likely pathways to increased radon reduction.

Table 7.5 illustrates the expected radon reduction (RR) for several practical hardware changes as made to the SD Mines RRS, which serves as a reference. The estimates of

RR provided are conservative in that only modest changes in the parameter of interest (*e.g.*, the input air temperature or columns length) are presumed to be the result of the hardware change. The rows *Heating purge air by 20°C* and *Add more pumps ($\tilde{S} = 5$)* illustrate how if the hardware change results in a larger effect, more significant gains in radon reduction are expected.

Heating the purge air increases radon reduction at each of the selected make-up air flows (50, 100, and 200 scfm). The increase in purge air temperature is chosen to be modest for this discussion (only 10 and 20°C) because of the practical challenge of ensuring heat is not overwhelmingly lost to the valves, piping, and other materials making up the purge line. Similarly, the presumed cooling of the input air is only 10°C in order to reflect the typical challenge of cooling air, particular for target temperatures close to freezing.

Adding additional pumps increases radon reduction particularly at high flows, while possibly undermining radon reduction below about 50 scfm. Because pumps and associated hardware and maintenance can be costly, improving pumping speed to increase radon reduction is expected to be a strategy best suited for high-flow applications. For low-flow applications, one might consider active temperature control, for example.

Lengthening columns by a factor of two can provide cost-effective gains in radon reduction, particularly at around 100 scfm. Further lengthening of the columns (to have a carbon bed length of, say, 480 cm) should be considered with caution, as longer columns are expected to require higher pumping speeds and/or a compound-column approach to overcome the added impedance. In this example, the column length has been only doubled to 240 cm, and so simply increasing pumping speed is expected to suffice. However, using compound columns is likely the better choice, as it can reduce the impedance during regeneration (allowing for lower pressure for the same pumps). Therefore, substituting each 240 cm column for two 120 cm columns (run in series during filtering and

parallel during regeneration) is expected to provide better radon reduction than what is considered here, and at a lower cost (by a third).

A practical RRS build with excellent performance might be designed to have active heating of the purge-flow air, compound columns (made from PVC or some other appropriate plastic based around pressure and temperature requirements) that operate in series during filtering (driven by an appropriately chosen blower) and parallel during regeneration and slowfill. Additional chillers may be employed to cool the input air (and may even make a dehumidifier unnecessary). If funding allowed, an additional pump is expected to improve regeneration and be particularly advantageous when combined with the compound columns. As informed by leak-tightness criteria throughout the system, less costly wafer-style valves and PVC hardware may be used to further offset the of both commissioning and operations. Because such a system will have not been constructed this way before, it is sensible to install temperature (RTD and IR), pressure, and relative humidity sensors at multiple locations within each column and perhaps in key locations throughout the system (such as in the input air ducting and at locations after the heated purge-flow line). The exact details of such a dream system should be modified to fit one's application, but would be expected to provide excellent radon reduction (of $\sim 10^5$) over a large flow domain, possibly extending beyond 200 scfm.

7.15.3 Using the Simulation to Inform Leak-tightness Criteria

With the RRS being a *vacuum*-swing adsorption system, replacing columns with longer ones or filling columns with different adsorption media can often introduce leaks that will need to be fixed. Because it can be challenging to fix leaks, it is important to have well-motivated leak-tightness goals for different parts of the system. While back-of-the-envelope calculations can provide excellent first-order (and sometimes much better) estimates of required leak-tightness, the simulation can provide additional insight into leak-tightness criteria for different regions of the system. Figure 7.101 shows predictions based on the assumption that air having a radon concentration of 100 Bq/m³ is able to

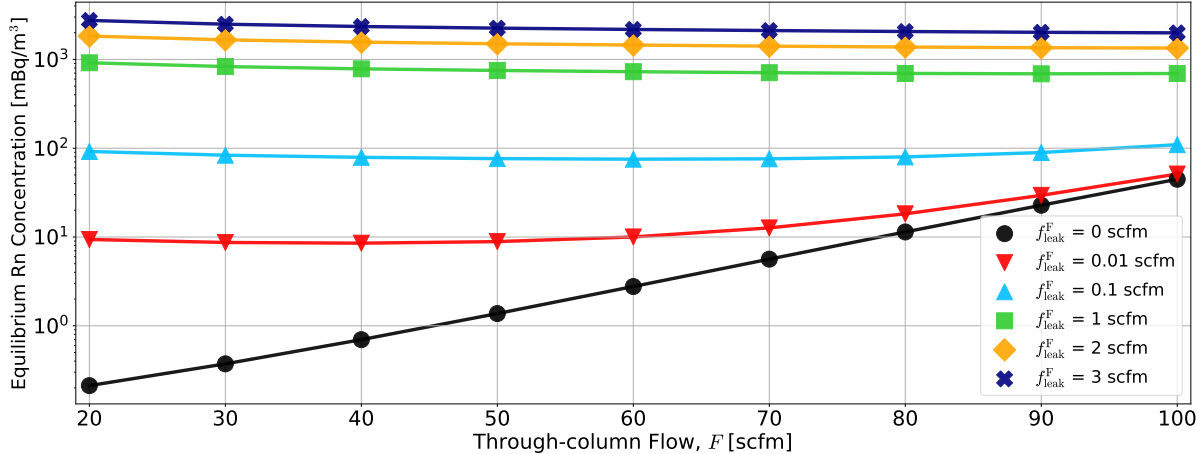


Figure 7.101: Air with radon concentration 100 Bq/m³ is made to flow into the filtering column at the output end with leak rate $f_{\text{leak}}^{\text{F}}$. As $f_{\text{leak}}^{\text{F}}$ increases, system performance decreases throughout the flow domain. Not surprisingly, as we dilute the output with high-radon air, the radon concentration of the outgoing air (colored shapes) increases according to a weighted average: $C = C_{\text{out}} [F_{\text{cr}} / (F_{\text{cr}} + f_{\text{leak}}^{\text{F}})] + C_{\text{lab}} [f_{\text{leak}}^{\text{F}} / (F_{\text{cr}} + f_{\text{leak}}^{\text{F}})]$, where C_{out} is the radon concentration leaving the filtering column without a leak and the flow of make-up air supplied to the cleanroom $F_{\text{cr}} = F - f_{\text{purge}}$.

leak with flow $f_{\text{leak}}^{\text{F}}$ (in units of scfm) into the low-radon output of the filtering column. Specifically for the SD Mines RRS, this could represent high-radon air leaking through the gate valve used to bypass the RRS (where there is a pressure differential of about 10 inches of water or about 19 Torr), resulting in radon being re-introduced to the low-radon air supplying the SD Mines cleanroom.

Due to the pressure differential of almost an atmosphere between the lab space and within the regenerating column, a more common case is where high-radon air is leaking into a regenerating column through the column lid and/or associated connections. By monitoring the pressure rate-of-rise $\Delta P / \Delta t$ within the column, and knowing the evacuated air volume V , one may estimate the flow $f_{\text{leak}}^{\text{R}}$ of high-radon air entering the column through the leak or leaks as so:

$$f_{\text{leak}}^{\text{R}} = \frac{V}{P_{\text{atm}}} \frac{\Delta P}{\Delta t}, \quad (7.135)$$

where P_{atm} is local atmospheric pressure. Figure 7.102 shows predictions for varying leak rates $f_{\text{leak}}^{\text{R}}$. While the purge flow f_{purge} is set to the default value of 7 scfm, the simulation updates this value by adding to it $f_{\text{leak}}^{\text{R}}$. That is, the pressure during regeneration is

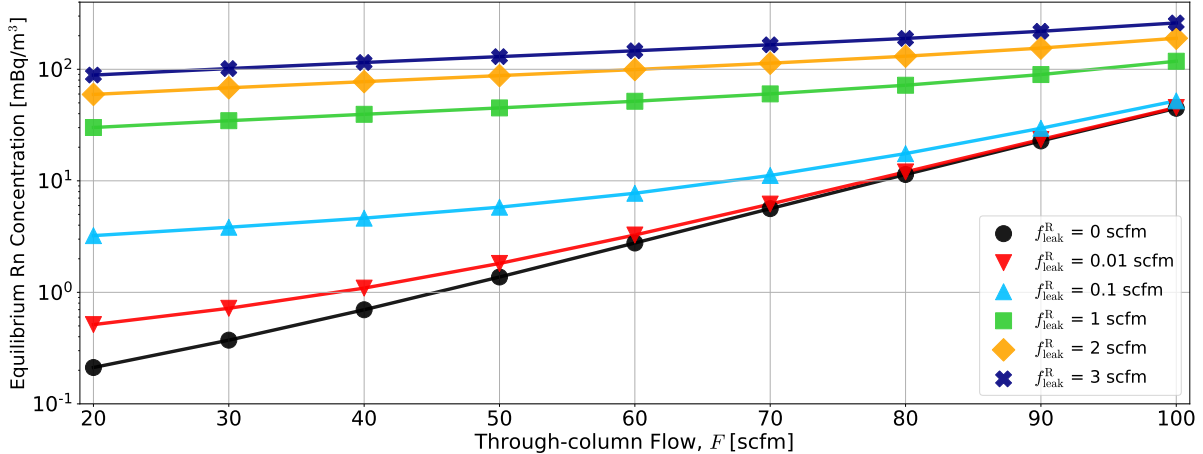


Figure 7.102: Similar to Fig. 7.101, air with radon concentration 100 Bq/m³ is made to flow into the regeneration column at the purge-flow end with leak rate $f_{\text{leak}}^{\text{R}}$. As $f_{\text{leak}}^{\text{R}}$ increases, system performance decreases throughout the flow domain. By introducing additional radon to the regenerating column, the regenerating stage is compromised; the radon still in the regenerating column then exits during the subsequent filtering stage.

slightly increased according to the total flow passing through the purge valve and the presumed leak.

For example, let's say that the RRS must supply make-up air of 80 scfm at less than 100 mBq/m³. The through-column flow F required is the make-up flow plus the purge flow f_{purge} , yielding $F = 80 \text{ scfm} + f_{\text{purge}} = 87 \text{ scfm}$. By inspecting Fig. 7.102, we see that a leak rate smaller than about 1 scfm during regeneration is sufficient. Therefore, the required rate-of-rise is calculated from Eq. 7.135:

$$\frac{\Delta P}{\Delta t} \leq f_{\text{leak}}^{\text{R}} \frac{P_{\text{atm}}}{V} \approx 6.8 \text{ Torr/min} = 408 \text{ Torr/hour}, \quad (7.136)$$

where local atmospheric pressure $P_{\text{atm}} = 680 \text{ Torr}$ and the column volume $V \approx 100 \text{ cf}$, as comprised of the physical air volume of the carbon (about 16 cf), the volume above and below the carbon bed and within vacuum connections (about 12 cf), and the volume of nitrogen that is expected to adsorb to the carbon surface (about 1.2% by mass, or 71 cf) [166, 167]. For the SD Mines RRS, we had a very conservative rate-of-rise target of $\Delta P/\Delta t = 5 \text{ Torr/hour}$, which would require $f_{\text{leak}}^{\text{R}} \leq 0.012 \text{ scfm}$. The rate-of-rise often achieved for this system is below 1 Torr/hour, so $f_{\text{leak}}^{\text{R}} \leq 0.0025 \text{ scfm}$.

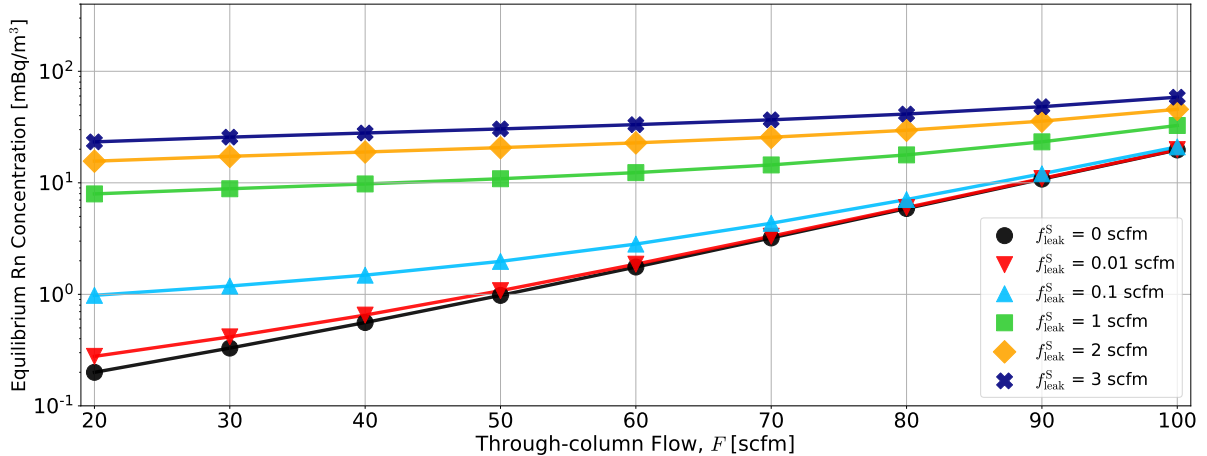


Figure 7.103: All radon atoms that flow into the slowfill column due to a leak (on the purge-flow side) with flow rate $f_{\text{leak}}^{\text{S}}$ can exit the column during the subsequent filtering stage. The slowfill time is calculated by the simulation according Eq. 7.116, but with the air leaking into the column added the purge flow f_{purge} .

Though it is unlikely that a leak would exist during the slowfill stage but not during regeneration, one could imagine, for example, a valve becoming leaky in its closed state, causing such a situation. Therefore, Fig. 7.103 shows predictions for the case where high-radon lab air leaks with flow $f_{\text{leak}}^{\text{S}}$ into a column at the purge-flow side, but only during the slowfill stage. The flow of air leaking into the slowfill column essentially increases the purge flow, raising the column to atmospheric pressure more quickly; therefore, the slowfill time is adjusted within the simulation according to Eq. 7.116, but with the substitution $f_{\text{purge}} \rightarrow f_{\text{purge}} + f_{\text{leak}}^{\text{S}}$.

Chapter 8

The SD Mines Table-top System

The Table-top System (TTS) provides infrastructure for understanding the transport of radon through a column packed with some kind of media, typically granules of activated carbon. The TTS is designed to perform a break-through curve (BTC) measurement, with the system build focused on flexibility in measurements, low-cost, and ease of use. The intent is for BTC measurements to be performed quickly and repeatedly while changing parameters that are expected to influence the characteristics of radon transport, such as the flow rate, temperature, or relative humidity of the carrier gas. The system has a small footprint of only about 3 square feet with a height of about 7 feet, and is on large, lockable wheels to allow for convenient relocation.

As described in Section 7.4.1, a BTC measurement is performed by flowing high-radon air through a carbon column that has very little radon initially in it, and measuring the radon activity of the air coming out the other end as a function of time. The radon adsorbs to the carbon and thus moves more slowly through the column than the air (or whatever is being used as the carrier gas). The measured radon concentration versus time ideally has the form of a sigmoid or S-curve. The inflection point of this curve (where the second derivative changes sign) is defined as the break-through time t_b and the spread in the sigmoid relates to the diffusion coefficient D of radon spreading throughout the carbon per unit time.

8.1 An Overview of the Physical TTS

As shown in Fig. 8.1, sample air from the lab space, SD Mines cleanroom (CR), or some other source is pressurized by an air compressor against an inline (MKS: Model#: GE50A008154SBV020) mass-flow controller (MFC). If the source gas is already pressur-

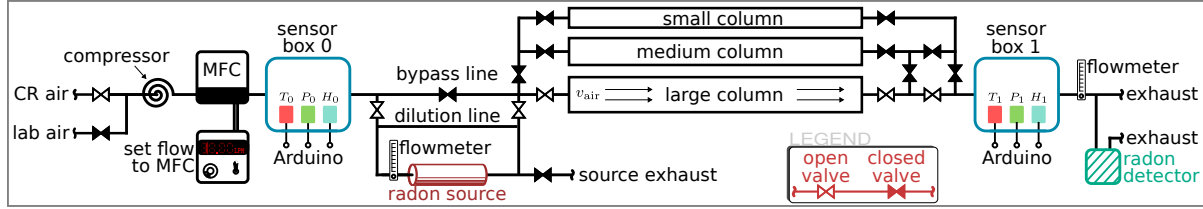


Figure 8.1: Table-top System diagram. Please refer to the text body for its description. The valves in this diagram are configured to pass air first through the radon source and then the large column. When the **dilution line** is not being used, the physical tube and associated barb-style T-fittings are removed (such that gas passes only through the radon source). A valve is not used to close off the dilution line when it is not being used; this is because when the line is being used, the valve that was employed (a 1/4-inch needle valve) restricted too much flow, and resulted in no *measured* flow through the radon source (though it was likely off just scale).

Column	Inner Diameter [inches]	Length, L [ft]	Internal Volume, V [m ³]
Small	1.5	4 ± 0.17	0.006 [†]
Medium	2	4 ± 0.17	0.010 [†]
Large	3	5 ± 0.17	0.028 [†]

Table 8.1: Table-top system column geometry. The lengths here refer to the approximate length of the carbon bed within the PVC assembly, not the total outer length of the assembly itself. [†]The propagated uncertainty in L results in an uncertainty of about 4% in V .

ized (as is the case with a N₂ cylinder), a line regulated to between 10-30 psi should be connected directly to the inlet of the MFC using 1/4-inch compression. The end user sets the desired flow on the MFC power supply and readout unit (MKS: Model#: 246C) that monitors and controls the volumetric flow through the system. Directly after the MFC, the air stream passes through **sensor box 0** where the temperature, pressure, and relative humidity of the air are measured and recorded. After the first sensor box, the user may choose to pass the air stream through the **bypass inline** or the **flowmeter** and then a **radon source**. With or without using the **dilution line** that allows the system flow to not be subject to flow limitations of the radon source, ²²²Rn is introduced to the air stream. A valve directly after the radon source allows air to pass to a **source exhaust** line (used for purging the large amount of radon that builds up within the source). Depending on the configuration of valves just before and after the columns, the air stream may be passed through any one column, or all three columns in either

series or parallel. The **small**, **medium**, and **large** columns have diameters of 1.5, 2, and 3 inches respectively and contain the same activated carbon as used in the SD Mines Radon Reduction System (more details on their geometry provided in Table 8.1). After passing through one or more columns, and through the post-column valve assembly, the air stream passes through **sensor box 1**, where characteristics of the air are again measured. The air stream then passes through an inline **flowmeter**, allowing the user to compare the outlet air flow with the MFC set point such that the system leak rate may be inferred. Finally, the air stream passes through a T-fitting, where most is exhausted and some (< 1 slpm) is sampled by a Durridge RAD7 **radon detector** [118].

The plumbing is built with flexible semi-transparent nylon tubing and compression fittings. These parts could be easily swapped out for or rebuilt from more robust stainless steel hardware, if warranted. The system as it is, however, handles slight overpressure (~ 1000 Torr absolute) very well. The sensor boxes are a bit fragile however, as they are constructed in part from acrylic. To avoid a potential kinetic hazard to the user, a polycarbonate window shields the user from direct line of sight to the sensor boxes. The system tends to have a leak rate of less than 10% of the set input flow. From the low-pressure tests performed, this type of hardware appears to tolerate an underpressure of half or a quarter of an atmosphere without any issues. Because we are primarily passing dry air or N₂ through the system, corrosion has not been a concern; however, this may require further consideration if we begin to routinely introduce additional moisture to the carrier gas, especially combined with increased temperature in parts of the system.

8.2 Details Important to TTS Operation

The MFC requires at least a 10 psi pressure differential to function correctly and can control flow from 0 to 20 slpm (for N₂, which is very similar to air). For other gases, a calibration knob on the back of the controller must be appropriately set (as described in the device manual).

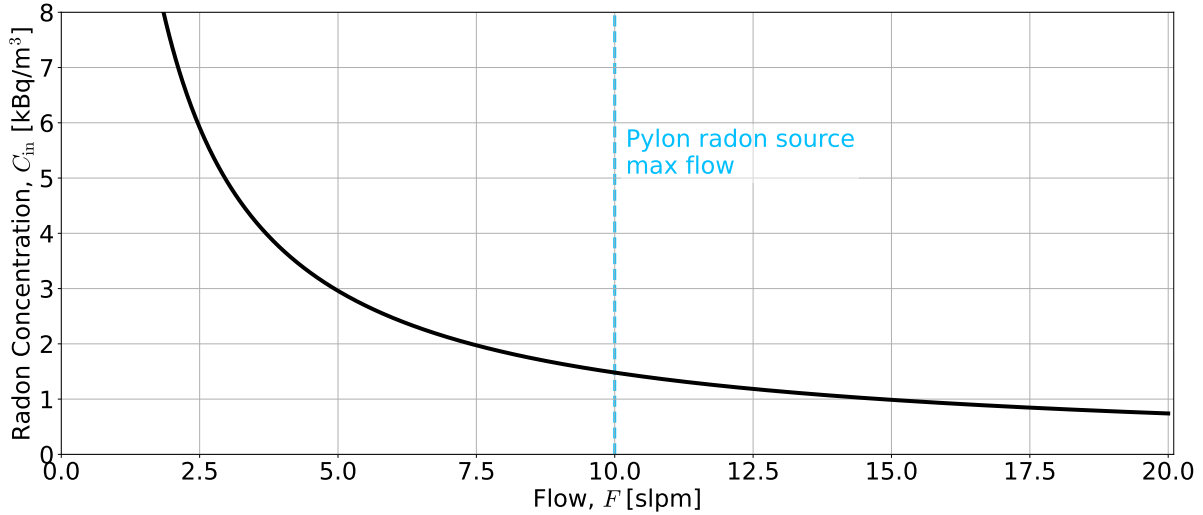


Figure 8.2: The radon concentration (black curve), due to the Pylon radon source, passing into a column or columns depends on the flow of carrier gas (air or N₂, for example) passing through and, when using the dilution line, around the source. The number of radon atoms created by decays of the long-lived ²²⁶Ra within the source is essentially constant in time. Therefore, passing a larger volume per unit time F through the source reduces the concentration of radon in the outgoing air by $1/F$. The maximum flow allowed to pass through the Pylon radon source is 10 slpm (blue dashed line). Larger through-column flow must be obtained by using the dilution line to partially bypass the source, since the flow through the source must be limited to 10 slpm.

No more than 10 slpm is supposed to be flowed through the Pylon radon source that is employed by this system. For this reason, a dilution line was installed, allowing gas to pass around the radon source [168]. Whether the dilution line is active or not, the radon concentration C_{in} (Bq/m³) of the air stream passing into a column may be calculated as

$$C_{\text{in}} = \frac{A_{\text{src}}}{F\tau + V_{\text{src}}}, \quad (8.1)$$

where A_{src} is the activity of the radon source (Bq), F is the flow through the column (m³/s), the radon mean lifetime $\tau = 5.516$ days = 4.766×10^5 s, and V_{src} is the internal volume of the radon source (m³), which can be safely ignored when $F\tau \gg V_{\text{src}}$, which is almost always the case; for example, at $F = 1$ slpm, $F\tau/V_{\text{src}} \sim 4 \times 10^4 \gg 1$. The inline flowmeter before the radon source allows the user to ensure that not all air is passing around the source. Another important requirement of the Pylon radon source is that air passing through it shall not exceed a relative humidity of < 10% (as inferred by the requirement that a cobalt sulfate (CoSO₄) desiccant drying column is meant to be used

inline before the source). Figure 8.2 shows the radon concentration passing into a column for the particular radon source activity $A_{\text{src}} = 117.5 \pm 4.7 \text{ kBq}$ of this system.

Because the radon concentration of the air entering a column is usually much larger than that of the air in the ambient lab space, it is not routinely necessary to purge a column with low-radon gas (such as boil-off N₂). It is, however, routine to flush the column with lab air before starting a BTC measurement. Though the initial readings of radon concentration made by a radon detector sampling the air exiting the column will be non-zero, this initial baseline does not significantly influence the inferred break-through time or the width of the sigmoid function, as the baseline value is typically < 10% of that of the air leaving the radon source.

The air passing through a column with cross-sectional area A , and packed with carbon granules, has an estimated velocity

$$v_{\text{air}} = \frac{1}{\epsilon_T} \frac{F}{A}, \quad (8.2)$$

where the *total porosity* $\epsilon_T = 0.8$, as introduced in Section 4.3, and F is the air flow through the column. The average radon velocity v_{Rn} is proportional to v_{air} and expressed as

$$v_{\text{Rn}} = f_A v_{\text{air}} \exp(-T_{\circ}/T), \quad (8.3)$$

where the critical temperature of adsorption $T_{\circ} = 3500 \text{ K}$ [102] and T is the carbon surface temperature (K), taken in this example to be 293 K (= 20 °C). The adsorption factor f_A (unitless) is observed to be a function of air speed as determined by SD Mines RRS BTC measurements (see Section 7.13.3) and has the form

$$f_A(v_{\text{air}}) = av_{\text{air}} + b, \quad (8.4)$$

where the empirical fitting parameter $a = 415.8 \text{ s/m}$ and $b = 32.2$ (unitless), providing v_{air} has units of m/s. The radon velocity is typically about 4000 times smaller than the speed of air passing through the column.

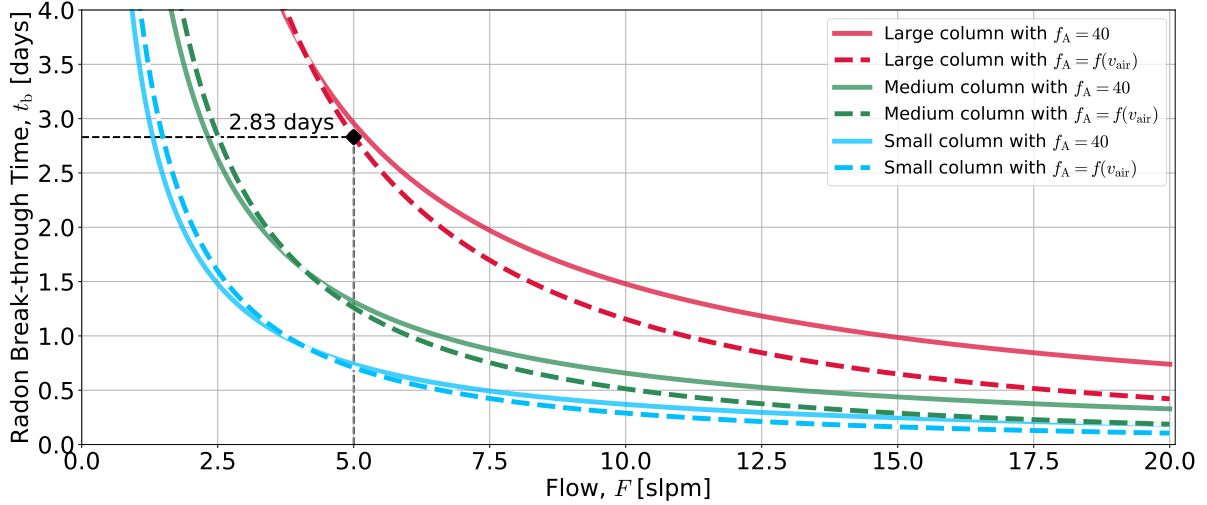


Figure 8.3: The break-through time $t_b = L/v_{Rn}$ and is plotted for two assumptions regarding the radon velocity v_{Rn} : (1) the adsorption factor f_A is presumed constant and set equal to 40 (solid curves) and (2) the value of the adsorption factor f_A is obtained from the model given by Eq. 8.4 (dashed curves). The model-dependent estimate of t_b is expected to be more accurate, with one datum lying on the prediction curve (black diamond) as inferred from a measured BTC at 5 slpm.

Figure 8.3 shows the expected break-through time t_b for a BTC performed with the TTS as a function of the set air flow rate F , and column size (small, medium or large). The solid curves represent the case when $f_A = 40$ for all F , while the dashed curves represent f_A being a function of v_{air} according to the model inferred from SD Mines RRS BTC data (Eq. 8.4). Both sets of curves are sufficient for planning a BTC measurement (*e.g.*, how much N₂ gas will be required to perform a run lasting $2t_b$), though the model-inferred values are expected to be more accurate. The analysis of one BTC performed by the TTS at 5 slpm produced a best-fit t_b of 2.83 ± 0.01 days and is represented by the black diamond on this figure. Though this point shows a preference for the model-inferred value of f_A , more data needs to be collected and analyzed.

8.3 Sensors and Their Readout

Each sensor box contains two sensor modules: the DHT22, which measures temperature and relative humidity, and the BME280, which measures temperature, relative humidity, and pressure. Both of these sensors are small and inexpensive, and the redundancy in

temperature and relative humidity is welcome, as the most responsive and/or accurate sensor can be quoted while the other acts as a check. Each sensor is read out by a dedicated **Arduino** that communicates via serial to a single **Raspberry Pi 3B** mini PC. A single script called `Master.py` initiates a new data-taking run without needing any additional input from the end user (*e.g.*, it automatically chooses the next run number and starts taking data with a standard configuration). The measured data is then plotted as a time series in real time for the user, while also being saved to disk in a crash-resistant way.

In hindsight (after building more systems for sensor readout and recording), the following comments are made in hope that they may be useful when making improvements to the TTS. It would have been simpler, easier, and more intuitive to the end user to have all of the sensors read out by the **GPIO** board of a **Raspberry Pi 3/4B**. Each sensor would then be called through Python. The sensor then responds with the value measured where it may be plotted, saved to disk, or anything else. As it is, the **Raspberry Pi** calls an **Arduino** via serial and hopes that the measurement being performed by the Arduino had *just* finished. Because this frequently won't be the case, a checksum verification routine is in place *that does work* but wouldn't be needed at all if the sensors were read out directly by the **GPIO** board. For real-life examples of how to read out sensors connected directly to a **Raspberry Pi 3/4B** using Python, see repositories for the SD Mines RRS RTD system or the SD Mines Cleanroom Monitoring System (Section 6.4).

8.3.1 Early Results: Water Vapor Passing Through A Carbon Column

Figure 8.4 shows the recorded relative humidity H of the air passing through the large column as measured at the system input (sensor box 0: H_0) and output (sensor box 1: H_1). The temperature measured at each sensor box agreed mutually within *sim*0.14 degrees Celsius, as the temperature of the entire system is primarily driven by the ambient temperature of the lab. At the beginning of the run, both H_0 and H_1 are very low (< 5%) as the source air feeding the TTS compressor was being drawn from

the SD Mines CR, which was overpressured with low-radon, dry air produced by the SD Mines RRS (and water was deliberately not being added to condition the CR air by the CR HVAC). Just before the 1-day mark, the SD Mines RRS was put in bypass mode. In this mode, high-radon air from the lab space, having a typical relative humidity of about 20-40% depending the time of day and, more generally, the weather, was forced into the CR providing the required make-up air of about 100 scfm, but without any radon reduction. The volume-replacement time τ , also called the characteristic time of perfect mixing, within the CR varies according to the make-up air flow rate F ; because the SD Mines CR has an internal volume $V_{cr} \approx 58 \text{ m}^3$ and $F = 100 \text{ scfm} = 0.047 \text{ m}^3/\text{s}$, we calculate $\tau = V/F \approx 20 \text{ min}$. The relative humidity within the CR increased quickly and therefore so did the source air to the TTS compressor, thus resulting in a similarly sharp increase in H_0 . At this time (at about 1 day), humid air was passing into the large column, but had not yet passed completely through the column and wouldn't for at least another day. At around 2.4 days, we measured the first uptick in H_1 ; from that time onward, we observed a steady increase in the relative humidity of the air exiting the column, until it reached a steady state at around 4.5 days. From this measurement, we infer a break-through time of water vapor passing through the large column of about 2 days.

The air flow through the large column was 7.5 slpm. The average speed v_H in which humidity (water vapor) passes through the column is inferred from its break-through time t_H as

$$v_H = L/t_H, \quad (8.5)$$

where L is the column length. If we presume that v_H is proportional to the air speed v_{air} , we may obtain the proportionality factor f_H as defined by

$$v_H = f_H v_{air} = L/t_H. \quad (8.6)$$

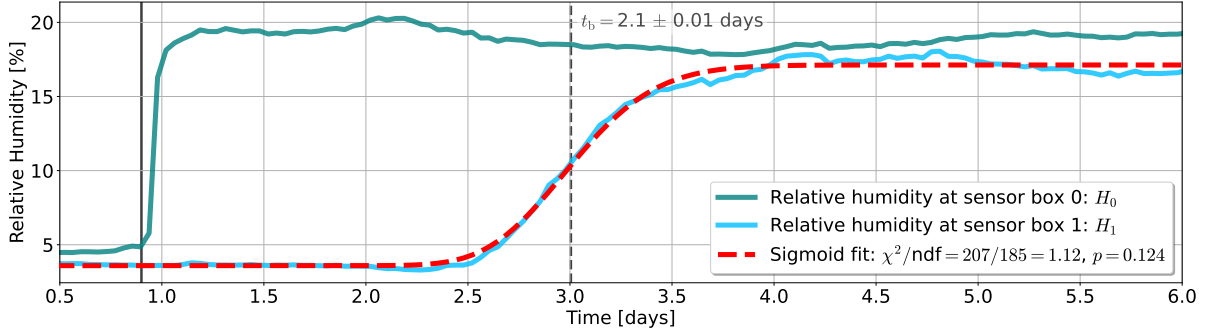


Figure 8.4: The relative humidity H_0 in sensor box 0 (teal curve), located at the system input was initially very low (a few percent) and then sharply increased as high-humidity (about 20%) lab air was sourced by the TTS air compressor. After an average time of about 2 days, the relative humidity H_1 measured in sensor box 1 (blue curve), located at the system output, had increased to the inflection point of a sigmoid-like curve, believed to represent water vapor slowly moving through the column and diffusing along the way (similar as how radon does). The outlet relative humidity H_1 was fit (dashed red curve) by a Sigmoid function (see Section 7.4.1) yielding water-vapor break-through time $t_H = 3.004 \pm 0.006$ days (dashed gray curve) and diffusion coefficient $D_H = 0.1353 \pm 0.0006 \text{ cm}^2/\text{day}$. The uncertainty on the DHT22 humidity sensor is quoted to be $\pm 2\text{-}5\%$ of the measured value (between 0 and 100%) [169, 170]. The goodness-of-fit found in the legend presumes an uncertainty that is the average of the quoted range, 3.5%; this presumed uncertainty is clearly much larger than actual, and thus likely overestimates the goodness-of-fit. The vertical gray line at 0.9 days represents the time when high-humidity was first introduced to the column input (and is used in determining t_H).

With $L = 5 \text{ ft}$, $t_H = 2 \text{ days}$, and $v_{\text{air}} = F/A = 2.7 \text{ cm/s}$, with the column cross-sectional area $A = \pi \left(\frac{3 \times 2.54}{2}\right)^2 = 46 \text{ cm}^2$, the proportionality factor $f_H = 0.3 \times 10^{-3}$ (unitless).

8.4 Future Studies and Discussion

With the TTS being built around flexibility, there are many exciting studies that have not been brought to fruition. One such study is to better understand the **influence of temperature** on radon adsorption. The temperature in this context refers to the temperature of the carbon surface, not the carrier gas. The TTS, however, measures the temperature of the gas entering and exiting the column, which may be related to the temperature of the carbon surface and thus radon adsorption (though perhaps with some caveat relating to, for example, the thermal mass of the carbon). A more robust temperature measuring setup may provide insight into how the gas temperature relates to the surface temperature (as the gas temperature is presumably more easily controlled

in a radon reduction system) and guide future effort on active heating/cooling systems in general.

A sketch of such a system update might involve installing additional resistive temperature devices (RTDs) within and around the column. Importantly, infrared (IR) sensors could be installed within the carbon granules, providing a non-contact means for assessing the surface temperature of the carbon. To modify the temperature of the carrier gas (though one might rely on ambient changes in temperature), an inline heater may be used to increase the gas temperature just before the column, ensuring that other system hardware, such as the radon source, is not damaged by the higher temperature gas. Alternatively or in addition, the carbon bed could be heated by wrapping a thermal blanket around the column (and allowing for the required heat-up time before starting a run) or using an induction system; whereby electrically coupling to the carbon, a current is induced, resulting in Joule heating of the carbon granules. This last method, using inductive heating, is expected to be a more challenging approach (though some work was already done on this during a Senior Design Project in 2021-22), but with the advantage of directly heating the carbon while only indirectly heating surrounding materials (via convective and radiative losses).

Another intriguing study is to better understand the **influence of pressure** on the diffusion of radon within the column during a BTC measurement. The expectation is that the diffusion coefficient is inversely proportional to the pressure in the column. To modify the pressure within a column, a vacuum may be placed directly after the column. The valve (or perhaps a more suitable valve) just before the column would provide high impedance to the gas flowing through it, thus resulting in a pressure drop at that location. The impedance of the column itself is expected to result in only a small pressure gradient (not more than 25% or so). By constraining the amount of gas flow through the valves before and after the column (just before the vacuum pump), the user may roughly choose the pressure within the column. It would therefore be useful to install pressure sensors

at a few locations within the column to monitor the average pressure and the pressure gradient across the carbon bed. Because these types of sensors are inexpensive, the total cost of such an update would not likely exceed a few hundred USD (with the expectation that some fittings and other hardware would need to be replaced).

Yet another study is to better understand the **influence of water vapor** within the carrier gas on radon adsorption. The expectation is that water vapor (related to the humidity of the gas) adsorbs and possibly condenses on the carbon surface. This may result in fractional coverage that eliminates possible adsorption sites for radon atoms. Alternatively, it may be the case that water molecules are effective at shielding the carbon surface from the radon atom and thus reducing the strength or frequency of the induced-dipole adsorption that would otherwise take place between the radon atom and the carbon surface.

While water may be easily introduced to the carrier gas by using, for example, a bubbler, there are two important issues when increasing the relative humidity of the carrier gas through the TTS. The first is that the Pylon radon source requires that the through-flow gas has a low relative humidity. Therefore, water should be introduced only after the radon source. This presents the practical issue that sensor box 0 is before the radon source, and therefore the user would not have a measurement of the amount of water added (that is, the increase in relative humidity). This can be circumvented by installing relative humidity sensors within the column (a good place to have sensors anyway). The second concern is similar, but its solution appears easier to implement. Once high-humidity gas begins exiting the column, it would be sampled by a radon detector. The Durridge RAD7 typically used also prefers low-humidity air (< 10%). Because the RAD7 only requires < 1 slpm of sample gas, a possible solution is to simply add an inline drying column filled with water-adsorbing desiccant (a consumable) or a Durridge Drystik, a device that removes water from the sample gas continuously without any type of consumption.

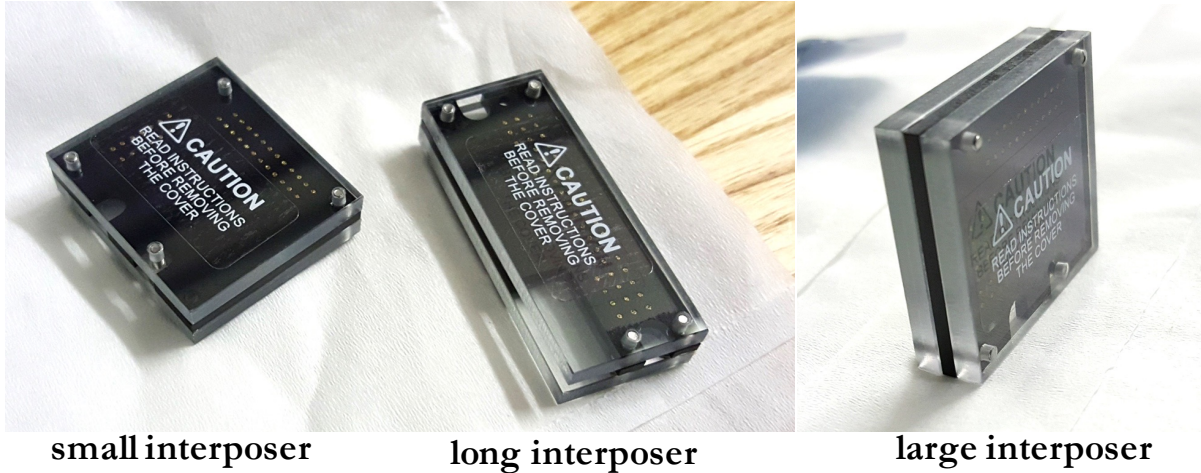


Figure 9.1: Three interposer boards (protected by clear plastic) with slightly different sizes (denoted as small, long, and large) act as representatives of all interposer boards that may be used. Copper fuzz buttons are embedded in holes within each board, seen here as small, gold colored dots.

Chapter 9

Assay of Interposer Boards

Interposer boards are small plastic plates containing conductive copper contacts used for detector readout and are to be located with line-of-sight to a SuperCDMS SNOLAB detector. Interposer boards containing so-called fuzz buttons were sandwiched between plastic for storage (see Fig. 9.1). The faces of the interposer boards were, therefore, afforded line-of-sight protection from radon daughter implantation. The side walls of the interposer boards, however, had no such protection. These boards were stored for several years in an environment that is assumed to have a radon concentration of $\sim 100 \text{ Bq}/\text{m}^3$. The SuperCDMS SNOLAB experiment aims for a $10 \mu\text{Bq}/\text{cm}^2$ goal in surface ^{210}Pb for these boards.

The faces and sidewalls of each of the three interposer boards have slightly differing geometries, described in Table 9.1. The position of the interposer boards during assay is

Interposer board	Length [cm]	Width [cm]	Thickness [cm]	Sidewall Area [cm ²]	Face Area [cm ²]
Small	2.88	2.77	0.78	2.3	8.0
Long	4.15	1.69	0.76	3.2	7.0
Large	4.13	3.84	0.76	3.2	15.9

Table 9.1: Dimensions of interposer boards with systematic uncertainties ± 0.02 cm.

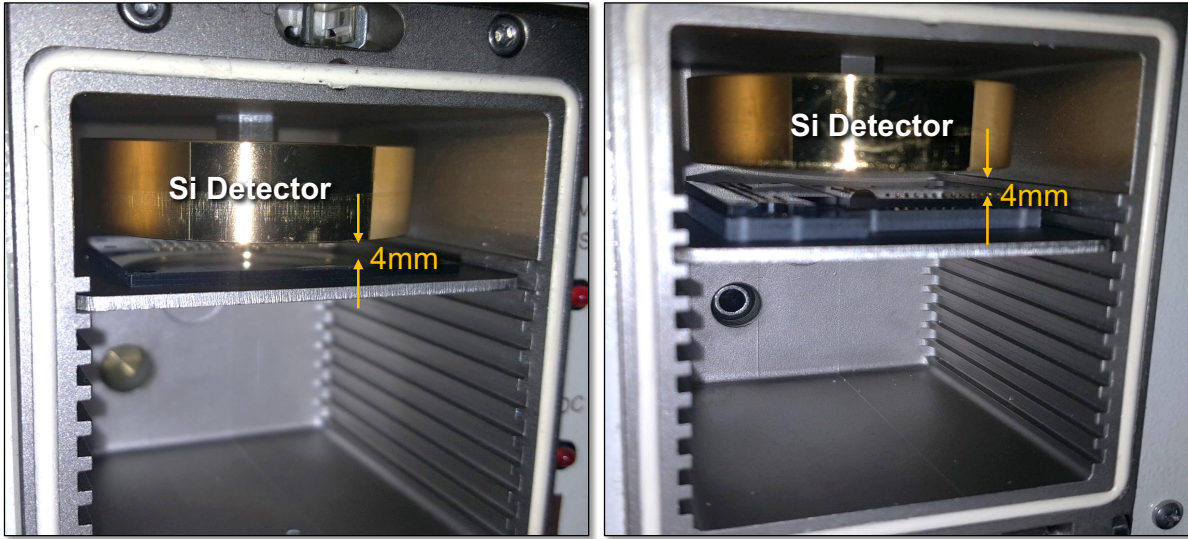


Figure 9.2: Interposer faces, with clear plastic removed, exposed to the detector with a separation of 4 mm.

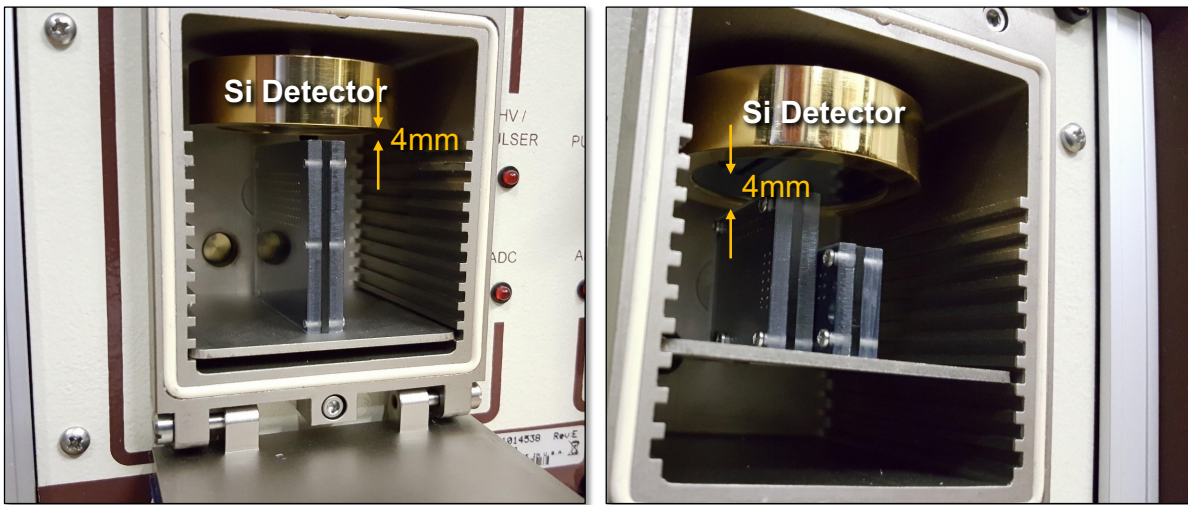


Figure 9.3: Interposer sidewalls exposed to the detector with a separation of 4 mm.

shown by Fig. 9.2 and Fig. 9.3, with corresponding efficiencies estimated by a toy Monte Carlo simulations, found in Table 9.2.

Interposer Assay	Sidewall Efficiency [decimal]	Face Efficiency [decimal]
Small and Long	0.24	0.21
Large	0.30	0.22

Table 9.2: Detection efficiencies for alpha decays on interposer surfaces, as illustrated by Fig. 9.2 and Fig. 9.3.

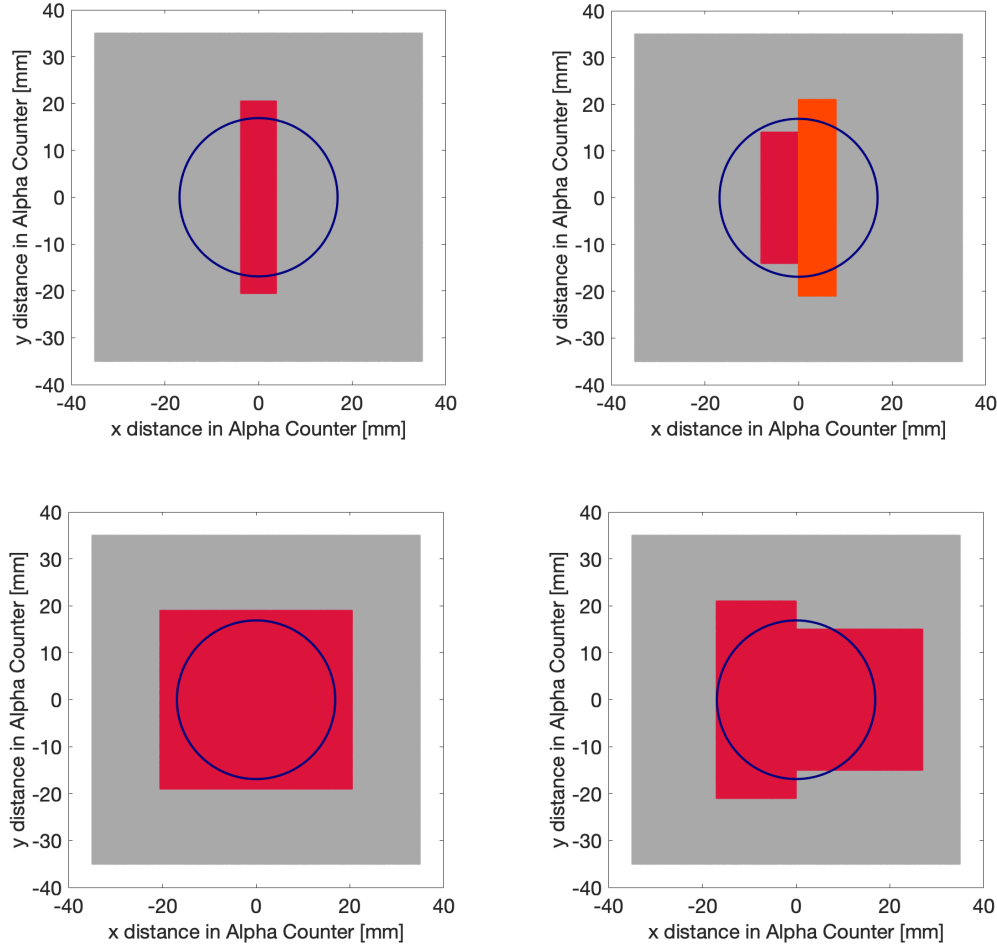


Figure 9.4: Random x - y locations are generated (gray). Locations within the sample are selected (red or orange). The **top left** plot represents the orientation of the large interposer sidewall assay. The **top right** plot represents the small (red) and long (orange) interposers with their sidewalls facing the detector. The long interposer is partially shadowed by the small interposer (due to its larger height) and is accounted for by the simulation. The **bottom left** plot represents the orientation of the large interposer face assay. The **bottom right** plot represents the small and long interposers with their faces facing the detector.

The simulation that calculates efficiency is built upon code that was originally written by John Roberts. Referring to Fig. 9.4, the 2D shape of a sample is described by its vertices. Events ($N \sim 10^7$) are generated with random locations within the (x - y) plane.

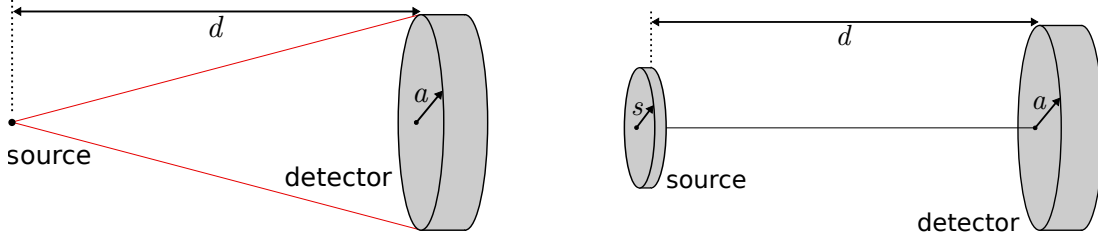


Figure 9.5: **Left:** A point source (dot) is a distance d from the detector (disc) with radius a . Red lines illustrate the solid angle seen by the detector. **Right:** A source (small disc), with radius s , is a distance d from the detector (large disc) with radius a . The disc source is concentric with the detector.

Of these events, those within the sample's 2D geometry are selected, and denoted as N_{sample} . An isotropically-random direction is then assigned to each of these selected events. Each event with a trajectory that passes through the detector is counted, adding up to N_{counted} . The efficiency is then $\epsilon = N_{\text{counted}}/(N_{\text{sample}} - N_{\text{missed}}) = N_{\text{counted}}/N_{\text{missed}}$.

In order to check that the efficiencies found by simulation are reasonable, we recall the solid angle of a point source separated by a distance d from a detector with radius a (as illustrated by Fig. 9.5: left):

$$\Omega = 2\pi \left(1 - \frac{d}{\sqrt{d^2 + a^2}} \right), \quad (9.1)$$

with the efficiency then found as $\epsilon = \Omega/(4\pi)$. With $d = 4$ mm and $a = 16.9$ mm, we arrive at $\epsilon \approx 0.38$. This, of course, is a gross over estimate for any of these assay orientations, but provides a hard upper limit.

Improving our constraint on the efficiency for the large face, for example, we consider the case of a disc source with radius s a distance d from a detector of radius a (as illustrated by Fig. 9.5: right). The effective solid angle averaged over the surface of the the source is given by solving the integral:

$$\Omega = \frac{4\pi a}{s} \int_0^\infty \frac{\exp(-dk) J_1(sk) J_a(ak)}{k} dk, \quad (9.2)$$

where $J_1(x)$ are Bessel functions [77]. Though no analytic solution exists, a good approximation has been found (also printed in [77]):

$$\Omega \approx 2\pi \left[1 - \frac{1}{(1+\beta)^{1/2}} - \frac{3}{8} \frac{\alpha\beta}{(1+\beta)^{5/2}} + \alpha^2[F1] - \alpha^3[F2] \right], \quad (9.3)$$

Assay	Run Number	Detector Bay 1 (or) Large Interposer [cpd]	Detector Bay 2 (or) Small and Long Interposer [cpd]
Sidewalls	256	1.86 ± 0.36	1.93 ± 0.37
Background	257	1.14 ± 0.29	2.22 ± 0.40
Faces	263	2.14 ± 0.39	1.94 ± 0.37
Background	264	2.30 ± 0.57	1.71 ± 0.49

Table 9.3: Integrated rate (in counts per day) within the 200 keV ^{210}Po ROI for each run. Uncertainties are found as \sqrt{N}/t_{live} , where N is the total number of counts within the ROI during the live-time t_{live} . The “Run Number” column is included for posterity (and will agree with the logs taken during these assays).

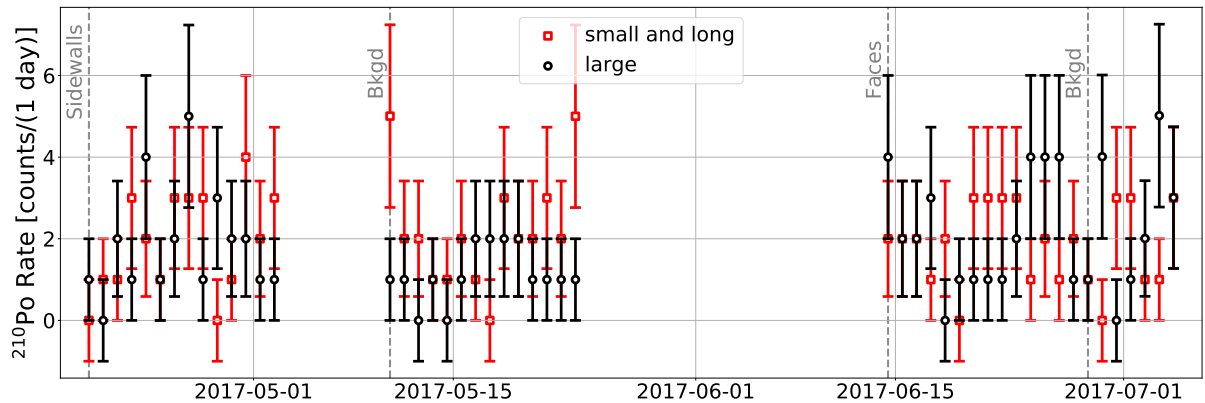


Figure 9.6: Event rate as a function of time for interposer assay runs, with a background run following each assay.

where

$$\begin{aligned} F1 &= \frac{5}{16} \frac{\beta}{(1 + \beta)^{7/2}} - \frac{35}{64} \frac{\beta^2}{(1 + \beta)^{9/2}} \\ F2 &= \frac{35}{128} \frac{\beta}{(1 + \beta)^{9/2}} - \frac{315}{256} \frac{\beta^2}{(1 + \beta)^{11/2}} + \frac{1155}{1024} \frac{\beta^3}{(1 + \beta)^{13/2}}, \end{aligned}$$

and

$$\alpha = \left(\frac{s}{d}\right)^2 \text{ and } \beta = \left(\frac{a}{d}\right)^2.$$

Assuming the source radius is the same as half of the short side of the large face, we have the values: $d = 4$ mm, $a = 16.9$ mm, and $s = 19.2$ mm. This results in the efficiency of $\epsilon \approx 0.28$. This is still a slight over estimate, but appears to indicate that the simulation value of $\epsilon = 0.22$ is not surprisingly small.

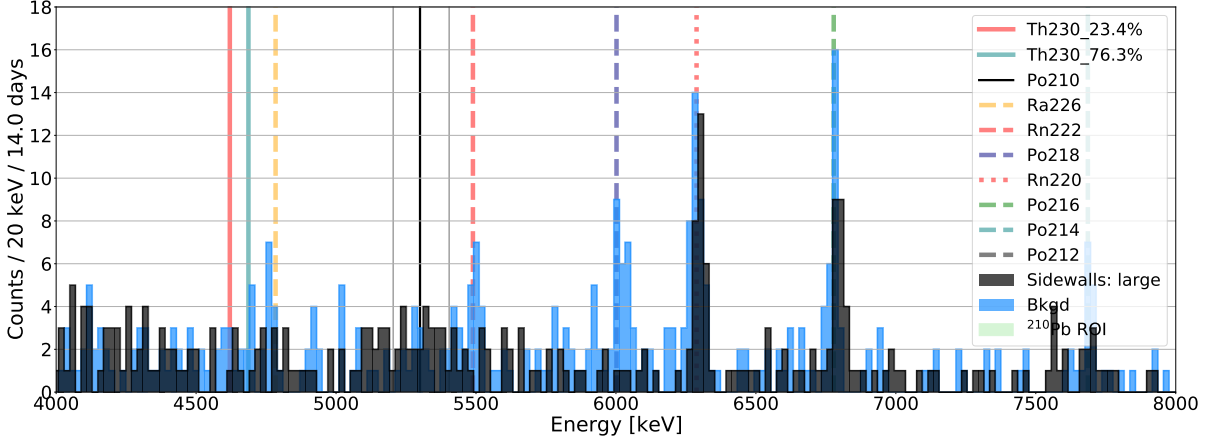


Figure 9.7: Energy histogram for large interposer sidewall assay (black) against its proceeding background run (blue).

The assay of the sidewalls had a live-time of 14 days, followed by a background run of the same duration. The assay of the faces also had a live-time of 14 days, while the following background run was performed for only 7 days. Each background run was setup identically to the preceding assay, but with the sample removed. The measured rates for each run is listed in Table 9.3. The complete time-series of these runs is shown by Fig. 9.6.

Energy histograms indicate that the rate measured for both the faces (Fig. 9.7 and Fig. 9.8) and sidewalls (Fig. 9.9 and Fig. 9.10) is consistent with detector background rates within the same region of interest (ROI). The ^{220}Rn and ^{214}Po peaks appear to be correctly calibrated within at least one 20 keV energy bin. Therefore, the ROI, having a chosen width of 200 keV, appears to capture close to 100% of the ^{210}Po peak.

The Alpha Duo background rate (within the ^{210}Po ROI) is the sum of two possible sources: (1) events originating from the bulk and/or surface of the Si detector and (2) events originating from the inside surface of the detector bay. Because it is unclear what fraction of events come from either of these two sources, no background subtraction has been attempted. This results in a conservative upper limit on the quoted ^{210}Po rate for the sidewall and face assays. The 95% confidence limit on the rate, $R_{95\%}$, is set by the

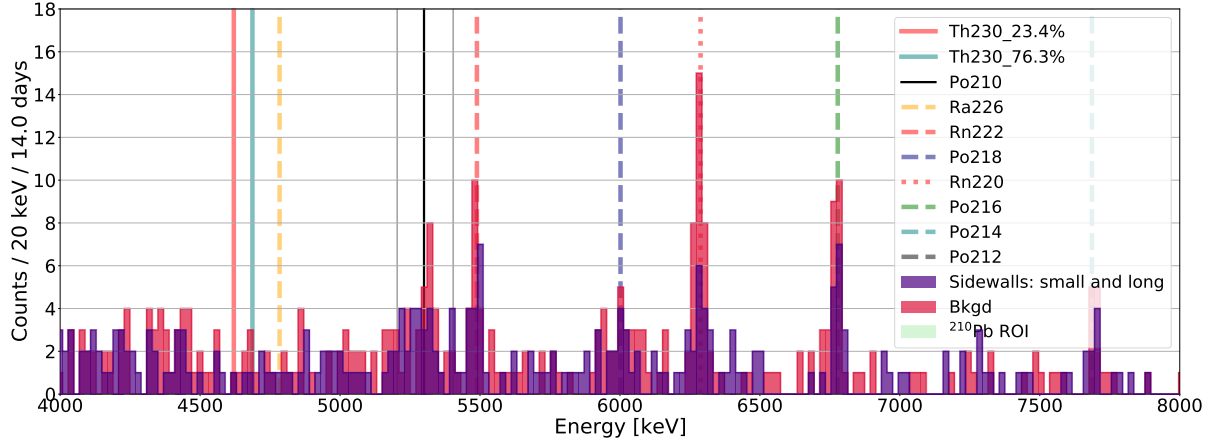


Figure 9.8: Energy histogram for small and long interposers sidewall assay (indigo) against its proceeding background run (crimson).

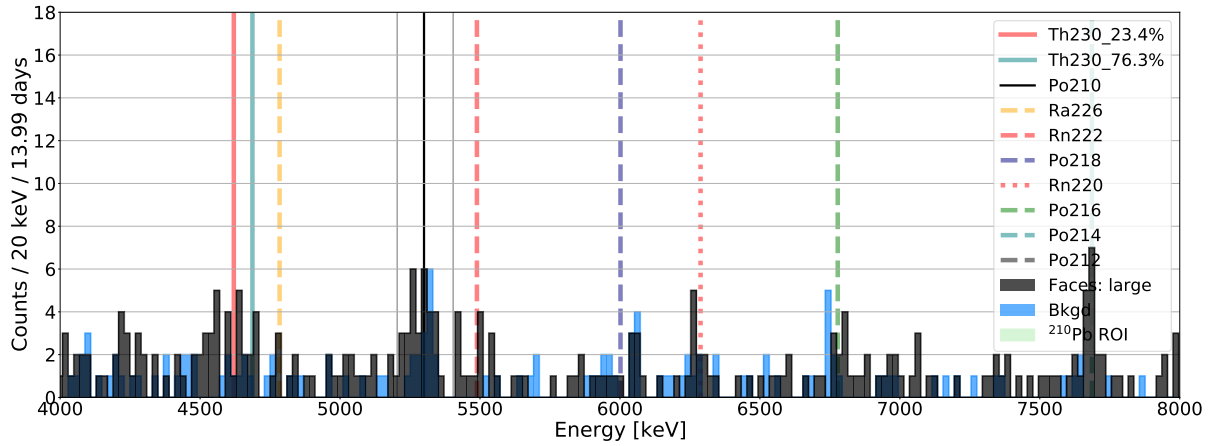


Figure 9.9: Energy histogram for large interposer face assay (black) against its proceeding background run (blue).

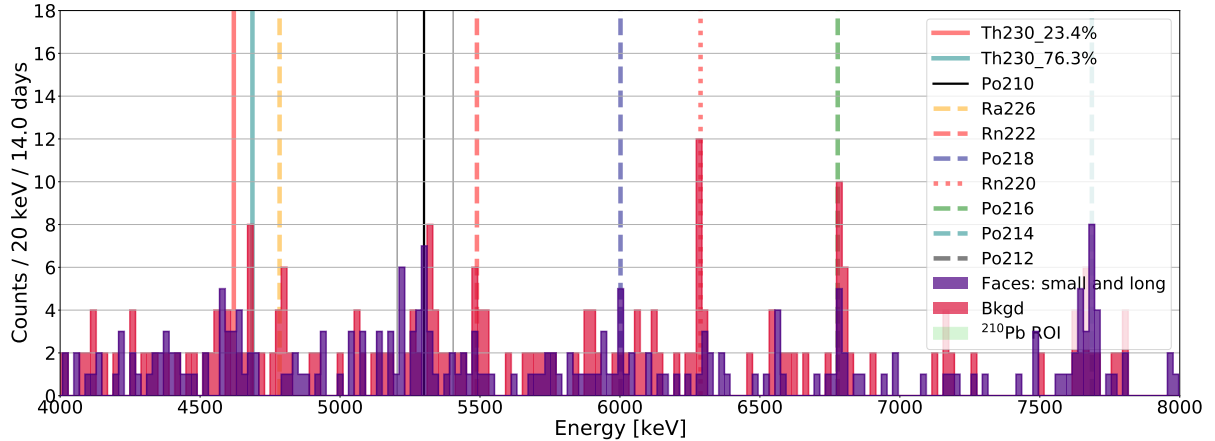


Figure 9.10: Energy histogram for small and long interposer face assay (indigo) against its proceeding background run (crimson).

Assay	Large Interposer (95% C.L.)		Small and Long Interposer (95% C.L.)	
	[cpd]	[$\mu\text{Bq}/\text{cm}^2$]	[cpd]	[$\mu\text{Bq}/\text{cm}^2$]
Sidewalls	2.54	30.61	2.57	22.53
Faces	2.85	9.44	2.39	8.79
Totals	—	12.99	—	24.82

Table 9.4: 95% upper-confidence limits of interposer ^{210}Po assays. The area-weighted average is between the sidewall and face rate. The totals are area weighted.

relation:

$$R_{95\%} = \bar{R} + Z \frac{\sigma}{\sqrt{N}}, \quad (9.4)$$

where \bar{R} is the mean rate within the ROI, $Z = 1.96$, the upper end point of the range containing 95% of the normal distribution, σ is the standard deviation of the measured rate R , and $N = 14$, the sample size (as the total rate measured was saved to disc once per day for two weeks). These confidence limits are listed in Table 9.4, along with the resulting surface contamination in units of $\mu\text{Bq}/\text{cm}^2$.

Chapter 10

Removal of ^{210}Pb by Etch of Crystalline Detector Sidewalls

This chapter describes published work [171] conducted through a collaboration between SD Mines and Texas A&M. Several subsections have been copied verbatim from the published paper, as well as some figures and their captions that would not benefit from being changed. Discussions on intermediate calculations (such as how the detection efficiency was estimated) and measured energy spectra have been included here to further describe the work conducted.

Portions of the published paper that are quoted verbatim are presented in blue text, such as the paragraph below.

This [work] describes a newly-developed etching technique for the sidewalls of solid-state crystal detectors. A Si crystal core was exposed to high-radon air, depositing ^{210}Pb on the core's surface. The core's sidewall was assayed by an alpha counter sensitive to ^{210}Po alpha decays before and after the etching technique was performed to infer the reduction in ^{210}Pb due to the etch.

10.1 ^{210}Pb Deposition from High-Radon Air Exposure

This section is quoted verbatim from the published paper, but with the exposure setup and radon-decay chain figures remade entirely.

A 76 mm \times 25.4 mm polished Si crystal was fabricated with SuperCDMS sensors. Following fabrication, the crystal was coated with Logitech OCON-200 bonding wax and sandwiched between two borosilicate glass disks to protect the circuit and reduce substrate chipping during coring. The coring process was performed on a standard Bridgeport Mill using hardware custom-designed to aid in substrate cooling. The diamond-

coated coring bit (1.000 ± 0.005 in diameter) was custom-fabricated by Keen-Kut Products, Hatward California.

Two of the cores produced were used for this study. They were exposed to high-radon air (having a radon concentration of $\sim 30 \text{ MBq/m}^3$) for 18 days and then another 13 days (with a 1-day assay of the ^{210}Po decay rate in between). Figure 10.1 illustrates the experimental setup during the last 13 days (the second exposure), which consisted of a ^{222}Rn source supplied by Pylon [172], exposure vessel, inline flow meter, and Durridge RAD7 in a closed loop with the air inside circulated by the RAD7's internal pump. The 18-day exposure (the first exposure) used a hand-siphon pump in place of the RAD7.

During exposure, ^{222}Rn decays through its so-called fast daughters ^{218}Po , ^{214}Pb , ^{214}Bi , and ^{214}Po (see the radon chain in Fig. 10.2). These fast daughters, usually positively charged [173], may settle on nearby surfaces [174]. Subsequent alpha decays may then embed the daughters of order 10 nm into the surface. As a result, some ^{210}Pb is embedded and concentrated just below the surface from the sustained radon exposure.

Prior to each exposure, the setup was flushed with low-radon lab air. If sufficient mixing is obtained, the radon concentration within the exposure vessel is

$$C_{\text{Rn}}(t) = \frac{A_{\text{source}}}{V_{\text{source}} + V_{\text{vess}}} \left[1 - \exp \left(-\frac{t}{\tau_{\text{Rn}}} \right) \right], \quad (10.1)$$

where the ^{222}Rn source activity $A_{\text{source}} = 118 \pm 5 \text{ kBq}$ and its inner volume $V_{\text{source}} = 0.2$ liters. The volume of the exposure vessel $V_{\text{vess}} = 3.5$ liters and the radon mean lifetime $\tau_{\text{Rn}} = 5.51$ days. The exponential factor reflects radon growing into equilibrium within the setup volume.

During the first exposure, a siphon pump was used to circulate the gas. For the second exposure, the siphon pump was replaced by a RAD7, making use of its internal pump. The RAD7 demonstrated that sufficient mixing was achieved, so the time dependence of the radon concentration during the second exposure should be described by Eq. 10.1.

The relative amounts of ^{210}Pb , ^{210}Bi , and ^{210}Po on the Si core at the beginning of the pre-etch assay influence the time dependence of the ^{210}Po decay rate. If the radon

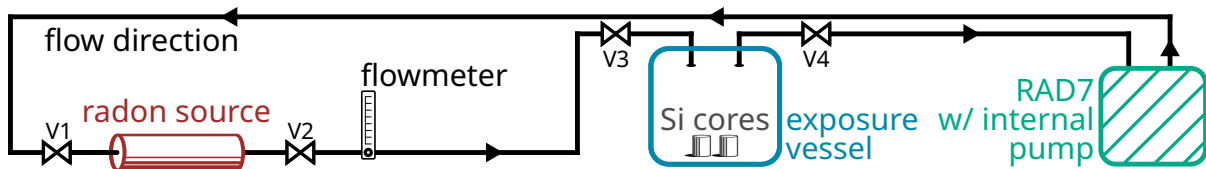


Figure 10.1: During the second exposure, radon emanates from the radon source into the air within the closed system. An inline flowmeter indicates the circulation rate provided by the RAD7's internal pump. The RAD7 also measures the radon activity of the air passing through it. The valves V1 through V4 are open during the exposure, but may be closed afterward such that the high-radon air may be safely purged to an exhaust line (not shown). During the first exposure, the RAD7 in this figure is substituted with an inline hand-siphon pump.

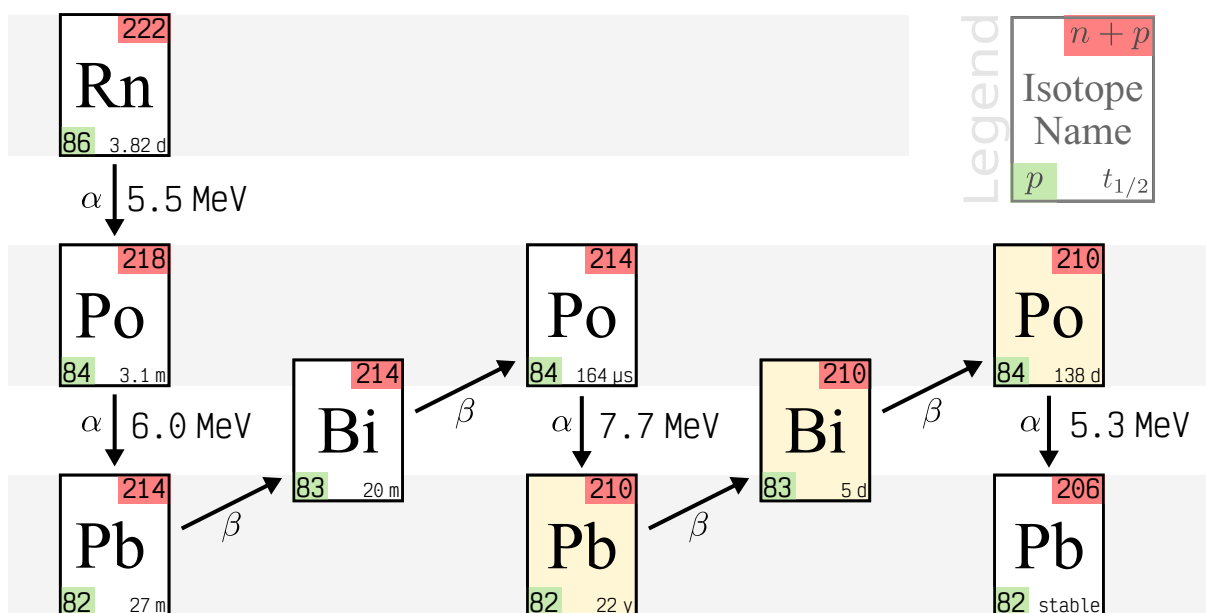


Figure 10.2: ^{222}Rn decay chain with legend shows the atomic number (the number of protons $Z = p$), mass number (the number of protons and neutrons $A = n + p$), and half-life $t_{1/2}$ of isotopes. Radon and its progeny prior to ^{210}Pb have relatively short half-lives. ^{210}Pb has a long half-life of 22.3 years from which ^{210}Po (having a half-life of 138 days) will grow into equilibrium over several months.

concentration during exposure is understood, then the radioactive-decay equations may be solved to provide the relative abundance of each radon daughter. Thus, the ^{210}Po rate due to the second exposure can be modeled with a single fitting parameter accounting for the unknown absolute deposition rate. The ^{210}Po rate due to the first exposure is characterized by three free parameters, representing the ^{210}Pb , ^{210}Bi , and ^{210}Po at the end of the exposure, ensuring a conservative limit is set.

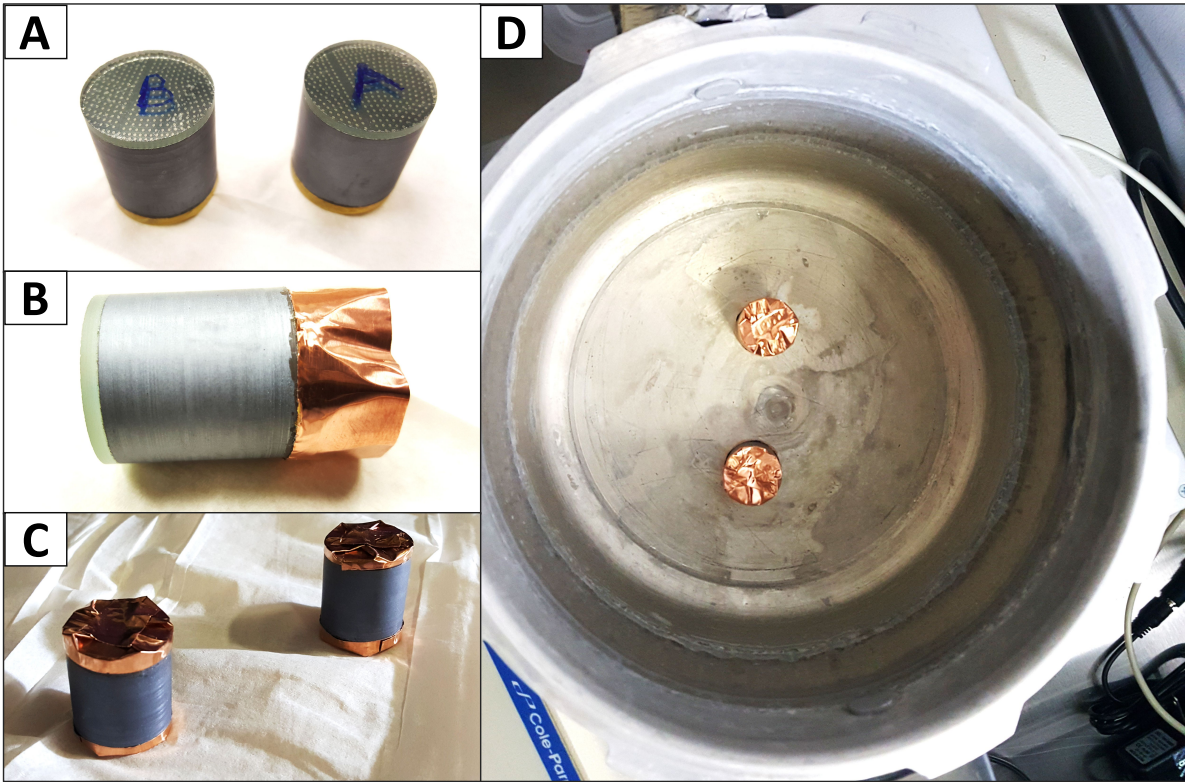


Figure 10.3: Si core preparation and exposure geometry. (A): Wax on the faces protects delicate sensors from the etch and handling. (B): Copper foil shields charged daughters from the influence of static charge on the wax. (C): Si cores have copper foil in place and are ready for the high-radon exposure. (D): Si cores are placed roughly equidistant between the vessel walls. This configuration likely produces non-uniform radon-daughter deposition on core sidewalls.

The exposure vessel was cylindrical with input and output feedthroughs penetrating its hemispherical lid. As seen in Fig. 10.3, copper foil was used to shield radon daughters from static charge on the wax that could reduce deposition on the core sidewalls. The cores were placed within the exposure vessel roughly equidistant between the vessel walls. The lack of radial symmetry in the core placement suggests non-uniform deposition with respect to the axial rotation of each core.

10.2 Alpha Duo α Spectrometer

Radon daughters are implanted in the Si core surface from the high-radon exposure; those that undergo alpha decay can be detected by the Alpha Duo α Spectrometer [175]. The Alpha Duo has two pressure-regulated detection chambers (see Fig. 10.4). Each



Figure 10.4: The Ortec Alpha Duo alpha spectrometer is shown with one detector bay closed and the other open. The open bay shows the inside of a vacuum chamber where a sample may be placed on an adjustable shelf below the Si detector. The detection chamber has a height $H = 44 \pm 0.25$ mm (when the shelf is at its lowest position), width $W = 52 \pm 0.25$ mm, and depth $D = 56 \pm 0.25$ mm.

chamber, sometimes called a detector bay, has an adjustable shelf that may be used to position a sample between 4 mm to 44 mm below a 51-mm-diameter Si detector that is fixed at the top of the chamber. When an alpha particle passes into the Si detector, the particle's kinetic energy is deposited according to its energy loss dE/dx . Each incident alpha travels a short distance (up to ~ 10 microns) in the Si detector where its kinetic energy is deposited, producing electron-hole pairs that are subjected to a 50 V potential, resulting in a change in the measured current. The integral of this current pulse is proportional to the alpha's energy, which may be used to infer the radioactive decay that produced it. The Alpha Duo is sensitive to event energies between about 1 and 10 MeV with an energy resolution of ≤ 20 keV (based on the FWHM from a ^{241}Am point source) [175].

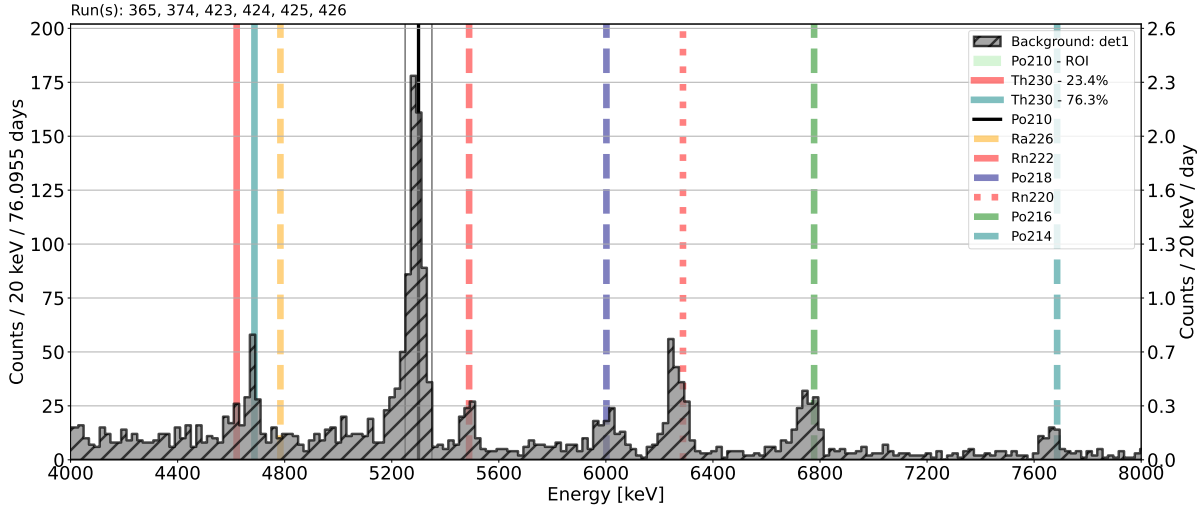


Figure 10.5: Background energy spectrum of the SD Mines Alpha Duo detector 1. Background measurements for the SD Mines Alpha Duo detector bay 1 were taken before and after each Si core assay and combined to form a single histogram (filled region). The ^{210}Po region of interest (ROI) has a width of 100 keV from 5250 to 5350 keV (light green vertical column) and has an average rate of 7.2 ± 2.7 counts/day.

Figure 10.5 shows combined background runs taken before and after Si core assays. A background run is a measurement performed exactly as the assay, but with no sample within the detection chamber. The ^{230}Th peaks are due to contamination of the shelf, which is blocked by the Si core during assays. The rate of ^{222}Rn at 5.5 MeV depends on the chamber pressure, with a higher pressure resulting in a higher concentration of radon and thus an increased rate. The rate of ^{218}Po and ^{214}Po also increases with the rate of ^{222}Rn . The rate of ^{220}Rn determines the rate of its daughters ^{216}Po and ^{212}Po . The aforementioned backgrounds have energy peaks sufficiently far away from the ^{210}Po region of interest (ROI) such that they are not expected to influence the ^{210}Po rate inferred. The ^{210}Po background rate is primarily determined by ^{210}Pb embedded in the face of the Si detector and is 7.2 ± 2.7 counts/day within the 100 keV ROI (from 5250 to 5350 keV). This ^{210}Po background rate is about 3 times larger than the typical rate from a newly fabricated detector.

10.2.1 Detection Efficiency for a Si Core

The probability of an alpha particle leaving the Si core surface is slightly more than 50% due to the curvature of the sidewall. A yet smaller fraction of those that leave the surface have trajectories that pass through the Alpha Duo Si detector, located directly above the sidewall of the Si core. If the number of alphas incident on the Si detector is N_i and the number of alphas not incident is N_{ni} , then the detection efficiency

$$\varepsilon \equiv \frac{N_i}{N_{ni} + N_i}. \quad (10.2)$$

While one could calculate the efficiency analytically using the sample and detector geometry, instead we use a toy Monte Carlo simulation (MC).

The toy MC consists of three major parts: (1) the generation of N random initial locations of alpha decays on the Si core surface, (2) the generation of an isotropically-random angle assigned to each generated alpha decay, and (3) a condition to test whether the alpha particle trajectory passes through the Si detector or not. The trajectories that pass through the detector represent the incident events with a total count of N_i , with those not incident having a total count $N_{ni} = N - N_i$.

Figure 10.6 shows a 3D depiction of the toy MC simulation, but with a reduced number of random events for visual clarity ($N = 5000$). With $N = 10^5$, alphas leaving the Si core are estimated to be detected with efficiency $\epsilon = 9.1^{+0.1}_{-0.1}\%$. This efficiency also passes a basic sanity check: half of all alphas have a direction leaving the Si core (not entering it), and only half of those have an upward component (toward the Alpha Duo detector). So far, this crude estimate of the efficiency is $\frac{1}{2} \cdot \frac{1}{2} = \frac{1}{4}$. Further consideration of the sample and detector geometry, an alpha leaving the Si core nearest the detector (at $\theta = \pi/2$, as shown by Fig. 10.7) has a larger solid angle than an alpha furthest from the detector (at $\theta = 0$ or π). If we estimate (by eye) that the detection probability of an alpha nearest the detector is $\frac{1}{2}$ and furthest from the detector is $\frac{1}{5}$, and further presume that the remaining alphas are split evenly between these two probabilities, we obtain an efficiency estimate of $\frac{1}{4} \cdot (\frac{1}{2} \cdot \frac{1}{2} + \frac{1}{2} \cdot \frac{1}{5}) = \frac{5}{60}$, or about 9%. While uncertainty in

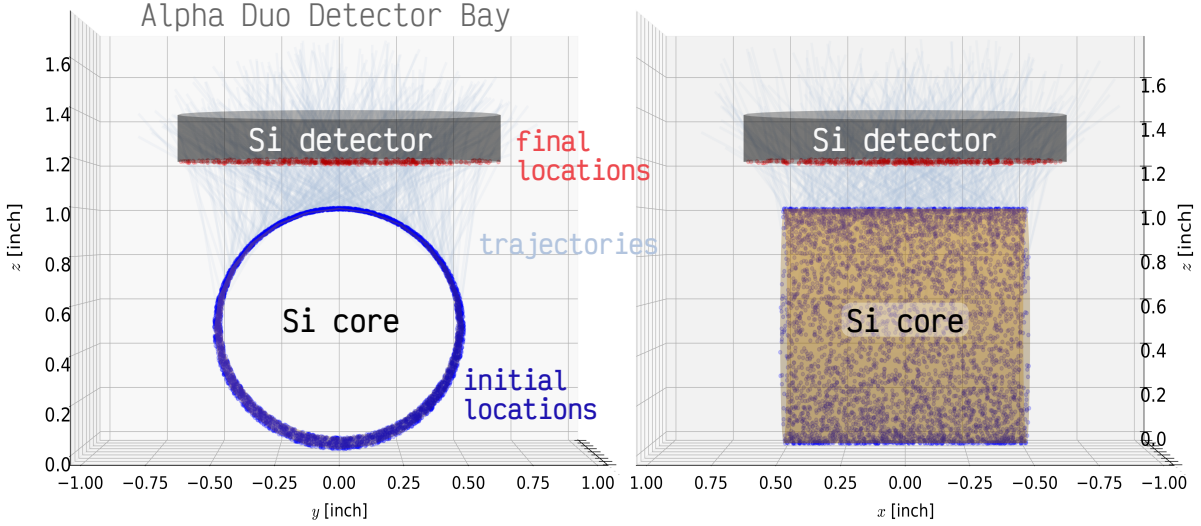


Figure 10.6: The toy MC with $N = 5000$ (for clarity) represented as a 3D scatter plot. Randomly generated **initial locations** of alpha decays on the **Si core** sidewall are shown by blue dots. An isotropically-random angle is assigned to each initial location; those decays with **trajectories** incident on the **Si detector** are shown by gray lines, with their **final locations** shown as red dots. The *left* plot shows the rendering with the x axis facing out of the page, while the *right* plot has the y axis facing out of the page.

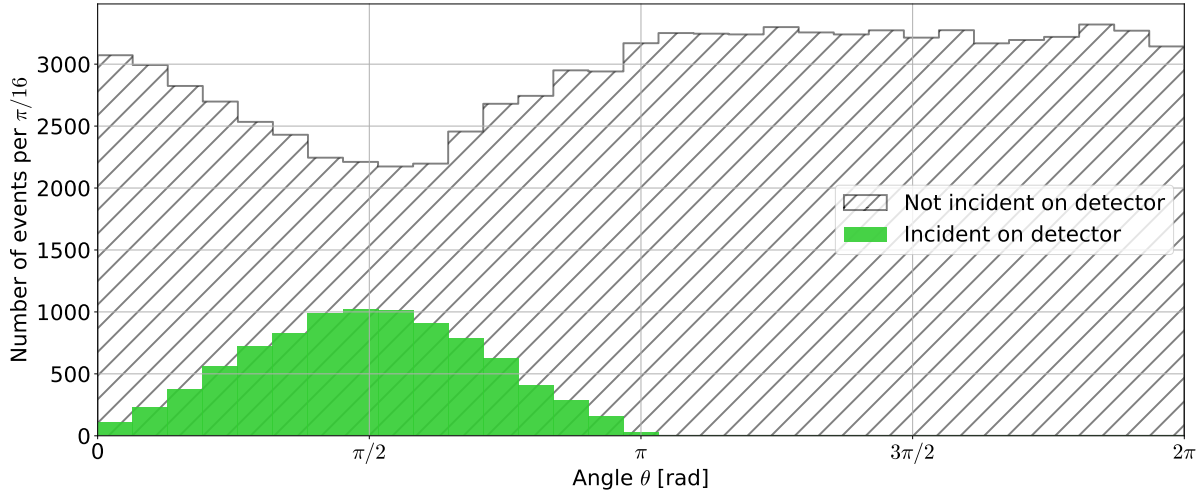


Figure 10.7: The number of alpha particles that are incident on the Alpha Duo Si detector (or not) depends on the angle θ where the parent decayed on the Si core surface. The region of the Si core surface closest to the Si detector (facing up) is at $\theta = \pi/2$.

the efficiency directly affects the quoted contamination (Eq. 10.5), it does *not* affect the quoted limit on the reduction of implanted ^{210}Pb (see Section 10.6), as a ratio is taken.

Figure 10.7 shows the number of incident and not-incident events as a function of the initial decay location angle θ on the Si core for $N = 10^5$ randomly generated decays.

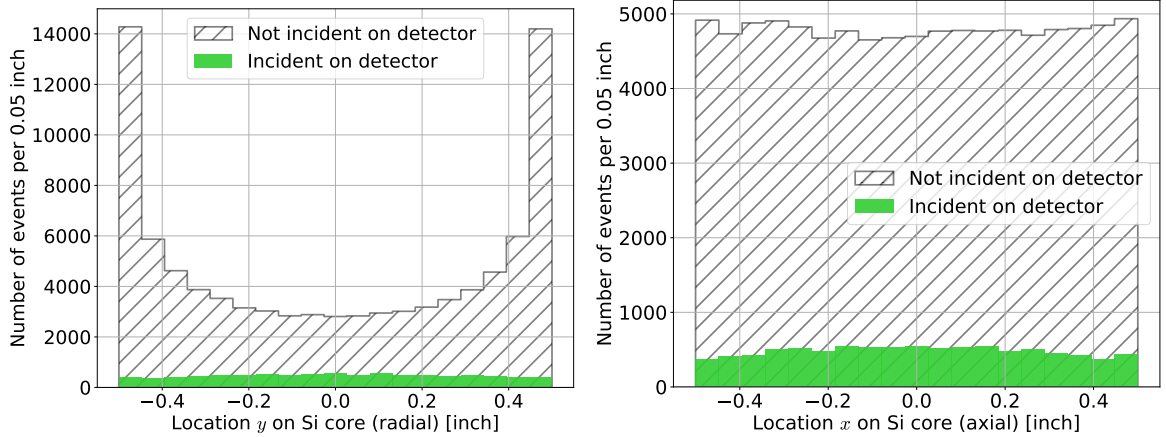


Figure 10.8: The number of alpha particles incident on the Alpha Duo Si detector (or not) depending on decay location x and y . **Left:** The event rate for alpha decays *not* incident on the detector (hatched curve) is largest at values of $y \sim r$, where Si core radius $r = 0.5$ inch. **Right:** The event rate for alpha decays incident on the detector (green, filled curve) is largest at the axial location $x = 0$. As x moves away from zero, the incident event rate drops off slightly as the solid angle of incidence for decaying alphas becomes increasingly small (as these decays takes place further from the center of the Si detector).

The side region of the Si core closest to the Alpha Duo detector is at the angle $\theta = \pi/2$, where the fraction of events that are incident on the detector is maximal. As the decay location angle approaches 0 or π , the incident events approach zero, as the solid angle for the event's trajectory not blocked by the Si core approaches zero.

Figure 10.8 shows the number of incident and not-incident events as functions of the locations x (along the Si core's longitudinal axis) and $y = r \sin(\theta)$ (along the Si core's radial axis), with the Si core radius $r = 0.5$ inch. As expected, the distribution of *not* incident events is concave up for values of y approaching the Si core's radius of 0.5 inch. At $y = 0.5$ inch, an alpha produced by decay must travel nearly straight upward to deposit energy in the Si detector, resulting in the number of incident events being minimal. Also expected, the distribution of incident events is essentially flat over locations x , but with a slight reduction as either end is approached (due to the reduced solid angle for event trajectories passing through the detector).

10.3 Pre-etch Assay

This section is quoted verbatim from the published paper, but with an updated figure showing core rotation and placement. A paragraph describing the energy spectrum has also been added.

Though the pre-etch assay was performed on two Si cores that were both exposed to high-radon air, only the one that was eventually etched and re-assayed will be further discussed.

An Ortec Alpha Duo alpha spectrometer [175] counted the ^{210}Po rate on the sidewall of the Si core. The consistent placement and rotation of the Si core within the Alpha Duo detector bay was important to ensure that the same region of the core's sidewall was counted, as variation in the amount of ^{210}Pb deposited as a function of rotation was likely, due to the placement geometry during exposure. Reproducibility of each angle of rotation minimized this possible systematic due to inadvertent rotation.

During the pre-etch assay, the Si core was periodically removed and replaced in the detector bay at an angle of rotation $\theta = 0^\circ$, 120° , and 240° as measured from the horizontal. The angle of the core was tracked by a line-like feature of the sensors on its face (see Fig. 10.9). Consistent core placement in the horizontal plane was guided by concentric recesses in the detector bay shelves. During handling, nitrile gloves were worn and only the detector faces were touched. This ensured that contaminants were neither added nor removed from the core's sidewall.

Figure 10.10 shows the energy spectrum of the pre-etch assay with the core rotation at zero degrees. The observed ^{210}Po rate is significantly higher than the background rate, indicating a successful high-radon exposure. Figure 10.11 shows the ^{210}Po rate increasing over time as the embedded ^{210}Pb decays via ^{210}Bi to ^{210}Po .

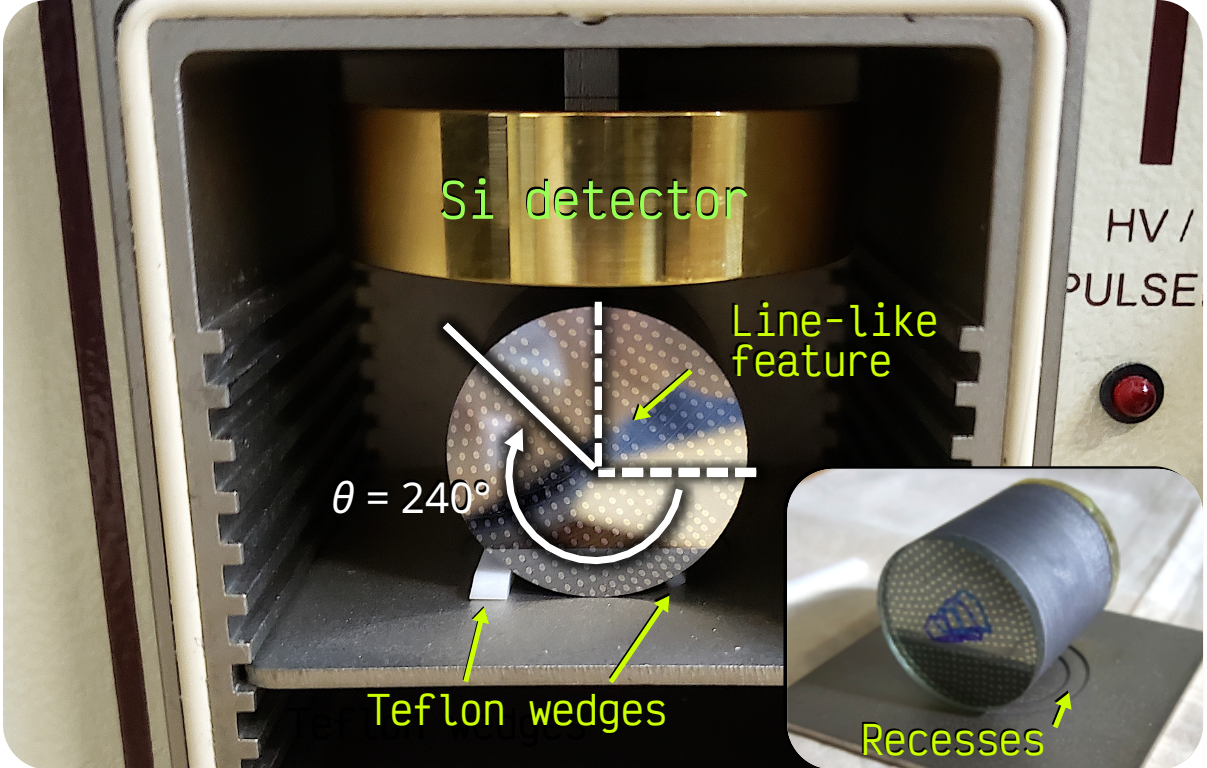


Figure 10.9: Si core sitting inside the Alpha Duo counter detector bay. Low-rate Teflon wedges ensure the core does not roll during measurement. A line-like feature between sensors on the core’s face is used to track core rotation as measured clockwise from the horizontal. Inset shows the concentric recesses that were used to ensure consistent placement on the detector bay shelf.

10.4 Fitting the Pre-etch Data

The Bateman equation B_n describes the number of atoms of the n ’th daughter produced by a radioactive parent [81]:

$$B_n(t) = \sum_{i=1}^n \left[N_i \times \left(\prod_{j=1}^{n-1} \lambda_j \right) \times \sum_{j=i}^n \left(\frac{\exp(-\lambda_j t)}{\prod_{p=i, p \neq j}^n (\lambda_p - \lambda_j)} \right) \right], \quad (10.3)$$

where λ_i is the i ’th daughter’s decay constant (for our case, $n = 3$ and $i = 1, 2, 3$ refers to ${}^{210}\text{Pb}$, ${}^{210}\text{Bi}$, and ${}^{210}\text{Po}$).

The two exposures are considered independently and, built upon Eq. 10.3, added together. The expected signal representing the detected ${}^{210}\text{Po}$ decay rate $S(t)$ has free parameters representing the initial ${}^{210}\text{Pb}$, ${}^{210}\text{Bi}$, and ${}^{210}\text{Po}$ atoms at the end of the first exposure, abbreviated as $N_{\text{Pb}}^{(1)}$, $N_{\text{Bi}}^{(1)}$, $N_{\text{Po}}^{(1)}$ and the initial ${}^{210}\text{Pb}$ at the end of the second

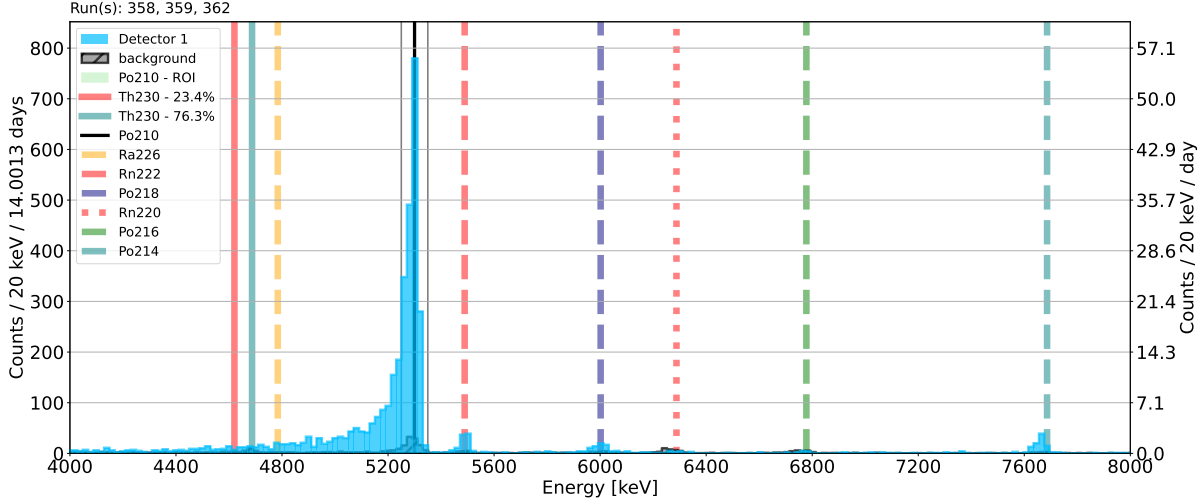


Figure 10.10: After the high-radon exposures, ^{210}Pb embedded in the zero-degree region of the Si core surface decays to ^{210}Bi and then to ^{210}Po . The ^{210}Po decay rate increases over time according to the 22.3 year half-life of ^{210}Pb . After counting for two weeks, the measured energy spectrum (filled, blue curve) shows a significant increase in the ^{210}Po rate (130 counts/day in 100 keV ROI) over the background rate of ~ 7 counts/day (hatched curve).

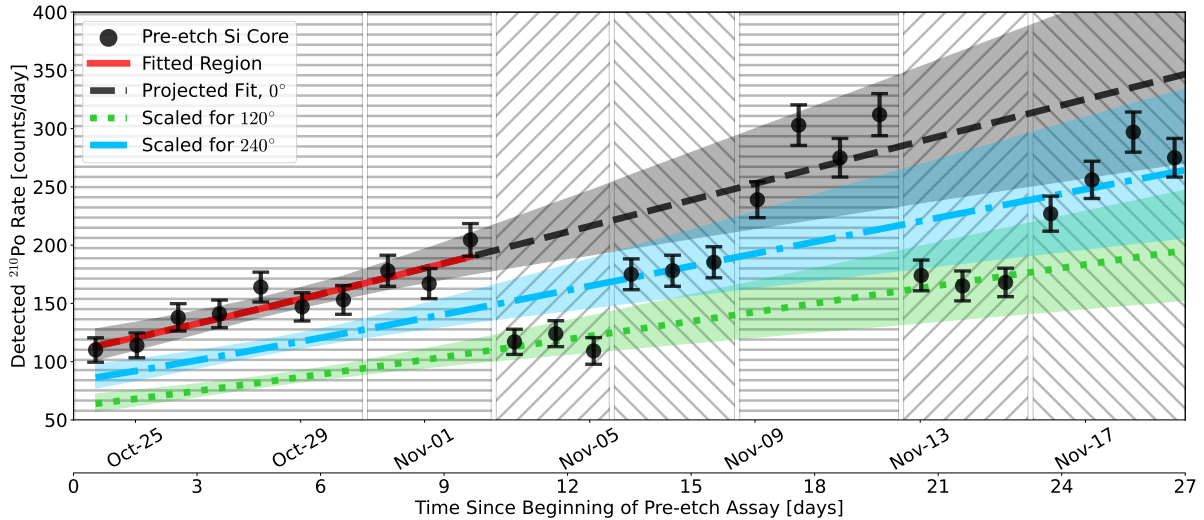


Figure 10.11: Pre-etch data (dots with 1σ error bars) at varying core rotations. The hatch marks in the background of the plot indicate the 0° (horizontal), 120° (up to the right), and 240° (down to the right) rotation of the core. The signal function was fit to the first $\theta = 0^\circ$ data run (represented by the solid curve) with $\chi^2/\text{ndf} = 7.3/9$, p-value = 0.7. Its projection (dashed curve) agrees with the second $\theta = 0^\circ$ run within statistical uncertainties on the best fit (upper shaded region). Days 11-13 show a lower rate for $\theta = 120^\circ$ (dotted curve), as do days 14-16 for $\theta = 240^\circ$ (dot-dashed curve), and each is consistent with its second run (see Table 10.1). Both the $\theta = 120^\circ$ and $\theta = 240^\circ$ curves and their shaded uncertainty regions are found by scaling the best-fit $\theta = 0^\circ$ curve by the best-fit scaling parameter A shown in Table 10.1. Not shown is the earlier one-day assay, which measured 21 ± 6 counts per day (cpd) compared to the best-fit 21^{+12}_{-8} cpd for that time.

exposure, abbreviated $N_{\text{Pb}}^{(2)}$:

$$\begin{aligned} S(t; N_{\text{Pb}}^{(1)}, N_{\text{Bi}}^{(1)}, N_{\text{Po}}^{(1)}, N_{\text{Pb}}^{(2)}) = \epsilon \lambda [B(t; N_{\text{Pb}}^{(1)}, N_{\text{Bi}}^{(1)}, N_{\text{Po}}^{(1)}) \\ + \Theta(t - \Delta t) B(t - \Delta t; N_{\text{Pb}}^{(2)})], \end{aligned} \quad (10.4)$$

where $B_{n=3}(t)$ is denoted as just $B(t)$ and Δt is the time between the beginning of the first and second exposures. The detector efficiency is ϵ , the ^{210}Po decay constant $\lambda = 5.813 \times 10^{-8} \text{ s}^{-1}$, and the second term is multiplied by the Heaviside function.

Equation 10.4 was fit to the ($\theta = 0$) one-day assay after the first exposure and the first 10 days of the ($\theta = 0$) assay after the second exposure. Figure 10.11 shows this fit, but focused on the pre-etch assay after the second exposure for clarity. The inferred surface contamination Σ on the measured ($\theta = 0$) side of the Si core at the beginning of the pre-etch assay (prior to etch) was

$$\Sigma_{\text{Pb}} = 137_{-60}^{+53} \text{ Bq/m}^2, \quad \Sigma_{\text{Bi}} = 101_{-23}^{+25} \text{ Bq/m}^2, \quad \text{and} \quad \Sigma_{\text{Po}} = 7_{-1}^{+1} \text{ Bq/m}^2, \quad (10.5)$$

with 1σ uncertainties found by toy Monte Carlo (see Section 10.4.2).

Each run at each angle of core rotation was fit, with a single scaling parameter, against the signal function fit to the first 0° run. That is, the 0° fit of $S(t)$, was scaled to fit each run as

$$F(t) = A \times S(t), \quad (10.6)$$

where A is a best-fit scaling parameter. Table 10.1 lists values of A and its uncertainty σ_A for both runs at each core rotation. The difference between the two scaling factors for each angle is consistent with statistical uncertainties.

10.4.1 The Number of Free Parameters and Relative Abundance

As introduced in Section 10.1, if we know the time dependence of the radon concentration during an exposure, we may calculate the relative abundance of each decay product. The absolute amount of any daughter is not known without knowing the deposition efficiency. The time dependence of the radon concentration during the first exposure is

θ	0°	120°	240°
A_1	1.00	0.56	0.76
A_2	1.05	0.57	0.77
σ_{A_1}	0.02	0.03	0.06
σ_{A_2}	0.05	0.02	0.03
$ A_1 - A_2 $	0.05	0.01	0.01

Table 10.1: Angle dependence and reproducibility. A_1 and A_2 represent the scaling factors for the first and second runs at each angle relative to the first 0° run, with σ_{A_1} and σ_{A_2} their respective fit uncertainties. The difference between these scaling factors $|A_1 - A_2|$ for each angle is consistent with statistical uncertainties.

not well known, as the efficiency of the hand siphon pump that was employed is not well understood. For the second exposure, a RAD7 was used to measure the radon concentration while using its internal pump to circulate the gas within the closed exposure system (see Fig. 10.1).

The radioactive-decay equations are a system of differential equations:

$$\begin{aligned}\dot{N}_0 &= -\lambda_0 N_0 \\ \dot{N}_1 &= -\lambda_1 N_1 + \lambda_0 N_0 \\ &\dots \\ \dot{N}_n &= -\lambda_n N_n + \lambda_{n-1} N_{n-1},\end{aligned}$$

where $N_i(t)$ is the number atoms of the i^{th} species and λ_i is its decay constant (with $i = 0, 1, \dots, n$ referring to ^{222}Rn , ^{218}Po , ..., ^{210}Po). Using an ODE solver (in Python), a program was written that solves this system of differential equations for a time-dependent radon concentration (*i.e.*, $N_0 = f(t)$, where t is time). In the case that N_0 is time-independent, solving the radioactive-decay equations yields the Bateman equation (Eq. 10.3). Figure 10.12 (top) shows the estimated amount of each radon daughter (in atoms) using a reasonable guess for the radon concentration during the first exposure (a stepped exponential, where a step occurs each time the hand siphon is used) and the RAD7 measurement during the second exposure.

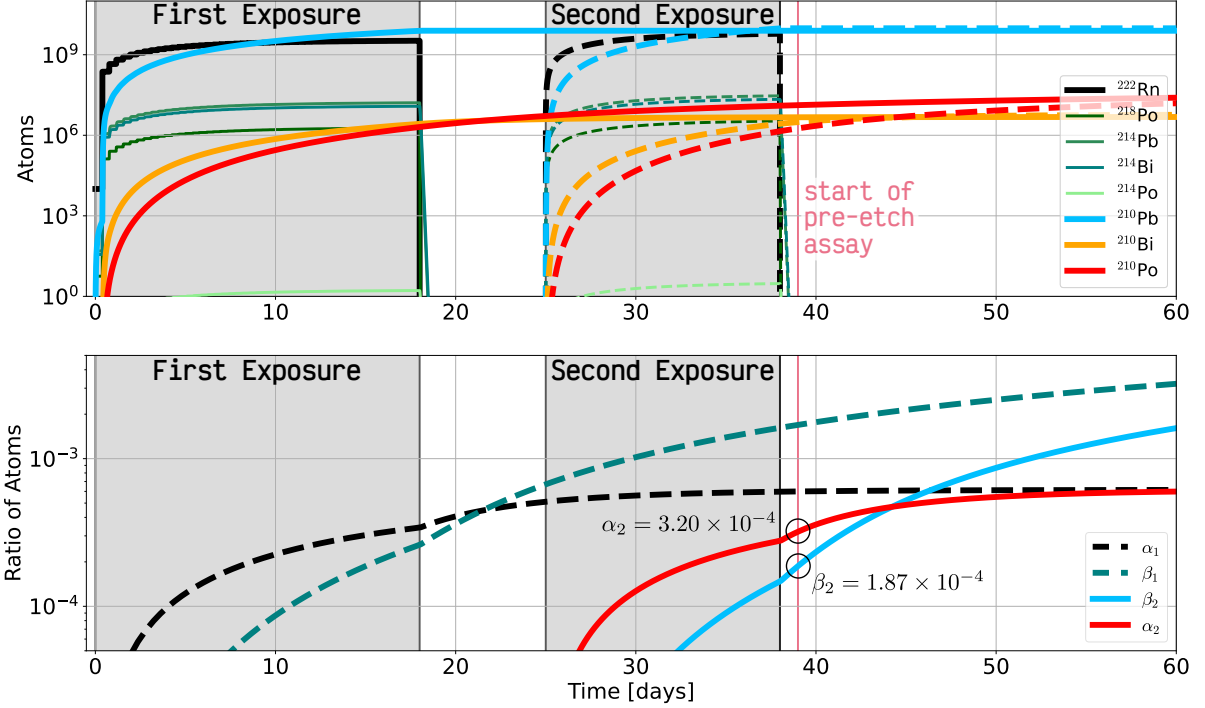


Figure 10.12: **Top:** The number of atoms of each radon daughter is calculated using a presumed step-exponential radon concentration during the first exposure (solid curves). Similarly, the number of atoms of each daughter is calculated from the measured radon concentration during the second exposure (dashed curves). The ^{210}Po rate from these two exposures is expected to be proportional the sum of the solid and dashed red curves. **Bottom:** Dividing ^{210}Bi and ^{210}Po curves by that of ^{210}Pb produced by the first exposure yields α_1 and β_1 respectively. The relative abundance factors α_2 and β_2 are calculated similarly for the second exposure, with their values at the start of the pre-etch assay (black circles) determined as $\alpha_2 = 3.20 \times 10^{-4}$ and $\beta_2 = 1.87 \times 10^{-4}$.

The relative abundances of ^{210}Bi and ^{210}Po compared with ^{210}Pb at the end of the second exposure are defined by the proportionality constants

$$\alpha_2 \equiv N_{\text{Bi}}^{(2)} / N_{\text{Pb}}^{(2)} \quad \text{and} \quad \beta_2 \equiv N_{\text{Po}}^{(2)} / N_{\text{Pb}}^{(2)}, \quad (10.7)$$

respectively. Similarly, the relative abundances of ^{210}Bi and ^{210}Po at the end of the first exposure are defined by the constants

$$\alpha_1 \equiv N_{\text{Bi}}^{(1)} / N_{\text{Pb}}^{(1)} \quad \text{and} \quad \beta_1 \equiv N_{\text{Po}}^{(1)} / N_{\text{Pb}}^{(1)}, \quad (10.8)$$

though these *cannot* be determined accurately by solving the decay equations (as the pre-exposure amounts of ^{210}Bi and ^{210}Po are not known and neither is the time dependence of the radon concentration during the first exposure). Figure 10.12 (bottom) shows the

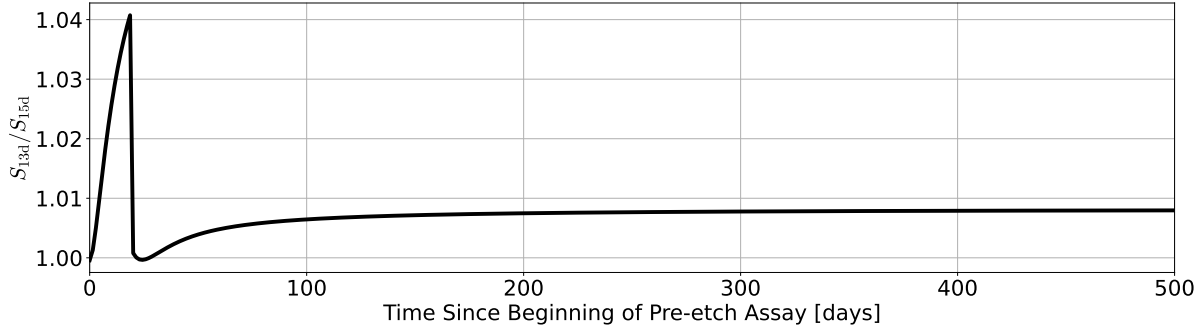


Figure 10.13: Equation 10.4 is fit to the pre-etch zero-degree data using the 13-day values of α_2 and β_2 , denoted as S_{13d} . Similarly, S_{15d} represents the best-fit using the 15-day values of α_2 and β_2 . The ratio of these fits S_{13d}/S_{15d} shows that at late time (~ 400 days) the fractional difference between the best fits is $< 1\%$. Because $S_{13d} > S_{15d}$ at late time, using S_{15d} provides a more-conservative limit on the removal of radon daughters by etching.

calculated abundances as a function of time. At the end of the second exposure (denoted by black circles),

$$\alpha_2 = 3.20 \times 10^{-4} \text{ and } \beta_2 = 1.87 \times 10^{-4}, \quad (10.9)$$

There is a small caveat here: the RAD7 data for the second exposure and all intermediate calculations and plots indicate the second exposure lasted 13 days. The relative abundance factors used, however, are for a 15-day exposure. The difference is essentially negligible (making the reported reduction after etching *more* conservative by a less than a percent), as may be seen by Fig. 10.13. Noting this discrepancy here, I will continue to use the 15-day exposure value for α_2 and β_2 , as it doesn't significantly change other reported values—and may well be correct based on details of the exposure and assay timeline that have not been identified during this rewriting (3 years later). The “correct” abundances for a 15-day exposure are

$$\alpha_2^{15d} = 3.45 \times 10^{-4} \text{ and } \beta_2^{15d} = 2.35 \times 10^{-4}. \quad (10.10)$$

with fractional changes of $\alpha_2/\alpha_2^{15d} \approx 0.93$ and $\beta_2/\beta_2^{15d} \approx 0.80$.

Though the goal is to calculate the relative abundance of ^{210}Bi and ^{210}Po during the second exposure, this simple model produces a very good representation of the measured pre-etch ^{210}Po rate, as shown by Fig. 10.14. This plot also provides an overview of both

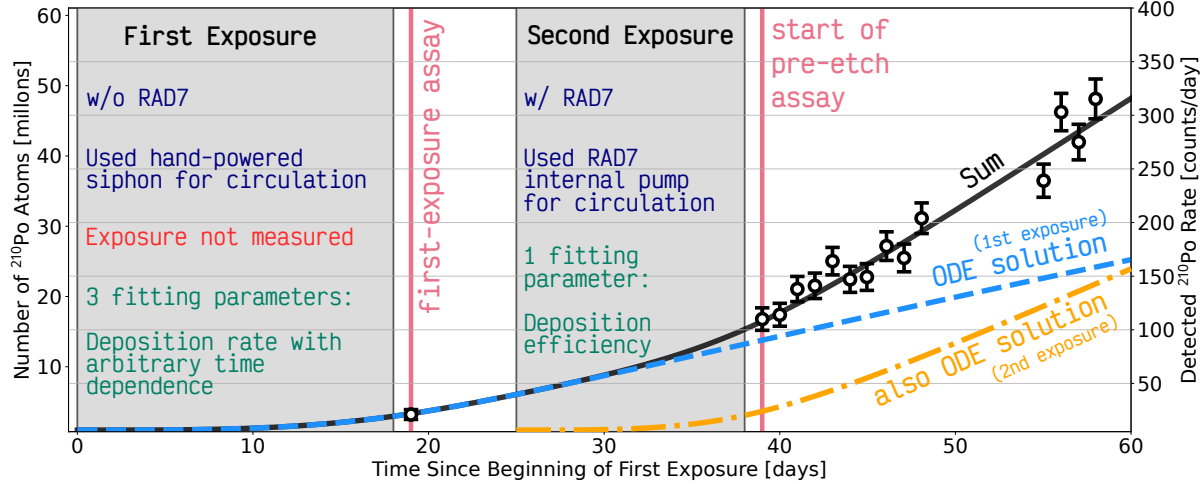


Figure 10.14: The first (18 day) and second (13 day) high-radon exposures are primarily different in how gas was circulated within the closed system, where a hand siphon was employed for the fist exposure while a RAD7 was employed for the second. The radioactive-decay equations were solved to predict the ^{210}Po rate from each exposure (denoted as *ODE solution*), with their sum showing good agreement with the measured pre-etch data. During the first exposure, the arbitrary time dependence on the radon concentration means that we can't predict the relative abundance of ^{210}Bi and ^{210}Po and must fit each, along with the amount of ^{210}Pb that was deposited, independently. By knowing the time dependence of the radon concentration during the second exposure, we *can* predict relative abundances and only need to fit a single parameter representing the deposition efficiency for the second exposure.

high-radon exposures, their main differences, and the ^{210}Po rate estimated from solving the radioactive-decay equations for each exposure (dashed and dot-dashed curves). The ^{210}Po rate predicted from each exposure is added together to produce a good model for the expected ^{210}Po (solid curve).

10.4.2 Toy Monte Carlo Simulation of the Time-dependent ^{210}Po Rate

Uncertainties on the best-fit numbers of ^{210}Pb , ^{210}Bi , and ^{210}Po atoms at the beginning of the pre-etch assay were estimated by toy Monte Carlo simulation using Eq. 10.4. Ten million unique combinations of $N_{\text{Pb}}^{(1)}$ (*i.e.*, the number of ^{210}Pb atoms from the first exposure), $N_{\text{Bi}}^{(1)}$, $N_{\text{Po}}^{(1)}$, and $N_{\text{Pb}}^{(2)}$ (*i.e.*, the number of ^{210}Pb atoms from the second exposure) were drawn from uniform distributions and used to produce curves built by the signal equation (see Eq. 10.4). Each curve was compared to the measured ^{210}Po rate, and those passing a 1σ cut on the resulting χ^2 produced a 1σ band. That is, passing the

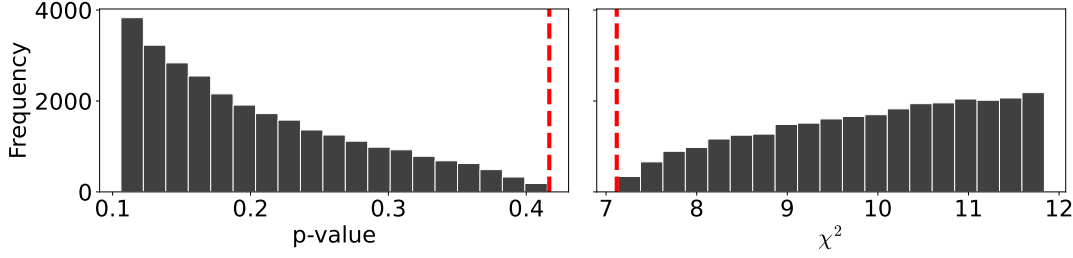


Figure 10.15: The p-values (left plot) and χ^2 values (right plot) are shown for the generated curves built on Eq. 10.4 that have passed the 1σ cut. The p-value and χ^2 of the best-fit curve is shown by the red dashed lines.

parameter	domain	best-fit value	min 1σ	max 1σ
$N_{\text{Pb}}^{(1)}$	$[0, 2 \times 10^7]$	1.2×10^7	5.2×10^6	1.8×10^7
$N_{\text{Bi}}^{(1)}$	$[0, 2 \times 10^4]$	4.2×10^3	8.3×10^3	1.3×10^4
$N_{\text{Po}}^{(1)}$	$[0, 2 \times 10^4]$	4.2×10^3	1.7×10^4	2.5×10^4
$N_{\text{Pb}}^{(2)}$	$[0, 2 \times 10^8]$	1.4×10^7	8.8×10^3	3.1×10^7

Table 10.2: Domains and best-fit value for each thrown parameter in units of number of atoms. The best-fit values were found by simultaneous χ^2 minimization (compare with Fig. 10.16).

condition

$$\Delta\chi_{\nu}^2 = \Delta\chi_4^2 = \chi^2 - \chi_{\min}^2 \leq 4.72, \quad (10.11)$$

where χ_{\min}^2 is from the best fit of the signal equation to data and 4.72 is the value of $\Delta\chi^2$ at 1σ and $\nu = 4$ free parameters. With $\chi_{\min}^2 = 7.1$, the condition becomes $\chi^2 \leq 4.72 + 7.1 = 11.82$. Figure 10.15 shows the p-values and χ^2 for the passed curves, with the best-fit values illustrated by the red dashed lines.

The domain of each thrown parameter and the best-fit value is shown in Table 10.2. Of the 10^7 parameter combinations thrown, 21,108 passed the 1σ cut. Figure 10.16 shows that passed parameter combinations were drawn from a sufficiently large sample of random combinations.

Because the relative abundances of ^{210}Bi and ^{210}Po are calculated for the second exposure, where the time dependence of the radon concentration is better known, histograms of $N_{\text{Bi}}^{(2)}$ and $N_{\text{Po}}^{(2)}$ are proportional to $N_{\text{Pb}}^{(2)}$, as the only free parameter representing the

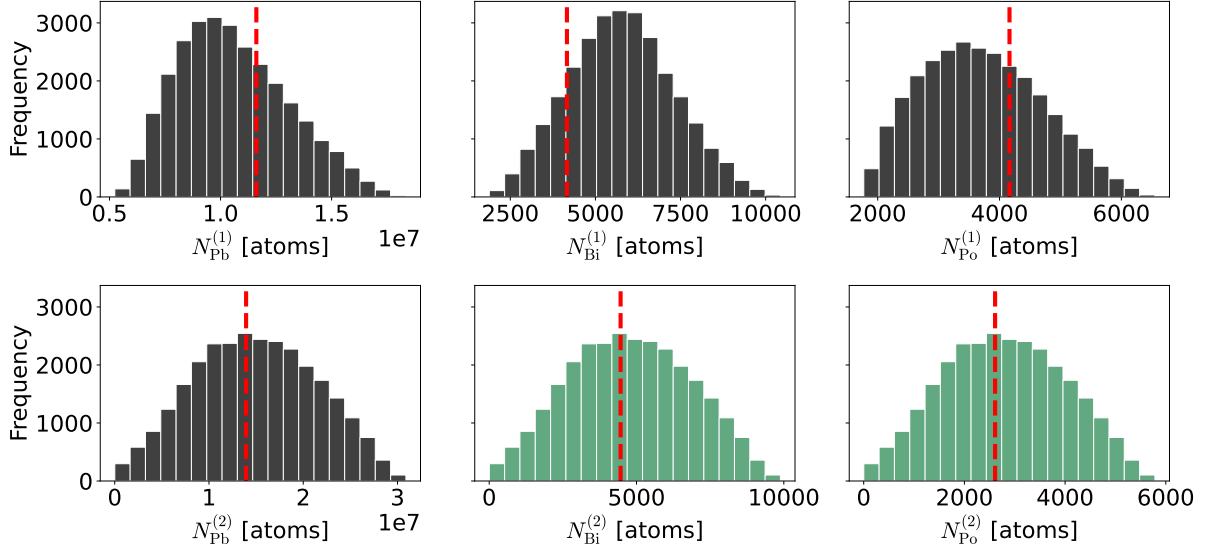


Figure 10.16: After placing a 1σ cut on the χ^2 for curves (built from Eq. 10.4), the histograms of the passed parameter combinations (of $N_{\text{Pb}}^{(1)}$, $N_{\text{Bi}}^{(1)}$, $N_{\text{Po}}^{(1)}$, and $N_{\text{Pb}}^{(2)}$) are distributed around the best-fit values (red dashed lines). The histograms of $N_{\text{Bi}}^{(2)}$ and $N_{\text{Po}}^{(2)}$ are proportional to $N_{\text{Pb}}^{(2)}$, with proportionality factors α_2 and β_2 (Eq. 10.9) determined by solving the radon-decay equations, along with the known radon concentration during the second exposure.

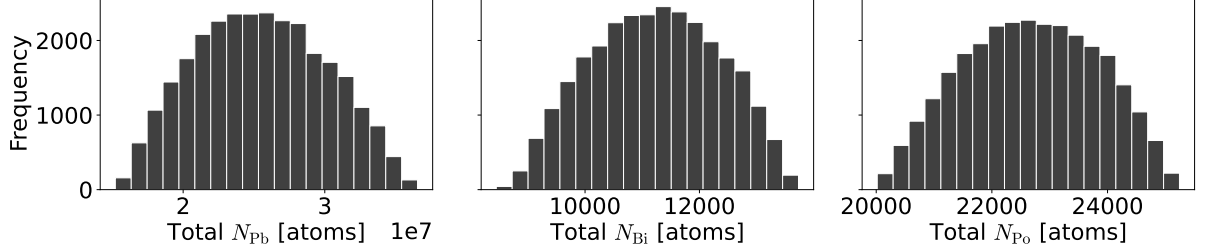


Figure 10.17: Distributions of total inferred N_{Pb} , N_{Bi} , and N_{Po} at the start of the pre-etch assay for 1σ solutions. The minimum and maximum of each distribution provide upper and lower uncertainties for the surface contaminations quoted by Eq. 10.5.

second exposure is $N_{\text{Pb}}^{(2)}$. The proportionality factors α_1 and β_1 are determined by the best-fit values of $N_{\text{Pb}}^{(1)}$, $N_{\text{Bi}}^{(1)}$, and $N_{\text{Po}}^{(1)}$ and are therefore not known a priori.

Figure 10.17 shows histograms for the total inferred N_{Pb} , N_{Bi} , and N_{Po} at the start of the pre-etch assay (as a result of both high-radon exposures) for curves passing the 1σ cut. The minimum and maximum of each distribution, once converted to Bq/m^2 , provide the estimated 1σ uncertainties presented by Eq. 10.5. The total number of

^{210}Pb atoms N_{Pb} is calculated as

$$N_{\text{Pb}} = N_{\text{Pb}}^{(1)} \times \exp\left(-\frac{t_{\text{between}}}{\tau_{\text{Pb}}}\right) + N_{\text{Pb}}^{(2)}, \quad (10.12)$$

where the time between the start of the first-exposure and pre-etch assays $t_{\text{between}} = 20$ days and the mean lifetime of ^{210}Pb $\tau_{\text{Pb}} = 11,743$ days.

While the inferred contamination used for setting the limit on the reduction of implanted daughters after etching presumes that the second exposure lasted 15 days, the 13-day exposure values have been included below.

$$\Sigma_{\text{Pb}} = 138^{+59}_{-56} \text{Bq/m}^2, \quad \Sigma_{\text{Bi}} = 99^{+25}_{-22} \text{Bq/m}^2, \quad \text{and} \quad \Sigma_{\text{Po}} = 7^{+1}_{-1} \text{Bq/m}^2, \quad (10.13)$$

Compared these values with those presented by Eq. 10.5, one may confirm that the difference between the two presumptions is negligible.

Figure 10.18 shows the correlation between thrown parameters $N_{\text{Pb}}^{(1)}$, α_1 , β_1 , and $N_{\text{Pb}}^{(2)}$, where the relative abundance factors have been adopted to emphasize the amount of ^{210}Bi and ^{210}Po that has grown in from the deposited ^{210}Pb atoms during the first exposure. Because the ^{210}Po rate depends on the amount of ^{210}Pb deposited during either of the two high-radon exposures, $N_{\text{Pb}}^{(1)}$ and $N_{\text{Pb}}^{(2)}$ are inversely correlated, and is seen by the lower-left scatter plot. Similarly, when $N_{\text{Pb}}^{(1)}$ is smaller, the grow-in fraction α_1 is made larger, as seen by the top-left scatter plot, such that the ^{210}Po rate remains constant.

10.5 Etching Technique

This section is quoted verbatim from the published paper.

After high-radon exposure, the Si core received a heavy etch treatment with a mixture of 80% nitric acid, 16% hydrofluoric acid, and 4% acetic acid within a large Nalgene tub. The substrate diameter was measured to be 25.446 ± 0.001 mm prior to etching. The substrate was then placed into a PTFE basket and dunked into the acid solution for 30 seconds. Following the acid dunk, the substrate was dunked and rinsed with DI water. The substrate diameter was again measured and found to be 25.430 ± 0.001 mm,

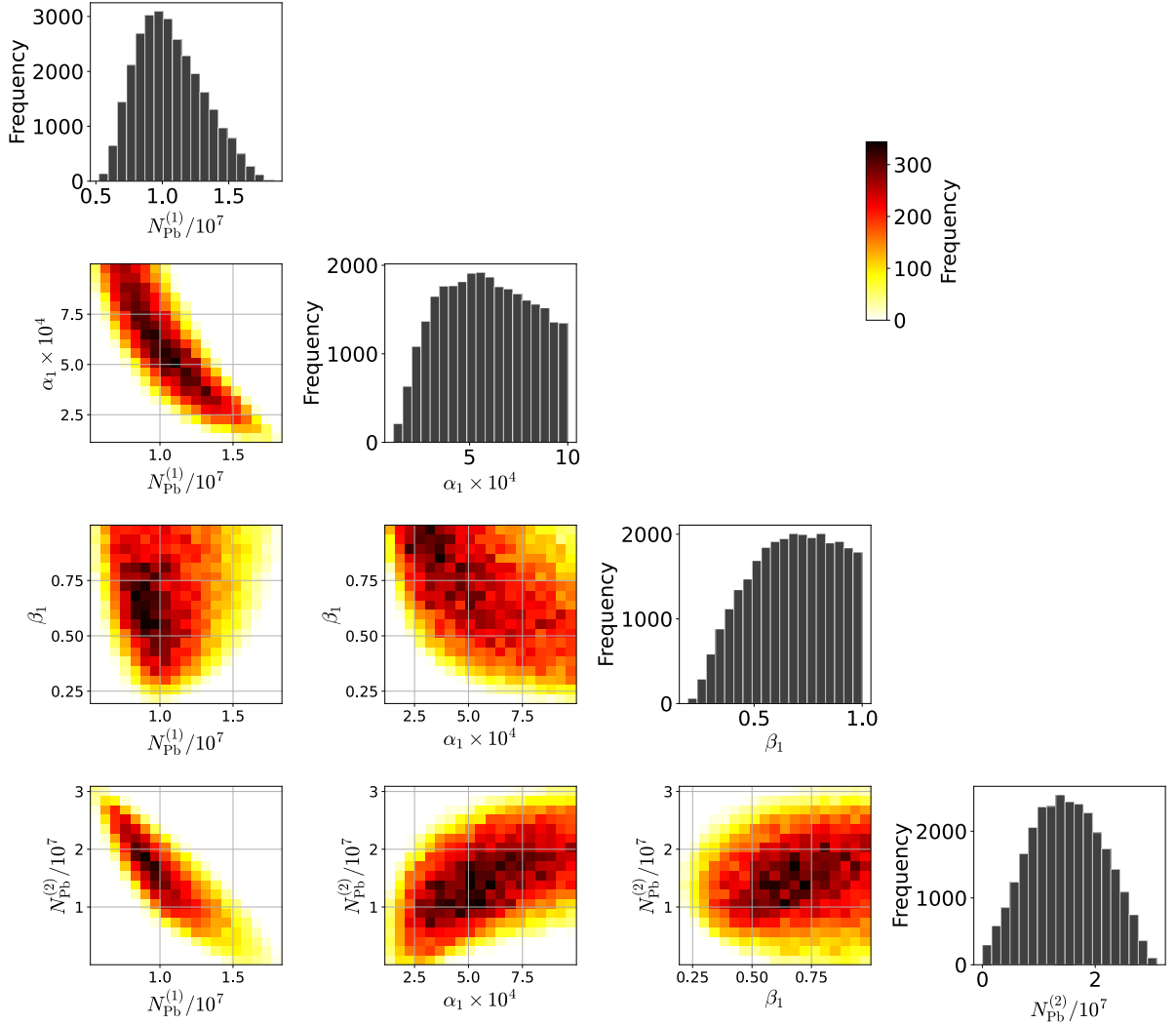


Figure 10.18: The correlation between the free parameters of the toy MC used to obtain contamination uncertainties shows expected trends. The number of ^{210}Pb atoms $N_{\text{Pb}}^{(1)}$ and $N_{\text{Pb}}^{(2)}$ deposited during the first and second exposure respectively are inversely correlated (lower-left scatter plot). For larger values of $N_{\text{Pb}}^{(1)}$ (and therefore lower values of $N_{\text{Pb}}^{(2)}$), α_1 is selected to be smaller, favoring less ^{210}Bi already present on the surface (top-left scatter plot); similar reasoning applies to the bottom-center scatter plot of $N_{\text{Pb}}^{(2)}$ and α_1 . The histograms along the diagonal are similar to those of Fig. 10.16, but in terms of α_1 and β_1 (and excluding the degenerate $N_{\text{Bi}}^{(2)}$ and $N_{\text{Po}}^{(2)}$ parameters).

indicating that $16 \pm 1 \mu\text{m}$ was removed—much more than the $\sim 0.1 \mu\text{m}$ implantation depth of radon daughters.

The glass was removed from both sides of the Si core by heating it to 100°C and sliding the glass away. Placing the Si core in a beaker with high-purity trichloroethylene

removed the remaining wax. The Si core was then rinsed with DI water and cleaned using isopropanol, acetone, methanol, and then blown dry with nitrogen.

10.6 Post-etch Assay and Observed ^{210}Pb Reduction

This section is quoted verbatim from the published paper, but with a figure showing the energy spectrum for the post-etch assay added, along with a couple words making reference to it.

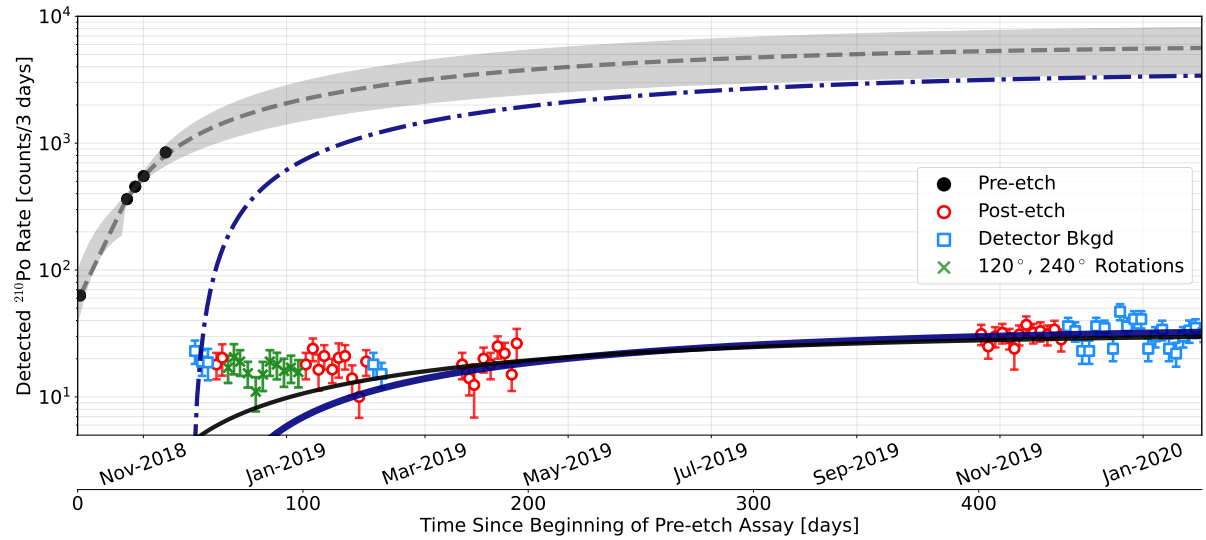


Figure 10.19: The signal function (Eq. 10.4) is fit (dashed line) to the pre-etch ^{210}Po rate (solid black circles). Its projection shows the expected grow-in from implanted ^{210}Pb with its 1σ band shown in light gray around it. Applying the Optimum Interval method [176, 177] to the post-etch ^{210}Po rate (red circles) using the 1σ lower limit of the signal function projection results in a scaled function at 90% confidence level upper limit (solid black curve) that corresponds to a reduction of (at least) $110\times$. In the case that the etch removes all ^{210}Bi and ^{210}Po , the 1σ lower limit on the signal after etch changes (navy dot-dashed curve) and produces a 90% upper limit (thick navy curve) corresponding to a reduction of (at least) $99\times$. The post-etch assay agrees with background measurements (blue squares) taken early and late in the post-etch assay (indicating an increase in the detector background with time). Though not used for this reduction measurement, $\theta = 120^\circ$ and $\theta = 240^\circ$ runs are also shown (green \times 's).

While the Si core sidewall was being etched, a background measurement was made with the detector unchanged except that the core was not present. After the etch was finished, the core sidewalls were again counted. Figure 10.19 shows the pre- and post-etch assays. Again, between post-etch runs, a background measurement was made and showed that the post-etch rate was consistent with the background rate (see Fig. 10.20).

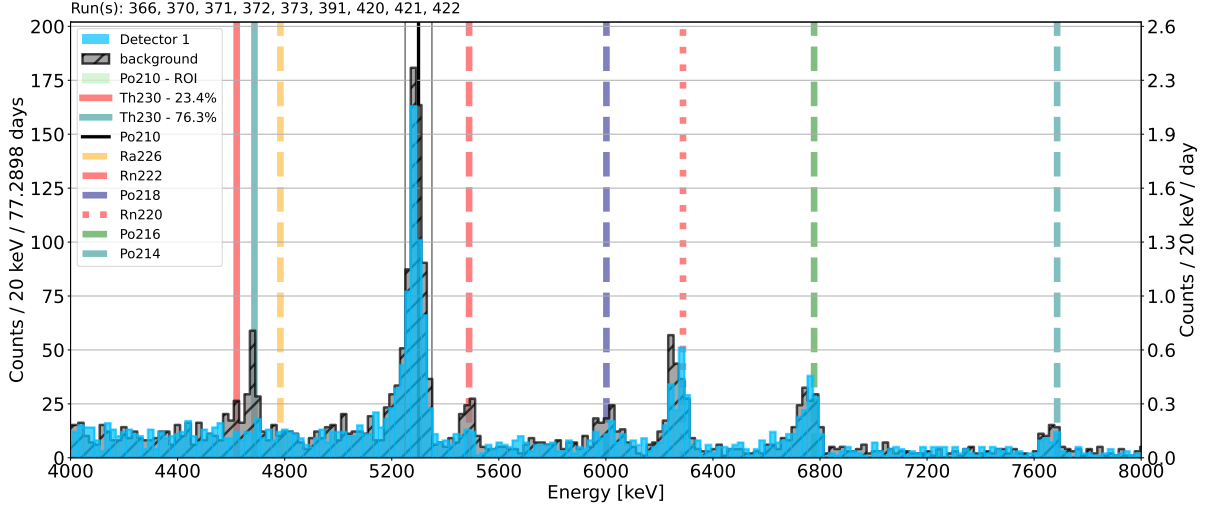


Figure 10.20: After etching the Si core sidewall, the measured ^{210}Po rate at the rotation of zero degrees (blue curve) is consistent with the background rate (hatched curve). The ^{230}Th peaks are only seen in the background spectrum because the Si core blocks the ^{230}Th contamination that was on shelf surface (and was successfully cleaned off after this study concluded using the cleaning procedure described in the ORTEC Alpha Duo user manual).

Though the $\theta = 0^\circ$ angle was the primary focus, $\theta = 120^\circ$ and $\theta = 240^\circ$ rates were also measured and were also consistent with the background rate.

The Optimum Interval (OI) method allows a limit to be set, with or without knowledge of the background, providing the expected signal is understood [176, 177]. After etching, the expected signal is still $S(t)$, but scaled by a reduction factor that represents the effect of the sidewall etch. The OI method returns the reduction factor $R \equiv 1/A$, as defined by Eq. 10.6, that can be stated at 90% confidence limit (C.L.). By this method, a reduction of $R > 110$ at 90% C.L. on the 1σ -lower-limit ^{210}Po rate was found, if all isotopes are removed equally.

The removal of ^{210}Pb , ^{210}Bi , and ^{210}Po from the surface of Ge was similarly studied by M. Wójcik and G. Zuzel [178]. They found that ^{210}Po (^{210}Pb) was removed more efficiently from rougher (smoother) surfaces, by almost a factor of 10. Because the Si core sidewall assayed in this study would be considered a rough surface, ^{210}Po was likely preferentially removed.

If ^{210}Po was indeed preferentially removed by this etch, the expected signal would then represent ^{210}Po growing in from the ^{210}Pb not removed by the etch. By assuming all ^{210}Bi and ^{210}Po are removed, this analysis indicates, rather conservatively, a ^{210}Pb reduction of $R > 99$ at 90% C.L.

Though the OI method can account for knowledge of the background and would likely provide a stronger limit on reduction, the background rate has not been used. This is because it is not yet known how the background rate changes with the Si core inside the Alpha Duo detector bay. Some line-of-sight backgrounds are blocked and this would need to be better understood. In addition, the observed reduction is already sufficiently large that, for this study, additional work is unwarranted.

10.7 Conclusions

This section is quoted verbatim from the published paper.

By comparing the ^{210}Po rates before and after the sidewall-etching technique was performed, a reduction of $R > 99$ at 90% C.L. was found for ^{210}Pb . This limit assumes all ^{210}Bi and ^{210}Po were removed by the etch thus making the statement of ^{210}Pb reduction conservative.

The application of this sidewall-etching technique applied to SuperCDMS SNOLAB, for example, would reduce the detector sidewall surface contamination, directly improving the experiment's sensitivity. The technique also provides a method to salvage a detector unintentionally subjected to high rates of radon-daughter deposition.

Bibliography

- [1] Planck Collaboration *et al.*, “Planck 2015 results. XIII. Cosmological parameters,” *A&A*, vol. 594, Sept. 2016.
- [2] J. D. Simon and M. Geha, “The Kinematics of the Ultra-faint Milky Way Satellites: Solving the Missing Satellite Problem,” *ApJ*, vol. 670, pp. 313–331, Nov. 2007.
- [3] SDSS Collaboration *et al.*, “The Sloan Digital Sky Survey: Technical Summary,” *AJ*, vol. 120, pp. 1579–1587, Sept. 2000.
- [4] Y. Sofue and V. Rubin, “Rotation Curves of Spiral Galaxies,” *ARA&A*, vol. 39, pp. 137–174, Jan. 2001.
- [5] J. F. Navarro, “The Structure of CDM Halos,” *arXiv e-prints*, Nov. 1995.
- [6] T. Hamblye, “On the stability of particle dark matter,” p. 98, Jan. 2010.
- [7] D. Clowe, M. Bradač, A. H. Gonzalez, M. Markevitch, S. W. Randall, C. Jones, and D. Zaritsky, “A Direct Empirical Proof of the Existence of Dark Matter,” *ApJ*, vol. 648, pp. L109–L113, Sept. 2006.
- [8] B. Fields and S. Sarkar, “Big-Bang nucleosynthesis (Particle Data Group mini-review),” *arXiv e-prints*, Jan. 2006.
- [9] R. J. Cooke, M. Pettini, R. A. Jorgenson, M. T. Murphy, and C. C. Steidel, “Precision Measures of the Primordial Abundance of Deuterium,” *ApJ*, vol. 781, Jan. 2014.
- [10] R. J. Cooke, M. Pettini, K. M. Nollett, and R. Jorgenson, “The Primordial Deuterium Abundance of the Most Metal-poor Damped Lyman- α System,” *ApJ*, vol. 830, Oct. 2016.
- [11] A. Coc and E. Vangioni, “Primordial nucleosynthesis,” *International Journal of Modern Physics E*, vol. 26, Jan. 2017.
- [12] Y. Ali-Haïmoud, C. M. Hirata, and M. Kamionkowski, “Metals at the surface of last scatter,” *Phys. Rev. D*, vol. 83, Apr. 2011.
- [13] M. Pospelov and J. Pradler, “Big Bang Nucleosynthesis as a Probe of New Physics,” *Annual Review of Nuclear and Particle Science*, vol. 60, pp. 539–568, Nov. 2010.
- [14] J. Baur, N. Palanque-Delabrouille, C. Yèche, C. Magneville, and M. Viel, “Lyman-alpha forests cool warm dark matter,” *J. Cosmology Astropart. Phys.*, vol. 2016, Aug. 2016.
- [15] M. Viel, J. Weller, and M. G. Haehnelt, “Constraints on the primordial power spectrum from high-resolution Lyman α forest spectra and WMAP,” *MNRAS*, vol. 355, pp. L23–L28, Dec. 2004.

- [16] P. Gondolo, “Introduction to Non-Baryonic Dark Matter,” *arXiv e-prints*, Mar. 2004.
- [17] D. Wands, O. F. Piattella, and L. Casarini, “Physics of the cosmic microwave background radiation,” Apr. 2015.
- [18] C. L. Bennett, D. Larson, J. L. Weiland, N. Jarosik, G. Hinshaw, N. Odegard, K. M. Smith, R. S. Hill, B. Gold, M. Halpern, E. Komatsu, M. R. Nolta, L. Page, D. N. Spergel, E. Wollack, J. Dunkley, A. Kogut, M. Limon, S. S. Meyer, G. S. Tucker, and E. L. Wright, “Nine-year wilkinson microwave anisotropy probe (wmap) observations: Final maps and results,” Dec. 2012.
- [19] W. Hu and S. Dodelson, “Cosmic microwave background anisotropies,”
- [20] D. Scott and G. F. Smoot, “Cosmic Microwave Background Mini-review,” *arXiv e-prints*, May 2010.
- [21] M. Fukugita, C. J. Hogan, and P. J. E. Peebles, “The Cosmic Baryon Budget,” *ApJ*, vol. 503, pp. 518–530, Aug. 1998.
- [22] R. Gavazzi, T. Treu, J. D. Rhodes, L. V. E. Koopmans, A. S. Bolton, S. Burles, R. J. Massey, and L. A. Moustakas, “The Sloan Lens ACS Survey. IV. The Mass Density Profile of Early-Type Galaxies out to 100 Effective Radii,” *ApJ*, vol. 667, pp. 176–190, Sept. 2007.
- [23] G. Bertone, D. Hooper, and J. Silk, “Particle dark matter: evidence, candidates and constraints.,” *Phys. Rep.*, vol. 405, pp. 279–390, Jan. 2004.
- [24] R. Durrer, “The cosmic microwave background: The history of its experimental investigation and its significance for cosmology,” June 2015.
- [25] M. Lisanti, “Lectures on Dark Matter Physics,” pp. 399–446, Jan. 2017.
- [26] J. Buch, J. S. C. Leung, and J. Fan, “Using Gaia DR2 to constrain local dark matter density and thin dark disk,” *J. Cosmology Astropart. Phys.*, vol. 2019, Apr. 2019.
- [27] R. Massey, T. Kitching, and J. Richard, “The dark matter of gravitational lensing,” *Reports on Progress in Physics*, vol. 73, Aug. 2010.
- [28] B. W. Lee and S. Weinberg, “Cosmological Lower Bound on Heavy Neutrino Masses,” *Phys. Rev. Lett.*, vol. 39, pp. 165–168, 1977.
- [29] J. L. Feng, “Dark Matter Candidates from Particle Physics and Methods of Detection,” *ARA&A*, vol. 48, pp. 495–545, Sept. 2010.
- [30] G. Jungman, M. Kamionkowski, and K. Griest, “Supersymmetric dark matter,” *Phys. Rep.*, vol. 267, pp. 195–373, Mar. 1996.
- [31] D. Hooper, “TASI 2008 Lectures on Dark Matter,” *arXiv e-prints*, Jan. 2009.
- [32] R. W. Schnee, “Introduction to Dark Matter Experiments,” pp. 775–829, Mar. 2011.

- [33] B. Sadoulet, T. Shutt, N. Wang, A. Cummings, P. Barnes, J. Beeman, J. Emes, E. E. Haller, A. Lange, and Y. Giraud-Heraud, “Doped semiconductors as thermal and ballistic phonon detectors,” in *Low temperature Detectors for Neutrinos and Dark Matter III*, pp. 227–241, Jan. 1990.
- [34] T. Shutt, N. Wang, A. Cummings, B. Sadoulet, P. Barnes, J. Emes, Y. Giraud-Héraud, A. Lannge, J. Rich, and R. Ross, “Development of a cryogenic dark matter detector.,” *IEEE Transactions on Nuclear Science*, vol. 37, pp. 547–552, Apr. 1990.
- [35] CDMS Collaboration *et al.*, “Exclusion Limits on the WIMP-Nucleon Cross Section from the Cryogenic Dark Matter Search,” *Phys. Rev. Lett.*, vol. 84, pp. 5699–5703, June 2000.
- [36] R. Bernabei, P. Belli, F. Montecchia, W. di Nicolantonio, A. Incicchitti, D. Prosperi, C. Bacci, C. J. Dai, L. K. Ding, H. H. Kuang, and J. M. Ma, “Searching for WIMPs by the annual modulation signature,” *Physics Letters B*, vol. 424, pp. 195–201, Apr. 1998.
- [37] P. Belli, R. Bernabei, A. Bottino, F. Donato, N. Fornengo, D. Prosperi, and S. Scopel, “Extending the DAMA annual-modulation region by inclusion of the uncertainties in astrophysical velocities,” *Phys. Rev. D*, vol. 61, Jan. 2000.
- [38] R. Bernabei, P. Belli, R. Cerulli, F. Montecchia, M. Amato, G. Ignesti, A. Incicchitti, D. Prosperi, C. J. Dai, H. L. He, H. H. Kuang, and J. M. Ma, “On the investigation of possible systematics in WIMP annual modulation search,” *European Physical Journal C*, vol. 18, pp. 283–292, Dec. 2000.
- [39] J. P. Filippini, *A Search for WIMP Dark Matter Using the First Five-Tower Run of the Cryogenic Dark Matter Search*. PhD thesis, UNIVERSITY OF CALIFORNIA, BERKELEY, 2008.
- [40] SuperCDMS Collaboration *et al.*, “Beyond the CDMS-II Dark Matter Search: SuperCDMS,” pp. 801–806, Jan. 2005.
- [41] CDMS Collaboration *et al.*, “Results from the final exposure of the cdms ii experiment,” Dec. 2009.
- [42] J. M. Carmona, S. Cebrián, E. García, I. G. Irastorza, G. Luzón, A. Morales, J. Morales, A. Ortiz de Solórzano, J. Puimedón, M. L. Sarsa, and J. A. Villar, “Neutron background at the Canfranc underground laboratory and its contribution to the IGEX-DM dark matter experiment,” *Astroparticle Physics*, vol. 21, pp. 523–533, Aug. 2004.
- [43] SuperCDMS Collaboration *et al.*, “Results from the super cryogenic dark matter search (supercdms) experiment at soudan,” Aug. 2017.
- [44] SuperCDMS Collaboration *et al.*, “Low-mass dark matter search with CDMSlite,” *Phys. Rev. D*, vol. 97, Jan. 2018.
- [45] SuperCDMS Collaboration *et al.*, “New Results from the Search for Low-Mass Weakly Interacting Massive Particles with the CDMS Low Ionization Threshold Experiment,” *Phys. Rev. Lett.*, vol. 116, Feb. 2016.

- [46] SuperCDMS Collaboration *et al.*, “Search for Low-Mass Weakly Interacting Massive Particles with SuperCDMS,” Phys. Rev. Lett., vol. 112, June 2014.
- [47] R. Calkins and SuperCDMS Collaboration, “The SuperCDMS Soudan high threshold WIMP search and the planned SuperCDMS SNOLAB experiment,” vol. 718, May 2016.
- [48] SuperCDMS Collaboration *et al.*, “Cdmslite: A search for low-mass wimps using voltage-assisted calorimetric ionization detection in the supercdms experiment,” Sept. 2013.
- [49] A. J. Anderson, *A Search for Light Weakly-Interacting Massive Particles with SuperCDMS and Applications to Neutrino Physics*. PhD thesis, Massachusetts Institute of Technology, June 2015.
- [50] R. Agnese, *SIMULATING THE SUPERCDMS DARK MATTER DETECTOR RESPONSE AND READOUT*. PhD thesis, University of Florida, 2017.
- [51] S. Hertel, *Advancing the Search for Dark Matter: from CDMS II to SuperCDMS*. PhD thesis, Massachusetts Institute of Technology, June 2012.
- [52] C. Kittel, *Introduction to Solid State Physics*. John Wiley & Sons, Inc, 8th ed., 2005.
- [53] D. R. Barker, *SuperCDMS Background Models for Low-Mass Dark Matter Searches*. PhD thesis, The University of Minnesota, 2018.
- [54] S. W. Leman, “Invited review article: Physics and monte carlo techniques as relevant to cryogenic, phonon, and ionization readout of cryogenic dark matter search radiation detectors,” *Review of Scientific Instruments*, vol. 83, Sept. 2012.
- [55] B. Cabrera, M. Pyle, R. Moffatt, K. Sundqvist, and B. Sadoulet, “Oblique propagation of electrons in crystals of germanium and silicon at sub-Kelvin temperature in low electric fields,” Apr. 2010.
- [56] J. Lindhard, “On the properties of a gas of charged particles,” *Kgl. Danske Videnskab. Selskab Mat.-fys. Medd.*, vol. Vol: 28, No. 8, Jan. 1954.
- [57] M. Pyle, *Optimizing the Design and Analysis of Cryogenic Semiconductor Dark Matter Detectors for Maximum Sensitivity*. PhD thesis, Stanford University, 2012.
- [58] SuperCDMS Collaboration *et al.*, “Demonstration of surface electron rejection with interleaved germanium detectors for dark matter searches,” May 2013.
- [59] SuperCDMS Collaboration *et al.*, “Projected sensitivity of the SuperCDMS SNOLAB experiment,” Phys. Rev. D, vol. 95, Apr. 2017.
- [60] N. Kurinsky, P. Brink, B. Cabrera, R. Partridge, M. Pyle, and SuperCDMS Collaboration, “SuperCDMS SNOLAB Low-Mass Detectors: Ultra-Sensitive Phonon Calorimeters for a Sub-GeV Dark Matter Search,” Jan. 2016.

- [61] CREST II Collaboration *et al.*, “Results on light dark matter particles with a low-threshold CRESST-II detector,” *European Physical Journal C*, vol. 76, Jan. 2016.
- [62] SuperCDMS Collaboration *et al.*, “New Results from the Search for Low-Mass Weakly Interacting Massive Particles with the CDMS Low Ionization Threshold Experiment,” *Phys. Rev. Lett.*, vol. 116, no. 7, 2016.
- [63] SuperCDMS Collaboration *et al.*, “Search for low-mass wimps with supercdms,” Feb. 2014.
- [64] LUX Collaboration *et al.*, “Improved Limits on Scattering of Weakly Interacting Massive Particles from Reanalysis of 2013 LUX Data,” *Phys. Rev. Lett.*, vol. 116, Apr. 2016.
- [65] SuperCDMS Collaboration, “Supercdms snolab technical design report,” Sept. 2018.
- [66] J. Street, R. Bunker, E. H. Miller, R. W. Schnee, S. Snyder, and J. So, “Radon mitigation for the SuperCDMS SNOLAB dark matter experiment,” vol. 1921, Jan. 2018.
- [67] H. Simgen, “Radon assay and purification techniques,” in *American Institute of Physics Conference Series* (L. Miramonti and L. Pandola, eds.), vol. 1549 of *American Institute of Physics Conference Series*, pp. 102–107, Aug. 2013.
- [68] J. White, R. Schnee, R. Bunker, M. Bowles, P. Cushman, M. Epland, M. Pepin, and V. Guiseppe, “Removal of Long-Lived Radon Daughters by Electropolishing Thin Layers of Stainless Steel,” Oct. 2012.
- [69] SuperCDMS Collaboration, “Supercdms snolab preliminary design report,” May 2017.
- [70] B. D. Cornell, *A Dark Matter Search Using the Final SuperCDMS Soudan Dataset and the Development of a Large-Format, Highly-Multiplexed, Athermal-Phonon-Mediated Particle Detector*. PhD thesis, California Institute of Technology, 2018.
- [71] NuMI Collaboration *et al.*, “The NuMI neutrino beam,” *Nuclear Instruments and Methods in Physics Research A*, vol. 806, pp. 279–306, Jan. 2016.
- [72] S. Liu, *The Limiting Background in a Detector Testing Facility for SuperCDMS at SNOLAB*. PhD thesis, Queen’s University, 2011.
- [73] D. Jardin, *A Likelihood Search for Low-mass Dark Matter via Inelastic Scattering in SuperCDMS*. PhD thesis, Southern Methodist University, 2019.
- [74] J. F. Ziegler, “The stopping and range of ions in matter.”
- [75] G. Perumpilly, V. E. Guiseppe, and N. Snyder, “Modeling surface backgrounds from radon progeny plate-out,” *AIP Conference Proceedings*, vol. 1549, Aug. 2013.

- [76] K. Kobayashi, “Identification of ^{210}Pb and ^{210}Po in the bulk of copper samples with a low-background alpha particle counter,” *AIP Conf. Proc.*, vol. 1921, no. 1, 2018.
- [77] G. F. Knoll, *Radiation Detection and Measurement*. John Wiley and Sons, 4th ed., 2010.
- [78] F. James, *Statistical Methods in Experimental Physics*. World Scientific Publishing Co. Pte. Ltd., 2nd ed., 2006.
- [79] W. T. Doughty, *SuperCDMS Soudan High Threshold WIMP Search*. PhD thesis, University of California, Berkeley, 2006.
- [80] D. Akerib, P. Barnes Jr., P. Brink, B. Cabrera, R. Clarke, R. Gaitskell, S. Golwala, M. Huber, M. Kurylowicz, V. Mandic, J. Martinis, P. Meunier, N. Mirabolfathi, S. Nam, M. Perillo-Isaac, T. Saab, B. Sadoulet, R. Schnee, D. Seitz, T. Shutt, G. Smith, W. Stockwell, K. Sundqvist, and S. White, “Design and performance of a modular low-radioactivity readout system for cryogenic detectors in the cdms experiment,” *Nuclear Instruments and Methods in Physics Research Section A: Accelerators, Spectrometers, Detectors and Associated Equipment*, vol. 591, no. 3, pp. 476–489, 2008.
- [81] H. Bateman, “Solution of a system of differential equations occurring in the theory of radioactive transformations,” *Proc. Cambridge Philos.*, vol. 15, pp. 423–427, 1910.
- [82] V. E. Guiseppe, C. D. Christofferson, K. R. Hair, and F. M. Adams, “A review and outlook for the removal of radon-generated Po-210 surface contamination,” in *Low Radioactivity Techniques 2017 (LRT 2017)*, vol. 1921 of *American Institute of Physics Conference Series*, Jan. 2018.
- [83] J. Reichenbacher, “Radiopurity screening and radiological model for dune,” CoS-SURF, May 2017.
- [84] N. A. of Sciences, *Radon and its Decay Products in Indoor Air*. John Wiley & Sons, 1st ed., 1988.
- [85] N. A. of Sciences, *Health Effects of Exposure to Radon: BEIR VI*. NATIONAL ACADEMY PRESS, 1st ed., 1999.
- [86] C. Garzillo, M. Pugliese, F. Loffredo, and M. Quarto, “Indoor radon exposure and lung cancer risk: a meta-analysis of case-control studies,” *Translational Cancer Research*, vol. 6, no. Suppl 5, 2017.
- [87] A. Zangwill, *Physics at Surfaces*. Cambridge University Press, 1988.
- [88] D. D. Do, *ADSORPTION ANALYSIS: EQUILIBRIA AND KINETICS*. Imperial College Press, 1998.
- [89] A. Groß, *Adsorption on Surfaces*, pp. 101–163. Berlin, Heidelberg: Springer Berlin Heidelberg, 2009.
- [90] E. Zaremba and W. Kohn, “Theory of helium adsorption on simple and noble-metal surfaces,” *Phys. Rev. B*, vol. 15, pp. 1769–1781, Feb. 1977.

- [91] H. Swenson and N. P. Stadie, “Langmuir’s theory of adsorption: A centennial review,” *Langmuir*, vol. 35, no. 16, pp. 5409–5426, 2019. PMID: 30912949.
- [92] F. Reif, *Fundamentals of Statistical and Thermal Physics*. McGraw-Hill, Inc., 1965.
- [93] J. Crank, *The Mathematics of Diffusion*. Oxford Science Publications, 2nd ed., 1992.
- [94] R. L. Grob, *Modern Practice of Gas Chromatography*. John Wiley and Sons, 2nd ed., 1985.
- [95] A. S. Said, *Theory and Mathematics of Gas Chromatography*. Heidelbarg Basel New York, 1st ed., 1981.
- [96] C. Loudon and K. McCulloh, “Application of the Hagen-Poiseuille Equation to Fluid Feeding through Short Tubes,” *Annals of the Entomological Society of America*, vol. 92, pp. 153–158, Jan. 1999.
- [97] C. A. Cramers, J. J. Rijks, and C. Schutjes, “Factors determining flow rate in chromatographic columns,” *Chromatographia*, vol. 14, pp. 439–444, 1981.
- [98] Crane, *Flow of Fluids Through Valves, Fittings and Pipe. Technical Paper No. 410 (TP-410)*. Crane Co., 2010.
- [99] Calgon Carbon, “Calgon Carbon A Kuraray Company.”
- [100] W. L. McCabe, J. C. Smith, and P. Harriot, *Unit Operations of Chemical Engineering* (seventh ed.). McGraw-Hill, 2005.
- [101] A. T. James and A. J. P. Martin, “Gas-liquid partition chromatography: the separation and micro-estimation of volatile fatty acids from formic acid to dodecanoic acid,” *Biochemical Journal*, vol. 50, pp. 679–690, Mar. 1952.
- [102] K. P. Strong and D. M. Levins, “Dynamic adsorption of radon on activated carbon,” tech. rep., United States, 1979.
- [103] LZ Collaboration *et al.*, “LUX-ZEPLIN (LZ) Technical Design Report,” *arXiv e-prints*, Mar. 2017.
- [104] A. Nachab, “Radon reduction and radon monitoring in the NEMO experiment,” *AIP Conf. Proc.*, vol. 897, pp. 35–38, 2007.
- [105] G. Benato, D. Biare, C. Bucci, L. D. Paolo, A. Drobizhev, R. W. Kadel, Y. G. Kolomensky, J. Schreiner, V. Singh, T. Sipla, J. Wallig, and S. Zimmermann, “”Radon mitigation during the installation of the CUORE $0\nu\beta\beta$ decay detector”,” Nov. 2017.
- [106] ATEKO a.s., “Continuous flow radon-mitigation system,” 2018.
- [107] A. Pocar, “Low background techniques for the Borexino nylon vessels,” vol. 785, pp. 153–162, Sept. 2005.
- [108] A. P. Pocar, *Low background techniques and experimental challenges for Borexino and its nylon vessels*. PhD thesis, Princeton University, Jan. 2003.

- [109] J. Street, R. Bunker, C. Dunagan, X. Loose, R. W. Schnee, M. Stark, K. Sundarnath, and D. Tronstad, “Construction and measurements of an improved vacuum-swing-adsorption radon-mitigation system,” vol. 1672, Aug. 2015.
- [110] D. Grant, A. Hallin, S. Hanchurak, C. Krauss, S. Liu, and R. Soluk, “Low Radon Cleanroom at the University of Alberta,” in *American Institute of Physics Conference Series* (R. Ford, ed.), vol. 1338 of *American Institute of Physics Conference Series*, pp. 161–163, Apr. 2011.
- [111] DEAP Collaboration *et al.*, “Search for dark matter with a 231-day exposure of liquid argon using DEAP-3600 at SNOLAB,” *Phys. Rev. D*, vol. 100, July 2019.
- [112] H. Back, A. Alton, F. Calaprice, C. Galbiati, A. Goretti, C. Kendziora, B. Loer, D. Montanari, P. Mosteiro, and S. Pordes, “Depleted argon from underground sources,” *Physics Procedia*, vol. 37, pp. 1105–1112, 2012. Proceedings of the 2nd International Conference on Technology and Instrumentation in Particle Physics (TIPP 2011).
- [113] H. O. Back, F. Calaprice, C. Condon, E. de Haas, R. Ford, C. Galbiati, A. Goretti, T. Hohman, A. Inanni, B. Loer, D. Montanari, A. Nelson, and A. Pocar, “First Large Scale Production of Low Radioactivity Argon From Underground Sources,” *arXiv e-prints*, Apr. 2012.
- [114] G. Heusser, W. Rau, B. Freudiger, M. Laubenstein, M. Balata, and T. Kirsten, “ ^{222}Rn detection at the microBq/m³ range in nitrogen gas and a new Rn purification technique for liquid nitrogen,” *Appl Radiat Isot*, vol. 52, pp. 691–695, Mar 2000.
- [115] X. R. Liu, “Ultra-low level radon assays in gases,” in *Low Radioactivity Techniques 2015 (LRT 2015)*, vol. 1672 of *American Institute of Physics Conference Series*, Aug. 2015.
- [116] K. Hosokawa, A. Murata, Y. Nakano, Y. Onishi, H. Sekiya, Y. Takeuchi, and S. Tasaka, “Development of a high-sensitivity 80 L radon detector for purified gases,” *Progress of Theoretical and Experimental Physics*, vol. 2015, Mar. 2015. 033H01.
- [117] Y. Nakano, H. Sekiya, S. Tasaka, Y. Takeuchi, R. A. Wendell, M. Matsubara, and M. Nakahata, “Measurement of radon concentration in super-Kamiokande’s buffer gas,” *Nuclear Instruments and Methods in Physics Research A*, vol. 867, pp. 108–114, Sept. 2017.
- [118] DURRIDGE Company, Inc., “RAD7 Radon Detector.”
- [119] ATEKO a.s., “ATEKO radon removal systems,” 2020.
- [120] S. Zhang, H. Wang, J. Liu, and C. Bao, “Measuring the specific surface area of monolayer graphene oxide in water,” *Materials Letters*, vol. 261, 2020.
- [121] Shapiro, Ascher, *The Dynamics and Thermodynamics of Compressible Fluid Flow*, vol. 1. Jon Wiley & Sons, Inc., 1st ed., 1953.

- [122] M. J. Moran, H. N. Shapiro, D. D. Boettner, and B. M. B., *Fundamentals of Engineering Thermodynamics*. John Wiley and Sons Inc., New York, NY, 8th ed., 2014.
- [123] M. J. Moran and H. N. Shapiro, *Fundamentals of Engineering Thermodynamics*. John Wiley and Sons Inc., New York, NY, 5th ed., 2006.
- [124] J. Devriendt, *Lecture Notes on Thermodynamics & Statistical Mechanics*. University of Oxford, 1st ed., 2021.
- [125] M. Plischke and B. Bergersen, *Equilibrium Statistical Physics*. World Scientific Publishing Co. Pte. Ltd., 3rd ed., 2006.
- [126] T. R. S. Mohn, *Heat Capacity Measurements of Porous Materials at Cryogenic Temperatures*. PhD thesis, Norwegian University of Science and Technology, June 2012.
- [127] I. Urieli, “Engineering thermodynamics - a graphical approach.”
- [128] The Engineering Toolbox, “Air - density vs. pressure and temperatures.”
- [129] The Engineering Toolbox, “Overall heat transfer coefficients.”
- [130] J. M. Coulson and J. F. Richardson, *Coulson and Richardson’s Chemical Engineering*, vol. 2. Butterworth-Heinemann, 5th ed., 2002.
- [131] The Engineering Toolbox, “Convective heat transfer.”
- [132] The Engineering Toolbox, “Metals, metallic elements and alloys - thermal conductivities.”
- [133] R. Verma, H. Nagendra, S. Kasthuriengan, N. Shivaprakash, and U. Behera, “Thermal conductivity studies on activated carbon based cryopanel,” *IOP Conference Series: Materials Science and Engineering*, vol. 502, Apr. 2019.
- [134] The Engineering Toolbox, “Moist air - water vapor and saturation pressure.”
- [135] C. R. Nave, “Hyperphysics: Saturated vapor pressure, density for water.”
- [136] S. Qi, K. J. Hay, M. J. Rood, and M. P. Cal, “Equilibrium and heat of adsorption for water vapor and activated carbon,” *Journal of Environmental Engineering*, vol. 126, no. 3, pp. 267–271, 2000.
- [137] J. G. Bell, M. J. Benham, and K. M. Thomas, “Adsorption of carbon dioxide, water vapor, nitrogen, and sulfur dioxide on activated carbon for capture from flue gases: Competitive adsorption and selectivity aspects,” *Energy & Fuels*, vol. 35, no. 9, pp. 8102–8116, 2021.
- [138] J. K. Brennan, T. J. Bandosz, K. T. Thomson, and K. E. Gubbins, “Water in porous carbons,” *Colloids and Surfaces A: Physicochemical and Engineering Aspects*, vol. 187-188, pp. 539–568, 2001.
- [139] P. McCord, “Composition of air.”
- [140] E. L. Pace, “Argon Adsorbed on a Graphitic Surface. The Heat of Adsorption from Lattice Liquid Theory,” *The Journal of Chemical Physics*, vol. 27, pp. 1341–1346, Aug. 2004.

- [141] R. Schnee, “The jacobi model for radon daughter plateout.” Internal note for the LZ Dark Matter Search Experiment, jun 2016.
- [142] The Engineering Toolbox, “Dry bulb, wet bulb and dew point temperatures.”
- [143] C. R. Nave, “Hyperphysics.”
- [144] F. Weigel, “Radon,” *Chemiker-Zeitung*, vol. 102(9), pp. 287–99, Nov. 1978.
- [145] DURRIDGE Company, Inc., *RAD AQUA Continuous Radon in Water Accessory for the RAD7 User Manual*. 900 Technology Park Dr, Billerica, MA 01821, 2021.
- [146] R. A. Sloto and L. A. Senior, “Radon in the ground water of chester county, pennsylvania,” Tech. Rep. 120-98, U.S. Geological Survey, Reston, VA, 1998.
- [147] S. Mittal, A. Rani, and R. Mehra, “Estimation of radon concentration in soil and groundwater samples of northern rajasthan, india,” *Journal of Radiation Research and Applied Sciences*, vol. 9, no. 2, pp. 125–130, 2016. Special issue on: “Current Research and Future Trends in Biotechnology for a Healthy and Green Word”.
- [148] R. B. Bird, W. E. Stewart, and E. N. Lightfoot, *Transport Phenomena*. John Wiley & Son, NY, 2nd ed., 2002.
- [149] J. C. Slattery and R. B. Bird, “Calculation of the diffusion coefficient of dilute gases and of the self-diffusion coefficient of dense gases,” *AICHE Journal*, vol. 4, no. 2, pp. 137–142, 1958.
- [150] K. Pushkin *et al.*, “Study of radon reduction in gases for rare event search experiments,” *Nuclear Instruments and Methods in Physics Research A*, vol. 903, pp. 267–276, Sept. 2018.
- [151] P. S. Foundation, “Floating point arithmetic: Issues and limitations.”
- [152] P. R. Bevington and K. D. Robinson, *Data Reduction and Error Analysis for the Physical Sciences*. McGraw Hill, 3rd ed., 2016.
- [153] NIST/SEMATECH, “e-handbook of statistical methods.”
- [154] D. A. McQuarrie, *Mathematical Methods for Scientists and Engineers*. Viva Books Private Limited, 1st indian edition ed., 2009.
- [155] W. H. Press, S. A. Teukolsky, W. T. Vetterling, and B. P. Flannery, *Numerical Recipes The Art of Scientific Computing*. Cambridge, 3rd ed., 2007.
- [156] The SciPy Community, “scipy.optimize.curve_fit.”
- [157] J. J. Moré, “The levenberg-marquardt algorithm: Implementation and theory,” in *Numerical Analysis* (G. A. Watson, ed.), (Berlin, Heidelberg), pp. 105–116, Springer Berlin Heidelberg, 1978.
- [158] M. Mayerhofer, J. Govaerts, N. Parmentier, H. Jeanmart, and L. Helsen, “Experimental investigation of pressure drop in packed beds of irregular shaped wood particles,” *Powder Technology*, vol. 205, no. 1, pp. 30–35, 2011.

- [159] P. M. Pojer, J. R. Peggie, R. S. O'Brien, S. B. Solomon, and N. Keith, "Performance of a diffusion barrier charcoal adsorption 222rn monitor under conditions of varying humidity and temperature," *Health Physics*, vol. 58, no. 1, 1990.
- [160] S. I. Shefsky, D. Rose, and C. G. Parsons, "A study of radon adsorption on activated carbon as a function of temperature," in *Proceedings of the 1993 International Radon Conference*, 1993.
- [161] D. Marx, L. Joss, M. Hefti, R. Pini, and M. Mazzotti, "The role of water in adsorption-based co2 capture systems," *Energy Procedia*, vol. 37, pp. 107–114, 2013. GHGT-11 Proceedings of the 11th International Conference on Greenhouse Gas Control Technologies, 18-22 November 2012, Kyoto, Japan.
- [162] F. Rouquerol, J. Rouquerol, and K. Sing, "Chapter 9 - adsorption by active carbons," in *Adsorption by Powders and Porous Solids* (F. Rouquerol, J. Rouquerol, and K. Sing, eds.), pp. 237–285, London: Academic Press, 1999.
- [163] llvm-admin team, "The llvm compiler infrastructure."
- [164] Anaconda, "Numba: Numba makes python code fast."
- [165] Westlake Pipe & Fittings, "Pressure ratings of thermoplastic fittings."
- [166] Y. Sun and P. Webley, "Preparation of activated carbons with large specific surface areas from biomass corncob and their adsorption equilibrium for methane, carbon dioxide, nitrogen, and hydrogen," *Industrial & Engineering Chemistry Research*, vol. 50, July 2011.
- [167] Sentry Air System Inc, "Activated carbon adsorption index chart."
- [168] Pylon, "Radon source."
- [169] R. A. Koestoter, N. Pancasaputra, I. Roihan, and Harinaldi, "A simple calibration methods of relative humidity sensor dht22 for tropical climates based on arduino data acquisition system," *AIP Conference Proceedings*, vol. 2062, no. 1, 2019.
- [170] Lady Ada, "Dht11, dht22 and am2302 sensors."
- [171] J. Street, R. Mahapatra, E. Morrison, M. Platt, and R. Schnee, "Removal of 210pb by etch of crystalline detector sidewalls," *Nuclear Instruments and Methods in Physics Research Section A: Accelerators, Spectrometers, Detectors and Associated Equipment*, vol. 976, 2020.
- [172] Pylon, "Rn222 source," 2020.
- [173] J. Porstendorfer, "Physical Parameters and Dose Factors of the Radon and Thoron Decay Products," *Radiation Protection Dosimetry*, vol. 94, pp. 365–373, Apr. 2001.
- [174] E. S. Morrison, E. H. Miller, T. Frels, R. W. Schnee, and J. Street, "Radon Daughter Plate-out onto Teflon," in *Topical Workshop on Low Radioactivity Techniques: LRT 2017* (D. L. Leonard, ed.), American Institute of Physics Conference Series, Aug. 2017.
- [175] Ortec, "Alpha duo," 2019.

- [176] S. Yellin, “Finding an upper limit in the presence of an unknown background,” *Phys. Rev. D*, vol. 66, Aug. 2002.
- [177] S. Yellin, “Extending the optimum interval method, ,” Sept. 2007.
- [178] M. Wójcik and G. Zuzel, “²²⁶ra, ²¹⁰pb, ²¹⁰bi and ²¹⁰po deposition and removal from surfaces and liquids,” *Journal of Radioanalytical and Nuclear Chemistry*, vol. 296, pp. 639–645, Sept. 2012.



Figure A.1: CalgonCarbon OVC 4x8 activated carbon shown with one United States quarter for scale.

Appendices

Activated Carbon

The SD Mines Radon-Reduction System uses \sim 200 kg (per column) of CalgonCarbon OVC 4x8 activated carbon (shown in Fig. A.1) as an adsorbent (for radon). Activated carbon is highly porous (see the datasheet that is Fig. A.2) and has a substantial surface area (as indicated by specific-surface-area assays, with summaries shown in Fig. A.3 and Fig. A.4).

OVC 4X8
Safety Data Sheet

Calgon Carbon®

Issued: 04/20/2015
Supersedes: 12/30/2011
Version: 1.0

SECTION 1: Identification of the Substance/Mixture and of the Company/Undertaking

1.1. Product identifier

Product name	: OVC 4X8
Product form	: Substance
CAS No	: 7440-44-0
Product code	: 12359
Synonyms	: Activated Carbon

1.2. Relevant identified uses of the substance or mixture and uses advised against

Use of the substance/mixture	: Adsorbent
------------------------------	-------------

1.3. Details of the supplier of the safety data sheet

Calgon Carbon Corporation
P.O. Box 717
Pittsburgh, PA 15230
412-787-6700

1.4. Emergency telephone number

Emergency number	: CHEMTRAC (24 HRS): 1-800-424-9300
------------------	-------------------------------------

SECTION 9: Physical and Chemical Properties

9.1. Information on basic physical and chemical properties

Physical state	: Solid
Appearance	: Granular, powder, or pelletized substance
Color	: Black
Odor	: Odorless
Odor threshold	: No data available
pH	: No data available
Relative evaporation rate (butylacetate=1)	: Not applicable
Melting point	: Not applicable
Freezing point	: Not applicable
Boiling point	: Not applicable
Flash point	: No data available
Auto-ignition temperature	: > 220 °C
Decomposition temperature	: No data available
Flammability (solid, gas)	: > 220 °C
Vapor pressure	: Not applicable
Relative vapor density at 20 °C	: Not applicable
Apparent density	: 0.4 - 0.7 g/cc
Solubility	: Insoluble.
Log Pow	: Not applicable
Log Kow	: Not applicable
Viscosity, kinematic	: Not applicable
Viscosity, dynamic	: Not applicable
Explosive properties	: No data available
Oxidising properties	: No data available
Explosive limits	: No data available

9.2. Other information

No additional information available

Figure A.2: Selected parts of the CalgonCarbon OVC 4x8 activated carbon datasheet.

StarDriver V2.03	Gemini 2375 V5.01	Serial # 3233	Page 23
<hr/>			
File Name: C:/TA/DATA/BET/JOSEPH~1/ACTCAR~1/ACTCARBA.MGD			
Sample ID: ACT Carbon A			
Setup Group: ACT Carbon A			
Started: 10/4/3818 2:30:54PM	Sat. Pressure: 723.88 mmHg	Meas. Freespace: 1.1364 cm ³	
Completed: 10/4/3818 5:25:32PM	Sample Weight: 0.3835 g	Evac. Time: 6.000000 minutes	
Report Time: 10/4/2018 4:02:09PM	Equil. Interval: 5 secs		
Evac. Rate: 300.0 mmHg/min			
Analysis Mode: Equilibration			
<hr/>			
Summary Report			
Area			
Single Point Surface Area at P/Po 0.24980660 :	958.9867	m ² /g	
BET Surface Area:	945.7408	m ² /g	
Langmuir Surface Area:	1303.9505	m ² /g	
Micropore Area:	795.7770	m ² /g	
External Surface Area:	149.9638	m ² /g	
BJH Adsorption Cumulative Surface Area of pores between 1.700000 and 300.000000 nm Diameter:	128.1804	m ² /g	
BJH Desorption Cumulative Surface Area of pores between 1.700000 and 300.000000 nm Diameter:	127.5839	m ² /g	
Volume			
Single Point Adsorption Total Pore Volume of pores less than 40.0460 nm Diameter at P/Po 0.94952888:	0.474114	cm ³ /g	
Micropore Volume:	0.385035	cm ³ /g	
BJH Adsorption Cumulative Pore Volume of pores between 1.700000 and 300.000000 nm Diameter:	0.081934	cm ³ /g	
BJH Desorption Cumulative Pore Volume of pores between 1.700000 and 300.000000 nm Diameter:	0.081239	cm ³ /g	
Pore Size			
Adsorption Average Pore Diameter (4V/A by BET):	2.0053	nm	
BJH Adsorption Average Pore Diameter (4V/A):	2.5568	nm	
BJH Desorption Average Pore Diameter (4V/A):	2.5470	nm	

Figure A.3: Specific-surface-area assay of the SD Mines RRS activated carbon (sample A).

StarDriver V2.03	Gemini 2375 V5.01	Serial # 3233	Page 23
<hr/>			
File Name: C:/TA/DATA/BET/JOSEPH~1/SAMPLE~1/SAMPLEB.MGD			
Sample ID: Sample B			
Setup Group: Sample B			
Started: 10/8/3818 3:19:20PM	Sat. Pressure: 728.95 mmHg	Meas. Freespace: 1.2084 cm ³	
Completed: 10/8/3818 6:21:39PM	Sample Weight: 0.3420 g	Evac. Time: 6.000000 minutes	
Report Time: 10/8/2018 4:57:59PM	Equil. Interval: 5 secs		
Evac. Rate: 300.0 mmHg/min			
Analysis Mode: Equilibration			
<hr/>			
Summary Report			
Area			
Single Point Surface Area at P/Po 0.24981822 :	1095.1153	m ² /g	
BET Surface Area:	1085.9462	m ² /g	
Langmuir Surface Area:	1502.9800	m ² /g	
Micropore Area:	857.3467	m ² /g	
External Surface Area:	228.5995	m ² /g	
BJH Adsorption Cumulative Surface Area of pores between 1.700000 and 300.000000 nm Diameter:	189.4085	m ² /g	
BJH Desorption Cumulative Surface Area of pores between 1.700000 and 300.000000 nm Diameter:	186.2759	m ² /g	
Volume			
Single Point Adsorption Total Pore Volume of pores less than 40.9608 nm Diameter at P/Po 0.95068934:	0.537554	cm ³ /g	
Micropore Volume:	0.413788	cm ³ /g	
BJH Adsorption Cumulative Pore Volume of pores between 1.700000 and 300.000000 nm Diameter:	0.110420	cm ³ /g	
BJH Desorption Cumulative Pore Volume of pores between 1.700000 and 300.000000 nm Diameter:	0.106764	cm ³ /g	
Pore Size			
Adsorption Average Pore Diameter (4V/A by BET):	1.9800	nm	
BJH Adsorption Average Pore Diameter (4V/A):	2.3319	nm	
BJH Desorption Average Pore Diameter (4V/A):	2.2926	nm	

Figure A.4: Specific-surface-area assay of the SD Mines RRS activated carbon (sample B).

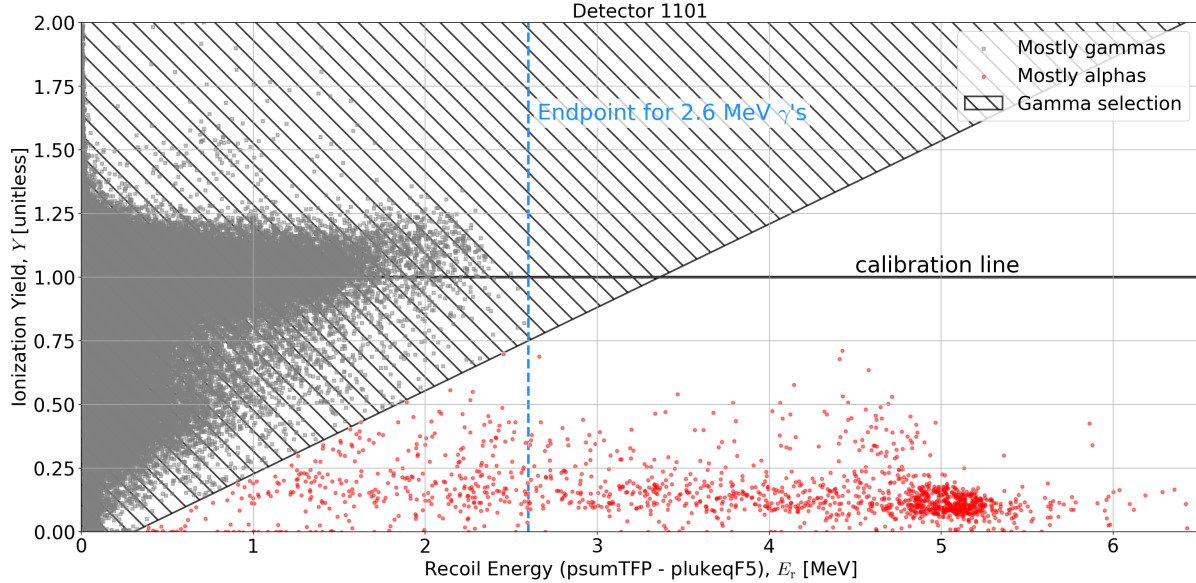


Figure B.1: Ionization yield versus recoil energy for SuperCDMS Soudan detector 1101 showing ^{210}Po alpha selection.

Appendices

Surface Contamination of SuperCDMS Soudan Detectors: Additional Figures

The key plots of the ^{210}Pb and ^{210}Po contamination analysis presented in Chapter 3 are shown for each SuperCDMS Soudan detector analyzed (1101, 1104, 1105, 1106, 1108, 1111, 1112, and 1114).

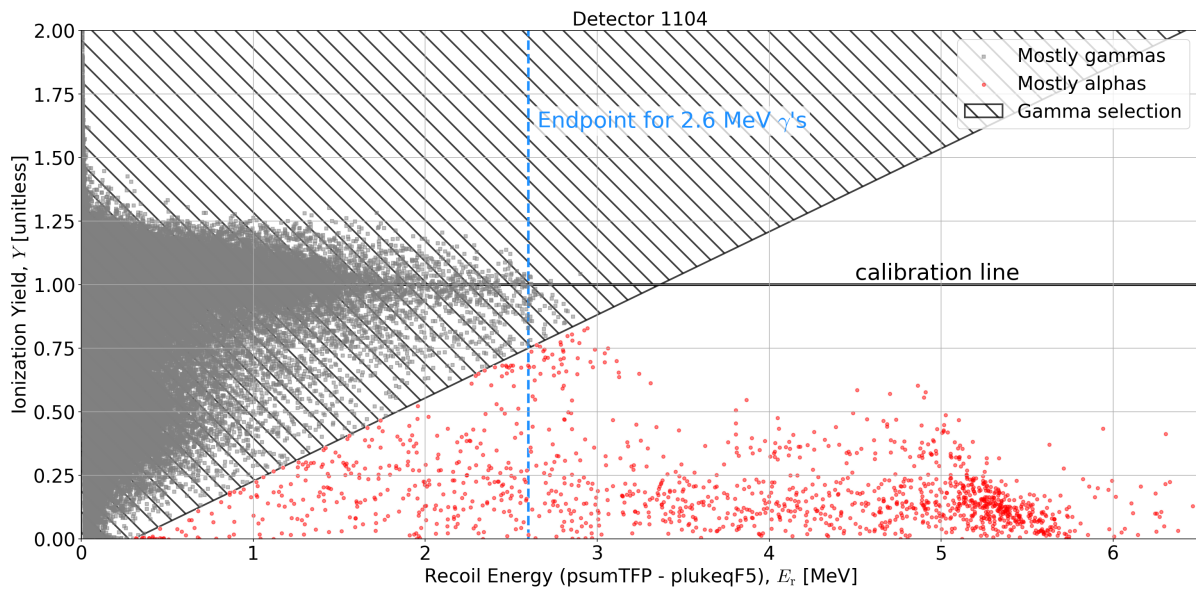


Figure B.2: Ionization yield versus recoil energy for SuperCDMS Soudan detector 1104 showing ^{210}Po alpha selection.

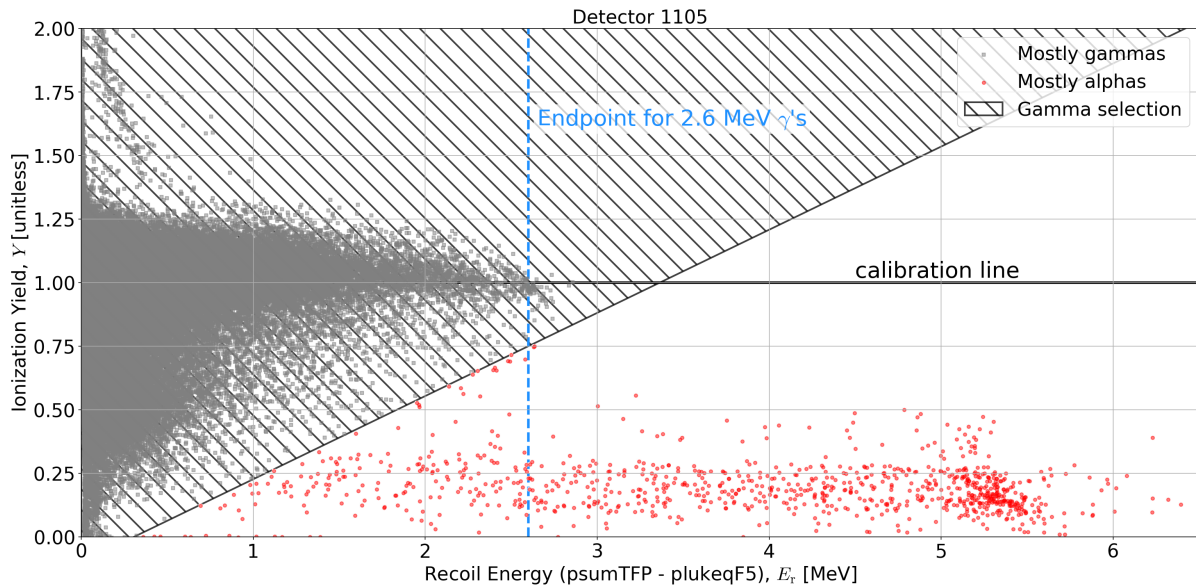


Figure B.3: Ionization yield versus recoil energy for SuperCDMS Soudan detector 1105 showing ^{210}Po alpha selection.

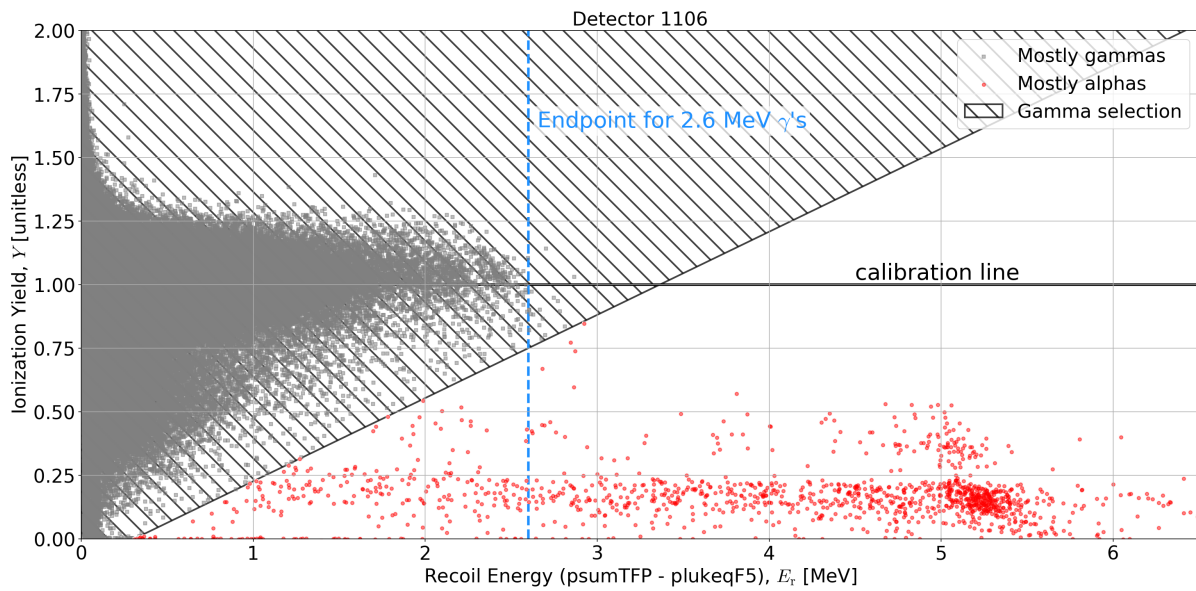


Figure B.4: Ionization yield versus recoil energy for SuperCDMS Soudan detector 1106 showing ^{210}Po alpha selection. Recall that PBS1 and PDS1 were not functional.

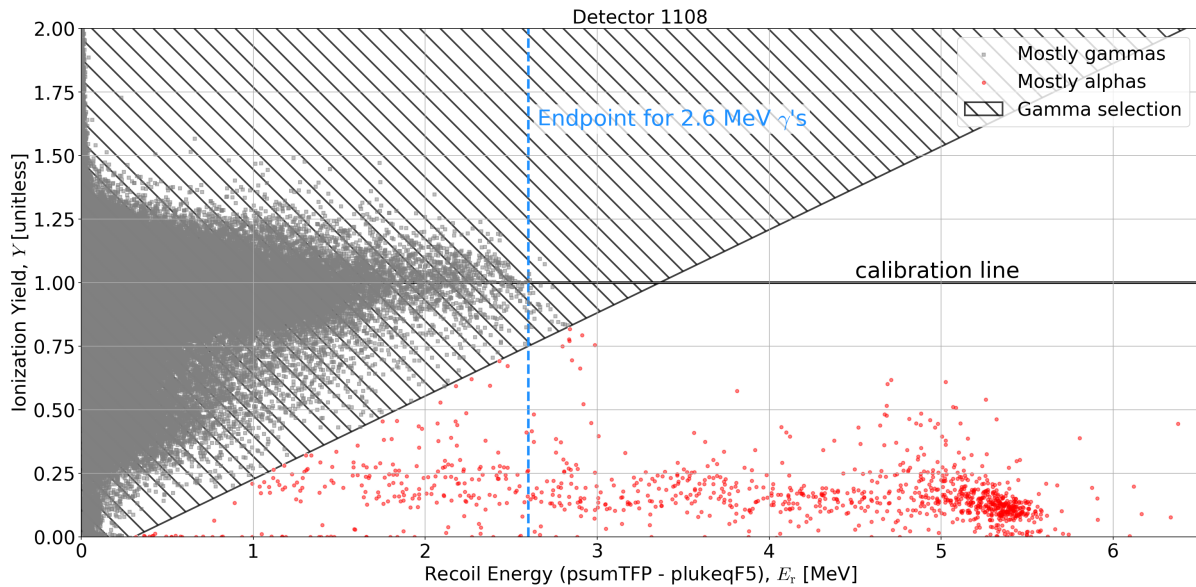


Figure B.5: Ionization yield versus recoil energy for SuperCDMS Soudan detector 1108 showing ^{210}Po alpha selection.

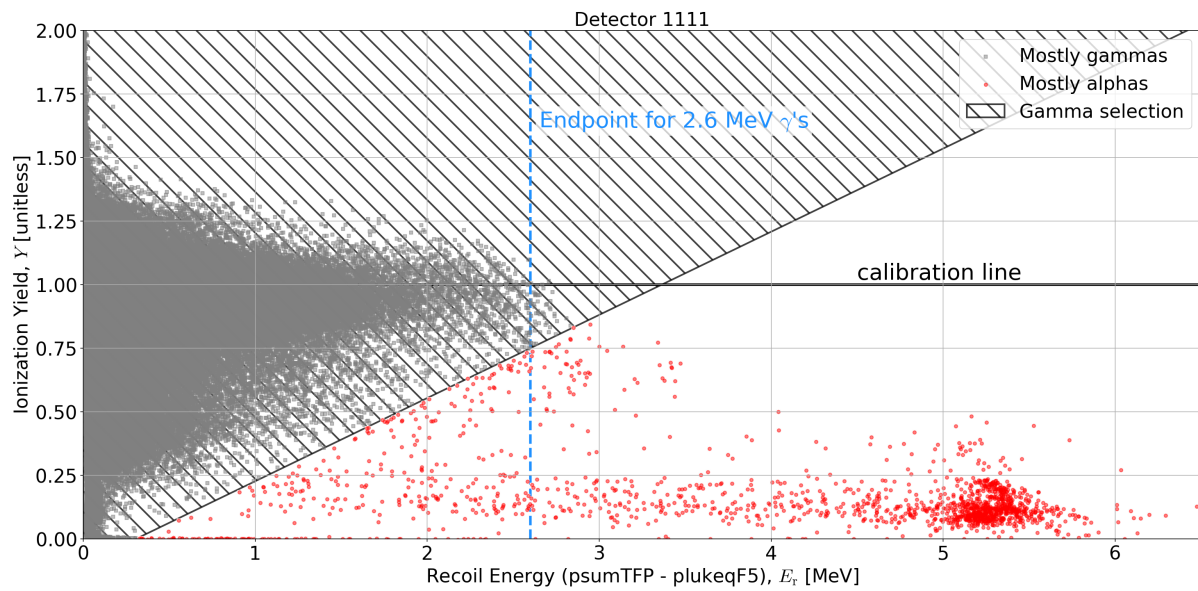


Figure B.6: Ionization yield versus recoil energy for SuperCDMS Soudan detector 1111 showing ^{210}Po alpha selection.

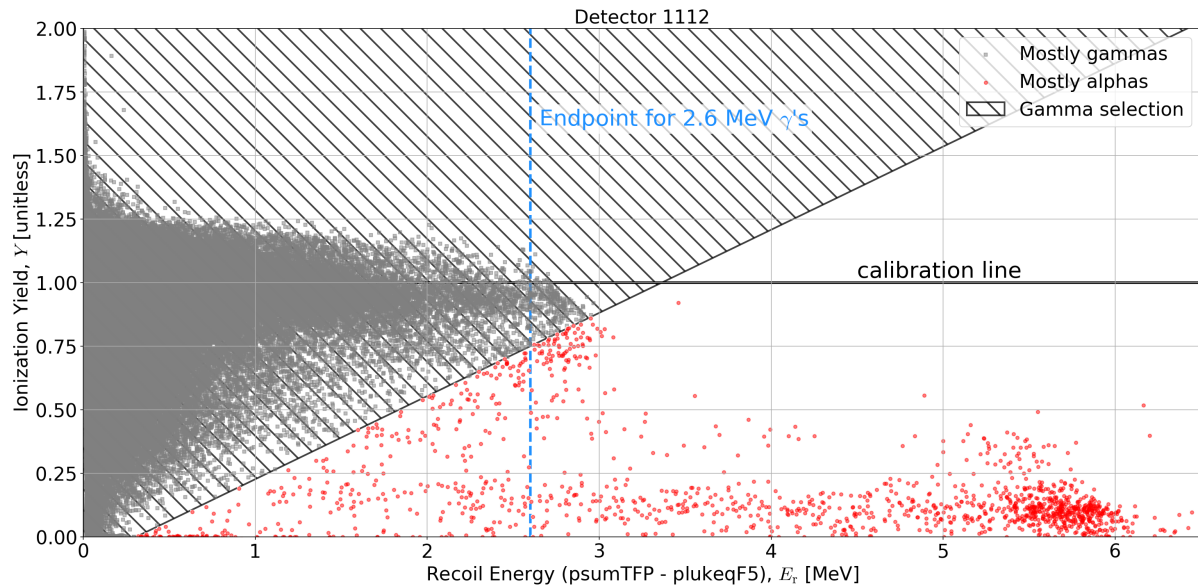


Figure B.7: Ionization yield versus recoil energy for SuperCDMS Soudan detector 1112 showing ^{210}Po alpha selection.

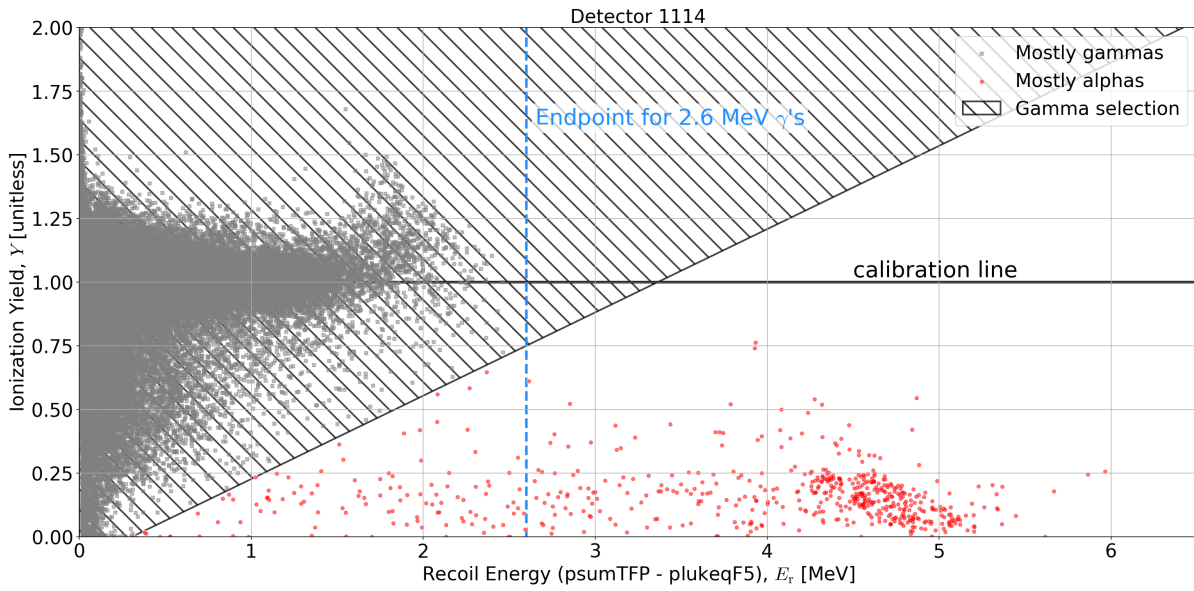


Figure B.8: Ionization yield versus recoil energy for SuperCDMS Soudan detector 1114 showing ^{210}Po alpha selection.

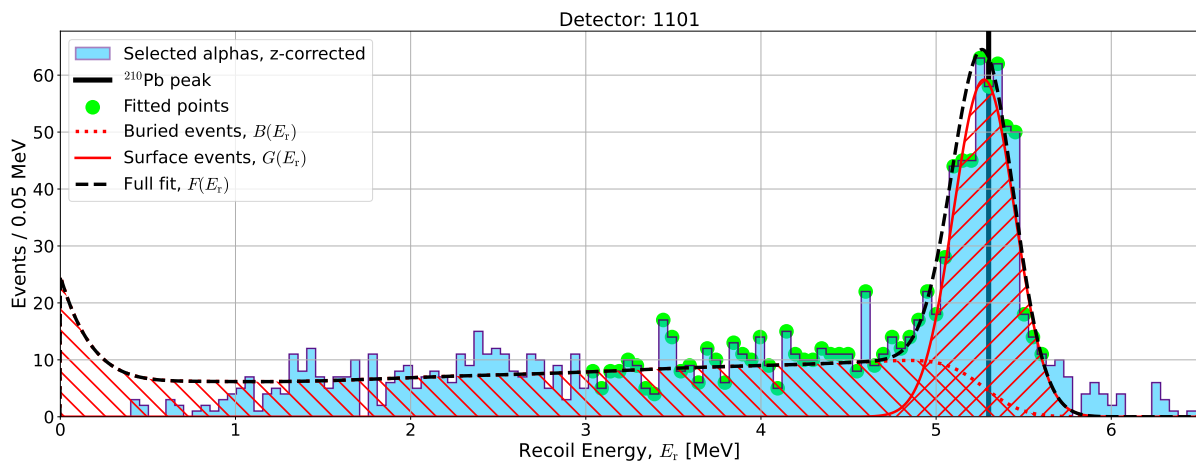


Figure B.9: Recoil energy spectrum for ^{210}Po alphas for SuperCDMS Soudan detector 1101 fitted by the spectrum developed in Section 3.4.

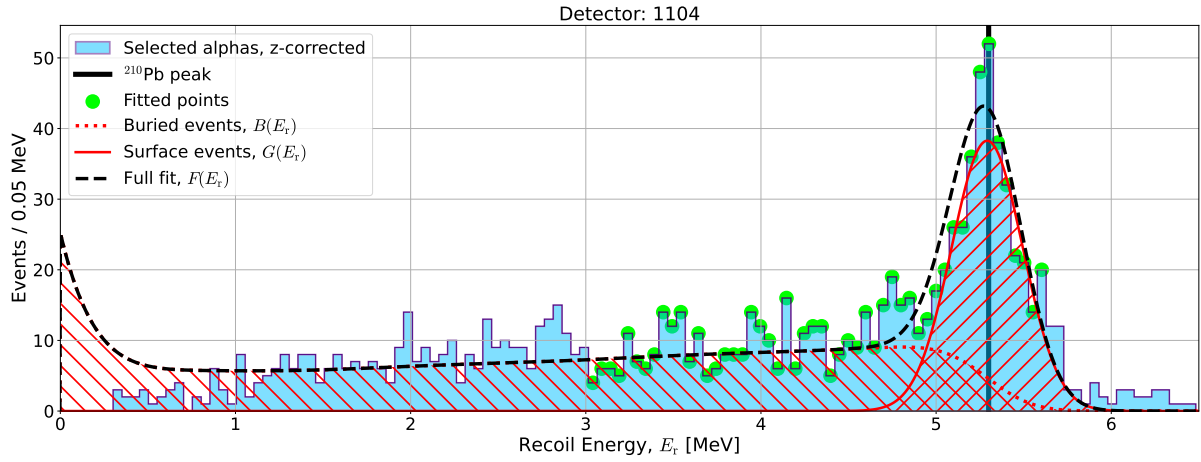


Figure B.10: Recoil energy spectrum for ^{210}Po alphas for SuperCDMS Soudan detector 1104 fitted by the spectrum developed in Section 3.4.

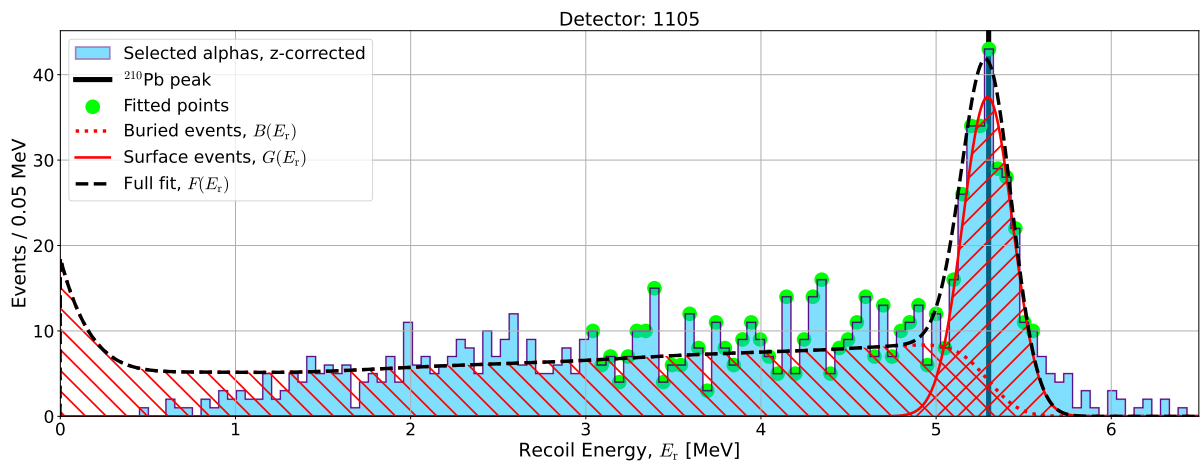


Figure B.11: Recoil energy spectrum for ^{210}Po alphas for SuperCDMS Soudan detector 1105 fitted by the spectrum developed in Section 3.4.

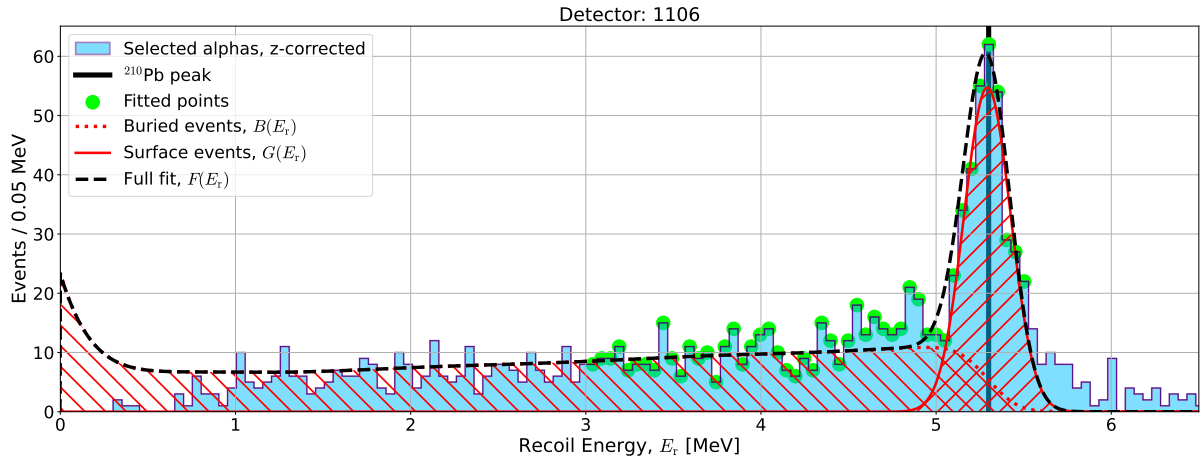


Figure B.12: Recoil energy spectrum for ^{210}Po alphas for SuperCDMS Soudan detector 1106 fitted by the spectrum developed in Section 3.4. Recall that PBS1 and PDS1 were not functional.

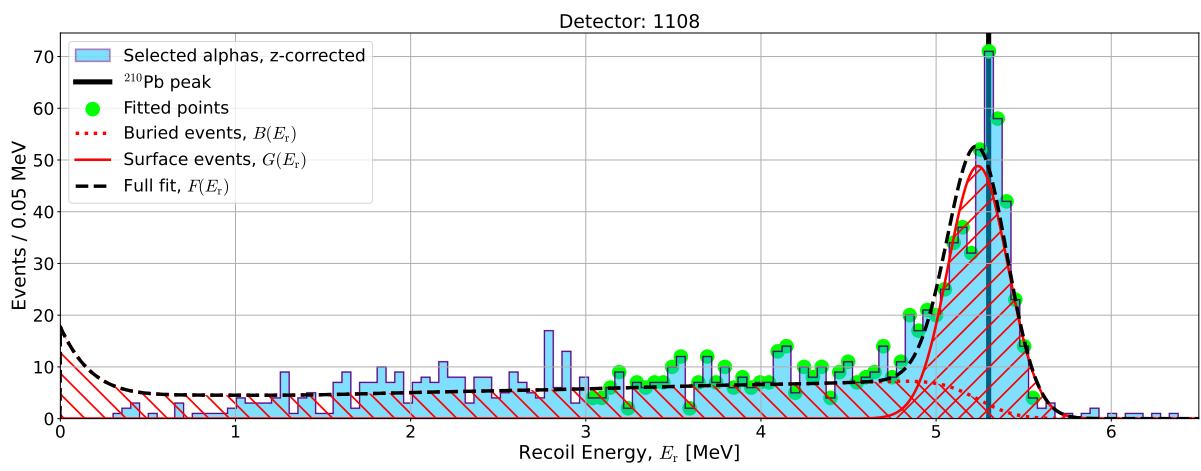


Figure B.13: Recoil energy spectrum for ^{210}Po alphas for SuperCDMS Soudan detector 1108 fitted by the spectrum developed in Section 3.4.

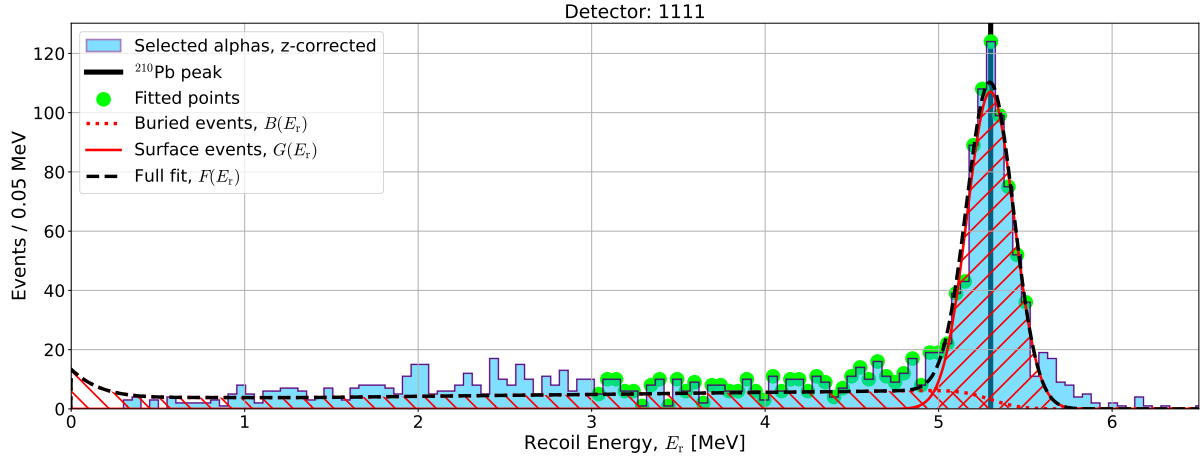


Figure B.14: Recoil energy spectrum for ^{210}Po alphas for SuperCDMS Soudan detector 1111 fitted by the spectrum developed in Section 3.4.

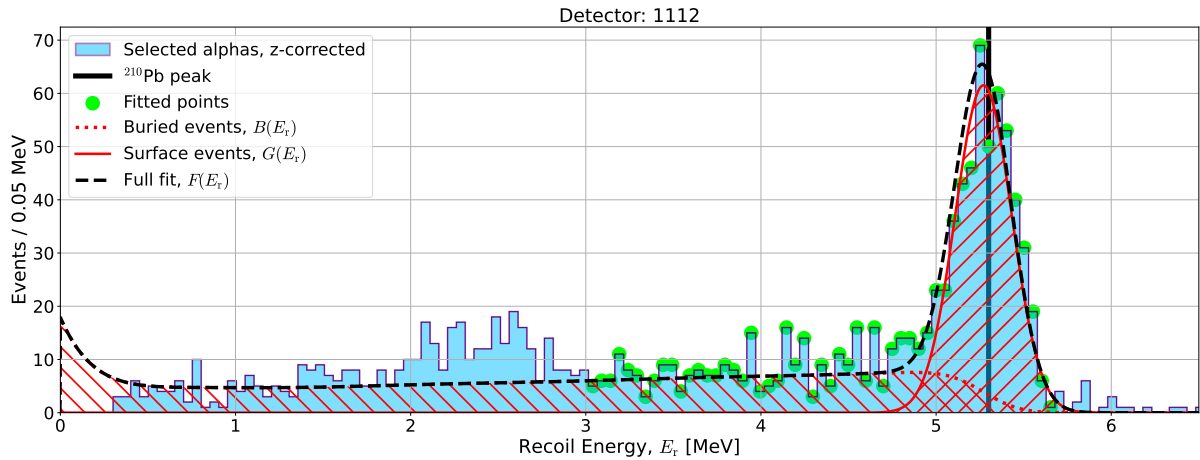


Figure B.15: Recoil energy spectrum for ^{210}Po alphas for SuperCDMS Soudan detector 1112 fitted by the spectrum developed in Section 3.4.

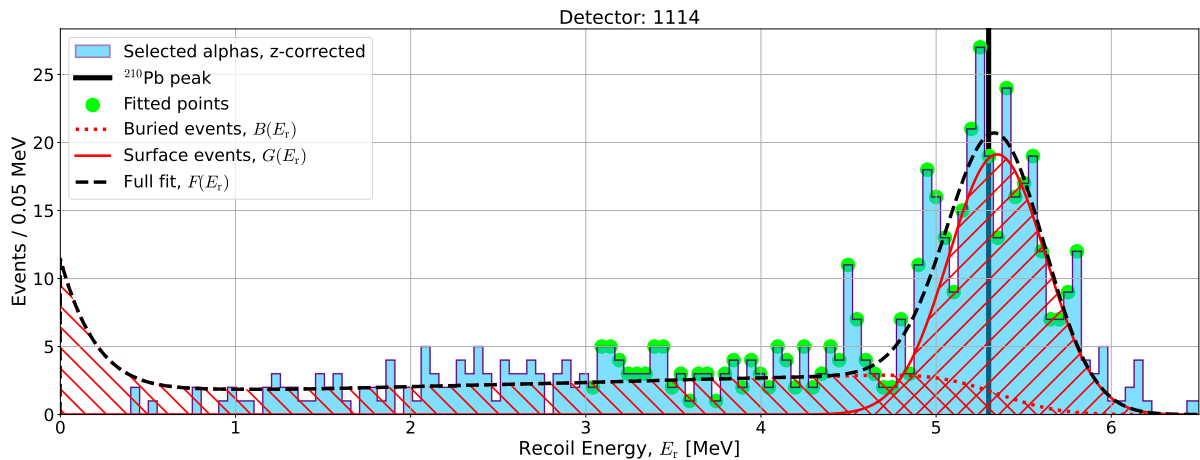


Figure B.16: Recoil energy spectrum for ^{210}Po alphas for SuperCDMS Soudan detector 1114 fitted by the spectrum developed in Section 3.4.

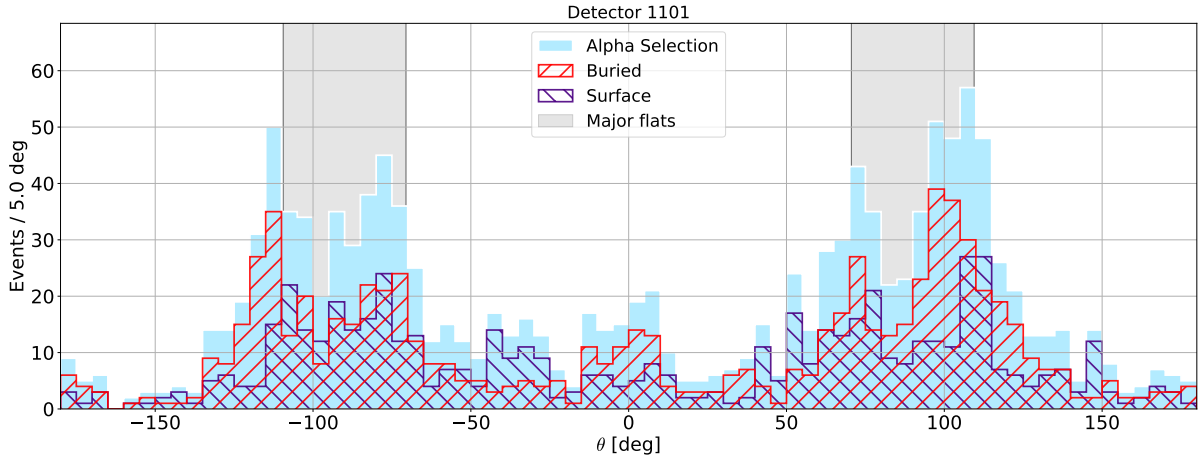


Figure B.17: The ^{210}Po event rate versus angle θ for SuperCDMS Soudan detector 1101.

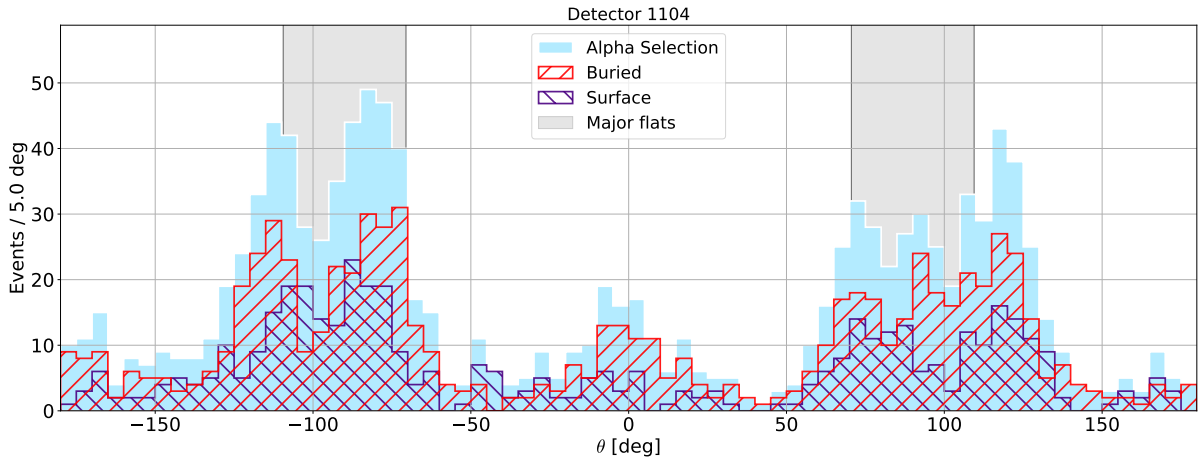


Figure B.18: The ^{210}Po event rate versus angle θ for SuperCDMS Soudan detector 1104.

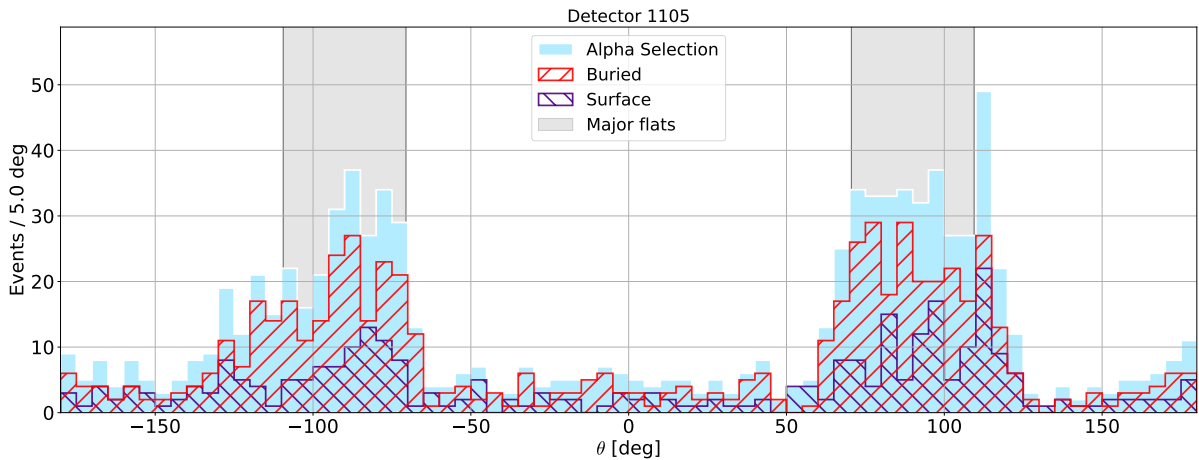


Figure B.19: The ^{210}Po event rate versus angle θ for SuperCDMS Soudan detector 1105.

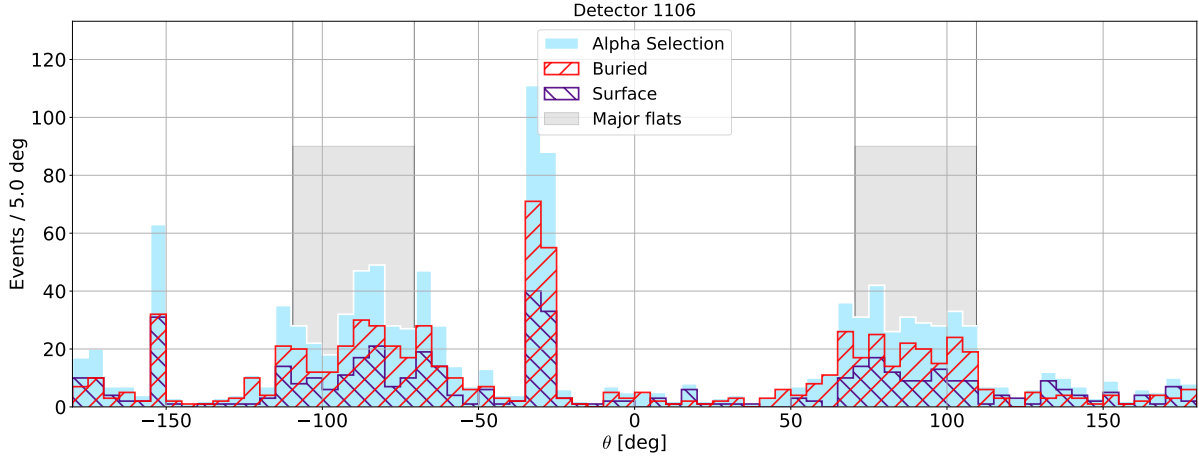


Figure B.20: The ^{210}Po event rate versus angle θ for SuperCDMS Soudan detector 1106. Recall that PBS1 and PDS1 were not functional, resulting in a non-physical event position reconstruction (as illustrated by the large rate at around -40° and -150°).

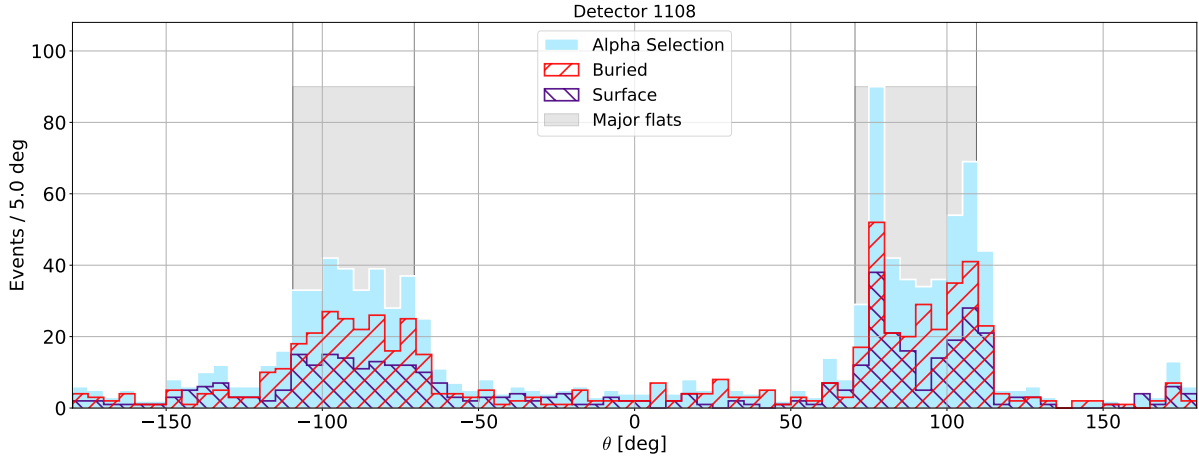


Figure B.21: The ^{210}Po event rate versus angle θ for SuperCDMS Soudan detector 1108.

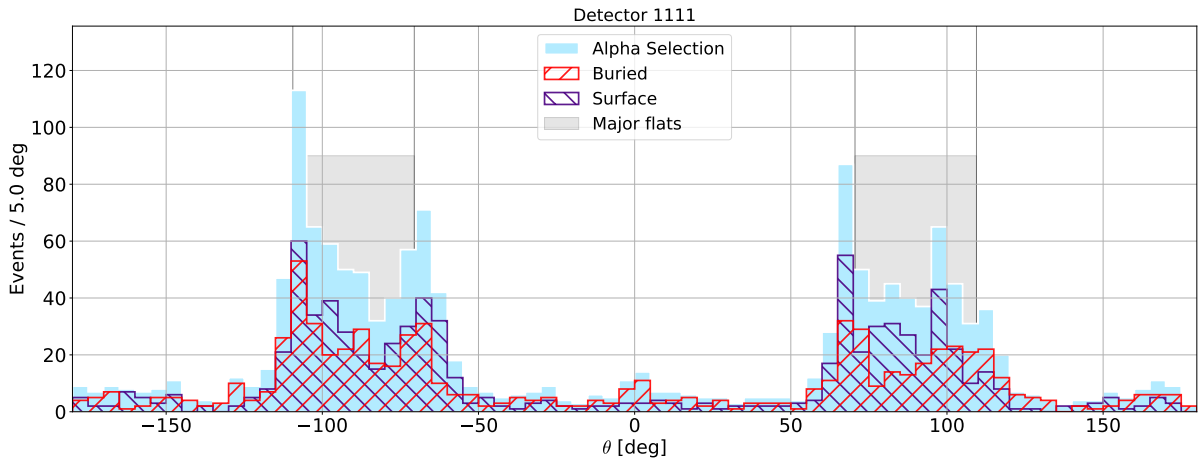


Figure B.22: The ^{210}Po event rate versus angle θ for SuperCDMS Soudan detector 1111.

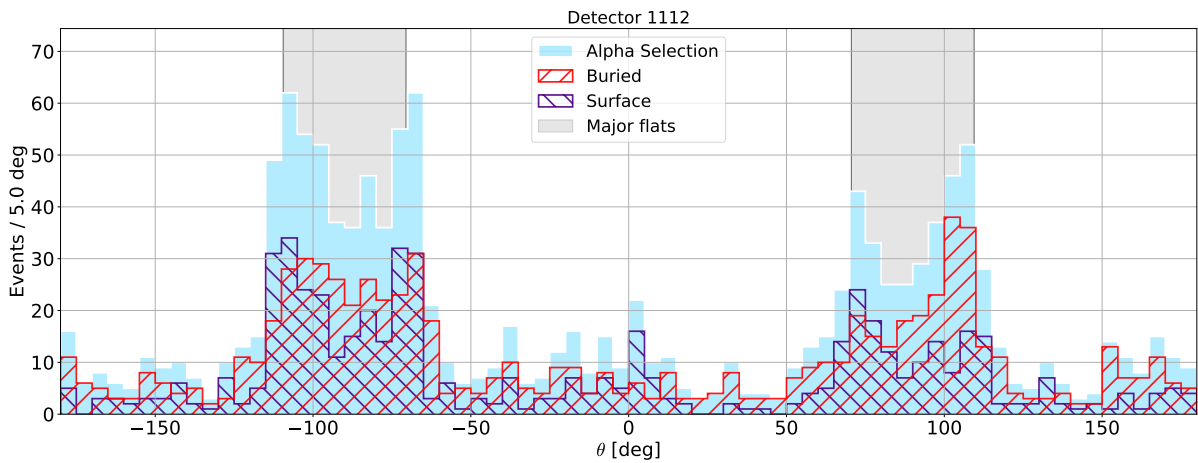


Figure B.23: The ^{210}Po event rate versus angle θ for SuperCDMS Soudan detector 1114.

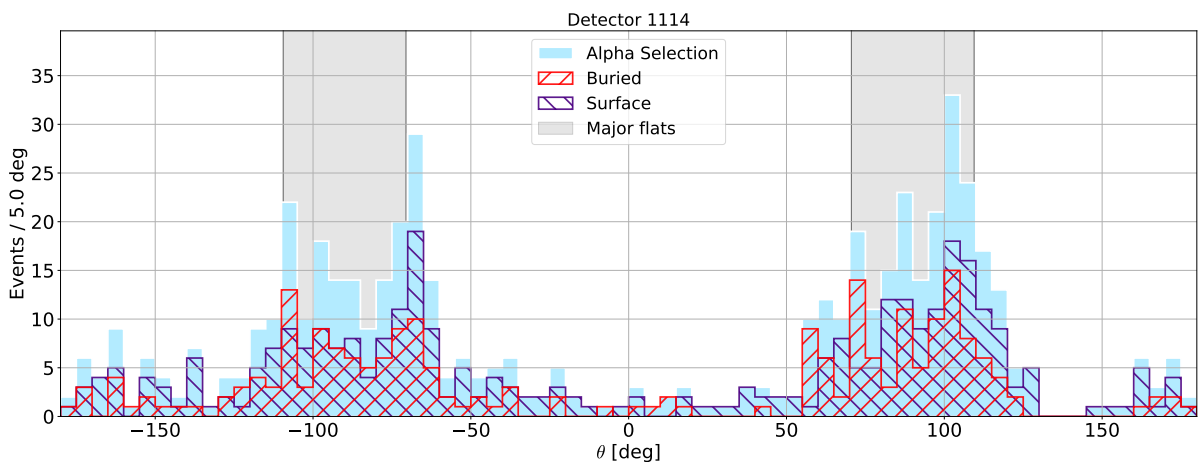


Figure B.24: The ^{210}Po event rate versus angle θ for SuperCDMS Soudan detector 1114.

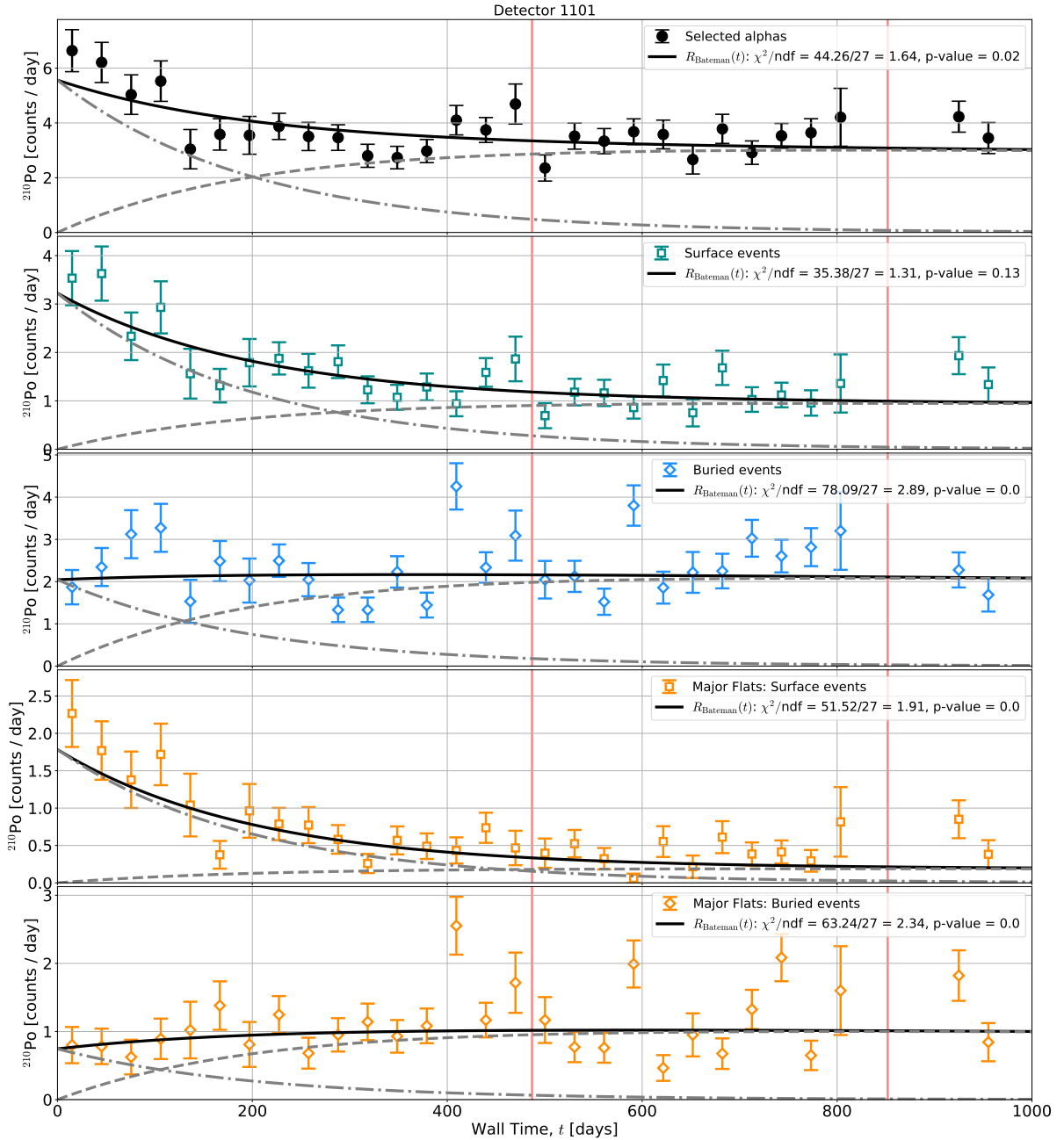


Figure B.25: Efficiency-corrected ^{210}Po rate versus time for SuperCDMS Soudan detector 1101.

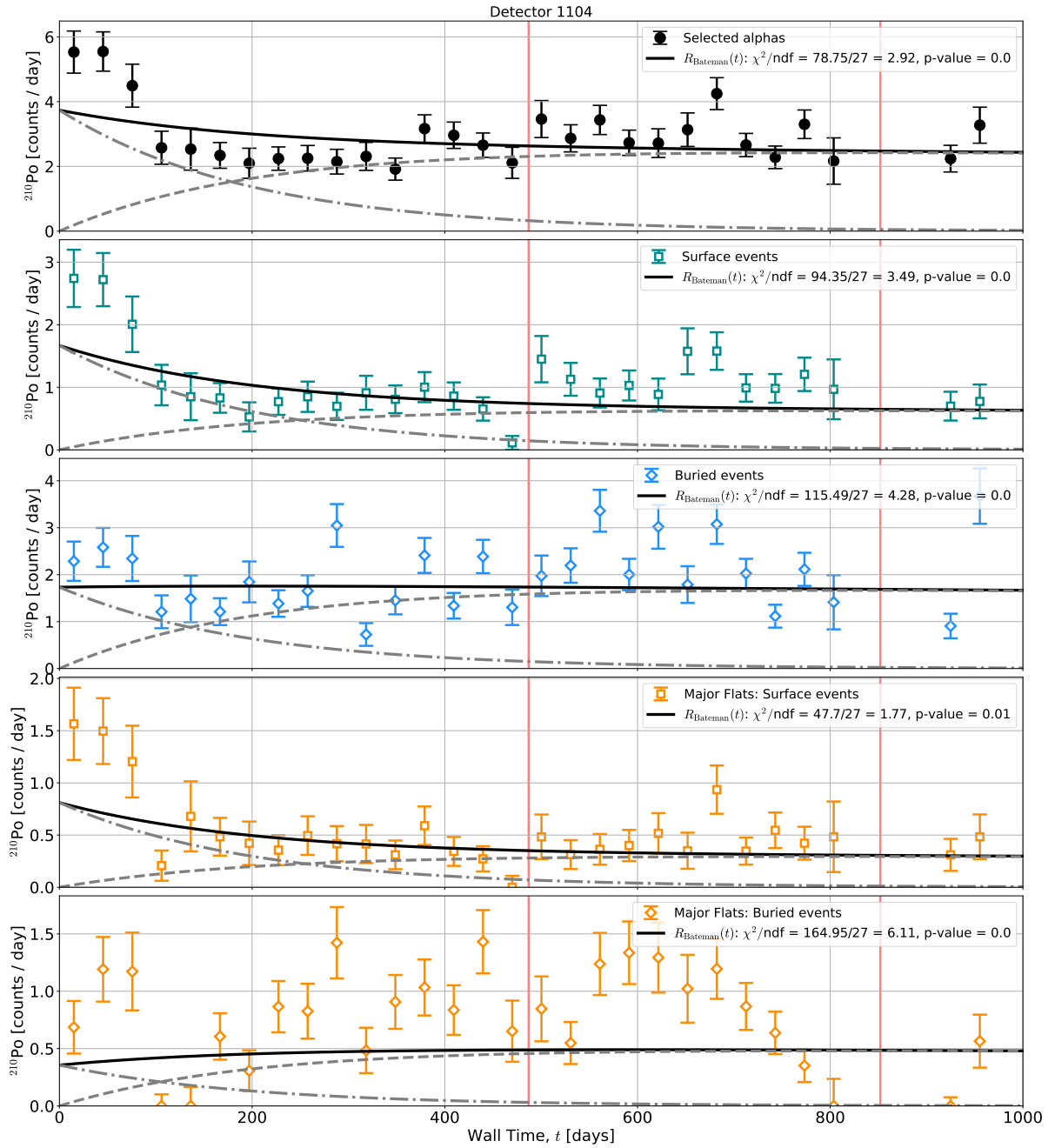


Figure B.26: Efficiency-corrected ^{210}Po rate versus time for SuperCDMS Soudan detector 1104.

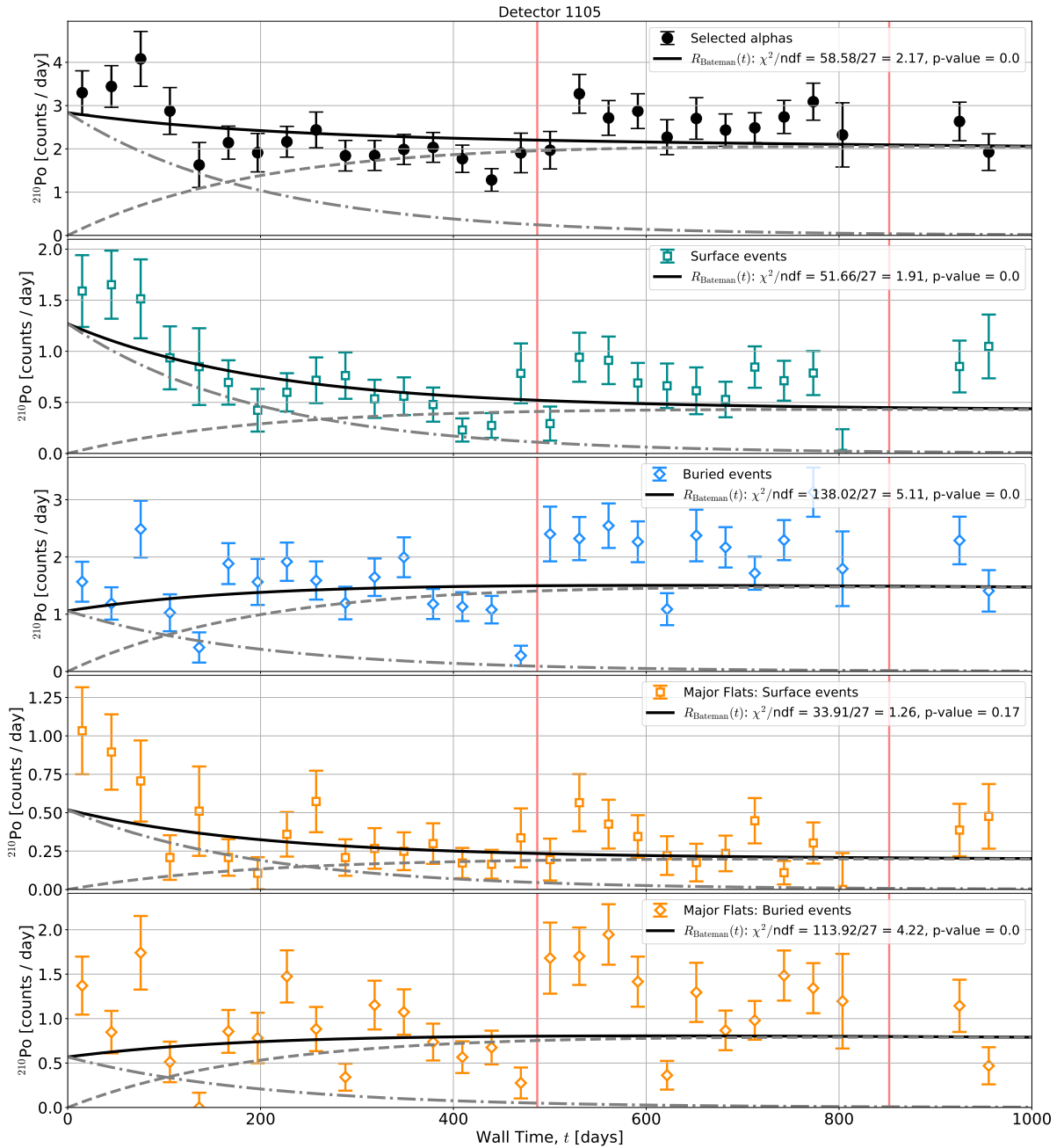


Figure B.27: Efficiency-corrected ^{210}Po rate versus time for SuperCDMS Soudan detector 1105.

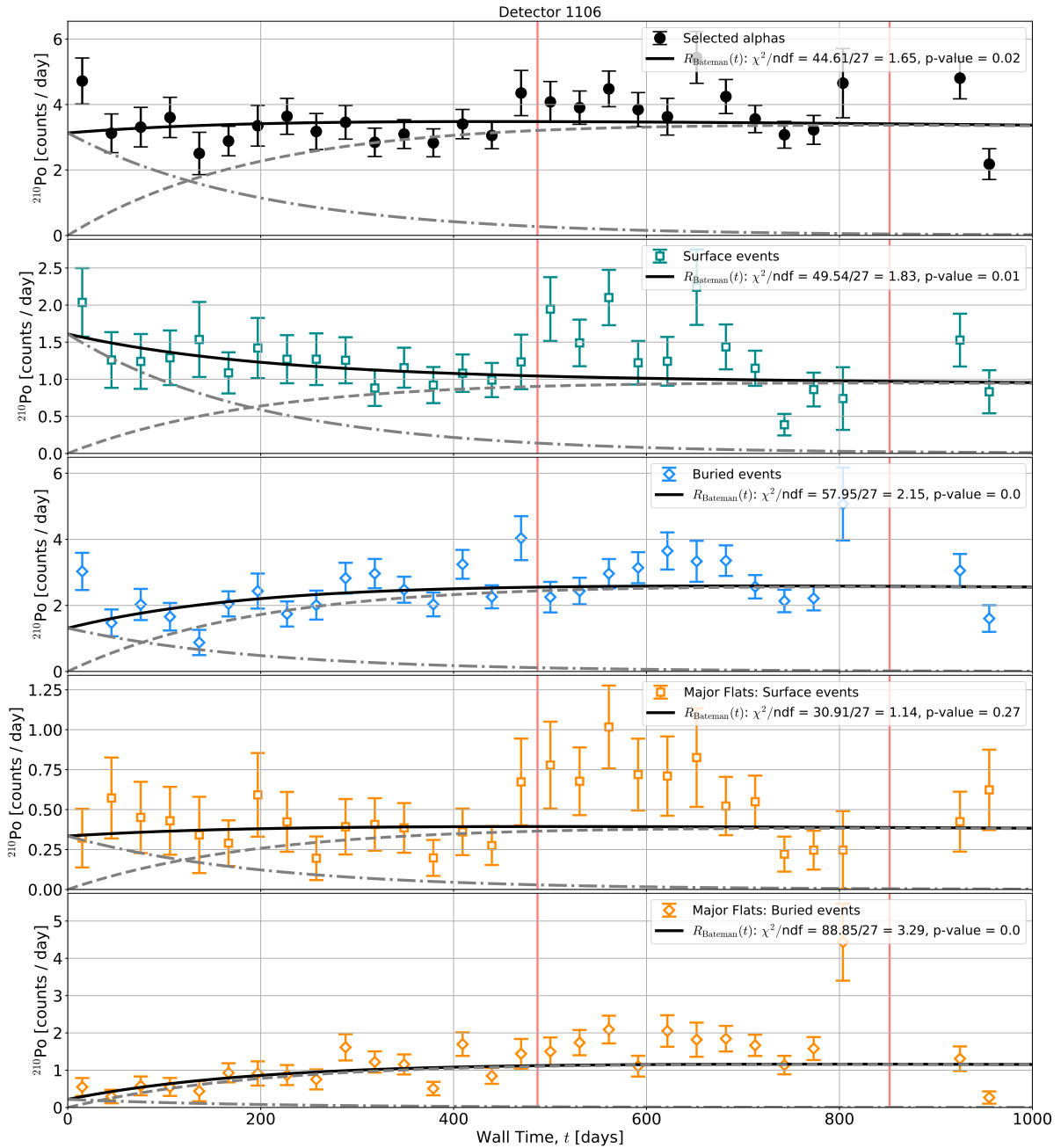


Figure B.28: Efficiency-corrected ^{210}Po rate versus time for SuperCDMS Soudan detector 1106. Recall that PBS1 and PDS1 were not functional.

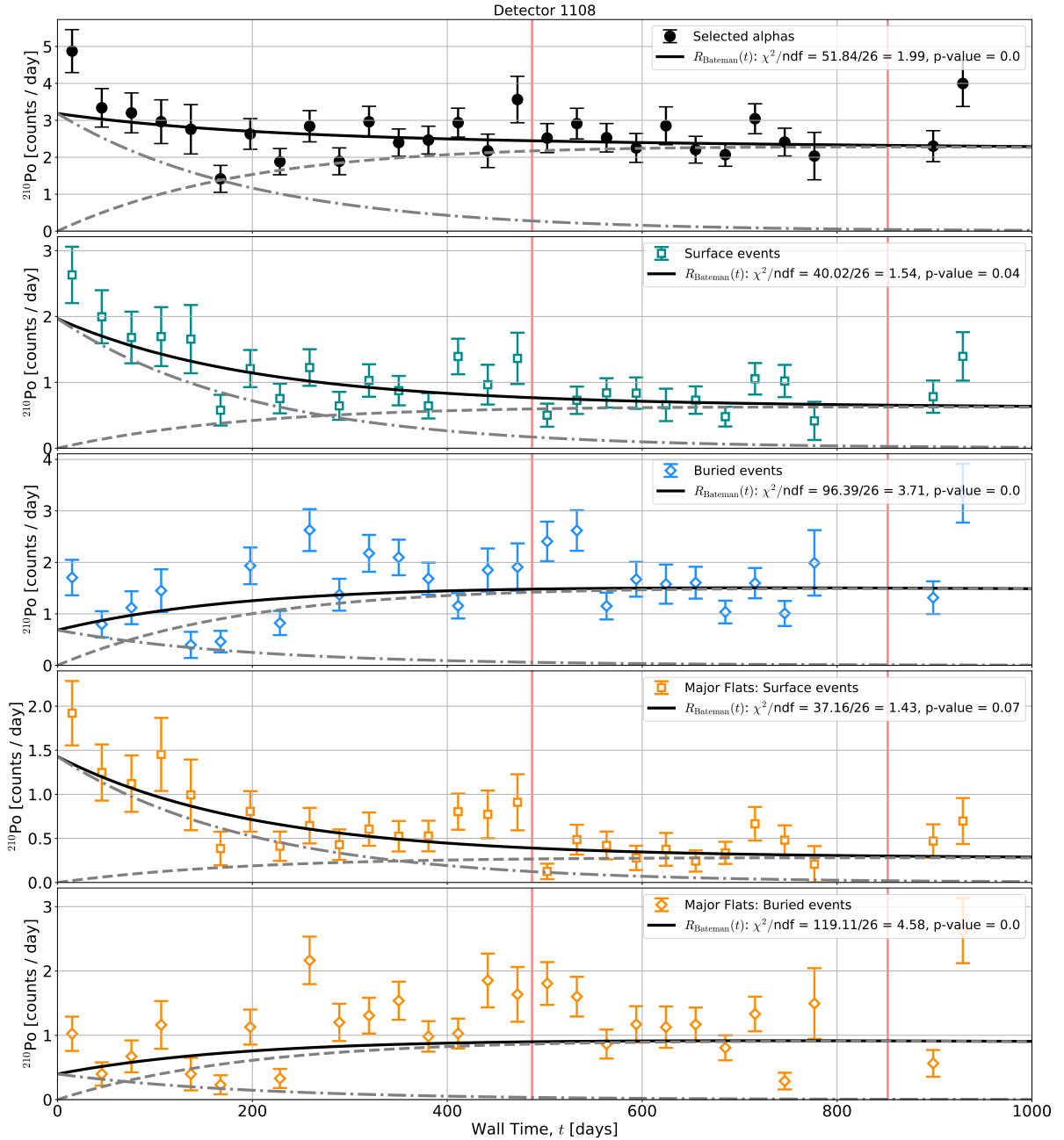


Figure B.29: Efficiency-corrected ^{210}Po rate versus time for SuperCDMS Soudan detector 1108.

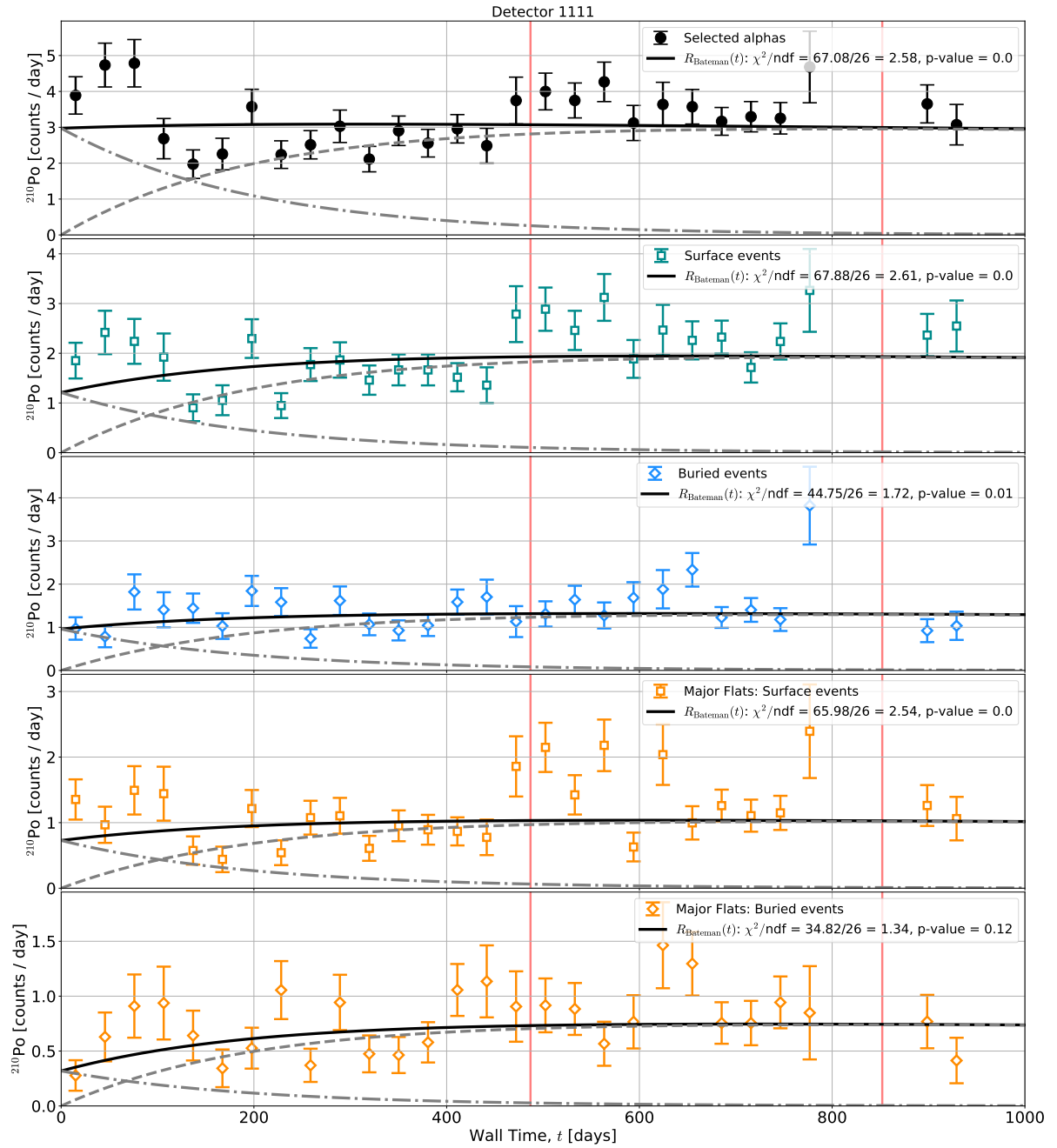


Figure B.30: Efficiency-corrected ^{210}Po rate versus time for SuperCDMS Soudan detector 1111.

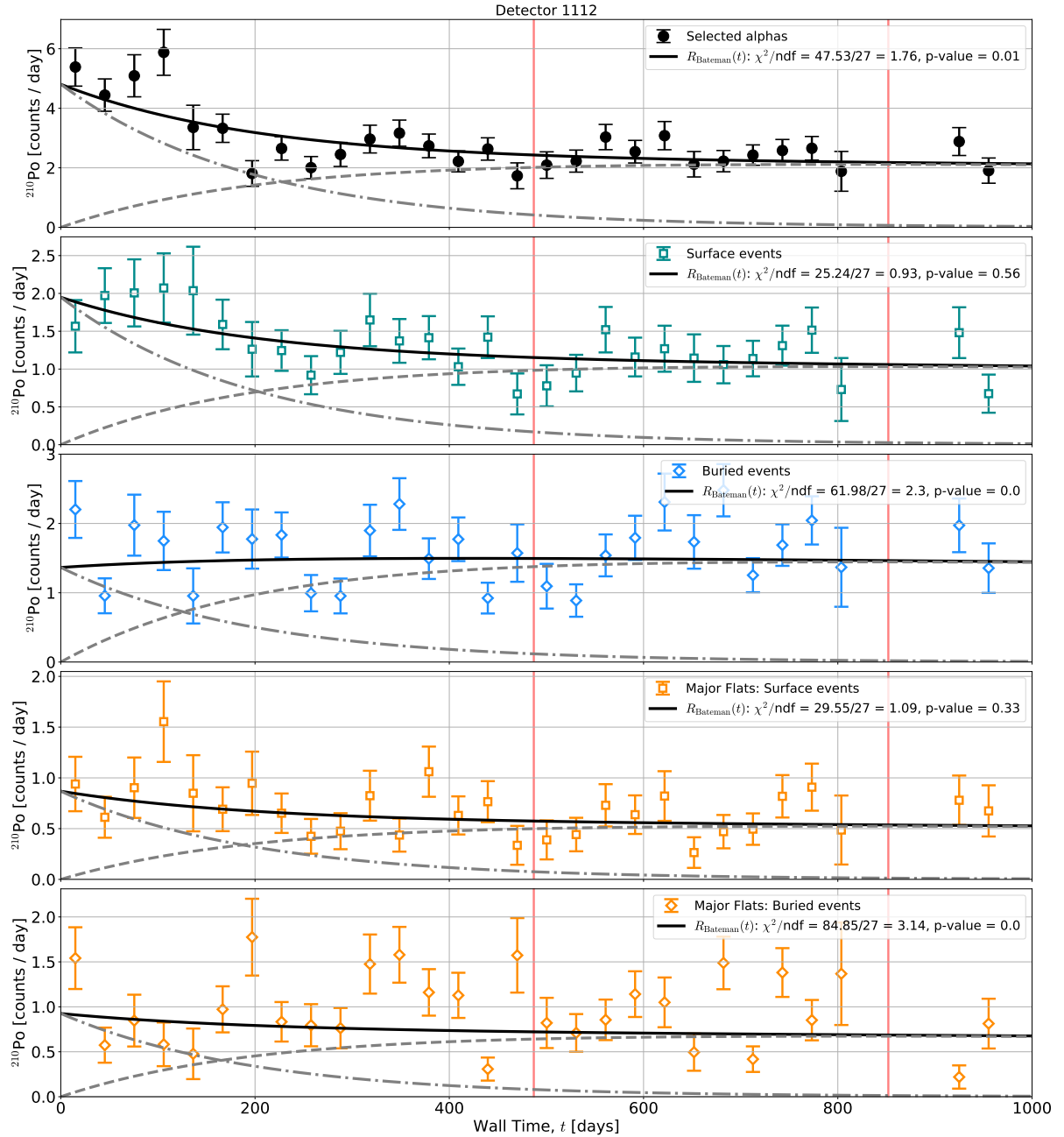


Figure B.31: Efficiency-corrected ^{210}Po rate versus time for SuperCDMS Soudan detector 1112.

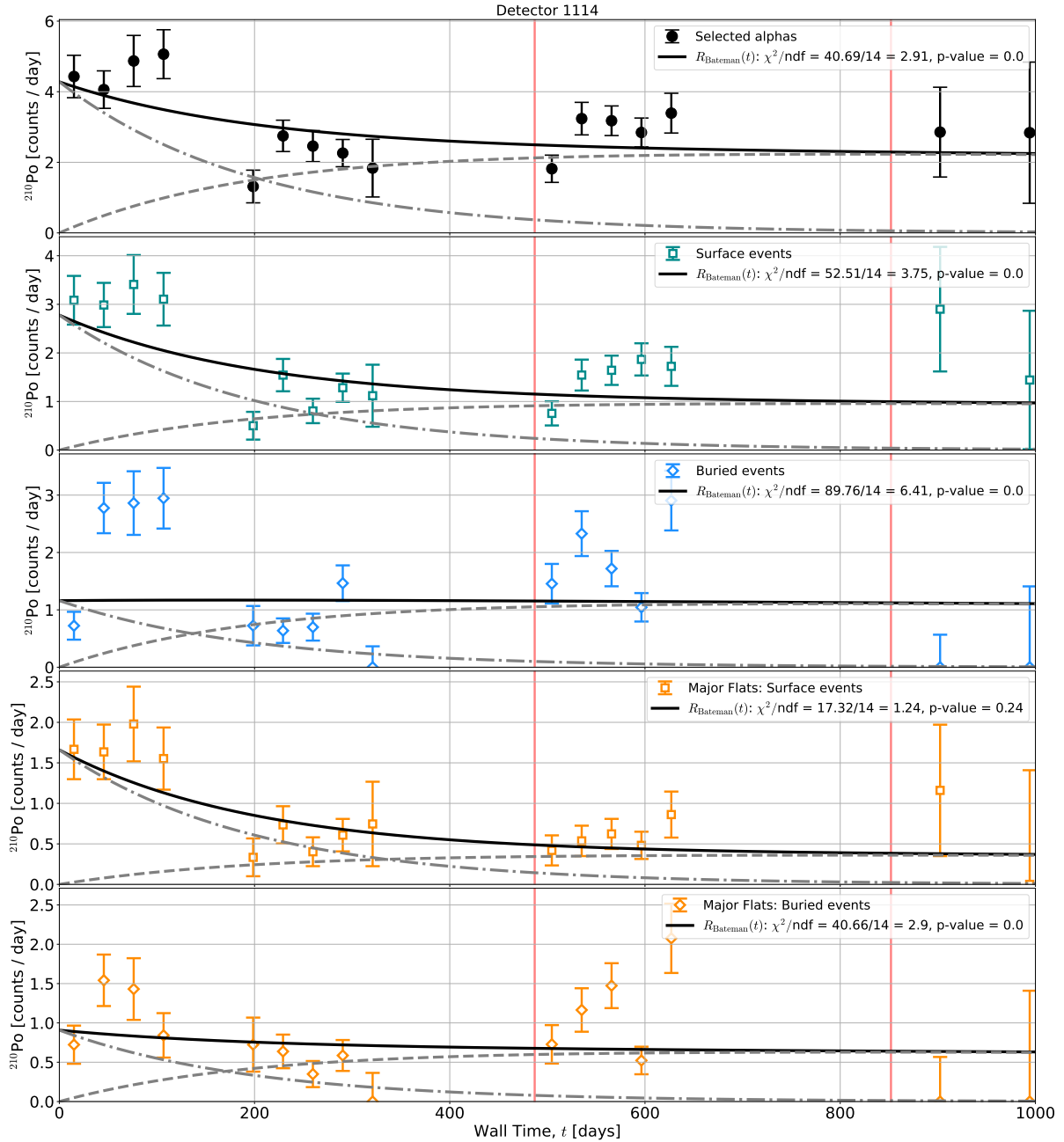


Figure B.32: Efficiency-corrected ^{210}Po rate versus time for SuperCDMS Soudan detector 1114.

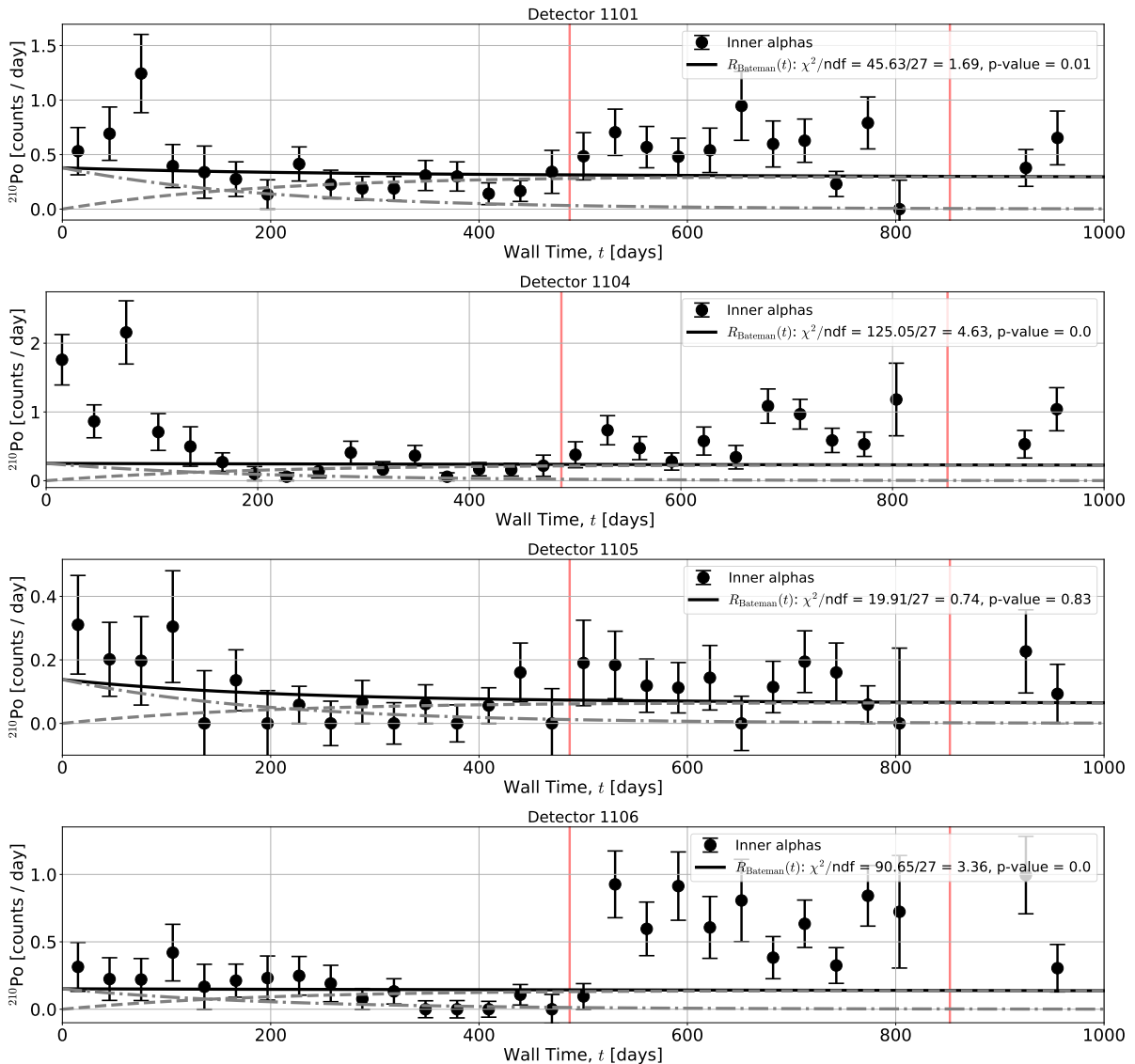


Figure B.33: Efficiency-corrected ^{210}Po inner (face) event rate versus time for SuperCDMS Soudan detector 1101-1106.

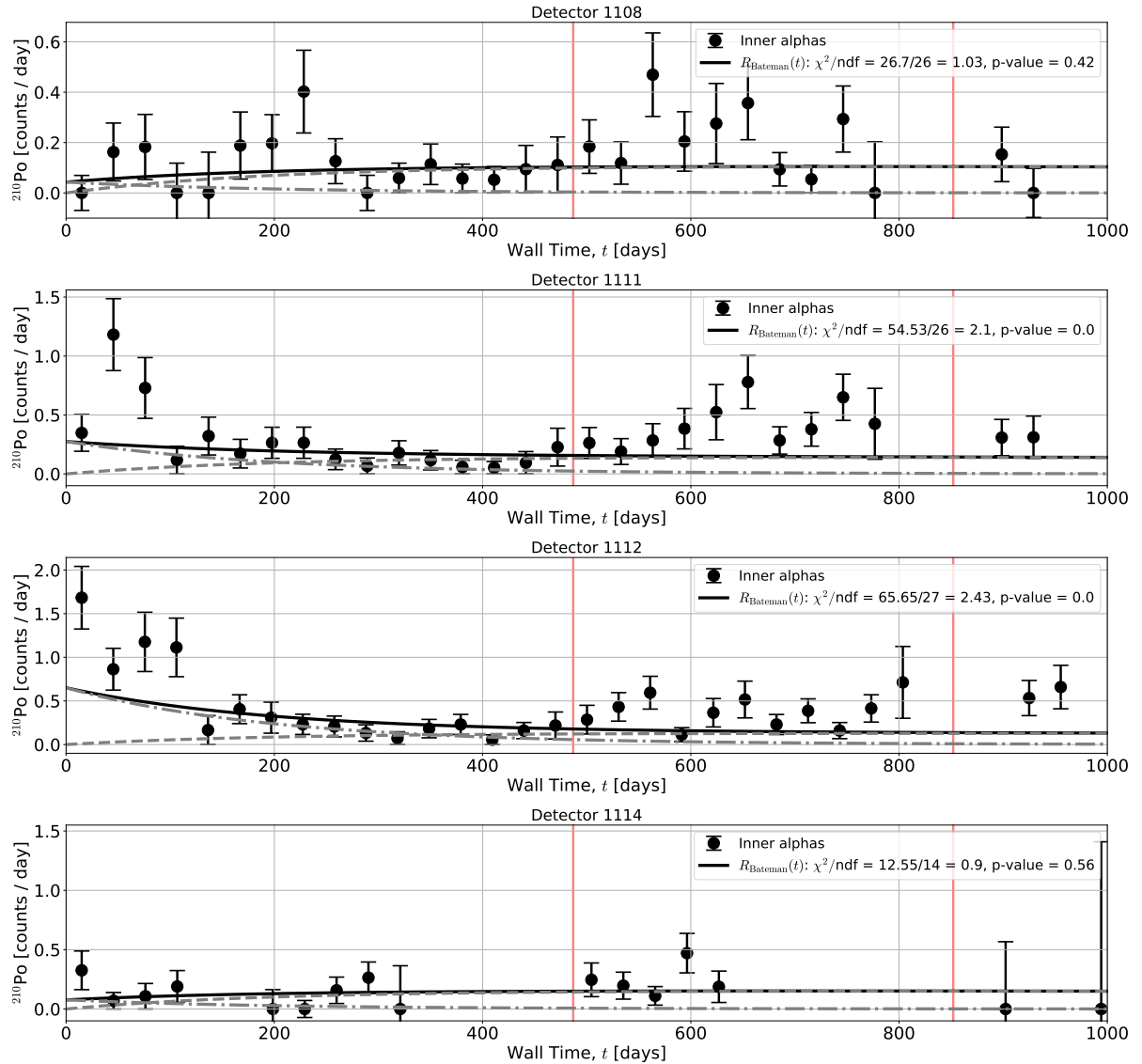


Figure B.34: Efficiency-corrected ^{210}Po inner (face) event rate versus time for SuperCDMS Soudan detector 1108-1114.

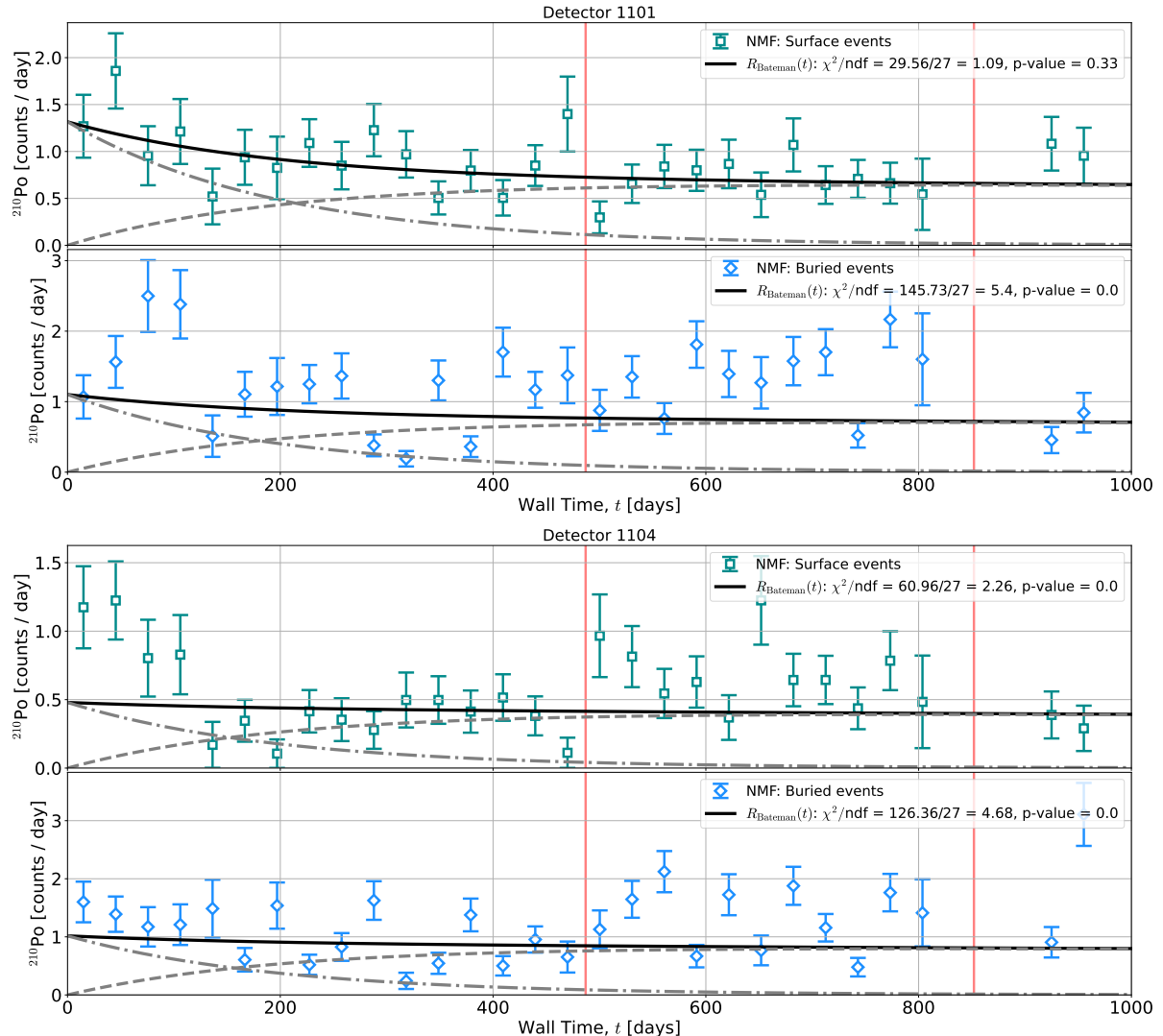


Figure B.35: Efficiency-corrected ^{210}Po (neither-major-flat) event rate versus time for SuperCDMS Soudan detectors 1101 and 1104.

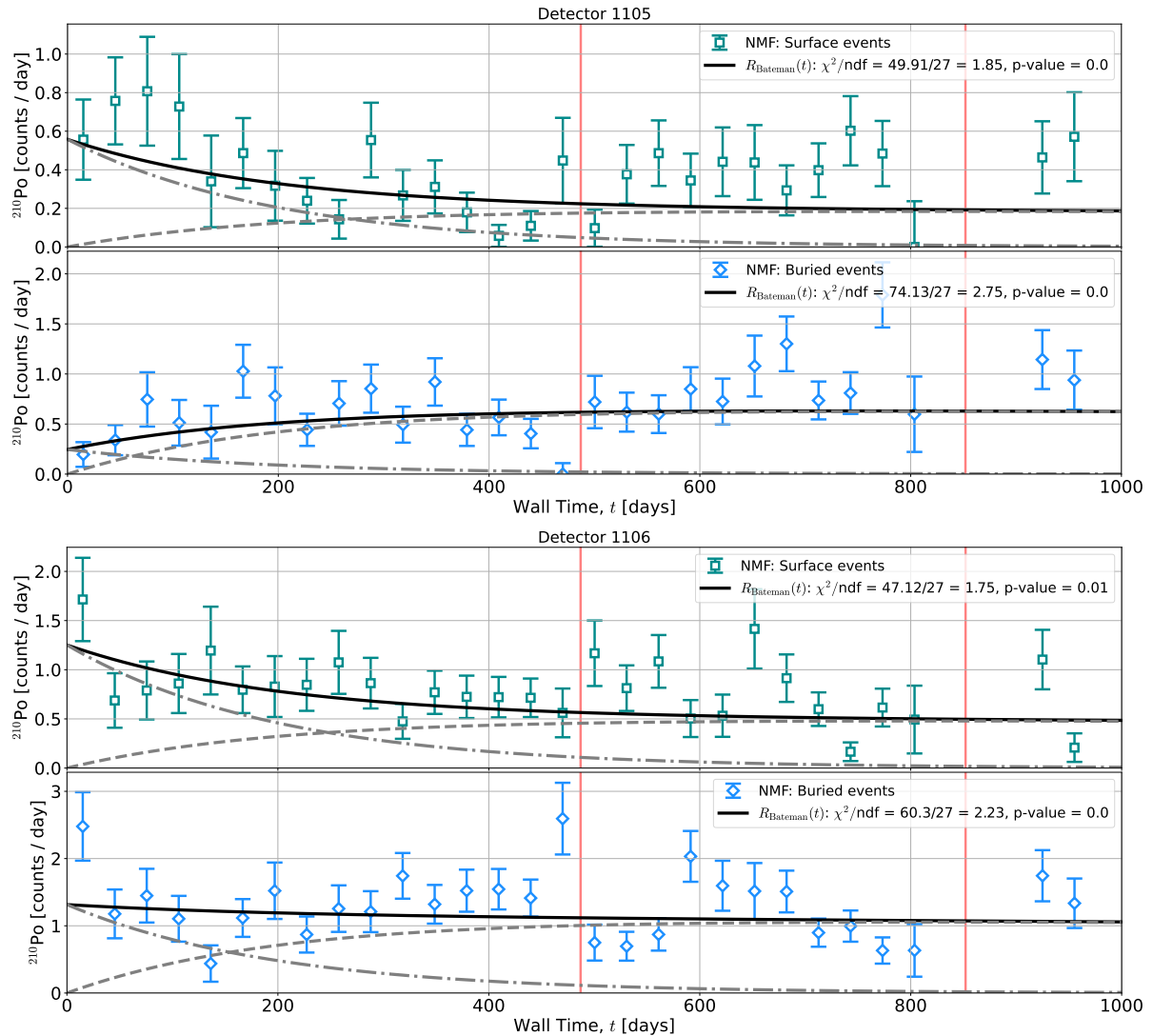


Figure B.36: Efficiency-corrected ^{210}Po (neither-major-flat) event rate versus time for SuperCDMS Soudan detectors 1105-1106.

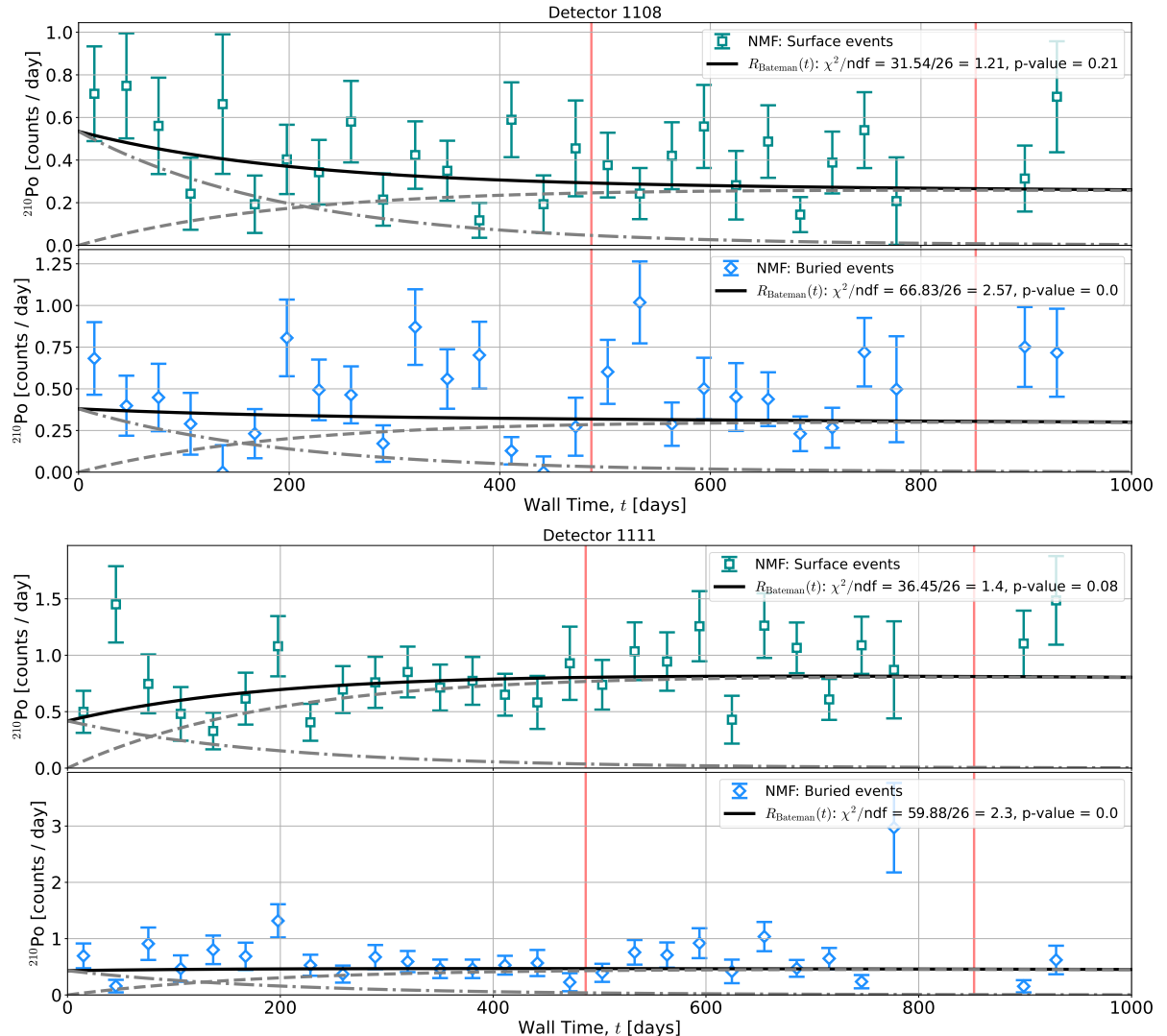


Figure B.37: Efficiency-corrected ^{210}Po (neither-major-flat) event rate versus time for SuperCDMS Soudan detectors 1108 and 1111.

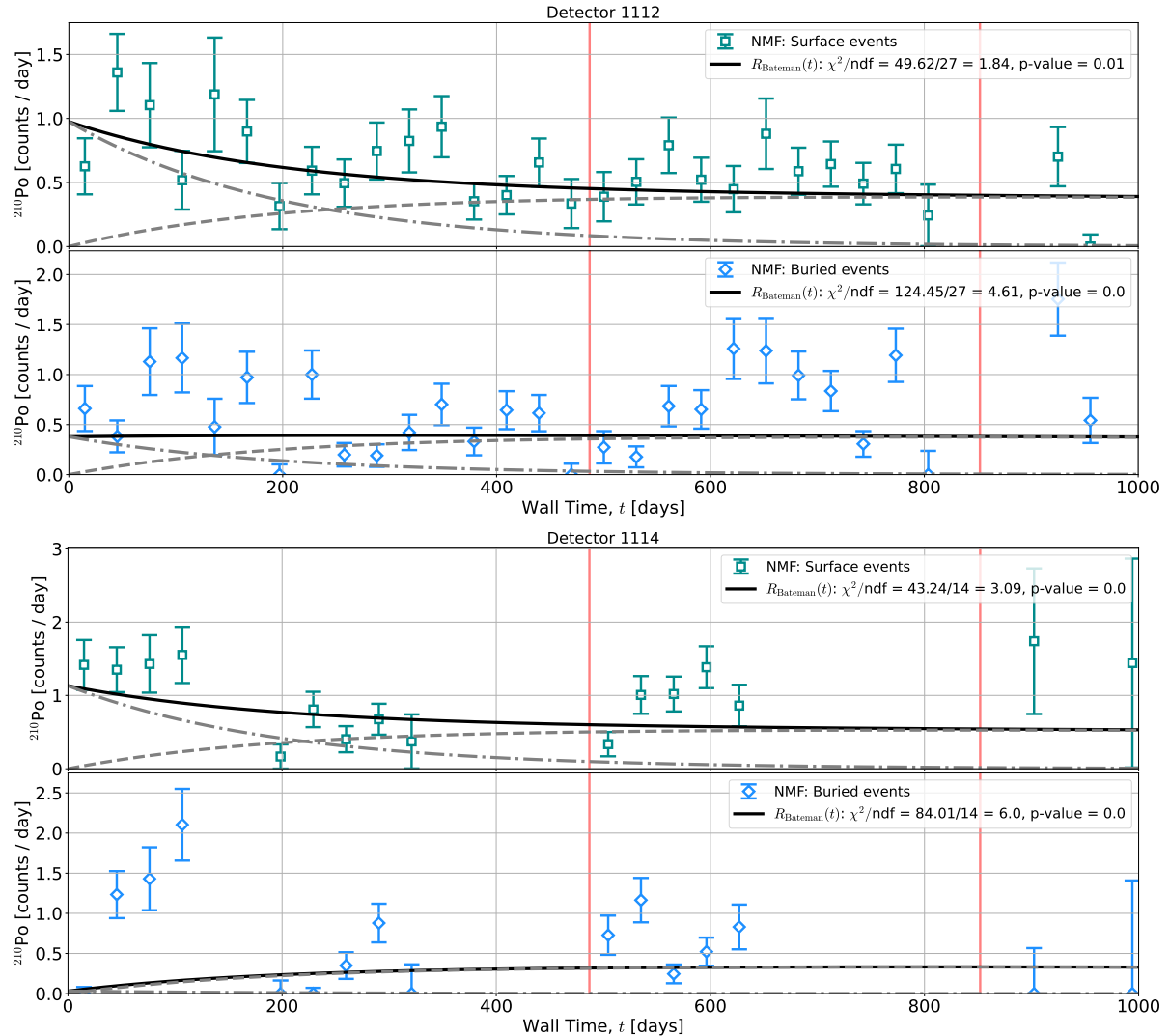


Figure B.38: Efficiency-corrected ^{210}Po (neither-major-flat) event rate versus time for SuperCDMS Soudan detectors 1112 and 1114.

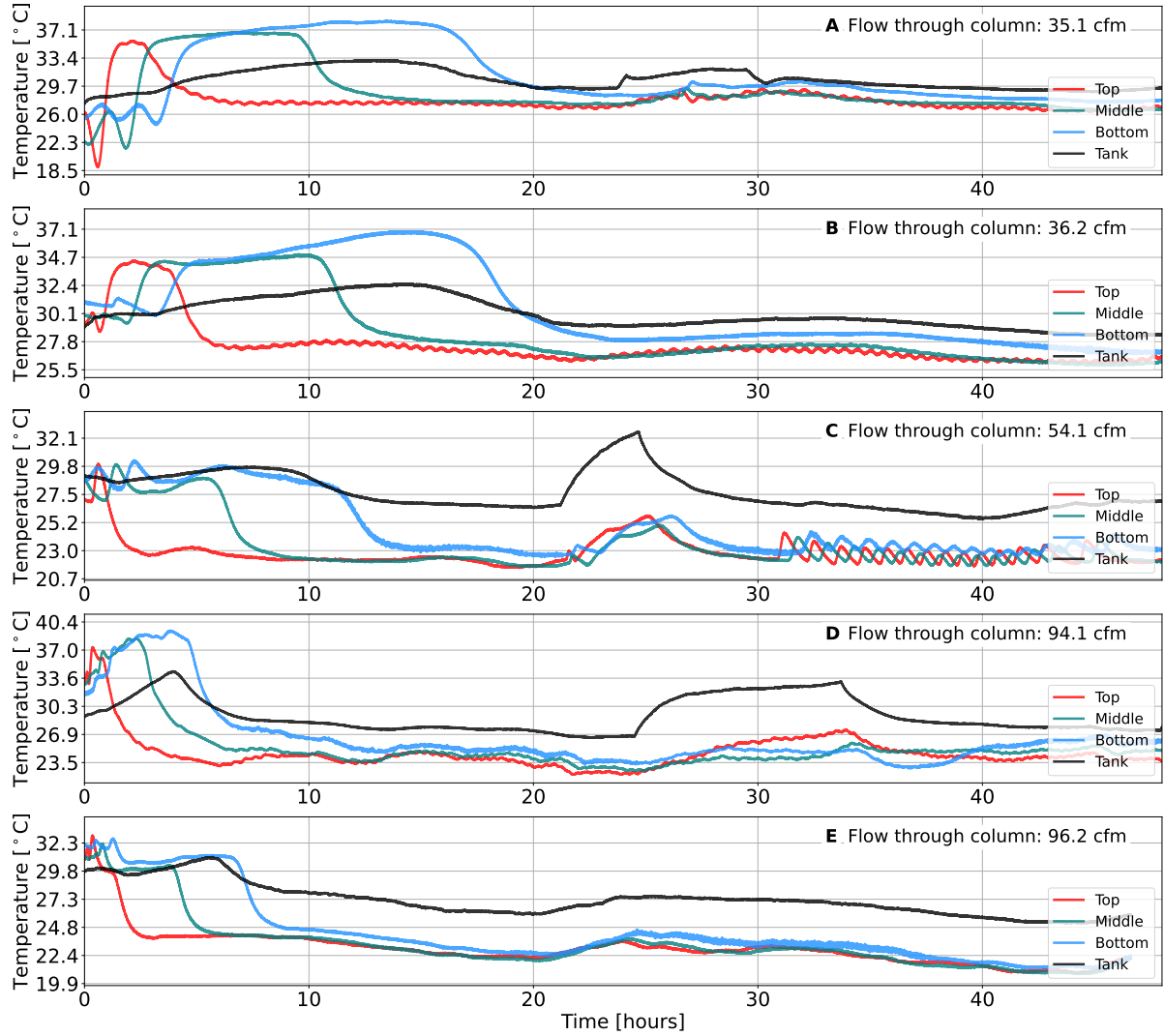


Figure C.1: Temperature measured within a single column during BTC operation. Bold letter labels on each plot (**A** through **E**) are referenced in the text body. The saw-tooth feature around 22 and 25 hours for **C** and **D** respectively are due to the pump room door being closed, which reduced ventilation that resulted in the ambient temperature of the room increasing.

Appendices

Measured Temperature During BTCs and RCs

Figure C.1 shows several examples of BTC temperature data, all sharing the feature of having a jump in temperature during the first part of the run, with a duration longer when the air flow is lower.

The temperature measured during RCs also appears to show early-time behavior that then disappears and becomes steady. Figure C.2 shows examples of RC temperature reaching lower temperature during the early regeneration stages, but eventually reaching a higher steady state profile. This feature also appears to depend on flow rate of the input air (with each of these data taking at the same purge-flow rate). Furthermore, at higher flow, where more water is expected to be added to the carbon bed, the temperature range between stages (filtering and regeneration) appears larger than during the lower flow runs (with all other system parameters held constant). These observations lend credibility to the water content hypothesis, though direct estimates of the change in temperature seem less compelling.

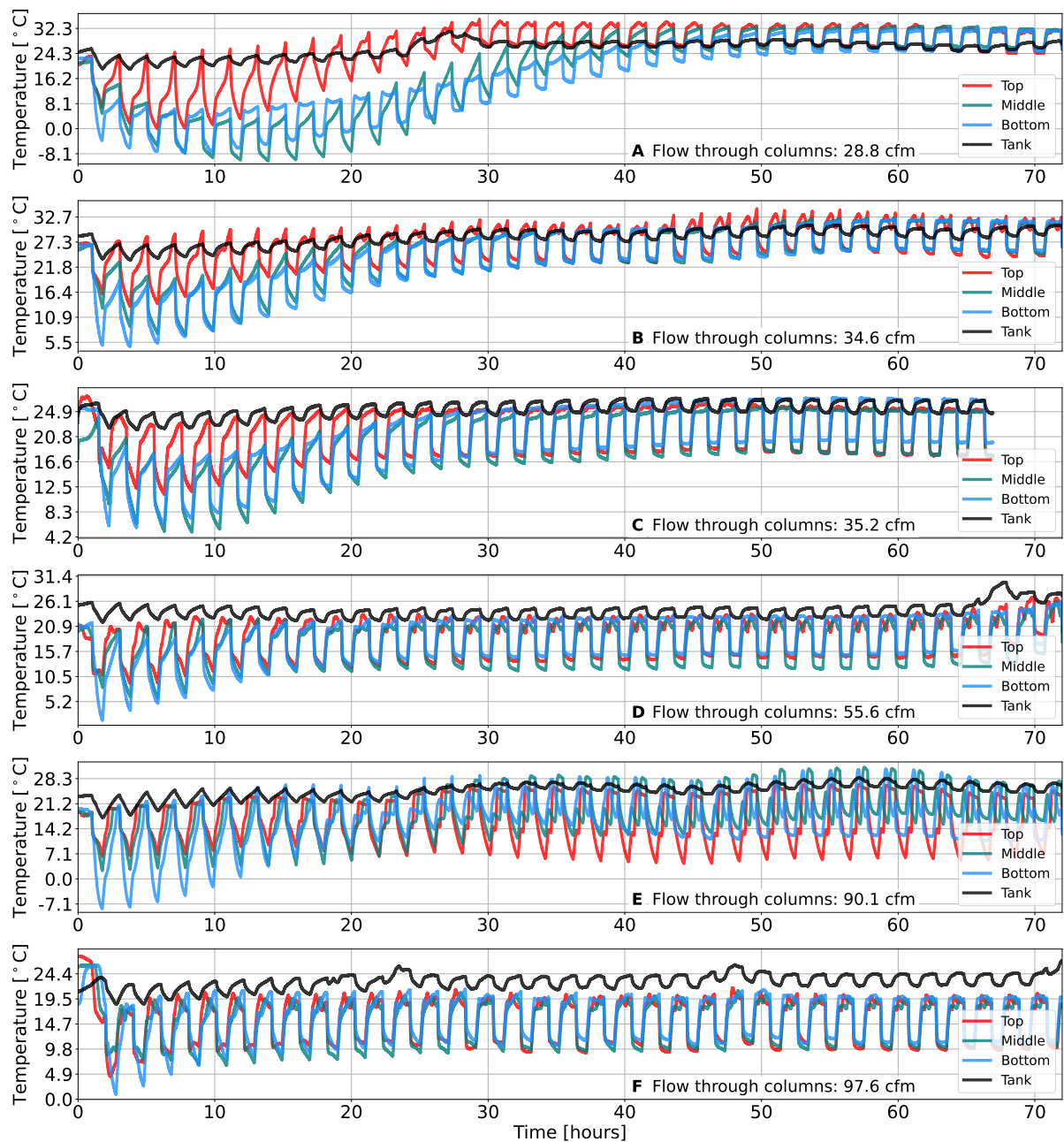


Figure C.2: Temperature measured within a single column during swing mode. Bold letter labels on each plot (A through F) are referenced in the text body.

Vita

Joseph Street was born in Englewood, CO in April of 1987. He was educated at home by his diligent mother and graduated high school in 2005. Joseph later attended Purdue University and graduated in 2013 with a major in physics and minor in mathematics. Joseph then attended the South Dakota School of Mines and Technology where he received a master's degree in materials engineering and science in 2016 and a master's degree in physics in 2017.